ASME
SETTING THE STANDARD

Journal of Fluids Engineering

Published Monthly by ASME

VOLUME 129 • NUMBER 7 • JULY 2007

Transactions of the ASME, Journal of Fluids Engineering (ISSN 0098-2202) is published monthly by The American Society of Mechanical Engineers, Three Park Avenue, New York, NY 10016. Periodicals postage paid at New York, NY and additional mailing offices.
POSTMASTER: Send address changes to Transactions of the ASME, Journal of Fluids Engineering, c/o THE AMERICAN SOCIETY OF MECHANICAL ENGINEERS, 22 Law Drive, Box 2300, Fairfield, NJ 07007-2300.
CHANGES OF ADDRESS must be received at Society headquarters seven weeks before they are to be effective. Please send old label and new address.

TECHNICAL PAPERS

(Contents continued on inside back cover)

This journal is printed on acid-free paper, which exceeds the ANSI Z39.48-1992 specification for permanence of paper and library materials. ♾™
♻ 85% recycled content, including 10% post-consumer fibers.

Journal of Fluids Engineering Volume 129, Number 7 JULY 2007

The ASME Journal of Fluids Engineering is abstracted and indexed in the following:

Applied Science & Technology Index, Chemical Abstracts, Chemical Engineering and Biotechnology Abstracts (Electronic equivalent of Process and Chemical Engineering), Civil Engineering Abstracts, Computer & Information Systems Abstracts, Corrosion Abstracts, Current Contents, Ei EncompassLit, Electronics & Communications Abstracts, Engineered Materials Abstracts, Engineering Index, Environmental Engineering Abstracts, Environmental Science and Pollution Management, Excerpta Medica, Fluidex, Index to Scientific Reviews, INSPEC, International Building Services Abstracts, Mechanical & Transportation Engineering Abstracts, Mechanical Engineering Abstracts, METADEX (The electronic equivalent of Metals Abstracts and Alloys Index), Petroleum Abstracts, Process and Chemical Engineering, Referativnyi Zhurnal, Science Citation Index, SciSearch (The electronic equivalent of Science Citation Index), Shock and Vibration Digest, Solid State and Superconductivity Abstracts, Theoretical Chemical Engineering

Development and Implementation of an Experimental-Based Reduced-Order Model for Feedback Control of Subsonic Cavity Flows

E. Caraballo
Graduate Student

J. Little
Graduate Student

M. Debiasi
Post Doctoral Researcher

M. Samimy[1]
Professor
e-mail: samimy.1@osu.edu

Gas Dynamics and Turbulent Laboratory,
Collaborative Center for Control Science,
Department of Mechanical Engineering,
GDTL/AARL,
2300 West Case Road,
The Ohio State University,
Columbus, OH 43235-7531

This work is focused on the development of a reduced-order model based on experimental data for the design of feedback control for subsonic cavity flows. The model is derived by applying the proper orthogonal decomposition (POD) in conjunction with the Galerkin projection of the Navier-Stokes equations onto the resulting spatial eigenfunctions. The experimental data consist of sets of 1000 simultaneous particle image velocimetry (PIV) images and surface pressure measurements taken in the Gas Dynamics and Turbulent Laboratory (GDTL) subsonic cavity flow facility at the Ohio State University. Models are derived for various individual flow conditions as well as for their combinations. The POD modes of the combined cases show some of the characteristics of the sets used. Flow reconstructions with 30 modes show good agreement with experimental PIV data. For control design, four modes capture the main features of the flow. The reduced-order model consists of a system of nonlinear ordinary differential equations for the modal amplitudes where the control input appears explicitly. Linear and quadratic stochastic estimation methods are used for real-time estimation of the modal amplitudes from real-time surface pressure measurements. [DOI: 10.1115/1.2742724]

1 Introduction

The flow characteristics over and through aerodynamic devices are of great importance since they dictate the overall behavior of the systems. Hence, a great deal of research effort has been devoted to controlling or modifying the dynamic characteristics of various types of flows with the overall goal of improving the systems' performance in terms of noise radiation, drag, mixing, etc. Different approaches have been explored, ranging from simple passive control to sophisticated active control. Passive control techniques have positive effects on the flow conditions for which they are designed but create negligible or, in some cases, adverse effects when used outside their designed operating range. Active control techniques, generally used in open-loop fashion, have also shown good results under design conditions, but cannot adapt in off-design circumstances [1]. In recent years, closed-loop flow control has gained popularity within the fluid dynamics community since it has the potential to increase the efficiency of systems over a wide range of operating conditions.

The benchmark case selected in our study is the flow over a shallow cavity [2], a configuration present in many practical applications that has been examined by numerous researchers over several decades (e.g., [3–5]). This flow is characterized by a strong coupling between flow dynamics and the flow-generated acoustic field that produces a self-sustained resonance known to cause, among other problems, store damage and airframe structural fatigue failure in weapon bays. A comprehensive review of this phenomenon and of different control and actuation strategies developed for its suppression is given in Cattafesta et al. [6] and Rowley and Williams [7].

Several methods can be used to develop feedback controllers for flow control. Some successful approaches to date have used experiments for the development of models (e.g., [8–10]), but have limitations since the control laws are developed either on an ad hoc basis or for a model that may not sufficiently capture the dynamics of the fluid/actuator interaction over a wide range of operating conditions and desired outputs. In the case of cavity resonance, more flexible approaches based on system identification have also been used to develop low-order models (e.g., [6,11]). The current effort at the Gas Dynamics and Turbulence Laboratory (GDTL) of the Ohio State University is focused on further steps in the design of more general and robust control laws by introducing systematic methods for order reduction of models based on the Navier-Stokes equations and for the derivation of control laws based on these models. This paper will deal with the former—the model development.

One of the major problems with the design of a model-based closed-loop flow control system is the complexity of the governing Navier-Stokes equations, which are a set of highly nonlinear partial differential equations with a wide range of spatial and temporal scales in high Reynolds number flows of practical interest. Therefore, in order to design and successfully implement closed-loop control, it is necessary to develop a simpler model of the system that captures the important dynamic characteristics of the flow and the effects of actuation while remaining amenable to control design. A well-known technique for deriving low-dimensional models is the proper orthogonal decomposition (POD). This technique uses the spatial correlation tensor to extract eigenmodes—the most dynamically significant features in the flow (and arguably the only entities that can effectively be controlled)—but does not preserve the time evolution of these eigenmodes. For flow analysis purposes, the time evolution of eigenmodes, or modal amplitudes, can be obtained by projecting the instantaneous flow field onto the POD basis. This requires time-resolved velocity data, which can be obtained from accurate numerical simulations or experiments. There are still unresolved

[1]Corresponding author.

Contributed by the Fluids Engineering Division of ASME for publication in the JOURNAL OF FLUIDS ENGINEERING. Manuscript received August 16, 2006; final manuscript received January 22, 2007. Assoc. Editor: Phillip M. Ligrani.

issues with the former in complex high-speed flows while the latter still requires further development of megahertz rate flow diagnostics in high-speed flows [12].

For many flow control applications, these approaches are unrealistic and the POD modal amplitudes must be obtained using alternative methods. One of such methods is the Galerkin projection, which transforms the complex governing equation into a simpler set of equations. This is obtained by projecting the governing flow equations onto the spatial basis of the POD modes, thereby eliminating the need for time-resolved data. The resultant state equation that can be employed for controller design is in the form of a system of nonlinear ordinary differential equations (ODEs) for the modal amplitudes. The system of equations can be recast in a form expressing the control input explicitly as required in application of the tools of control theory for the development of feedback control. The values of modal amplitudes are then updated in real time by exploiting stochastic estimation methods that correlate the velocity field with a variable that can be measured continuously in time, such as surface pressure [13–16].

The steps outlined above have been used in this work to derive a reduced-order model of the cavity flow, which captures the dynamics of the flow as well as the effect of the control input, and to design a feedback control system that can be implemented experimentally. This work continues our previous efforts based on numerical [17] and experimental data [15,16,18] and extends them toward the design and implementation of a real-time feedback controller that directly utilizes measurements of physical flow quantities. This work is part of a larger multidisciplinary effort in the development of a basic understanding and implementation of feedback flow control techniques [2].

In Secs. 2 and 3, we will introduce the flow facility used in this study, the POD and Galerkin methods adopted for deriving the reduced-order model, and the stochastic estimation approach used for real-time estimation of the model variables directly from dynamic pressure measurements.

2 Experimental Facility

The experimental facility is described in detail in Debiasi and Samimy [19]. It is an instrumented, optically accessible wind tunnel that operates in a blow-down fashion with atmospheric exhaust. The filtered, dried air is conditioned in a stagnation chamber before entering a smoothly contoured converging nozzle to the 50.8 mm by 50.8 mm test section. The facility can run continuously in the subsonic range between Mach 0.20 and 0.70.

A shallow cavity is recessed in the test section with a depth $D=12.7$ mm and length $L=50.8$ mm for an aspect ratio $L/D=4$. For control, the flow is forced at the cavity shear layer receptivity region by a two-dimensional (2D) synthetic jet-type actuator issuing at 30 deg relative to the main flow from a 1 mm slot embedded in the cavity leading edge spanning the width of the cavity (Fig. 1). A Selenium D3300Ti compression driver provides the mechanical oscillations necessary to create the zero net mass, nonzero net momentum flow for actuation. The actuator signals are produced by either a BK Precision 3011A function generator for open-loop forcing or by a dSPACE 1103 digital signal processor control board in closed-loop studies and are amplified by a Crown D-150A amplifier in both cases.

The "snapshots" of the flow field, required for the development of the low-dimensional models, are acquired and processed using a LaVision Inc. PIV system. Details of the PIV system, procedure, and results are presented in Little et al. [20]. The main flow is seeded with submicron (Di-Ethyl-Hexyl-Sebacat) particles using a four-jet atomizer upstream of the stagnation chamber. This location allows homogenous dispersion of the particle seed throughout the test section. A dual-head Spectra Physics PIV-400 Nd:YAG laser operating at the second harmonic (532 nm) is used in conjunction with spherical and cylindrical lenses to form a thin ($\sim$1 mm), vertical sheet spanning the length of the cavity at the middle of the test section width. In order to minimize beam reflections, a small slot cut into the cavity floor allows the laser sheet to exhaust and diffuse in a sealed light trap. The time separation between the laser pulses used for PIV can be tuned according to the flow velocity, seeding density, and interrogation window size. For Mach 0.30 flow in our facility, this value is 1.8 μs. Two images, corresponding to the pulses from each laser head, were acquired by a 2000 by 2000 pixel CCD camera equipped with a 90 mm macrolens with a narrow bandpass optical filter. The images were divided into 32 by 32 pixel interrogation windows, which contained 6–10 seed particles each. For each image, subregions were cross correlated using multipass processing with 50% overlap. The resulting vector fields were post-processed to remove any remaining spurious vectors. This setup gives a velocity vector grid of 128 by 128 over the measurement domain, which translates to each velocity vector being separated by $\sim$0.4 mm. Figure 2 is a phase-averaged PIV image of the velocity field for the baseline flow at M=0.30, which clearly shows the freestream uniform velocity and the vortical structures inside the cavity, typical of this resonant flow.

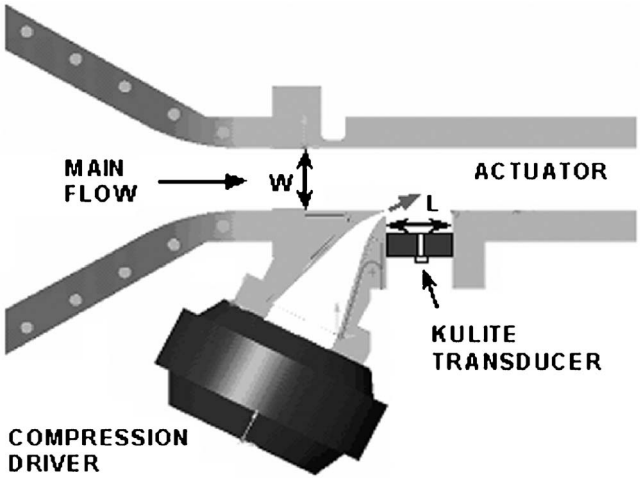

Fig. 1 Schematic of the experimental setup showing the incoming flow, the actuation location, and other geometrical details

Flush-mounted Kulite® transducers were placed on various locations on the walls of the test section for dynamic pressure measurements (Fig. 3). The sensors have a nearly flat frequency response up to $\sim$50 kHz and are powered by a signal conditioner that amplifies and low-pass filters the signals at 10 kHz. For state estimation, dynamic pressure measurements were recorded simultaneously with the PIV measurements using a National Instruments (NI) PCI-6143 S-Series data acquisition board mounted on a Dell Precision Workstation 650. The system allows simultaneous sampling of eight channels with a maximum sampling frequency of 250 kHz per channel. Each pressure recording was bandpass filtered between 100 Hz and 10 kHz to remove unwanted frequency components. In the current study, 1000 PIV snapshots were recorded for each flow/actuation condition explored. For each PIV snapshot, 128 samples from the laser Q-switch signal and from each of the transducers of Fig. 3 were acquired at 50 kHz. The laser Q-switch signal indicates the time at which the PIV data were acquired. The NI board was triggered by a programmable timing unit housed in the PIV system that activated the beginning of the acquisition to allow the Q-switch TTL to fall approximately in the middle of the 128 pressure data points. The simultaneous sampling of the laser Q-switch signal with the pressure signals allows synchronization of the pressure time traces and the instantaneous velocity field. Additional, longer pressure

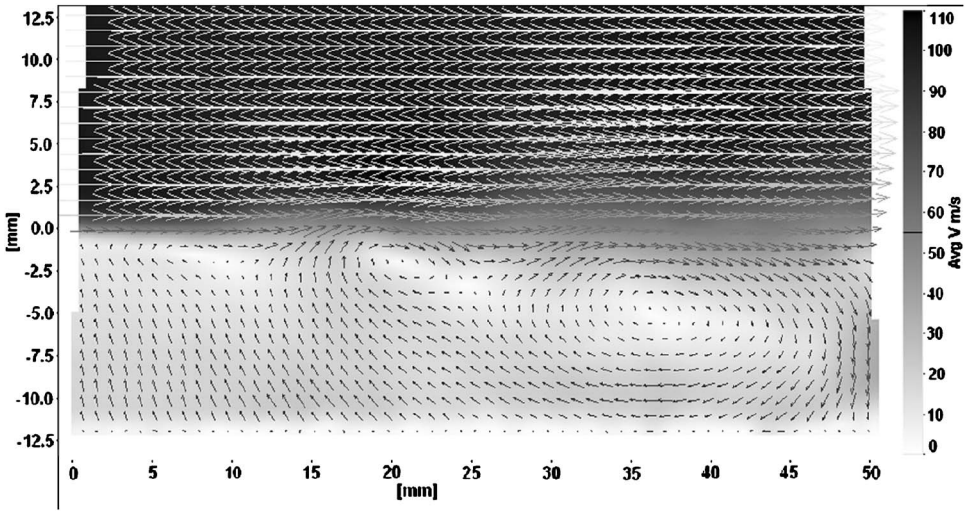

Fig. 2 Phase-averaged PIV images of the Mach 0.30 flow over the cavity; vector field superimposed on an absolute velocity contour

recordings of 262,144 samples per channel acquired at 200 kHz were also used to derive SPL spectra as described in Debiasi et al. [21].

Data for several flow conditions were saved for the cavity at Mach 0.30. To simplify the identification of each flow condition, the notation of Table 1 is used. An "M" added in front of the notation indicates the results obtained for the solution of the reduced-order model; e.g., MB refers to the model based on the baseline flow case. Details of the selection process of the flow conditions shown in Table 1 are discussed by Debiasi and Samimy [19] and Samimy et al. [22]. In general, these flow conditions were selected because they generated noticeable changes in the baseline flow, by reducing the dominant frequency or introducing multiple peaks at lower amplitude.

3 Reduced-Order Modeling

The primary goal of this research program is the development of tools and procedures for feedback control based on reduced-order models. In this section, we will discuss the tools used in the development of the reduced-order model and the issues encountered and addressed in the process. The focus will be on derivation of reduced-order models of the cavity flow from simultaneous PIV and surface pressure measurements. This approach comprises the following steps discussed in this section. First, spatial eigenmodes or POD modes of the flow are derived from the PIV measurements. Second, the Navier-Stokes equations tailored for the flow are projected onto the POD modes by using the Galerkin projection method to obtain the reduced-order model of the flow. This produces a set of ordinary nonlinear differential equations for the modal amplitudes governing the time evolution of the POD modes. In the third and final step, the reduced-order model is updated in real time by using stochastic estimation that correlates the modal amplitudes to surface pressure measurements.

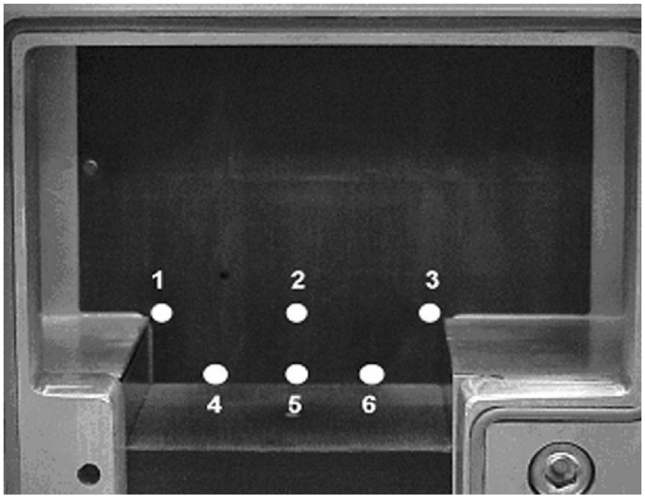

Fig. 3 Location and numbering of Kulite pressure transducers in the cavity geometry

3.1 POD Method. The POD method was introduced by Lumley [23] as an objective tool for extracting energy-containing large-scale structures in turbulent flows. A detailed explanation of the method can be found in Holmes et al. [24] and Delville et al. [25]. The original or classical POD method favored large sets of time-resolved data at a few spatial locations (e.g., hot wire anemometry [26]). Two decades later, Sirovich [27] extended the POD approach and developed the snapshot method, which favors spatially resolved but time-uncorrelated snapshots of the flow field like those obtained using laser-based planar flow diagnostics, e.g., particle image velocimetry (PIV) and planar Doppler velocimetry (PDV).

In this study, we adopted the snapshot method based on PIV data. The fundamental steps of the method require the definition of a suitable inner product operator [28]. For the case of compressible flow, Rowley [29] and Freund and Colonius [30] highlighted the advantages of using vectors that group the independent flow variables and then define the appropriate inner product op-

Table 1 Nomenclature for various flow cases

Case	Forcing frequency (Hz)	Comments
B	—	Baseline flow
F1	1610	Open-loop forcing
F2	1830	Open-loop forcing
F3	3250	Open-loop forcing
F4	3920	Open-loop forcing
BF#	—	Combination of snapshots of B and F#
BF#F#	—	Combination of snapshots of B and the two F#

Note: #=1,2,3, or 4 represents the open loop set used.

erator. Experimental measurements indicated that the spanwise component of the velocity (w) was negligibly small in comparison to the other two components, and accordingly, we define such a vector as $\boldsymbol{q}(\boldsymbol{x},t)=[u(\boldsymbol{x},t),v(\boldsymbol{x},t),c(\boldsymbol{x},t)]$, where u, v, and c are the local values of the velocity components and of the speed of sound. The inner product operator is defined in such a way that the final quantity makes physical sense (i.e., all the variables involved have the same dimensions). Following Rowley et al. [28], the inner product, for any two vectors ($\boldsymbol{q}_1$ and $\boldsymbol{q}_2$) in the flow field, is defined as

$$\langle \boldsymbol{q}_1,\boldsymbol{q}_2\rangle_\alpha|_S = \int_S \left(u_1u_2 + v_1v_2 + \frac{2\alpha}{\gamma-1}c_1c_2\right)d\boldsymbol{x} \tag{1}$$

where $\alpha=1$ and γ is the ratio of specific heats, and the integration is performed over the flow domain S.

For the range of flow Mach numbers used in this work the cavity flow is assumed to be isentropic, as the temperature is low and density variations are small. The stagnation temperature is taken as the mean of the values registered at the beginning and end of every experiment. Then, the local speed of sound is obtained from the stagnation enthalpy of the flow and the local velocity.

The POD snapshot approach uses M snapshots of the flow and casts the fluctuations of the flow realizations, $\boldsymbol{q}'(\boldsymbol{x},t)=[u'\ v'\ c']$, in terms of $N<M$ spatial orthonormal modes or POD modes, $\boldsymbol{\varphi}_i(\boldsymbol{x})$, each modulated in time by a modal amplitude $a_i(t)$

$$\boldsymbol{q}'(\boldsymbol{x},t) \cong \sum_{i=1}^{N} a_i(t)\boldsymbol{\varphi}_i(\boldsymbol{x}) \tag{2}$$

The POD modes, or spatial eigenfunctions, are a reduced basis of modes that captures the coherent structures, the dominant features present in the flow. Each mode is a linear combination of the instantaneous flow fields as

$$\boldsymbol{\varphi}_i(\boldsymbol{x}) = \sum_{k=1}^{M} A_{ik}(t)\boldsymbol{q}'(\boldsymbol{x},t_k) \tag{3}$$

The matrix A is obtained by solving the eigenvalue problem

$$C(t,t_k)A = \lambda A \tag{4}$$

where $C(t,t_k)$ is the two-point correlation tensor of independent snapshots, i.e., PIV images, integrated over the spatial domain of interest, defined as

$$C(t,t_k) = \frac{1}{M}\langle \boldsymbol{q}(\boldsymbol{x},t),\boldsymbol{q}(\boldsymbol{x},t_k)\rangle|_S \tag{5}$$

The procedure above reduces the eigenvalue problem from one that depends on the number of grid points to one that depends only on the number M of snapshots or ensembles used. Then the ith modal amplitude of a known flow field, $\boldsymbol{q}'(\boldsymbol{x},t)$, can be obtained from

$$a_i(t) = \int_s \boldsymbol{q}'(\boldsymbol{x},t)\boldsymbol{\varphi}_i(\boldsymbol{x})d\boldsymbol{x} \tag{6}$$

The number M of snapshots required to obtain a representative spatial basis for the flow is defined based on the following considerations. The number should be high enough to show convergence of the mean kinetic energy captured by the POD modes. For the baseline flow, Fig. 4 shows the percent of energy recovered by the POD modes as the number of snapshots increases in intervals of 100. About 400 snapshots are sufficient to produce convergence in the first 40 modes. Similar results were observed for the other cases in Table 1.

The number of snapshots should also provide convergence of the turbulent kinetic energy of the flow at different locations on the domain S. For the baseline flow, Fig. 5 shows that the mean turbulent kinetic energy at several locations in the shear layer converges when more than about 700 images are used. Therefore, to obtain the spatial basis for the reduced-order model of this flow, at least 700 images are required to assure that the set contains sufficient statistical events to represent the flow behavior.

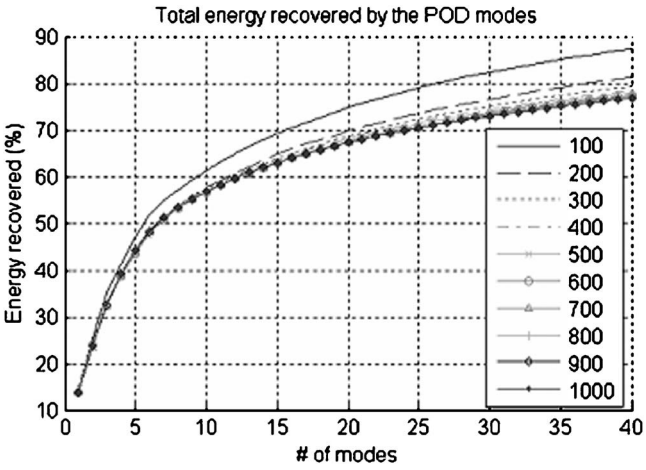

Fig. 4 Total energy recovered by the POD modes for increasing number of snapshots

Finally, we checked the number of snapshots M for which the shape of each mode becomes stable. Figure 6 shows the first mode of the fluctuating normal velocity v' of the baseline flow obtained using 500 and 1000 snapshots. It can be noted that increasing the number of snapshots from 500 to 1000 does not change the structures present in the modes or their organization. The larger number produces a smoother (cleaner) representation of the structures captured by the modes since the small-scale effects are captured by the higher modes added to the system. However, there is little change in the energy content of the modes, especially at low order. No appreciable shape changes were observed by using more than about 800 snapshots. Similar results were observed for the forced cases F1–F4 in Table 1. Based on these analyses, 1000 PIV snapshots of the flow field were acquired as described in the experimental section and used in the derivation of the modes and their modal amplitude.

The number of modes N used to reconstruct the flow field using the POD expansion depends on the nature of the problem and the final purpose of the model obtained. A nominal criterion for the POD method to accurately represent the flow is that it must retain the modes necessary to capture 99% of the mean turbulent kinetic energy [27]. For our cavity flow, this requires about 500 POD

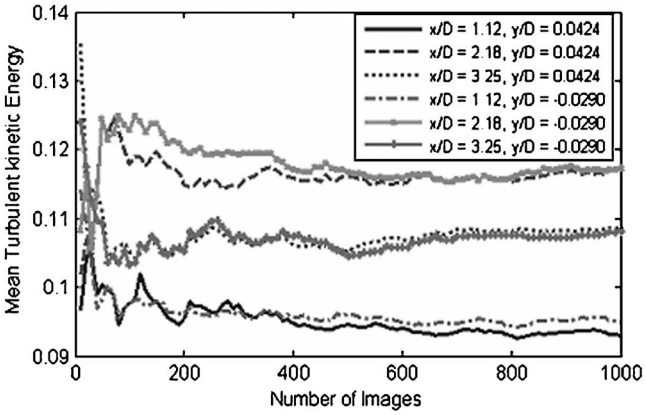

Fig. 5 Mean turbulent kinetic energy of the cavity flow at different locations in the shear layer

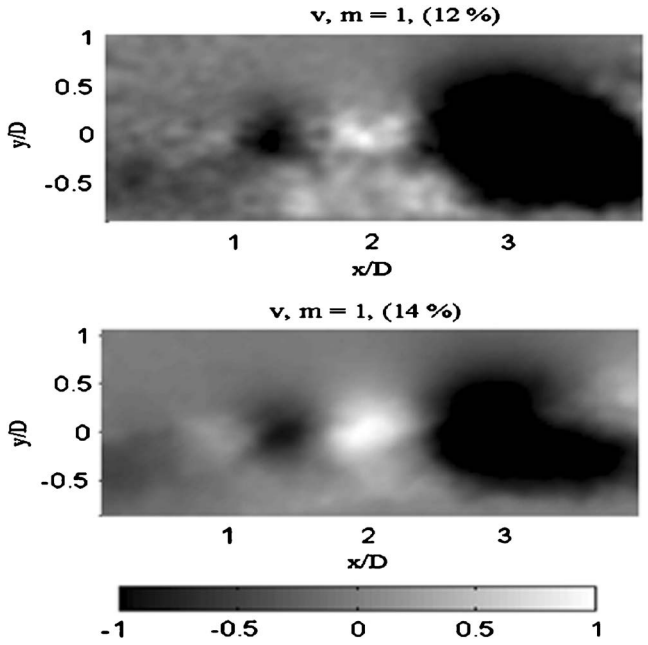

Fig. 6 First POD mode of the normal fluctuating velocity (v') for the cavity flow: Top 500 snapshots, bottom 1000 snapshots

modes. However, with ~130 POD modes for the cavity flow, 90% of the energy is recovered, which is acceptable for a subsequent analytical study of the flow dynamics but is too high for real-time description and control of the flow. In the process of designing the controller, it is desirable to minimize the number of modes (states to control) since the complexity of the controller increases significantly with additional modes. In order to evaluate the trade-off between accuracy and simplicity, we analyzed the impact of decreasing the number of modes in the overall reconstruction of the different flows. Figure 7 compares a PIV snapshot of the baseline case to its reconstructions obtained using 130, 30, and 4 POD modes. The lower number of modes yields a reconstruction that, while less accurate with filtered-out smaller scales, still captures the main features of the flow. Similar observations were obtained for other snapshots of this flow and of the F1–F4 cases. Accordingly, we decided to limit to $N=4$ the number of modes used in deriving the models for subsequent control design.

As Rempfer [31] noted, one of the limitations of the POD method is that it cannot reproduce the actual behavior of the flow if its conditions are different from those for which the model has been obtained. Noack et al. [32] has illustrated this by using numerical simulations of the wake behind a cylinder. To offset this limitation, researchers have developed two approaches. One is to create models based on several flow conditions in order to provide a richer description of the flow dynamics. Taylor and Glauser [33] and Glauser et al. [13] obtained a "global" POD spatial basis from combinations of several flow conditions. Another approach is to add shift modes and control modes [32,34] to take into account the changes in the flow condition. We elected to adopt the first technique by creating a model for individual flow conditions as well as for the combination of some of the cases, which are later used for feedback control design. In the following, we compare and discuss the POD bases obtained for the different cases of Table 1.

Figure 8 shows the first four POD modes of the five individual flow conditions listed in Table 1. It can be observed that the baseline POD modes (*a*) exhibit three structures, each represented by a pair of a positive (white) and negative (black) features. This is consistent with the baseline flow resonating at the third Rossiter mode. The two forced flows F1 (*b*) and F2 (*c*) show two sets of structures, each structure consists of a pair of positive and negative features, consistent with forcing the flow near and at the second Rossiter mode, respectively. The structures present in these two forced cases are larger than those of the baseline case, as expected. The F3 flow (*d*) is forced at a frequency slightly higher than the natural resonance and shows a behavior similar to that of the baseline. The F4 flow is forced at a frequency just below the fourth Rossiter mode and excites a subharmonic close to the second Rossiter mode. This reduces the acoustic noise by creating a multimode resonance between the natural and the subharmonic frequency [10]. Correspondingly, we observe two structures in the first two modes and three on the third while the fourth mode is not well defined, which may be linked to the multimode behavior of the flow.

The size and organization of the structures captured by the POD modes seem to correlate to the modal distribution of energy. It can be seen from Fig. 9(*a*) that more energy is recovered by modes

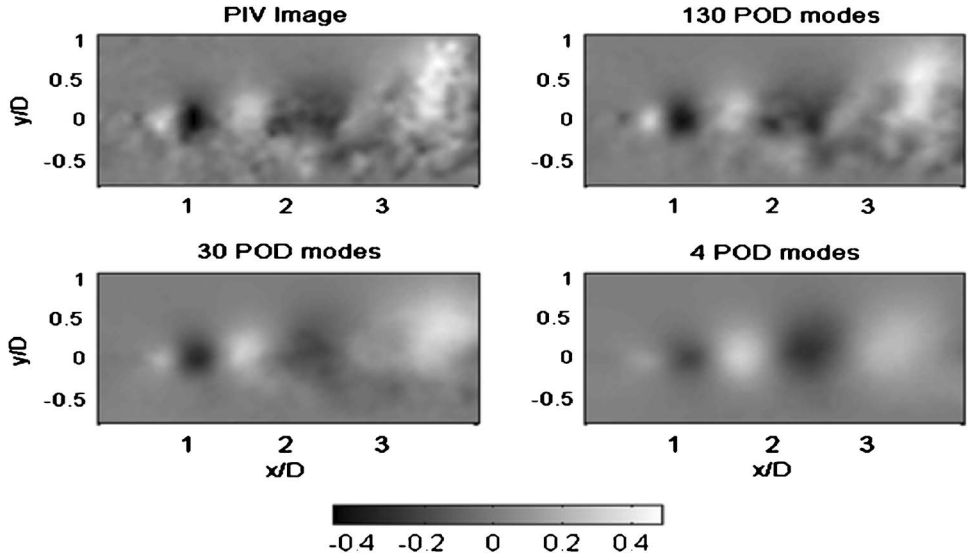

Fig. 7 Comparison of the normal velocity fluctuation from the PIV measurements with reconstruction using 130, 30, and 4 POD modes

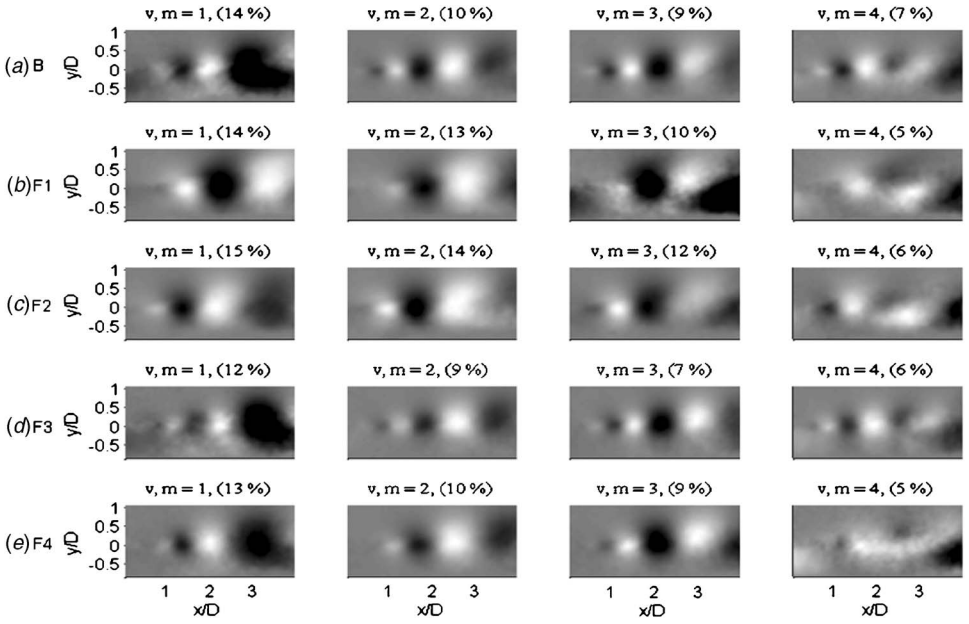

Fig. 8 First four POD modes of the normal velocity fluctuations (v') for different flow conditions

1–3 in the F1 and F2 cases, i.e., in flows with larger, more organized shear-layer structures. In terms of cumulative modal energy balance, Fig. 9(*b*), the larger energy recovery of these modes is not compensated by the lower recovery of the successive modes 4–6. This is particularly visible for F2. Conversely, cases F3 and F4, characterized by smaller and less organized structures, exhibit a lower energy recovery in the early modes. The energy recovery of all the successive modes appears to be similar for all the cases explored in this work.

We combined the B and F1–F4 flow cases to obtain the "composite" cases BF1, BF2, BF1F2, and BF3, BF4, BF3F4. Figure 10 shows the first four modes for all these combinations. It can be seen that in each combination the modes capture some of the characteristics of the individual cases. The first and fourth modes resemble the baseline flow, and the second and third modes seem to capture the forced flow behavior. Overall, the combined cases show structures of similar shape and size.

Once the POD bases were obtained for the different flow cases, the next step requires the estimation of the modal amplitude for each case. For our approach, this necessitates the derivation of a reduced set of ordinary differential equations through the application of the Galerkin projection method.

3.2 Galerkin Projection and Low-Dimensional Model. The POD expansion enables the description of the flow field based on a limited number of modes once the evolution of the corresponding mode amplitudes is known. A system of equations that describes such evolution represents the reduced-order model of the flow. We use the Galerkin projection method to obtain the reduced-order model of the cavity flow dynamics, which consists of a system of ordinary differential equations for the modal amplitude $\boldsymbol{a}(t)=[a_1(t),a_2(t),\ldots,a_N(t)]$. The method relies on the projection of the governing equations of the flow, the compressible Navier-Stokes equations, onto the orthogonal basis of POD modes. This transforms the complex system of nonlinear partial differential equations into a system of nonlinear ordinary differential equations that is more amenable for control analysis and design. In our study, we adopted the two-dimensional form of the Navier-Stokes equations based on the work of Rowley [30]

$$\frac{Dc}{Dt} + \frac{\gamma - 1}{2} c \nabla \cdot \boldsymbol{u} = 0$$

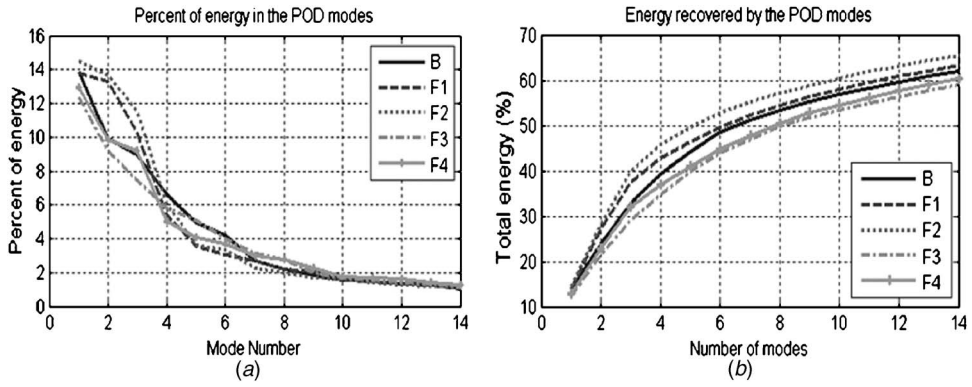

Fig. 9 Energy recovered by the POD modes: (*a*) total energy and (*b*) individual mode energy

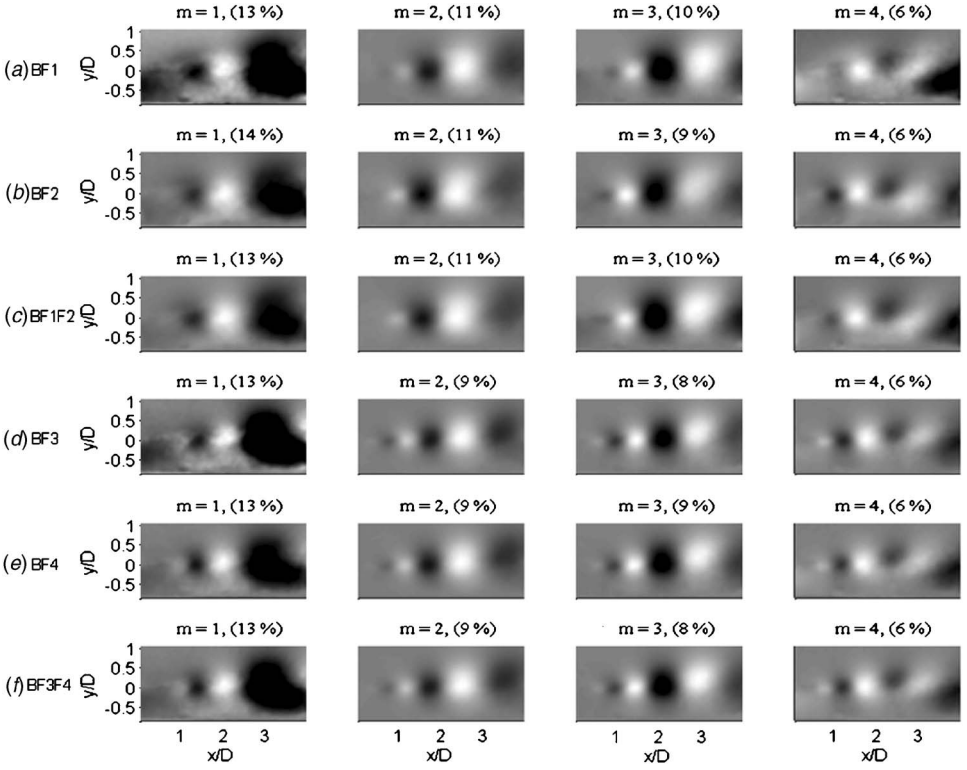

Fig. 10 First four POD modes of the normal velocity fluctuations (v') for different combinations of the experimental flow conditions

$$\frac{D\boldsymbol{u}}{Dt} + \frac{2}{\gamma - 1} c \nabla c = \frac{\mu}{\rho} \nabla^2 \boldsymbol{u} \tag{7}$$

where $\boldsymbol{u} = (u, v)$ is the velocity vector and c is the local speed of sound.

In general, the Galerkin projection procedure involves the following steps. The flow variables are first expressed in terms of their mean component and of the POD expansion of their fluctuating components (Eq. (2)). These expressions are introduced in the governing equations (Eqs. (7)), which are projected onto the basis of POD modes by taking the inner product of each term with the POD modes, according to the operator defined in Eq. (1). This procedure yields a system of nonlinear ordinary differential equations for the modal amplitude where the number N of modes used in the POD expansion defines the number of equations.

These equations are of little use for control design, as the control input is not separated from the rest of the flow, i.e., the control effect is implicit in the model. Therefore, some modification of the above process is required in order to obtain a different reduced-order model where the control effect appears explicitly. To this aim, we separate the effect of boundary excitation from the remaining terms of the POD-based model so that it appears in the set of ODEs as a separate external input. The procedure, presented in more detail in Efe and Özbay [35,36] and Samimy et al. [37], is briefly discussed here.

The general idea is to separate the control input of the system by dividing the entire flow domain into two subdomains, as shown in Fig. 11. One smaller region, S_2, comprises the physical region where the synthetic jet excitation is dominant, whereas a second larger region, S_1, contains the rest of the flow field. The total flow domain can then be expressed as $S := S_1 \cup S_2$. This partitioning captures the effect of the forcing input boundary condition and its influence over the spatial domain individually.

Based on the above considerations, the steps of our Galerkin projection procedure are as follows: The flow variable vector in the total flow domain is expressed as

$$\boldsymbol{q}(\boldsymbol{x}, t) = \boldsymbol{q}_m(\boldsymbol{x}) + \sum_{i=1}^{N} a_i(t) \boldsymbol{\varphi}_i(\boldsymbol{x}) \tag{8}$$

where $\boldsymbol{q}_m$, a_i, and $\boldsymbol{\varphi}_i$ denote the mean flow, the ith modal amplitude (a scalar operating simultaneously on the three values of $\boldsymbol{q}$), and the ith spatial basis, respectively. Replacing Eq. (8) in the governing equations (Eqs. (7)) leads to an expression of the form

$$\sum_{i=1}^{N} \dot{a}_i(t) \boldsymbol{\varphi}_i(\boldsymbol{x}) = \boldsymbol{f}\left\{ \boldsymbol{q}(\boldsymbol{x}, t), \frac{\partial}{\partial x} \boldsymbol{q}(\boldsymbol{x}, t), \ldots \right\} \equiv \boldsymbol{f}(\boldsymbol{x}, t) \tag{9}$$

where the left-hand side stems from the time derivatives in Eq. (7) and the right-hand side groups all the other terms of Eq. (7). In the Galerkin projection, the inner products of both sides of Eq. (9) are taken with the POD modes. Because of the orthonormality of the modes, the only terms surviving on the left-hand side correspond to the modes projecting onto themselves

$$\dot{a}_i(t) = \langle \boldsymbol{\varphi}_i(\boldsymbol{x}), \boldsymbol{f}(\boldsymbol{x}, t) \rangle|_S, \quad i = 1, 2, \ldots, N \tag{10}$$

It is important to notice that $\langle \boldsymbol{\varphi}_i(\boldsymbol{x}), \boldsymbol{f}(\boldsymbol{x}, t) \rangle|_S = \langle \boldsymbol{\varphi}_i(\boldsymbol{x}), \boldsymbol{f}(\boldsymbol{x}, t) \rangle|_{S_1} + \langle \boldsymbol{\varphi}_i(\boldsymbol{x}), \boldsymbol{f}(\boldsymbol{x}, t) \rangle|_{S_2}$ holds true by the definition of the inner product.

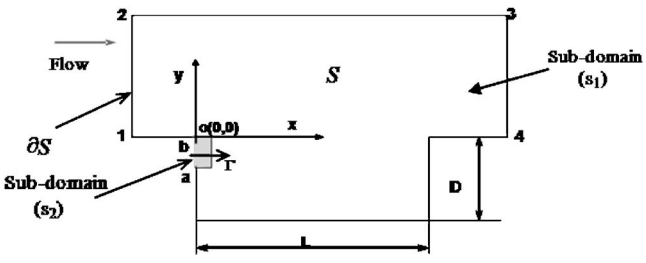

Fig. 11 Schematic of the cavity showing two subdomains s_1 and s_2

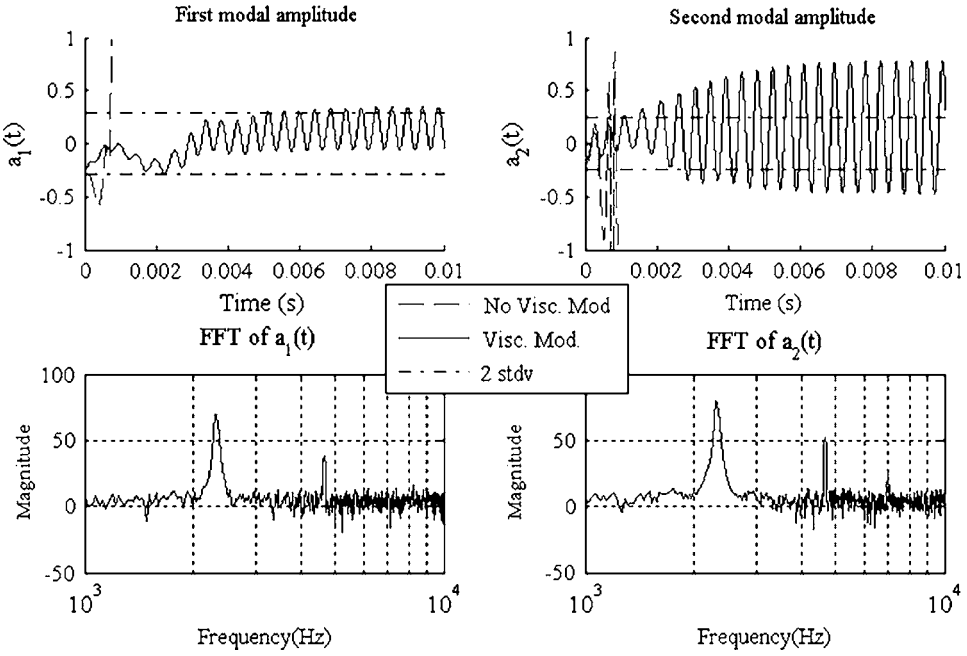

Fig. 12 Effect of the additional viscous term in the solution of the Galerkin system, baseline flow model four modes

That is, the partitioning of the flow domain corresponds to calculating an integral over two domains, the union of which gives the original domain of the problem while the intersection is an empty set. Therefore, Eq. (10) can be more explicitly written

$$\dot{a}_i(t) = \langle \boldsymbol{\varphi}_i(\boldsymbol{x}), \boldsymbol{f}(\boldsymbol{x},t)\rangle|_{S_1} + \langle \boldsymbol{\varphi}_i(\boldsymbol{x}), \boldsymbol{f}(\boldsymbol{x},t)\rangle|_{S_2}, \quad i = 1,2,\ldots,N \tag{11}$$

Since the boundary excitation $\Gamma(t)$ accounts for the flow characteristics in the S_2 subdomain, we can write

$$\boldsymbol{q}_m(\boldsymbol{x})|_{s_2} + \sum_{i=1}^{N} a_i(t)\boldsymbol{\varphi}_i(\boldsymbol{x})|_{s_s} = \Gamma(t) \tag{12}$$

and in (11), the terms corresponding to the left-hand side of (12) can be replaced with the excitation $\Gamma(t)$. With this modification and depending on the form of the vector function $\boldsymbol{f}$, the procedure described will yield a nonautonomous set of ODEs capturing the dynamics in the following form:

$$\dot{a}_i(t) = F^i + \sum_{j=1}^{N} G^{ij}a_j(t) + \sum_{j=1}^{N}\sum_{k=1}^{N} H^{ijk}a_j(t)a_k(t) + B^i\Gamma(t) + \sum_{j=1}^{N} \bar{B}^{ij}\Gamma(t)a_j(t) \tag{13}$$

A more detailed treatment of the control separation technique and of the straightforward but tedious calculation of the terms in the matrices A and B is presented in Efe and Özbay [35,36] for a simpler system.

The solution of the system (13) obtained for the individual flow cases of Table 1 often diverged. This was observed for each case using various initial conditions. We attribute this behavior to numerical errors in calculating the derivative terms in the system of equations and to the use of a finite number N of modes to describe the flow which not only loses some flow details but also fails to capture the energy transfer process between the N retained modes and the neglected ones. To overcome the second problem, Couplet et al. [38] and Noack et al. [39] proposed the introduction of an additional viscous term, the modal eddy viscosity $\tilde{\nu}_i$. This additional viscosity term is added to the model to maintain the overall flow energy balance, but it also compensates for other small errors introduced in the derivation of the model. Adding the modal eddy viscosity modifies Eq. (13) into

$$\dot{a}_i(t) = \bar{F}^i + \sum_{j=1}^{N} [(\nu + \tilde{\nu}_i)L^{ij} + \bar{G}^{ij}]a_j(t) + \sum_{j=1}^{N}\sum_{k=1}^{N} H^{ijk}a_j(t)a_k(t) + B^i\Gamma(t) + \sum_{j=1}^{N} \bar{B}^{ij}\Gamma(t)a_j(t) \tag{14}$$

where νL^{ij} accounts for the viscous contribution (from the Navier-Stokes equations) of F^i and G^j in Eq. (13) and $\bar{F}^i$ and $\bar{G}^{ij}$ are the inviscid parts of the same matrices. The value of the modal eddy viscosity $\tilde{\nu}_i$ is obtained from an energy balance of Eq. (14) [38], and has the form

$$\tilde{\nu}_i = \nu - \frac{\bar{G}^{ii}\lambda_i + H^{ijk}\langle a^i a^j a^k\rangle}{l^{ii}\lambda_i} \tag{15}$$

where λ_i is the eigenvalue of each POD mode and the operator angular brackets (not to be confused with the inner product previously defined) represent the time average of its arguments. This new term changes for each mode and adjusts for the numerical errors and energy transfer left unaccounted for by the neglected modes.

Figure 12 compares the solution of Eqs. (13) and (14) for the first and second modal amplitudes of the baseline model using $N=4$ modes. It can be noted that the system without the additional viscous term degenerates very quickly, while the system with the modal eddy viscosity evolves in a bounded fashion between the two standard deviations of the modal amplitudes obtained from the PIV snapshots. For $N=4$ modes, the dampening effect of the modal eddy viscosity seems to somewhat reduce the resonance frequency of the Galerkin system (Eq. (14)) (from the experimental 2800 Hz to 2300 Hz). We observed that using a larger number of modes mitigates this discrepancy, but as previously remarked, this option would yield a system intractable from a control design

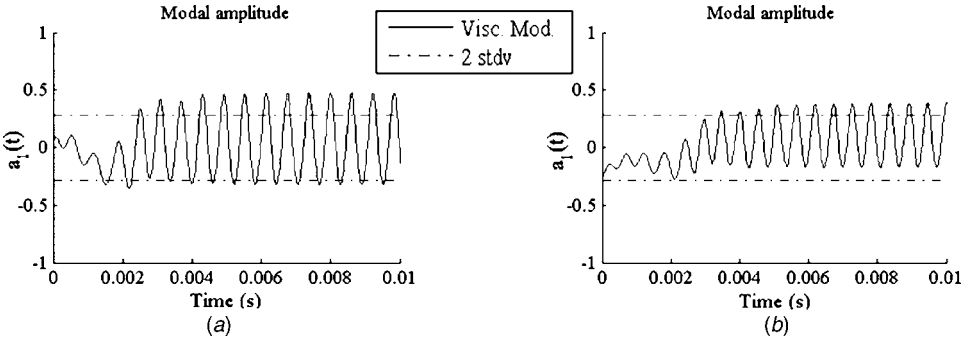

Fig. 13 Solution of the Galerkin system for two different models: (*a*) MF4 and (*b*) MBF4

perspective.

Analogous benefits and tradeoffs were observed for the other two modes and for the modes of other flow cases. For instance, Fig. 13 shows the evolution of the first modal amplitude of the model based on the F4 case and of the model based on a combination of the B and F4 cases. As before, the values evolve within two standard deviations of the corresponding mode values from the PIV snapshots. It was also observed, as noted above, that the frequency of oscillation of the solution obtained with the modified model is slightly lower than the experimental value, which we relate to the introduction of additional viscous dissipation. We should also note that the system trajectories of Figs. 12 and 13 converged to the same values, irrespective of the initial condition used for the solution of Eq. (14), indicating the occurrence of a stable limit cycle.

Equation (14) can be compactly expressed in vector notation useful for control analysis

$$\dot{\boldsymbol{a}} = A(\boldsymbol{a}) + B(\boldsymbol{a})\Gamma \tag{16}$$

where A is a matrix that groups $\bar{F}^i$ and all the terms that depend only on $a(t)$ and B is a matrix that groups all the terms which depend on $\Gamma(t)$. Equation (16) represents the reduced-order model sought for the design of a feedback controller.

3.3 Stochastic Estimation. In the experimental implementation of the controller based on the reduced-order model described by Eq. (16), the model variables (i.e., the values of the modal amplitudes) must be updated in real time. Since the update rate required for real-time feedback control has to be about an order of magnitude higher than the frequencies associated with the dynamics of large-scale structures in the flow, an update based on PIV diagnostics is impossible. Therefore, a means must be found to update the modal amplitudes based on a flow variable that can be reliably measured in real time. Such a variable in our experimental setup is represented by the pressure fluctuations in different locations of the test section. Also, in any practical implementation of such a technique, real-time flow variable measurements on the surface would perhaps be the only option for real-time updating. The update is done by using stochastic estimation (SE) to correlate the modal amplitudes to the dynamic surface pressure measurements.

Stochastic estimation, first proposed by Adrian [40] as a method to extract coherent structures from a turbulent flow field, estimates flow variables at any location by using statistical information about the flow at a limited number ($\mathcal{L}$) of locations. Although linear stochastic estimation has often been used in the literature, Naguib et al. [41] used both linear and quadratic terms for a more accurate estimate of the flow field from wall pressure measurements. For the cavity flow, the improvement in the accuracy of the technique by using this combination was confirmed by Ukeiley and Murray [14] and by Caraballo et al. [42]. Similar observations were presented by Ausseur et al. [43] for the case of flow separation control.

Initially, we implemented the stochastic estimation by utilizing the instantaneous measurement of the surface pressure at each sensor (static approach). A recent analysis of the different effects of various model-based controllers [44] raised the suspicion that some of the observed differences could be caused by an "overfitting" of the quadratic SE to the specific data set used for the derivation of each model using Eq. (16). That is, the quadratic SE could fail to accurately estimate the modal amplitudes for pressure values other than those used for its derivation. This could be related to deficiencies in the static approach when used to capture the dynamic behavior of the system and to the reduced number of sensors available. To correct this and avoid an overfitting by the quadratic estimation, we decided to evaluate if any benefit could be gained by using the less fitting linear SE where, however, richer dynamics of the flow are recovered by using one or more previous "time samples" of the measured pressure fluctuations. For a fair and more complete comparison, we also adopted this dynamic approach to quadratic estimation as well.

To simplify the mathematical treatment of the derivation each time delay included, previous time samples are considered as an additional set of sensors. Therefore, the pressure fluctuations can be represented by

$$p'_j = p'_k(t - s\Delta t) \quad j = 1, \ldots, \mathcal{L}(s+1), \quad k = 1, \ldots, \mathcal{L},$$
$$s = 0, 1, 2, \ldots \tag{17}$$

where Δt is the time delay, which is equal to the sampling time, $\mathcal{L}$ is the number of sensors, and s is the number of delays. For the case of linear SE, the expression used to estimate $\hat{a}_i(t)$ at any time t is

$$\hat{a}_i(t) = C_l^{ij} p'_j, \quad i = 1, \ldots, N \tag{18}$$

C_l is the matrix of the estimation coefficients obtained by minimizing the average mean square error e_i between the values of $a_i(t_r)$ obtained with Eq. (5) at the times t_r of the PIV snapshots, and the ones $\hat{a}_i(t_r)$ estimated from the pressure data recorded simultaneously with the snapshots as discussed in Sec. 2, That is,

$$e_i = \langle [\hat{a}_i(t_r) - a_i(t_r)]^2 \rangle, \quad r = 1, \ldots, M \tag{19}$$

Once the estimation matrix C_l is obtained, it can be used in Eq. (18) to estimate the modal amplitude from the surface pressure measurements. Similarly, for quadratic SE, the expression used to obtain the estimated values of $\hat{a}_i(t)$ is

$$\hat{a}_i(t) = C_q^{ij} p'_j + D_q^{ijk} p'_j p'_k, \quad i = 1, \ldots, N, \quad j,k = 1, \ldots, \mathcal{L}(s+1),$$
$$s = 0, 1, 2, \ldots \tag{20}$$

where C_q and D_q are matrices of the estimation coefficients obtained as in the linear case. Additional details on the procedure to obtain the estimation matrices for the quadratic estimation are

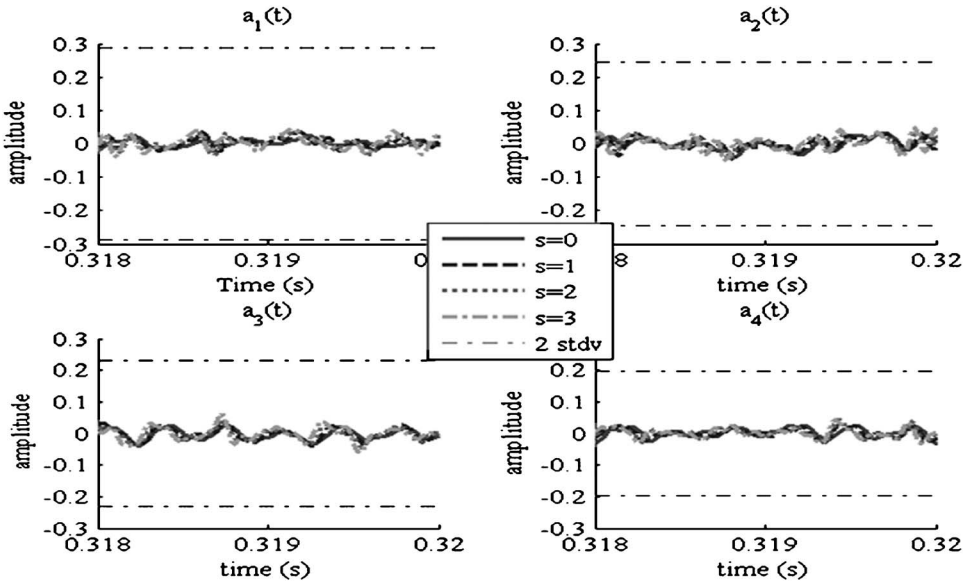

Fig. 14 Linear stochastic estimation of the modal amplitude using zero to three time steps back (*s*=0–3), from experimental data in comparison to two standard deviation (2 stdv) of the modal coefficient from PIV data

available in Ukeiley and Murray [14]. In our experimental setup, the real-time measurements of surface pressure used for estimation were taken at the locations of transducers 1–6 in the cavity test section (Fig. 3).

Figure 14 shows the linear estimation of the four modal amplitudes from the dynamic surface pressure measurements of the baseline flow. For all the modal amplitudes, we can observe that the effect of using up to previous three time samples is negligible. The modal amplitudes oscillate at the same frequency (2850 Hz) of the pressure fluctuations, i.e., the resonant frequency of the baseline flow. In all cases, the maximum values of the amplitude are significantly smaller than two standard deviations of the corresponding modal amplitudes calculated from PIV data.

Figure 15 shows the corresponding results with the use of the quadratic SE. The estimated amplitudes are somewhat noisier, but peaks at the flow resonant frequency can still be clearly distinguished. Comparison to two standard deviations of the PIV-derived modal amplitudes suggests that quadratic SE produces estimates more consistent with the results from experimental measurements. Furthermore, with quadratic SE the effect of using previous time samples is not negligible. The experimental implementation of feedback control based on the model (Eq. (16)) updated with Eq. (18) or (20) suggests that more effective control can be achieved using the quadratic SE with one or more backward time samples [44].

The methods presented and discussed in the previous sections have been used to develop and implement a real-time feedback controller for suppressing the resonance of a Mach 0.3 flow over a shallow cavity. Figure 16 shows the effect of the LQ controller on the cavity flow for the MB and MBF4 models. It can be ob-

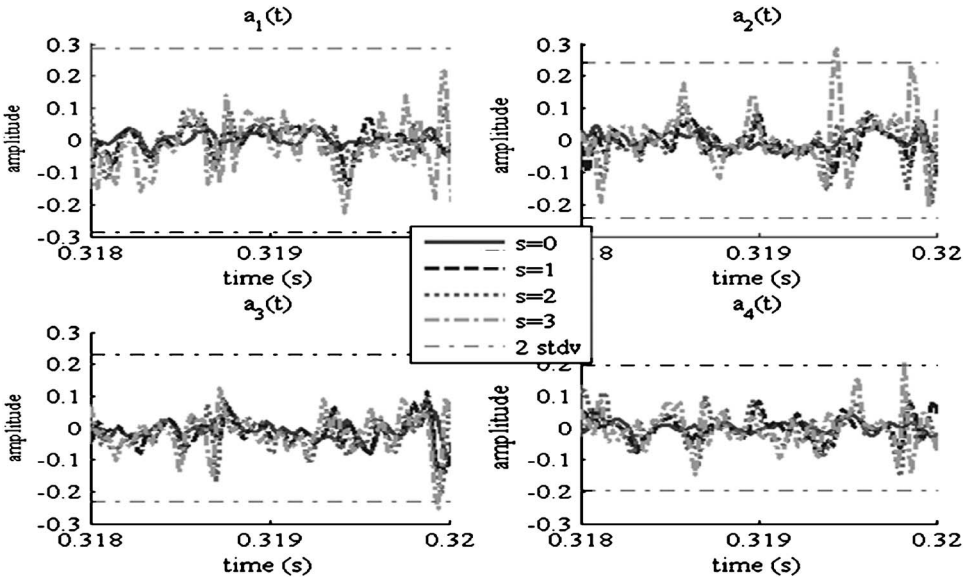

Fig. 15 Quadratic stochastic estimation of the modal amplitude using zero to three time steps back (*s*=0–3), from experimental data in comparison to two standard deviation (2 stdv) of the modal coefficient from PIV data

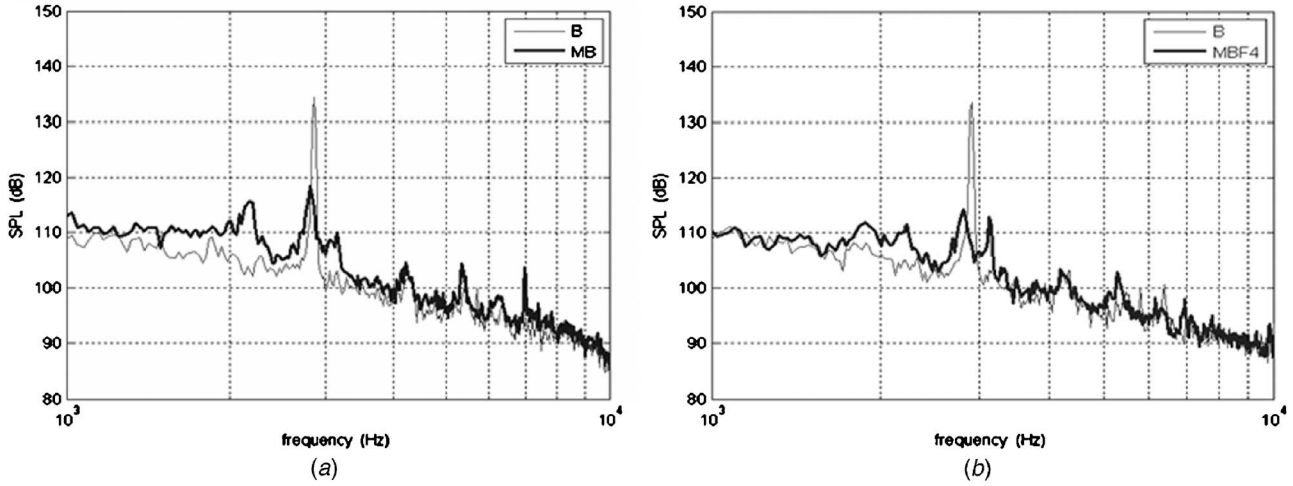

Fig. 16 SPL spectra obtained from sensor 5 (Fig. 3) in closed-loop experiments with LQ design based on baseline flow model, MB (*a*), and combined flow model, MBF4 (*b*)

served that the dominant resonant mode is significantly reduced by introduction of the controller based on the reduced-order model presented and discussed above. Details of the flow physics and the design of linear quadratic (LQ) controllers based on the model (Eq. (16)) and their experimental implementation and results are discussed in Samimy et al. [18,22], Debiasi et al. [44], Yuan et al. [17], and Caraballo et al. [16]. It suffices here to mention that the best results were obtained with LQ controllers designed around the MB and MBF4 models updated in real time with the quadratic SE. These controllers are effective in the Mach range 0.27–0.32, indicating that they possess some robustness with respect to departure from the design conditions of Mach 0.3.

4 Conclusions

This paper presents and discusses the procedure that we used to develop and update, in real time, a reduced-order model for feedback control of a subsonic cavity flow. Starting from PIV data and using the snapshot-based proper orthogonal decomposition (POD) in conjunction with Galerkin projection of the Navier-Stokes equations onto the POD eigenfunctions, we derived reduced-order models of different flows. Linear and quadratic stochastic estimation were used for real-time update of the model variables from dynamic surface pressure measurements as required for the implementation of the controller. Models for individual flows as well as combinations of flow cases were explored.

In all cases, the snapshot-based POD requires at least 700 PIV images to achieve convergence of the mean turbulent kinetic energy and to obtain well-defined modal bases. POD reconstruction with about 30 modes shows good agreement with the PIV data. Only four modes are used to capture the main characteristics of the flow for control purposes. The modal energy distribution is similar for all the cases tested. More energy is recovered by the first few modes in the case of flows with larger, more organized shear-layer structures. Composite models, obtained by combining the PIV data of different flows, have POD modes that capture some of the characteristics of the individual flows.

We separate the flow spatial domain into a subdomain where the effect of actuation is relevant and another subdomain that comprises the remainder of the flow. The Galerkin projection of the Navier-Stokes onto the POD modal basis is performed in these subdomains. This produces a reduced-order model of the flow in terms of the modal amplitudes where the control effect appears explicitly. An additional viscous term is added to the model to account for the energy balance with the neglected POD modes and to dampen small numerical errors arising in the derivation procedure.

For real-time update of the model variables, we developed linear and quadratic stochastic estimation procedures that can operate statically (i.e., based on instantaneous values of the pressure) or dynamically by accounting for one or more previous pressure samples. The dynamic quadratic estimation seems to provide a better approximation of the model variables and produces more effective control. Further improvements should be possible by refining the separation of control in the reduced-order model and by optimizing the number and location of the pressure sensors used in the stochastic estimation.

Acknowledgment

This work is supported, in part, by the AFRL/VA and AFOSR through the Collaborative Center of Control Science (Contract No. F33615-01-2-3154). The authors would like to thank Andrea Serrani, James Myatt, James DeBonis, R. C. Camphouse, and Xin Yuan for help and fruitful discussions. Fruitful exchanges with Bern Noack, Dietmar Rempfer, Mark Glauser, and Lawrence Ukeiley are greatly appreciated.

References

[1] Gad-el-Hak, M., 2000, *Flow Control—Passive, Active, and Reactive Flow Management*, Cambridge University Press, Cambridge, England.
[2] Samimy, M., Debiasi, M., Caraballo, E., Malone, J., Little, J., Özbay, H., Efe, M. Ö., Yan, P., Yuan, X., DeBonis, J., Myatt, J. H., and Camphouse, R. C., 2004, "Exploring Strategies for Closed-Loop Cavity Flow Control," AIAA Paper No. 2004-0576.
[3] Rossiter, J. E., 1964, "Wind Tunnel Experiments on the Flow Over Rectangular Cavities at Subsonic and Transonic Speeds," RAE Tech. Report No. 64037, and Aeronautical Research Council Reports and Memoranda No. 3438.
[4] Heller, H. H., and Bliss, D. B., 1975, "The Physical Mechanisms of Flow-Induced Pressure Fluctuations in Cavities and Concepts for Their Suppression," AIAA Paper No. 75-491.
[5] Rockwell, D., and Naudascher, E., 1978, "Review—Self-Sustaining Oscillations of Flow Past Cavities," ASME J. Fluids Eng., **100**, pp. 152–165.
[6] Cattafesta, L. N., III, Williams, D. R., Rowley, C. W., and Alvi, F. S., 2003, "Review of Active Control of Flow-Induced Cavity Resonance," AIAA Paper No. 2003-3567.
[7] Rowley, C., and Williams, D., 2006, "Dynamics and Control of High-Reynolds-Number Flow Over Open Cavities," Annu. Rev. Fluid Mech., **38**, pp. 251–276.
[8] Traub, L. W., Miller, A., Ukpai, U. I., Rediniotis, O., Jeong, G., and Kim, K., 2003, "Reconfigurable Synthetic Jet Actuation and Closed-Loop Flow Control," AIAA Paper No. 2003-0217.
[9] Patel, M. P., Kolacinski, R. M., Prince, T. S., Ng, T. T., and Cain, A. B., 2003, "Flow Control Using Intelligent Control Modules for Virtual Aerodynamic Shaping," AIAA Paper No. 2003-3663.
[10] Yan, P., Debiasi, M., Yuan, X., Little, J., Özbay, H., and Samimy, M., 2006, "Experimental Study of Linear Closed-Loop Control of Subsonic Cavity Flow," AIAA J., **44**(5), pp. 929–938.
[11] Rowley, C., and Williams, D., 2003, "Control of Forced and Self-Sustained

Oscillations in the Flow Past a Cavity," AIAA Paper No. 2003-0008.
[12] Thurow, B. S., Jiang, N., Lempert, W. R., and Samimy, M., 2005, "Development of Megahertz-Rate Planar Doppler Velocimetry for High-Speed Flows," AIAA J., **43**(3), pp. 500–511.
[13] Glauser, M. N., Higuchi, H., Ausseur, J., and Pinier, J., 2004, "Feedback Control of Separated Flows (Invited)," AIAA Paper No. 2004-2521.
[14] Ukeiley, L., and Murray, N., 2005, "Velocity and Surface Pressure Measurements in an Open Cavity," Exp. Fluids, **38**, pp. 656–671.
[15] Caraballo, E., Yuan, X., Little, J., Debiasi, M., Yan, P., Serrani, A., Myatt, J., and Samimy, M., 2005, "Feedback Control of Cavity Flow Using Experimental Based Reduced Order Model," AIAA Paper No. 2005-5269.
[16] Caraballo, E., Yuan, X., Little, J., Debiasi, M., Serrani, A., Myatt, J., and Samimy, M., 2006, "Further Development of Feedback Control of Cavity Flow Using Experimental Based Reduced Order Model," AIAA Paper No. 2006-1405.
[17] Yuan, X., Caraballo, E., Yan, P., Özbay, H., Serrani, A., DeBonis, J., Myatt, J. H., and Samimy, M., 2005, "Reduced-Order Model-Based Feedback Controller Design for Subsonic Cavity Flows," AIAA Paper No. 2005-0293.
[18] Samimy, M., Debiasi, M., Caraballo, E., Serrani, A., Yuan, X., Little, J., and Myatt, J. H., 2006, "Reduced-Order Model-based Feedback Control of Subsonic Cavity Flows—An Experimental Approach," Conference on Active Flow Control, Germany.
[19] Debiasi, M., and Samimy, M., 2004, "Logic-Based Active Control of Subsonic Cavity Flow Resonance," AIAA J., **42**(9), pp. 1901–1909.
[20] Little, J., Debiasi, M., and Samimy, M., 2006, "Flow Structure in Controlled and Baseline Subsonic Cavity Flows," AIAA Paper No. 2006-0480.
[21] Debiasi, M., Little, J., Malone, J., Samimy, M., Yan, P., and Özbay, H., 2004, "An Experimental Study of Subsonic Cavity Flow—Physical Understanding and Control," AIAA Paper No. 2004-2123.
[22] Samimy, M., Debiasi, M., Caraballo, E., Serrani, A., Yuan, X., Little, J., and Myatt, J. H., 2007, "Feedback Control of Subsonic Cavity Flows Using Reduced-Order Models," J. Fluid Mech. (to appear).
[23] Lumley, J., 1967, "The Structure of Inhomogeneous Turbulent Flows," *Atmospheric Turbulence and Wave Propagation*, Nauka, Moscow, pp. 166–176.
[24] Holmes, P., Lumley, J. L., and Berkooz, G., 1996, *Turbulence, Coherent Structures, Dynamical System, and Symmetry*, Cambridge University Press, Cambridge, England.
[25] Delville, J., Cordier, L., and Bonnet, J. P., 1998, "Large-Scale-Structure Identification and Control in Turbulent Shear Flows," *Flow Control: Fundamentals and Practice*, M. Gad-el-Hak, A. Pollard, and J. Bonnet, eds., Springer-Verlag, Berlin, pp. 199–273.
[26] Glauser, M., Eaton, E., Taylor, J., Cole, D., Ukeiley, L., Citrinity, J., George, W., and Stokes, S., 1999, "Low-Dimensional Descriptions of Turbulent Flows: Experiment and Modeling," AIAA Paper No. 1999-3699.
[27] Sirovich, L., 1987, "Turbulence and the Dynamics of Coherent Structures," Q. Appl. Math., **45**(3), pp. 561–590.
[28] Rowley, C. W., Colonius, T., and Murray, R., 2004, "Model Reduction for Compressible Flows Using POD and Galerkin Projections," Physica D, **189**, pp. 115–129.
[29] Rowley, C. W., 2002, "Modeling, Simulation and Control of Cavity Flow Oscillations," Ph.D. thesis, California Institute of Technology.
[30] Freund, J. B., and Colonius, T., 2002, "POD Analysis of Sound Generation by a Turbulent Jet," AIAA Paper No. 2002-0072.
[31] Rempfer, D., 2003, "Low-Dimensional Modeling and Numerical Simulations of Transition in Simple Shear Flows," Annu. Rev. Fluid Mech., **35**, pp. 229–265.
[32] Noack, B. R., Afanaisev, K., Morzyński, M., Tadmor, G., and Thiele, F., 2003, "A Hierarchy of Low-Dimensional Models for the Transient and Post-Transient Cylinder Wake," J. Fluid Mech., **497**, pp. 335–363.
[33] Taylor, J., and Glauser, M., 2004, "Towards Practical Flow Sensing and Control Via POD and LES Based Low-Dimensional Tools," ASME J. Fluids Eng., **126**(3), pp. 337–345.
[34] Siegel, S., Cohen, K., Seidel, J., and McLaughlin, T., 2005, "Tow Dimensional Simulations of a Feedback Controlled D-Cylinder Wake," AIAA Paper No. 2005-5019.
[35] Efe, M. Ö., and Özbay, H., 2003, "Proper Orthogonal Decomposition for Reduced Order Modeling: 2D Heat Flow," *IEEE Int. Conf. on Control Applications (CCA'2003)*, Istanbul, pp. 1273–1278.
[36] Efe, M. Ö., and Özbay, H., 2003, "Integral Action Based Dirichlet Boundary Control of Burgers' Equation," *Proc. IEEE Int. Conf. on Control Applications (CCA'2003)*, Istanbul, Turkey, pp. 1267–1272.
[37] Samimy, M., Debiasi, M., Caraballo, E., Özbay, H., Efe, M. O., Yuan, X., DeBonis, J., and Myatt, J. H., 2003, "Closed-Loop Active Flow Control: A Collaborative Approach," AIAA Paper No. 2003-0058.
[38] Couplet, M., Sagaut, P., and Basdevant, C., 2003, "Intermodal Energy Transfer in a Proper Orthogonal Decomposition-Galerkin Representation of a Turbulent Separated Flow," J. Fluid Mech., **491**, pp. 275–284.
[39] Noack, B., Tadmor, G., and Morzynski, M., 2004, "Low-Dimensional Models for Feedback Flow Control. Part I: Empirical Galerkin Models," AIAA Paper No. 2004-2408.
[40] Adrian, R. J., 1979, "On the Role of Conditional Averages in Turbulent Theory," *Turbulence in Liquids*, Science Press, Princeton.
[41] Naguib, A., Wark, C., and Juckenhoefel, O., 2001, "Stochastic Estimation and Flow Sources Associated With Surface Pressure Events in a Turbulent Boundary Layer," Phys. Fluids, **13**(9), pp. 2611–2616.
[42] Caraballo, E., Malone, J., Samimy, M., and DeBonis, J., 2004, "A Study of Subsonic Cavity Flows—Low Dimensional Modeling," AIAA Paper No. 2004-2124.
[43] Ausseur, J. M., Pinier, J. T., Glauser, M. N., Higuchi, H., and Carlson, H., 2006, "Experimental Development of a Reducer-Order Model for Flow Separation Control," AIAA Paper No. 2006-1251.
[44] Debiasi, M., Little, J., Caraballo, E., Yuan, X., Serrani, A., Myatt, J. H., and Samimy, M., 2006, "Influence of Stochastic Estimation on the Control of Subsonic Cavity Flow—A Preliminary Study," AIAA Paper No. 2006-3492.

Optimal Location of a Synthetic Jet on an Airfoil for Stall Control

R. Duvigneau[1]
e-mail: Regis.Duvigneau@sophia.inria.fr

A. Hay
e-mail: hay@vt.edu

M. Visonneau
e-mail: Michel.Visonneau@ec-nantes.fr

Laboratoire de Mécanique des Fluides CNRS
UMR6598,
Equipe Modélisation Numérique,
Ecole Centrale de Nantes,
rue de la Noë, 44321 Nantes, France

This study deals with the optimization of the location of a synthetic jet on the suction side of an airfoil to control stall. The optimal location is found by coupling a time-accurate flow solver with adaptive mesh refinement/coarsening techniques and an automatic optimization algorithm. The flow and jet are modeled by the unsteady Reynolds-averaged Navier-Stokes equations (URANSE) with a near-wall low-Reynolds number turbulence closure. An unstructured grid refinement/coarsening method is used to automatically generate meshes adapted to the presence of the synthetic jet at a prescribed location. An optimization algorithm modifies the location of the synthetic jet to determine the best actuator location to increase the time-averaged lift for high angles of attack. The proposed methodology is applied to optimize the location of a synthetic jet on the suction side of the NACA 0012 airfoil at a Reynolds number $\mathrm{Re}=2\times10^6$ *and incidences of* 18 deg *and* 20 deg. *Finally, a physical analysis of the influence of the synthetic jet location on the control efficiency is proposed to provide some guidelines for practical jet positioning.* [DOI: 10.1115/1.2742729]

1 Introduction

Flow control using synthetic jets has been an active topic of research for many years. Indeed, it was shown experimentally that flows can be modified by introducing jets with ad hoc properties to obtain desired characteristics [1]. Some numerical investigations of lift enhancement using synthetic jets found in the literature use time-accurate solutions of the Reynolds-averaged Navier-Stokes equations. Wu et al. [2] investigated post-stall lift enhancement for a NACA 0012 airfoil using a normal suction/blowing jet located at 2.5% of the chord and found that lift enhancement in the post-stall regime can be achieved, as was reported in experiments. Steady blowing as well as oscillatory jet actuations were simulated by Donovan et al. [3] and compared to experimental measurements. The same configuration was also studied by Ekaterinaris [4], who tested some different jet parameters.

These studies provide useful information to help engineers who need to control the flow around an airfoil to delay stall. However, some questions remain open: For a particular airfoil, at a given Reynolds number and specific angles of attack, where should a synthetic jet be located to delay stall? Which frequency should be employed? What is the minimum jet velocity requires to achieve satisfactory flow control?

To answer these questions, we tested coupling between a time-accurate flow solver and an optimization algorithm and applied it to delay stall on a NACA 0015 airfoil [5,6]. The simultaneous optimization of the jet frequency, amplitude, and orientation significantly increased the control efficiency ($+34\%\,C_L$). However, the influence of the jet location on stall delay was not taken into account in this previous study because it was not possible, at that time, to automatically generate grids adapted to variable jet locations.

To overcome this limitation and provide a methodology allowing the automatic optimization of the jet location, we proposed coupling of a time-accurate flow solver, an adaptive mesh refinement/coarsening technique, and an automatic optimization algorithm. The numerical methods used in the flow solver are described in the first section. Then, we provide details on the grid refinement/coarsening techniques used to automatically generate a mesh adapted to the jet location. The optimization procedure is finally presented. Although our ultimate goal is simultaneous optimization over all parameters (frequency, amplitude, direction, and location), we prefer at the present time to focus on the optimization of the jet location only. In the following section, the procedure is applied to determine the optimal location of a synthetic jet to delay stall for the NACA 0012 airfoil at Reynolds number $\mathrm{Re}=2\times10^6$ for two values of the angle of attack. Finally, the characteristics of the controlled flow are studied to understand the relationship between jet location and control efficiency.

2 Flow Solver

The numerical simulation of stall control is performed by the ISIS-CFD flow solver, developed by EMN (Equipe Modélisation Numérique, i.e., CFD Department of the Fluid Mechanics Laboratory). The prediction of massively separated flows, such as those encountered in stall control, is a difficult task because results are highly dependent on the choice of turbulence and transition models for which knowledge and numerical modeling are very incomplete. Although large eddy simulation (LES) approaches may be more suitable for such flows, we have chosen to use the unsteady Reynolds-averaged Navier-Stokes equations (URANSE). Indeed, for practical and cost-effectiveness considerations, LES is still prohibitive for high Reynolds numbers, particularly in a design optimization framework.

The incompressible unsteady Reynolds-averaged Navier-Stokes equations can be written as (using the generalized form of Gauss' theorem)

$$\frac{\partial}{\partial t}\int_V \rho dV + \int_S \rho(\vec{U}-\vec{U}_d)\cdot\vec{n}dS = 0 \tag{1a}$$

$$\frac{\partial}{\partial t}\int_V \rho U_i dV + \int_S \rho U_i(\vec{U}-\vec{U}_d)\cdot\vec{n}dS = \int_S (\tau_{ij}I_j - pI_i)\cdot\vec{n}dS + \int_V \rho g_i dV \tag{1b}$$

where V is the domain of interest, or control volume, bounded by a closed surface S moving at a velocity $\vec{U}_d$ with a unit outward normal vector $\vec{n}$. $\vec{U}$ and p represent, respectively, the velocity and

[1]Corresponding author. INRIA — Projet Opale, 2004 route des lucioles, BP 93, 06902 Sophia-Antipolis, France.

Contributed by the Fluids Engineering Division of ASME for publication in the JOURNAL OF FLUIDS ENGINEERING. Manuscript received June 6, 2006; final manuscript received January 24, 2007. Assoc. Editor: Surya P. Vanka.

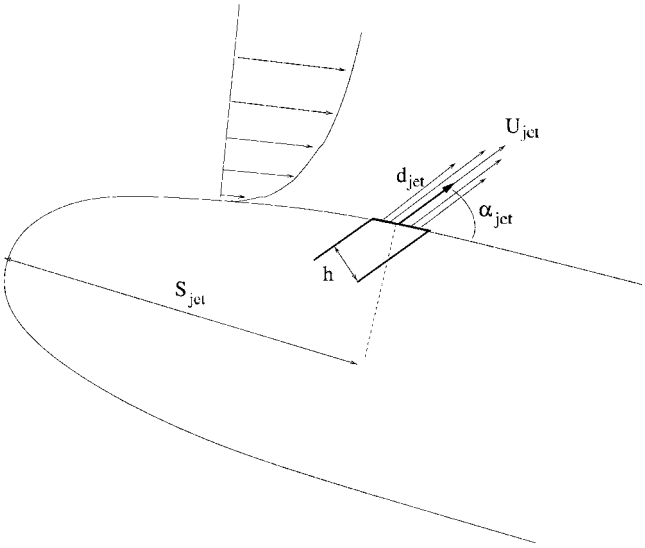

Fig. 1 Configuration of the computations

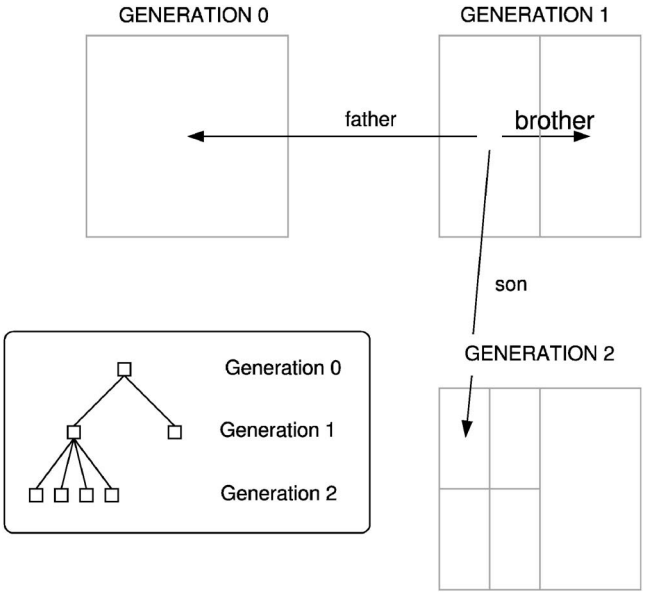

Fig. 2 Relationship between the different generations of elements

pressure fields. τ_{ij} and g_i are the components of the viscous stress tensor and the gravity, whereas I_j is the identity vector whose components vanished, except for the component j, which is equal to unity.

All flow variables are stored at the geometric center of arbitrary shaped cells. Volume and surface integrals are evaluated with second-order accurate approximations. Numerical fluxes are reconstructed on mesh faces by linear extrapolation of integrand from the neighboring cell centers. A centered scheme is used for the diffusion terms, whereas a combination of upwind and centered schemes is applied to the convective terms. The combination used results from a blending based on a continuous exponential scheme involving the signed Peclet number at the face [7].

A pressure equation is obtained in the spirit of Rhie and Chow [8]. Momentum and pressure equations are solved in a segregated manner like in the SIMPLE coupling procedure [9].

A second-order backward difference scheme is used to discretize time. All spatial terms appearing in Eqs. (1*a*) and (1*b*) are treated in a fully implicit manner.

Several turbulence closures are available in the flow solver, ranging from linear eddy-viscosity models to full second-order closures. We have opted for the near-wall low-Reynolds number $k-\omega$ SST model of Menter [10] because it behaves satisfactorily for separated flows over airfoils. Turbulent variables k and ω are obtained by solving transport equations discretized in a manner similar to that used for the momentum equations.

The synthetic jet actuator is modeled as a suction/blowing-type boundary condition. We prescribe the following velocity distribution at the jet lips:

$$\vec{U} = U_{\text{jet}} \sin(2\pi N_{\text{jet}} t) f(\xi) \vec{d}_{\text{jet}} \tag{2}$$

where $\vec{d}_{\text{jet}}$ is a unit vector in the direction of the jet. α_{jet} is the angle between $\vec{d}_{\text{jet}}$ and the wall (Fig. 1). $f(\xi)$ is the velocity distribution across the jet inlet. $f(\xi)=\sin^2(\xi)$ is used to accurately describe the jet flow [3]. For the turbulent variables, normal gradients of value zero are imposed at the jet boundary for both k and ω. The jet width is usually very small with respect to the length scale of the problem. Thus, the grid should be especially fine in the vicinity of the slot to provide a detailed description of the jet boundary layer interaction. Such grids are generated automatically using the local adaptive mesh procedure described in Sec. 3.

3 Adaptive Techniques

3.1 Principle. An automatic local adaptive mesh procedure (*h*-refinement) is well suited to track the temporal evolution of the jet and to maintain a fine computational grid around it. Moreover, an automatic grid adaptation frees the user from the tedious task of generating a mesh suitable for any jet position. Indeed, using mesh adaptation, one can start from a coarse uniform grid that is refined thanks to an explicit error indicator. We use a simple refinement indicator based on the distance to the jet location. Thus, the cell size within a sphere surrounding the jet slot can be controlled to provide a precise description of the jet velocity distribution and sufficient resolution of its interaction with the wall boundary layer. This section presents the basic features of the adaptive procedure.

3.2 Data Structure. An appropriate data structure is required to ensure a simple yet flexible and fast mesh adaptation. Our local mesh adaptation procedure is based on the notion of a relationship between the successive generations of elements of the grids and stores the information in a treelike data structure (see Fig. 2). This approach is used to efficiently store and retrieve data for control volumes, of arbitrary shapes as well as for all mesh faces. They are presented here only for the control volumes but similar notions apply to the faces of the grids [11,12]. The initial mesh consists of elements of generation 0, and a first refinement step leads to the birth of elements of generation 1. A control volume tagged for refinement becomes a father and is split into several sons (which share a brotherly relationship while the father and its sons form a family). Further refinement steps will induce genesis of elements of generation 2 and so on. It should be emphasized that this structure does not restrict the generality of the grid adaptation process because it does not require information about how the elements are refined. Besides, negative generations can exist because cell agglomeration can coarsen the initial grid when required [11]. Such a data structure permits one to address several problems at once. First, the unrefinement of a family (thus, of a previously refined cell) becomes straightforward since it corresponds to the recovery of its father (and also the destruction of its sons). Thus, the refinement/unrefinement process becomes fully dynamic and quick to achieve. Second, it guarantees exact recovery of the initial mesh if refinement is no longer necessary in some area of the computational grid, as is the case with unsteady problems.

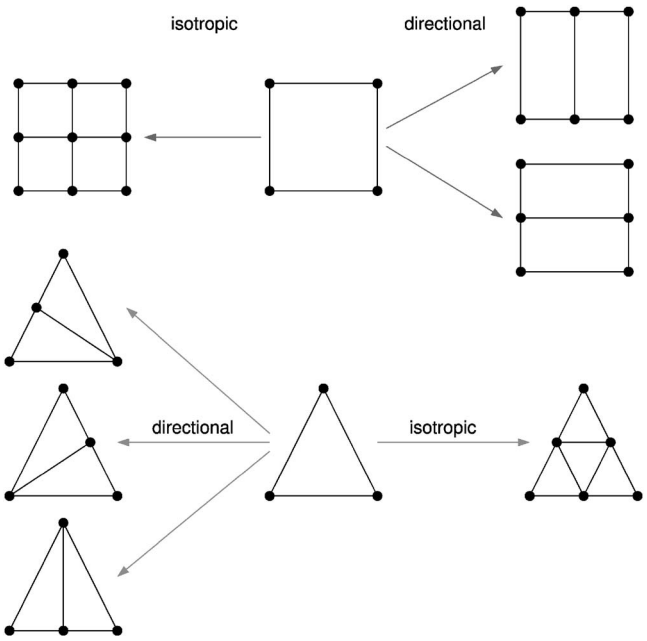

Fig. 3 Refinement of two-dimensional volumes

3.3 Grid Alteration. During the refinement process, each control volume tagged for refinement is split into several smaller ones of the same topology. Thus, a son inherits the topology of its father and the difference is restricted to cell size. This ensures that the initial desired local mesh quality is preserved everywhere throughout the simulation. For two-dimensional grids, as illustrated in Fig. 3, the refinement process can occur with a possible directional sensitivity for flows with simple features.

In the present study, meshes are only refined in the tangential direction to the wall. Indeed, by construction, grids are already very fine in the normal direction to the wall. We emphasize that adapted grids require no specific treatment in the flow solver. A nonrefined neighbor of a refined cell presents a so-called hanging node, which is accounted for naturally by our face-based finite-volume method: a face with a hanging node is simply seen as several smaller faces.

Special treatments are necessary when refining a curved boundary surface because two requirements have to be fulfilled when a new node is added on the surface of the body:

- The node must be placed on the exact geometry, which should be described either analytically or by a CAD description readable by the flow solver.
- For convex boundaries and high aspect ratio cells, the inclusion of a new node on the surface of the body should not generate neighboring cells with negative volumes.

To avoid ill-conditioned near-wall cells, we move the grid in accordance with the discrete boundaries' deformation by generalizing the mesh deformation tools already included in the flow solver and previously used for shape optimization studies [13,14]. For two- and three-dimensional cases, a lineal and torsional spring analogy is employed to control the deformation of the grid. The association of lineal and torsional springs provides a powerful mesh deformation tool that maintains the grid quality near the wall even for high deformations [15].

4 Optimization Procedure

4.1 Optimization Loop. Design optimization consists of maximizing an objective function f that depends on the design variables D and the flow variables $Q(D)$. The governing equations of the flow $R[D,Q(D)]=0$ are considered as constraints that must be satisfied at each step of the design procedure. Some bound constraints must be added to the problem to find a realistic solution. Thus, the variation domain of design variables is usually closed. From a mathematical point of view, the problem may be expressed as

$$\text{Maximize } f[D,Q(D)]$$

$$\text{Constrained to } R[D,Q(D)]=0$$

$$L_i \leq D \leq L_s$$

In the present work, the objective function is the time-averaged lift coefficient C_l of the airfoil. It is evaluated after all transient effects have vanished, by integrating the instantaneous lift coefficient over several flow cycles

$$f[D,Q(D)] = \frac{1}{t_2 - t_1}\int_{t_1}^{t_2} C_l[D,Q(D)]dt \tag{3}$$

In practice, the integration is performed over five flow cycles. Numerical experiments have shown that this interval of integration is large enough to ensure that time-dependency effects be negligible. The design variable D is the location of the synthetic jet s_{jet} on the suction side of the airfoil (see Fig. 1). Other parameters, such as frequency, amplitude, and direction, are fixed during optimization to focus on the analysis of the location dependency. Therefore, the optimization procedure consists of several unsteady flow simulations for a synthetic jet with different locations, whose value is modified by the optimization algorithm. Thus, the design procedure is described by the following steps:

1. Generation of a baseline grid X_0
2. Initialization of the design variables D_0
3. Step $k=0$
4. Generation of an adapted grid $X_k(D_k)$
5. Unsteady simulation of the flow $Q_k(D_k)$
6. Evaluation of the lift $f(D_k,Q_k(D_k))$
7. Correction ΔD_k by the optimization algorithm
8. Update $D_{k+1}=D_k+\Delta D_k$, $k=k+1$
9. Go to step 4

until the convergence of the design variables is achieved.

4.2 Optimization Strategy. Gradient-based optimizers are popular because of their efficiency since they can reach a maximum of the objective function in a number of evaluations lower than zero-order methods. However, some difficulties arise when used on complicated realistic problems. The evaluation of the derivatives of the objective function for a sophisticated simulation process is a nontrivial task. Their evaluation is usually based on an adjoint formulation that relies on the differentiation of the flow solver [16]. This task is tedious when high-order discretization schemes on unstructured grids are used or complex turbulence models are employed. This approach often requires a priori simplification of the problem, neglecting turbulence sensitivities for instance, or using first-order discretization schemes, which provides an approximated gradient [16]. All in all, this approach appears restricted to moderately complicated problems and its use for massively separated flows remains a challenge.

To overcome these limitations, we chose a derivative-free algorithm that is easier to implement in a complex numerical framework. Furthermore, this approach is less sensitive to numerical noise because no information about the derivatives is needed to predict the optimization path. The number of flow evaluations required is higher than that needed by gradient-based methods, but it remains reasonable, as soon as the number of design variables is low, which is the case in the present study.

4.3 Algorithm. We chose an optimizer relying on an iteratively updated quadratic interpolating model of the objective function, inspired from the work of Marazzi and Nocedal [17]. Assuming that the value of the objective function is known as a set of sample points, including the best point x_k, a local quadratic interpolating model q_k is built at each optimization step k. For a quadratic model, $(1/2)(n+1)(n+2)$ sample points are needed, where n is the number of design variables

$$q_k(x_k+s) = f(x_k) + g_k^T s + \tfrac{1}{2} s^T H_k s \tag{4}$$

The unknown coefficients g_k and H_k are determined by solving a linear system, expressing the interpolation condition at the sample points.

Assuming that the model q_k is valid in a ball of radius ρ_k centered at x_k, called the trust region, a subproblem is solved at each iteration to minimize q_k in this region

$$\text{Minimize} \quad q_k(x) \quad x \in \mathcal{R}^n$$

$$\text{Constraint to} \quad \|x - x_k\| \leq \rho_k \tag{5}$$

Contrary to response surface techniques that rely on a global and approximated model using a large number of sample points, the present method minimizes a local and interpolated model at each iteration. This cheap operation can be easily performed using a Newton step, for instance. Once the solution $\tilde{x}$ of the subproblem (5) is determined, the value of the objective function recomputed at the new point $\tilde{x}$ is then included in the set of sample points to replace x_{far}, the farthest point from $\tilde{x}$. This promotes inclusion of promising points in the set of sample points, thus improving the quality of the model. The radius of the trust region is then updated. The efficiency of the model is evaluated as follows:

$$e_k = \frac{f(\tilde{x}) - f(x_k)}{q_k(\tilde{x}) - q_k(x_k)} \tag{6}$$

If it is satisfactory, i.e., $e_k > \alpha$ (e.g., $\alpha = 0.8$), the trust region radius is increased because the model seems to be accurate and a larger step may be taken. If the efficiency is poor, i.e., $e_k < \beta$ (e.g., $\beta = 0.1$), the radius is reduced. Finally, the procedure goes on using the updated model and trust region. The algorithm is fully analyzed and validated for several problems in the paper by Marazzi and Nocedal [17].

5 Mesh Refinement Study

A grid refinement study is first performed on a typical configuration to determine how fine the mesh should be to obtain an accurate representation of the controlled flow. To this end, flows obtained on grids with different refinement levels are compared. A synthetic jet of width $h = 0.5\%\, l$ is arbitrarily located at 20% of the chord l of a NACA 0012 airfoil. The Reynolds number is $\text{Re} = 2 \times 10^6$, and the angle of attack is set to 18 deg. The nondimensional actuation frequency is $N_{\text{jet}} L/U_\infty = 1$, whereas the nondimensional amplitude of the jet is $U_{\text{jet}}/U_\infty = 1$. The angle of the jet direction with respect to the wall is $\alpha_{\text{jet}} = 30$ deg. The flow is initialized using the fields obtained from a previous simulation without actuation. The nondimensional time step is $\Delta t = 0.002$, which ensures an accurate description of each flow cycle. Turbulence is modeled with the $k-\omega$ SST model of Menter [10]. Flow computations are performed on four grids. The first grid is the baseline mesh $\mathcal{M}_0$. It is composed of 66,110 quadrangle cells in the vicinity of the airfoil and its wake, and triangles in the rest of the domain (see Fig. 4). The distance between the first point and the wall corresponds to $y^+ = 0.2$. The second grid $\mathcal{M}_1$ is the one-generation grid anisotropically refined in the tangential direction in a sphere of radius $5\%\, l$ centered at the jet center. The third grid $\mathcal{M}_2$ is the two-generation grid refined in two spheres of radius $5\%\, l$ and $4\%\, l$. The fourth grid $\mathcal{M}_3$ is the three-generation grid refined in three spheres of radius $5\%\, l$, $4\%\, l$, and $3\%\, l$ (see Fig. 5). Table 1 details the size of the grids and the number of faces on the jet boundary for each of them.

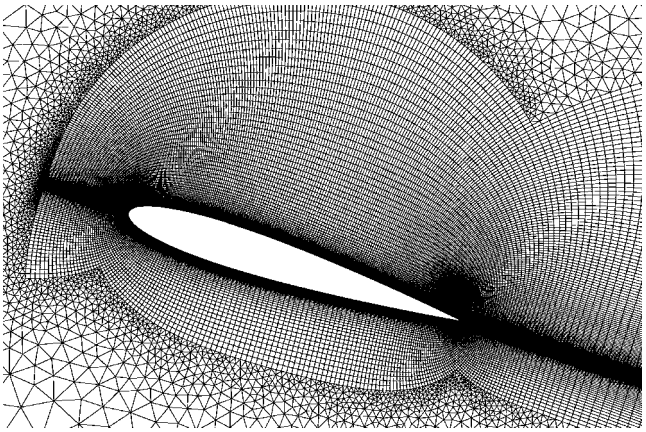

Fig. 4 Baseline grid

A comparison of the lift coefficient histories obtained with the different grids after all transient effects have vanished is shown in Fig. 6. As can be seen, results using grids $\mathcal{M}_2$ and $\mathcal{M}_3$ are very close to each other. This indicates that the two-generation grid $\mathcal{M}_2$ is fine enough to describe the actuated flow. Hence, we use this grid for the optimization problem detailed in Sec. 6.

6 Optimization of the Jet Location

6.1 Presentation of the Test Case. Now that computations with adaptive grids rely on a safe basis, we turn to optimization problems. The physical configuration of the problem as well as the numerical parameters are identical to those used for the grid refinement study. However, we consider two angles of attack, 18 deg and 20 deg, to quantify the influence of the angle of attack on the optimal actuator location.

The flow without actuation is characterized by a steady recirculation zone located at the trailing edge for the incidence 18 deg. Two steady vortices are present on most of the suction side of the airfoil for the incidence 20 deg (Fig. 7). Actually, these configurations correspond to flows at maximum lift and just after stall (Fig. 8).

The characteristics of the actuator are also the same as those used for the grid refinement study, except for the incidence of 20 deg for which the jet amplitude is increased to $U_{\text{jet}}/U_\infty = 1.5$. Lower values yield poor control at this incidence. The initial jet location is arbitrarily set to $s_0 = 20\%\, l$.

Finding an optimal jet location requires about 15 time-accurate flow simulations. For each one, time integration is carried out until a nondimensional time $t = 25$, to ensure that transcient effects have vanished. This requires roughly 500 CPU hours for each single optimization procedure.

6.2 Lift Enhancement. Lift enhancement obtained at both incidences is shown in Fig. 8 for a synthetic jet located at the initial and optimal positions. For an angle of attack of 18 deg, the lift increases only by ~5% with respect to the baseline airfoil. This is likely due to the fact that computations were performed in the vicinity of the maximum lift for the baseline airfoil. The actuation effects for the initial and optimized jet locations look similar. Actually, the initial point appears to be very close to the optimal one. However, for an angle of attack of 20 deg (post-stall regime), the results exhibit larger improvements. The lift increases due to the jet actuation by ~43% for the initial location and 57% for the optimized location. Thus, the benefit obtained by optimizing the jet location is clearly established for this case.

The time-averaged lift evolution with respect to the jet position

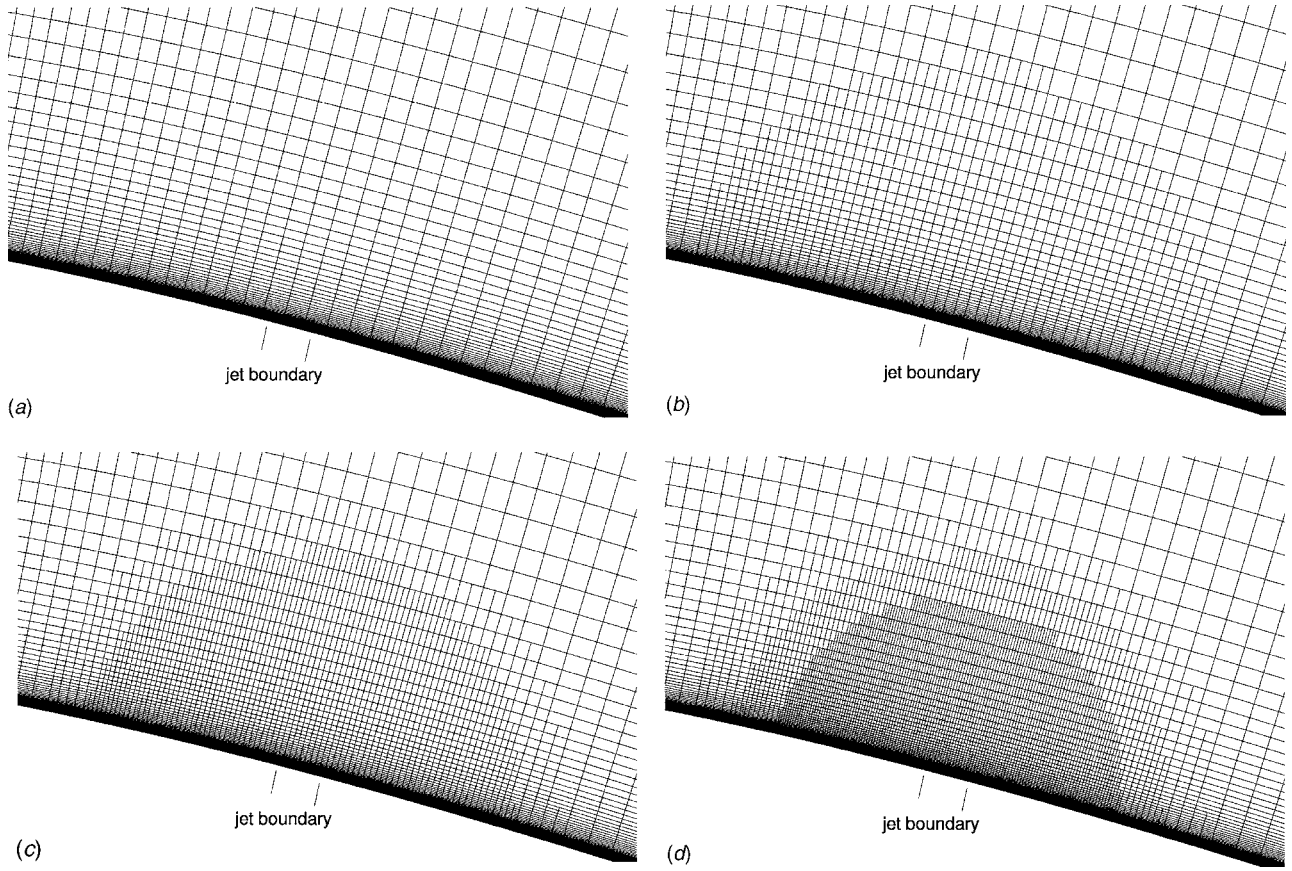

Fig. 5 Successive refined grid

is shown in Fig. 9. The evolution of the lift for an angle of attack of 18 deg is rather smooth, and the maximum is reached for $s_{\text{opt}}^{18}=0.23l$. The low variations of the lift can be explained in two ways: First, the incidence is close to the maximum lift incidence for the baseline airfoil. Thus, only moderate gains can be expected so that the amplitude of the synthetic jet is quite low. For an angle of attack of 20 deg, the influence of the actuator location on the lift is much larger. Thus, the optimization of the jet location yields significant improvements of the control efficiency. The maximum is reached for $s_{\text{opt}}^{20}=0.14l$, which is closer to the leading edge than in the previous case. However, the lift evolution exhibits some oscillations in the vicinity of the optimal location. The source of these oscillations is unclear. They may be due to a physical phenomenon yielding local optima caused by the strong nonlinearity of the flow in the vicinity of the synthetic jet. They may also be due to modeling uncertainties, since turbulence modeling using URANSE in the presence of a synthetic jet is still questionable. Additional flow analyses were performed a posteriori with actuator positions close to those for which oscillations were observed. They confirmed the occurrence of sudden lift variations as the jet is moved. Yet, no satisfactory explanation of their origin was found.

Table 1 Grids size

Mesh	Number of cells	Jet boundary faces
$\mathcal{M}_0$	66,110	2
$\mathcal{M}_1$	68,116	5
$\mathcal{M}_2$	71,401	8
$\mathcal{M}_3$	76,429	16

6.3 Flow Analysis. Flows are now analyzed to understand how the jet location influences the control efficiency. The temporal evolutions of the lift coefficient along one flow period are depicted in Figs. 10 and 11 for both incidences. Three jet locations are considered:

- upstream of the best location: $s=10\%l$ for both incidences
- at the best location: $s_{\text{opt}}^{18}=23\%l$ and $s_{\text{opt}}^{20}=14\%l$

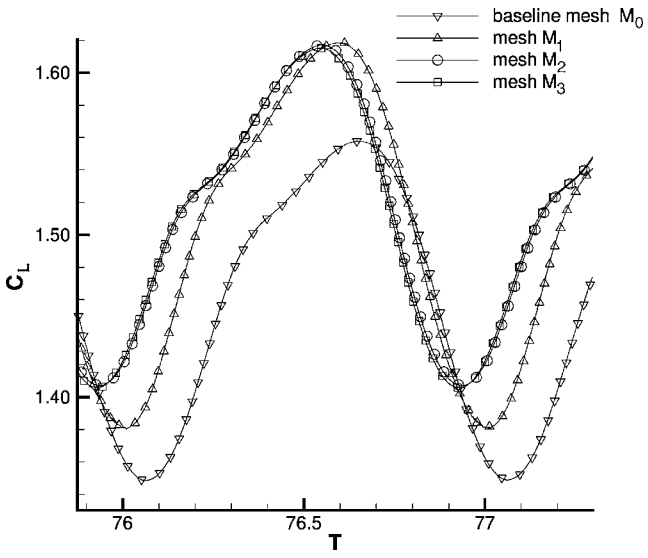

Fig. 6 Grid refinement study

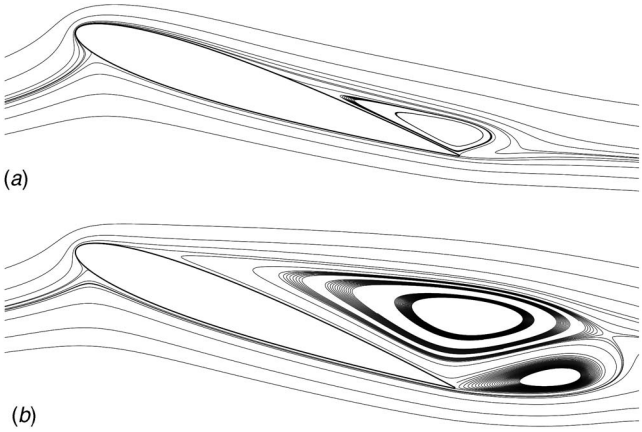

Fig. 7 Streamlines without actuation

- downstream the best location: $s=30\%l$ for an incidence of 18 deg and $s=20\%l$ for an incidence of 20 deg

Jet blowing is also presented in Figs. 10 and 11 to correlate it with lift evolution. Figures 12–15 show the pressure coefficient on the airfoil at maximum and minimum lift times for the three jet locations described above. Finally, Figs. 16–21 show streamlines at maximum and minimum lift times for the same jet locations. The arrow indicates the precise jet location on the airfoil.

6.3.1 Incidence 18 deg

From $s=10\%l$ *to* $s_{\text{opt}}^{18}=23\%l$. The lift histories (Fig. 10) show that the minimum lift value increases as the jet is moved downstream from $s=10\%l$ to $s_{\text{opt}}^{18}=23\%l$. This lift increase is caused by the suction peak enhancement (Fig. 13). This behavior can be explained by the fact that the minimum lift time, which corresponds to vortex shedding (Figs. 16(*b*) and 17(*b*)), is moved from blowing times to suction times (Fig. 10). Indeed, the suction peak is enhanced when the jet is in suction mode and reduced as it is blowing. Therefore, the increase of the minimum lift can be explained by a switch of the phase between the blowing/suction and the vortex shedding, due to the modification of the jet location.

The maximum lift is maintained (Fig. 10), as the jet is moved downstream. At the maximum lift time, a vortex is growing on the suction side of the airfoil for $s=10\%l$ (Figs. 16(*a*)), yielding an increase of the pressure level on the suction side (Fig. 12), whereas for $s_{\text{opt}}^{18}=23\%l$ the flow is still attached until the trailing

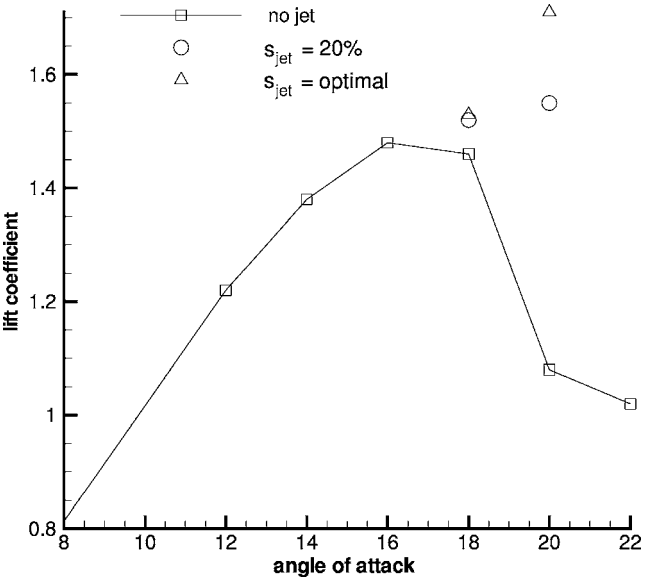

Fig. 8 Lift coefficient with respect to the angle of attack

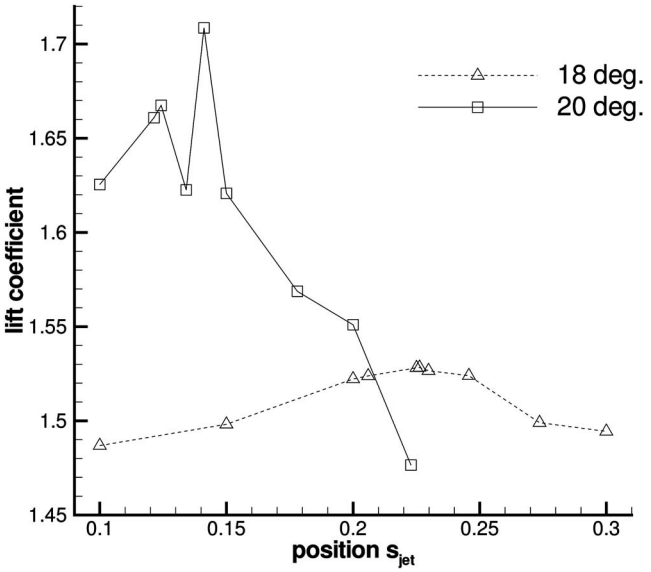

Fig. 9 Lift coefficient with respect to the jet position

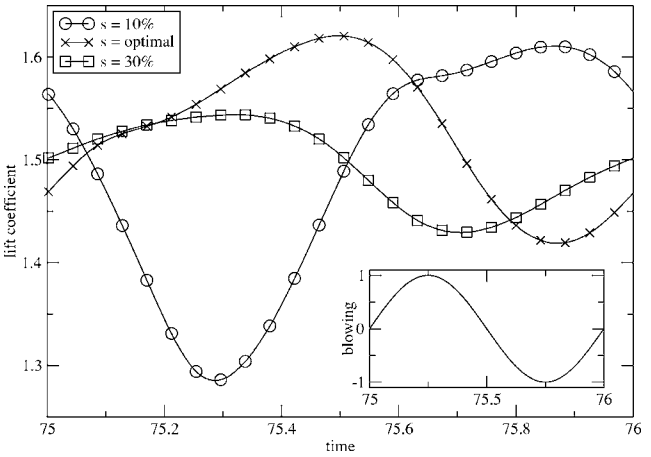

Fig. 10 Lift coefficient history for incidence 18 deg

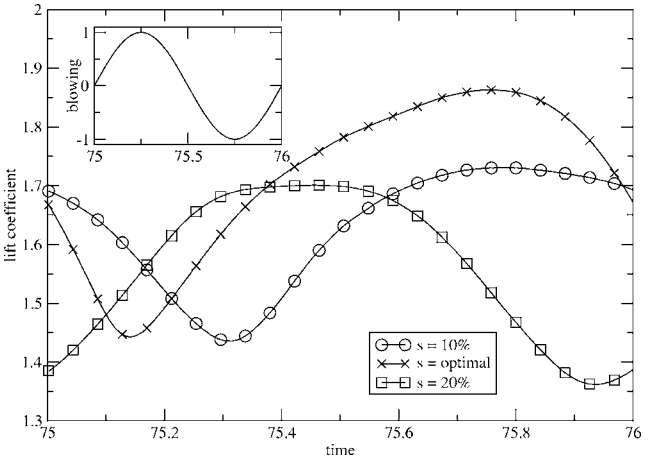

Fig. 11 Lift coefficient history for incidence 20 deg

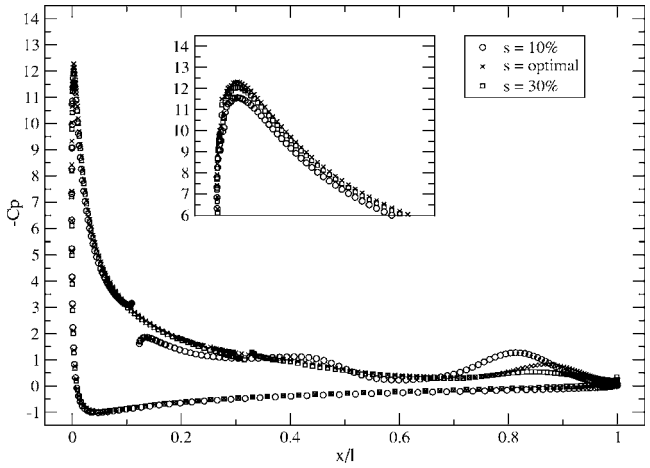

Fig. 12 Pressure coefficient at the maximum lift time for incidence 18 deg

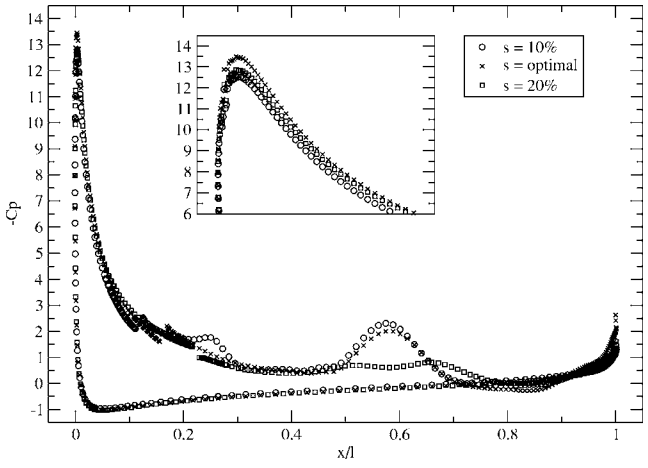

Fig. 15 Pressure coefficient at the minimum lift time for incidence 20 deg

edge (Fig. 17(*a*)), yielding a lower pressure level on the suction side, particularly at the suction peak. Nevertheless, this improvement is balanced by a slight suction effect in the vicinity of the vortices for $s=10\%l$ (Fig. 12), due to a more intense vorticity (Figs. 16(*a*)). Moreover, the suction effect of the jet for $s=10\%l$ at this time compensates the high level pressure at the suction peak explained previously. Finally, the lifts for the two locations are quite similar.

From $s_{\text{opt}}^{18}=23\%l$ *to* $s=30\%l$. The lift histories (Fig. 10) show that the minimum lift value is globally maintained as the jet is

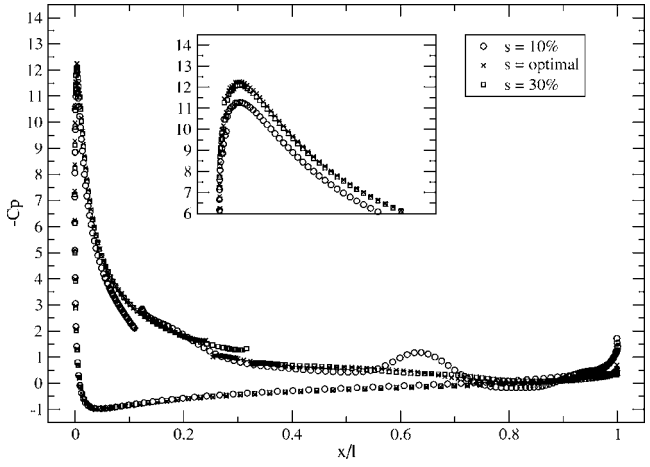

Fig. 13 Pressure coefficient at the minimum lift time for incidence 18 deg

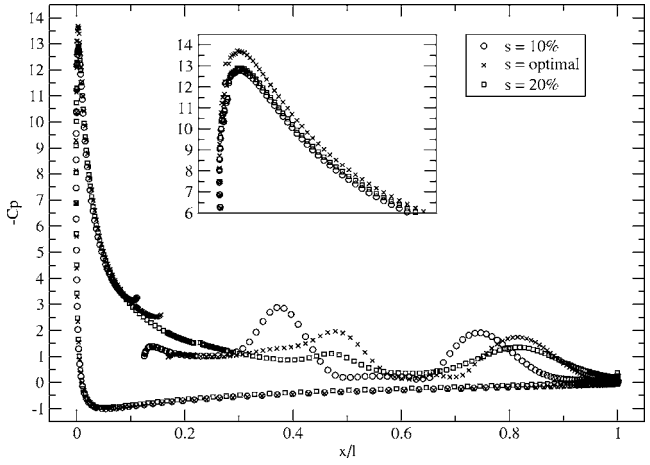

Fig. 14 Pressure coefficient at the maximum lift time for incidence 20 deg

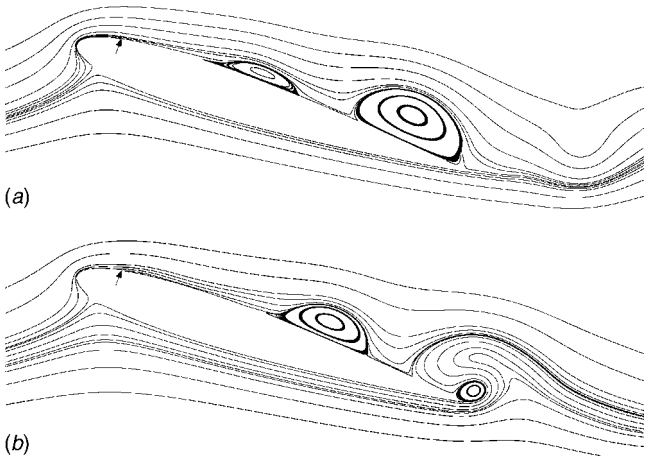

Fig. 16 Incidence 18 deg, $s=0.1l$

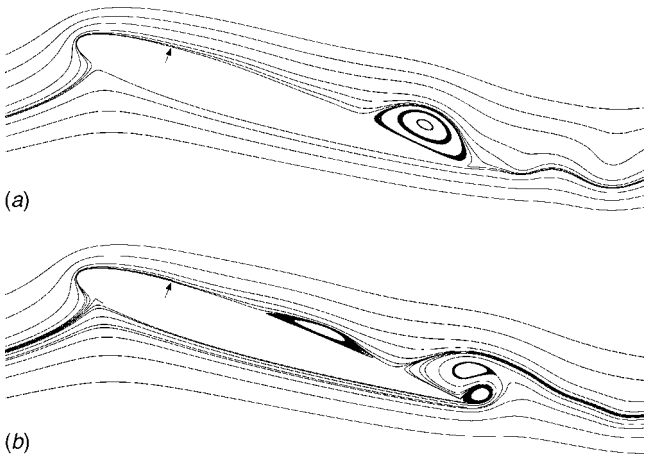

Fig. 17 Incidence 18 deg, $s=s_{\text{opt}}^{18}$

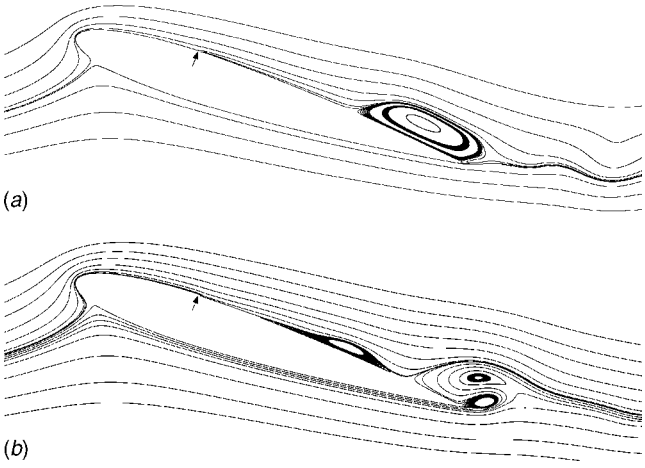

Fig. 18 Incidence 18 deg, $s=0.3l$

moved downstream from $s_{opt}^{18}=23\%l$ to $s=30\%l$, whereas the maximum lift decreases. At the minimum lift time, the suction peak enhancement due to the jet suction is slightly reduced because the jet location is moved downstream since the distance between the jet and the suction peak increases (Fig. 13). However, this effect is balanced by the fact that the growing vortex is delayed for $s=30\%l$ (Figs. 17(*b*) and 18(*b*)). At the maximum lift time, the lift decrease can be explained by a larger vortex located at the trailing edge for $s=30\%l$ (Figs. 17(*a*) and 18(*a*)).

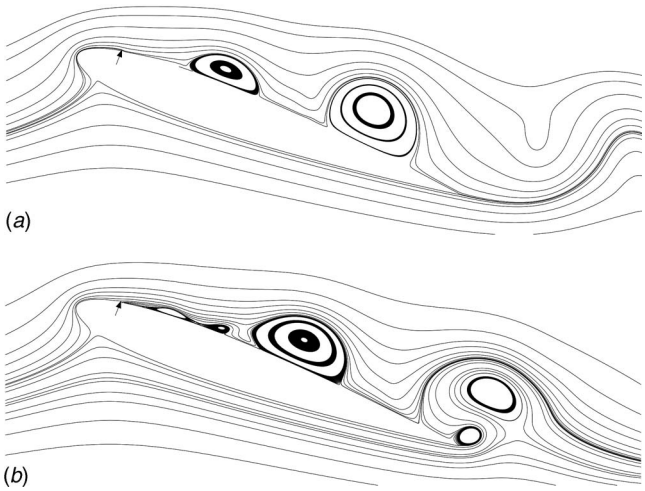

Fig. 19 Incidence 20 deg, $s=0.1l$

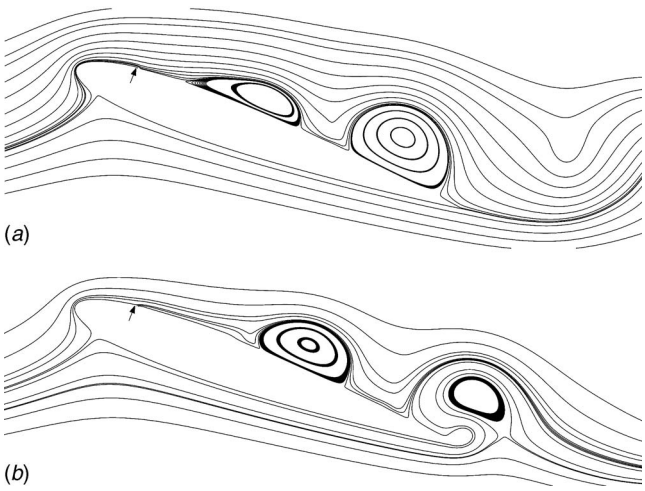

Fig. 20 Incidence 20 deg, $s=s_{opt}^{20}$

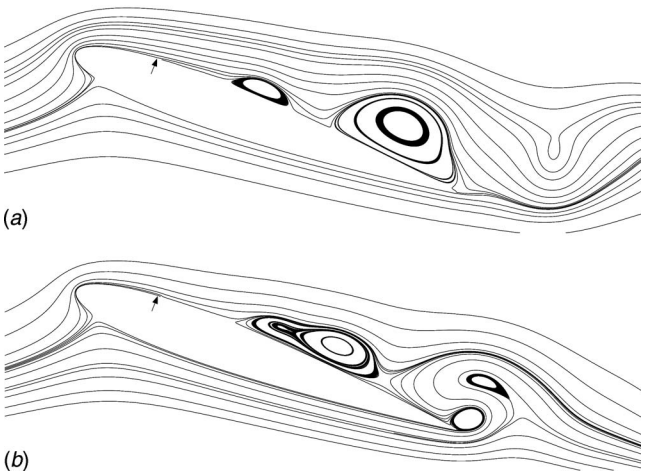

Fig. 21 Incidence 20 deg, $s=0.2l$

6.3.2 Incidence 20 deg

From $s=10\%l$ to $s_{opt}^{20}=14\%l$. As can be seen in Fig. 11, the minimum lift is maintained as the synthetic jet is moved from $s=10\%l$ to $s_{opt}^{20}=14\%l$. For $s=10\%l$, vortices are generated very close to the leading edge (Fig. 19(*b*)) yielding a decrease of the suction peak (Fig. 15). This is not the case for $s_{opt}^{20}=14\%l$ (Fig. 20(*b*)). However, this change is balanced by a slight pressure decrease at the vortices' locations for $s=10\%l$, due to a more intense vorticity field (Figs. 15 and 19(*b*)). Finally, the lift curves are similar for the two jet locations.

The maximum lift is far higher for the optimized jet location (Fig. 11). The pressure distribution along the airfoil clearly shows that this is due to the enhancement of the suction peak as the jet is moved downstream (Fig. 14). For $s=10\%l$, the vortex is located slightly closer to the leading edge (Fig. 14), yielding a decrease of the level of the suction peak.

From $s_{opt}^{20}=14\%l$ to $s=20\%l$. As the jet is moved downstream from $s_{opt}^{20}=14\%l$ to $s=20\%l$, both maximum and minimum lifts are decreased. Indeed, at the minimum lift time, the flow is detached over more than half of the suction side of the airfoil for $s=20\%l$, including low intensity vortices (Fig. 21(*b*)) and yielding a flat pressure distribution (Fig. 15). Hopefully, the effect is partially balanced by the enhancement of the suction peak due to the sucking jet. At the maximum lift time, the lift is lower for $s=20\%l$ than for $s_{opt}^{20}=14\%l$, since vortices have a lower intensity and the jet is blowing, which result in a lower suction effect at the vortices' locations as well as at the suction peak (Fig. 14).

6.4 Synthesis. These results lead us to propose some key ideas to explain the control efficiency changes as the synthetic jet is moved along the suction side of the airfoil:

- Enhancement of the suction peak by the jet—If the synthetic jet is located close to the leading edge, it excites the suction peak: during the jet-suction phase, the suction peak is enhanced, whereas during the jet-blowing phase, the suction peak is reduced. This mechanism weakens as the jet is moved downstream.
- Temporal phase between the vortex shedding and the suction/blowing effects—For some jet locations, vortex shedding occurs in phase with the suction peak enhancement by the sucking jet. Then, the lift decrease due to the

vortex shedding is compensated by a higher suction peak.
- Location of the vortices' birth—As the synthetic jet is moved upstream, the location where vortices are generated moves upstream as well. It results in a pressure increase at the suction peak and a decrease of the lift.
- The intensity of vortices.

If the synthetic jet is located close to the leading edge, the vortices generated are more intense, causing a stronger suction effect as they move along the airfoil.

Conclusion

A methodology for automatically finding the optimal location of a synthetic jet is proposed by coupling of a time-accurate flow solver, an adaptive mesh refinement/coarsening technique, and an optimization algorithm. Unsteady Reynolds-averaged Navier-Stokes equations (URANSE) are solved with a near-wall low-Reynolds number turbulence closure to obtain the controlled flow around the airfoil. An unstructured grid refinement/coarsening method is used to automatically generate meshes adapted to the presence of the synthetic jet. Finally, an optimization algorithm searches for the best location of a synthetic jet to maximize lift.

This methodology is demonstrated by optimizing the location of a synthetic jet on the suction side of the NACA 0012 airfoil for a Reynolds number $\mathrm{Re}=2\times10^6$ at incidences of 18 deg and 20 deg for stall control purposes. Results show that the influence of the jet location on the control efficiency is moderate at the incidence of 18 deg. However, the jet location has a stronger effect at an incidence of 20 deg. At this angle, lift increases by +43% for the initial jet location and by +57% for the optimal location. Then, the usefulness of the proposed approach is demonstrated. One can also note that the optimal locations found at the incidences 18 deg and 20 deg are different.

Analysis of the controlled flows yields guidelines for practical jet positioning: enhancement of the suction peak by the jet, the temporal phase between the vortex shedding and the suction/blowing effects, the location of the vortices' birth, and the intensity of the vortices seem to have a critical influence on the control efficiency.

References

[1] Seifert, A., Darabi, A., and Wygnanski, I., 1996, "Delay of Airfoil Stall by Periodic Excitation," AIAA J., **33**(4), pp. 691–707.

[2] Wu, J. M., Lu, X. Y., Denney, A. G., Fan, M., and Wu, J. Z., 1997, "Post-stall Lift Enhancement on an Airfoil by Local Unsteady Control. Part i. Lift, Drag and Pressure Characteristics," AIAA Paper No. 97–2063.

[3] Donovan, J. F., Kral, L. D., and Cary, A. W., 1998, "Active Flow Control Applied to an Airfoil," AIAA Paper No. 98–0210.

[4] Ekaterinaris, J. A., 2003, "Active Flow Control of Wing Separated Flow," ASME FEDSM'03 Joint Fluids Engineering Conference, Honolulu, HI, USA.

[5] Duvigneau, R., and Visonneau, M., 2004, "Simulation and Optimization of Aerodynamic Stall Control Using a Synthetic Jet," 2nd AIAA Flow Control Conference, Portland, AIAA Paper No. 2004-2315.

[6] Duvigneau, R., and Visonneau, M., 2006, "Optimization of a Synthetic Jet Actuator for Aerodynamic Stall Control," Comput. Fluids, **35**, pp. 624–638.

[7] Demirdžić, I., and Muzaferija, S., 1995, "Numerical Method for Coupled Fluid Flow, Heat Transfer and Stress Analysis Using Unstructured Moving Meshes With Cells of Arbitrary Topology," Comput. Methods Appl. Mech. Eng. **125**, pp. 235–255.

[8] Rhie, C. L., and Chow, W. L., 1982, "A Numerical Study of the Turbulent Flow on an Isolated Airfoil With Trailing Edge Separation," AIAA/ASME 3rd Joint Thermophysics Fluids, Plasma and Heat Transfer Conference, AIAA Paper No. 82-0998.

[9] Issa, R. I., 1985, "Solution of the Implicitly Discretized Fluid Flow Equations by Operator-Splitting," J. Low Temp. Phys., **62**, pp. 40–65.

[10] Menter, F. R., 1993, "Zonal Two-Equations $k-\omega$ Turbulence Models for Aerodynamic Flows," AIAA Paper No. 93-2906.

[11] Hay, A., and Visonneau, M., 2005, "Adaptive Mesh Strategy Applied to Turbulent Flows," C. R. Acad. Sci., Ser. Mecanique, **333**(1), pp. 103–110.

[12] Hay, A., Leroyer, A., and Visonneau, M., 2006, "H-Adaptive Navier-Stokes Simulations of Free-Surface Flows Around Moving Bodies," J. Mar. Sci. Technol., **11**(1), pp. 1–18.

[13] Duvigneau, R., and Visonneau, M., 2001, "Shape Optimization for Incompressible and Turbulent Flows Using the Simplex Method," AIAA Paper No. 2001-2533.

[14] Duvigneau, R., Visonneau, M., and Deng, G. B., 2003, "On the Role Played by Turbulence Closures for Hull Shape Optimization at Model and Full Scale," J. Mar. Sci. Technol., **8**(1), pp. 11–25.

[15] Hay, A., and Visonneau, M., 2005, "Local Mesh Adaptation and Remeshing Technique Applied to a Multiple Element Airfoil," 17th AIAA Computational Fluid Dynamics Conference, Toronto, Ontario, Canada, AIAA Paper No. 2005-5337.

[16] Nielsen, E. J., and Anderson, W. K., 1999, "Aerodynamic Design Optimization on Unstructured Meshes Using the Navier-Stokes Equations," AIAA J., **37**(11), pp. 1411–1419.

[17] Marazzi, M., and Nocedal, J., 2002, "Wedge Trust Region Methods for Derivative Free Optimization," Math. Program., **91**(2), pp. 289–305.

PIV Measurement of Separated Flow in a Square Channel With Streamwise Periodic Ribs on One Wall

Lei Wang
Heat Transfer Division,
Lund University,
Box 118,
SE-221 00, Lund, Sweden

Jiri Hejcik
Faculty of Mechanical Engineering,
Brno University of Technology,
616 69, Brno, Czech Republic

Bengt Sunden[1]
Heat Transfer Division,
Lund University,
Box 118,
SE-221 00, Lund, Sweden
e-mail: Bengt.Sunden@vok.lth.se

In this study, particle image velocimetry (PIV) is used to investigate the physical process of separated flow in a square channel roughened with periodically transverse ribs on one wall. The ribs obstruct the channel by 15% of its height and are arranged 12 rib heights apart. The Reynolds number, based on the bulk-mean velocity and the corresponding hydraulic diameter of the channel, is fixed at 22,000. Assuming flow periodicity in the streamwise direction, the investigated domain is between two consecutive ribs. The emphasis of this study is to give some insight into the turbulence mechanism associated with separation, reattachment, and subsequent redevelopment. Results are included for mean velocity, friction coefficient, vorticity thickness, Reynolds shear stress, anisotropy parameter, and production of turbulent kinetic energy and shear stress. Based on the two-point correlation profiles, Taylor microscales are derived to reveal the sizes of the turbulence structure in the longitudinal and lateral directions. Moreover, Galilean decomposition is applied to the instantaneous velocity fields. The result shows that the separated shear layer is dominated by the large-scale, unsteady vortical structures.
[DOI: 10.1115/1.2742723]

Keywords: Separated Flow, Turbulence Properties, PIV

1 Introduction

Ribbed duct flows are encountered in numerous engineering applications, e.g., turbine blades and combustor walls cooling. The flow behind a rib is typically characterized by flow separation and subsequent reattachment. Flow in a separated shear layer is complicated by the presence of reverse flow and a high level of the turbulence intensity. Despite the substantial progress in experimental and numerical studies on turbulent flows with separation, our understanding of this phenomenon is far from complete. The first review of the experimental data for separated flow was provided by Bradshaw and Wong [1] for flow over a backward-facing step. Based on the single point measurement, they concluded that the shear layer split into two parts at the reattachment point and the bifurcation caused a rapid decrease in turbulence shear stress. Troutt et al. [2] showed that the separated shear layer was dominated by the large-scale vortices that retained their organization far downstream of the reattachment region. Ruderich and Fernholz [3] indicated a self-similar behavior for the mean and fluctuating quantities in a short region upstream of the reattachment point. The data of Castro and Haque [4] showed that the turbulent structure of the separated shear layer differed from that of a plane mixing layer between two streams. On the other hand, they argued that the flow close to the wall within the recirculation region had some features reminiscent of a laminar boundary layer in a favorable pressure gradient. Thereafter, Hasan [5] confirmed that the reattaching shear layer did split into two and a low-frequency flapping motion of the shear layer is observed. In the numerical simulation of turbulent flow over a backward-facing step, Le et al. [6] pointed out that the turbulent kinetic energy budget in the recirculation region is similar to that of a turbulent mixing layer.

Previous research mostly focused on the flow with separation induced by a backward-facing step that is considered to be the benchmark to study this phenomenon. The flow past a rib is more complicated because it involves an additional separation in the upstream region of the obstacle. On the other hand, the geometry of a rib has also an essential influence on the flow separation and reattachment. According to Fröhlich et al. [7], separation from continuous and curved surfaces displays a strong spatial and temporal fluctuation of the separation line; meanwhile, the mean location of reattachment is sensitively dependent on that of separation. These characteristics imply that the separation from contoured protrusions is more elusive than that from obstacles with a sharp edge.

In this study, square-shaped, transversely placed ribs are employed to investigate the separated flow in a square channel. In order to highlight the physical mechanism of flow separation, only one wall of the channel is fitted with periodic ribs. The ribs obstruct the channel by 15% of its height and are arranged 12 rib heights apart. The inter-rib spacing is set such that the reattachment is allowed to take place on the portion between consecutive ribs and a distinct redevelopment region is introduced prior to a reseparation over the next rib.

Many numerical and analytical studies [8–11] were carried out to investigate the characteristics of flow separation in a ribbed channel based on the direct numerical simulation (DNS) or large-eddy simulation (LES) techniques. Corresponding to the numerous simulation works, very few experimental works, however, were executed to give high-resolution velocity measurements and turbulent properties. Based on the literature review, Islam et al. [12] conducted an experimental study on the turbulent water flow in a rib-roughened rectangular channel by particle image velocimetry (PIV).

Given the limited body of experimental data, experiments are performed to study the unsteady turbulent flow inside a square, ribbed channel. In the present study, the two-dimensional PIV technique is implemented to measure the instantaneous velocity fields and turbulent statistical quantities. The research reported

[1]Corresponding author.

Contributed by the Fluids Engineering Division of ASME for publication in the JOURNAL OF FLUIDS ENGINEERING. Manuscript received March 17, 2006; final manuscript received January 4, 2007. Assoc. Editor: James A. Liburdy

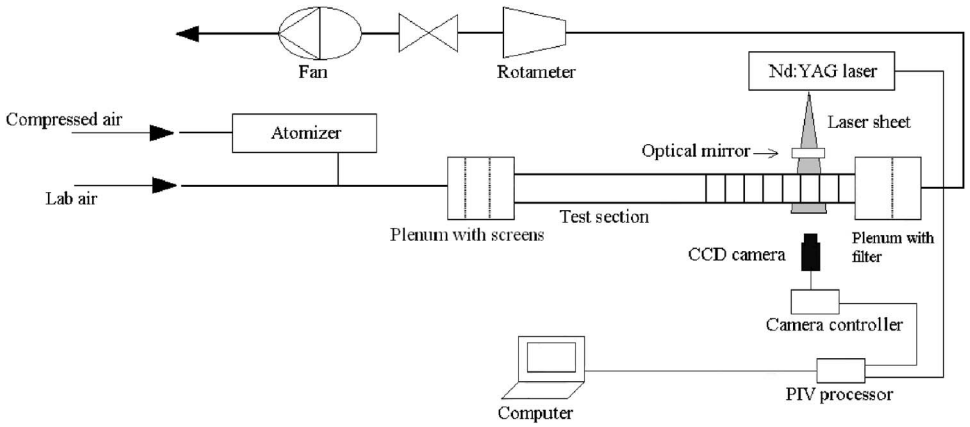

Fig. 1 Sketch of experimental setup

here is undertaken to fulfill two objectives, i.e., to gain insight into the physical process of separation and to provide experimental data of ribbed channel flows for validation of CFD models.

2 Experimental Setup and Procedures

The experimental setup consists of a 750 mm smooth channel followed by a rib-roughened section of equal length, as illustrated in Fig. 1. The cross section of the internal channel and ribs is 50 mm $\times$ 50 mm and 7.5 mm $\times$ 7.5 mm, respectively. The pitch-to-rib-height ratio P/e is fixed at 12, and the blockage ratio e/H is equal to 0.15, as shown in Fig. 2. Plexiglas plates are used to provide visual and optical access. Eight ribs, with the last one fixed at the position $x/D_h = 29$ (D_h is the hydraulic diameter of the channel), are employed in the test section. Assuming flow periodicity in the streamwise direction, the investigated domain lies between the sixth and seventh ribs, in which the fully developed turbulence is deemed to have been reached.

A commercially available PIV system developed by Dantec Dynamics is used in the present investigation. The system is arranged to measure the velocity fields in the vertical symmetry plane and the horizontal plane of the ribbed channel. Oil-based aerosol with mean particle diameter of 1 μm is generated by a TSI 9306 six-jet atomizer. The concentration of the seeding particles is regulated by the compressed air pressure and the number of Laskin nozzles. In order to get homogeneous trace particles, the channel inlet is preceded by a plenum with two screens. A Quantel Q-switched Nd:YAG laser provides the pulsed illumination with a wavelength of 532 nm. The duration of each pulse is 10 ns, and the maximum output energy is 120 mJ. The light-sheet thickness in the test section is kept at 0.8 mm. A digital camera containing a CCD chip with 1280 $\times$ 1024 pixels and a Nikon AF Micro 60f/2.8D lens with an optical filter are used to record the particle images. The field of view ranges from 65 mm $\times$ 52 mm up to 98 mm $\times$ 78 mm in the vertical planes and 90 mm $\times$ 72 mm in the horizontal planes. Using a window size of 32 $\times$ 32 pixels with 50% overlap, the velocity map contains, for instance, 69 $\times$ 57 vectors for a spatial domain 55 mm $\times$ 45 mm in the vertical plane.

The time interval between laser pulses is set such that the particles move at the most eight pixels between the pair of images. In the present experiment, the time interval varies from 10 μs to 20 μs, depending on the velocity magnitude and the desired resolution. Within each window, the number of seeding particles is >5 and the particle image size projected onto the CCD sensor is ~ 3 pixels. FFT-based cross-correlation coupled with a two-dimensional Gaussian fit is applied to find the correlation peak position. Assuming that the measured particle displacement is accurate to the extent between 0.01 and 0.1 pixels, which is the commonly accepted range, the experimental uncertainty in the instantaneous velocity measurement is estimated to be $<2\%$. The sample size is another error source for the mean and fluctuating velocity statistics. According to Gao [13], it was found that 250 instantaneous velocity samples could provide a reasonable accuracy. In the present study, 500 images are generated for each measurement plane, which results in a total sampling time of ~ 8 min under the circumstances that the time interval between recordings is set as a default value, namely, 1 s. The uncertainties of the velocity gradient $d\langle u\rangle/dy$ and shear stress $\langle -u'v'\rangle$ are estimated to be within 5% and 10%, respectively.

During the experiments, the laser beam enters the square channel vertically by means of an optical mirror that turns the horizontal laser sheet 90 deg upward. The laser-sheet position is controlled by an accurate traversing system on which the optical mirror is fixed. Two-dimensional velocity measurements are made in the vertical symmetry plane and horizontal plane, respectively. The Reynolds number, based on the bulk-mean velocity in the smooth channel (U_0=6.7 m/s) and the corresponding hydraulic diameter, is 22,000. Throughout this paper, the length and velocity are scaled by e and U_r, respectively, in which e represents the rib height, and U_r is mean velocity along the centerline of the ribbed channel. In the present measurement, U_r is equal to 9.7 m/s.

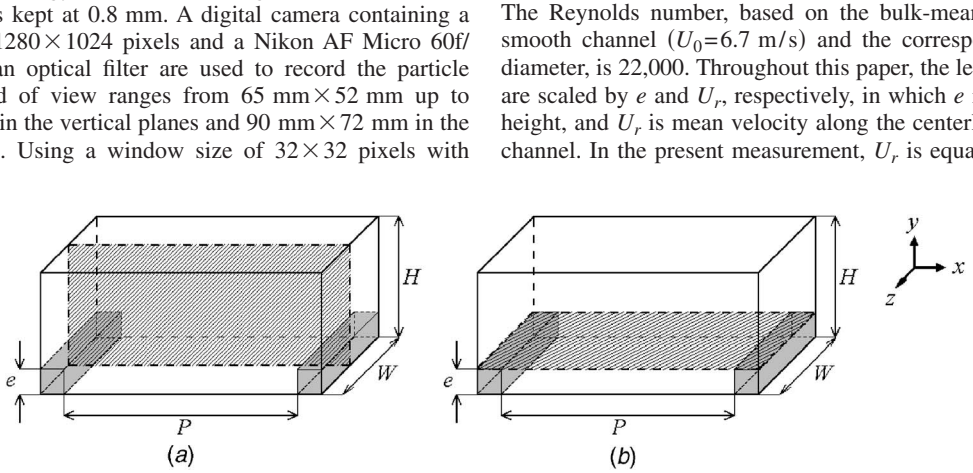

Fig. 2 Rib configuration and measurement planes: (*a*) vertical symmetry plane and (*b*) horizontal plane

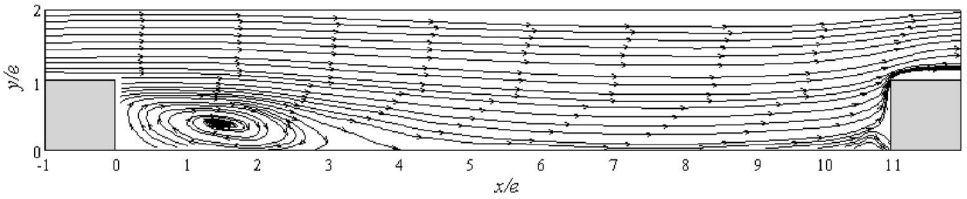

Fig. 3 Streamlines of the mean flow

3 Results and Discussion

3.1 General View of the Mean Flow Field. The time-averaged streamlines in Fig. 3 display the major global flow characteristics in the ribbed channel. The introduction of ribs locally reduces the cross section of the channel and gives rise to mainstream flow acceleration around these obstacles. The flow separates at the sharp edge of the upstream rib, forming a separation bubble that is bounded by the free shear layer and the ribbed wall. Downstream of the reattachment point, a new boundary layer redevelops gradually until it reseparates in front of the next rib.

Figure 4 gives the skin-friction coefficient development, which reveals the variation of the near-wall velocity. It should be mentioned here that the skin-friction coefficient is normalized by the inlet velocity U_0. The positive values occurring in the region $0 < x/e < 0.5$ suggest that a secondary vortex is formed in the concave corner as the backward flow approaches the vertical surface of the rib. At the reattachment point ($x/e=3.6$), the wall shear stress is vanishing. Incidentally, the position of the reattachment point is found to be coincident with the location of the maximum heat transfer coefficient (see [14]). In the region $0.5 < x/e < 3.6$, the negative value of the skin-friction coefficient characterizes the reverse flow, which reaches the maximum at $x/e=2$. Downstream of the reattachment point, a sharp increase of the skin friction in the region $3.6 < x/e < 8$ indicates acceleration in the inner part of the redeveloping boundary layer. Further downstream, as the flow impinges on the vertical face of the next rib, the boundary layer is retarded by the adverse pressure gradient and the skin friction falls quickly to zero ($9 < x/e < 11$).

Figure 5 shows the mean streamwise velocity at different downstream locations plotted against the height above the ribbed wall. The locations are chosen such that the flow regions having particular characteristics can be represented. In the leeward corner immediately downstream the rib ($x/e=0.1$), the fluid is virtually stationary. Above the top of the rib ($1.0 < y/e < 1.5$), however, the velocity gradient in the normal direction undergoes a sharp increase. The reverse flow at $x/e=2$ is followed by the reattachment point ($x/e=3.6$), where the velocity gradient on the wall is zero. Downstream of the reattachment point ($x/e=6,8$), the persistent dips of velocity profiles in the outer part region imply that the redeveloping boundary layer is still subjected to a moderately adverse pressure gradient. Thus, the inner part acceleration associated with the outer part deceleration makes the redevelopment of the boundary layer quite different from the behavior of an equilibrium boundary layer.

Figure 6 presents the mean vertical velocity at the plane $y/e=1.1$. The negative velocities in the region $1 < x/e < 8$ indicate a downwash motion toward the ribbed wall. In the cooling process, the downwash motion entrains the relative cold fluid from the mainstream to the hot surface, which, in a sense, enhances the heat transfer rate. In Fig. 6, the maximum negative value is observed at position $x/e=3$, which is slightly upstream of the reattachment point. The magnitude of the maximum negative value is $\sim 0.04 U_r$.

3.2 Instantaneous Flow Structures. When flow separates at the edge of a rib, spanwise vortices are generated in the shear layer due to the Kelvin-Helmholtz instability. To identify these vortical structures in an instantaneous velocity field, the reference frame velocity should be varied. When the reference frame velocity matches the convection velocity of an eddy, it becomes recog-

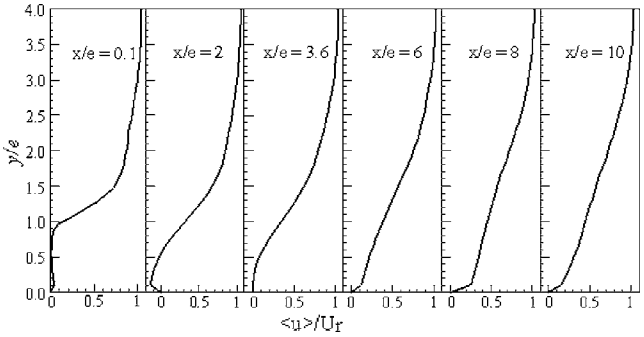

Fig. 5 Mean streamwise velocity profiles

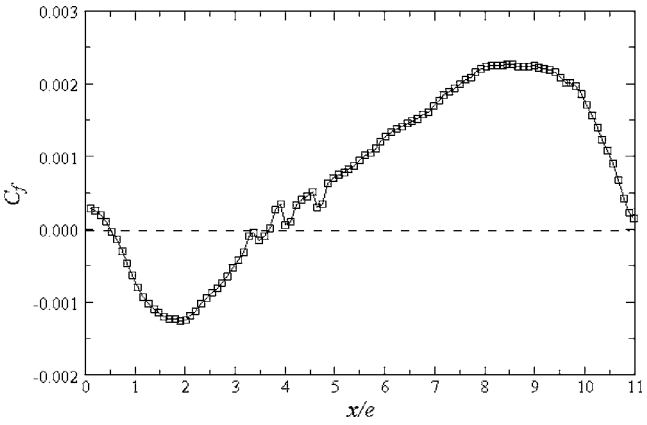

Fig. 4 Skin-friction coefficient along the ribbed wall

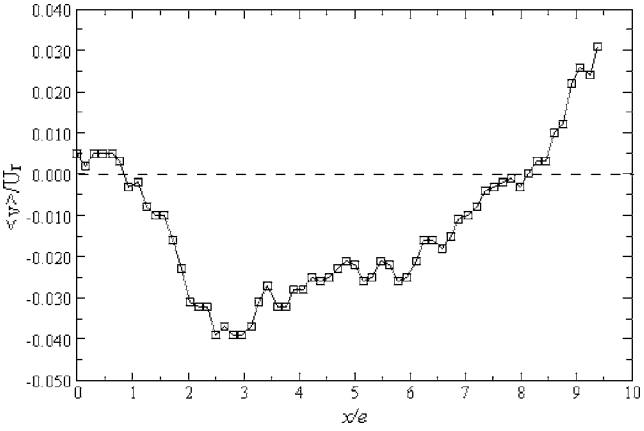

Fig. 6 Mean vertical velocity at $y/e=1.1$

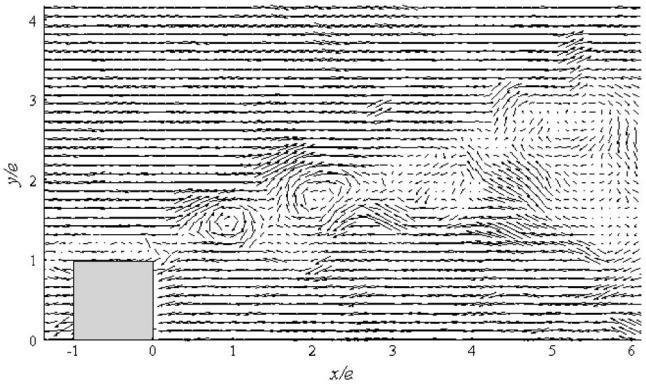

Fig. 7 Visualization of vortices; the reference frame velocity is U_f=5.0 m/s ($0.52U_r$)

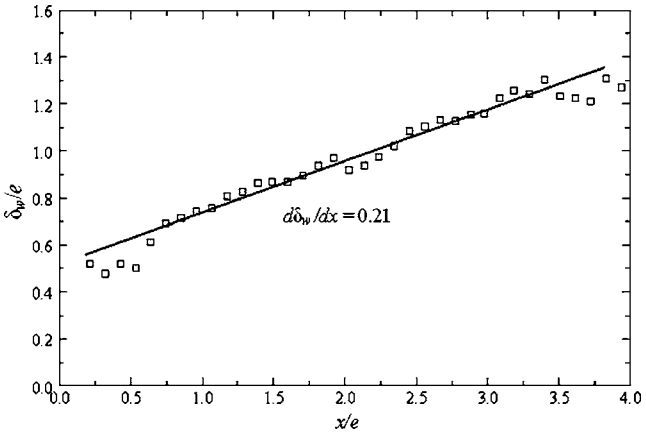

Fig. 9 Vorticity thickness growth along the separated shear layer

nizable as a roughly circular pattern. This method of visualization of structured, coherent elements embedded in the flow field is called Galilean decomposition [15].

Figure 7 shows an instantaneous velocity vector field in which the reference frame moves at U_f=5.0 m/s ($0.52U_r$). Figure 7 clearly displays two distinct vortices being shed downstream of the rib. The vortices have a size of the order of half a rib height and are inclined at approximately ~20 deg with respect to the x-axis. The visualization provides strong evidence that the separated shear layer is dominated by the large-scale energetic vortices, although no information is obtained on whether or not the vortices are uniform in the spanwise direction. In another instantaneous flow field plotted in Fig. 8, four vortices are seen, which are aligned nearly parallel to the ribbed wall except the one at x/e=3 that is slightly lower than the others. The reference frame velocity in Fig. 8 is U_f=3.7 m/s ($0.38U_r$). The lower part vortex at x/e=3 probably relates to the downwash motion of the shear layer that entrains the vortical structures towards the wall. In addition, it is found that the most downstream vortex in Fig. 8 extends to x/e=5.6, which is much larger than the time-mean reattachment length (X_r/e=3.6). However, the farthest downstream vortex in Fig. 7 just reaches to the location of x/e=2. This is probably associated with the growth and contraction of the separated region, commonly called "shear-layer flapping" [5].

To quantify the time-mean development of the separated shear layer, the growth of the shear layer is expressed by a measure called vorticity thickness δ_w. The vorticity thickness is defined as

$$\delta_w = \frac{u_2 - u_1}{(d\langle u\rangle/dy)_{\max}} \tag{1}$$

where $(d\langle u\rangle/dy)_{\max}$ is the maximum velocity gradient in the shear layer, and u_2 and u_1 are the speeds of the upper and lower streams in the mixing layer, respectively [16]. In this work u_2 is the bulk velocity above the top of a rib and u_1=0. Figure 9 shows the development of the vorticity thickness along the shear layer from the leading edge of the rib. The rate of growth is found to be linear, and the slope $d\delta_w/dx$ has a value of 0.21, which agrees well with the previous result of 0.18 for a single-stream mixing layer, for example [16].

3.3 Profiles of Turbulent Properties. In what follows, statistical properties associated with turbulence, such as Reynolds shear stresses, anisotropy parameters, and production of turbulent kinetic energy and Reynolds shear stress are presented and discussed in Figs. 10–14. These profiles provide information of the turbulence structure of nonequilibrium flow involving separation, reattachment, and subsequent redevelopment toward a turbulent boundary layer. Figure 10 presents the profiles of normalized turbulent Reynolds shear stresses at different streamwise locations. The position at x/e=0.1 is not included here because the high-velocity gradients very close to the rib wall give rise to considerable uncertainties to the results. As expected, all the shear stresses have a peak at certain distance from the surface. In the separation zone (x/e=2 and 3.6), the location of maximum shear stress is at y/e =1. In the post-reattachment region (x/e=6, 8, and 10), however, the peak moves progressively outward. Figure 11 shows the features of the maximum shear stress plotted against streamwise

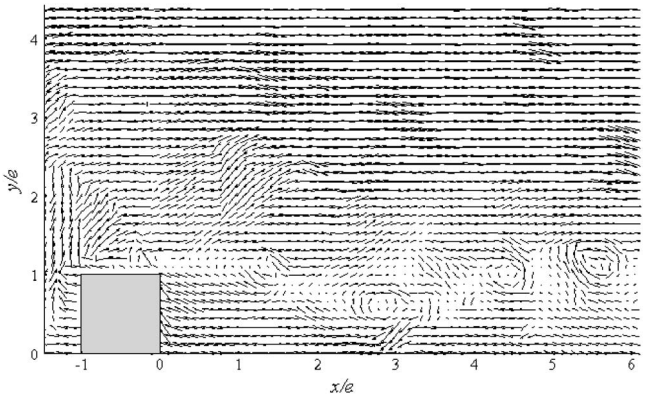

Fig. 8 Visualization of vortices; the reference frame velocity is U_f=3.7 m/s ($0.38U_r$)

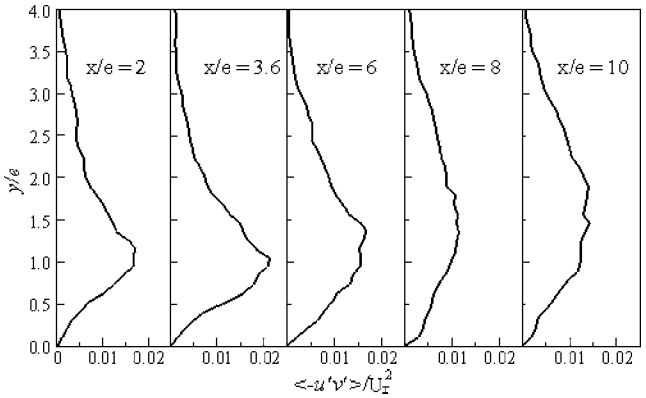

Fig. 10 Reynolds shear stress profiles

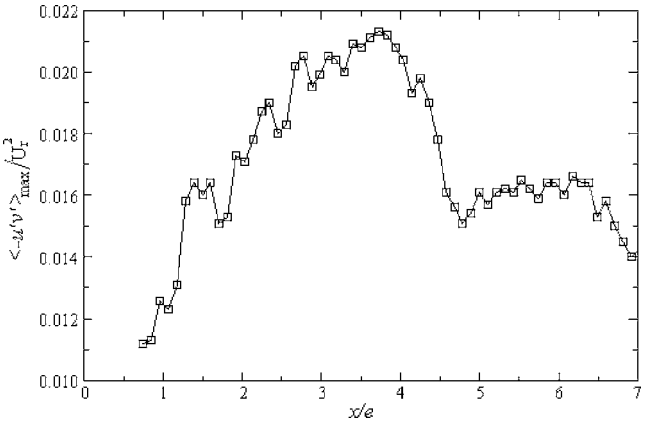

Fig. 11 Maximum shear stress distribution

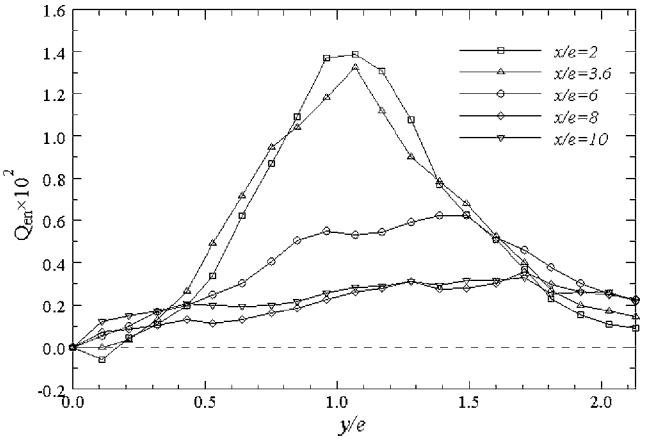

Fig. 13 Turbulent kinetic energy production

distance. The general level of the maximum shear stress rises gradually with increasing distance up to the reattachment point, and then decreases rapidly between $x/e=3.7$ and 4.7. Following the rapid decay after reattachment, a short plateau of constant maximum values is then observed in the region $5<x/e<6.5$. The rapid decrease of maximum turbulent shear stress just downstream of reattachment was also reported by other researchers. Bradshaw and Wong [1] attributed the decrease in shear stress to the supposed decrease in turbulence length scale. An alternative way of explaining the fall is provided by Chandrsuda and Bradshaw [17], who found the increase in energy dissipation leads to the sudden drop of shear stress. More recently, Bandyopadhyay [18] demonstrated via careful visualization studies that the longitudinal vortex pairs disintegrate quite rapidly beyond reattachment and small-scale motions quickly develop; it is this process giving rise to the sudden fall in the Reynolds stress.

The development of the anisotropy parameter, $\langle u'u'\rangle/\langle v'v'\rangle$, is shown in Fig. 12. The semi-logarithmic scale is employed to examine the inner-wall behavior. It is evident that the anisotropy parameter reaches a value of the order of 12 in the innermost wall region except near reattachment, where a sharp decrease ($\langle u'u'\rangle/\langle v'v'\rangle \approx 3$) is recognized. This phenomenon is probably associated with the singularity at the reattachment point, i.e., the normal velocity component $\langle v\rangle$ is of the nearly same order of magnitude as the streamwise component $\langle u\rangle$. The more isotropic turbulence near reattachment suggests that the two-component turbulent flow cannot be applied to represent the behavior of fluctuating velocities. Further away from the surface, for $y/e>1$, a moderate increase in the ratio $\langle u'u'\rangle/\langle v'v'\rangle$ is observed for all the streamwise positions.

Turbulent kinetic energy production $\mathbf{Q}_{en}$, expressed by $\mathbf{Q}_{en}=\langle -u'v'\rangle \partial\langle u\rangle/\partial y$, and Reynolds shear stress production $\mathbf{Q}_{ss}$, expressed by $\mathbf{Q}_{ss}=\langle v'v'\rangle \partial\langle u\rangle/\partial y$, are shown in Figs. 13 and 14, respectively. The quantities in both figures are normalized by U_r^3/e. It is evident that both the terms exhibit distinct peaks at $y/e=1$ for the region upstream of the reattachment point ($x/e=2$ and 3.6). Further inspection of the maximum turbulence production shows that the peak is approximately coincident with the inflection point ($d^2\langle u\rangle/dy^2=0$), that means, the velocity gradient $d\langle u\rangle/dy$ at the inflexion point plays a dominant role in the production of turbulence. Beyond reattachment, the maximum moves progressively outwards coupled with the reduction of its quantity, which is substantiated by the Reynolds shear stress displayed in Fig. 10. Furthermore, the near-wall turbulence features in the recirculation zone, for example, $x/e=2$, shows a sign reversal in the turbulence production for both kinetic energy and the shear stress. This fact indicates that the other contributions, such as the pressure strain, must outweigh the production term to maintain the turbulent kinetic energy and shear stress at a positive level.

Another fundamental test is to compute two-point correlations, which give an indication of the spatial structure of the flow. The size of the structures is roughly twice the distance between the origin and the point where the correlation coefficient levels off to zero. The two-point correlation coefficient is defined as

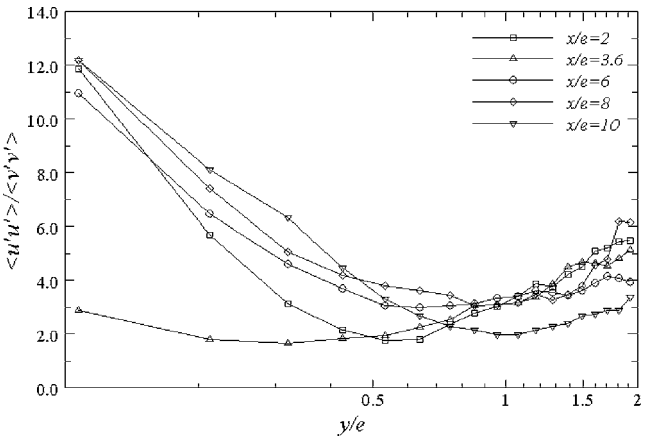

Fig. 12 Anisotropy parameter

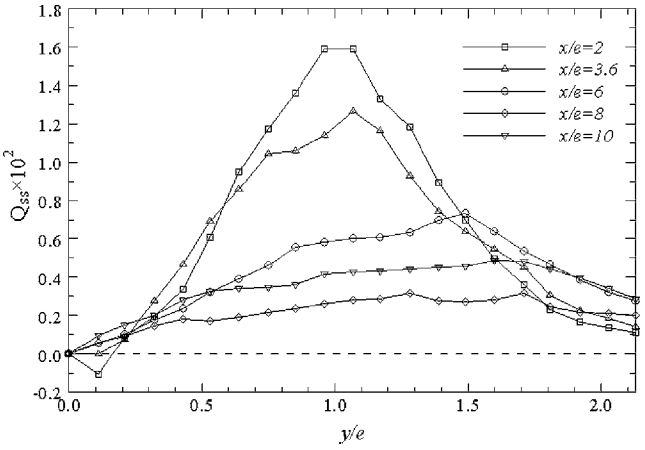

Fig. 14 Reynolds shear stress production

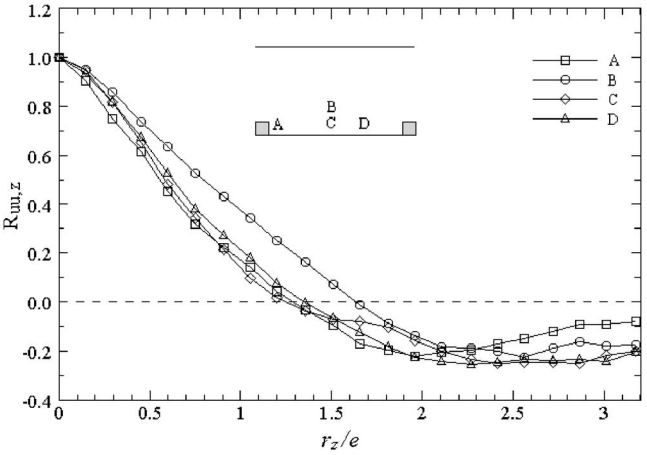

Fig. 15 Spanwise u' correlation coefficient at different points ($x/e, y/e$) in the flow field: A (0.5, 1), B (5.5, 2), C (5.5, 1), and D (8, 1)

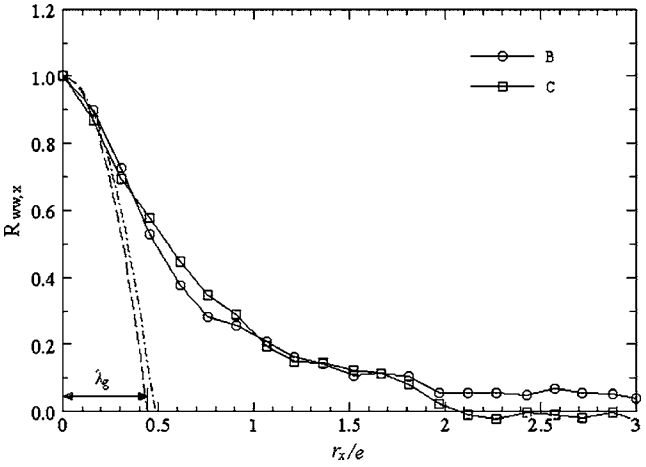

Fig. 17 Streamwise w' correlation coefficient

$$R_{u_i u_i, x_j} = \frac{\langle u_i'(x_{j0}) u_i'(x_j) \rangle}{\sqrt{\langle u_i'^2(x_{j0}) \rangle} \sqrt{\langle u_i'^2(x_j) \rangle}} \tag{2}$$

where u_i' is an instantaneous velocity fluctuation and x_{j0} is a fixed location. The distance between the two points is expressed by $r_{x_j} = x_j - x_{j0}$. Figure 15 shows the distribution of the streamwise velocity correlation $R_{uu,z}$ in the spanwise direction. Four points ($x/e, y/e$) in the symmetry plane ($z/W=0$) are selected as the origin, i.e., A (0.5, 1), B (5.5, 2), C (5.5, 1) and D (8, 1), respectively. Apart from point A, which is immediately downstream separation, the other three are located in the post-reattachment zone. Moreover, to examine the length scale for different heights, point B (at $y/e=2$) is placed above the others. It is apparent that all the points at $y/e=1$ show a similar size of the spanwise structures and the correlation virtually vanishes at $1.3e$. For point B, however, the correlation length is $\sim 1.7e$. In addition, it is noted that all the points demonstrate pronounced negative values down to −0.2 for large spanwise separation. This is likely caused by the streamwise vortices which are inclined in the vertical direction [7]. From Fig. 15, it is hard to figure out the largest scales because the correlation does not vanish for all points within $r_z = 3.2e$, which is half the width of the channel.

In what follows, the longitudinal two-point correlations $R_{uu,x}$ and lateral two-point correlations $R_{ww,x}$ will be exhibited. The principal direction is along the x-axis. For clarity, points B and C are chosen as the origin, respectively. The profiles of $R_{uu,x}$ are shown in Fig. 16, in which u' displays considerable coherence over a streamwise distance of more than half of the inter-rib spacing. Moreover, the coherence increases with wall distance ($y/e > 1$). As the correlation coefficient is down to 0.2, $r_x/e = 5.5$, and 3.8 for points B and C, respectively. The large longitudinal correlation length indicates that the fluctuations u' are mainly produced by the large-scale, inactive motions, as suggested by Townsend [19]. Figure 17 shows the distribution of $R_{ww,x}$. The lateral correlation length is substantially shorter than that of the longitudinal counterpart, as revealed by the faster decay near the origin. For both points, the correlation coefficients virtually level off to zero at $r_x/e = 2$. Unlike the development of $R_{uu,z}$, no obvious negative values are discerned in $R_{ww,x}$ which otherwise is exactly identical with $R_{uu,z}$ under the circumstance of isotropic turbulence. Based on the profiles correlation, Taylor's longitudinal microscales λ_f and lateral microscales λ_g are derived, respectively. λ_f and λ_g are defined as

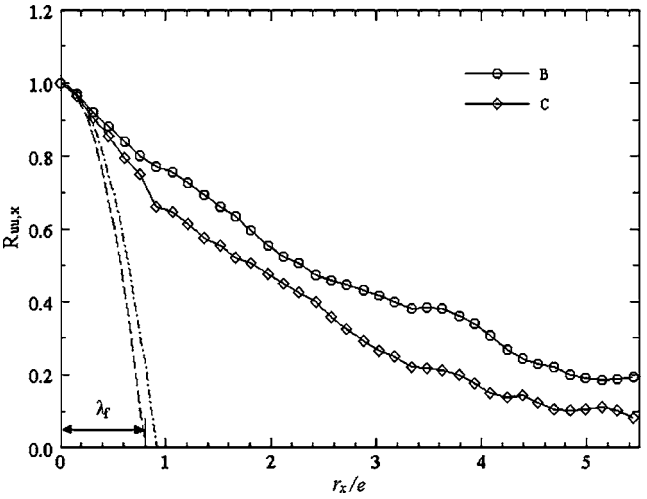

Fig. 16 Streamwise u' correlation coefficient

$$R_{uu,x} = 1 - \frac{x^2}{\lambda_f^2} \tag{3}$$

$$R_{ww,x} = 1 - \frac{x^2}{\lambda_g^2} \tag{4}$$

Equation (3) or (4) defines a parabola with vertex at the point $x = 0$, where it osculates the correlation curve, λ_f or λ_g is obtained from the intersection of the parabola with the x-axis. The results are illustrated in Table 1. It is clear that the both microscales at the plane $y/e=2$ are larger than that at $y/e=1$. For isotropic turbulence, the relation between λ_f and λ_g is represented by $\lambda_f = \sqrt{2}\lambda_g$. In the present case, the remarkable deviation of ratio λ_f/λ_g from $\sqrt{2}$ suggests that the local turbulence is far from isotropic. Furthermore, the increase of λ_f/λ_g for $y/e > 1$ implies that the local turbulence becomes more anisotropic. This phenomenon is also borne out by the rise of anisotropy parameters, as shown in Fig. 13.

Table 1 Taylor's microscales

y/e	λ_f/e	λ_g/e	λ_f/λ_g
1	0.80	0.44	1.82
2	0.91	0.48	1.90

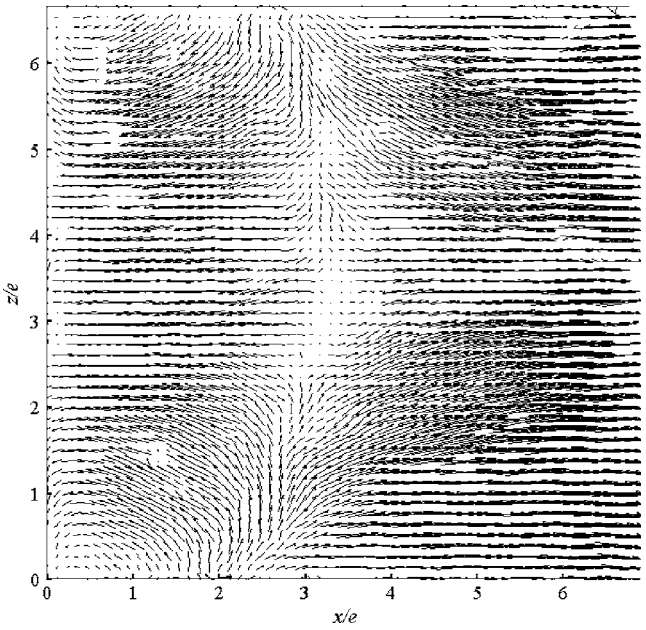

Fig. 18 Mean velocity vector plot near the ribbed wall

3.4 Flow Fields in Horizontal Planes. The mean velocity vectors in a plane very close to the ribbed wall ($y \approx 1$ mm) is plotted in Fig. 18, in which the spanwise reverse flow associated with a curved reattachment line is clearly observed. In addition, the corner eddy on each side just downstream the rib is shown in Fig. 18. Based on these data, the mean reattachment length X_r is determined by the location at which the mean velocity $\langle u \rangle$ is zero. According to Fig. 19, the reattachment length is ~3.5 rib heights on the centerline, which is in agreement with the result in Fig. 5. However, the curvature of the reattachment line is not exactly symmetrical in the spanwise direction.

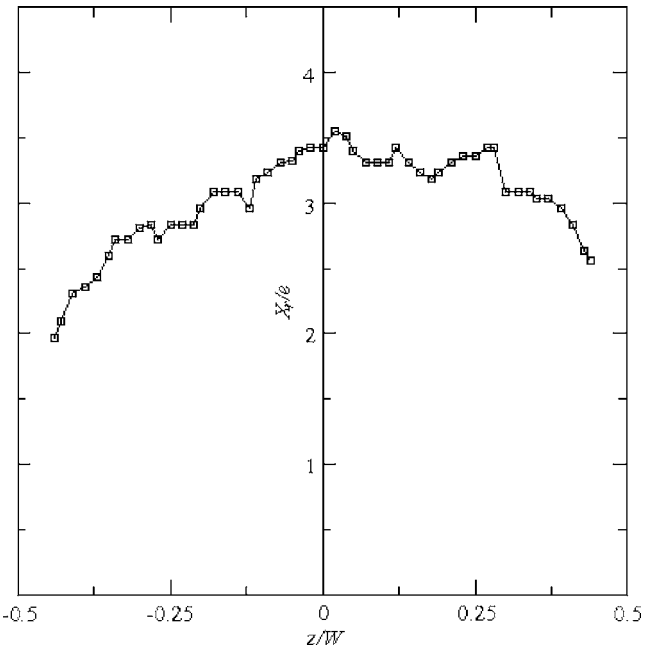

Fig. 19 Mean reattachment length in the spanwise direction

4 Conclusions

The present study examines experimentally the flow structures and turbulent properties associated with the flow separation in a square, ribbed channel by using PIV. The Reynolds number, based on the bulk-mean velocity and the channel hydraulic diameter, is fixed at 22,000. The ribs obstruct the channel by 15% of its height and are arranged 12 rib heights apart. Because of the flow periodicity, the investigated domain ranges from the sixth to seventh ribs. Two-dimensional velocity measurements are made in the vertical symmetry plane as well as the horizontal planes, respectively.

The instantaneous velocity gives evidence that the separated shear layer is dominated by the coherent vortices which are generated by the Kelvin-Helmholtz instability. Similar to the plane mixing layers, the growth rate of the separated shear layer is linear with respect to the streamwise direction. Moreover, it is noted that the turbulence production, for both turbulent kinetic energy and shear stress, has a remarkable peak at $y/e=1$, which is approximately coincident with the inflection point $d^2\langle u \rangle/dy^2=0$.

Two distinct features near reattachment are characterized in the present study. First, the maximum shear stresses decrease rapidly just downstream of the reattachment. Second, the anisotropy parameters deviate to a small extent from unity at reattachment. Further downstream of the reattachment, the acceleration in the inner part coupled with deceleration in the outer part makes the redevelopment of the boundary layer different from the behaviour of an equilibrium boundary layer.

Two-point correlation profiles give the spatial structure of the flow. The profiles of $R_{uu,z}$ at different positions display the pronounced negative values in the spanwise direction. However, such a phenomenon is not observed in the lateral correlation $R_{ww,x}$. Finally, it is found that the Taylor lateral microscales λ_g, derived from the profiles of $R_{ww,x}$, are of the order of half a rib height.

Acknowledgment

The current research is financially supported by the Swedish National Energy Agency (STEM) and Swedish Research Council (VR).

Nomenclature

C_f = skin-friction coefficient
D_h = hydraulic diameter of the channel
e = rib height
H = height of the channel
P = rib pitch
$\mathbf{Q}_{en}$ = production of turbulent kinetic energy
$\mathbf{Q}_{ss}$ = production of Reynolds shear stress
$R_{uu,x}$ = streamwise u' correlation coefficient
$R_{uu,z}$ = spanwise u' correlation coefficient
$R_{ww,x}$ = streamwise w' correlation coefficient
$\langle u \rangle$ = mean streamwise velocity
u' = instantaneous fluctuation of streamwise velocity
U_0 = bulk-mean velocity in the smooth channel
U_f = reference frame velocity
U_r = scaling velocity
$\langle -u'v' \rangle$ = Reynolds shear stress
$\langle v \rangle$ = mean vertical velocity
v' = instantaneous fluctuation of vertical velocity
w' = instantaneous fluctuation of spanwise velocity
x = streamwise direction
Xr = reattachment length
y = vertical direction
z = spanwise direction
δ_w = vorticity thickness
λ_f = Taylor's longitudinal microscale
λ_g = Taylor's lateral microscale

References

[1] Bradshaw, P., and Wong, F. Y. F., 1972, "The Reattachment and Relaxation of a Turbulent Shear Layer," J. Fluid Mech., **52**, pp. 113–135.

[2] Troutt, T. R., Scheelke, B., and Norman, T. R., 1984, "Organized Structures in a Reattaching Separated Flow Field," J. Fluid Mech., **143**, pp. 413–427.

[3] Ruderich, R., and Fernholz, H. H., 1986, "An Experimental Investigation of a Turbulent Shear Flow With Separation, Reverse Flow, and Reattachment," J. Fluid Mech., **163**, pp. 283–322.

[4] Castro, I. P., and Haque, A., 1987, "The Structure of a Turbulent Shear Layer Bounding a Separation Region," J. Fluid Mech., **179**, pp. 439–468.

[5] Hasan, M. A. Z., 1992, "The Flow Over a Backward Facing Step Under Controlled Perturbation: Laminar Separation," J. Fluid Mech., **238**, pp. 73–96.

[6] Le, H., Moin, P., and Kim, J., 1997, "Direct Numerical Simulation of Turbulent Flow Over a Backward-Facing Step," J. Fluid Mech., **330**, pp. 349–374.

[7] Fröhlich, J., Mellen, C. P., Rodi, W., Temmerman, L., and Leschziner, M. A., 2005, "Highly Resolved Large-Eddy Simulation of Separated Flow in a Channel With Streamwise Periodic Constrictions," J. Fluid Mech., **526**, pp. 19–66.

[8] Miyake, Y., Tsujimoto, K., and Nagai, N., 2002, "Numerical Simulation of Channel Flow With a Rib-Roughened Wall," J. Turbul., **3**, pp. 1–17.

[9] Cui, J., Patel, V. C., and Lin, C. L., 2003, "Large-Eddy Simulation of Turbulent Flow in a Channel With Rib Roughness," Int. J. Heat Fluid Flow, **24**, pp. 372–388.

[10] Nagano, Y., Hattori, H., and Houra, T., 2004, "DNS of Velocity and Thermal Fields in Turbulent Channel Flow With Transverse-Rib Roughness," Int. J. Heat Fluid Flow, **25**, pp. 393–403.

[11] Leonardi, S., Orlandi, P., Djenidi, L., and Antonia, R. A., 2004, "Structure of Turbulent Channel With Square Bars on One Wall," Int. J. Heat Fluid Flow, **25**, pp. 384–392.

[12] Islam, M. S., Haga, K., Kaminaga, M., Hino, R., and Monde, M., 2002, "Experimental Analysis of Turbulent Flow Structure in a Fully Developed Rib-Roughened Rectangular Channel With PIV," Exp. Fluids, **33**, pp. 296–306.

[13] Gao, X., 2002, "Heat Transfer and Fluid Flow Investigations in Ribbed Ducts and Impinging Jets Using Liquid Crystal Thermography and PIV," Ph.D. thesis, Division of Heat Transfer, Department of Energy Sciences, Lund Institute of Technology, Lund, Sweden.

[14] Wang, L., and Sundén, B., 2005, "Experimental Investigation of Local Heat Transfer in a Square Duct With Continuous and Truncated Ribs," Exp. Heat Transfer, **18**, pp. 179–197.

[15] Adrian, R. J., Christensen, K. T., and Liu, Z.-C., 2000, "Analysis and Interpretation of Instantaneous Turbulent Velocity Fields," Exp. Fluids, **29**, pp. 2756–290.

[16] Brown, G. L., and Roshko, A., 1974, "On Density Effects and Large Structure in Turbulent Mixing Layers," J. Fluid Mech., **64**, pp. 775–816.

[17] Chandrsuda, C., and Bradshaw, P., 1981, "Turbulence Structure of a Reattaching Mixing Layer," J. Fluid Mech., **110**, pp. 171–194.

[18] Bandyopadhyay, P. R., 1989, "Instabilities and Large Structures in Reattaching Boundary Layers," AIAA J., **29**, pp. 1149–1155.

[19] Townsend, A. A., 1961, "Equilibrium Layers and Wall Turbulence," J. Fluid Mech., **11**, pp. 97–120.

Turbulent Jet Mixing Enhancement and Control Using Self-Excited Nozzles

Uri Vandsburger
Department of Mechanical Engineering,
Virginia Polytechnic Institute and State University,
Blacksburg, VA 24061

Yiqing Yuan
Department of Powertrain Virtual Simulation,
Advanced Vehicle Engineering,
CIMS 484-01-13,
DaimlerChrysler Corporation,
Auburn Hills, MI 48326-2757

A new self-excited jet methodology was developed for the mixing enhancement of jet fluid with its surrounding, quiescent, stagnant, or coflowing fluid. The nozzles, of a square or rectangular cross section, featured two flexible side walls that could go into aerodynamically-induced vibration. The mixing of nozzle fluid was measured using planar laser-induced fluorescence (PLIF) from acetone seeded into the nozzle fluid. Overall, the self-excited jet showed enhanced mixing with the ambient fluid; for example, at 390 Hz *excitation a mixing rate enhancement of 400% at* $x/D=4$ *and 200% at* $x/D=20$ *over the unexcited jet. The mixing rate was sensitive to the excitation frequency, increasing by 60% with the frequency changing from 200 to* 390 Hz *(corresponding to a Strouhal number from 0.052 to 0.1). It was also observed that the mixing rate increased with the coflow velocity. To explain the observed mixing enhancement, the flow field was studied in detail using four-element hot wire probes. This led to the observation of two pairs of counter rotating large-scale streamwise vortices as the dominant structures in the excited flow. Shedding right from the nozzle exit, these inviscid vortices provided a rapid transport of the momentum and mass between the jet and the surrounding fluid at a length scale comparable to half-nozzle diameter. Moreover, the excited jet gained as much as six times the turbulent kinetic energy at the nozzle exit over the unexcited jet. Most of the turbulent kinetic energy is concentrated within five diameters from the nozzle exit, distributed across the entire jet width, explaining the increased mixing in the near field.* [DOI: 10.1115/1.2745840]

Introduction

Rapid mixing is the key to efficient and environment-friendly operation of many industrial and propulsion devices involving jet flows. In particular, driven by increasingly stringent regulations on emissions, the recent development of lean premixed combustion technology calls for improved mixing of fuel and air within the combustor, and of combustion products and dilution air at the combustor exit.

Since the early 1970s, a variety of jet control methods have been developed to enable predefined or interactive manipulation of the mixing process. Due to the Kelvin-Helmholtz instability, the shear layer of a jet rolls up naturally into periodic vortex rings, and then stretches into large-scale structures (vortices). These vortices pair and break down in a semi-organized fashion in an unexcited jet, while they can be strengthened and stabilized by periodic stimulation. For instance, Binder and Favre-Marinet [1] found that the jet spreading rate was increased by introducing velocity pulsation to the upstream of a nozzle with a spinning butterfly valve. Curtet and Girard [2] used an oscillating piston upstream of the nozzle exit to induce fluctuations in jet velocity. Zaman and Hussain [3] demonstrated that the formation and subsequent pairing of the vortices could be controlled by proper periodic stimulation. Single frequency forcing was also employed by Bouchard and Reynolds [4] to control jet growth by either enhancing or suppressing vortex pairing. These widely studied single-frequency modulation methods excite the jet column instability; i.e., preferred mode. Dual-frequency excitation was also proposed. For example, Lee and Reynolds [5] properly combined axial and azimuthal modes to alter the structure and momentum transport of round jets. The increase of spreading rates using noncircular jets, such as triangular jets of Gutmark et al. [6] and elliptical jets of Ho and Gutmark [7], were investigated. When the ratio of axial to transverse excitation frequencies was two, jets were bifurcated into two distinct jets and the spreading angle was increased dramatically with excitation amplitude, according to Parekh et al. [8]. Juvet and Reynolds [9] showed that the entrainment was increased significantly when the ratio of axial to helical excitation frequencies was a noninteger. However, frequency modulation was observed to be ineffective in the far field due to phase decorrelation. Since jet flow was found unstable to various spatial instability modes as reported by Batchelor and Gill [10], Plaschko [11], and Yoda [12], azimuthal mode modulation emerged as a better control strategy for far-field mixing. The seminal work in this area was done by the group of Wygnanski; e.g., Cohen and Wygnanski [13,14], who measured and modeled the jet evolution for single and multiple spatial mode excitations. The spreading rate and direction of isovelocity contours in the far field were found controllable with spatial mode excitations, as shown by Vandsburger and Ding [15]. Known as dynamic mode control, phase modulation and switching modulation were proposed by Ding [16] to eliminate phase decorrelation. More recently, Wiltse and Glezer [17] proposed direct excitation of the small scales within the dissipation range of free shear flows with a frequency that is an order of magnitude lower than the passage frequency of the Kolmogorov scale.

The technical implementation of these methods is subject to the gain in mixing rate and the cost in energy required to achieve the mixing enhancement. Based on shear flow instabilities, these methods may lose effectiveness to a certain degree within practical combustors where high coflow and swirl are present since the growth rate of instabilities is adversely affected by the decrease in velocity gradient between the jet and coflow. The near-field mixing performance of these methods is another issue because it generally takes a few nozzle diameters of distance for the small instability vortices to grow into large-scale structures.

A multifaceted study of the enhancement of jet and surrounding fluid mixing has been executed in the Reacting Flows Laboratory

Contributed by the Fluids Engineering Division of ASME for publication in the JOURNAL OF FLUIDS ENGINEERING. Manuscript received September 13, 2006; final manuscript received January 3, 2007. Assoc. Editor: Juergen Kompenhans.

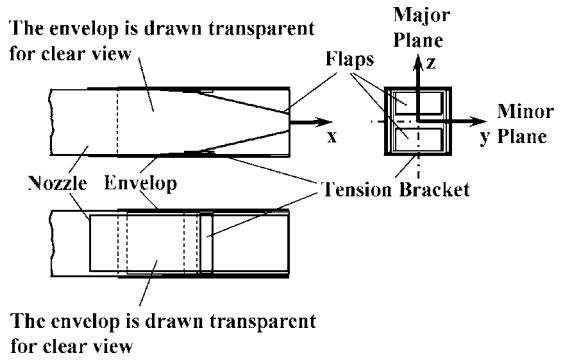

Fig. 1 Schematic of the self-excited nozzle

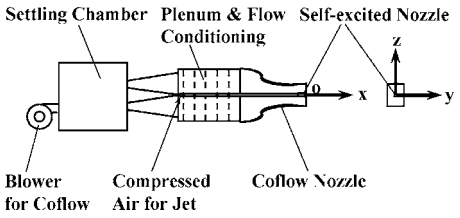

Fig. 2 Test tunnel and the coordinate system

at Virginia Tech, motivated by the drive towards lean premixed combustion, for the purpose of lowering pollutant emissions. For this application, the search is for improved fuel-air mixing, and combustion products and dilution-air mixing. While several methods have been developed in the 1990s, active and passive, one of the tests for possible technical implementation is the cost in energy (and therefore the efficiency penalty) required to achieve this mixing enhancement.

Thus, the objectives of this study were as follows:

- Develop a feasible actuation methodology to further improve jet mixing while minimizing required energy input;
- Quantitatively evaluate the mixing rate of the excited jet;
- Clarify flow dynamic mechanisms responsible for the enhanced mixing;
- Examine the effects of major geometric and operating conditions on mixing characteristics.

Motivated by these practical engineering concerns, the impetus for a new category of mixing control methodologies has been established. These devices should make use of inviscid flow dynamics of the whole jet body. As an example, from a companion study reported earlier by Yuan and Vandsburger [18] and Yuan [19], a 200–300% mixing rate enhancement over a conical nozzle in the near field has been achieved with a radially lobed nozzle. This is driven by a pair of large-scale, counter-rotating, streamwise vortices shedding right from the nozzle exit plane.

In the present paper, a study of self-excited nozzle characteristics is discussed. Self-excitation is not a novel concept in the study of mixing layers and jets. For instance, a vibrating ribbon was used by Schubauer and Skramstad [20] to excite Tollmien-Schlichting (T-S) waves across a span of a flat-plate boundary layer over half a century ago. The two-dimensional instability modes in a planar mixing layer shedding from a small oscillation spanwise flap mounted at the trailing edge of the flow partition was studied by Oster and Wygnanski [21]. A self-excited circular whistling nozzle was first reported by Hill and Greene [22], and a self-excited elliptic whistler nozzle was also studied by Husain and Hussain [23]. Nevertheless, these studies were fundamentally different from the self-excited nozzles addressed here in both the configuration and self-excitation mechanism.

Technical Approach

A new self-excited jet methodology was tested for the enhancement of jet fluid mixing with its surrounding fluid, either stagnant or coflowing. The nozzles had a square or rectangular cross section, and key features were the flexibility of the two side walls, as shown in Fig. 1, and the ability to control the excitation frequency.

The self-excited nozzles were made from square and rectangular brass tubes, with two sides replaced by polyethylene or stainless steel shim stock. These two free sides became excited upon the occurrence of jet flow. Within a range of flow rates, a stable and harmonic vibration can be attained, manifested by a pure tone. The vibration frequency depends on the geometric dimensions of the flaps such as length, width, and thickness, the density of the flap material, the elasticity of the flaps in its normal direction, the geometric dimensions of the nozzle, and the density and velocity of the jet and coflowing fluids. The most convenient way to control the frequency is by moving a tension bracket along the nozzle axis, which alters the effective length of the flaps. For given nozzle geometry and flow conditions, as the bracket is moved downstream, the effective length of the flaps is reduced and the frequency increases, and vice versa. The amplitude, however, is restricted by the nozzle walls and therefore remained identical during the tests. Since the vibrating flaps are typically in phase, the amplitude is half of the nozzle height. Although the nozzle can be made partially modulated, i.e., partially closed and opened periodically; the present study only deals with fully modulated nozzles; i.e., completely closed and then completely opened periodically. Note that for the self-excitation to occur, the flap tips are not necessarily flush with the nozzle exit. When they extend out from the nozzle, the amplitude can become larger than the nozzle height and the flaps can easily get fractured. Thus, the flaps were mounted flush with nozzle exit in the present study.

Two square nozzles, one 11.3 mm by 11.3 mm and the other 8.1 mm by 8.1 mm, along with two rectangular nozzles, were studied. The rectangular nozzles had a 1:2.52 and 1:4.72 height-to-width aspect ratio, with an exit area identical to that of the smaller square nozzle. The self-excitation frequency of these nozzles could be adjusted in the range of 200 Hz to 2000 Hz.

Experimental and Analytical Methods

The jet fluid mixing was studied both qualitatively and quantitatively, by means of flow visualization, and detailed mapping of the velocity and nozzle fluid concentrations, respectively. The jet mass transfer and mixing were quantified via an entrainment ratio and a mixing parameter. Proposed mechanisms for the observed mixing enhancement are based on detailed structural and spectral analysis of the flow field.

Jet Facilities. The experiments were conducted in a wind tunnel that generated a jet in a coflow, as shown in Fig. 2. In most cases, a square self-excited nozzle was tested at a Reynolds number of 31,000, based on the hydraulic diameter of the nozzles and the average jet exit velocity. Three nozzles of aspect ratios 1:1, 1:2.52, and 1:4.72 were tested at Reynolds numbers of 17,000 and 10,000. During the experiments, the jet exit mass flow rates were kept identical in order to enable comparisons among nozzles under various conditions.

Data Acquisition and Reduction. The concentration field of nozzle fluid was measured using planar laser-induced fluorescence (PLIF) from acetone with the experimental setup shown in Fig. 3. A pulsed XeCl excimer laser (wavelength 308 nm, 40–60 mJ per pulse, pulse duration 12 ns) was used as the light source, and the laser beam was formed into a sheet approximately 0.8 mm thick at the waist using three UV grade cylindrical lenses. The jet was seeded with acetone (CH_3-CO-CH_3) as molecular tracer with a mole fraction of around 1%. Since the optical depth of the acetone seeded flow was about 170 cm and the typical width of the jet flow was of the order of 10 cm, the medium was considered op-

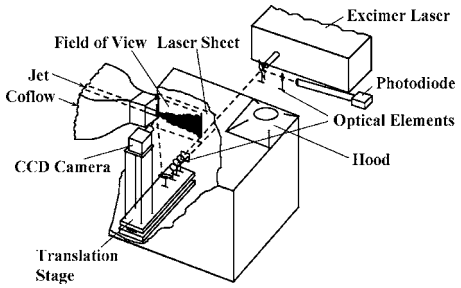

Fig. 3 PLIF experimental setup for nozzle fluid concentration measurements

tically thin and the light absorption was negligible. A gated, intensified CCD (ICCD) camera of 640×480 active pixel elements was used to acquire the images. In the experiments, 50 frames were collected to form an averaged raw image in every transverse plane. Various corrections were applied to the data of raw images. These included background signal, laser intensity distribution, and camera pixel-to-pixel variation images. The corrections followed the procedures outlined in van Cruyningen et al. [24].

For phase-locked data collection, the pure tone generated by the vibrating flaps was detected by a microphone. The signal was band filtered and amplified by electronic circuits and then used for triggering the excimer laser, the ICCD camera, and the data acquisition board.

The velocity field was measured using a four-sensor hot-wire anemometer system consisting of an Auspex Model AVOP-4-100 probe and an AA Lab Systems Model AN-1003 anemometer. The probe was mounted on a computer controlled 3-D traverse stage. The method described in Wittmer [25] was used for the calibration of the probe and the conversion of voltage data into velocity data.

Analysis of Data. A mixing index was developed for quantifying the mixing rate of free jets issuing from the different nozzles.

The spatial unmixedness employed by Vranos et al. [26] and Liscinsky et al. [27] requires a fully mixed mass fraction, which is only available in the case that mass is conserved in a confined volume, e.g., in the case of ducted jet flows, or in the case that the amount of mass moving out of the confined volume is known. Nevertheless, for a free jet, the concentration decays toward zero instead of a certain value at the end of mixing. This very fact that the lack of a perfectly mixed concentration makes their parameter not applicable for free jets. Therefore, a mixing index $I_m(x)$ was defined as follows

$$I_m(x) \equiv \frac{\bar{C}_{\text{avg}}(x)}{\bar{C}_{\text{var}}(x)} \tag{1}$$

where $\bar{C}_{\text{avg}}(x)$is the normalized mean concentration over all points within the calculation domain A_1 at a downstream station x, as shown in Fig. 4. A_1 is so determined that within this domain the integrated mass of tracer at all downstream stations is equal to that at the first station, i.e., nozzle exit. $\bar{C}_{\text{var}}(x)$ is the normalized concentration variation over all points in the calculation domain A_2 at a downstream station x. A_2 is a circular domain of a diameter that is three times the hydraulic diameter of the nozzle. Note that the C_{avg} denotes different quantities in the following formulas:

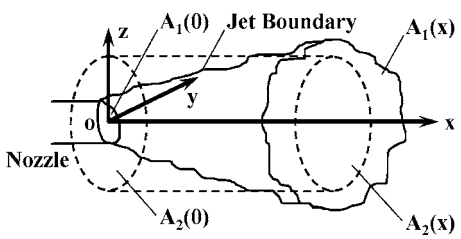

Fig. 4 Domains for the definition of the mixing index

$$\bar{C}_{\text{avg}}(x) = [C^{A1}_{\text{avg}}(0) - C^{A1}_{\text{avg}}(x)]/C^{A1}_{\text{avg}}(0) \tag{2}$$

$$\bar{C}_{\text{var}}(x) = C^{A2}_{\text{rms}}(x)/C^{A2}_{\text{avg}}(x) \tag{3}$$

The larger the mixing index, the higher the ability the nozzle has to transfer the jet fluid from the centerline and distribute it uniformly in the space; i.e., the better mixing performance.

Results and Discussion

First, the concentration field of the self-excited jet is examined quantitatively to evaluate the mixing process. This is followed by a detailed discussion of the corresponding velocity field to clarify the fluid mechanics underlying the enhanced mixing.

Concentration Field. The spreading angle and length of potential core of a jet are direct measures of the momentum and mass transfer processes. These characteristics are examined first qualitatively by comparing the concentration field of the self-excited jet to the unexcited jet from the same nozzle, followed by a discussion of the mixing rate using the index defined above. The effects of excitation frequency, coflow, and nozzle aspect ratio are also addressed. In general, the initial condition of the jet and coflow is depicted with the momentum-flux ratio

$$\lambda_e = \left(\frac{\rho_c U_c^2}{\rho_j U_j^2}\right)^{1/2} \tag{4}$$

In this study, since the jet and coflow fluids are both air, λ_e is reduced to velocity ratio λ:

$$\lambda = \frac{U_c}{U_j} \tag{5}$$

The side view of the major plane in which the flaps vibrate and the end view of the time-mean concentration fields of the unexcited and excited jets for coflow-to-jet velocity ratio $\lambda=0$ and 0.3 are shown in Fig. 5. With coflow, the unmixed jet fluid core ends at $x/D=10$ for the unexcited jet (c), while it ends at $x/D=1$ for the excited jet (d). Without coflow, the unmixed jet fluid core extends to $x/D=8$ for the unexcited jet (a), compared to $x/D=2$ for the excited jet (b). The substantially shortened core of the jet is strong evidence of enhanced mixing. This is one of the features that distinguishes the self-excited nozzles from other jet instability based mixing control methods. A typical instability based mixing control involves introduction of small perturbation near the nozzle exit. In general, the excited instabilities take several diameters of downstream distance to grow into structures that are large enough to reshape the jet column and jet core. Therefore, the jet core is usually much longer than that in the self-excited jet. Also noticeable is the large expansion angle of the excited jet in the major plane, indicative of improved mass transfer of jet fluid off the jet axis. It is observed that the jet fluid mixing with the surroundings increases with coflow for the self-excited nozzle, while it decreases for the unexcited nozzle. This is explainable through the different mechanisms involved; that is, shear layer growth for the unexcited nozzle versus vectoring of the flows for the self-excited nozzle. In a natural rectangular jet, the fluid motion is parallel to the jet axis near the nozzle exit. On the contrary, the vibration of the flaps can cause the jet fluid moving outward in the spanwise direction off the jet axis, i.e., vectoring. This phenomenon and its mechanism will be discussed further in the following text.

Compared to the sharp boundary of the unexcited jet, the boundary of the excited jet gets blurred after $x/D=10$, as shown in Figs. 5(b) and 5(d). In fact, the streamwise decay of jet fluid concentration in the excited jet is much faster than that in the unexcited jet, which is direct evidence of enhanced mixing. Under

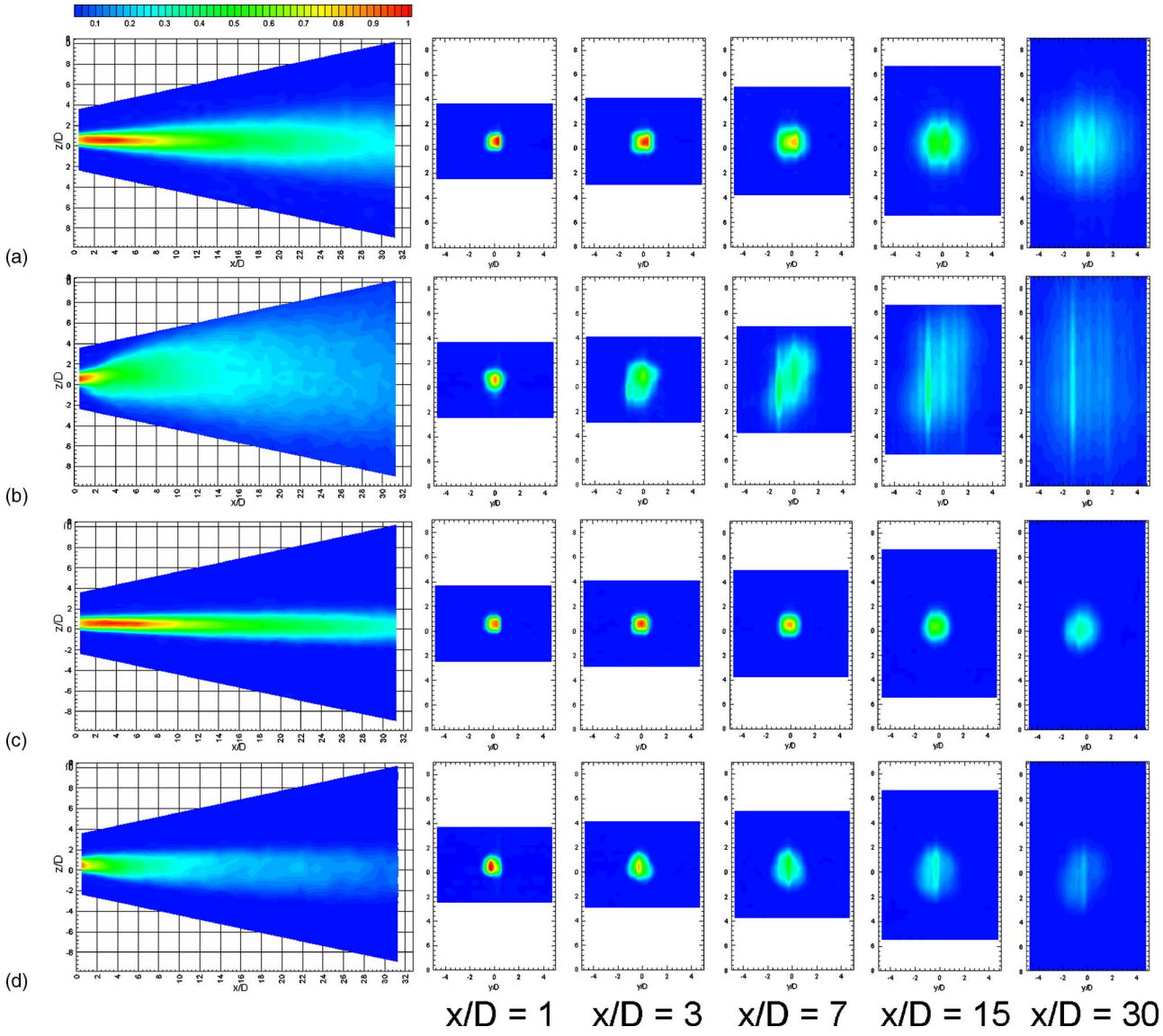

Fig. 5 Concentration maps for a square nozzle; Re=17,000, St=0.12; (*a*) Unexcited, λ=0; (*b*). Excited, λ=0; (*c*). Unexcited, λ=0.3; (*d*). Excited, λ=0.3.

excitation, the jet expands significantly in the major plane, with no visible change in the minor plane compared to the unexcited jet. In the presence of coflow, the visible part of the concentration contours shrinks as the coflow velocity increases, regardless of the existence of excitation. However, the jet fluid is spread into a larger cross-sectional area with lower concentration for the excited jet than the unexcited jet.

With the specific geometry of the nozzle and the flaps used in our experiments, the excitation frequency could vary in a range from 200 Hz to 2000 Hz by adjusting the tension bracket. The mixing enhancement through excitation is shown in Fig. 6. Compared with the unexcited jet (f_e=0 Hz), the mixing index of the excited jet increases by up to 400% at x/D=4, and 200% at x/D=20. Also noticeable is that for the excited jet, the mixing index increases sharply from nozzle exit to x/D=4, while for the unexcited jet, the mixing index increases almost linearly in the near field. Clearly, the sharply increased mixing rate in the near field of the excited jet explains the drastic reduction of the mean concentration in this area observed earlier in concentration contours. Farther downstream, beyond x/D=14 in the excited jet, there is another dramatic increase in mixing index, which appears to be a result of the mixing transition that causes the nonuniformity of the jet fluid to decrease even in the molecular level.

The sensitivity of the mixing rate to the excitation frequency is shown in Fig. 6 as well. For example, when λ=0.058, as excitation frequency increases from 200 Hz to 390 Hz, i.e., St=0.052 (dotted lines) to 0.1, the mixing index increases from 0.8 to 1.3 at x/D=20, which is an increase over 60%; when λ=0.23, the mixing index increases from 1.09 to 1.9 at x/D=20, an increase of about 75%. This is due to a larger amount of kinetic energy delivered by the flaps into the flow at higher frequencies.

The mixing rate was observed to increase with the coflow velocity. For instance, as velocity ratio increases from 0.058 to 0.23, the mixing index increases from 0.37 to 0.77 at x/D=8 for the jet excited at 390 Hz, i.e., St=0.1 (dashed lines), which is an increase over 100%; at x/D=20, the mixing index increases from 1.3 to 1.9, an increase of about 50%.

After noticing the effect of self-excitation on jet mixing, the potential benefit of an asymmetric nozzle cross section was examined. This was partly motivated by the multiple scales existing in elliptic nozzles. An examination of rectangular nozzles showed that they do not offer any advantages over the square nozzle, as seen in Fig. 7. The mixing rate of the square nozzle was the highest among the three tested nozzles, while the mixing rate of

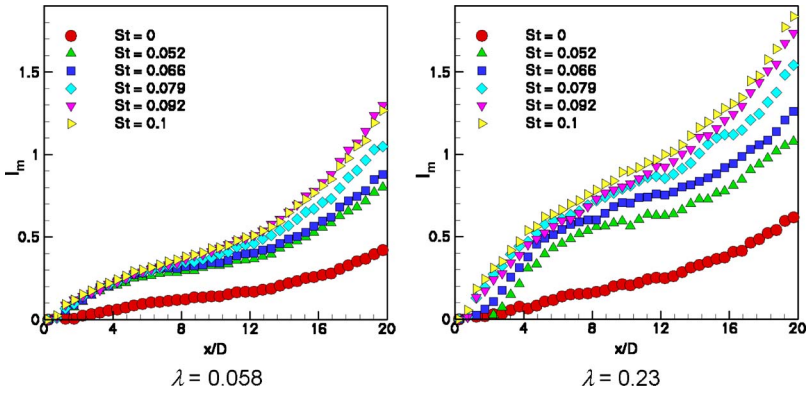

Fig. 6 Mixing index of a self-excited square nozzle for various excitation frequencies and velocity ratios; Re=31,000

the 1:2.52 aspect ratio nozzle is higher than that of the 1:4.72 ratio nozzle. This is valid in the entire range of coflow from $\lambda=0.076$ to $\lambda=0.3$. As the aspect ratio increases, the nozzle height decreases, and so does the area where the coflow is entrained into the jet near the minor plane. As a result, the mass entrainment from the coflow may decrease and the mixing deteriorates with increasing aspect ratio.

Flow Field Characteristics. The flow dynamics underlying the enhanced mixing using self-excited nozzles is discussed next. The initial velocity profiles of the jet are examined first. Based on velocity vector maps and turbulent kinetic energy maps, the flow mechanisms for large- and small-scale mixing are revealed. The energy cascade in the mixing process is also investigated with spectral analysis of the flow field.

The mean and fluctuation exit axial velocity profiles of the jets across an unexcited square nozzle are shown in Fig. 8. The bell-shaped mean velocity profile suggests a fully developed turbulent flow at the nozzle exit, with the maximum located at the geometric center of the nozzle. The turbulence level is about 7% of the mean flow in the center portion of the jet flow, but nearly 17.3% in the shear layer. It is known that high turbulence level in the initial part of the jet is an unfavorable condition for shear flow excitation based on small disturbance amplification since the controlled perturbation can be overpowered by the background turbulence noise. In contrast, this has little effect on self-excited nozzles since the mixing process is driven by the inviscid flow dynamics as indicted later.

The phase-resolved cross-sectional velocity vector maps at 36 deg of phase angle of the excited jet issuing from the 1:4.72 nozzle in a coflow ($\lambda=0.5$) are shown in Fig. 9. The phase angle of 0 deg corresponds to the moment when the flaps touch each other and are just about to separate, i.e., the minimum opening of the nozzle. The data for the 1:4.72 nozzle are presented here because the large-scale vortices are spaced farther apart and therefore can be shown most clearly. Two pairs of counter-rotating vortices (CVPs) are obvious at $x/D=4$, which roll up right from the nozzle exit and grow with downstream distance. In the far field, the strength of these CVPs decreases with the distance from nozzle, as indicated by the decrease in transverse velocity components. In addition, strong convection from coflow into the jet in the minor plane can be clearly seen at all axial stations, even at $x/D=0.5$. These CVPs improve the entrainment and large-scale mixing in the near field of the excited jet.

The velocity vector maps in the major and minor planes of the same jet at 0 deg phase angle are shown in Fig. 10. Unlike a natural rectangular jet, because of the inflection of the flaps, the excited jet undergoes vectoring in the major plane immediately at the nozzle exit plane; this occurs in most of the time of the excitation cycle.

The roll-up mechanism of the observed CVPs can be explained by the characteristics of pressure field around the nozzle exit induced by the vibrating flaps, as shown in Fig. 11. As the flaps move apart (*a*), the static pressure in the wake of the flaps decreases. As a result, the ambient fluid is induced into the jet in the minor plane. The strong spanwise and lateral velocity components, outward in the major plane and inward in the minor plane, cause a circulation around each corner of the nozzle (*b*). These vortices involve the main stream of both jet and coflow and their roll-up is not a result of the growth of instabilities in the shear layer. In other words, these vortices are not initiated by the velocity gradient in the shear layer. Therefore, they are basically inviscid in nature. It is these large-scale, streamwise vortices that

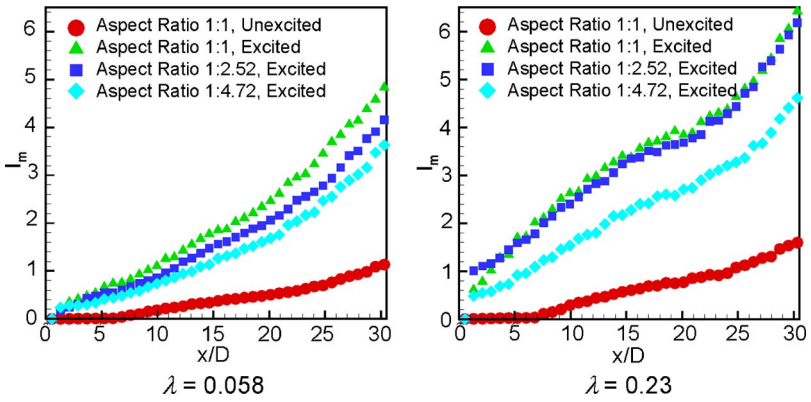

Fig. 7 Effect of nozzle aspect ratio on mixing index; Re=17,000, St=0.12

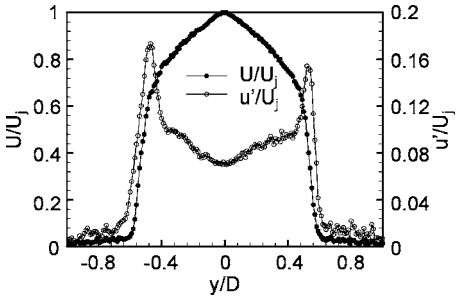

Fig. 8 Mean axial velocity and turbulent intensity profiles across a natural square jet at $x/D=0.2$

dominate the jet mixing process. As flaps move to the center (c), the pressure behind the flaps decreases and the spanwise and lateral velocity components both turn inward toward the jet axis. As a result, this portion of the cycle has little contribution to the roll-up of CVPs.

Due to the ambiguity of hot-wire measurements in detecting reverse flows, the large-scale CVPs are not visible in the side view of the mean flow field. Nevertheless, these CVPs can be clearly seen in the field of scalar characteristics, for instance, turbulent kinetic energy. Figure 12 presents side-view turbulent kinetic energy maps of the excited 1:4.72 jet in a coflow ($\lambda=0.5$). The turbulent kinetic energy is concentrated in the entire near field of the jet from nozzle exit to $x/D=3$–5 and widely spread in the

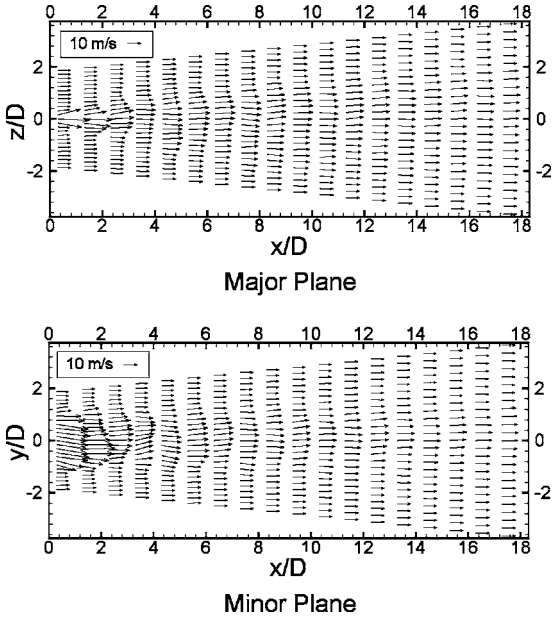

Fig. 10 Velocity vector maps of the excited 1:4.72 jet at 0 deg phase of cycle; Re=10,000, $\lambda=0.5$, St=0.19

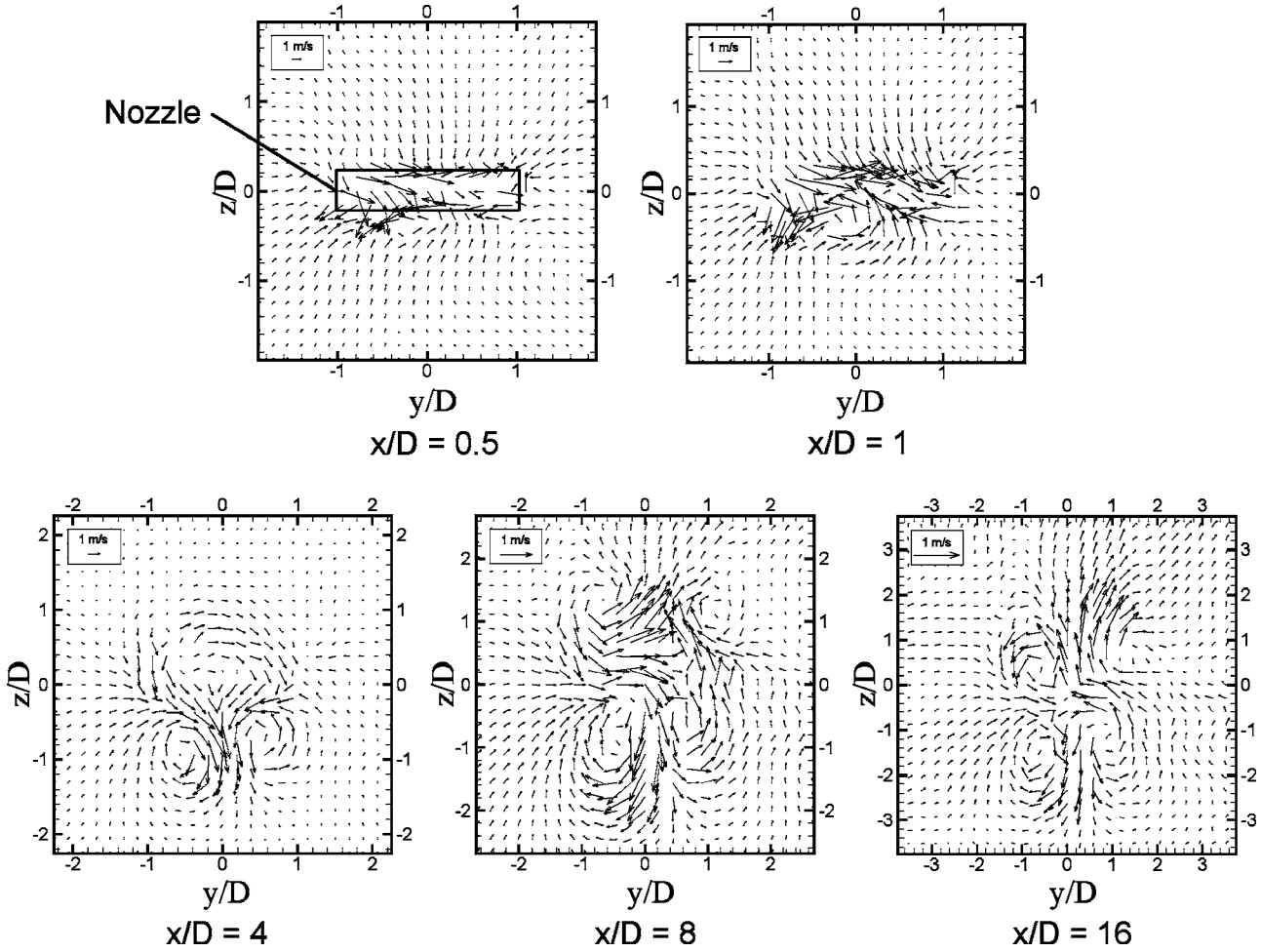

Fig. 9 End-on velocity vector maps of the excited 1:4.72 jet; phase=0 deg, Re=10,000, $\lambda=0.5$, St=0.19

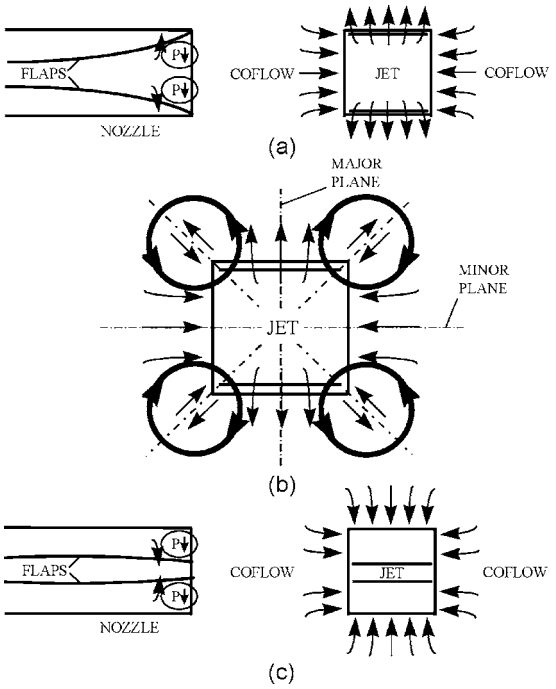

Fig. 11 Schematic of the flow entrainment induced by excitation near the nozzle exit and roll-up of the large-scale streamwise vortices

spanwise direction. This is indicative of strengthened small-scale mixing. Noticeable also are the staggered large-scale streamwise vortices. The different convection velocities of large-scale vortices can be a result of imperfect symmetry of the flaps or unequal vectoring angles.

To examine the energy cascade in the mixing process, power spectra of the velocity signal measured on the centerline of the 1:4.72 self-excited jet at various downstream stations are shown in Fig. 13. In the near field, the spectral components at the excitation frequency of 475 Hz and its harmonic at 950 Hz are larger than any other spectral contents in the flow, with featureless distribution below the excitation frequency. At $x/D=6$, the harmonic peak vanishes and only the fundamental (excitation) frequency dominates the flow, indicating the beginning of the mixing transition. At $x/D=8$, the fundamental peak disappears, signifying the completion of mixing transition. Farther downstream from there, the magnitude of spectral components within the frequency range of 500 Hz to 2000 Hz consistently decreases, an indication of a more isotropic turbulence.

The dominant turbulence scales in the excited jet flow can be better seen in the period-averaged power spectra over an excitation cycle (Fig. 14). With no distinguishable peaks below the one corresponding to the excitation frequency, the diminution in the amplitude of higher frequency spectral components starts immediately above the excitation frequency. This demonstrates the energy cascade from the large-scale vortices formed in the near field down to smaller scale turbulence at which dissipation ultimately

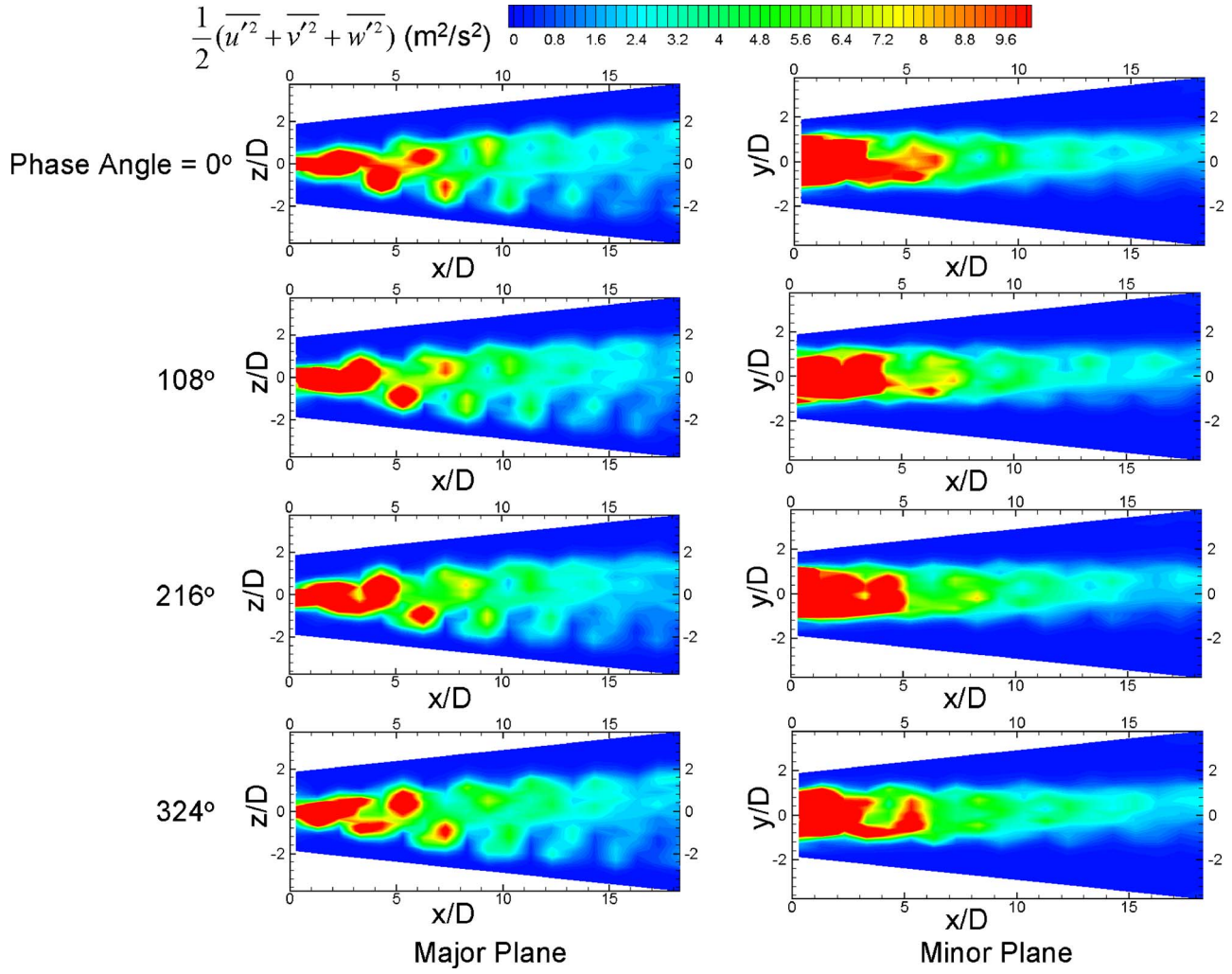

Fig. 12 Turbulent kinetic energy maps of the excited 1:4.72 jet; Re=10,000, λ=0.5, St=0.19

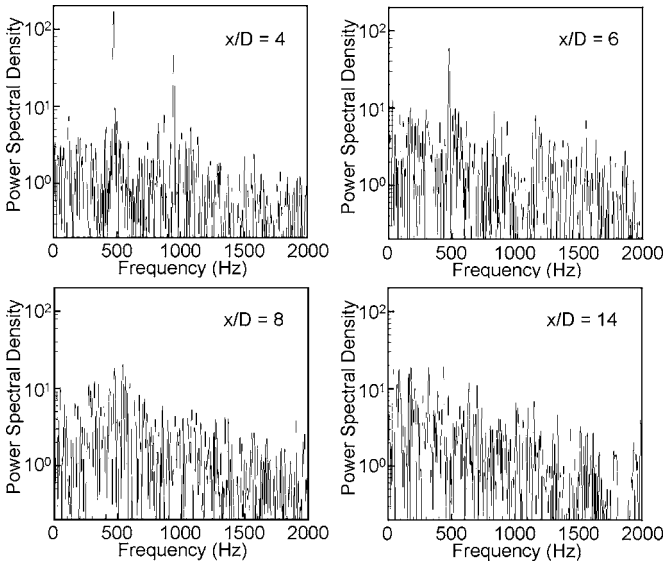

Fig. 13 Power spectra of the excited 1:4.72 jet along its centerline; Re=10,000, λ=0.5, St=0.19

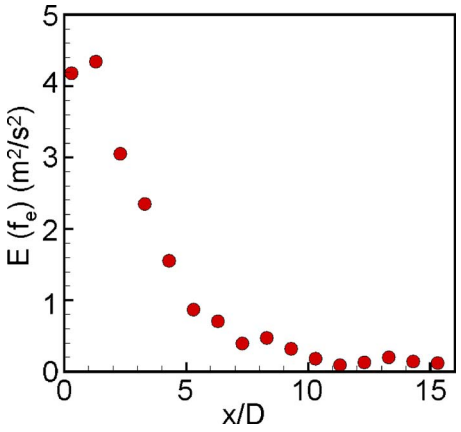

Fig. 15 Streamwise variation of the spectral component at the excitation frequency of the excited 1:4.72 jet along its centerline; Re=10,000, λ=0.5, St=0.19, f_e=475 Hz

takes place. Farther downstream, the decay of the spectral distribution begins at lower wave numbers. Moreover, because the characteristic local (centerline) velocity decreases with downstream distance, the spectral peak at the excitation frequency continuously migrates towards the high wave numbers where the dissipation finally takes place. The second harmonic is the only prominent higher harmonics of the excitation frequency. It decays rapidly with downstream distance at a rate similar to the fundamental peak and disappears at about 14 diameters downstream. The lack of subharmonics of the excitation frequency within the spectra indicates the absence of pairing processes in the formation and decay of the jet.

Shown in Fig. 15 is the streamwise decay of the spectral energy component at the excitation frequency. Clearly, the breakdown of the large-scale vortices is complete at approximately $x/D=10$, where most of the kinetic energy the jet gained from the self-excitation has been dissipated and the jet becomes a small-scale dominant, isotropic turbulence flow.

Conclusions

A new self-excitation method was conceived and tested to enhance the mixing of jet fluid with its surrounding fluid. The con-

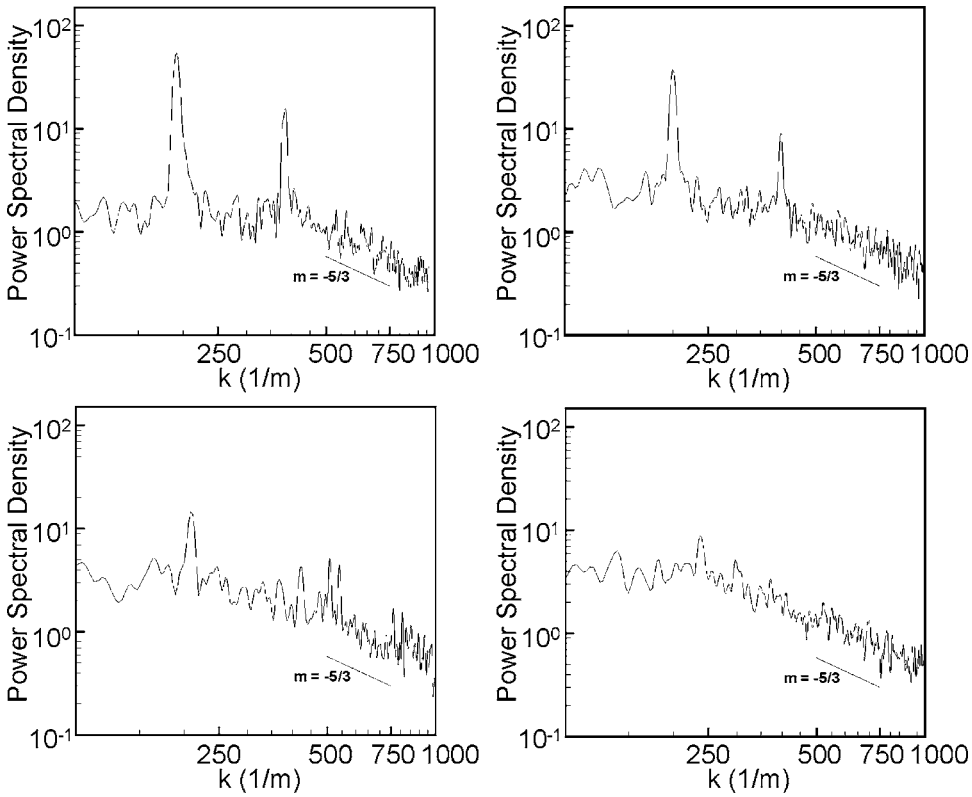

Fig. 14 Period-averaged power spectra of the excited 1:4.72 jet along its centerline; Re =10,000, λ=0.5

centration and velocity fields of jets emanating from square and rectangular shaped nozzles were studied in order to clarify the mixing performance and the flow mechanisms responsible for the performance of the excited jet.

The quantitative examination of the concentration field indicated that the mixing rate increased substantially in the excited jet. A mixing rate enhancement of 400% by $x/D=4$ and 200% by $x/D=20$ over the unexcited jet were observed with 390 Hz excitation (St=0.1). Featuring large expansion in the major plane and very short unmixed jet fluid core, the excited jet exhibited a much faster streamwise decay in jet fluid concentration than the unexcited jet. Within the frequency range tested, for constant deflection amplitude the mixing rate was observed to increase with frequency and coflow velocity. Two stages in the evolution of the excited jet where the mixing rate dramatically increased were observed. The first was from nozzle exit to $x/D=4$, where the mixing rate was increased mainly due to large-scale ambient fluid entrainment. The second stage was downstream from $x/D=14$, where the increase of the mixing rate was primarily due to enhanced small-scale mixing.

The square nozzle exhibited a higher mixing rate than the rectangular nozzles.

The detailed mapping of the velocity field revealed the existence of two pairs of counter-rotating, large-scale streamwise vortices centered around the nozzle corners that dominated the excited jet flow. Becoming visible at four diameters from the nozzle exit, these vortices were induced by the periodic oscillation of local static pressure in the mean flow at the nozzle exit. These vortices were inviscid in nature, with a spanwise or lateral velocity magnitude of typically an order of 10% to 20% of the mean flow. This intensive radial-circumferential convection provided a rapid transport of the momentum and mass between the jet and the surrounding fluid at a length scale comparable to the nozzle dimensions. Large-angle vectoring starting right from the nozzle exit in the major plane of the excited jet was observed. As a consequence, the penetration of the coflow into the jet column in the minor plane occurred immediately downstream the nozzle exit plane.

The near field of the flow exhibited a high degree of complexity with strong three-dimensional characteristics. Compared to a jet excited by small-amplitude perturbation, this large amplitude excitation significantly advanced the occurrence of the streamwise vortices, and therefore, the large-scale mixing. Moreover, the excited jet gained as much as six times the turbulent kinetic energy at the nozzle exit over the unexcited jet. Most of the turbulent kinetic energy is concentrated within five diameters from the nozzle exit across the entire width of the jet. This is indicative of advanced and strengthened small-scale mixing. The mixing transition takes place at roughly $x/D=7$, as observed in the spectral analysis of the velocity signal.

The proposed and tested active, self-excited nozzle has been shown to offer significant enhancement of nozzle fluid mixing with coflowing fluid streams. The practical application of the concept must await prolonged testing to satisfy reliability, availability, and maintainability criteria, which is mostly a material issue.

Acknowledgment

This work was partially funded by the AGTSR Program as a subcontract from DOE (1994–1997). The authors wish to acknowledge Dr. Dan Fant for his project monitoring effort. Y. Yuan would also like to thank F. Caldwell and S. LePera for their assistance in circuit design and software coding. This work constituted part of the doctoral work of Y. Yuan.

Nomenclature

A_1 = downstream cross-sectional area in which the integrated mass of tracer is equal to its initial value at the nozzle exit plane

A_2 = a circular shaped downstream cross-sectional area that has a diameter of three times the hydraulic diameter or equivalent diameter of the nozzle

$C_{avg}(x)$ = mean concentration at a downstream station x

$\bar{C}_{avg}(x)$ = normalized mean concentration over all points falling in the calculation domain A_1 at a downstream station x

$C_{rms}(x)$ = root-mean-square of concentration at a downstream station x

$\bar{C}_{var}(x)$ = normalized concentration variation over all points in the calculation domain A_2 at a downstream station x

D = nozzle equivalent diameter

E = power spectral density

f_e = excitation frequency

k = wave number or index

I_m = Nondimensional mixing index

Re = Reynolds number

St = Strouhal number

u' = fluctuation velocity

U = time-mean velocity

U_c = time-mean velocity of the coflow at the nozzle exit plane

U_j = time-mean centerline velocity of the jet at the nozzle exit

x,y,z,t = streamwise, lateral, spanwise, time coordinates, respectively

Greek Symbols

λ = coflow-to-jet velocity ratio at the nozzle exit

λ_e = coflow-to-jet momentum flux ratio at the nozzle exit

ρ_j = density of jet fluid

ρ_c = density of coflow fluid

References

[1] Binder, G., and Favre-Marinet, M., 1973, "Mixing Improvement in Pulsating Turbulent Jets," *ASME Symposium on Fluid Mechanics of Mixing*.

[2] Curtet, R. M., and Girard, J. P., 1973, "Visualization of a Pulsating Jet," *ASME Symposium on Fluid Mechanics of Mixing*.

[3] Zaman, K. B. M. Q., and Hussain, A. K. M. F., 1980, "Vortex Pairing in a Circular Jet Under Controlled Excitation. Part 1. General Jet Responses," J. Fluid Mech., **101**, pp. 449–491.

[4] Bouchard, E. E., and Reynolds, W. C., 1981, "Effect of Forcing on the Mixing-Layer Region of a Round Jet," *AIAA Unsteady Turbulent Shear Flows Conference*, Toulouse, France, pp. 402–411.

[5] Lee, M., and Reynolds, W. C., 1985, "Bifurcating and Blooming Jets," *5th Symposium on Turbulent Shear Flows*, pp. 1.7–1.12.

[6] Gutmark, E., Schadow, K. C., Parr, D. M., Harris, C. K., and Wilson, K. J., 1985, "The Mean and Turbulent Structure of Noncircular Jets," *AIAA Shear Flow Control Conference*, Boulder, CO, AIAA Paper No. 85-0546.

[7] Ho, C. M., and Gutmark, E., 1987, "Vortex Induction and Mass Entrainment in a Small-Aspect-Ratio Elliptic Jet," J. Fluid Mech., **179**, pp. 383–405.

[8] Parekh, D. E., Reynolds, W. C., and Mungal, M. G., 1987, "Bifurcation of Round Air Jets by Dual-Mode Acoustic Excitation," AIAA Paper No. 87-0164.

[9] Juvet, P. J., and Reynolds, W. C., 1989, "Entrainment Control in an Acoustically Controlled Shrouded Jet," AIAA Paper No. 89-0969.

[10] Batchelor, G. K., and Gill, A. E., 1961, "Analysis of the Stability of Axisymmetric Jets," J. Fluid Mech., **14**, pp. 529–551.

[11] Plaschko, P., 1979, "Helical Instabilities of Slowly Divergent Jets," J. Fluid Mech., **92**, pp. 209–215.

[12] Yoda, M., 1992, "The Instantaneous Concentration Field in the Self-Similar Region of a High Schmidt Number Round Jet," Ph.D. thesis, Department of Aeronautics and Astronautics, Stanford University, Stanford, CA.

[13] Cohen, J., and Wygnanski, I., 1987, "The Evolution of Instabilities in the Axisymmetric Jet, Part 1," J. Fluid Mech., **176**, pp. 191–219.

[14] Cohen, J., and Wygnanski, I., 1987, "The Evolution of Instabilities in the Axisymmetric Jet, Part 2," J. Fluid Mech., **176**, pp. 221–235.

[15] Vandsburger, U., and Ding, C., 1995, "The Spatial Modulation of a Forced Triangular Jet," Exp. Fluids, **18**, pp. 239–248.

[16] Ding, C., 1995, "Methodologies for Active Control of Free Shear Flows," Ph.D. thesis, Department of Mechanical Engineering, Virginia Polytechnic Institute and State University, Blacksburg, VA.

[17] Wiltse, J. M., and Glezer, A., 1998, "Direct Excitation of Small-Scale Motions

in Free Shear Flows," Phys. Fluids, **10**, pp. 2026–2036.
[18] Yuan, Y., and Vandsburger, U., 1998, "An Experimental Study of Subsonic Turbulent Jets Issuing From Radially Lobed Nozzles," *Proceedings of the 1998 ASME Fluid Engineering Division Summer Meeting*, Washington, DC, ASME FEDSM98-4885.
[19] Yuan, Y., 2000, "Jet Fluid Mixing Control Through Manipulation of Inviscid Flow Structures," Ph.D. thesis, Department of Mechanical Engineering, Virginia Polytechnic Institute and State University, Blacksburg, VA.
[20] Schubauer, G. B., and Skramstad, H. K., 1947, "Laminar Boundary Layer Oscillation and Stability of Laminar Flow," J. Aerosp. Sci., **14**, pp. 68–78.
[21] Oster, D., and Wygnanski, I., 1982, "The Forced Mixing Layer Between Parallel Streams," J. Fluid Mech., **123**, pp. 91–130.
[22] Hill, W. G., Jr., and Greene, P. R., 1977, "Increased Turbulent Jet Mixing Rates Obtained by Self-Excited Acoustic Oscillation," ASME J. Fluids Eng., **99**, pp. 520–525.
[23] Husain, H. S., and Hussain, F., 1999, "The Elliptic Whistler Jet," J. Fluid Mech., **397**, pp. 23–44.
[24] van Cruyningen, I., Lozano, A., and Hanson, R. K., 1990, "Quantitative Imaging of Concentration by Planar Laser-Induced Fluorescence," Exp. Fluids, **10**, pp. 41–49.
[25] Wittmer, K. S., 1996, "Turbulent Flowfield Downstream of a Perpendicular Airfoil–Vortex Interaction," Ph.D. thesis, Department of Aerospace and Ocean Engineering, Virginia Polytechnic Institute and State University, Blacksburg, VA.
[26] Vranos, A., Liscinsky, D. S., True, B., and Holdeman, J. D., 1991, "Experimental Study of Cross-Stream Mixing in a Cylindrical Duct," *AIAA/SAE/ASME/ASEE 27th Joint Propulsion Conference*, Sacramento, CA.
[27] Liscinsky, D. S., True, B., and Holdeman, J. D., 1994, "Mixing Characteristics of Directly Opposed Rows of Jets Injected Normal to a Crossflow in a Rectangular Duct," AIAA Paper No. 94-0217.

Sensitivity of a Square Cylinder Wake to Forced Oscillations

Sushanta Dutta

P. K. Panigrahi

K. Muralidhar

Department of Mechanical Engineering,
Indian Institute of Technology Kanpur,
Kanpur 208016, India

The wake of a square cylinder at zero angle of incidence oscillating inline with the incoming stream has been experimentally studied. Measurement data are reported for Reynolds numbers of 170 and 355. The cylinder aspect ratio is set equal to 28 and a limited study at an aspect ratio of 16 has been carried out. The frequency of oscillation is varied around the Strouhal frequency of a stationary cylinder, and the amplitude of oscillation is 10–30% of the cylinder size. Spatial and temporal flow fields in the cylinder wake have been studied using particle image velocimetry and hot-wire anemometry, the former providing flow visualization images as well. A strong effect of forcing frequency is clearly seen in the near wake. With an increase in frequency, the recirculation length substantially reduces and diminishes the time-averaged drag coefficient. The time-averaged vorticity contours show that the large-scale vortices move closer to the cylinder. The rms values of velocity fluctuations increase in magnitude and cluster around the cylinder as well. The production of turbulent kinetic energy shows a similar trend as that of spanwise vorticity with the former showing greater asymmetry at both sides of the cylinder centerline. The instantaneous vorticity contours show that the length of the shear layer at separation decreases with increasing frequency. The effect of amplitude of oscillation on the flow details has been studied when the forcing frequency is kept equal to the vortex-shedding frequency of the stationary cylinder. An increase in amplitude diminishes the time-averaged drag coefficient. The peak value of rms velocity increases, and its location moves upstream. The length of the recirculation bubble decreases with amplitude. The reduction in drag coefficient with frequency and amplitude is broadly reproduced in experiments with the cylinder of lower aspect ratio. [DOI: 10.1115/1.2742736]

Keywords: square cylinder, forced inline oscillation, drag coefficient, Strouhal number, recirculation length

1 Introduction

Bluff body wakes have been extensively investigated in view of their applications to wind engineering, hydrodynamics, aerodynamics, and electronics cooling. Such wakes display characteristics that are distinct to the object shape, Reynolds number, and distance in the streamwise direction. At high Reynolds numbers, the wake structure is complex, owing to unsteadiness and turbulence. In the lower range of the Reynolds number, recent studies with a cylinder of square cross section show that the flow field along with unsteadiness is three-dimensional, even in nominally two-dimensional geometries. In many practical applications, the flow complexity can be exploited for attaining varying degrees of control.

Active flow control using riblike structures is a recent topic of research and requires understanding of the coherent flow structures. The rib can be a cylinder of square cross section. Control is implemented by using an independent external disturbance or a feedback control system resulting in cylinder oscillations. Depending on the direction of motion with respect to the main flow direction, the oscillation may be transverse or inline. Modification of the flow field can significantly reduce or enhance the intensity of the wake.

Griffin and Ramberg [1] reviewed the wake structure of a circular cylinder oscillating inline with the incident steady flow at Re=190. Vortex shedding was seen to be synchronized with the oscillation of the cylinder in a range of frequencies near twice the shedding frequency. In one experiment, two vortices of opposite sign were shed for one cycle of cylinder motion. In another, one vortex was shed for each cycle of oscillation. Ongoren and Rockwell [2] studied near-wake flow structures arising from a transversely oscillating cylinder over a Reynolds number range of 584–1300 with the hydrogen bubble technique. The authors studied three different geometries (circular, triangular, and square) over a wide range of frequencies from subharmonic to superharmonic. The study showed a distinct phase relationship between body motion and vortex shedding for the three harmonic ranges. Roussopoulos [3] studied feedback control of vortex shedding for flow past a circular cylinder at an intermediate Reynolds number using flow visualization and hot-wire techniques. A loudspeaker was used as an actuator and the hot-wire sensor as the control. Vortex suppression was not possible if the control sensor was located too far downstream of the cylinder, even when the sensor could clearly detect the shedding. Also, suppression was not possible if the feedback loop was highly tuned to the shedding frequency. Gu et al. [4] studied, numerically and experimentally, the timing of vortex formation for a transversely oscillating circular cylinder. With an increase in the excitation frequency, the vortices were seen to move closer to the cylinder until a limiting position was reached and the vortices switched to the opposite sides of the cylinder. Tao et al. [5] reported a feedback experiment with a hot-wire probe, wherein visualization was conducted using a dye-injection technique for flow past a circular cylinder. The flow visualization images clearly showed complete vortex suppression and enhancement for various feedback conditions. Krishnamoorthy et al. [6] studied near-wake phenomena behind a transversely oscillating circular cylinder in the Reynolds number range of 1250–1500. While keeping the amplitude of cylinder oscillation fixed, the frequency of oscillation was varied. At the lower excitation frequency in the lock-in regime, the authors observed two pairs of vortices shed from the cylinder per cycle of cylinder oscillation. When the critical excitation frequency crossed the lock-in regime, one pair of vortices was shed from the cylinder.

Contributed by the Fluids Engineering Division of ASME for publication in the JOURNAL OF FLUIDS ENGINEERING. Manuscript received July 18, 2006; final manuscript received January 19, 2007. Assoc. Editor: James A. Liburdy.

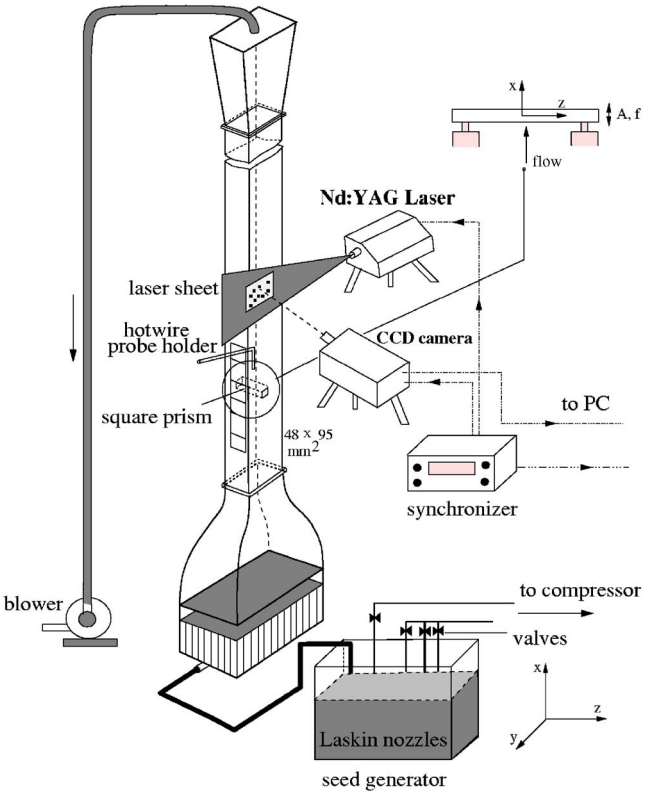

Fig. 1 Schematic drawing of the experimental apparatus

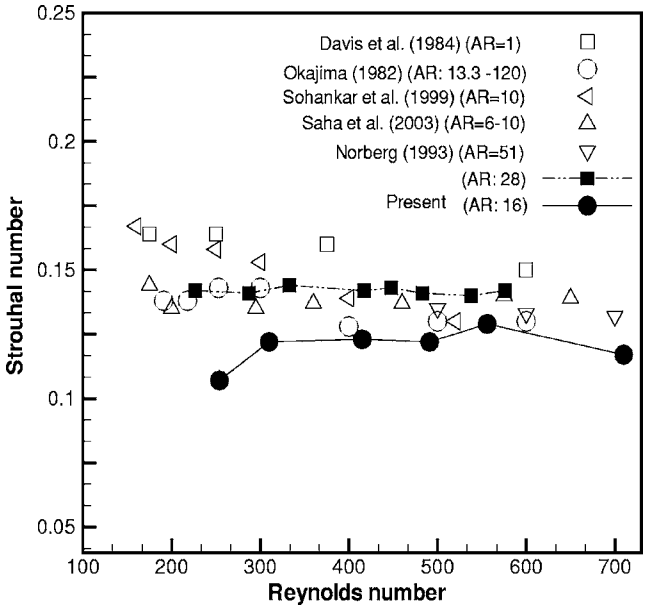

Fig. 2 Validation in terms of Strouhal number as a function of Reynolds number for flow past a square cylinder at zero angle of incidence

Cetiner and Rockwell [7] studied lock-in phenomena and dynamic loading of a circular cylinder for streamwise forced oscillations with respect to the mean flow direction over a wide range of Reynolds number ($405 < \mathrm{Re} < 2482$). Particle image velocimetry was used for the study. The authors correlated the vortex pattern with the force coefficients. The authors showed that the lock-in phenomenon is possible for streamwise oscillations because it is in transverse oscillations of the cylinder. Sarpkaya [8] reviewed vortex-induced oscillations of circular cylinders and categorized fundamental aspects of the wake behavior. Yang et al. [9] numerically studied flow past a transversely oscillating rectangular cylinder in channel flow. The authors captured flow details at a Reynolds number of 500. It was concluded that the wake pattern is dominated by the oscillations of the cylinder. Nobari et al. [10] reported numerical simulation results for flow past an oscillating circular cylinder for Reynolds numbers up to 300. Both transverse and inline oscillations were studied for various frequencies and amplitudes. The effect of the oscillation parameters on the time-averaged drag coefficient was discussed. The authors compared the results of their numerical simulations to experimental data and found a good match. Nishihara et al. [11] studied the effect of streamwise oscillation on wake pattern and fluid dynamic forces of a circular cylinder in a water tunnel using laser Doppler veloci-

Table 1 Comparison of the time-averaged drag coefficient with the published literature for flow past a stationary square cylinder

Authors	Nature of study	Aspect ratio	Blockage	Re	C_D
Davis and Moore [18]	Numerical (2D)	—	0.170	470	1.95
Sohankar et al. [19]	Numerical (3D)	6	0.055	400	1.67
Saha et al. [20]	Numerical (3D)	6–10	0.100	400	2.21
Present	Experimental	16	0.030	410	2.32
		28	0.060	420	2.03

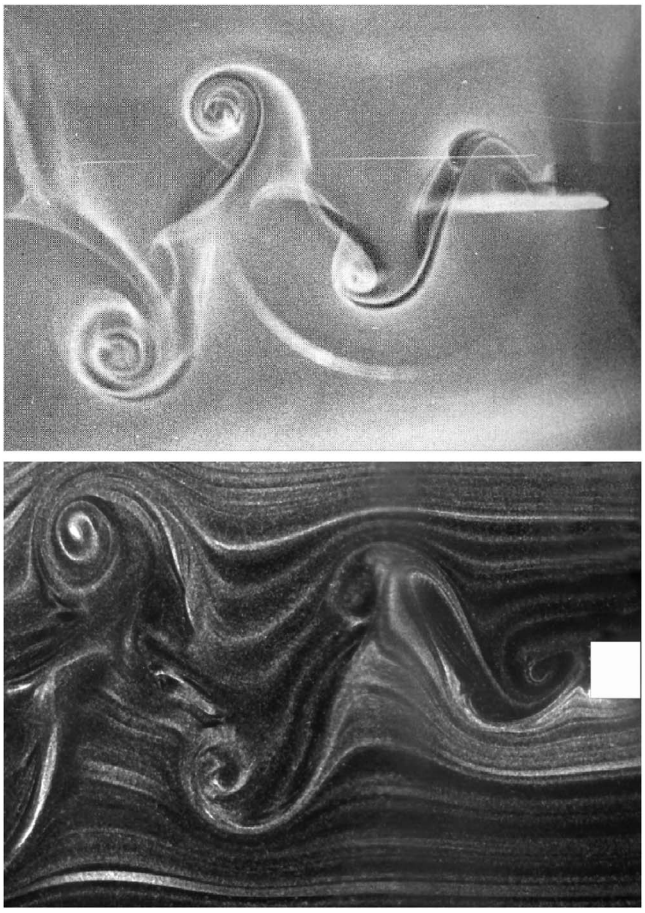

Fig. 3 Flow visualization images for inline oscillations of a square cylinder ($f/f_0=2$, below) with a circular cylinder (above) as reported by Griffin and Ramberg [1]

Table 2 Drag coefficient as a function of forcing frequency. Values outside brackets indicate momentum deficit; values within brackets include the contribution of velocity fluctuations on the time-averaged drag

f/f_o	Re=170	Re=355
0	1.48 (1.94)	1.41 (1.86)
0.5	1.13 (1.62)	0.78 (1.15)
1.0	0.94 (1.42)	0.83 (1.09)
2.0	1.05 (1.47)	0.58 (0.79)

metry (LDV) and flow visualization. The authors identified two ranges of the reduced velocity where distinct flow phenomena are observed. In the lower range ($V_r < 2.5$) symmetric vortex shedding was to be seen, whereas in the higher range ($V_r > 2.5$), alternate vortex shedding was realized.

The detailed literature review suggests that the study on effect of cylinder oscillation is primarily limited to the circular cylinder. The difference between the square and circular cylinders is the uniqueness of the location of the separation point. For the former, it is fixed at the upstream corners. For a circular cylinder, flow separation depends on the Reynolds number and freestream turbulence level. In the present work, flow past a prismatic cylinder of square cross section has been considered. The motivation for studying this geometry arises from the use of square ribs for flow control. Experiments have been conducted with an oscillating cylinder in the intermediate range of Reynolds number (170 and 355). The frequency has been varied around that of vortex shedding from a stationary cylinder. The oscillation amplitude is varied above the threshold value, while keeping the frequency equal to that of vortex shedding. For the range of parameters considered, the cylinder oscillations provide small perturbation to the wake of the square cylinder. The flow field has been explored experimentally using particle image velocimetry (PIV), hot-wire anemometry (HWA), and flow visualization. The influences of frequency and amplitude on the instantaneous and time-averaged properties of the wake of the cylinder are examined. The Reynolds number and aspect ratio effect on the wake characteristics have also been reported.

2 Apparatus and Instrumentation

Experiments have been carried out in a vertical test cell made of Plexiglas with air as the working fluid (Fig. 1). The test cell has two optical windows, one for the passage of the laser sheet and the other for recording by the camera. The cross section of the test cell is 9.5×4.8 cm^2, and the overall length is 2 m. The active length of the test cell, where measurements have been carried out, is 0.3 m. A contraction ratio of 10:1 ahead of the test section has been used. Cylinders of square cross section (3 mm and 3.4 mm edge) used for the experiments are made of Plexiglas and machined for sharp edges. Therefore, the respective aspect ratios (=length/edge) in the experiments are equal to 16 and 28. Most results have been reported for an aspect ratio of 28. With reference to Fig. 1, the x-axis is vertical and aligned with the mean flow direction. The z-axis coincides with the cylinder axis, and the y-axis is perpendicular to x and z.

The flow in the test section is set up by using the suction side of a blower driven by a voltage-stabilized single-phase motor. The freestream turbulence level in the approach flow was quite small; it was found to be less than the background noise of the anemometer (<0.05%). Flow parallelism in the approach flow was better than 98% over 95% of the width of the test cell. Stable velocities in the range of 0.5–3 m/s were realized in the test cell to cover the Reynolds number range of 100–800.

Measurements of the velocity field over selected planes were carried out using a particle image velocimetry system. The PIV system comprises a double-pulsed Nd:YAG laser (New Wave Lasers, $\lambda = 532$ nm), 15 mJ/pulse, a Peltier-cooled 12 bit CCD camera (PCO Sensicam) with a frame speed of 8 Hz, a synchronizer, a frame grabber, and a dual processor PC. The CCD is an array of 1280×1024 pixels. A Nikon 50 mm manual lens was attached to the CCD camera for covering the field of interest. The field of view for PIV measurements was 40 mm $\times$ 35 mm. From an initial size of 64×64, the final interrogation size of 16×16 pixels was arrived at by an adaptive cross-correlation method [12]. A total of 5561 velocity vectors were obtained with a spatial resolution of 0.5 mm. Inconsistent velocity vectors were eliminated by local median filtering. The time-averaged and rms velocity fields were obtained by averaging a sequence of 200 velocity vector images, corresponding to total time duration of 50 s. The instantaneous flow visualization images were recorded using the PIV system itself with a reduced particle density with a laser pulse width of 25 μs and an exposure time of 4 ms. Laskin nozzles were used to produce seeding particles from corn oil.

Local time-averaged velocity and velocity fluctuations were measured using a hot-wire anemometer (DANTEC). An X-wire probe was used for measuring two components of velocity. With the square cylinder placed horizontally, the X configuration was formed in the vertical plane. The two wires of the probe were calibrated against a pitot-static tube connected to a digital manometer (Furness Controls, 19.99 mm H_2O). The anemometer output voltage was collected in a PC through a data acquisition card (National Instruments) with LABVIEW software. Flow visualization was carried out in the test cell itself using a light sheet of the pulsed Nd:YAG laser with a reduced particle density. The cylinder was oscillated by mounting it over two electromagnetic actuators (Spranktronics) located outside the sidewalls of the test section. A small gap in the text section filled with soft rubber allowed the motion of the cylinder during actuation. Oscillation amplitude was estimated under no flow conditions by directly imaging the

Table 3 Strouhal number as a function of forcing frequency

f/f_0	Re=170	Re=355
0	0.138	0.154
0.5	0.135	0.151
1.0	0.135	0.151
2.0	0.138	0.154

Table 4 Recirculation length as a function of forcing frequency. The dimension is scaled by the edge of the cylinder.

f/f_0	Re=170	Re=355
0	2.80	2.50
0.5	3.20	2.17
1.0	1.93	1.97
2.0	0.50	1.50

Table 5 Drag coefficient, Strouhal number, and the dimensionless recirculation length as a function of forcing amplitude. $f/f_o=1$, Re=170. Values outside brackets indicate momentum deficit; values within brackets include the contribution of velocity fluctuations on the time-averaged drag. The recirculation length is scaled by the edge of the cylinder.

A/B	C_D (corrected)	St	Recirculation length
0	1.48 (1.94)	0.138	2.80
0.025	1.71 (2.27)	0.138	2.43
0.1	0.94 (1.42)	0.138	1.93
0.17	0.85 (1.14)	0.138	1.52
0.26	0.81 (1.10)	0.138	1.50
0.32	1.05 (1.40)	0.138	1.10

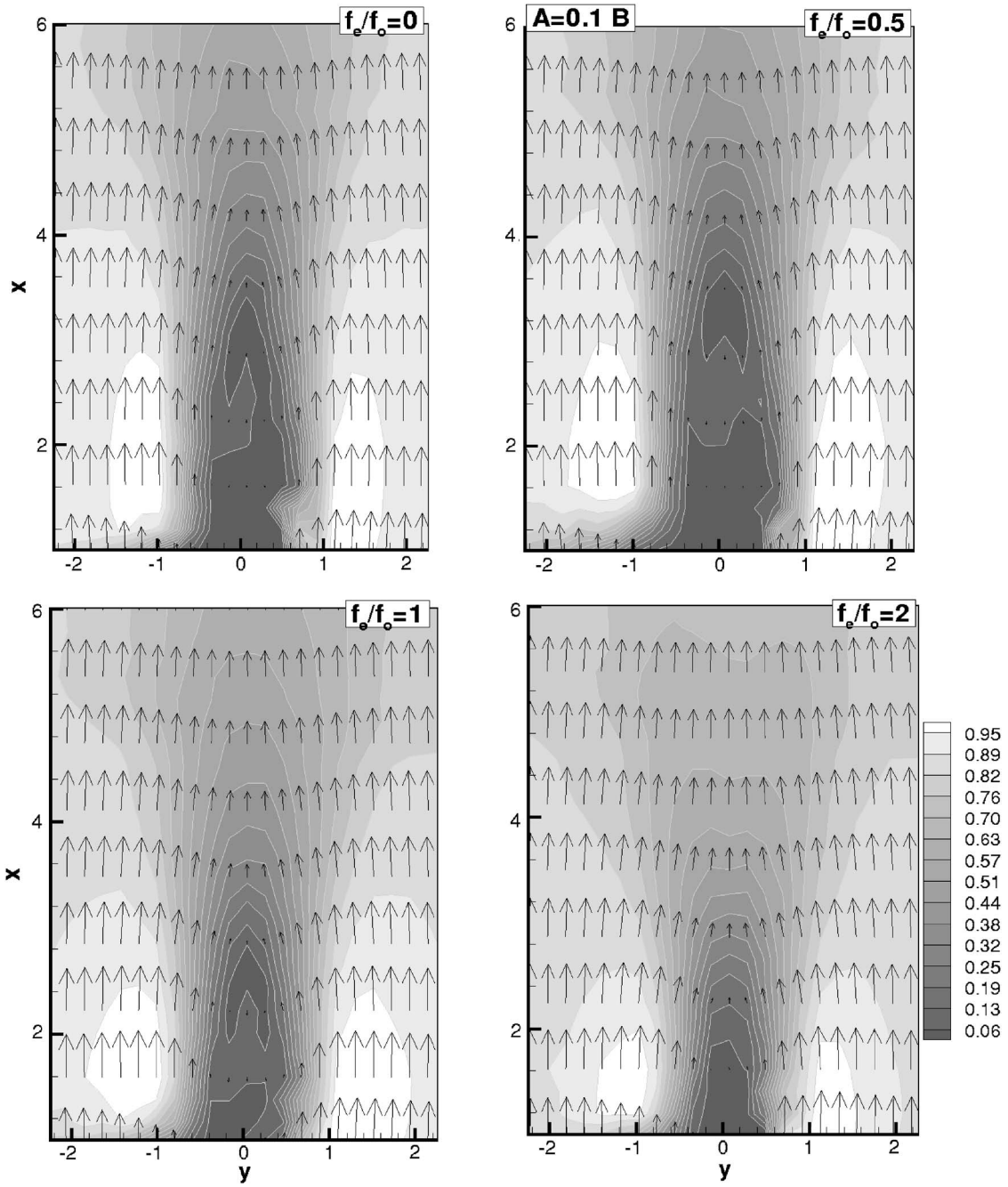

Fig. 4 Time-averaged nondimensional velocity vectors above an oscillating cylinder: Effect of frequency ratio, Re=170, *A*/*B*=0.1; flooded contours represent the absolute velocity magnitude

cylinder with the PIV camera and calibrating the pixel displacement of the cylinder with respect to the cylinder size. The actuator frequency and amplitude were adjustable through a control unit that is interfaced to a PC. The cylinders were excited at different harmonics of the shedding frequency in the streamwise direction. The amplitude of excitation was set by a voltage input to the electromagnetic actuator.

3 Uncertainty and Validation

The seeding of flow with oil particles, calibration, laser light reflection and variation in background illumination, image digitization, calculation of cross correlation, velocity gradients, and out-of-plane particle motion affect the repeatability of PIV measurements. Tracer particles need to follow the main airflow without any lag. For the particle size utilized and the range of frequencies in the wake, a slip velocity error of 0.3–0.5% relative to the instantaneous local velocity is expected. A second source of error in velocity measurement is due to the weight of the particle. In the present experiments, the effect of particle weight was examined by conducting experiments at a fixed Reynolds number by varying the size of the cylinder and air speed. The streamline plot and the dimensionless size of the recirculation region were found to be identical in each case, and independent of the fluid speed. The noise due to background light was minimized by using a bandpass filter (around the wavelength of the laser) before the camera sensor. The x- and y-component velocity profiles from PIV measurements compared very well to those from the hot wire in the far field region, confirming the proper implementation of both the

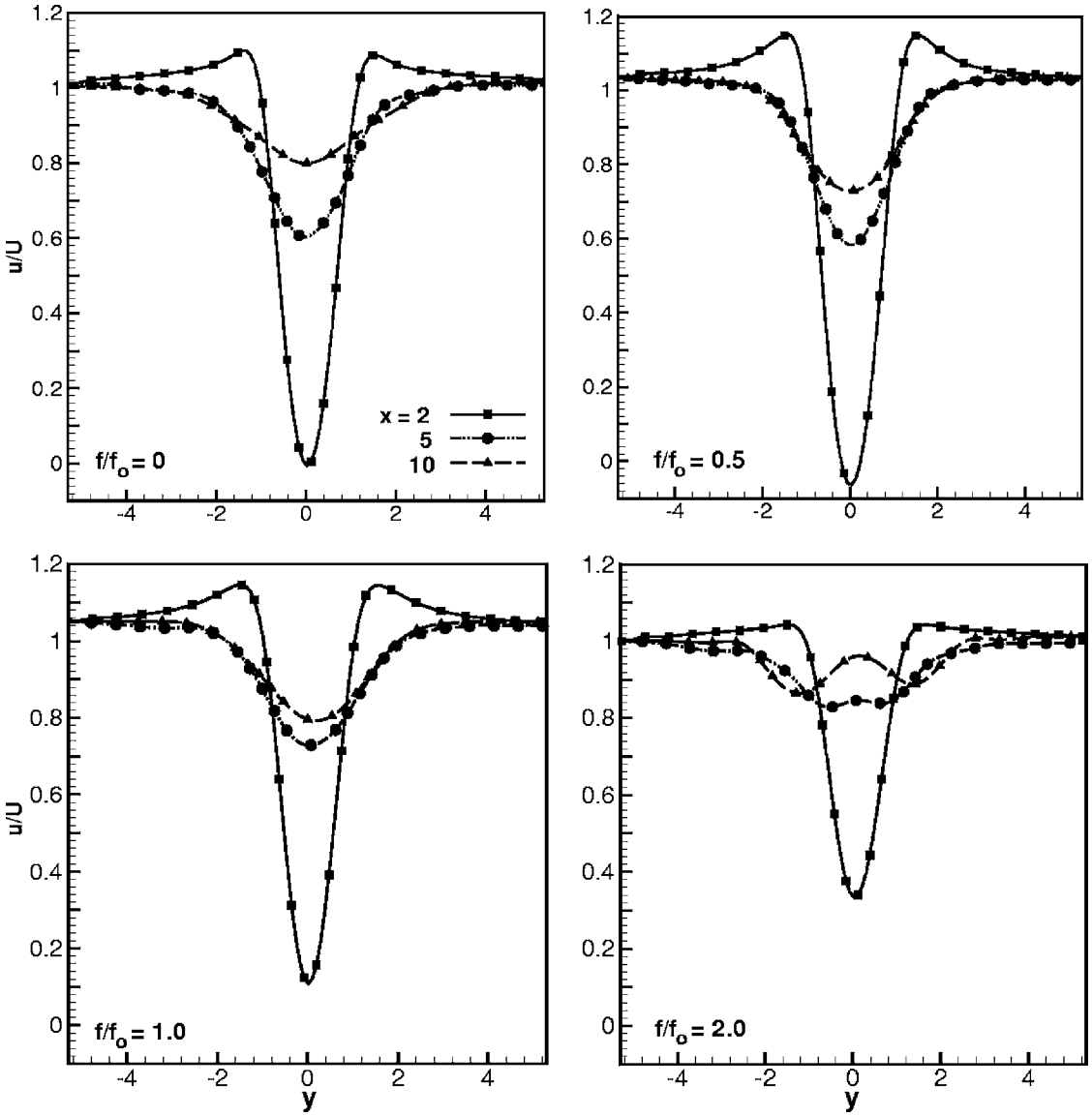

Fig. 5 Time-average *u*-velocity profiles above an oscillating cylinder at various *x*-locations: Effect of frequency ratio, Re=170, *A*/*B*=0.1

techniques and the measurement procedure. From repeated measurements (with Reynolds number kept constant to within ±1%), the uncertainty in drag coefficient was determined to be within ±5%. The uncertainty in Strouhal number was ±2%.

In experiments, the oil particle size was ~2–3 μm while the pixel size was 6.7 μm. The size of the particle image on the pixel array was estimated as 14–15 μm from a histogram distribution of light intensity over an interrogation spot. This yields a particle image-to-pixel ratio of slightly greater than 2 and fulfills the criterion recommended by Chang and Liu [13]. Other criteria, including the number of particles per interrogation spot and the average in-plane displacement discussed by Keane and Adrian [14], have also been accounted for. These criteria of particle size and number of particles per interrogation spot reduce the uncertainty in locating the peak of the cross-correlation function.

Measurements have been validated against published results for a stationary cylinder in terms of drag coefficient (Table 1), Strouhal number (Fig. 2), and visualization images (Fig. 3) in the intermediate range of Reynolds numbers. A reasonably good match of drag coefficient and Strouhal number with the literature was obtained. Figure 3 shows a comparison of flow visualization images of the square cylinder from the present work to that of the circular cylinder, as reported by Griffin and Ramberg [1]. In both experiments, the cylinders are subjected to inline oscillations at twice the Strouhal frequency. The two images show considerable similarity in terms of the wake structure.

4 Results and Discussion

The vortex formation in the near wake determines the wake structure and the forces on the cylinder. Shedding may be symmetric or asymmetric, depending on the forcing frequency. The pattern of vortex formation and the associated inline and transverse force components depend on the Keulegan-Carpenter number, KC=$2\pi A/B$, reduced velocity ($V_r=U/fB$), and velocity ratio, $U/2\pi fA$ [7,8]. Here, A is the amplitude of oscillation, B the cylinder size, and f the forcing frequency in hertz. In addition, the symbol f_0 is used for the vortex-shedding frequency of the stationary cylinder under identical experimental conditions. The present study reports results for a Keulegan-Carpenter number

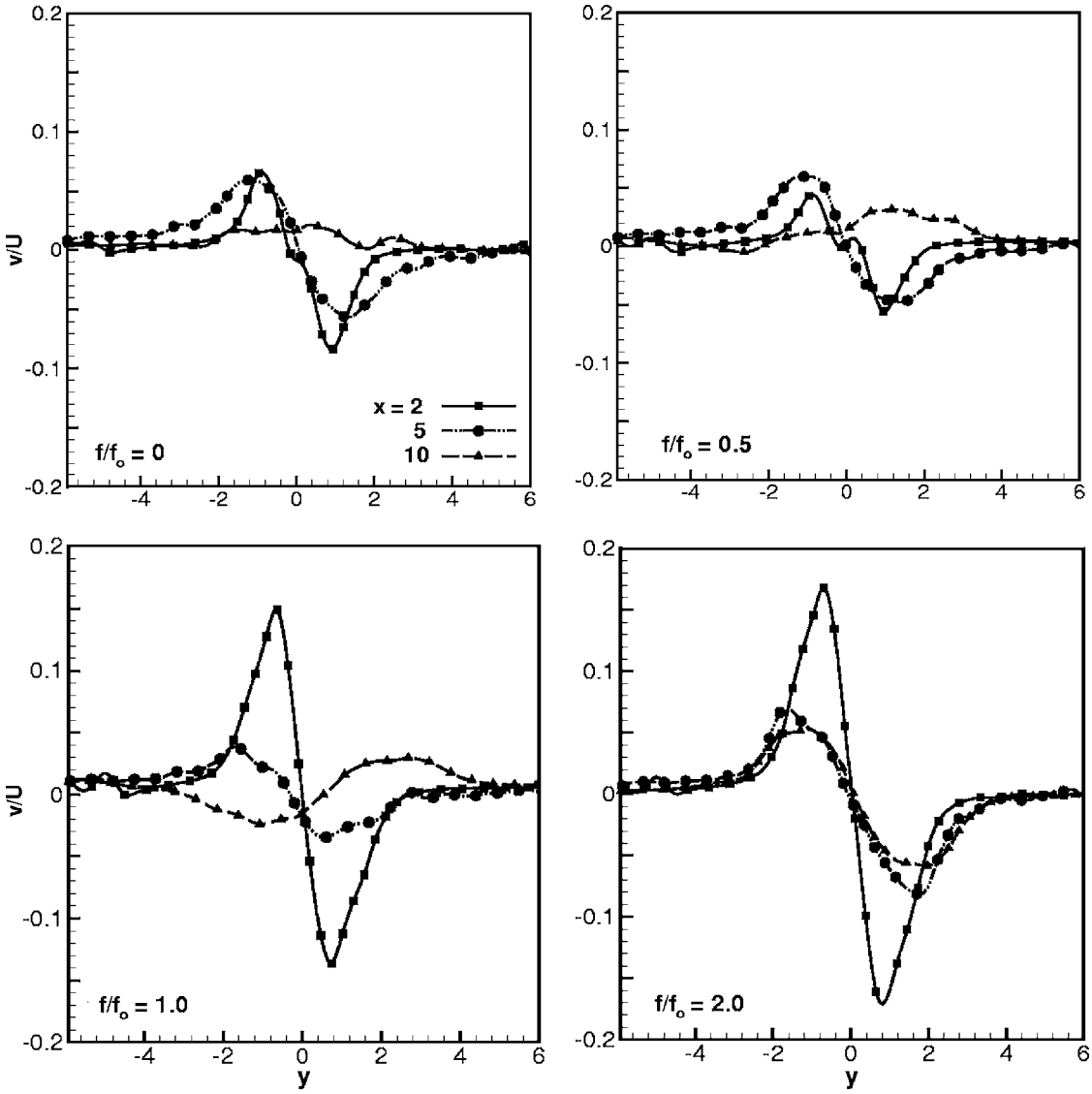

Fig. 6 Time-average *v*-velocity profiles above an oscillating cylinder at various *x*-locations: Effect of frequency ratio, Re=170, $A/B=0.1$

KC<2, reduced velocity range of 3–15, and a velocity ratio of 6–9. These parameters are such that they classify the cylinder oscillations as small perturbations to the wake.

For a stationary cylinder, the time-averaged flow field is symmetric about the x-z plane (the plane that carries the cylinder axis). Symmetry of this type breaks down for an oscillating cylinder. This is because the edge shedding a vortex and moving in the streamwise direction would produce a longer shear layer, when measured from the mean cylinder position. In contrast, an edge shedding a vortex but moving in a direction opposed to the main flow would produce a shorter shear layer. The contributions of fluid acceleration to shear layer instability at these time instants are also in opposite directions. The related asymmetry is expected to be small for small oscillation amplitudes. Asymmetry is expected to increase with the amplitude of oscillation.

The term "lock-on" is used to convey the idea that body motion is synchronized with the cycle of vortex shedding. The vortex-shedding frequency is then equal to the forcing frequency. For forcing frequencies well below lock-on, one can expect the shedding frequency to be close to the Strouhal frequency. The results presented below show that nonlinear interactions result in the appearance of additional harmonics in the power spectra.

The present work considers two Reynolds numbers (Re=170 and 355) and various amplitudes of oscillation and frequency. The frequency of oscillations is varied near the vortex-shedding frequency ($f/f_0=0.5$, 1, and 2) and amplitude (A/B) varied from 0.05 to 0.3. Here, the threshold amplitude of oscillation (namely, $A/B=0.05$) below which the wake remains unaffected is taken into account [1]. Results have been presented mainly for a cylinder aspect ratio of 28. The effect of decreasing the aspect ratio to 16 is briefly discussed.

4.1 Drag Coefficient and Strouhal Number. The drag coefficient reported here arises from the combined effect of momentum deficit and time-averaged turbulent stresses at the outflow plane of the wake. It has been determined as a time-averaged quantity from a PIV data set of 200 images. Factors such as added mass are not included in the calculation. The drag coefficient has been determined from the profiles of velocity and velocity fluctuations across the entire test cell at a streamwise location of $x=10$. Farther downstream ($x=15$), the time-averaged velocity field was significantly distorted by the presence of the wall and was not preferred. Since the plane $x=10$ is not sufficiently far away from

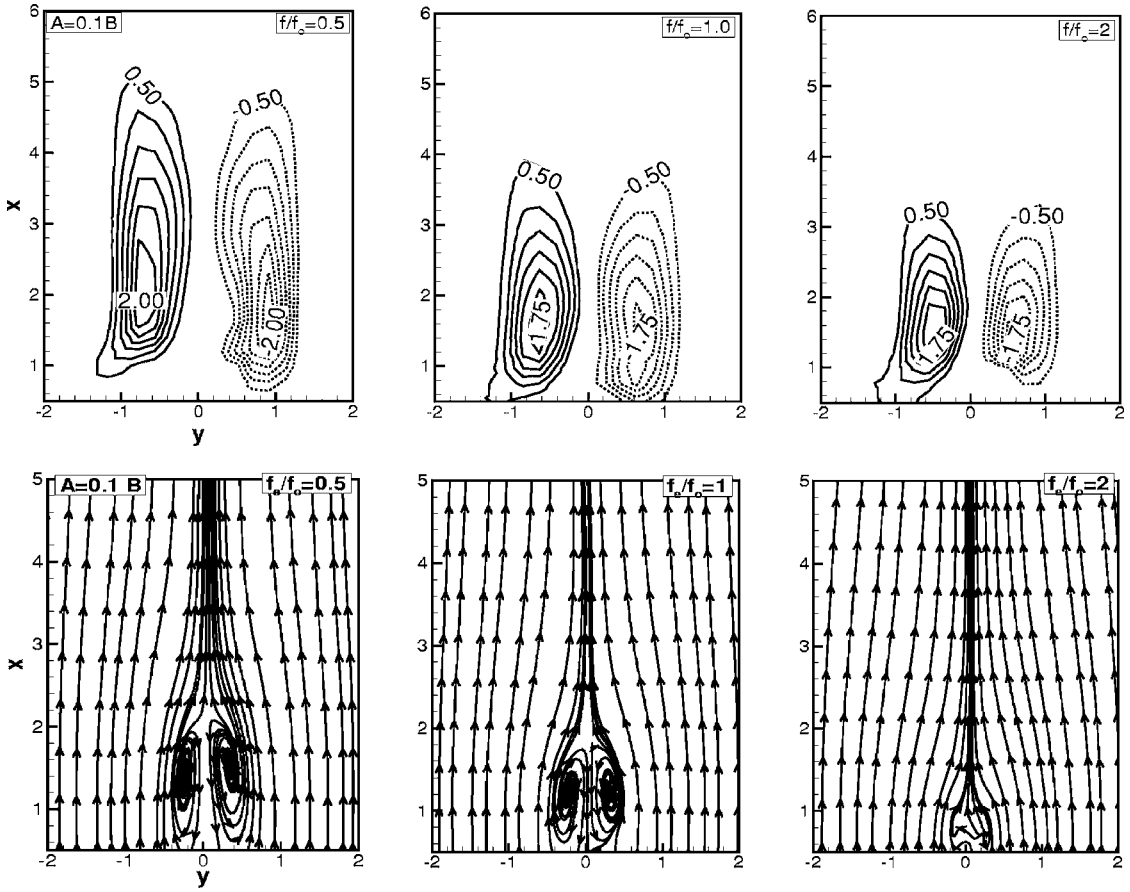

Fig. 7 Time-averaged spanwise vorticity field (top) and streamlines (below) in the wake of an oscillating square cylinder as a function of the forcing frequency, Re=170, $A/B=0.1$

the cylinder, the correction arising from turbulent stresses is expected to be significant. The drag coefficient has been calculated from the extended formula

$$C_D = 2\int_{-\infty}^{\infty} \frac{u}{U}\left(1-\frac{u}{U}\right)dy + 2\int_{-\infty}^{\infty}\left(\frac{\overline{v'^2}-\overline{u'^2}}{U^2}\right)dy$$

Here, the first term is the momentum deficit of the time-averaged flow field and the second term is the contribution of the turbulent fluctuations. The Strouhal number has been calculated from the spectral peak of the velocity trace recorded by the hot-wire anemometer.

Table 2 presents the drag coefficient measured at various frequencies of oscillation. The amplitude of oscillation is kept constant in these experiments at $A/B=0.1$. Drag coefficients have been calculated for two Reynolds numbers (Re=170 and 355). The drag coefficient decreases with respect to a stationary cylinder for an increase in the forcing frequency at both Reynolds numbers. There is a slight increase in drag coefficient when the frequency ratio increases from one to two (at Re=170), but the values are consistently smaller than for a stationary cylinder. The above trends are realized for a drag coefficient based on the momentum deficit alone as well as the total value. These results can be understood against measurements of flow patterns described in the later sections.

Table 3 presents the Strouhal number data as a function of frequency of oscillation at two Reynolds numbers (Re=170 and 355). No significant change in Strouhal number as a function of forcing frequency is observed, although its overall value increases with an increase in Reynolds number. This result is to be interpreted to mean that a significant spectral peak at the Strouhal frequency of a stationary cylinder was seen for all forcing frequencies. However, the cylinder oscillation modifies the wake structures sufficiently to reduce the momentum deficit and hence drag coefficient with respect to the stationary cylinder. Power spectra are discussed in Sec. 4.7.

The recirculation length of the time-averaged wake normalized by the edge of the cylinder in cross section is given in Table 4 as a function of frequency. This quantity diminishes with increasing frequency at both Reynolds numbers. The recirculation length scales with base pressure on the rear side of the cylinder in the sense that smaller base pressures result in longer recirculation lengths. Hence, a reduction in the recirculation length is indicative of a higher base pressure and a lower drag.

Drag coefficient and Strouhal number as functions of the amplitude of excitation are presented in Table 5. The excitation frequency is kept fixed and equal to that of vortex shedding of a stationary cylinder. A constant Strouhal number is observed with increase in amplitude of excitation indicating that the amplification of the fundamental mode is the highest among all modes and no other harmonic dominates over the basic vortex shedding process. The drag coefficient (along with the recirculation length) generally decreases with an increase in amplitude. However, when the amplitude reaches 0.32, the turbulent stresses provide a significant contribution to drag and the total drag coefficient starts to increase. The recirculation length, however, shows a continuously decreasing trend.

4.2 Velocity Field. The time-averaged velocity vectors and velocity profiles for various oscillation frequencies are shown in Figs. 4–6 for a Reynolds number of 170. Both x- and y-axes have been nondimensionalized with the cylinder size. The shaded con-

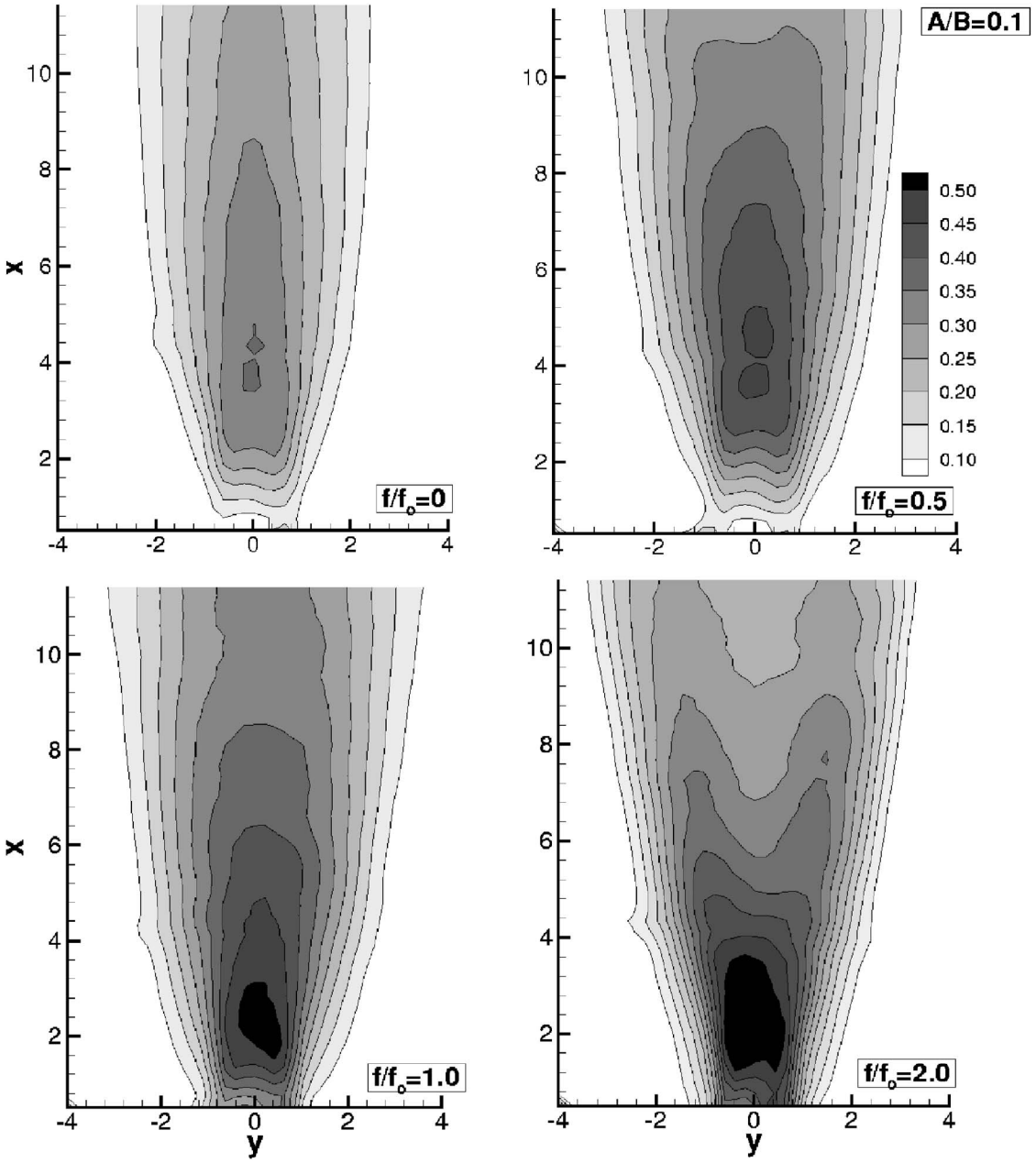

Fig. 8 Nondimensional contours of turbulent intensity in the wake of an oscillating square cylinder as a function of the forcing frequency, Re=170, A/B=0.1

tours are of resultant velocity, being the darkest in zones of small velocity magnitude. The velocity vectors in the near wake are seen to be affected by the forced oscillations. The overall shapes of the flooded velocity contours are similar for frequency ratios of 0, 0.5, and 1, but different for $f/f_0=2.0$. For this frequency ratio, the drag coefficient shows a marginal increase with respect to frequency ratio of unity (Table 2). The corresponding far-wake velocity profile shows branching in the contours and a double hump in the u-velocity profile (Fig. 5). The slight increase in drag coefficient at a frequency ratio of 2 (with respect to unity) is thus explained in terms of a broader wake that, in turn, lowers the base pressure. The origin of the broadening is explained with respect to the instantaneous plots of Sec. 4.5.

The v velocity is affected significantly by cylinder oscillations (Fig. 6). The magnitude of peak v velocity increases with an increase in the oscillation frequencies and is the highest at $f/f_o=2.0$. The overall increase in v velocity indicates greater interaction between the vortices of the neighboring shear layer. An increase in the transverse velocity with frequency is indicative of higher flow entrainment into the wake. It is, in turn, responsible for a reduction in the size of the recirculation zone (Fig. 4, also see Sec. 4.3). The shape and size of the flooded velocity contours demonstrates that the size of the recirculation zone is indeed a function of the excitation frequency. Equivalently, the magnitude of the centerline u velocity can be seen to increase in the near wake (Fig. 5).

4.3 Vorticity Field and Streamlines. Figure 7 shows the time-averaged spanwise vorticity contours for various frequency ratios (0.5, 1.0, and 2.0) at an amplitude of oscillation $A/B=0.1$. With an increase in frequency, Fig. 7 shows that the vortices, on average, move closer to the cylinder and get concentrated in the near wake. For the amplitude considered, the maximum strength of the vortices does not change significantly with the frequency of

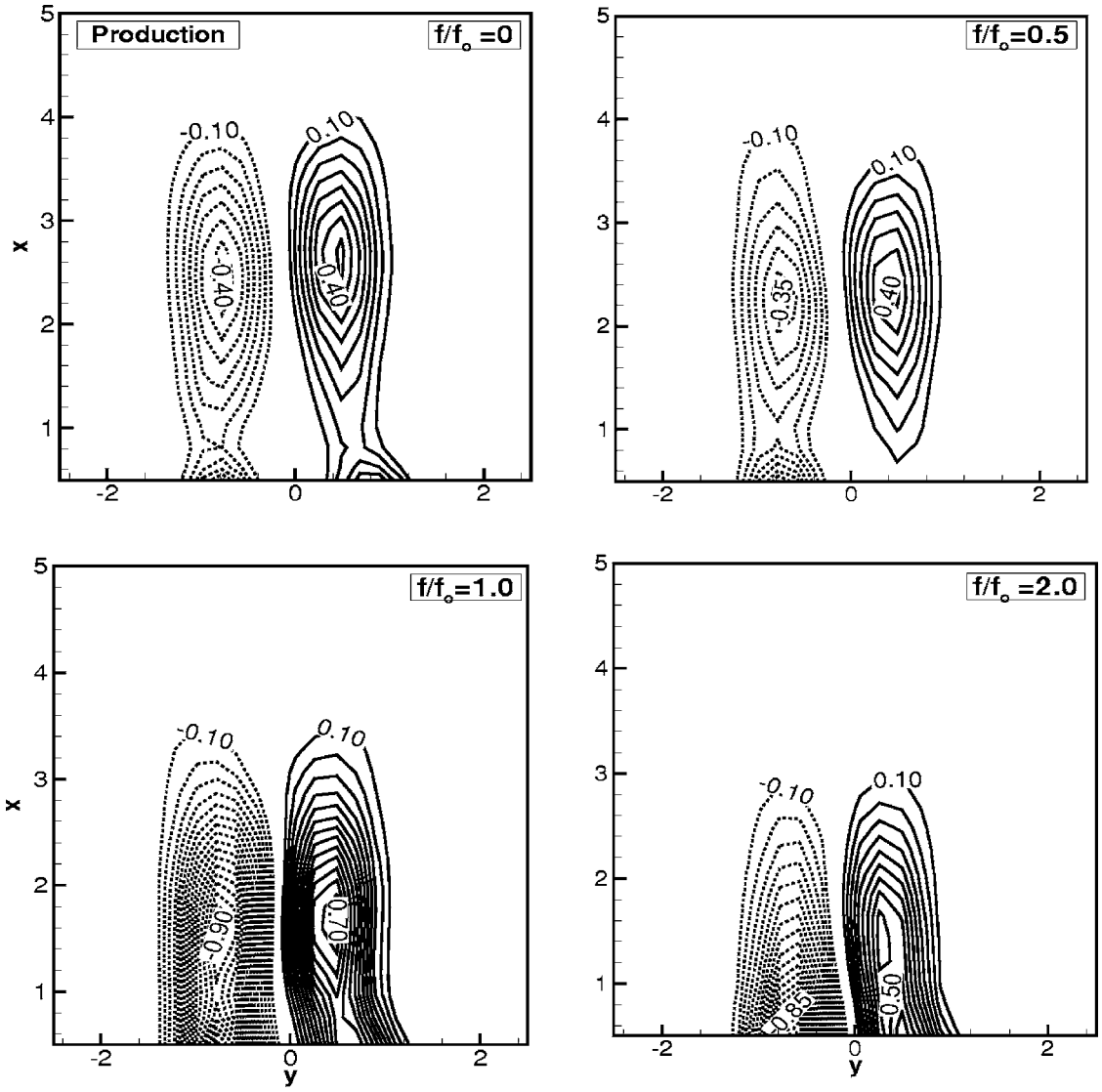

Fig. 9 Dimensionless production of turbulent kinetic energy, Re=170, A/B=0.1

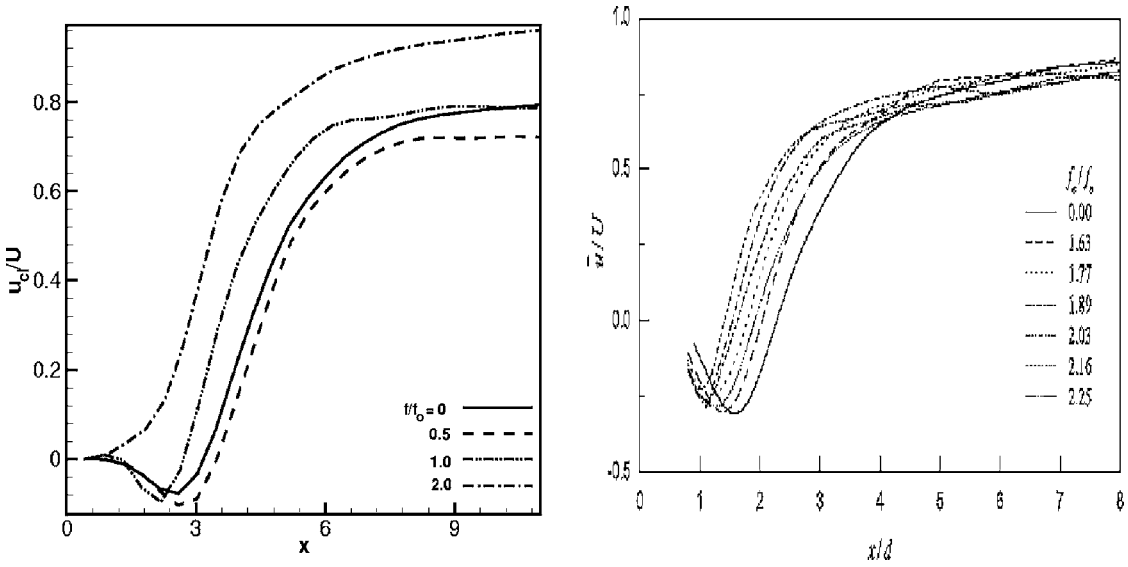

Fig. 10 Comparison of centerline recovery of streamwise velocity of the present study (left) at various oscillation frequencies with Konstantinides et al. [15] (right). The reference study is for a circular cylinder.

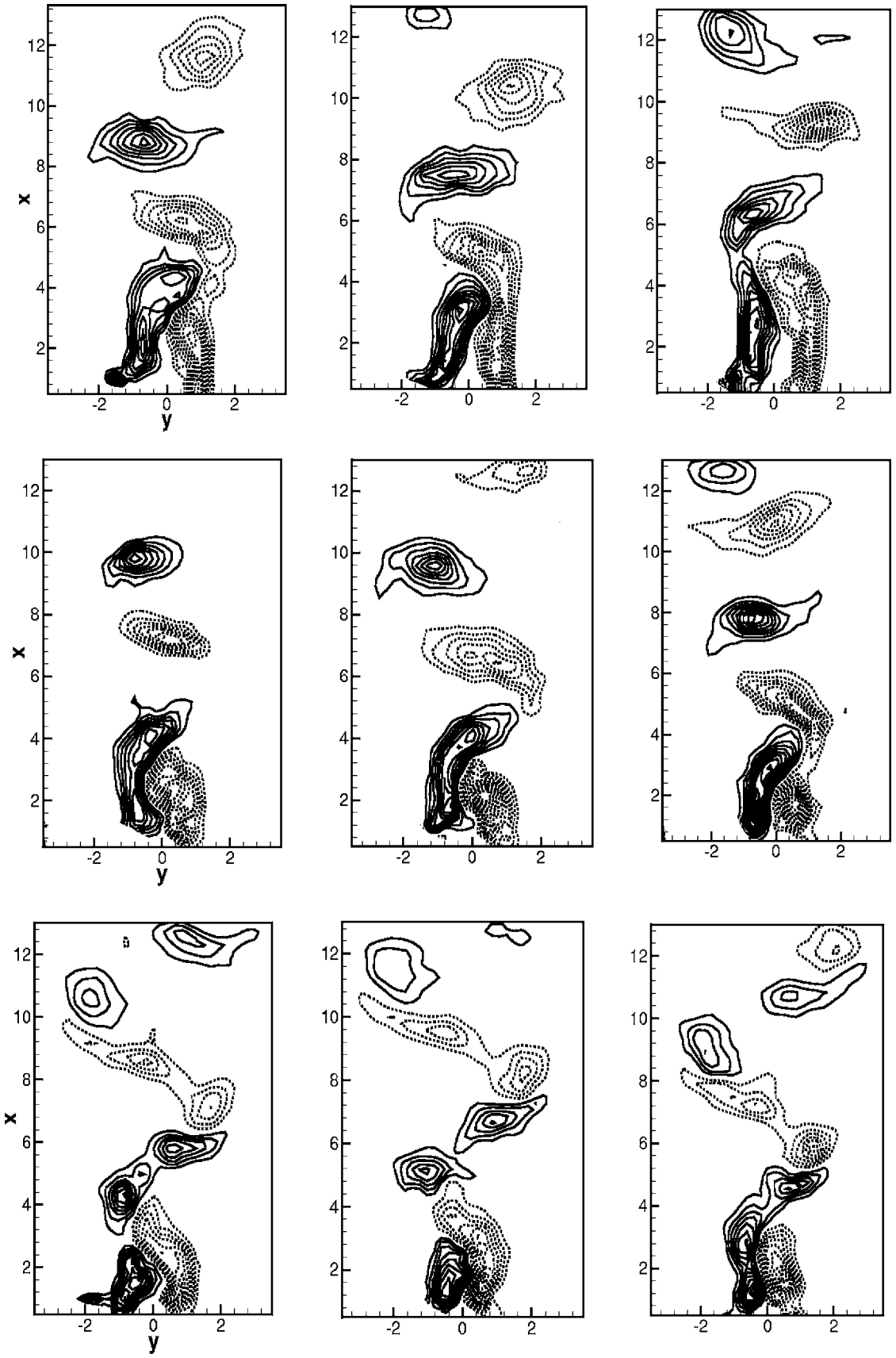

Fig. 11 Instantaneous spanwise vorticity contours above an oscillating cylinder. First row: $f/f_0=0.5$; second row: $f/f_0=1$; third row: $f/f_0=2$. $A/B=0.1$; maximum, minimum, and increments in ω_z are 3, −3, 0.25.

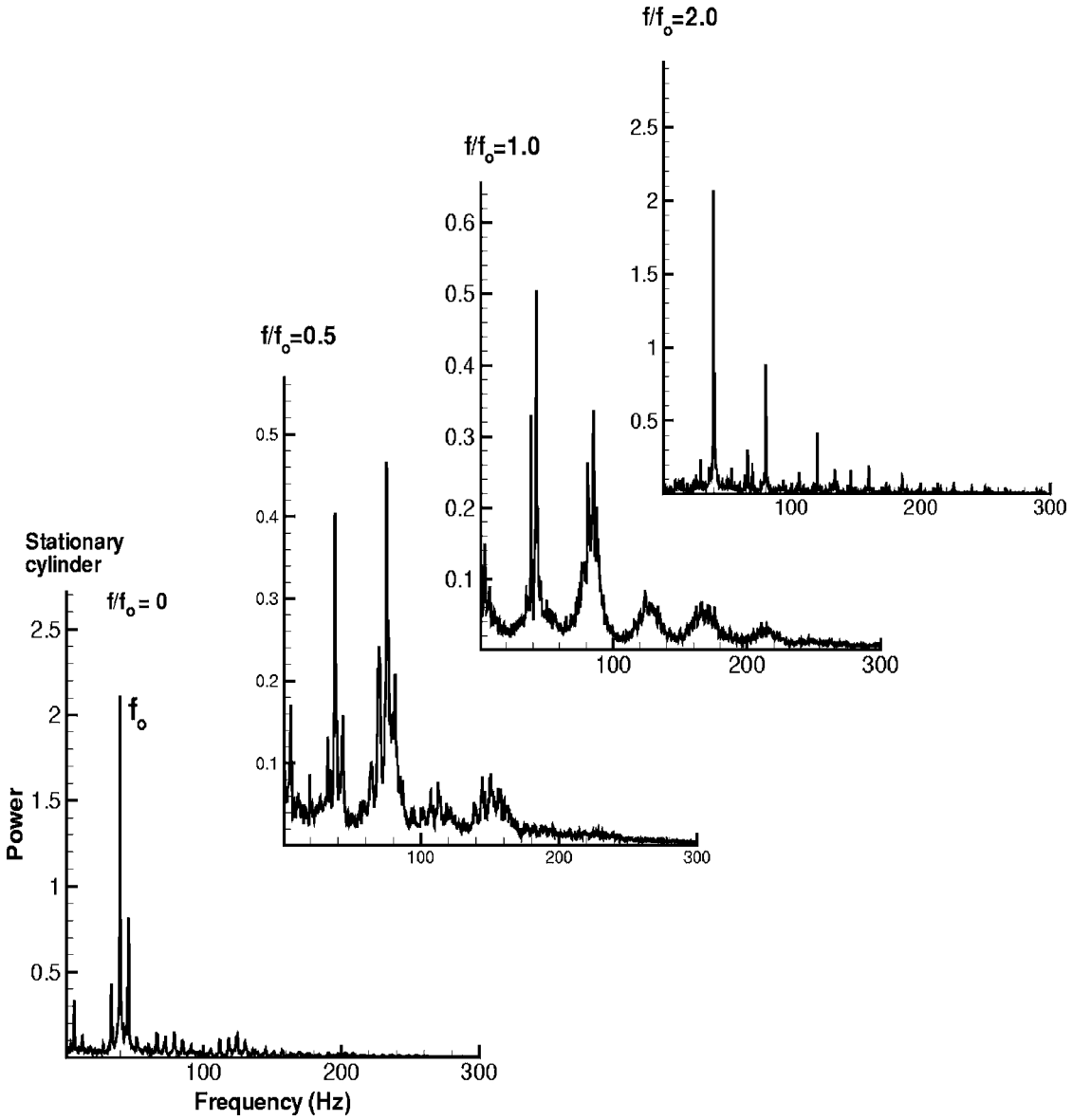

Fig. 12 Power spectra of the transverse velocity component in the wake of an oscillating cylinder; Re=170

oscillation. Vorticity concentration in the near field region has also been observed in the context of circular cylinder oscillations [4]. The movement of the point of maximum vorticity toward the cylinder confirms the reduction in the size of the recirculation zone of Fig. 4.

Vorticity in the wake can be traced to the shear layer separating at the cylinder corners. Subsequently, it is swept along the wake, while being diffused by the fluid viscosity. The vorticity production in the wake is proportional to the velocity difference between the main stream and the cylinder centerline velocity. The time instants at which flow separation takes place on each side of the cylinder correspond to distinct phases in the cylinder oscillation. Hence, the strengths of the vortices on either side of the cylinder are not necessarily of equal strength. Vortices are also subjected to strain fields imposed by the near field vortices. The vorticity contours of Fig. 7 show that for the present experiments, the effect of forced oscillations on flow symmetry is small. The sizes of two oppositely oriented vortices are close to each other and the peak values are close as well. However, the mechanism of vorticity distribution or budgets in the wake region is dependent on the excitation frequency leading to the movement of maximum vorticity zone closer to the cylinder for the excited case. The influence on the time-averaged properties, such as drag coefficient, is, however, significant (Sec. 4.1).

Figure 7 also shows the streamline contours from the time-averaged velocity vectors at the midspan of the cylinder for Re $=170$. With an increase in excitation frequency, the streamline patterns show that the size of the recirculation bubble reduces. The shape of the streamline contour is similar to that of the vorticity contours except at excitation frequency $f/f_0=2$. The size of the recirculation bubble is smaller than that of the vorticity contour. The recirculation zone for $f/f_0=2$ is smaller than the measurement zone of this study. Therefore, the recirculation bubbles are not clearly seen at $f/f_0=2$. This trend has been observed for a circular cylinder by other authors, notably Konstantinides et al. [15]. Zdravkovich [16] pointed out that wakes of a cylinder forced to oscillate in either the transverse or the streamwise direction share several characteristics, including reduction in vortex formation length and an increase in base pressure. The reduction in vortex formation length in the synchronization range has also been observed for a circular cylinder oscillated in the transverse

direction [6]. The reduction in vortex formation length indicates directly an increase in the base pressure and hence a reduction in the drag coefficient.

4.4 Velocity Fluctuations. Figure 8 shows the spatial distribution of percentage turbulence intensity (based on two components of velocity fluctuations) for a Reynolds number of 170. The turbulence intensity has been normalized with the incoming velocity. With an increase in frequency, the location of maximum turbulence intensity moves closer to the cylinder. There is a strong effect of forcing frequency on the turbulence intensity field. It increases with oscillation frequency and is highest at $f/f_0=2$. The size of the maximum turbulence intensity zone widens in the transverse direction, with an increase in excitation frequency. This observation is to be expected since advective transport of turbulent kinetic energy across the wake is governed by the fluctuating component of the transverse (v) velocity. A double peak in turbulence intensity appears on each side of the cylinder for $f/f_0=2$. This result was noted for the time-averaged velocity profile as well (Fig. 5). Hence, the field of velocity fluctuations is seen to relate to the distribution of the time-averaged streamwise velocity component. This indicates different vortex-shedding mechanisms for $f/f_0=2$ and have been discussed later in Secs. 4.6 and 4.8.

Figure 9 shows contours of the production term of kinetic energy of velocity fluctuations. This production term is defined as $\langle u'u'\rangle(\partial u/\partial x)+\langle v'v'\rangle(\partial v/\partial x)+\langle u'v'\rangle(\partial u/\partial y)+\langle u'v'\rangle(\partial v/\partial x)$ and is nondimensionalized by U^3/B. Regions of high production appear in regions of high rms velocity fluctuation of Fig. 8. In addition, the turbulent intensity production contour shape is similar to that of the time-averaged vorticity field (Fig. 7). However, the maximum magnitude of turbulent kinetic energy production distribution shows greater asymmetry between the two sides of the cylinder centerline compared to that of the vorticity for excitation frequency $f/f_0=1$ and 2. It may be noted that a higher v-velocity magnitude is seen at excitation frequencies of $f/f_0=1$ and 2 in Fig. 6. The higher value of turbulence production for these cylinder oscillation cases may be attributed to the greater magnitude of normal stresses.

4.5 Centerline Recovery. Figure 10 shows a comparison of recovery of centerline streamwise velocity with the data reported by Konstantinidis et al. [15] for various forcing frequencies. The trends in the two plots (for $f/f_0\geq 1$) are quite similar. With an increase in the forcing frequency, the vortex formation region, as measured by the distance over which negative streamwise velocities prevail, is seen to diminish in size.

Figure 10 shows that the centerline velocity drops to a minimum value and recovers subsequently for all excitation frequencies. The rate of recovery diminishes in the downstream direction. It is faster in the near field region and is also a function of the excitation frequency. With an increase in frequency, the recovery of centerline velocity is rapid for frequency ratios of 1 and 2. The PIV data of Fig. 4 also shows that the region of reversed flow decreases in size with an increase in excitation frequency when compared to a stationary cylinder. The centerline recovery is directly related to the wake width which, in turn, depends on entrainment at the edge of the wake. The greater v-velocity profile for cylinder oscillation at $f/f_0=1$ and 2 in Fig. 6 also confirms the greater entrainment from the mean flow. Figure 10 indicates an increase in entrainment with increasing frequency and the centerline recovery to be fastest at $f/f_0=2$ among all excitation frequencies considered.

The difference in centerline velocities in Fig. 10 for frequency ratios between 0 and 0.5 is small. This result is also brought out in Fig. 4, where the size of the recirculation zone is barely altered at $f/f_0=0.5$. In fact there is a slight increase, with the centerline velocity in Fig. 10 reaching an asymptotic value later, in comparison to a stationary cylinder. The reduction in drag coefficient at a

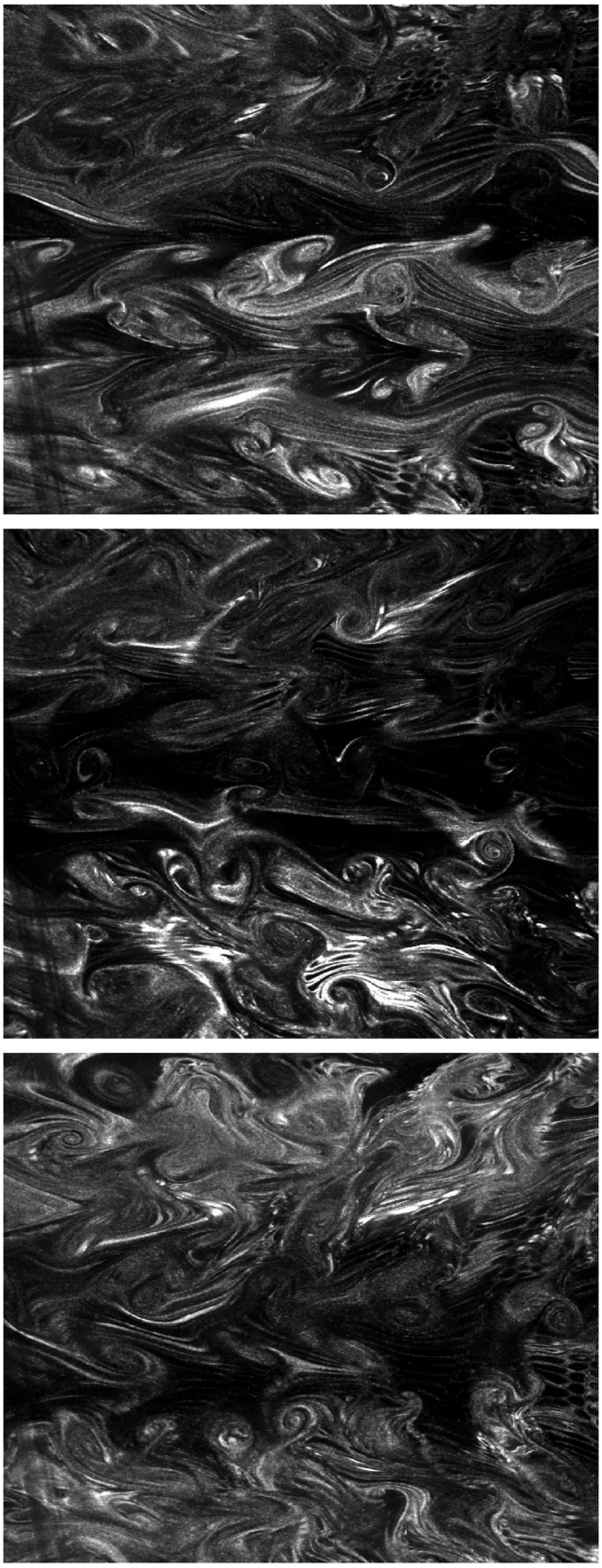

Fig. 13 Instantaneous flow visualization images on the *x-z* plane for various forcing frequencies ($f/f_0=0.5$, bottom; 1, middle; 2, top); 80% of the cylinder length is included in each frame. Main flow direction is from the right to the left.

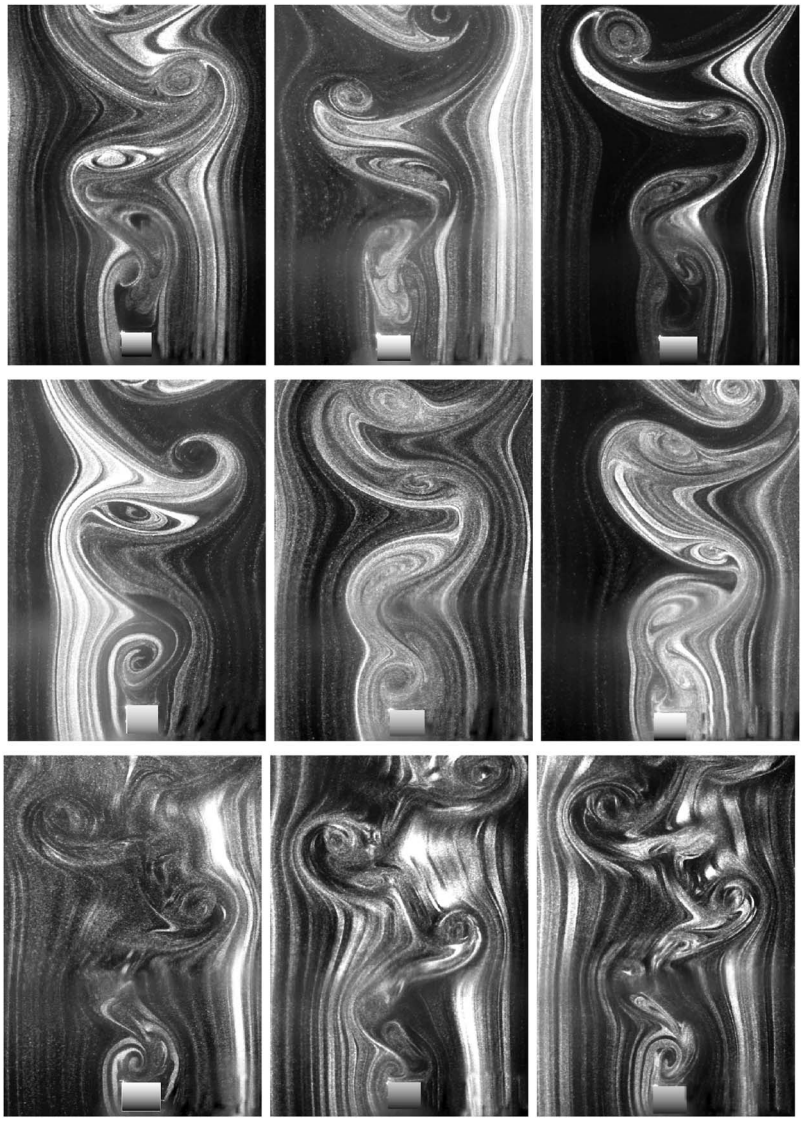

Fig. 14 Instantaneous flow visualization images in the *x-y* plane for various forcing frequencies (frequency ratios=0.5, 1, 2)

frequency ratio of 0.5 is related to the weakening of the base region though its size starts to diminish only at higher frequency ratios.

4.6 Instantaneous Spanwise Vorticity Field. Figure 11 shows instantaneous vorticity contours at selected instants of time for different frequencies of oscillation. As the frequency increases, the near-wake vortex pattern changes due to a change in the characteristics of vortex shedding. The vortices grow behind the cylinder and are subsequently shed. The vortex roll-up distance decreases with an increase in frequency. The vortex roll-up distance is the lowest at the highest excitation frequency ($f/f_0=2$). The reduction in the streamwise length scale carries over to the time-averaged data as well (Fig. 7). The alternate vortices shed from the cylinder are transported in the downstream direction. The vortex shed from one shear layer is drawn toward the other. This process repeats for both sides of the shear layer. The lateral movement of the vortices is the highest for an excitation of $f/f_0=2$. At this frequency of excitation, two neighboring vortices travel as a group having smaller streamwise separation compared to the subsequent pair of vortices. The dual peak in the streamwise velocity profile (Fig. 5) and that in the turbulence intensity distribution of Fig. 8 can be attributed to the higher lateral movement of the separated shear layers at $f/f_0=2$. The large spread of vorticity in the transverse direction at a frequency ratio of 2 is also indicative of a lower base pressure and slightly higher drag (Table 2).

Alternate shedding of vortices, typical of a stationary cylinder, is referred to as the *S* mode in the literature [8]. The lateral (transverse) movement of vortices is the *P* mode and is observed for transverse oscillation of the cylinder with respect to the mean flow direction, Williamson and Roshko [17]. In the present experiments, the shedding pattern is seen to be predominantly of the *S* type. At the frequency ratio $f/f_0=2$, a combination of *P* and *S* modes is observed.

4.7 Power Spectra. Figure 12 shows power spectra at a Reynolds number of 170 for three nondimensional forcing frequencies along with the stationary cylinder. The spectra were obtained from a long-time signal of 20,000 samples at a sampling rate of 1000 Hz. Spectra have been calculated based on the v component of velocity (at $x/B=5$ and $y/B=1$) and normalized by their respective areas under the curve. The time record involves at least 300 cycles of vortex shedding. For the low Reynolds number experiment (Re=170), a pure Karman vortex shedding pattern is observed for a stationary cylinder. It corresponds to a single

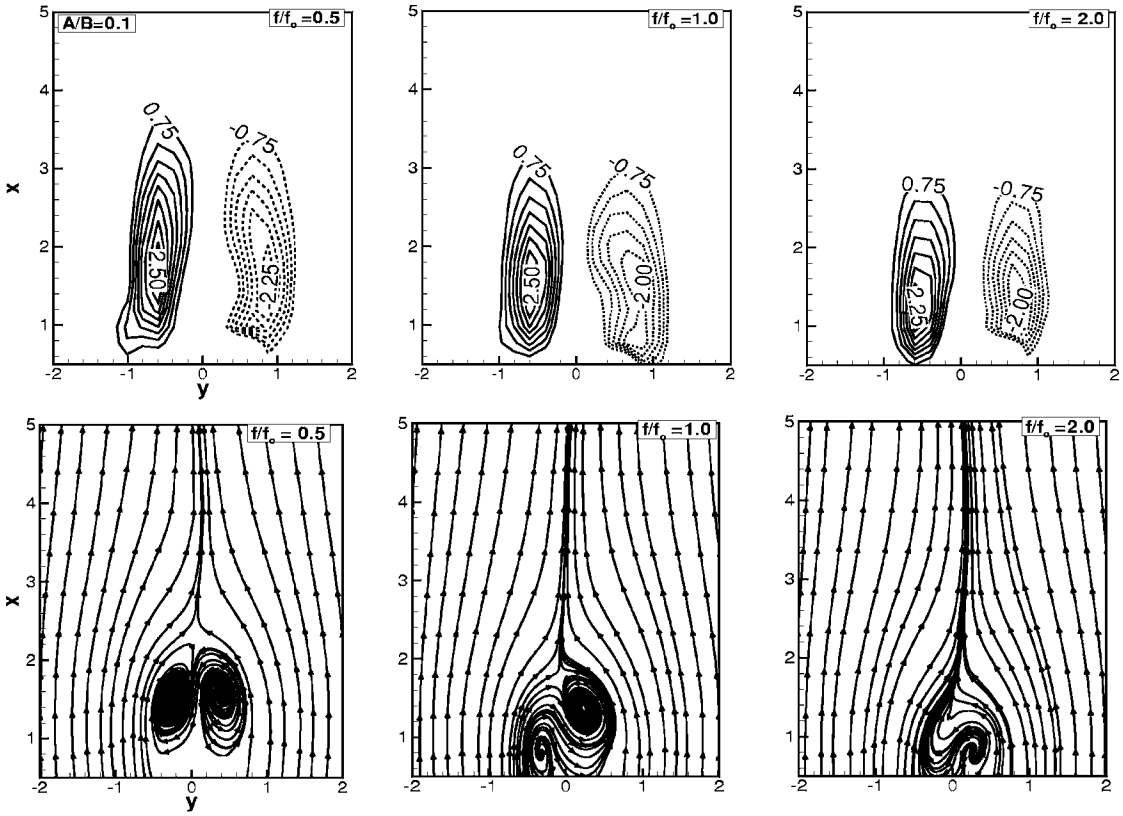

Fig. 15 Time-averaged spanwise vorticity contours (ω_z) and streamlines in the wake of a square cylinder at various frequency ratios (0.5,1,2) with a perturbation amplitude at A/B=0.1 and Re=355

sharply defined peak of vortex shedding in the spectra (at 39 Hz). With externally applied forcing frequency, Fig. 12 shows that a spectral peak is consistently seen at 39 Hz, though additional spectral peaks appear in the spectra. At a forcing frequency ratio of 0.5, the unsteadiness due to cylinder motion at a frequency of 19.5 Hz is not to be seen. Instead, a peak at 78 Hz higher than the one at 39 Hz is realized. The excitation at subharmonic frequency (f/f_0=0.5) has been observed to contribute toward vortex merging in the mixing layer. The absence of a spectral peak at f/f_0 =0.5 for square cylinder oscillation indicates absence of vortex merging phenomena due to subharmonic excitation. At a frequency ratio of unity, the cylinder motion reinforces vortex shedding and the peak shifts clearly to 39 Hz. The nonlinear interaction between the forcing signal and vortex-shedding frequency generates sum and difference frequencies in the spectrum and is responsible for the second peak. At a frequency ratio of 2, the peak remains at 39 Hz and its magnitude is significantly greater than at 0.5 and unity. An additional smaller peak corresponding to cylinder motion is seen at 78 Hz. The increase in the magnitude of the spectral peak to a value close to that of the stationary cylinder shows that lock-on conditions prevail in the wake. This is consistent with the data of Griffin and Ramberg [1], who show that lock-on should appear for an amplitude ratio of 0.1 and a frequency ratio of 2, but not for other frequency ratios. The authors also suggest that the flow field would be close to two-dimensional under lock-on conditions. This conjecture is supported by the flow visualization images of Fig. 13. Here, the particle traces tend to get straightened at the highest frequency ratio (f/f_0=2).

4.8 Flow Visualization Images. Figure 14 shows particle traces in the cylinder wake recorded using PIV at forcing frequencies of 0.5 (first row), 1 (second), and 2 (third). The first column corresponds to the instant when the cylinder is at its extreme top position. The second has the cylinder at the mean position, while the third column corresponds to the lowest position of the cylinder. The flow distribution for a stationary cylinder, namely, alternate shedding of vortices from either side of the cylinder, is quite similar to that corresponding to a frequency ratio of 0.5 and is not shown. The streamwise distance over which a vortex rolls up relative to the cylinder position known as vortex formation length decreases with an increase in frequency of oscillation. The reduction in the vortex formation length carries over to the time-averaged data as well (Fig. 7). For all three frequencies, the vortex detaches from the upstream corner during the passage of the cylinder in the downward direction. The phase corresponds to the extreme top position of the cylinder. For frequencies of 0.5 and unity, the centers of vortices essentially remain on one side of the midplane. At a frequency ratio of 2, the wake reveals new features. Eddies are shed jointly from both sides of the cylinder, while alternate shedding also persists with a phase difference. The wake reveals two length scales corresponding to the separating shear layer and the spacing between vortices. The centers of the shed vortices move across the cylinder midplane. There is a broadening of the wake as well. The interaction between the neighboring vortices of the opposite shear layer is interrupted by the intermediate vortex structure appearing behind the primary large-scale shed vortex. These factors result in the double-peaked distribution of rms velocity contours (Fig. 8), slight increase in drag coefficient (Table 2), and additional harmonics in the power spectra.

4.9 Effect of Reynolds Number. Results discussed above are mainly at a Reynolds number of 170. Experiments have also been conducted at a second Reynolds number of 355. Broadly, no difference was seen in the wake behavior. The time-averaged vorticity and streamline plots at the higher Reynolds number are shown in Fig. 15. The vorticity plots look similar to Fig. 7 at Re=170, though the peak vorticity at the higher Reynolds number is also

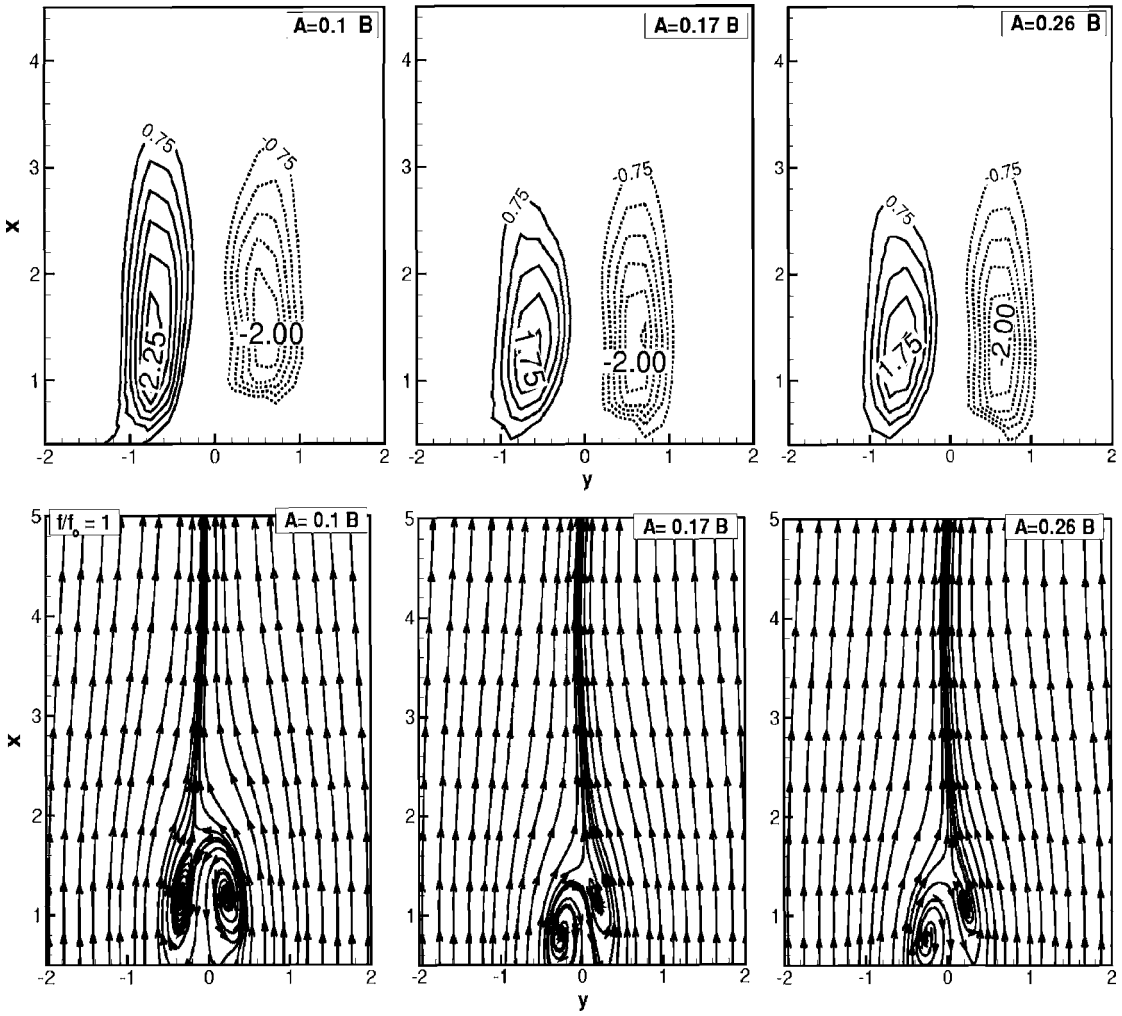

Fig. 16 Time-averaged vorticity and stream traces for various amplitudes of oscillation (A/B=0.1,0.17,0.26) at a forcing frequency f/f_0=1, Re=170

higher. To a first approximation, one can surmise that the effects of Reynolds number and frequency on the wake are independent. The effect of forced oscillations on flow symmetry is marginal, as seen from vorticity contours. The sizes of two oppositely oriented vortices are similar to each other, though not equal for the frequencies considered. The length of the recirculation bubble decreases with an increase in forcing frequency as in the lower Reynolds number experiments (Re=170). The streamline plots indicate greater asymmetry between the recirculation bubbles at the opposite sides of the cylinder centerline for excitation at f/f_0=1 and 2. The vortex formation length at both sides of the cylinder is affected to a greater extent for higher Reynolds number leading to greater asymmetry in flow structures at both sides of the cylinder.

4.10 Effect of Amplitude. In the present section, the effect of amplitude of oscillation on the flow structures is discussed. The forcing frequency is kept equal to the vortex-shedding frequency. With an increase in amplitude, the momentum flux pumped into the near wake of the cylinder increases. The vortex formation length reduces with an increase in the amplitude. These changes in the near-wake vortex formation process cause corresponding changes in the strength of the shed vortices. The increase in vortex strength can be interpreted as a corresponding increase in the rate of vorticity generation.

Time-averaged drag coefficient, Strouhal number, and recirculation length as functions of the amplitude of excitation are presented in Table 5. A constant Strouhal number is observed at all excitation amplitudes, indicating that the amplification of the fundamental mode is highest among all other modes and no other harmonics dominates over the vortex shedding with an increase in amplitude of excitation.

The time-averaged spanwise vorticity contours for various oscillation amplitudes are shown in Fig. 16. The time-averaged vorticity contour size reduces with increase in excitation amplitude, and the average vortex structure moves upstream toward the cylinder. An upstream migration of the large-scale vortex structure has also been observed earlier by Ongoren and Rockwell [2] for transverse oscillation experiments with cylinders of circular, square, and triangle cross sections.

Figure 16 also shows the streamline plot derived from the time-averaged velocity field. The size of the recirculation zone reduces with an increase in the amplitude of oscillation. When compared to the effect of forcing frequency on recirculation length, the effect of amplitude is less prominent. Simultaneously, an asymmetry in the flow field starts to appear. The increase in amplitude of oscillation makes the flow field asymmetric due to a distortion in the phase relationship between cylinder movement and the vortex shedding cycle. A strong coupling between oppositely oriented vortices is responsible for the asymmetry in the time-averaged data.

The effect of oscillation amplitude on the flow field can be understood from the following idealized context. Consider a situation where a cylinder moves in an infinite fluid and the superim-

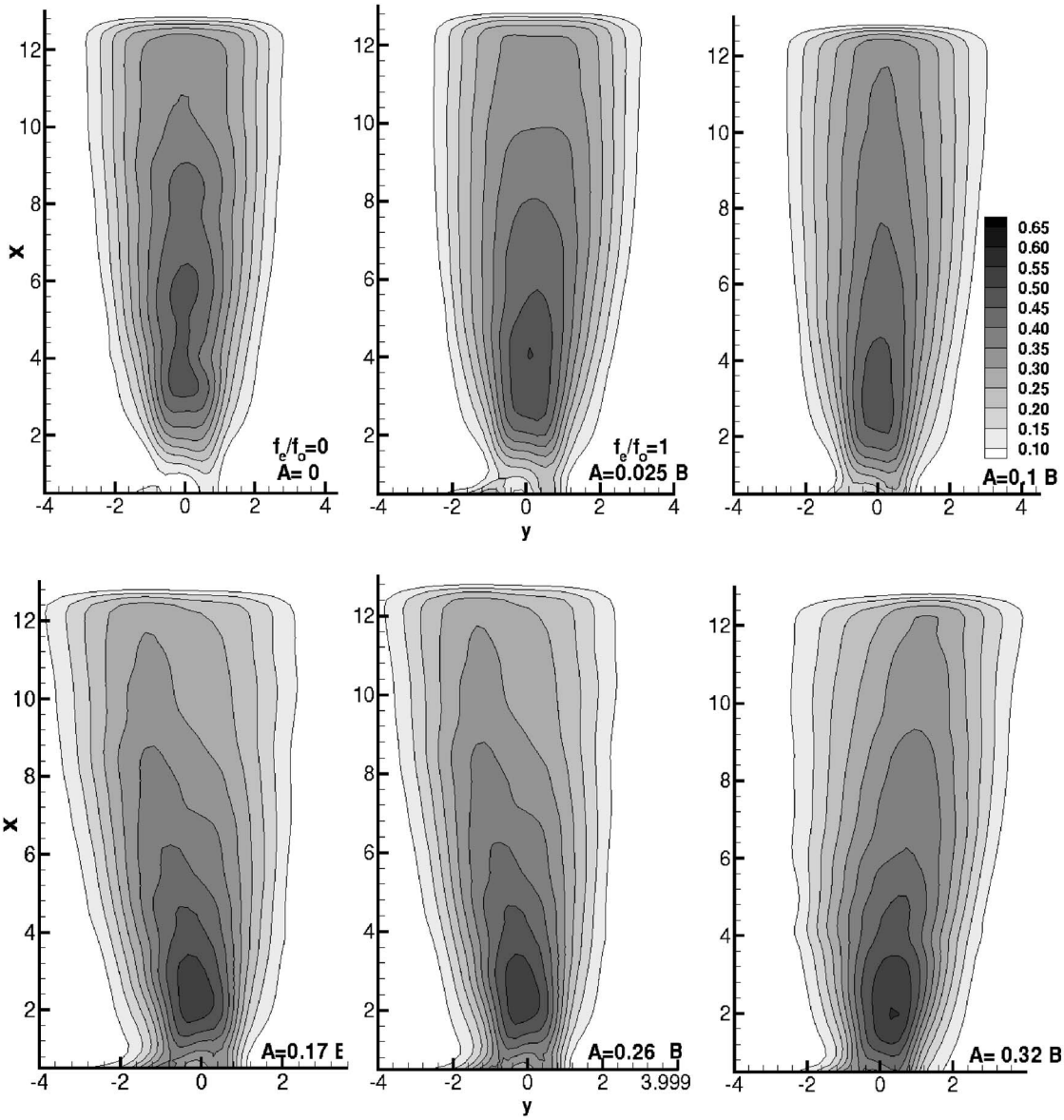

Fig. 17 Rms contours for various amplitudes of oscillation, Re=170

posed flow is zero. For a square cylinder with inline oscillations, two fixed stagnation points at the front and back of the cylinder are available. The resulting vortex-generation process can be described as follows. As the oscillating cylinder moves in the forward direction, two boundary layers develop on the cylinder wall. The separating flow creates two counterrotating vortices of equal magnitude and strength, resulting in geometrically similar vortex fields. The creation of vortices stops when the maximum forward location of the cylinder is reached and the cylinder starts its backward motion.

The vortex formation process is now repeated on the other side of the cylinder. In addition, the backward motion of the cylinder causes a splitting of the vortex pair, produced earlier by the forward motion, until, finally, flow reversal occurs. Thus, cylinder oscillation creates a strong damping effect in the near flow field and a concentration of vortices in the near wake of the cylinder. The higher the amplitude of oscillation is, the larger the damping effect is. One can now expect the superimposed flow to modulate the vortex-generation process described above because of vortex shedding.

Figure 17 shows the nondimensional turbulence intensity field at various amplitudes of oscillation. The turbulent intensity near the cylinder increases as more energy enters the flow field from cylinder excitation. The maximum intensity value moves toward the cylinder with an increase in excitation amplitude. The degree of asymmetry increases as well with an increase in the amplitude.

Figure 18 shows the power spectra of velocity signals in the near wake at different amplitudes of oscillation. With an increase in the amplitude of oscillation, multiple harmonics of the frequency of vortex shedding start to appear. At a particular amplitude ($A/B=0.32$), the flow field is dominated by the forcing frequency and only one dominant peak is seen in the power spectra. This may be considered as a lock-on state, and the flow can be considered increasingly two-dimensional with increase in amplitude.

4.11 Effect of Aspect Ratio. A limited study was carried out to investigate the effect of aspect ratio on the near wake of a cylinder under oscillatory conditions. While the aspect ratio considered in earlier sections was 28, the aspect ratio in the present discussion is 16. For definiteness, a Reynolds number of 170 is considered. The effects of frequency as well as amplitude of oscillation are investigated.

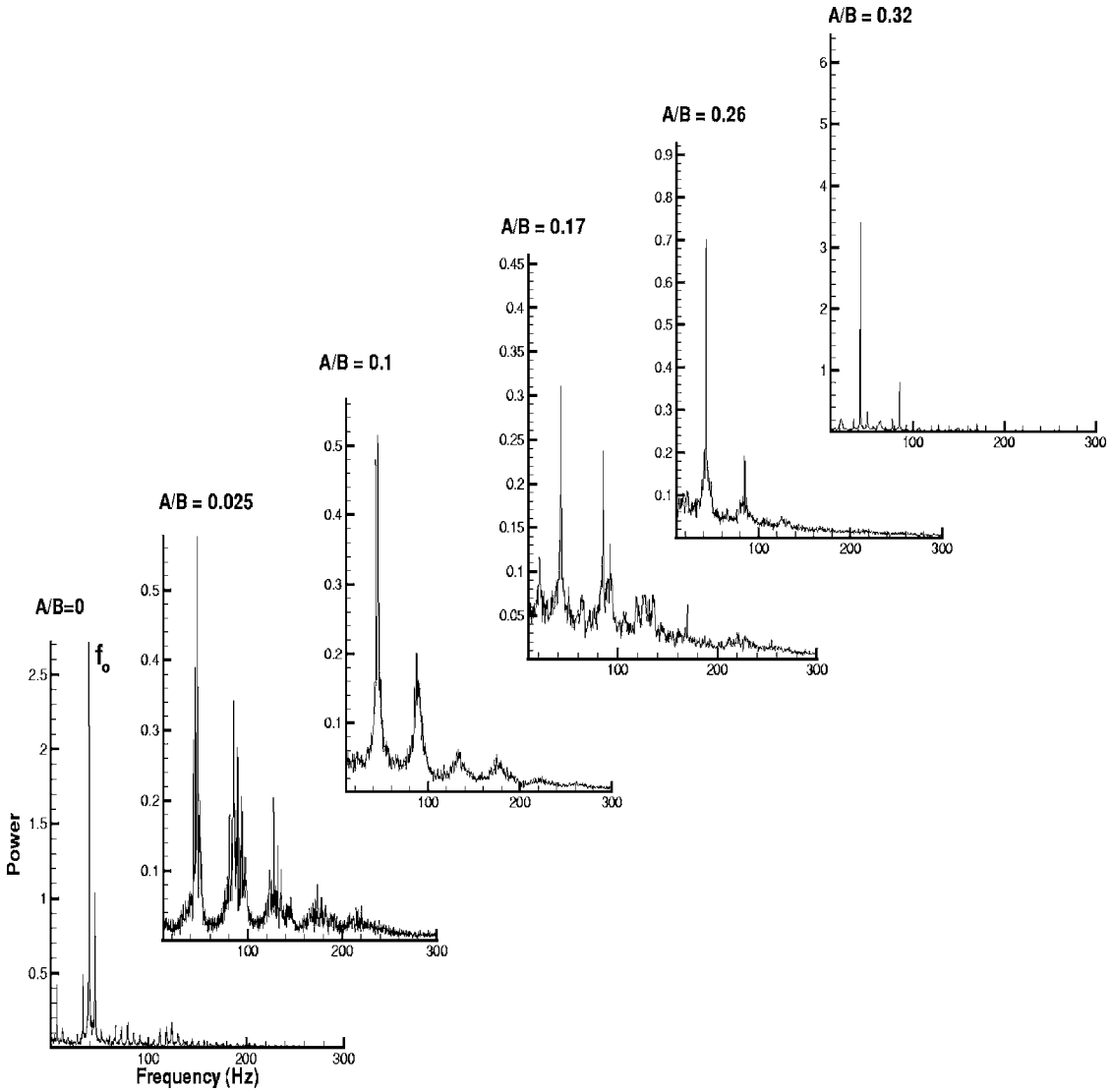

Fig. 18 Power spectra for various amplitudes of oscillation, Re=170

Table 6 summarizes the time-averaged drag coefficient data for two aspect ratios 16 and 28 for various frequencies and amplitudes of oscillation. In the study of the effect of frequency, the amplitude is kept constant at 0.1. In the second set of experiments, the forcing frequency is that of vortex shedding, while the amplitude is varied. The overall drag coefficient is lower at the higher aspect ratio for both unexcited and excited cylinders. A minimum in drag coefficient is seen for a frequency ratio $f/f_0=1.0$ for the two aspect ratios. This indicates that the end conditions due to the difference in aspect ratio do not alter the effect of cylinder oscillation. The magnitude of drag coefficient at AR=16 is uniformly higher when compared to the higher aspect ratio experiments. This effect of aspect ratio on drag coefficient was seen for a stationary cylinder as well. The drag coefficient diminishes rapidly with an increase in the amplitude of oscillation.

Figure 19 shows the time-averaged spanwise vorticity contours for various frequencies ($f/f_0=0.5$, 1.0, and 2.0) and amplitudes ($A/B=0.1$, 0.14, and 0.21) at the aspect ratio of 16. With an increase in the forcing frequency, the vortices concentrate near the rear surface of the cylinder. Similar trends were observed at the higher aspect ratio (Fig. 7). However, the strength of vorticity is higher in the lower aspect ratio experiment (Fig. 19) when compared to the higher one (Fig. 7). The higher vorticity at lower aspect ratio may be related to the confinement effects. The comparison of Fig. 19 (top) with Fig. 19 (bottom) indicates similar effects of excitation amplitude and frequency. Overall, aspect ratio does not alter the characteristics of the oscillating cylinder.

5 Conclusions

An experimental study of uniform flow past an oscillating square cylinder is reported. Measurement techniques are based on PIV, HWA, and flow visualization. The Reynolds number mainly considered is 170, while selected results for Re=355 have also been presented. The cylinder is oscillated using an electromagnetic actuator at around the vortex-shedding frequency of the equivalent stationary cylinder. The following conclusions have been arrived at in the study:

1. Effect of frequency ($A/B=0.1$; Re=170). A strong effect of forcing frequency is clearly to be seen in the near wake. The recirculation length reduces by a factor of 5 for an increase in frequency ratio from zero to two. The time-averaged drag

Table 6 Comparison of drag coefficient as a function of forcing frequency and amplitude for two aspect ratio (AR=16 and 28) at Re=170. Drag coefficients are based on the momentum deficit of the wake.

A/B	AR=16	AR=28
0	2.34	1.48
0.05	2.55	-
0.1	1.91	0.94
0.17	1.72	0.85
0.23	1.34	0.81
0.27	1.21	-
f/f_{o0}	AR=16	AR=28
0	2.34	1.48
0.5	2.61	1.13
1.0	1.91	0.94
2.0	2.02	1.05

acting on the cylinder is correspondingly lowered by ~25% from that of a stationary cylinder. The contribution of the turbulent stresses on the time-averaged drag coefficient is in the range of 30–50%, thus being significant in all experiments. The instantaneous vorticity contours show the length of the shear layer to be lowered before separation; hence, the longitudinal wavelength of the shed vortices reduces. With an increase in frequency, the large-scale vortices move closer to the cylinder. The rms velocity fluctuations cluster around the cylinder as well, though they spread in the transverse direction. Power spectra reveal lock-on conditions only at the highest frequency ratio.

2. Effect of amplitude ($f/f_0=1$; Re=170). The effect of increasing the amplitude at a given frequency leads to a reduction in the length of the recirculation bubble by ~57% of a stationary cylinder. The reduction in the time-averaged drag coefficient is ~30% when the highest amplitude ratio of 0.32. The time-averaged velocity profiles show asymmetry with increase in the perturbation amplitude. Asymmetry is related to the phase difference between the vortex-shedding mechanism and the cylinder motion. The peak value of rms velocity increases with amplitude, being 80% higher at the highest amplitude. The peak rms value also moves upstream toward the cylinder with an increase in the amplitude. Lock-on conditions were seen at the highest amplitude ratio of 0.32.
3. Effect of aspect ratio. With an increase in frequency and amplitude of oscillation, the recirculation length reduces. The time-averaged momentum deficits of the lower aspect ratio cylinder exceed those of the higher by a factor of 60%. However, the effects of forcing frequency and amplitude on the wake properties are similar at aspect ratios of 16 and 28.

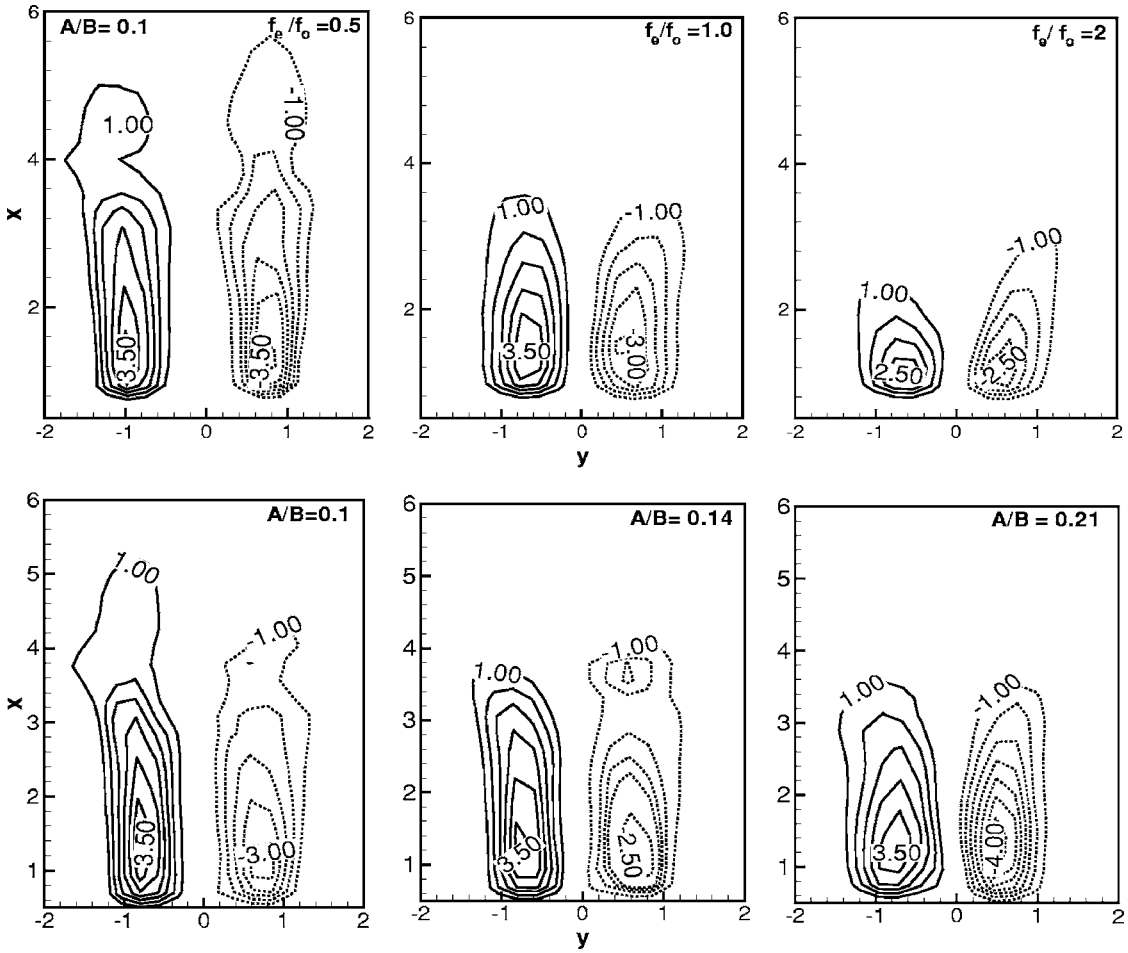

Fig. 19 Time-averaged spanwise vorticity contours (ω_z) for various forcing frequencies ($f/f_0=0.5,1,2$) (top) and amplitude ($A/B=0.1,0.14,0.21$) (bottom) at Re=170; aspect ratio=16

Acknowledgment

The authors acknowledge partial financial support received from the Naval Research Board, New Delhi, India, for this study.

Nomenclature

A = amplitude of oscillation, m
AR = aspect ratio, L/B
B = edge of the square cylinder, m
C_D = drag coefficient based on the average upstream velocity and B,
f = forcing frequency, Hz
f_o = vortex shedding frequency of stationary cylinder, Hz
KC = Carpenter number, $2\pi A/B$
L = length of the square cylinder, m
Re = Reynolds number based on cylinder diameter, $\rho UB/\mu$
rms = root-mean-square velocity, m/s
St = Strouhal number, fB/U
t = time
u = x component of velocity, m/s
U = upstream velocity, m/s
v = y component of velocity, m/s
V_r = reduced velocity, U/Bf
W = width of the test section, m
x,y,z = dimensionless coordinates from the cylinder center scaled by B

Greek symbols

μ = dynamic viscosity, kg/s m^2
ρ = density, kg/m^3
ω_z = spanwise component of the vorticity scaled by U/B

References

[1] Griffin, O. M., and Ramberg, S. E., 1976, "Vortex Shedding From a Cylinder Vibrating In-Line With an Incident Uniform Flow," J. Fluid Mech., **75**(2), pp. 257–271.
[2] Ongoren, A., and Rockwell, D., 1988, "Flow Structure From an Oscillating Cylinder Part 1. Mechanism of Phase Shift and Recovery in the Near Wake," J. Fluid Mech., **191**, pp. 197–223.
[3] Roussopoulos, K., 1993, "Feedback Control of Vortex Shedding at Low Reynolds Numbers," J. Fluid Mech., **248**, pp. 267–296.
[4] Gu, W., Chyu, C., and Rockwell, D., 1994, "Timing of Vortex Formation From an Oscillating Cylinder," Phys. Fluids, **6**(11), pp. 3677–3682.
[5] Tao, J. S., Huang, X. Y., and Chan, W. K. (1996), "A Flow Visualization Study on Feedback Control of Vortex Shedding From a Circular Cylinder," J. Fluids Struct., **10**, pp. 965–970.
[6] Krishnamoorthy, S., Price, S. J., and Paidoussis, M. P., 2001, "Cross-Flow Past an Oscillating Circular Cylinder: Synchronization Phenomena in the Near Wake," J. Fluids Struct., **15**, pp. 955–980.
[7] Cetiner, O., and Rockwell, D., 2001, "Streamwise Oscillations of a Cylinder in a Steady Current. Part 1. Locked-on States of Vortex Formation and Loading," J. Fluid Mech., **427**, pp. 1–28.
[8] Sarpkaya, T., 2004, "A Critical Review of the Intrinsic Nature of Vortex-Induced Vibrations," J. Fluids Struct., **19**, pp. 389–447.
[9] Yang, S. J., Cheng, T. R., and Fu, W. S., 2005, "Numerical Simulation of Flow Structures Around an Oscillating Rectangular Cylinder in a Channel Flow," Comput. Mech., **35**, pp. 342–351.
[10] Nobari, M. R. H., and Naderan, H., 2006, "Numerical Study of Flow Past a Cylinder With Cross Flow and Inline Oscillation," Comput. Fluids, **35**, pp. 393–415.
[11] Nishihara, T., Kaneko, S., and Watanabe, T., 2005, "Characteristics of Fluid Dynamic Forces Acting on a Circular Cylinder Oscillated in the Streamwise Direction and Its Wake Patterns," J. Fluids Struct., **20**, pp. 505–518.
[12] Westerweel, J., Dabiri, D., and Gharib, M., 1997, "The Effect of a Discrete Window Offset on the Accuracy of Cross-Correlation Analysis of PIV Recordings," Exp. Fluids, **23**, pp. 20–28.
[13] Chang, K.-A., and Liu, P. L.-F., 2000, "Pseudo Turbulence in PIV Breaking-Wave Measurements," Exp. Fluids, **29**, pp. 331–338.
[14] Keane, R. D., and Adrian, R. J., 1990, "Optimization of Particle Image Velocimeters. Part I: Double-Pulsed System," Meas. Sci. Technol., **1**, pp. 1202–1215.
[15] Konstantinidis, E., Balabani, S., and Yianneskis, M., 2003, "Effect of Flow Perturbations on the Near Wake Characteristics of a Circular Cylinder," J. Fluids Struct., **18**, pp. 367–386.
[16] Zdravkovich, M. M., 2003, *Flow Around Circular Cylinders*, Oxford University Press, London, Vol. 2.
[17] Williamson, C. H. K., and Roshko, A., 1988, "Vortex Formation in the Wake of an Oscillating Cylinder," J. Fluids Struct., **2**, pp. 355–381.
[18] Davis, R. W., and Moore, E. F., 1984, "A Numerical Study of Vortex Shedding From Rectangles," J. Fluid Mech., **116**, pp. 475–506.
[19] Sohankar, A., Norberg, C., and Davidson, L., 1999, "Simulation of Three-Dimensional Flow Around a Square Cylinder at Moderate Reynolds Numbers," Phys. Fluids, **11**(2), pp. 288–306.
[20] Saha, A. K., Muralidhar, K., and Biswas, G., 2003, "Investigation of Two and Three Dimensional Models of Transitional Flow Past a Square Cylinder," J. Eng. Mech., **129**(11), pp. 1320–1329.

Yoshiki Yoshida
Japan Aerospace Exploration Agency,
Kakuda Space Center,
1 Koganezawa, Kimigaya, Kakuda,
Miyagi 981-1525, Japan
e-mail: kryoshi@kakuda.jaxa.jp

Yoshifumi Sasao
JAXA Research Student
Tohoku University,
2-1-1 Katahira, Aoba-ku, Sendai
Miyagi 980-8577, Japan
e-mail: sasao@cfs.ifs.tohoku.ac.jp

Kouichi Okita
Japan Aerospace Exploration Agency,
Tsukuba Space Center,
2-1-1 Sengen, Tsukuba,
Ibaraki 305-8505, Japan

Satoshi Hasegawa

Mitsuru Shimagaki

Japan Aerospace Exploration Agency,
Kakuda Space Center,
1 Koganezawa, Kimigaya, Kakuda,
Miyagi 981-1525, Japan

Toshiaki Ikohagi
Institute of Fluid Science,
Tohoku University,
2-1-1 Katahira, Aoba-ku, Sendai
Miyagi 980-8577, Japan

Influence of Thermodynamic Effect on Synchronous Rotating Cavitation

Synchronous rotating cavitation is known as one type of cavitation instability, which causes synchronous shaft vibration or head loss. On the other hand, cavitation in cryogenic fluids has a thermodynamic effect on cavitating inducers because of thermal imbalance around the cavity. It improves cavitation performances due to delay of cavity growth. However, relationships between the thermodynamic effect and cavitation instabilities are still unknown. To investigate the influence of the thermodynamic effect on synchronous rotating cavitation, we conducted experiments in which liquid nitrogen was set at different temperatures (74 K, 78 K, and 83 K). We clarified the thermodynamic effect on synchronous rotating cavitation in terms of cavity length, fluid force, and liquid temperature. Synchronous rotating cavitation occurs at the critical cavity length of $Lc/h \cong 0.8$*, and the onset cavitation number shifts to a lower level due to the lag of cavity growth by the thermodynamic effect, which appears significantly with rising liquid temperature. Furthermore, we confirmed that the fluid force acting on the inducer notably increases under conditions of synchronous rotating cavitation.*
[DOI: 10.1115/1.2745838]

Introduction

In rocket engines, turbopumps are installed to achieve high thrust, and an inducer is installed upstream of the main impeller in the turbopump to obtain high suction performance. Unfortunately, under some operating conditions, cavitation instabilities such as rotating cavitation or cavitation surge are observed, frequently causing degradation of the performance or failure of the turbopump. Synchronous rotating cavitation is one type of cavitation instability, which results in head loss or synchronous shaft vibration [1].

On the other hand, the thermodynamic effect on cavitation is a favorable phenomenon in cryogenic fluids such as liquid hydrogen or liquid oxygen, well-known as propellants for liquid rocket engines. It slows down the growth of a cavity since thermal imbalance appears around the cavity due to heat transfer for evaporation. Because of this heat transfer, saturated vapor pressure in the cavity decreases due to the temperature drop, and the degree of cavity growth becomes smaller than that in water without the thermodynamic effect. Therefore, cavitation performance of the inducer in cryogenic fluids is improved. But the degree of improvement in performance depends on cascade design and thermodynamic property of working fluids. The strength of the thermodynamic effect can be evaluated by the thermodynamic function proposed by Brennen [2]. The relationships between the thermodynamic effect and cavitation instabilities, however, are poorly understood. To clarify these relationships, studies using freon R114 and hot water have been conducted by Franc et al. [3] and Cervone et al. [4], respectively.

In the present study, to investigate the relationship between the thermodynamic effect and cavitation instability, we focused on synchronous rotating cavitation. Furthermore, making full use of the ability of the test facility, in which the temperature of the working fluid can be varied, we conducted experiments with liquid nitrogen intentionally set at different temperatures (74 K, 78 K, and 83 K) in order to confirm the dependence of the thermodynamic effect on the temperature.

Experimental Facility and Procedures

Experimental Facility. Experiments were conducted in the Cryogenic Inducer Test Facility (CITF) at Kakuda Space Center of Japan Aerospace Exploration Agency (JAXA). Figure 1 shows the flow of the test facility. This facility has two tanks, one upstream (run-tank) and one downstream (catch-tank), and the temperature of the liquid nitrogen can be varied by regulating the pressure in the run-tank. Thanks to this capability, liquid nitrogen set at different temperatures can be used as the working fluid (Yoshida et al. [5]).

The test inducer, which was also used in the experiment by Kobayashi [6], has three blades with sweep cutback at the leading edge, and its solidity is about 2.1. The rotation speed of the inducer is 18,300 rpm, equal to that of an actual turbopump.

Experimental Procedures. Although the cavity length should be measured by visible observation, direct visualization inside the

Contributed by the Fluids Engineering Division of ASME for publication in the JOURNAL OF FLUIDS ENGINEERING. Manuscript received August 18, 2006; final manuscript received January 10, 2007. Assoc. Editor: Timothy J. O'Hern.

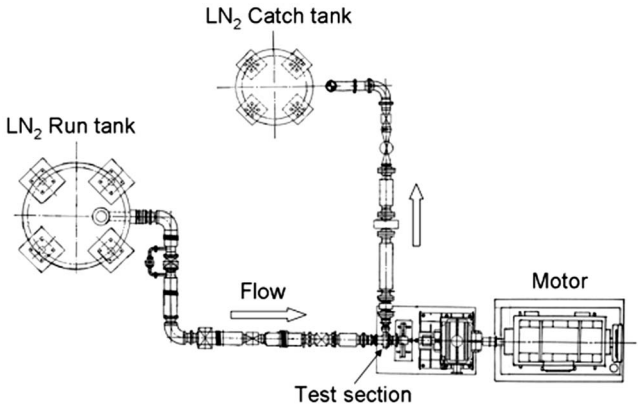

Fig. 1 Schematic diagram of the Cryogenic Inducer Test Facility

cavitating inducer is difficult for experiments using cryogenic fluids. To estimate the cavitating state of the inducer indirectly, therefore, eight pressure sensors (Pos. 1–Pos. 8) are installed along the blade from the leading edge to the trailing edge on the casing as shown in Figs. 2 and 3. The pressure sensors detect the cavitation near the blade tip, i.e., tip leakage vortex cavitation. However, sensors are unable to detect the cavitation in the backflow upstream of the inducer, i.e., backflow vortex cavitation.

Figure 4 shows typical wave forms of 50 revolution-averaged pressure fluctuations measured by the pressure sensor at Pos. 4. In this figure, a flat lower pressure region can be defined as the cavity region because it must reach saturated vapor pressure. Under synchronous rotating cavitation in Fig. 4, the flat region which shows the presence of the cavity is recognized except for one channel. Namely, the occurrence of uneven cavity distribution is expected within the three blades. On the other hand, in the normal state, three pressure drops due to the blade passing are indicated in one rotation, and there is no unevenness in the cavitating state of the three blades.

Using these wave forms at each position, contour plots describing the cavitation state in the blade channel is obtained. Figure 5 is drawn by rearrangement of the wave forms of all the sensors. These figures indicate the estimated cavity region for three typical cavitation numbers. The white lines and the blue area in these figures indicate the blades of the inducer and the estimated cavity

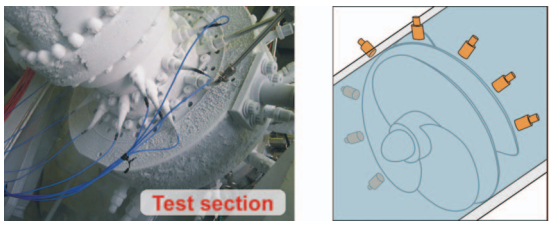

Fig. 2 Photograph and illustration of the test section installed pressure sensors to estimate cavitation region

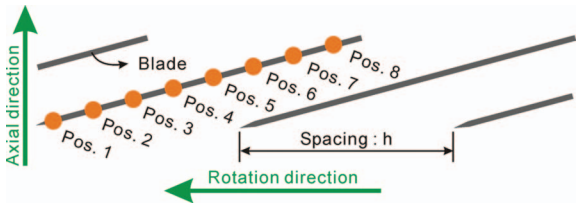

Fig. 3 Development view of the inducer showing location of pressure sensors along the inducer blade

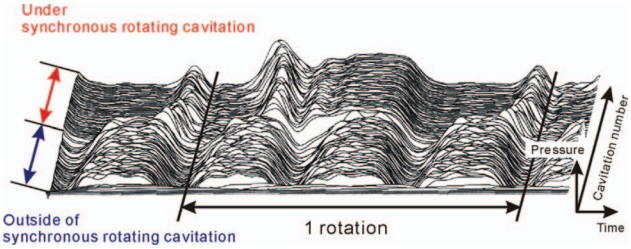

Fig. 4 Waterfall of pressure fluctuation under synchronous rotating cavitation and normal state at Pos. 4

region, respectively. In addition, cavitation number of these figures decreases from Fig. 5(*a*) to 5(*c*). Especially, unevenness of the cavity length is observed only in Fig. 5(*b*). This is synchronous rotating cavitation. Using these figures, the cavity length as an indication of cavitation can be estimated with the present indirect visualization (Yoshida et al. [7]).

Synchronous Rotating Cavitation and Thermodynamic Effect

Synchronous Rotating Cavitation. As we have already mentioned, synchronous rotating cavitation is one type of cavitation instability. Under this state, severe synchronous shaft vibration occurs due to the uneven fluid force acting on the inducer [1]. Figure 6 shows an example of the cavitation state under conditions of synchronous rotating cavitation in water experiment [8]. In these pictures, the unevenness of the cavity length (short, long, and middle) on each blade (blade 1–blade 3) can be clearly observed. However, synchronous rotating cavitation is not an unsteady phenomenon in which the unevenness of the cavity length

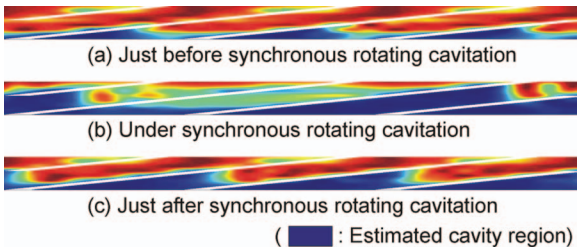

Fig. 5 Figures of estimated cavity region near synchronous rotating cavitation obtained from the measured pressure distribution

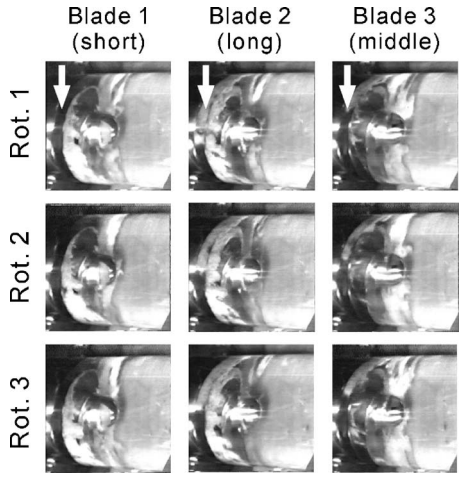

Fig. 6 Photographs of synchronous rotating cavitation which show the unequal cavity length of each blade

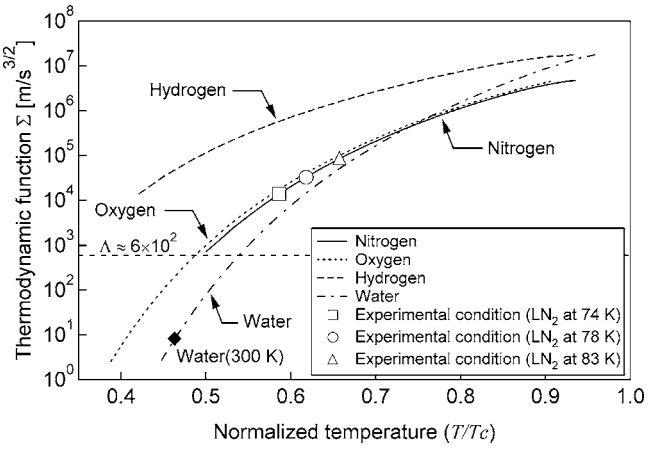

Fig. 7 Variations of the thermodynamic function Σ, including points of experimental conditions and water at 300 K

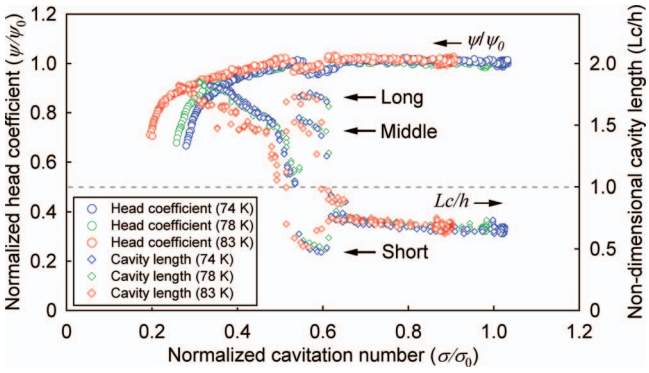

Fig. 8 Cavitation performances and cavity length of each channel for three temperatures of liquid nitrogen (74 K, 78 K, and 83 K), showing unequal cavity length under synchronous rotating cavitation (uncertainty in σ/σ_0=0.02, ψ/ψ_0=0.01, Lc/h=0.03)

propagates from blade to blade as in the case of rotating cavitation. Though the cavitation state in the inducer is surely "asymmetric" and "uneven," it does not change in rotation (Rot. 1–Rot. 3). From that viewpoint, synchronous rotating cavitation can be defined as a steady "anomalous" phenomenon.

Thermodynamic Effect. Thermal imbalance occurs around the cavity due to the transportation of evaporation heat from ambient fluid to the cavity. Consequently, cavity growth is delayed by decreasing the temperature and the saturated vapor pressure in the cavity. This effect appears distinctly in cryogenic fluids such as liquid hydrogen, liquid oxygen, and liquid nitrogen. It has been confirmed to improve suction performance in many experiments (Ruggeri et al. [9]).

In Brenen's analysis [2], thermodynamic function Σ (Eq. (1)) and dynamic fluid parameter Λ (Eq. (2)) have been proposed for a simple spherical cavity in a flow field. Comparing the magnitude of both parameters, we can estimate which influence is stronger:

$$\Sigma = \frac{(\rho_v L)^2}{\rho_l^2 C_{pl} T_\infty \sqrt{\alpha_l}} \quad (\mathrm{m/s^{3/2}}) \tag{1}$$

$$\Lambda = \sqrt{\frac{U^3 \sigma}{C}} \quad (\mathrm{m/s^{3/2}}) \tag{2}$$

Figure 7 shows variations of thermodynamic function for hydrogen, oxygen, nitrogen, and water between the triple point and the critical point. Temperature is on the horizontal axis and is normalized by critical temperature (T_c). In addition, points for experimental conditions (74 K (square), 78 K (circle), and 83 K (triangle)) and water at room temperature (300 K) are also plotted in this figure. Variations of the thermodynamic function for cryogenic fluids such as hydrogen, oxygen, and nitrogen are far larger than that of water at room temperature. Furthermore, in the whole region of experimental conditions (74 K, 78 K, and 83 K), the thermodynamic functions $\Sigma(\cong 1\times10^4-10^5\ \mathrm{m/s^{3/2}})$ are much greater than the dynamic fluid parameter $\Lambda(\cong 6\times10^2\ \mathrm{m/s^{3/2}})$. Thus, the thermodynamic effect is expected to appear under the present conditions hugely.

Experimental Results

Head Coefficient and Cavity Length. The diamond-shaped symbols in Fig. 8 show variations of nondimensional cavity length (Lc/h) versus normalized cavitation number (σ/σ_0) for each temperature condition (74 K (blue), 78 K, (green), and 83 K (red)). The reference value of the cavitation number (σ_0) is the same value given by each temperature of the working fluid. We defined the length from the leading edge of the blade to the trailing edge of the estimated cavity region as the cavity length (Lc). In other words, the length of the blue region along the blade in Fig. 5 is the cavity length. Additionally, Fig. 8 contains results of each channel of the inducer (i.e., three channels for the three-bladed inducer). The uncertainties in Fig. 8 are σ/σ_0=0.02, ψ/ψ_0=0.01, and Lc/h=0.03.

In the region where synchronous rotating cavitation occurs, unevenness of cavity length is manifested as three lengths (short, long, and middle), similar to the photographs in Fig. 6. Meanwhile, in the region without synchronous rotating cavitation, there is no unevenness of cavity length for each channel, and cavity length increases with decreasing cavitation number.

Head performance is considered in the following. The circles in Fig. 8 show variations of the inducer head (ψ/ψ_0) normalized by reference head coefficient (ψ_0). Within the range of the occurrence of synchronous rotating cavitation, the inducer head temporarily decreases since each blade has a different angle of attack due to the inequality of flow rate for each channel. After breaking away from the synchronous rotating cavitation, the cavity length of each blade becomes $Lc/h\cong1.0$. Hereupon, they rapidly lengthen to $Lc/h\cong1.5$. Inducer head drop then begins to gradually occur.

According to these results, for the three temperatures, the head drop is nearly equal at the same cavity length for all conditions. This means that the inducer head is strongly dependent on the cavity length. Furthermore, the cavity length is governed by the liquid temperature, namely the degree of the thermodynamic effect Σ as shown in Fig. 7.

Synchronous Rotating Cavitation and Thermodynamic Effect. Under synchronous rotating cavitation, differences in the unevenness of the cavity lengths (short, long, and middle) were not found, even though the liquid temperature differed. Thus, the thermodynamic effect does not affect the unevenness of the cavity length during synchronous rotating cavitation.

On the other hand, synchronous rotating cavitation occurs at about $Lc/h\cong0.8$ for every condition. Therefore, the origin of synchronous rotating cavitation must be governed only by the cavity length, which is inferred to be one type of fluid dynamic instability with cavitation. This result agrees with the theoretical analysis of the alternate blade cavitation calculated by Horiguchi et al. [10]. They reported that the alternate blade cavitation starts to occur when the cavity length approaches $Lc/h\cong0.65$ in even number of blade cascades.

Furthermore, the thermodynamic effect surely affects the development of the cavity length, so the cavitation number for which the cavity length reaches $Lc/h\cong0.8$ for 83 K becomes lower than

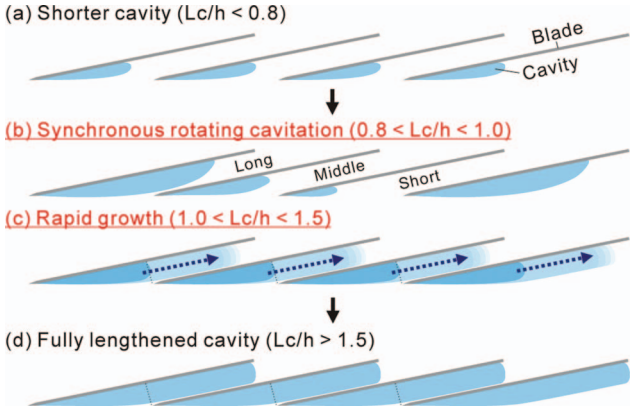

Fig. 9 Transition of cavitating state, including inducer-specific unstable region

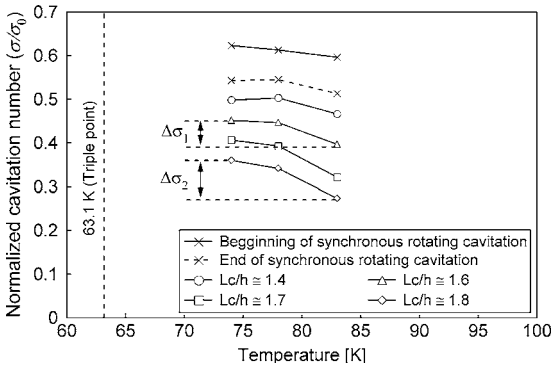

Fig. 10 Influence of temperature on cavity length between 74 K and 83 K (uncertainty in σ/σ_0=0.02, Lc/h=0.03)

that of 74 K. Thus, onset of the synchronous rotating cavitation shifts to the lower side of cavitation number due to the thermodynamic effect.

In Fig. 8, synchronous rotating cavitation appears at $Lc/h \cong 0.8$ and disappears at $Lc/h \cong 1.0$. After that, the cavity length lengthens rapidly from $Lc/h \cong 1.0$ to $Lc/h \cong 1.5$, with the length of each channel remaining equal. This region (from $Lc/h \cong 0.8$ to $Lc/h \cong 1.5$) is considered to be an unstable region for cavity growth. In other words, the cavity length for each channel exhibit breaking symmetry such as synchronous rotating cavitation, or lengthen rapidly with symmetry.

Discussion

Consideration of the Unstable Region. Here, we consider the inducer-specific unstable region. We expect that the trigger of synchronous rotating cavitation may be interference of the tip leakage vortex cavitation with the leading edge of the adjacent blade. Tip leakage vortex cavitation induces flow rate imbalance in each channel when it reaches the throat (Lc/h=1.0). The difference of the flow rate means that the effective angle of attack is not equal among blades. Thus, the cavity length (cavity volume) for each channel may be unequal. From the viewpoint of dynamics, this unevenness of cavity length can be classified into as a type of diverging instability. Because of this diverging instability, cavity length does not vary timewise if it is fully developed. The other type of instability is the lengthening of cavity length rapidly with maintenance of evenness. This phenomenon appears only after passage of Lc/h=1.0. After passing the throat of the cascade, the cavity is rigidly restricted by the channels. In other words, the cavitating state affecting the flow field completely changes over the throat ($Lc/h > 1.0$). Therefore, the cavity length (i.e., flow rate, effective angle of attack) for each blade must be equal, and every channel in the inducer seems to be choked by the rapid growth of the cavity.

Thus, for a shorter cavity within specific unstable region of the inducer ($0.8 < Lc/h < 1.0$), the behavior of the cavity has a degree of freedom in the cavitating state because the cavity is not fully constrained by the adjacent blade. Therefore, the cavitating state may be unstable and exhibit asymmetry such as synchronous rotating cavitation as shown in Figs. 9(*a*) to 9(*b*). On the other hand, for a longer cavity in an unstable region ($Lc/h > 1.0$), the cavity is rapidly lengthened since it cannot stay in that unstable region and cannot break the symmetry caused by loss of the degree of freedom, as shown Figs. 9(*c*) to 9(*d*). For this inducer, within the inducer-specific unstable region, cavitation in the inducer exhibit asymmetric (synchronous rotating cavitation) and symmetric (rapid growth) behavior due to transition of the location of the trailing edge of the cavity from the "leading edge" to the "blade channel."

Liquid Temperature and Cavity Length. Figure 10 shows the relationships between the temperature of liquid nitrogen and the cavity length. This figure indicates variations of the cavitation number which reaches a given cavity length. These cavity lengths are chosen from typical values greater than Lc/h=1.0. From this figure, it can be found that the cavitation number which reaches a given length becomes smaller since the thermodynamic effect is strengthened due to the rise in temperature of liquid nitrogen. For instance, comparing 74 K (left) and 83 K (right), the difference of cavitation number for each temperature can be shown as $\Delta\sigma_1$ for $Lc/h \cong 1.6$ and $\Delta\sigma_2$ for $Lc/h \cong 1.8$. It is obvious that $\Delta\sigma_2$ is greater than $\Delta\sigma_1$. This indicates that the thermodynamic effect is strengthened by the increase in cavity length and makes the growth of cavity length significantly slower. In addition, focusing on one cavity length, the difference of cavitation number for three temperatures tends to become smaller with falling temperature. It is considered that the temperature depression in the cavity (i.e., thermodynamic effect) decreases with decreasing thermodynamic function Σ, and is restricted physically when it approaches the triple point of nitrogen (63.1 K) [7].

Fluid Force and Shaft Vibration. Figure 11 shows variation of cavity length (Lc/h), estimated fluid force (F/F_{max}) (top), and the component of the synchronous shaft vibration from the displacement sensors (bottom), for a normal temperature of 78 K. Here,

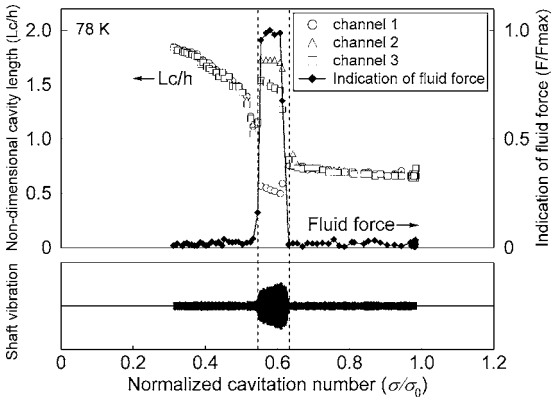

Fig. 11 Variations of cavity length, estimated fluid force and shaft vibration, indicating amplification of shaft vibration due to increasing the fluid force during occurrence of synchronous rotating cavitation (uncertainty in σ/σ_0=0.02, Lc/h=0.03, F/F_{max}=0.05)

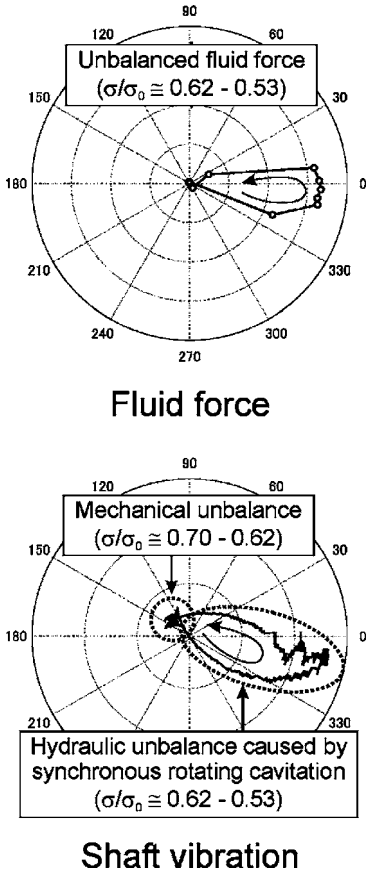

Fig. 12 Vector orbits of fluid force and shaft vibration, indicating similar phase change in vector orbit under conditions of synchronous rotating cavitation

estimated fluid force is computed by integrating the pressure distributions around the inducer casing. This estimated force is only an indication to evaluate the degree of fluid force acting on the inducer. The figure shows that the fluid force increases significantly under synchronous rotating cavitation. Moreover, the synchronous shaft vibration is clearly amplified because of the action of the fluid force caused by synchronous rotating cavitation.

Figure 12 presents the orbit of the fluid force vector under the synchronous rotating cavitation (top) and the synchronous component of the shaft vibration (bottom). It should be noted that the origin of the angles in these diagrams is not the same. From these figures, the directions of both vectors (fluid force and shaft vibration) are seen to change under synchronous rotating cavitation. Although the reason for the slight decrease in the amplitude of the shaft vibration under the synchronous rotating cavitation in Fig. 11 is unclear, the changing direction of the fluid force vector in Fig. 12 is expected to have some influence on it.

Moreover, for the vector orbit of the shaft vibration (bottom), the upper left position of the origin indicates mechanical unbalance as the normal state ($\sigma/\sigma_0=0.70-0.62$), and oval path on the lower right position shows the vector orbit under condition of the synchronous rotating cavitation ($\sigma/\sigma_0=0.62-0.53$). In addition, the direction of the arrows shows the direction of decrease in cavitation number. Comparison of the normal state with the synchronous rotating cavitation state indicates that the shaft vibration caused by the synchronous rotating cavitation is much greater than that in the normal state. Thus, the hydraulic unbalance caused by the synchronous rotating cavitation is expected to have a strong influence on the rotordynamics for inducers [6].

Conclusions

By experiments with liquid nitrogen set at different temperatures and considerations based on the cavity length, the following points were clarified:

(1) Synchronous rotating cavitation occurs at the same cavity length independent of the temperature. The critical cavity length at the onset of synchronous rotating cavitation was $Lc/h \cong 0.8$.
(2) The thermodynamic effect slows down the growth of cavity length. Growth of the cavity is distinctly delayed with rising liquid temperature.
(3) Due to the above results, the thermodynamic effect shifts the onset (critical) cavitation number of synchronous rotating cavitation to a lower side.
(4) However, differences in the unevenness of the cavity length under synchronous rotating cavitation was not prominent at the temperatures in the present experiments, thus indicating that the thermodynamic effect has no influence upon the unevenness of the cavity length.
(5) For this inducer, the unstable region can be considered from $Lc/h \cong 0.8$ to $Lc/h \cong 1.5$ where the cavitating state in the inducer must be asymmetry (synchronous rotating cavitation) or symmetry (rapid growth).
(6) The fluid force acting on the inducer significantly increases under synchronous rotating cavitation. The fluid force due to synchronous rotating cavitation has a far greater impact on the rotordynamics than the mechanical dynamic force due to the mass unbalance.

Acknowledgment

The authors would like to thank Mr. Kengo Kikuta of Ishikawajima-Harima Heavy Industries Co., Ltd. for his great help with data processing.

Nomenclature

C = chord of inducer
C_{pl} = specific heat of liquid
F = fluid force
$F_{\max}$ = maximum value of fluid force
h = spacing of cascade
L = latent heat
Lc = cavity length
T_∞ = ambient temperature
U = tip velocity of inducer
α_l = thermal diffusivity of liquid
Λ = dynamic fluid parameter defined by Eq. (2)
ρ_v = vapor density
ρ_l = liquid density
Σ = thermodynamic function defined by Eq. (1)
σ = cavitation number
σ_0 = reference value of cavitation number
ψ = head coefficient
ψ_0 = reference value of head coefficient

References

[1] Rosenmann, W., 1965, "Experimental Investigations of Hydrodynamically Induced Shaft Forces With a Three-bladed Inducer," Symposium on Cavitation in Fluid Machinery, pp. 172–195.
[2] Brennen, C. E., 1973, "The Dynamic Behavior and Compliance of a Stream of Cavitating Babbles," ASME J. Fluids Eng., **95**, pp. 533–541.
[3] Franc, J. P., Rebattet, C., and Coulon, A., 2004, "An Experimental Investigation of Thermal Effects in a Cavitating Inducer," ASME J. Fluids Eng., **126**, pp. 716–723.
[4] Cervone, A., Testa, R., and d'Agostino, L., 2005, "Thermal Effects on Cavitation Instabilities in Helical Inducers," J. Propul. Power, **21**(5), pp. 893–899.
[5] Yoshida, Y., Watanabe, M., Hasegawa, S., Hashimoto, T., Shimagaki, M., Yamada, H., and Shimura, T., 2004, "Cryogenic Inducer Test Facility in JAXA," (in Japanese), JAXA Research and Development Report No. JAXA-RR-05-042.

[6] Kobayashi, S., 2005, "Effects of Shaft Vibration on the Occurrence of the Asymmetric Cavitation in an Inducer" (in Japanese) Trans. Jpn. Soc. Mech. Eng., Ser. B, **71**(709), pp. 2303–2308.
[7] Yoshida, Y., Kikuta, K., Hasegawa, S., Shimagaki, M., Nakamura, N., and Tokumasu, T., 2007, "Thermodynamic Effect on a Cavitating Inducer in Liquid Nitrogen," ASME J. Fluids Eng., **129**, pp. 273–278.
[8] Maekawa, Y., 1996, "Experimental Study of Unsteady Cavitation on an Inducer" (in Japanese), Master's thesis, Osaka University.
[9] Ruggeri, R. S., and Moore, R. D., 1969, "Method for Prediction of Pump Cavitation Performance for Various Liquids, Liquid Temperatures, and Rotative Speeds," NASA TN D-5292.
[10] Horiguchi, H., Watanabe, S., Tsujimoto, Y., and Aoki, M., 2000, "A Theoretical Analysis of Alternate Blade Cavitation in Inducers," ASME J. Fluids Eng., **122**, pp. 156–163.

Angelo Cervone
Project Manager
Alta S.p.A.,
Via Gherardesca 5,
56121 Pisa, Italy
e-mail: a.cervone@alta-space.com

Cristina Bramanti
Post-Doc Fellow
ESA-ESTEC,
Keplerlaan 1,
Nordwijk, The Netherlands

Lucio Torre
Research Engineer
Alta S.p.A.,
Via Gherardesca 5,
56121 Pisa, Italy

Domenico Fotino
MS Student

Luca d'Agostino
Professor
Department of Aerospace Engineering,
University of Pisa,
Via G. Caruso,
56100 Pisa, Italy

Setup of a High-Speed Optical System for the Characterization of Flow Instabilities Generated by Cavitation

The present paper illustrates the setup and the preliminary results of an experimental investigation of cavitation flow instabilities carried out by means of a high-speed camera on a three-bladed inducer in the cavitating pump rotordynamic test facility (CPRTF) at Alta S.p.A. The brightness thresholding technique adopted for cavitation recognition is described and implemented in a semi-automatic algorithm. In order to test the capabilities of the algorithm, the mean frontal cavitating area has been computed under different operating conditions. The tip cavity length has also been evaluated as a function of time. Inlet pressure signal and video acquisitions have been synchronized in order to analyze possible cavitation fluid-dynamic instabilities both optically and by means of pressure fluctuation analysis. Fourier analysis showed the occurrence of a cavity length oscillation at a frequency of 14.7 Hz*, which corresponds to the frequency of the rotating stall instability detected by means of pressure oscillation analysis.* [DOI: 10.1115/1.2742738]

Introduction

In space propulsion, propellant feed turbopumps are a crucial component of all primary propulsion concepts powered by liquid propellant rocket engines. Severe limitations are associated with the design of high power density, dynamically stable machines capable of meeting the extremely demanding suction, pumping, and reliability requirements of current space transportation systems (Stripling and Acosta [1]).

In most cases, these pumps employ an inducer upstream of the centrifugal stage(s) in order to improve the suction performance and reduce the propellant tank pressure and weight. Significant cavitation levels typically occur in inducers and often lead to the development of flow instabilities that can seriously degrade the performance of the machine, or even cause its rapid failure.

According to Brennen [2], these flow instabilities can be divided into three main categories: global oscillations, local oscillations, and instabilities caused by radial or rotordynamic forces. Some of the most interesting and well-recognized instabilities in pumps and axial inducers are global oscillations, such as the *rotating stall* and the *rotating cavitation*, propagating in the azimuthal direction at angular speeds different from those of the pump (typically subsynchronous for rotating stall and supersynchronous for rotating cavitation). Other global oscillations are the *surge* and the *cavitation auto-oscillations*, system instabilities involving strong longitudinal flow and pressure oscillations of the whole suction line, typically occurring in noncavitating pumps for positive slopes of the characteristic curve (surge) and near breakdown conditions in cavitating turbopumps (cavitation auto-oscillations).

Contributed by the Fluids Engineering Division of ASME for publication in the JOURNAL OF FLUIDS ENGINEERING. Manuscript received September 14, 2006; final manuscript received January 15, 2007. Assoc. Editor Juergen Kompenhans. Paper presented at the 6th International Symposium on Cavitation CAV2006, Wageningen, The Netherlands, 11–15 September 2006.

Experimental investigations on the instabilities triggered by cavitation in axial inducers have been recently carried out at Alta S.p.A. (Cervone et al. [3]; Cervone et al. [4]). Experiments were conducted in the cavitating pump test facility, specifically intended for general-purpose experimentation on cavitating/noncavitating turbopumps, and its upgraded version, the cavitating pump rotordynamic test facility (CPRTF), which is especially dedicated to the investigation of rotordynamic fluid forces in forced vibration experiments with adjustable rotational and whirl speeds.

Tsujimoto and co-workers [5] introduced for the first time the cross-correlation and phase analysis technique in order to detect the frequency of oscillation and the spatial characteristics (i.e., rotating or axial) of the cavitating flow oscillations. This technique has also been used in Alta's experiments (Cervone et al. [3,4]).

The characterization of the flow instabilities by means of unsteady pressure measurements, however, is significantly more effective if accompanied by optical visualization of the cavitating flow on the inducer blades by means of high-speed movies.

Using the combination of these techniques, Tsujimoto and co-workers [5] detected the occurrence of rotating cavitation and other modes of oscillation on a scaled model of the LE-7 LOX turbopump inducer. They concluded that the rotating cavitation was probably caused by the occurrence of five cavitation regions extending upstream from the tip of the blades and slowly rotating. By analysis of the high-speed movies, they also detected a form of instability characterized by axial fluctuations (cavitation surge).

Kamijo and co-workers [6] detected the occurrence of a supersynchronous frequency in the spectra of the inlet pressure fluctuations and using high-speed camera movies; they could state that it was caused by the circumferential cavity length oscillation at the same frequency. They observed that both the tip vortex cavitation and the blade surface cavitation oscillated at approximately the same supersynchronous frequency and the same phase.

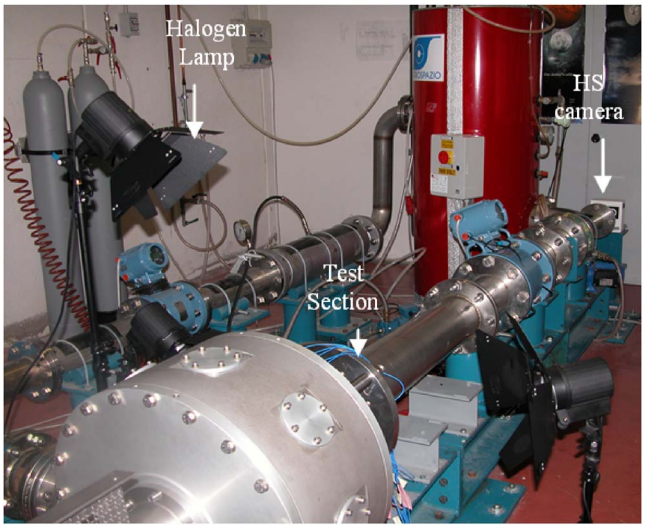

Fig. 1 The cavitating pump rotordynamic test facility

Using a high-speed camera at 7000 fps, Hashimoto et al. [7] plotted the cavitating surface as a function of the number of inducer revolutions, on a three-bladed inducer with dimensions similar to those of the LE-7 LOX pump inducer. They detected various modes of oscillation, including a backward-rotating and a forward-rotating cavitation, an attached cavitation, and a low cycle oscillation.

Recently, in French research laboratories, Jousselin et al. [8] used frontal images of a four-bladed inducer in order to extract the cavitating regions by means of an image processing code developed by the National Institute of Health. They plotted the nondimensional cavitating area as a function of the cavitation number at constant flow rate and as a function of the flow rate at constant cavitation number.

This paper is aimed at illustrating the following aspects of the present research activity at Alta S.p.A.:

- setup of the optical system in order to record frontal high-speed movies (up to 16,000 fps) on a three-bladed inducer;
- implementation of an image processing algorithm for extracting the blade cavitating areas from every frame;
- implementation of an automatic algorithm for calculating the tip cavity length;
- estimation and analysis of the blade cavitating areas;
- spectral analysis of the inlet pressure fluctuations by means of piezoelectric pressure transducers;
- spectral analysis of the cavity length fluctuations.

Experimental Apparatus

The cavitating pump rotordynamic test facility CPRTF (Fig. 1) has been designed to experimentally characterize the performance of pumps in a wide variety of alternative configurations (axial, radial, or mixed flow, with or without an inducer; Rapposelli, Cervone, and d'Agostino [9]). The facility operates in water at temperatures up to 90°C and is intended as a flexible apparatus readily adaptable to conduct experimental investigations on virtually any kind of fluid dynamic phenomena relevant to high performance turbopumps.

The test section (Fig. 2) is equipped with a rotating dynamometer, for the measurement of the forces and moments acting on the impeller, and a mechanism for adjusting and rotating the eccentricity of the impeller axis in the range 0–2 mm and ±3000 rpm. The inlet section, made of Plexiglas, is transparent in order to allow for optical visualization of cavitation on the test inducer.

The adjustable physical parameters of the experimental setup include the pump rotating speed and acceleration (by means of the engine controls), the mass flow (by means of a lamination valve), and the temperature and pressure of the working fluid (by means, respectively, of a heat exchanger and a bladder placed inside the tank).

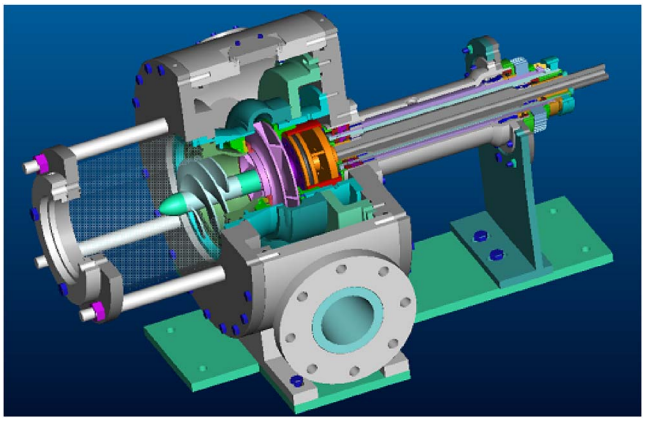

Fig. 2 Cut-out drawing of the CPRTF test section

For the present experimental work, the facility was assembled in a simplified configuration without the rotating dynamometer. The test section was equipped with three different series of pressure transducers. The inlet pressure is measured by means of an absolute pressure transducer installed upstream of the Plexiglas inlet section (Druck, model PMP 1400, 0–1.5 bar operating range, 0.25% precision class). The pressure rise, necessary for the characterization of the pump performance, is measured by means of two redundant differential pressure transducers installed between the inlet and the outlet sections of the test pump (Kulite, model BMD 1P 1500 100, 0–100 psid operating range, 0.1% precision class; Druck, model PMP 4170, 0–1 bar operating range, 0.08% precision class). The pressure fluctuations are analyzed by equipping the inlet section (Fig. 3) with flush-mounted piezoelectric pressure transducers (PCB M112A22, ICP® voltage mode-type, 0.1% class) located at three axial stations (inducer inlet, outlet, and at the middle of the axial chord of the blades, Fig. 3). At each axial station at least two transducers have to be mounted with a given angular spacing, in order to cross-correlate their signals for coherence and phase analysis. As a result, waterfall plots of the power spectral density of the pressure fluctuations can be obtained as functions of the cavitation number $\sigma = (p_{in} - p_V)/\frac{1}{2}\rho\Omega^2 r_T^2$, in order to detect the occurrence of instabilities. The axial or azimuthal nature of the detected instabilities

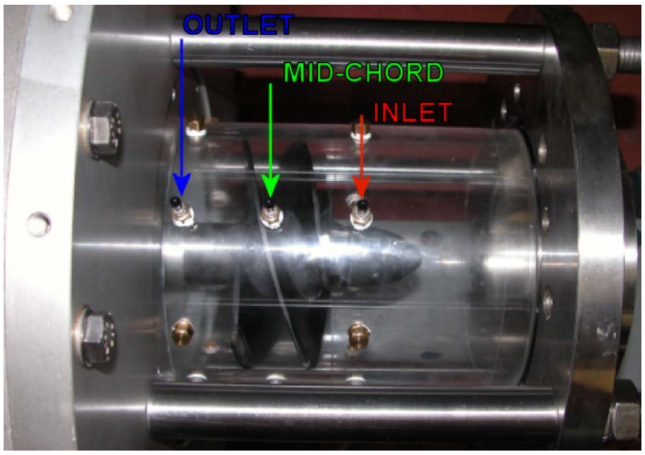

Fig. 3 The inlet section of the facility instrumented with piezoelectric pressure transducers

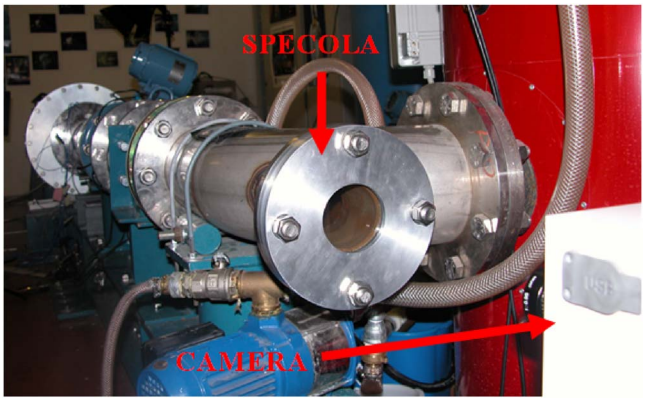

Fig. 4 The optical access at the end of the facility suction line

(and, in the second case, the number of rotating cells involved) can be determined by means of cross-correlation of the pressure signals from different locations.

The capabilities of the test facility have been improved after the installation of an integrated system for the optical analysis of the cavitating flow. The core of the system is represented by a high-speed video camera (Fastec Imaging model Ranger) having a record rate variable from 125 fps (maximum resolution 1280 $\times$ 1024) to 16,000 fps (maximum resolution 1280 $\times$ 32). It uses a monochrome complementary metal-oxide semiconductor sensor and its recording mode can be manual or triggered by the connection with a personal computer by means of USB port. The shutter speed ranges from 1$\times$ to 20$\times$ the recording rate. The required illumination level is provided by three halogen lamps produced by Hedler, each one having a power of 1250 W. The camera can also be synchronized with a stroboscopic light (Drelloscop 3009) having a maximum flash frequency of 1000 lamp/s with a frequency accuracy of 0.001%. The optical system is completed by a Nikon Coolpix 5700 digital photo camera, with optical 8$\times$ zoom, digital 4$\times$ zoom, a focal distance from 8.9 to 71.2 mm and a shutter speed from 1/4000 s to 8 s.

The characteristics of the facility make it possible to record both side movies, through the Plexiglas inlet section, and frontal movies, through an optical access placed at the end of the suction line (Fig. 4). Side movies provide indications on the extension of cavitation in the blade channels, whereas the frontal ones give information about the radial and circumferential extension of the cavities on the blades.

The preliminary results illustrated in this paper refer to the FIP162 inducer (Fig. 5): it is a three-bladed, aluminum-made axial pump of extremely simple helical geometry, with a tip radius of 81 mm, a hub radius of 22.5 mm, a tip blade angle of 9 deg, a tip solidity of 3.05, and 2 mm thick back-swept blades with blunt leading and trailing edges. It is manufactured by Fabbrica Italiana Pompe (FIP) S.p.A. for the food industry by welding the blades on the hub, therefore, it does not satisfy stringent geometric tolerances.

Image Processing Algorithm

A semi-automatic image processing algorithm has been developed to extract the regions of the image where cavitation is present. This algorithm has been implemented in a code that allows for automatically processing the frames of the movies taken by the high-speed camera and for analyzing the movie using the processed frames. The algorithm has been implemented in Matlab® and its flow chart is shown in Fig. 6. The input is a frame in grayscale format: a typical input image is shown in Fig. 7 (left).

The first step of the procedure is the manual selection of the inducer rotational axis for the first frame of the movie; this operation allows us to rotate all the processed frames around this point in order to obtain a movie in which the position of the blades is fixed.

Fig. 5 The FIP162 inducer

The next step is the so-called "segmentation technique" by which the cavitating regions are separated from the rest of the image. Several segmentation techniques have been proposed in the past (see, for example, Gonzalez and Woods [10]): the thresholding technique has been the one used in the present activity. By

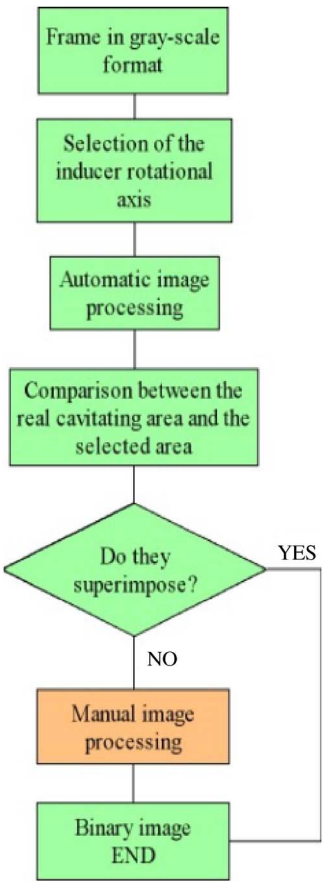

Fig. 6 Flow chart of the semi-automatic algorithm

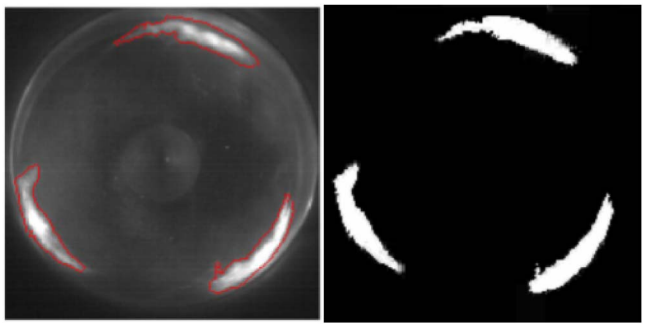

Fig. 7 Comparison between the original frame (left) and the processed binary image (right) in a sample case

this technique, the original grayscale image is converted in a binary image: the pixels having an intensity in the original image greater than a certain threshold value are set equal to 1 (i.e., they become white pixels), while all other pixels are set equal to 0 (i.e., they become black pixels). Despite its implementation simplicity, the main problem of this technique is the evaluation of the right value to be attributed to the threshold. There are several methods to automatically find this value according to the image histogram properties (Gonzalez and Woods [10], Kato et al. [11], Otsu [12]). The simplest way to find the right threshold is to choose an intermediate value between the two peaks shown by the typical brightness histogram of the input frame (Fig. 8).

In the present case it has not been possible to find a threshold value for the frame as a whole, so different threshold values have been used for the different regions into the image: the input frame is divided into several circular sectors (Fig. 9) and an automatic threshold value, evaluated using Otsu's method [12], is given for each sector.

An analysis of the brightness histogram for each circular sector (Fig. 10) showed that the standard deviation for the sectors in which there is no cavitation is very low, so the pixels of these sectors are set equal to 0 without setting any threshold value. Besides, in order to better analyze the cavitating regions on the blades, the central portion of the image (where other cavitating phenomena often occur) and the region outside the inducer are covered with black pixels (masked portions in Fig. 9). Thus, by calibrating the angular division of the frame, a good first-tentative image segmentation is obtained.

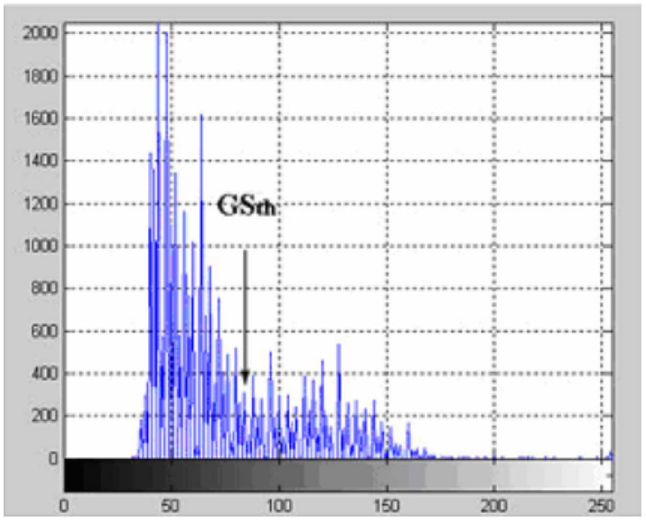

Fig. 8 Typical brightness histogram of an input frame

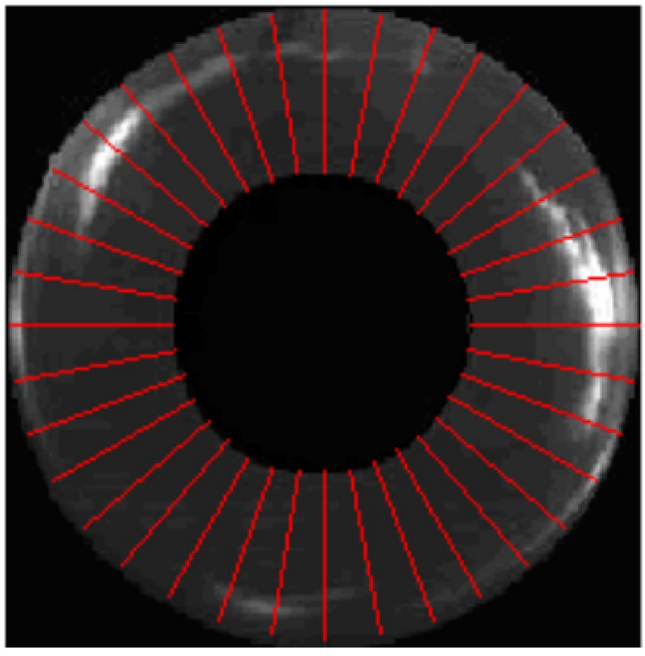

Fig. 9 Example of the image division and the masked portions

The contour of the white regions in the first-tentative binarized image is then superimposed to the grayscale frame (highlighted contour in Fig. 7, left): if it does not superimpose to the effective cavitating regions, the operator can manually process the frame selecting the right cavitating areas and setting a new threshold value by a trial-and-error technique until the right value is found (i.e., the value that produces a good result as by the operator's judgment, see Gonzalez and Woods [10]). An example of the resulting binary image is shown in Fig. 7 (right).

Blade Cavitating Area Estimation

The total frontal area of the cavitating regions on the inducer blades (S_{cav}) has been estimated by averaging the number of white pixels in all the frames of a movie taken at given flow conditions. This value has been normalized using the total frontal area of the inducer (S_{flow}).

A standard procedure has been adopted for the tests. The working fluid has been de-aerated before every test. In order to im-

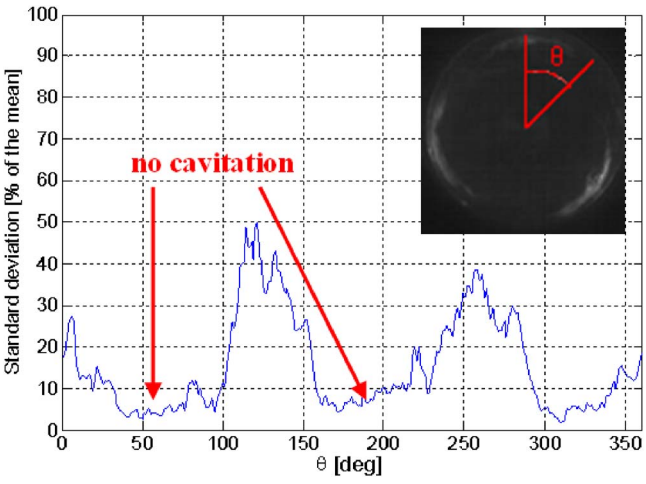

Fig. 10 Standard deviation of the brightness histogram as a function of the azimuthal coordinate θ

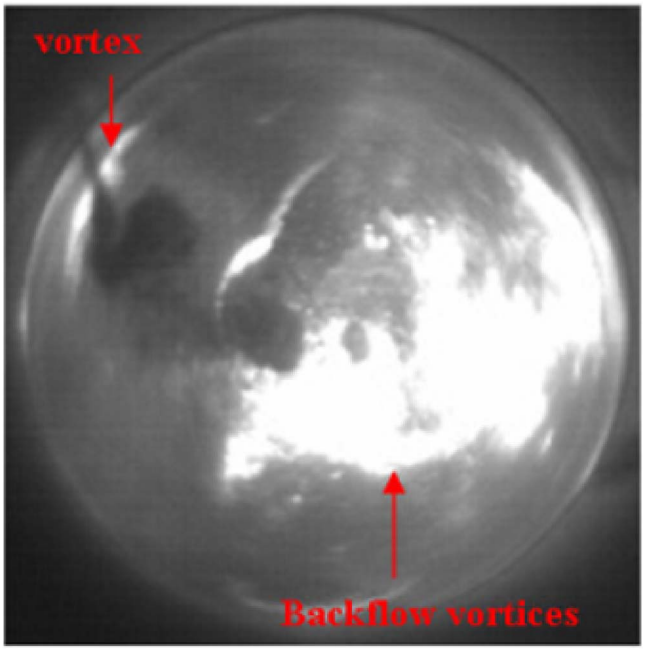

Fig. 11 Example of a frame which cannot be analyzed using the image processing

prove the image quality, excessively high cavitation levels have not been reached during the tests. For this reason, the inducer rotational speed has been set equal to 1500 rpm. Nevertheless, at low flow coefficients and cavitation numbers, the image processing algorithm described in the previous section cannot be used properly, due to the significant number of vortices and large cavitation regions in the inducer inlet flow. The water quality is significantly degraded, with a large number of cavitating nuclei and consequently adverse effects on light diffusion (Fig. 11).

High-speed movies have been recorded at constant flow rate, while the inducer inlet pressure has been decreased from high to low values using the vacuum pump.

The camera frame rate has been set equal to 1000 fps (i.e., 40 frames/revolution at 1500 rpm), at an image resolution of 640 $\times$480 pixels. This setup gave the possibility of optically analyzing the cavitation instabilities detected on the same inducer by unsteady pressure measurement analysis.

The plot presented in Fig. 12 shows the normalized frontal cavitating surface as a function of the cavitation number for several values of the flow coefficient. It is evident that the cavitating surface tends to decrease when the cavitation number increases. This aspect is also evident by observation of the frames shown in Fig. 13 and refer to a particular value of the flow coefficient.

The plot presented in Fig. 14, on the other hand, shows the normalized frontal cavitating surface as a function of the flow coefficient for several values of the cavitation number. It can be observed that the cavitating surface tends to decrease when the flow coefficient decreases.

The trend shown in Fig. 14 is in agreement with the free streamline solution proposed by Brennen and Acosta [13]. Their analytical model gives the following equation for the choked cavitation number (defined as the minimum cavitation number at which the cavity becomes infinitely long and below which there are no solutions):

$$\sigma_c = \left[1 + \sin\left(\frac{\alpha}{2}\right)\sec\left(\frac{\beta_b}{2}\right)\sin\left(\frac{\beta_b - \alpha}{2}\right) + 2d\sin^2\left(\frac{\beta_b}{2}\right) \right]^2 - 1$$

Figure 15 shows the choked cavitation number for the FIP162 inducer, as a function of the flow coefficient, according to the Brennen-Acosta model. It increases with the flow coefficient and

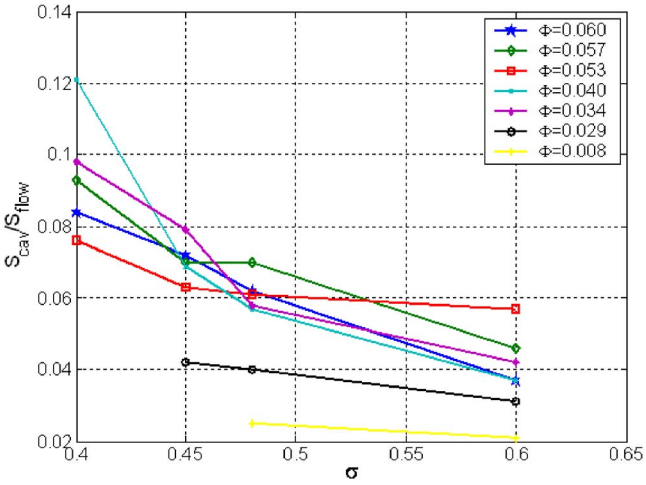

Fig. 12 Frontal cavitating surface as a function of the cavitation number for several values of the flow coefficient

reaches a maximum for $\Phi = 0.08$. This result is in agreement with the experimental observations presented in Fig. 14: at lower flow coefficients, the choked cavitation number decreases and, as a consequence, a smaller cavitating region is observed at a given value of the cavitation number σ. Furthermore, for the values of σ considered in the plot of Fig. 14, no strong backflow is observed at lower flow coefficients and significant vortices like those shown in Fig. 11 are not present.

Tip Cavity Length Estimation

The tip cavity length has been estimated using an automatic algorithm that scans every binary frame with a line rotating around the inducer axis at an angular pitch of 1 deg. When a white pixel is found along the scanning line after a completely black line, the cavitating region is assumed to begin; on the other hand, when every pixel along the scanning line becomes black, the cavitating region is assumed to finish (Fig. 16). The length of the

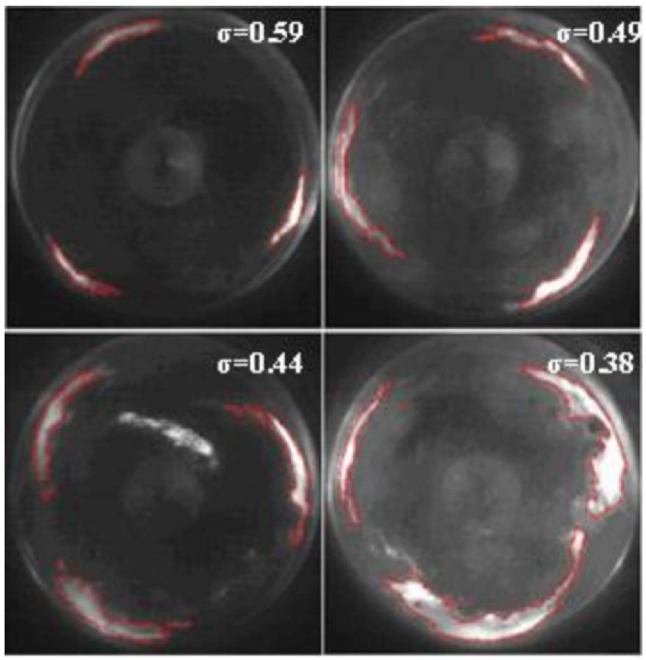

Fig. 13 Cavitating area development for a particular flow condition ($\Phi = 0.04$, $\Omega = 1500$ rpm, and frame sample rate=1000 fps)

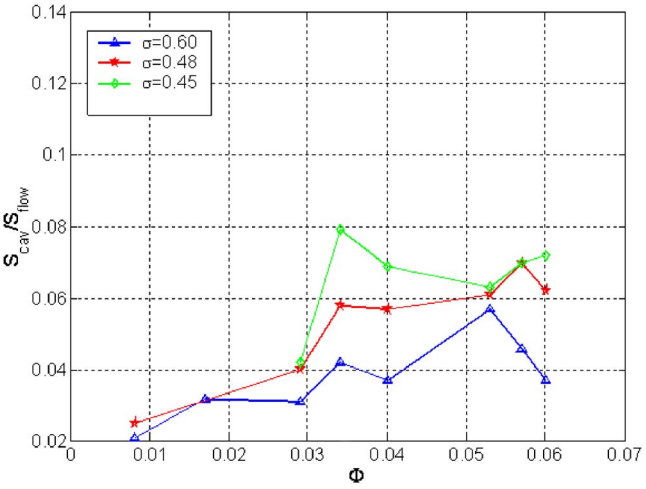

Fig. 14 Frontal cavitating surface as a function of the flow coefficient for several values of the cavitation number

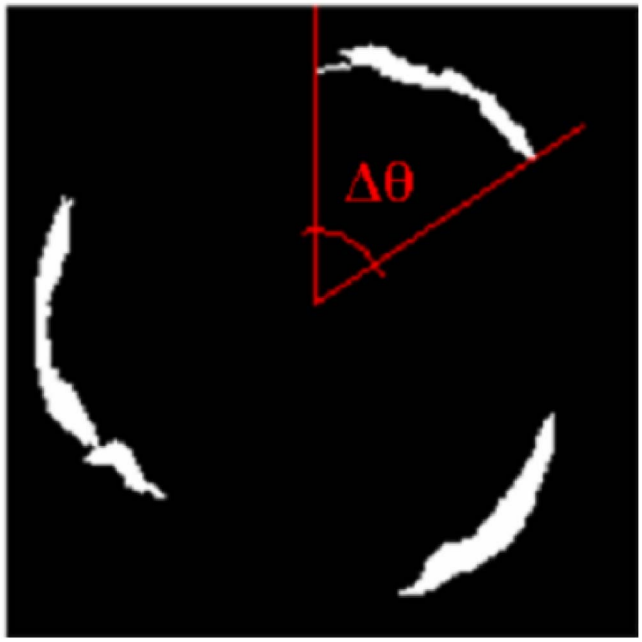

Fig. 16 Evaluation of the azimuthal extension of the cavitation on a blade

cavitating region is finally estimated by multiplying its azimuthal extension ($\Delta\theta$) by the radius at which the cavitating region has been examined.

Sometimes the cavitating region appears to be fragmented. This is due to the separation of small cavitating areas and to the presence of vortices between the real blade surface and the camera lens (Fig. 11). In this case, the algorithm takes into account the angular separation between the different cavitating regions and, if they are sufficiently close, they are considered as a unique cavitating region. Otherwise, if the cavitating regions are sufficiently distant, they are considered as effectively separated and only the length of the first one is taken into account.

This procedure has been applied to a binarized movie whose frames have been rotated around the inducer rotational axis in order to obtain fixed blade position. The following plots (Fig. 17) show the length of the cavitating region on the blades as a function of time, at given flow conditions.

Fourier Analysis of the Inlet Pressure and Cavity Length Fluctuations

In the experiments for the characterization of the flow instabilities, six piezoelectric transducers were mounted at the inducer inlet station (Fig. 3) at an angular spacing of 45 deg (Fig. 18), in order to characterize the occurrence and nature of instabilities.

Examination of the waterfall plots obtained in a previous paper (Cervone et al. [3]) shows the occurrence of several forms of instabilities. Among these, the rotating stall has been analyzed by means of both the inlet pressure fluctuations and the tip cavity length oscillations. To this purpose, pressure and movie acquisi-

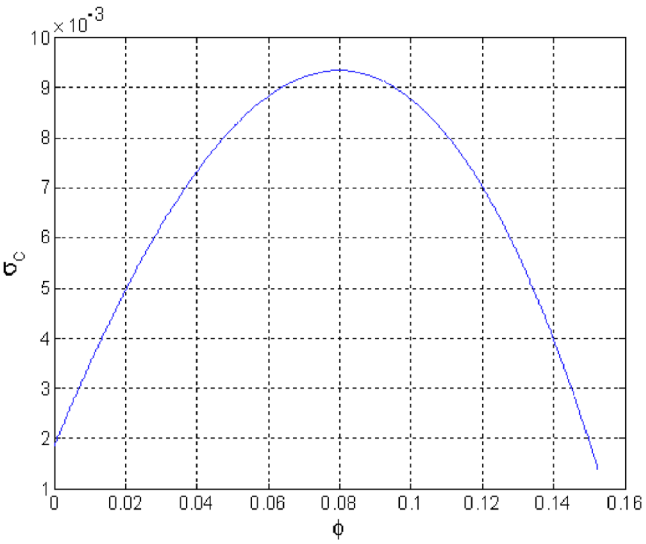

Fig. 15 Choked cavitation number as a function of the flow coefficient for the FIP162 inducer

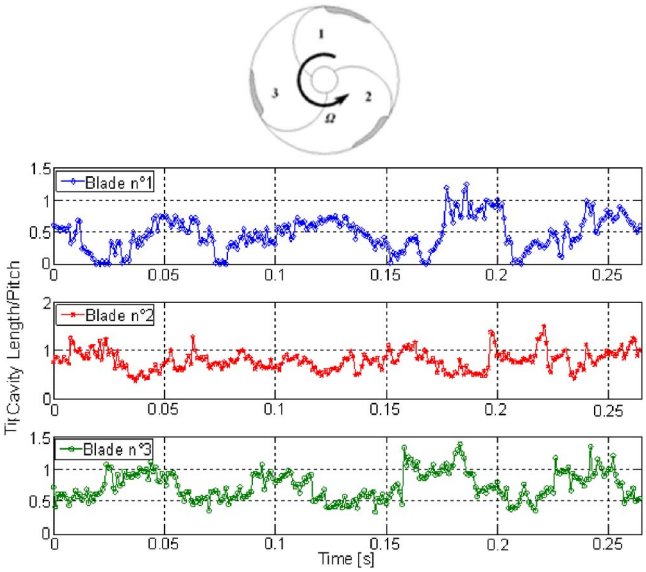

Fig. 17 Length of the cavitating regions on the blades as a function of time (Φ=0.034, σ=0.52, Ω=1500 rpm, and frame sample rate=1000 fps)

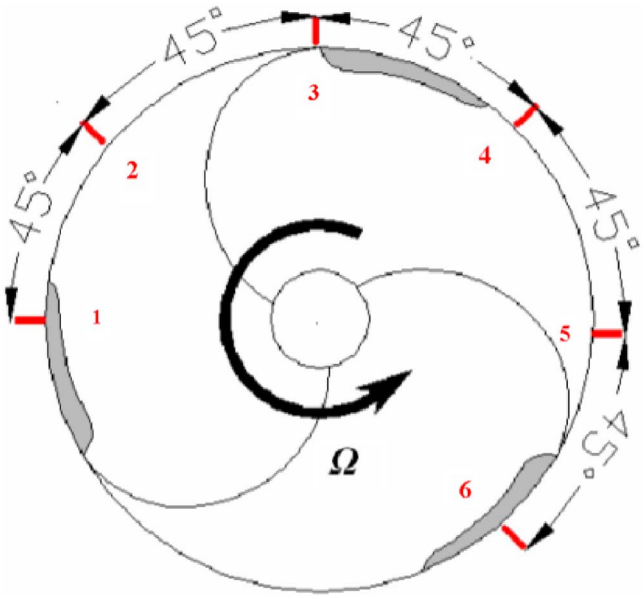

Fig. 18 Schematic of the piezoelectric transducers position at the inlet station

tions have been synchronized and different flow conditions have been investigated based on the results of the previous analysis (Cervone [3]).

Figure 19 shows the power density spectrum and the phase of the cross-correlation of the pressure signals by two transducers with 45 deg angular separation, calculated at a flow condition for which the rotating stall (f_1 frequency) is well recognizable. It can be observed that the phases of the cross-correlation are approximately equal to the adopted transducer angular spacing (Table 1). For this reason, f_1 represents a one cell subsynchronous rotating phenomenon (0.41Ω). The spectrum also shows a well-defined frequency peak at $f_2=\Omega-f_1$, probably caused by a nonlinear interaction between the rotating stall and the inducer rotational frequency, which suggests that f_1 represents a forward-rotating phenomenon.

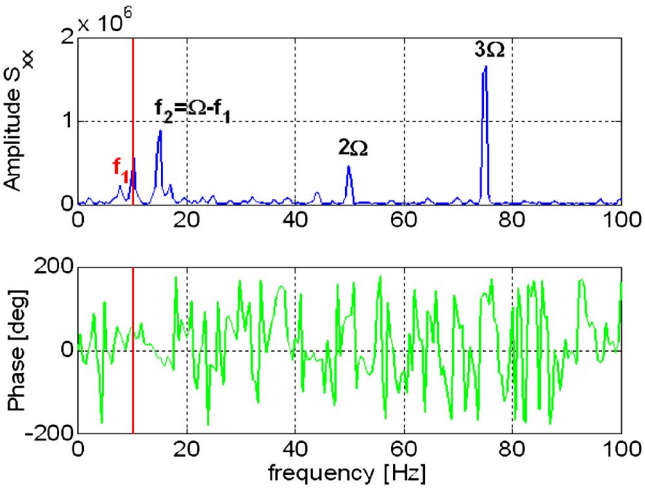

Fig. 19 Power density spectrum and phase of the cross-correlation of the pressure signals of two transducers with 45 deg angular separation ($\Phi=0.034$, $\sigma=0.52$, and $\Omega=1500$ rpm)

Table 1 Phases of the cross-correlation between the signal obtained by transducer 1 and the other transducers shown in Fig. 18

Frequency	$f_1=10.3$ Hz
Phases 1-2	45 deg
Phases 1-3	83 deg
Phases 1-4	126 deg
Phases 1-5	175 deg
Phases 1-6	220 deg

Fourier analysis of the tip cavity length oscillations shown in Fig. 17, calculated at the same flow conditions of Fig. 19, gives the results presented in Fig. 20.

A well-defined peak is detected in the power spectrum at a frequency of 14.7 Hz (f_c). The cross-correlation phases are 120 deg (blade 3-blade 2), 155 deg (blade 2-blade 1), and 85 deg (blade 1-blade 3). This means that the phenomenon is rotating clockwise in the rotating coordinate frame. The ratio of the mean angular separation of two adjacent cavitating regions to the relative cross-correlation phase is about 1 and this means that the oscillation involves just one single rotating cell.

The detected rotating stall has a frequency of 0.41Ω (10.3 Hz) in a fixed coordinate frame. The rotating speed of the inducer was 1500 rpm (25 Hz). As a consequence, in a coordinate frame rotating with the blades (as the one used to estimate the cavity length), the frequency of the rotating stall becomes $25-10.3=14.7$ Hz, which is just the observed value of f_c.

Figure 21 (top) shows a sinusoidal signal at frequency f_c, whose magnitude and phase have been calculated using a trial-and-error technique, superimposed to the nondimensional tip cavity length on the third blade, while Fig. 21 (bottom) shows the same sinusoidal signal shifted of an angle equal to the phase of the cross-correlation between blade 3 and blade 2.

Figure 22 shows the sinusoidal signals of Fig. 21 together with that obtained for the remaining blade (same frequency, phase calculated from the cross-correlation analysis). It is evident that the cavity propagates clockwise from the first blade to the third blade. It can also be observed that the mean cavity length on the first blade is lower than the other two (asymmetric cavitation, Fig. 23). The asymmetric cavitation is clearly generated by some kind of geometric imperfection on this blade and not, as it could also be supposed, by a nonuniform illumination of the inducer. If nonuniform illumination were experienced, in fact, a shorter cavity would be observed only in given sectors during each rotation and for all the blades, not just for one of them as shown by Fig. 22.

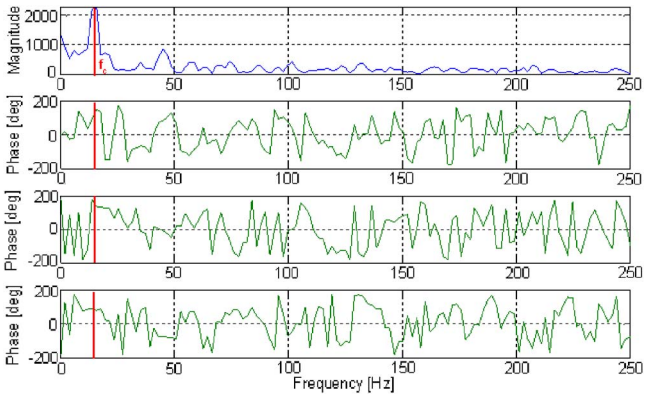

Fig. 20 Power spectrum of the tip cavity length on third blade (first plot). Phase of the cross-correlation between third and second blades (second plot), second and first blades (third plot), first and third blades (fourth plot).

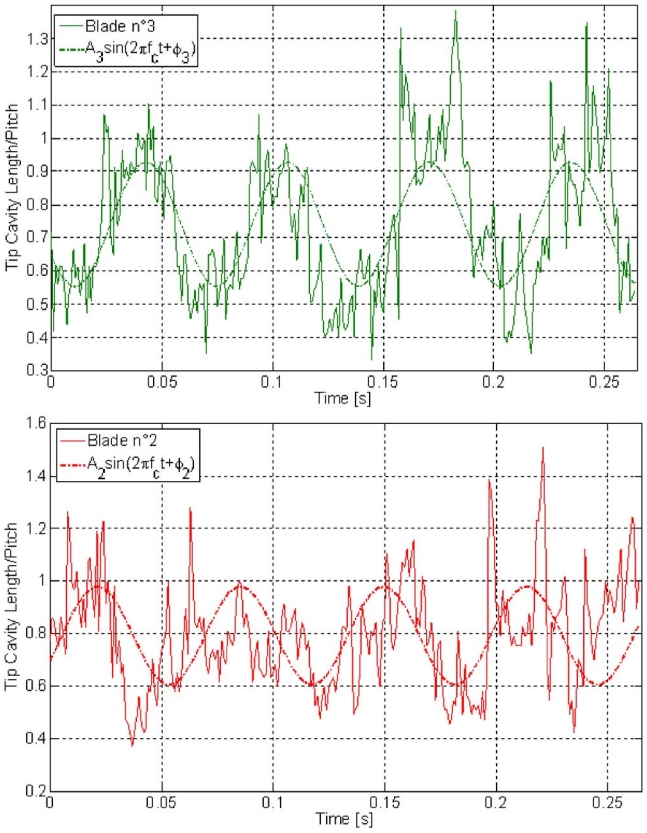

Fig. 21 Sinusoidal signal at frequency f_c superimposed to the measured nondimensional tip cavity length for blade 3 (top) and blade 2 (bottom)

Conclusions

The present research activity has allowed for the development and successful validation of a viable and effective tool, based on optical processing of high-speed video movies for quantitative analysis and diagnostics of cavitation instabilities in turbopump inducers. The capabilities of the semi-automatic algorithm created to implement the proposed technique have been improved by developing a procedure for the estimation of the frontal cavitating surface and the extension of the cavitating regions on the blades.

The application of the above technique to the analysis of cavitation in a test inducer lead to the detection of the rotating stall instability observed under the same operating conditions by means of Fourier analysis of the inlet pressure signals. The results confirm the potential of the proposed method in the characterization of cavitation-induced instabilities and suggest the possibility of extracting additional useful information on the nature, extent, and location of the cavitating regions on the inducer blades.

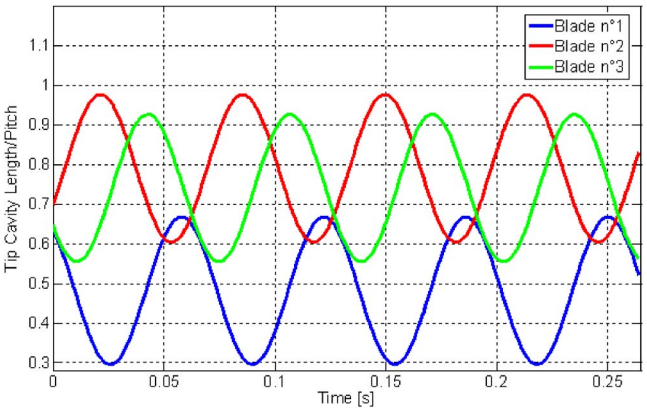

Fig. 22 Oscillation of the cavity length on the blades of the FIP inducer

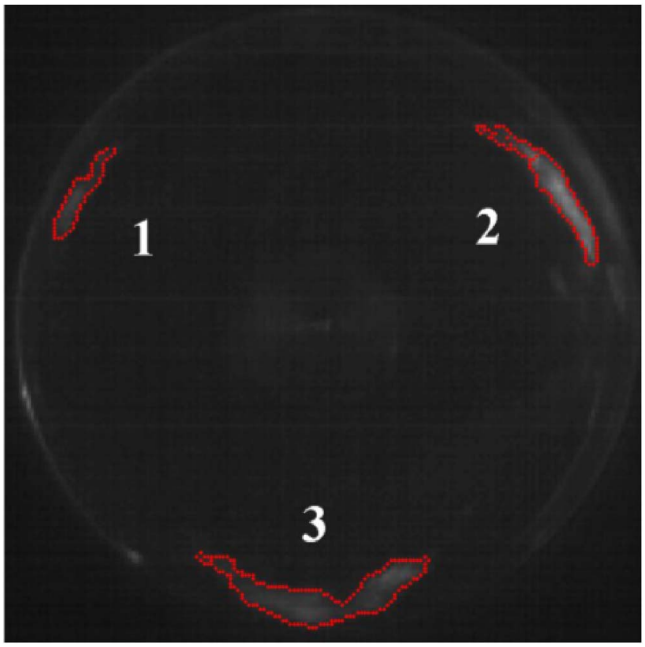

Fig. 23 Example of asymmetric blade cavitation

Acknowledgment

The present activity has been funded by the Agenzia Spaziale Italiana under contract No. I/016/05/0 for fundamental research, whose support is gratefully acknowledged. The authors would like to express their gratitude to Prof. Mariano Andrenucci, Prof. Renzo Lazzeretti, and Prof. Fabrizio Paganucci of the Dipartimento di Ingegneria Aerospaziale, Università di Pisa, Pisa, Italy, for their constant and friendly encouragement.

Nomenclature

A = amplitude of oscillations
b_t = blade thickness
d = b_t/n
f = frequency
n = normal blade spacing
p_{in} = inlet pressure
p_V = vapor pressure
Q = volumetric flow rate
r_t = inducer blade tip radius
S_{cav} = total cavitating surface on each blade
S_{flow} = inducer frontal surface
t = time
ν = kinematic viscosity
α = incidence angle
β_b = blade angle
Ω = rotational speed
Φ = flow coefficient $\Phi = Q/\pi\Omega r_T^3$
ϕ = phase of oscillations
ρ = density
σ = cavitation number
σ_c = choked cavitation number
θ = azimuthal coordinate
$\Delta\theta$ = azimuthal extension of the cavity at the tip of the blades

References

[1] Stripling, L. B., and Acosta, A. J., 1962, "Cavitation in Turbopumps—Part 1," ASME J. Basic Eng., **84**, pp. 326–338.

[2] Brennen, C. E., 1994, *Hydrodynamics of Pumps*, Concepts ETI, Inc. and Oxford University Press, Norwich, VT.

[3] Cervone, A., Testa, R., Bramanti, C., Rapposelli, E., and d'Agostino, L., 2005, "Thermal Effects on Cavitation Instabilities in Helical Inducers," J. Propul. Power, **21**(5), pp. 893–899.

[4] Cervone, A., Torre, L., Bramanti, C., Rapposelli, E., and d'Agostino, L., 2006, "Experimental Characterization of Cavitation Instabilities in a Two-Bladed Axial Inducer," J. Propul. Power, **22**(6), pp. 1389–1395.

[5] Tsujimoto, Y., Yoshida, Y., Maekawa, Y., Watanabe, S., and Hashimoto, T., 1997, "Observations of Oscillating Cavitation of an Inducer," ASME J. Fluids Eng., **119**, pp. 775–781.

[6] Kamijo, K., Shimura, T., and Tsujimoto, Y., 1994, "Experimental and Analytical Study of Rotating Cavitation," Proc. of ASME Cavitation and Gas-Liquid Flow in Fluid Machinery and Devices, Lake Tahoe, NV, Jun. 19–23.

[7] Hashimoto, T., Yoshida, M., Watanabe, M., Kamijo, K., and Tsujimoto, Y., 1997, "Experimental Study of Rotating Cavitation of Rocket Propellant Pump Inducers," J. Propul. Power, **13**(4), pp. 488–494.

[8] Jousselin, F., Courtot, Y., Coutier-Delgosha, O., and Reboud, J. L., 2001, "Cavitating Inducer Instabilities: Experimental Analysis and 2D Numerical Simulation of Unsteady Flow in Blade Cascade," Proc. of CAV2001—4th International Symposium on Cavitation, Pasadena, CA, Jun. 20–23.

[9] Rapposelli, E., Cervone, A., and d'Agostino, L., 2002, "A New Cavitating Pump Rotordynamic Test Facility," Proc. of AIAA Joint Propulsion Conference and Exhibit, Indianapolis, IN, Jul. 7–10, paper No. 2002-4285.

[10] Gonzalez, R. C., and Woods, R. E., 2002, *Digital Image Processing*, Prentice-Hall, New Jersey.

[11] Kato, K., Matudaira, Y., and Obara, H., 2003, "Flow Visualization of Cavitation With Particle and Bubble Image Processing," Proc. of ASME FEDSM—Fluids Engineering Division Summer Meeting, Honolulu, HI, Jul. 6–11.

[12] Otsu, N., 1979, "A Threshold Selection Method From Gray-Level Histograms," IEEE Trans. Syst. Man Cybern., **9**(1), pp. 62–66.

[13] Brennen, C. E., and Acosta, A. J., 1973, "Theoretical, Quasistatic Analyses of Cavitation Compliance in Turbopumps," J. Spacecr. Rockets, **10**(3), pp. 175–180.

Xavier Escaler
Center for Industrial Diagnostics (CDIF),
Universitat Politècnica de Catalunya (UPC),
Avinguda Diagonal 647,
08028 Barcelona, Spain
e-mail: escaler@mf.upc.edu

Mohamed Farhat
Laboratory for Hydraulic Machines
(LMH-IMHEF),
École Polytechnique Fédérale de Lausanne
(EPFL),
Avenue de Cour 33bis,
CH-1007 Lausanne, Switzerland
e-mail: mohamed.farhat@epfl.ch

Eduard Egusquiza
Center for Industrial Diagnostics (CDIF),
Universitat Politècnica de Catalunya (UPC),
Avinguda Diagonal 647,
08028 Barcelona, Spain
e-mail: egusquiza@mf.upc.edu

François Avellan
Laboratory for Hydraulic Machines
(LMH-IMHEF),
École Polytechnique Fédérale de Lausanne
(EPFL),
Avenue de Cour 33bis,
CH-1007 Lausanne, Switzerland
e-mail: francois.avellan@epfl.ch

Dynamics and Intensity of Erosive Partial Cavitation

An experimental work has been carried out to investigate the dynamic behavior and the intensity of erosive partial cavitation on a 2-D hydrofoil. Both sheet (stable) and cloud (unstable) cavitation have been tested in a cavitation tunnel for various free stream velocities. Special attention has been given to validate the use of acceleration transducers for studying the physical process. In particular, the modulation in amplitude of the cavitation induced vibrations in a high frequency band has allowed us to determine the shedding frequency and the relative intensity of the collapse process for each testing condition. Regarding the cavity dynamics, a typical Strouhal value based on its length of about 0.28 has been found for cloud cavitation; meanwhile, for sheet cavitation, it presents a value of about 0.16. Furthermore, the level of the vibration modulation in the band from 45 kHz *to* 50 kHz *for cloud cavitation shows a power law dependency on the free stream velocity as well as a good correlation with the pitting rate measured on stainless steel samples mounted on the hydrofoil.* [DOI: 10.1115/1.2742748]

Keywords: partial cavitation, vibration modulation, dynamics, erosion

1 Introduction

1.1 Unsteady Attached Cavities. Attached cavitation appears as macrocavities that develop and attach on a solid wall placed in the flow. The various forms of attached cavitation on the suction side of hydrofoils have been extensively investigated experimentally for many years by, for example, Franc and Michel [1] and Avellan et al. [2]. Numerical simulations (Kubota et al. [3]) and theoretical models (Watanabe et al. [4]) have also been developed, although the results have been very limited up to now. In general terms, two types of unsteadiness with distinctive character have been observed based on the attached cavity length l (Leroux et al. [5]). Partial cavitation occurs for $l/c<3/4$ and transitional cavitation occurs for $l/c>3/4$, where c is the chord length. An equivalent parameter is $\sigma/2i$ that has been found to be about 4 in the transition of these two types of cavitation and higher than 4 for partial cavitation by Kjeldsen et al. [6]. The experimental results seem to indicate that for transitional cavitation, the main cavity dynamics would be governed by a shock-wave phenomenon; meanwhile, for partial cavitation, the predominant mechanism is the re-entrant jet (Callenaere et al. [7]).

Partial cavitation on the suction side of a hydrofoil can present two different regimes, depending on the hydrodynamic conditions. One of them, i.e., sheet cavitation, is characterized by a thin stable cavity with a smooth and transparent interface. At the rear part, the cavity closure presents a slight and weak pulsation due to the shedding of small cavitation vortices. The other regime, i.e., cloud cavitation, shows a strong unsteadiness and a pulsating behavior that provokes significant oscillations of the cavity length. The cavity interface is wavy and turbulent. Large U-shaped transient cavities and clouds of cavities are shed away downstream of the cavity closure that collapses violently (Avellan and Dupont [8]). Strong pressure pulses are applied on the solid surface due to the shock waves emitted at the final stage of the cavity collapses (Avellan and Farhat [9]). Consequently, cloud cavitation is found to be a very aggressive form of partial cavitation with a high erosive power compared with sheet cavitation that seems to present a lower risk (Quang et al. [10]).

The majority of experimental and numerical studies have concluded that the shedding frequency of partial cavitation follows a Strouhal law based on the main cavity length. For cloud cavitation, the cavity dynamics clearly show a St_l value of about 0.30 (Leroux et al. [11]); nevertheless, there are no analogous results found for sheet cavitation up to now. The low intensity cavity fluctuations observed with sheet cavitation make it difficult to characterize its behavior.

1.2 Erosion in Hydraulic Machines. Cavitation erosion of runner/impeller blades is a common and relevant problem in hydraulic machinery. The experience based on erosion cases observed in the blades of actual water turbines seems to indicate that it is caused by a partial cavity starting next to the leading edge and with a maximum length below $\frac{3}{4}$ of the chord. When damage occurs, it is generally very aggressive and requires continuous inspection of the runner/impeller to prevent the blades from breaking off. Such strong erosive power appears to be related to the unsteady behavior of the attached partial cavity, as in an isolated hydrofoil (Bourdon et al. [12]). Nevertheless, the basic cavitation mechanisms in actual machines are not yet well known. It is believed that there is a strong interaction with the complex flow features induced by the machine dynamic behavior. For instance,

Contributed by the Fluids Engineering Division of ASME for publication in the JOURNAL OF FLUIDS ENGINEERING. Manuscript received October 13, 2006; final manuscript received January 15, 2007. Review conducted by Joseph Katz.

in turbines erosive cavitation is difficult to predict since it usually occurs only under certain machine operating conditions (Escaler et al. [13]). To improve our understanding of this phenomenon, it would be appropriate to carry out a detailed investigation of the dynamics and intensity of both sheet and cloud cavitation in the laboratory. Thinking in the latter application of these results in actual machines, where there are strong difficulties in installing instrumentation and measuring without significantly affecting the machine operation, it has been decided to base our research on vibration measurements.

1.3 Cavitation Induced Vibrations. General research on erosive cavitation was started with the idea that noise and vibrations could be used as indicators of cavitation erosive power (Kato et al. [14], Simoneau et al. [15], and Bourdon et al. [16]). Given a hydrofoil in a cavitation tunnel, partial cavities shed clouds of bubbles and cavitation vortices in a periodic way synchronized with the main cavity oscillation. The cloud collapse takes place just downstream of the main cavity and the solid wall is impacted by emitted shock waves. Each collapse results in a high pressure, short duration pulse that excites the structure like a hammer hitting in a small area. As a consequence, vibrations with a broadband spectral content reaching very high frequencies (above tenths of kHz) are induced on the structure at the end of each shedding period.

In laboratory measurements, dynamic pressure transducers flush mounted in the test section walls or embedded on the hydrofoil suction side can be used to characterize partial cavitation. Test section pressure signals are very useful to detect the pressure pulsations generated by the main cavity oscillation and the noise due to the cavity collapses. However, it is well known that only a given percentage of the collapses are close enough to the surface to provoke erosion. Therefore, these signals are not adequate if we are concerned about cavitation erosion quantification. Embedded hydrofoil wall pressure signals are obtained with small sized transducers that can only measure local phenomena occurring just above them. Usually, their number is small so that they monitor only a small area of the region of interest. Moreover, their use in real machines is difficult and expensive. Consequently, high frequency acceleration transducers mounted on the external parts of the hydrofoil support and as close as possible to it, are an alternative way of investigating the physical process behind erosive partial cavitation on hydrofoils. They are mechanically linked to the hydrofoil structure and they can detect all pulsating forces acting on the hydrofoil wall that are directly related to erosion.

1.4 Analysis of Vibrations. The use of high frequency vibrations for the study of cavitation erosion started with the evaluation of the overall acceleration level (RMS value) in a broadband frequency range. However, this quantifier is also dependent on the level of vibrations induced by the main free cavitation flow. An improvement of this method arose with the observation that the instantaneous vibration levels are lower during the cloud cavitation inception and its development period. Then, during the collapse stage, the levels obviously increase. As a result, the cavitation induced vibrations appear to be modulated in amplitude at the particular frequency of the main cavity dynamics. Moreover, the modulation level should be related to the erosion intensity. By an adequate demodulation technique, these frequencies can be extracted and their amplitude can be estimated. Abbot et al. [17] were able to validate in hydrofoils and in actual water turbines the use of full-wave rectification spectral analysis for this purpose. Nowadays, a similar modulation analysis is applied but based on digital signal processing [13] which gives more flexibility and the possibility to explore more in detail the experimental data. To finish, just indicate that the complete prediction of cavitation erosion is also dependent on the metallurgical characteristics of the material under attack.

1.5 Objectives. The main objective of the current work is to investigate the dynamic and erosive characteristics of both sheet and cloud cavitation by the use of cavitation induced vibrations. In particular, it is intended to find out the characteristic shedding frequency and the amplitude of the modulation energy. Considering the latter as an indicator of cavitation erosion intensity, its dependence with the free stream velocity will then be evaluated. It is also intended to find its correlation with the erosion rate measured on the material.

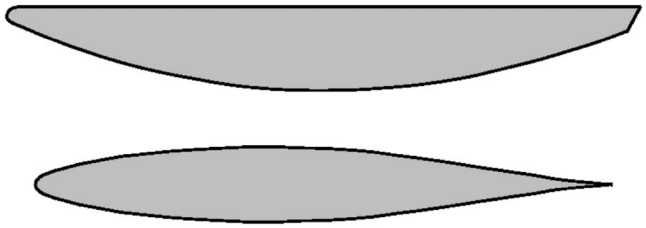

Fig. 1 Cross sections of the plane-convex (top) and of the NACA 65012 (bottom) hydrofoils

2 Experimental Setup and Procedure

2.1 High Speed Cavitation Tunnel. The experiments have been carried out in the Laboratory for Hydraulic Machines-École Polytechnique Fédérale de Lausanne (LMH-EPFL), high-speed cavitation tunnel. This closed loop with circulating water is specially designed for the study of cavitation in hydrofoils [18]. A free stream velocity (U_{inf}) up to a maximum of 50 m/s can be reached within a rectangular test section of $150 \times 150 \times 750$ mm^3. A revolving bedplate flange provides a rigid mounting base for the hydrofoil to be tested with the possibility of varying its angle of incidence (i). The cavitation number (σ), which is continuously controlled, can be adjusted as desired.

2.2 Hydrofoils. Two bi-dimensional hydrofoils with rounded leading edges have been used to generate erosive partial cavitation. One of them is a NACA 65012 and the other one has a plane-convex cross section with a flat suction side and a circular pressure side (see Fig. 1). Their chord lengths are 91.1 mm and 100 mm, respectively. They have a spanwise length of 150 mm and a maximum thickness of approximately 12 mm. To carry out erosion tests on materials, both hydrofoils permit us to install replaceable samples on their suction sides.

2.3 Flow Visualization. To identify the regime of the partial cavity and to measure its length, the hydrofoil suction side has been observed through the tunnel transparent windows by means of a digital CCD camera combined with a stroboscopic lamp. Typical photographs of sheet and cloud cavitation are shown in Fig. 2.

2.4 Vibration Measurement. The cavitation induced vibrations can be measured with miniature piezoelectric accelerometers Bruel&Kjaer type 8309 (BK) and Kistler type 8614A500M1 (K). Their theoretical mounted resonant frequencies are of about 180 kHz and 125 kHz, respectively. The BK is bolted, meanwhile, the K is fixed with wax to the structure. These transducers can be oriented in vertical (V) or horizontal (H) directions inside the revolving bedplate on a special support rigidly attached to the flange (see Fig. 3). The K accelerometers can also be attached on the flange (close) or on the external side of the bedplate (far) in a horizontal direction.

The signals from the transducer are filtered with a Wavetek Butterworth band-pass filter for noise reduction and anti-aliasing prior to being recorded with an analog-to-digital converter LeCroy 6810. The data are then transmitted to the PC acquisition software through a general purpose interface bus (GPIB) to computer automated measurement and control (CAMAC) interface module

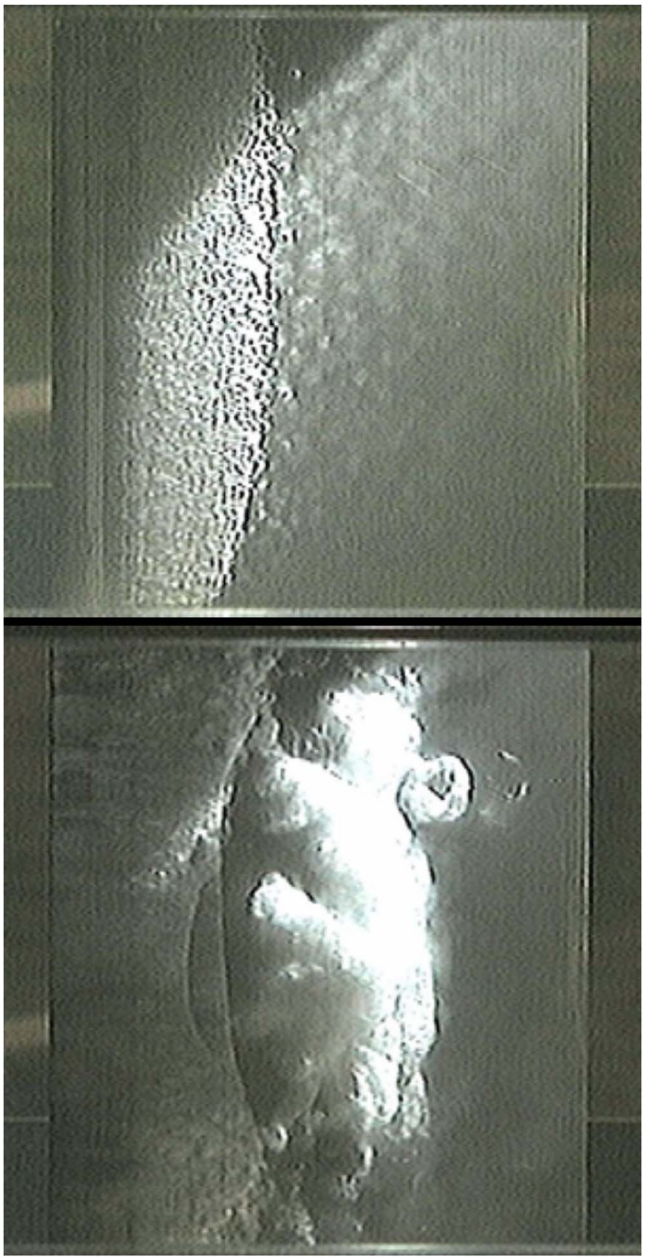

Fig. 2 Partial cavitation on a 2-D hydrofoil. Top: Sheet cavitation at U_{inf}=30 m/s, σ=0.7, and i=2 deg. Bottom: Cloud cavitation at U_{inf}=30 m/s, σ=1.2, and i=5 deg. Flow from left to right.

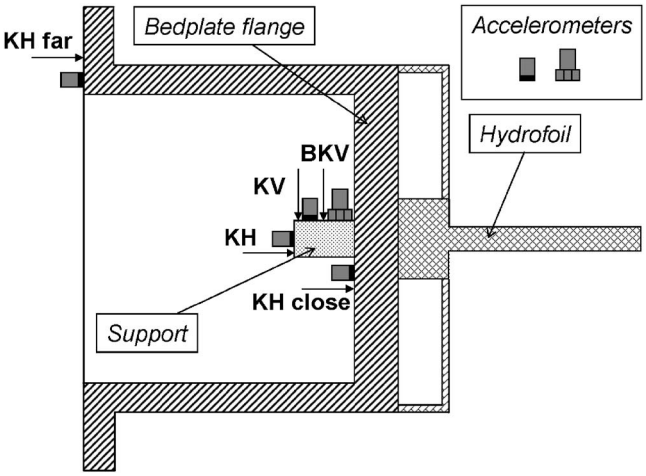

Fig. 3 Section of the hydrofoil, the revolving bedplate, and the support for the accelerometers. Schematic of the transducer locations and orientations.

LeCroy 6010. The low frequency cutoff is usually set at 2 kHz. Typical sampling frequencies are 200 kHz and 500 kHz.

2.5 Spectral Content and Amplitude Demodulation. The power spectral density (PSD) of the absolute accelerations is calculated from an averaged auto power spectrum using a smoothing Hanning window.

The raw time signals can be band-pass filtered in a given frequency band using an adjustable Butterworth digital filter with ripple 10, attenuation 40, and order 2. The envelope of the filtered time signal is obtained from the analytic signal using the Hilbert transform (see the details of this processing technique in [13]). The frequency content of the envelope shows the main amplitude modulation frequencies.

An example of the cavitation induced vibrations measured with the BK accelerometer in the band from 45 kHz to 50 kHz and the corresponding envelope is shown in Fig. 4. This signal corresponds to unstable cloud cavitation on the NACA hydrofoil tested at 30 m/s with 6 deg of incidence and a maximum cavity length of about 40% of the chord length.

3 Preliminary Tests

In order to define the final experimental configuration, a preliminary study of the influence of various measurement and analysis parameters was carried out.

First of all, two types of accelerometers and two orientations were simultaneously tested under cloud cavitation conditions on the plane-convex hydrofoil, in particular, the BKV, KV, and KH (refer to Fig. 3). Figure 5 shows the PSD and the amplitude modulation in the band from 45 kHz to 50 kHz of the measured vibrations. The two K sensors with different orientations measure a similar spectral content but it differs from the BK results. The advantage of this last sensor is that it can detect cavitation excitation up to frequencies of 200 kHz. Regarding the amplitude demodulation, this technique appears to work correctly for the same spectral band in the three measurements. A distinctive peak is found for a St_l number of 0.3 which is what is expected for a mean cavity length of 50% of the chord. In addition, the height of the modulating peak relative to its corresponding baseline is found to be the same for the three sensors. This indicates that, although the absolute level of the amplitude modulation is different, the envelopes are proportional among the sensors. Thus, the relative modulation level is analogous.

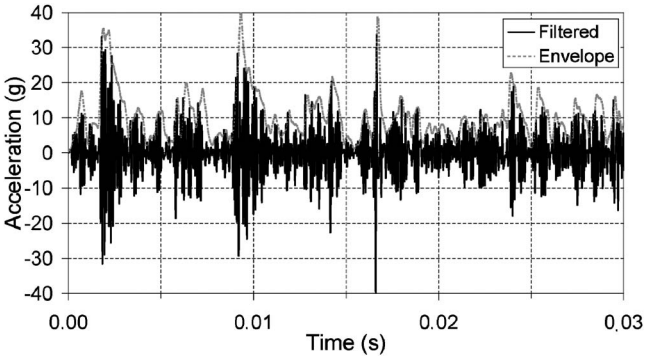

Fig. 4 Filtered time signal and corresponding envelope of cavitation induced vibrations in the band from 45 kHz to 50 kHz (i=6 deg, U_{inf}=30 m/s, l/c=0.4, and σ=1.6)

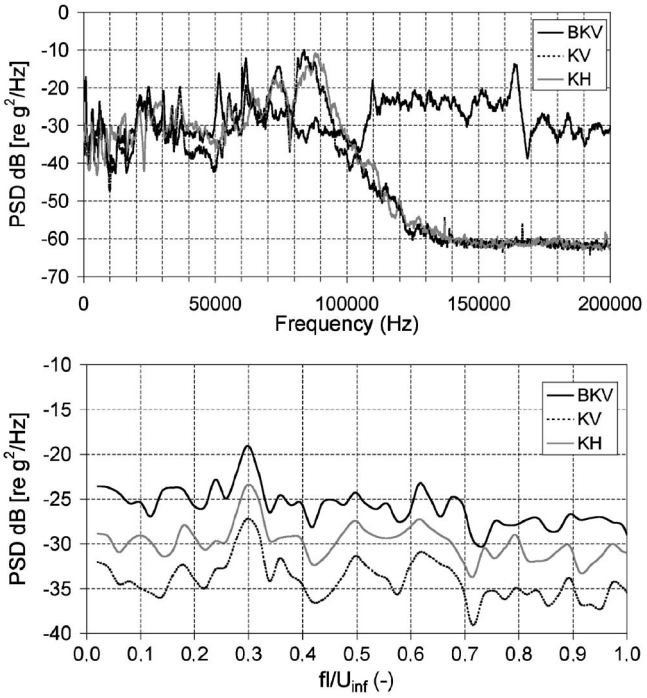

Fig. 5 PSD (top) and modulation in the band from 45 kHz to 50 kHz (bottom) of cloud cavitation vibrations measured on the plane-convex hydrofoil with BKV, KV, and KH (i=0.8 deg, U_{inf}=35 m/s, l/c=0.5, and σ=0.6)

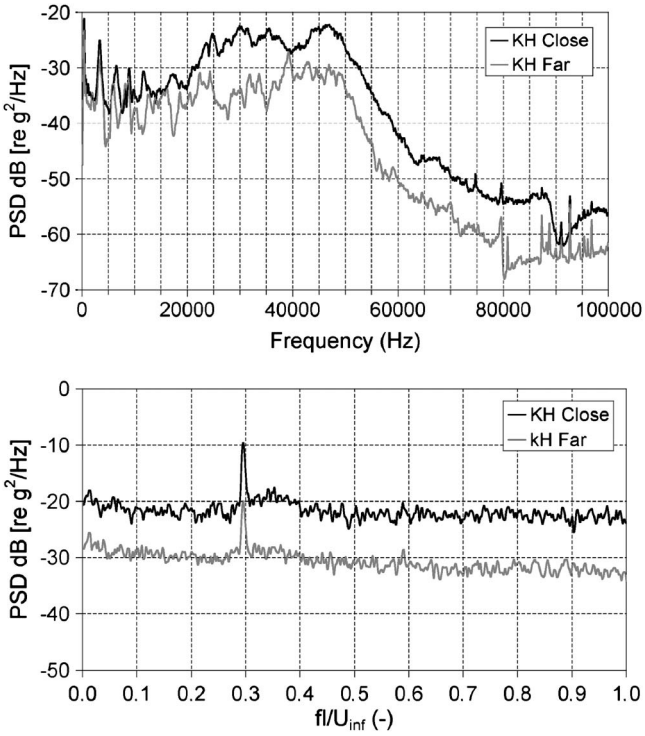

Fig. 6 PSD (top) and modulation in the band from 45 kHz to 50 kHz (bottom) of cloud cavitation vibrations measured on the plane-convex hydrofoil with two KH at different distances (i=5 deg, U_{inf}=35 m/s, l/c=0.3, and σ=1.1)

Second, the transmissibility properties of the hydrofoil and its support were also considered by comparing simultaneous measurements with the same type of accelerometer (K) and orientation (H) at two different distances from the source of excitation again with the plane-convex hydrofoil. In Fig. 6, the resulting spectral content and the amplitude modulation are plotted. As in the previous analysis, although the shape of the spectra presents slight differences, the peak of the main amplitude modulation frequency has about the same height within the two measurements. This indicates that in this particular setup, the signal is linearly and uniformly attenuated between the two measuring locations. Thus, the measured structural response to the hydraulic excitation can be considered as a valid indicator of the excitation characteristics.

Finally, the effect of selecting the frequency limits for the amplitude demodulation was also checked. In Fig. 7, the results obtained by filtering at various bands of 5 kHz width in the range from 5 kHz to 80 kHz are plotted together for a given BKV measurement with the NACA hydrofoil. Any band above 5 kHz is suitable to detect the main modulation frequency. However, only above 15 kHz are the modulation results analogous in terms of amplitude relative to the spectrum baseline, i.e., PSD_b.

Therefore, based on these preliminary results, it was decided to measure the vibrations during the final tests with the BK accelerometer in vertical orientation on the bedplate flange support. The frequency band from 45 kHz to 50 kHz was selected for the amplitude demodulation analysis of the vibrations because it showed a significant signal level.

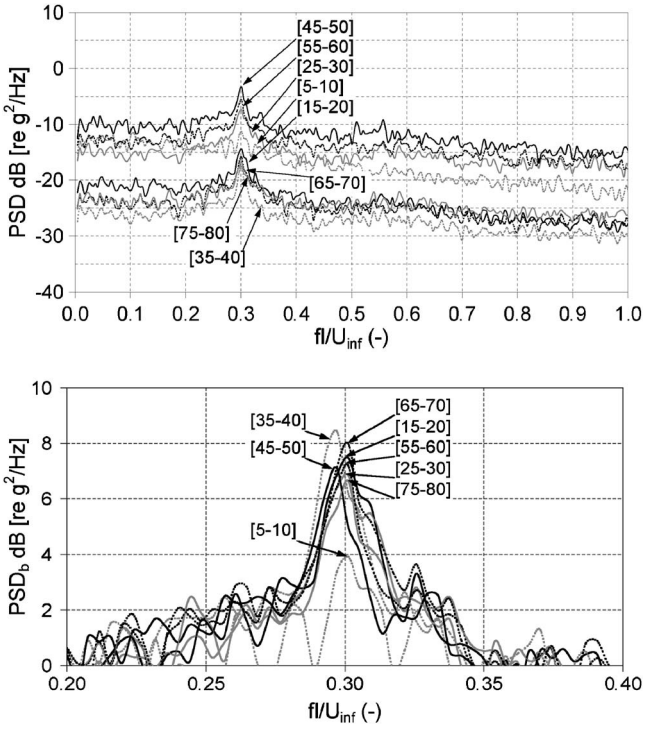

Fig. 7 Modulation results (top) and comparison of their amplitudes relative to the baselines (bottom) for different frequency bands (in kHz) of cloud cavitation vibrations measured on the NACA hydrofoil with BKV (i=6 deg, U_{inf}=30 m/s, l/c=0.4, and σ=1.6)

4 Final Erosion Tests

4.1 Hydrodynamic Conditions and Erosion Results. The vibration and erosion tests have been carried out at tunnel free stream velocities of 15, 20, 25, and 30 m/s with the NACA 65012 hydrofoil. The incidence angle has been fixed to 4 deg and 6 deg. The sigma has been adjusted to generate cavity lengths of about 20% and 40% of the chord length. Visual observation has permit-

Table 1 Testing conditions (i, l/c, U_{inf}) and corresponding values of σ, $\sigma/2i$, t, R_{ave}, τ, f_{max}, St_l, RMS value of accelerations and mean square value of AD_b in the band from 45 kHz to 50 kHz

i (deg)	l/c (%)	U_{inf} (m/s)	σ	$\sigma/2i$	t (s)	R_{ave} (μm)	τ (1/mm^2/s)	f_{max} (Hz)	St_l	RMS (g)	AD_b (g^2)
4	20	15	1.21	8.67			-	-	-	0.3	-
4	20	20	1.22	8.74			-	-	-	0.53	-
4	20	25	1.23	8.81			-	204.47	0.16	1.39	0.014
4	20	30	1.26	9.03			-	253.30	0.17	2.75	0.248
4	40	15	1.10	7.88			-	-	-	0.36	-
4	40	20	1.10	7.88			-	77.82	0.16	0.8	0.002
4	40	25	1.10	7.88			-	100.71	0.16	1.75	0.026
4	40	30	1.12	8.02			-	119.02	0.16	3.42	0.166
6	20	15	1.83	8.74	7200	16.8	5.8×10^{-6}	189.21	0.25	0.85	0.015
6	20	20	1.85	8.83	2400	19.3	5.2×10^{-5}	250.24	0.25	2.59	0.160
6	20	25	1.87	8.93	480	27.0	1.5×10^{-4}	387.57	0.31	5.03	0.404
6	20	30	1.90	9.07	100	27.7	4.2×10^{-4}	419.62	0.28	7.54	1.359
6	40	15	1.55	7.40	8100	17.1	6.9×10^{-6}	96.13	0.26	1.1	0.048
6	40	20	1.58	7.55	3600	34.2	1.2×10^{-4}	132.75	0.27	3.26	0.499
6	40	25	1.60	7.64	720	34.5	3.7×10^{-4}	175.48	0.28	6.16	2.002
6	40	30	1.62	7.74	150	40.8	3.5×10^{-3}	225.83	0.30	10.12	7.035

ted us to determine that stable sheet cavitation occurs for $i=4$ deg and unstable cloud cavitation for $i=6$ deg, independently of the rest of the parameters.

Erosion measurements have been carried out by Couty [19] on stainless steel 316L (inox) samples inserted in the NACA hydrofoil. The tests have been carried out during the material incubation period by selecting an adequate exposure time t. The surface of the sample has been measured after the test at certain locations along the chord with a 3-D laser profilometer and the pits have been identified and measured with a specific software. Due to the strong resistance of stainless steel, measurable erosion has only been obtained for the most aggressive cavitation conditions corresponding to $i=6$ deg. The material exposure time, the average pit radius R_{ave}, the average pitting rate τ, and the corresponding hydrodynamic testing conditions are given in Table 1. For additional information, please refer to [16].

4.2 Spectral Analysis. The averaged PSD of the raw cavitation induced vibrations measured with BKV during the tests are presented in Fig. 8. The effect of the free stream velocity on the spectral content is observed on each graph for fixed incidence angles and cavity lengths. Broadly speaking, the increase of U_{inf} increases the spectrum level uniformly in the entire frequency range from 1 kHz to 100 kHz. The spectra appear almost parallel in any range of frequencies.

In Fig. 9, there is a comparison of vibration spectral content at two incidence angles and at two cavity lengths for constant $U_{inf}=30$ m/s. It is observed that increasing i from 4 deg to 6 deg for the same l/c results in a significant uniform increase of the spectral content in the entire frequency band. For the same i, the effect

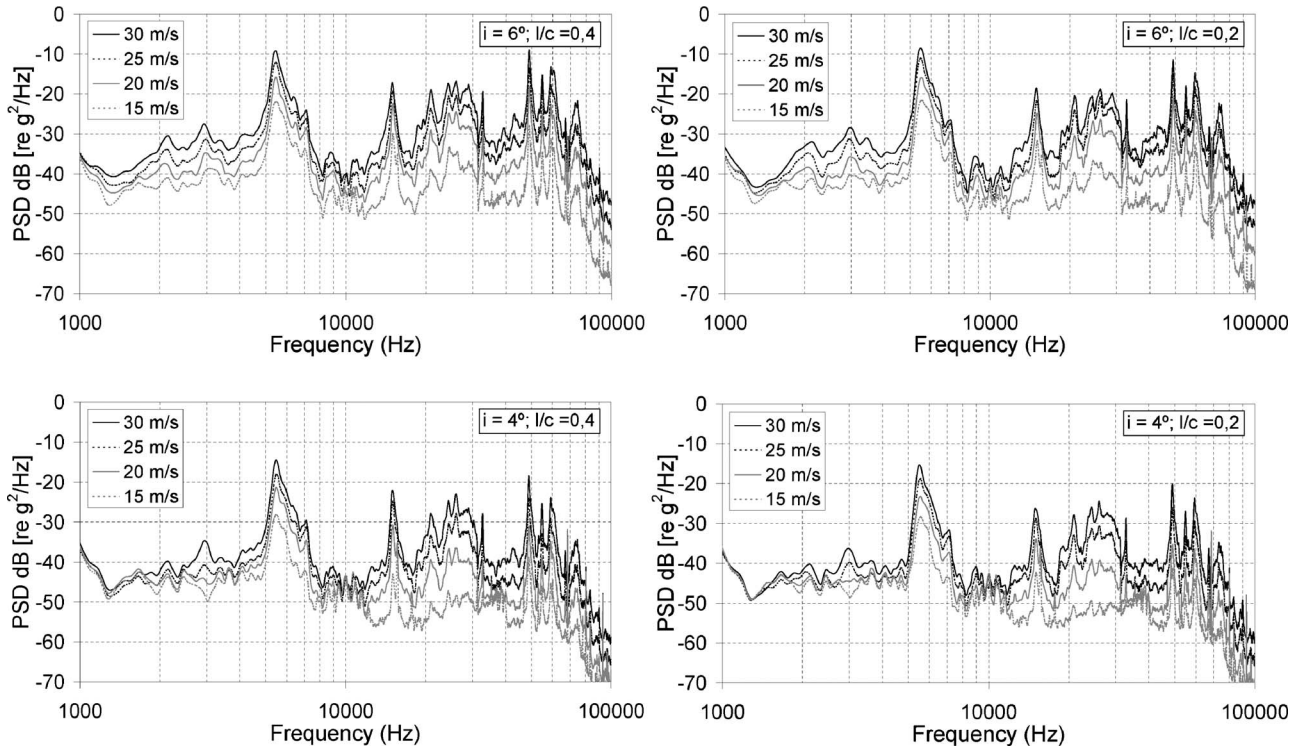

Fig. 8 PSD of the cavitation induced vibrations on the NACA hydrofoil

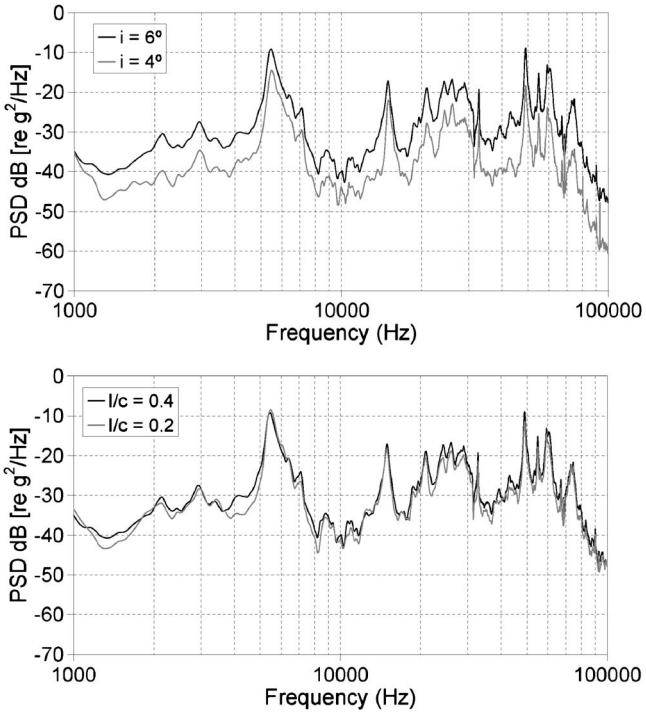

Fig. 9 Comparison of PSD at two incidence angles for the same l/c=0.4 (top) and at two cavity lengths for the same i =6 deg (bottom) for U_{inf}=30 m/s on the NACA hydrofoil

of increasing l/c from 0.2 to 0.4 do not show a significant change in the spectra except for a slight parallel increase. In fact, in the first situation, the type of cavitation is changing from sheet to cloud but in the second case, the same type of cavitation is maintained. A similar behavior is observed at any tested i and U_{inf}.

In order to quantify more precisely the energy content of the vibration signals, the RMS values of accelerations in the frequency band from 45 kHz to 50 kHz have been calculated and they are listed in Table 1. The corresponding overall mean square values have been plotted as a function of U_{inf} in Fig. 10. These results confirm that the excitation due to cloud cavitation (i =6 deg) is significantly stronger than that of sheet cavitation (i =4 deg). Moreover, increasing the cavity length for a given incidence angle from 20% to 40% of the chord also enhances the cavitation intensity. For all the types of partial cavitation, the effect of the flow velocity increase has a similar trend with a slope of around 6.4.

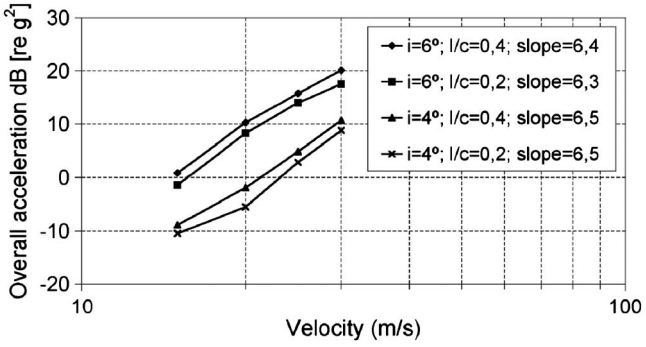

Fig. 10 Overall mean square value of accelerations as a function of U_{inf} in the band from 45 kHz to 50 kHz on the NACA hydrofoil

4.3 Amplitude Demodulation Analysis. The averaged PSD of the envelopes calculated for the filtered signal in the band from 45 kHz to 50 kHz are plotted in Fig. 11. For the lower free stream velocities at i=4 deg, the amplitude of the vibration acceleration was so low that no reliable demodulation results could be obtained. For the rest of testing conditions, a single amplitude modulation peak has been well identified. Considering the frequency value with maximum amplitude f_{max}, then, the corresponding Strouhal number St_l has been determined. For a more precise evaluation of the modulation energy, the width of the modulation peak and its height relative to the spectrum baseline have been considered. The curve defining the baseline has been calculated with a least-squares fit of the entire spectrum. The range of values around f_{max} with amplitude levels above the corresponding baseline values have then been considered as part of the modulation peak. And finally, the mean square modulation acceleration of the shedding frequency AD_b has been calculated by integrating over this frequency range the PSD values minus the baseline levels. All these results are listed in Table 1.

For all the tests with cloud cavitation corresponding to i =6 deg, the Strouhal number St_l lies in the range from 0.25 to 0.31 with an average value of about 0.275. However, when sheet cavitation is involved for tests with i=4 deg, St_l is about 0.16 on average. This is an interesting result that clearly points out a different behavior of the re-entrant jet mechanism for partial cavitation between stable (sheet) and unstable (cloud) regimes.

Another consideration related to the shedding process is observed from the fact that, when the length of the main cavity is reduced from 40% to 20% of the chord, the modulation peak is lowered and widened. This would indicate that for a longer cavity, there is a predominating type of collapsing structure with a quite constant shedding frequency; meanwhile, for shorter lengths, the shedding process is not so coherent, and then collapses of less intensity take place with a wider distribution of frequencies.

In Fig. 12, the mean square modulation acceleration AD_b is plotted as a function of U_{inf}. The effect of increasing the angle of incidence, the cavity length, and the flow velocity are also well identified. It must be noted that this intensity quantifier is more sensitive to the increase of U_{inf} than the overall acceleration level in the same band. For high incidence (i=6 deg), the slopes of the linear fits are around 6.7 and for low incidence (i=4 deg), they are even larger, reaching levels of about 10.9.

Finally, the correlation between the AD_b level and average pitting rate has been calculated and the result is plotted in Fig. 13 for the tests at i=6 deg. A linear behavior is identified for the cloud cavitation regime with a slope of about 1.1, which appears to agree with the results obtained by Abbot et al. [17] in 1993.

5 Conclusions

An experimental investigation on erosive partial cavitation has been carried out based on the measurement of cavitation induced vibrations in a broadband frequency range up to 100 kHz.

The use of acceleration transducers mounted on the test section is valid to study the physical characteristics of this type of cavitation.

The analysis of the vibrations' spectral content and the amplitude demodulation of the acceleration signals filtered from 45 kHz to 50 kHz permits us to quantify the cavitation intensity and to identify the main cavity shedding frequency.

A series of tests have been carried out with sheet (stable) and cloud (unstable) cavitation regimes using the NACA 65012 hydrofoil corresponding to incidence angles of 4 deg and 6 deg, respectively. In each regime, cavity lengths of about 20% and 40% of the chord have been reproduced at various free stream velocities from 15 m/s to 30 m/s.

The shedding process of cloud cavitation follows a constant Strouhal value based on the main cavity length of about 0.28, meanwhile, for sheet cavitation it follows a constant value of

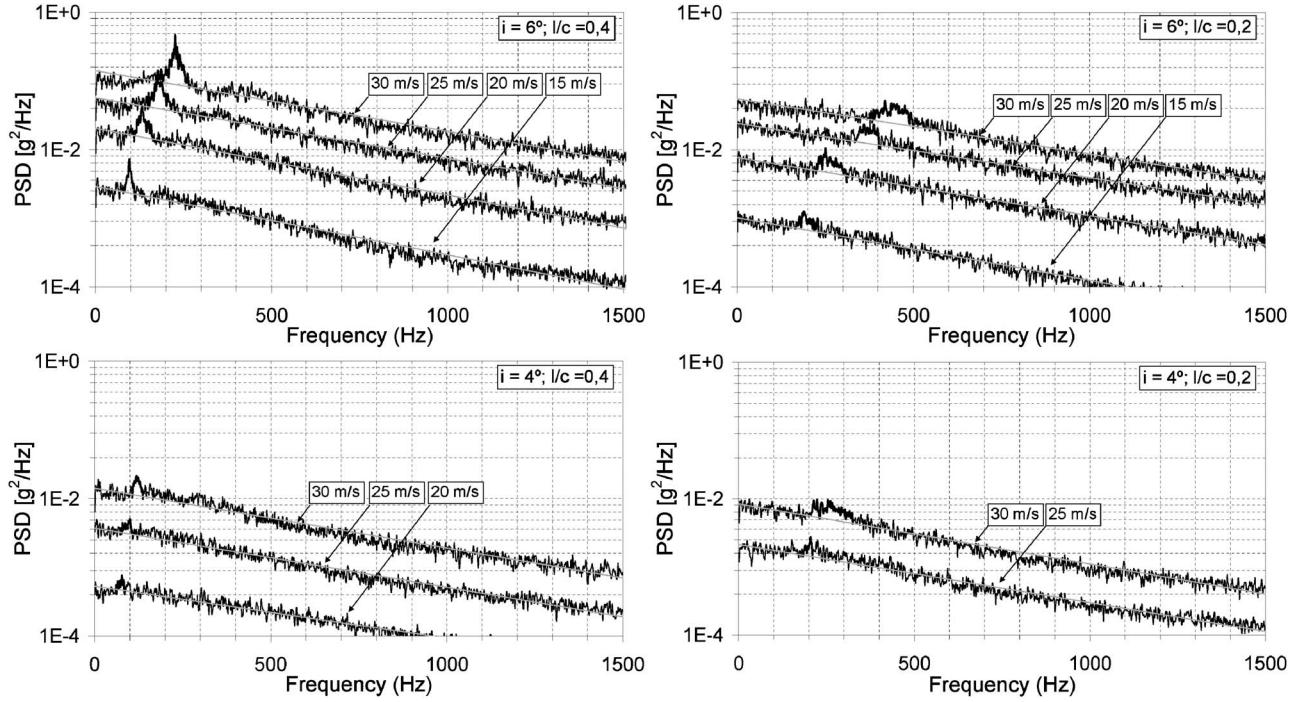

Fig. 11 PSD of vibration modulation spectra in the band from 45 kHz to 50 kHz on the NACA hydrofoil

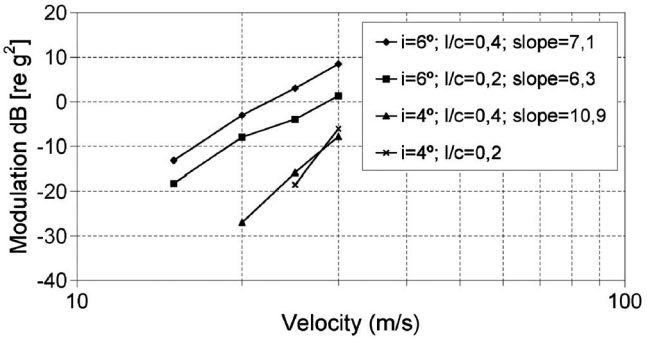

Fig. 12 Mean square level of the vibration modulation as a function of U_{inf} in the band from 45 kHz to 50 kHz on the NACA hydrofoil

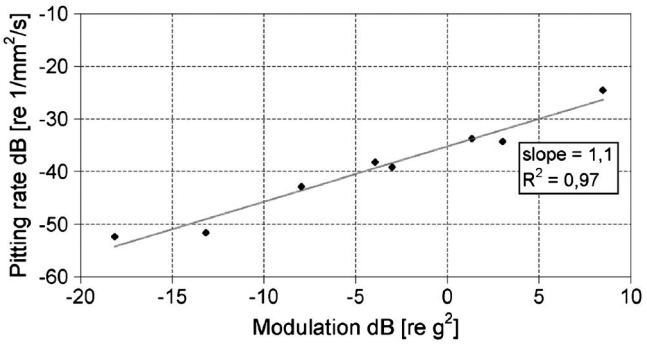

Fig. 13 Average pitting rate on stainless steel as a function of mean square level of the vibration modulation in the band from 45 kHz to 50 kHz at i=6 deg and linear fit for the NACA hydrofoil

about 0.16. At low free stream velocities, no modulation is detected for sheet cavitation. When the length of the main cavity is reduced from 40% to 20% of the chord, the modulation frequency peak is lowered and widened out.

The intensity of the erosive partial cavitation has been measured based on the mean square acceleration of the modulation frequency peak. The effect of increasing the flow free stream velocity has been well quantified for cloud cavitation. In particular, the intensity shows a power law dependency on the velocity with an exponent of about 6.7.

A good correlation has also been found between the modulation level and the actual average pitting rate measured on the hydrofoil stainless steel samples for cloud cavitation.

Acknowledgment

The members and technical staff of the LMH-EPFL Cavitation Group are thanked for their support and collaboration.

Nomenclature

AD_b = mean square modulation acceleration, relative to baseline (g^2)
BK = accelerometer Bruel&Kjaer 8309
c = hydrofoil chord length (m)
f = frequency (Hz)
f_{max} = frequency with maximum amplitude (Hz)
H = horizontal orientation
i = incidence angle (deg)
K = accelerometer Kistler 8614A500M1
l = attached cavity length (m)
p_{inf} = free stream pressure (Pa)
p_{ref} = reference pressure (Pa)
p_v = vapor pressure (Pa)
PSD = power spectral density (g^2/Hz)
PSD_b = PSD relative to baseline (g^2/Hz)
R_{ave} = average pit radius (μm)
RMS = root mean square
St_l = Strouhal number, $St_l = fl/U_{inf}$
t = exposure time (s)

U_{inf} = free stream velocity (m/s)
V = vertical orientation

Greek Letters

ρ = density (Kg/m^3)
σ = cavitation number, $\sigma=2(p_{ref}-p_v)/(\rho U_{inf}^2)$
τ = average pitting rate ($1/mm^2/s$)

References

[1] Franc, J. P., and Michel, J. M., 1985, "Attached Cavitation and the Boundary Layer: Experimental Investigation and Numerical Treatment," J. Fluid Mech., **154**, pp. 63–90.

[2] Avellan, F., Dupont, P., and Ryhming, I., 1988, "Generation Mechanism and Dynamics of Cavitation Vortices Downstream of a Fixed Leading Edge Cavity," *Proceedings of the 17th Symposium on Naval Hydrodynamics*, The Hague, The Netherlands, Session V, pp. 1–13.

[3] Kubota, A., Kato, H., and Yamaguchi, H., 1992, "A New Modelling of Cavitating Flows: A Numerical Study of Unsteady Cavitation on a Hydrofoil Section," J. Fluid Mech., **240**, pp. 59–96.

[4] Watanabe, S., Tsujimoto, Y., and Furukawa, A., 2001, "Theoretical Analysis of Transitional and Partial Cavity Instabilities," ASME J. Fluids Eng., **123**(3), pp. 692–697.

[5] Leroux, J.-B., Astolfi, J. A., and Billard, J. Y., 2004, "An Experimental Study of Unsteady Partial Cavitation," ASME J. Fluids Eng., **126**(1), pp. 94–101.

[6] Kjeldsen, M., Arndt, R. E. A., and Effertz, M., 2000, "Spectral Characteristics of Sheet/Cloud Cavitation," ASME J. Fluids Eng., **122**(3), pp. 484–487.

[7] Callenaere, M., Franc, J. P., Michel, J. M., and Riondet, M., 2001, "The Cavitation Instability Induced by the Development of a Re-Entrant Jet," J. Fluid Mech., **444**, pp. 223–256.

[8] Avellan, F., and Dupont, P., 1988, "Cavitation Erosion of the Hydraulic Machines: Generation and Dynamics of Erosive Cavities," *Proceedings of the 14th IAHR Symposium*, Trondheim, Norway, pp. 725–738.

[9] Avellan, F., and Farhat, M., 1989, "Shock Pressure Generated by Cavitation Vortex Collapse," *Proceedings of the 3rd International Symposium on Cavitation Noise and Erosion in Fluid Systems*, ASME Winter Annual Meeting, San Francisco, Vol. 88, pp. 119–125.

[10] Quang, L., Franc, J. P., and Michel, J. M., 1989, "Pressure Pulse Distribution Around Cavity Closure," *Proceedings of the 3rd International Symposium on Cavitation Noise and Erosion in Fluid Systems*, ASME Winter Annual Meeting, San Francisco, Vol. 88, pp. 111–118.

[11] Leroux, J.-B., Coutier-Delgosha, O., and Astolfi, J. A., 2005, "A Joint Experimental and Numerical Study of Mechanisms Associated to Instability of Partial Cavitation on Two-Dimensional Hydrofoil," Phys. Fluids, **17**, p. 052101.

[12] Bourdon, P., Simoneau, R., and Avellan, F., 1993, "Erosion Vibratory Fingerprint of Leading Edge Cavitation of a NACA Profile and of a Francis Model and Prototype Hydroturbine," *Proceedings of Bubble Noise and Cavitation Erosion in Fluid Systems*, ASME Winter Annual Meeting, New Orleans, Vol. 176, pp. 51–67.

[13] Escaler, X., Egusquiza, E., Farhat, M., and Avellan, F., 2006, "Detection of Cavitation in Hydraulic Turbines," Mech. Syst. Signal Process., **20**, pp. 983–1007.

[14] Kato, H., Ye, Y. P., and Maeda, M., 1989, "Cavitation Erosion and Noise Study on a Foil Section," *Proceedings of the 3rd International Symposium on Cavitation Noise and Erosion in Fluid Systems*, ASME Winter Annual Meeting, San Francisco, Vol. 88, pp. 41–46.

[15] Simoneau, R., Avellan, F., and Kuhn de Chizelle, Y., 1989, "On Line Measurement of Cavitation Erosion Rate on a 2D NACA Profile," *Proceedings of the 3rd International Symposium on Cavitation Noise and Erosion in Fluid Systems*, ASME Winter Annual Meeting, San Francisco, FED-Vol. 88, pp. 95–102.

[16] Bourdon, P., Simoneau, R., Avellan, F., and Farhat, M., 1990, "Vibratory Characteristics of Erosive Cavitation Vortices Downstream of a Fixed Leading Edge Cavity," *Proceedings of the 15th IAHR Symposium on Modern Technology in Hydraulic Energy Production*, Belgrade, Serbia, Vol. 1, Session H(3), pp. 1–12.

[17] Abbot, P. A., Arndt, R. E. A., and Shanahan, T. B., 1993, "Modulation Noise Analyses of Cavitating Hydrofoils," *Proceedings of Bubble Noise and Cavitation Erosion in Fluid Systems*, ASME Winter Annual Meeting, New Orleans, Vol. 176, pp. 83–94.

[18] Avellan, F., Henry, P., and Rhyming, I., 1987, "A New High Speed Cavitation Tunnel for Cavitation Studies in Hydraulic Machinery," *Proceedings of International Symposium on Cavitation Research Facilities and Techniques*, ASME Winter Annual Meeting, Boston, Vol. 57, pp. 49–60.

[19] Couty, P., 2001, "Physical Investigation of Cavitation Vortex Collapse," 2463, École Polytechnique Fédérale de Lausanne, Lausanne.

A Mean-Field Pressure Formulation for Liquid-Vapor Flows

Shi-Ming Li
e-mail: smli@vt.edu

Danesh K. Tafti
e-mail: dtafti@vt.edu

Department of Mechanical Engineering,
Virginia Polytechnic Institute and State University,
Blacksburg, VA 24060

A nonlocal pressure equation is derived from mean-field free energy theory for calculating liquid-vapor systems. The proposed equation is validated analytically by showing that it reduces to van der Waals' square-gradient approximation under the assumption of slow density variations. The proposed nonlocal pressure is implemented in the mean-field free energy lattice Boltzmann method (LBM). The LBM is applied to simulate equilibrium liquid-vapor interface properties and interface dynamics of capillary waves and oscillating droplets in vapor. Computed results are validated with Maxwell constructions of liquid-vapor coexistence densities, theoretical relationship of variation of surface tension with temperature, theoretical planar interface density profiles, Laplace's law of capillarity, dispersion relationship between frequency and wave number of capillary waves, and the relationship between radius and the oscillating frequency of droplets in vapor. It is shown that the nonlocal pressure formulation gives excellent agreement with theory. [DOI: 10.1115/1.2742730]

Introduction

Liquid-vapor systems have a wide range of applications in engineering systems, such as steam power plants, vapor compression cycles for refrigeration/air-conditioning, electronics cooling, and to micro- and nanoscale devices. One of the challenges in these systems is computing the time evolution of the boundary or interface between the phases. Interface dynamics of merging, splitting, twisting, and topological singularities must be resolved in a consistent and general framework. The most widely used methods are based on treating the phase boundary as a discontinuous interface. These can be broadly classified as: (i) fixed meshes with interface reconstruction [1], (ii) deforming unstructured meshes which follow the interface [2,3], (iii) fixed mesh interface tracking with surface tension forces introduced as volume forces [4], and (iv) fixed mesh interface tracking with surface tension forces and property variations smoothed and transferred to the underlying grid [5–8]. In the first two methods, surface tension forces are applied at the interfacial boundary, which relates the jump in the normal stress across the interface to the interfacial curvature, continuity in normal velocity across the interface, and continuity in tangential stresses. However, the methods break down when the interfacial thickness is comparable to the length scale of the phenomenon being examined, as in near-critical fluids (interface thickens considerably), moving contact lines along a solid surface, and extreme topological changes of the interface (breakup and coalescence of liquid droplets). The latter two methods avoid some of these problems by spreading the effects of surface tension over a few grid thicknesses.

Although all the discontinuous interface methods have their foundations in fluid dynamics, liquid-vapor systems, on the other hand, also require a thermodynamic basis to facilitate evaporation and condensation between the two phases. The diffuse interface method is based on the explicit recognition that phase interfaces undergo a rapid but smooth transition of physical quantities of the bulk phases. In flows with complex topological changes, and when the flow scales are commensurate with the thickness of the interface (near critical point), diffuse interface methods have clear advantages. Diffuse interface methods for liquid-vapor systems are based on the mean-field free energy of the fluid [9–14]. The mean-field theory provides a thermodynamically consistent and numerically simple framework to deal with liquid-vapor phase transitions (condensation, evaporation), interface capillarity, and hydrodynamics.

Within mean-field theory, the free energy density is represented by two components, one pertaining to the homogeneous energy density of the bulk fluid phases from classical equilibrium thermodynamics and the second due to the inhomogeneous or molecular attractive forces between dissimilar phases. Based on the molecular model of a hard sphere with an interparticle attraction potential, the total Helmholtz free energy can be represented by [15–17]

$$H = \int_V \psi[n(\mathbf{r})]d^3\mathbf{r} + \frac{1}{4}\int\int_V w(\mathbf{r},\mathbf{r}')[n(\mathbf{r}') - n(\mathbf{r})]^2 d^3\mathbf{r}d^3\mathbf{r}' \tag{1}$$

In Eq. (1), $\psi(n)$ is the local free energy density, n is the local fluid density, and V represents the volume of the system. The second term is the mean-field representation of the attraction between molecules accounting for inhomogeneities of fluid density at liquid-vapor interfaces. The interparticle pairwise attraction potential $-w(\mathbf{r},\mathbf{r}')$ is everywhere nonpositive. For a homogeneous system, the second term reduces to zero and Eq. (1) equates the free energy derived from equilibrium thermodynamics.

It was van der Waals (see [18]), who first proposed a theory based on the gradient of density (square-gradient theory) to predict the thickness of liquid-vapor interfaces and the surface tension forces acting at the interface. The general form of the free energy in square-gradient theory is expressed as [19]

$$H = \int_V \left\{ \psi[n(\mathbf{r})] + \frac{\kappa}{2}|\nabla n(\mathbf{r})|^2 \right\} d^3\mathbf{r} \tag{2}$$

where $\psi[n(\mathbf{r})]$ has the same definition as in Eq. (1) and the second term approximates the intermolecular attraction forces in Eq. (1) under the assumption of slow density variations. The constant κ is a measure of the interparticle attraction potential. The expression for pressure derived from Eq. (2) is given as [18,20,21]

$$p[n(\mathbf{r})] = p_o - \kappa n\nabla^2 n(\mathbf{r}) - \tfrac{1}{2}\kappa|\nabla n(\mathbf{r})|^2 \tag{3}$$

Contributed by the Fluids Engineering Division of ASME for publication in the JOURNAL OF FLUIDS ENGINEERING. Manuscript received July 10, 2006; final manuscript received December 28, 2006. Assoc. Editor: Theodore Heindel.

$$p_o = n\psi' - \psi \tag{4}$$

The first term in Eq. (3) is the homogeneous thermodynamic pressure, whereas the second and third terms quantify the *nonlocal* or inhomogeneous pressure at phase interfaces. For a homogeneous system, the second and third terms have no contribution, and Eqs. (3) and (4) reduce to the van der Waals' equation of state.

A number of two-phase diffuse interface methods have been developed under the umbrella of lattice Boltzmann methods (LBM) [20–28]. LBM, which has its origins in lattice-gas cellular automata and can also be derived from the continuous Boltzmann equation, operates in the mesoscopic regime on particle distribution functions on a lattice. Hence for engineering applications, it is a good compromise between continuum simulations at the macroscales, where much of the microphysics is averaged out, and molecular dynamics calculations, which are limited to process length and time scales at most in the nanometer and nanosecond range, respectively.

Central to many of the LBM methods for calculating two-phase flows is the use of the free energy based on the square-gradient theory [20,21,25,26]. As pointed out by several researchers, such as Sullivan [16], Zhang et al. [28], and van Giessen et al. [29], the square-gradient theory poses some limitations on the description of phase interfaces near a solid wall, where the impenetrable solid wall imposes a discontinuity on the fluid density near the wall. In a practical implementation, it is also not easy to obtain realistic contact angles and density distributions near a wall based on the square-gradient theory. Because of these difficulties, Briant et al. [30,31] in their application of the square-gradient model to contact line dynamics fix the contact angle a priori and do not allow it to change based on the flow dynamics. Hence, in such instances, it is more appropriate to work with the more general mean-field expression of free energy given by Eq. (1) [32].

The objective of this paper is to develop a consistent equation for pressure, starting from the general mean-field free-energy description given in Eq. (1). The consistency of the derived pressure equation is established theoretically by reducing it to the pressure given by the square-gradient theory in Eq. (3) under the assumption of slow density variations. The pressure equation is then implemented in the LBM and validated against known theoretical solutions of: (i) Density profiles across planar liquid-vapor interfaces, (ii) Maxwell construction of liquid-vapor coexistence systems, (iii) surface tension based on integrations of excess free energy, (iv) Laplace's law of capillarity for droplets in vapor, (v) the dispersion equation of capillary wave dynamics of interfaces, and (vi) Lamb's frequency relation of an oscillating droplet in vapor. It is established that the new pressure equation with its mean-field free-energy LBM gives good agreement with equivalent results from thermodynamics, molecular dynamics, and hydrodynamics for all the above test cases.

Mean-Field Pressure Equation

Classical thermodynamics of homogeneous fluids defines the fluid pressure as

$$p = -\left(\frac{\partial H}{\partial V}\right)_T \tag{5}$$

where H is the total Helmholtz free energy of a liquid-vapor system with a fixed mass, V has the same meaning of Eqs. (1) and (2), representing the volume of the fluid system, and T is the temperature.

First, the above definition of pressure for a homogeneous fluid is extended to an inhomogeneous fluid as

$$p = -\lim_{V\to\Lambda}\left(\frac{\partial H}{\partial V}\right)_T = -\left(\frac{\partial\left(\lim_{V\to\Lambda} H\right)}{\partial\Lambda}\right)_T \tag{6}$$

With this extension, we study the total free energy of fluid within the "very small-scale" volume Λ at the spatial point $\mathbf{r}$. A material surface is chosen as the boundary of the volume Λ, such that the volume Λ is very small in the macroscopic sense but large enough in the microscopic sense. The molecular exchange across the material surface is kept in dynamic balance, such that the enclosed mass m in the volume Λ is kept constant

$$m = \lim_{V\to\Lambda}\int_V n(\mathbf{r})d^3\mathbf{r} = \Lambda n(\mathbf{r}) \tag{7}$$

With this extension, the total free energy in the small volume Λ becomes

$$H = \lim_{V\to\Lambda}\int_V \Psi[n(\mathbf{r})]d^3\mathbf{r} = \Lambda\Psi[n(\mathbf{r})] \tag{8}$$

where $\Psi[n(\mathbf{r})]$ is the free-energy density of the nonhomogeneous fluid and has the following representation based on Eq. (1):

$$\Psi[n(\mathbf{r})] = \psi[n(\mathbf{r})] + \frac{1}{4}\int_V w(\mathbf{r},\mathbf{r}')[n(\mathbf{r}') - n(\mathbf{r})]^2 d^3\mathbf{r}' \tag{9}$$

Substitution of Eqs. (8) into Eq. (6) and using Eq. (7) gives

$$p = -\frac{\partial}{\partial\Lambda}(\Lambda\Psi[n(\mathbf{r})]) = n(\mathbf{r})\Psi'[n(\mathbf{r})] - \Psi[n(\mathbf{r})] \tag{10}$$

Furthermore, substituting Eq. (9) into Eq. (10), we finally obtain

$$p[n(\mathbf{r})] = p_o - n\int_V w(\mathbf{r},\mathbf{r}')[n(\mathbf{r}') - n(\mathbf{r})]d^3\mathbf{r}' - \frac{1}{4}\int_V w(\mathbf{r},\mathbf{r}')[n(\mathbf{r}') - n(\mathbf{r})]^2 d^3\mathbf{r}' \tag{11}$$

where p_o has the same form of Eq. (4).

Equation (11) is the new mean-field nonlocal pressure equation for a liquid-vapor system.

Validation With Square-Gradient Theory

Because the van der Waals' square-gradient theory [18,19] for liquid-vapor interfaces is a simplified version of the more general mean-field theory, both the free energy of Eq. (2) and the nonlocal pressure in Eq. (3) of the square-gradient theory should be a special case of Eqs. (1) and (11), respectively. To verify that Eq. (11) reduces to the nonlocal pressure of the square-gradient theory, we apply the following Taylor expansion:

$$n(\mathbf{r}') - n(\mathbf{r}) = (\mathbf{r}' - \mathbf{r})\cdot\nabla n(\mathbf{r}) + \tfrac{1}{2}[(\mathbf{r}' - \mathbf{r})\cdot\nabla]^2 n(\mathbf{r}) \tag{12}$$

where terms of order higher than $|\mathbf{r}' - \mathbf{r}|^2$ are neglected.

It is known that the interparticle pairwise attraction potential $w(\mathbf{r}' - \mathbf{r})$ is symmetric in the framework of the mean-field theory. As an example, many intermolecular interaction potentials can be approximated by the well-known Lennard-Jones potential as follows:

$$w_{\mathrm{L-J}}(\mathbf{r}' - \mathbf{r}) = 4\varepsilon\left[\left(\frac{\sigma}{\mathbf{r}' - \mathbf{r}}\right)^{12} - \left(\frac{\sigma}{\mathbf{r}' - \mathbf{r}}\right)^{6}\right] \tag{13}$$

where ε and σ are physical constants. The first term is the intermolecular repulsive potential, while the second term is the intermolecular attraction potential. It is seen that both the attractive and repulsive parts are symmetric around point $\mathbf{r}$. The symmetry arguments of both the interparticle attraction potential $w(\mathbf{r},\mathbf{r}')$ and the operator $(\mathbf{r}' - \mathbf{r})$ result in

$$\int_V w(\mathbf{r},\mathbf{r}')(\mathbf{r}' - \mathbf{r})\cdot\nabla n(\mathbf{r})d^3\mathbf{r}' = 0 \tag{14}$$

Substituting Eq. (12) into Eq. (11), neglecting terms of order higher than $|\mathbf{r}'-\mathbf{r}|^2$, and using Eq. (14)

$$p[n(\mathbf{r})] = p_o - \left[\frac{1}{6}\int_V w(\mathbf{r},\mathbf{r}')(\mathbf{r}'-\mathbf{r})\cdot(\mathbf{r}'-\mathbf{r})d^3\mathbf{r}'\right]n\nabla^2 n - \frac{1}{2}\left[\frac{1}{6}\int_V w(\mathbf{r},\mathbf{r}')(\mathbf{r}'-\mathbf{r})\cdot(\mathbf{r}'-\mathbf{r})d^3\mathbf{r}'\right]|\nabla n(\mathbf{r})|^2 \tag{15}$$

By using the following equality:

$$\kappa = \frac{1}{6}\int_V w(\mathbf{r},\mathbf{r}')(\mathbf{r}'-\mathbf{r})\cdot(\mathbf{r}'-\mathbf{r})d^3\mathbf{r}' \tag{16}$$

Eq. (15) reduces to Eq. (3). κ in Eq. (16) represents the second moment of the pairwise attraction potential, which is a measure of the strength of the interparticle attraction. Thus, we show that Eq. (11), obtained from the more general mean-field theory, is a general form of the nonlocal pressure that reduces to and is consistent with the square-gradient theory under the assumption of slow density variations.

Furthermore, by substituting Eqs. (12), (14), and (16) into Eq. (1), with terms higher than the order of $|\mathbf{r}'-\mathbf{r}|^2$ neglected, Eq. (1) can be shown to reduce to Eq. (2). That is, the free energy of the square-gradient theory is an approximation of the free energy of the more general mean-field theory to the order of $|\mathbf{r}'-\mathbf{r}|^2$.

Although the present mean-field nonlocal pressure distribution given in Eq. (11) is shown to reduce consistently to the nonlocal pressure representation of the square-gradient theory under the assumption of slow density variations, the mean-field nonlocal pressure in [28] given by

$$p[n(\mathbf{r})] = p_o - \frac{1}{2}n\int_V w(\mathbf{r},\mathbf{r}')[n(\mathbf{r}')-n(\mathbf{r})]d^3\mathbf{r}' \tag{17}$$

does not. Under the assumption of slow density variations, using the same procedures as described above, it can be shown that Eq. (17) instead reduces to

$$p[n(\mathbf{r})] = p_o - \frac{\kappa}{2}n\nabla^2 n(\mathbf{r}) \tag{18}$$

which does not agree with the classical square-gradient theory. The missing terms in Eq. (18) dominate the total nonlocal effects as the system moves away from the critical point.

Mean-Field Free-Energy LBM

The LBM implementation is the same as that described by Zhang et al. [28] with the nonlocal pressure described in the current paper by Eq. (11). The extensively used lattice Boltzmann Bhatnagar-Gross-Krook (BGK) [42] equation by Chen et al. [33] and Qian et al. [34] is used

$$f_i(\mathbf{x}+\mathbf{e}_i,t+1) - f_i(\mathbf{x},t) = \frac{1}{\tau}[f_i^{eq}(\mathbf{x},t) - f_i(\mathbf{x},t)] \quad i = 0,1,2,\ldots I, \tag{19}$$

where $\mathbf{x}$ and $\mathbf{e}_i$ represent lattice site and directions, respectively; t and τ are the time step and the collision relaxation time. I is the lattice link number. $f_i(\mathbf{x},t)$ is the particle distribution function, and $f_i^{eq}(\mathbf{x},t)$ is the equilibrium distribution which can be [34,35]

$$f_0^{eq} = n\left[d_0 - \frac{1}{c^2}\mathbf{u}\cdot\mathbf{u}\right] \tag{20}$$

$$f_i^{eq} = n\left[\frac{1-d_0}{I} + \frac{D}{c^2 I}\mathbf{e}_i\cdot\mathbf{u} + \frac{D(D+2)}{2c^4 I}(\mathbf{e}_i\cdot\mathbf{u})^2 - \frac{D}{2Ic^2}\mathbf{u}\cdot\mathbf{u}\right], \quad i = 1,2,\ldots I \tag{21}$$

The above representations of the equilibrium particle distribution functions are for a D-dimensional lattice with I links for each lattice site. Here, d_0 is the fraction of rest particles at equilibrium and is used to enhance numerical stability. c is the lattice particle speed, and $\mathbf{u}$ is the equilibrium velocity.

For liquid-vapor interfaces, a force term $\mathbf{F}$ is defined to represent the nonlocal pressure

$$\mathbf{F} = -\nabla\left\{p[n(\mathbf{r})] - \frac{c^2(1-d_0)}{D}n(\mathbf{r})\right\} \tag{22}$$

where $p[n(\mathbf{r})]$ is the new nonlocal pressure given by Eq. (11).

The force term $\mathbf{F}$ is then incorporated into the LBM through the equilibrium velocity $\mathbf{u}$ as [23,24]

$$n\mathbf{u} = \sum_{i=1}^{I} f_i\mathbf{e}_i + \tau\mathbf{F} \tag{23}$$

Following the standard Chapman-Enskog procedure, the Navier-Stokes-like equations for a liquid-vapor system are recovered from the above lattice Boltzmann configuration, having the fluid density n and fluid velocity $\mathbf{v}$ as follows:

$$n = \sum_{i=0}^{I} f_i \tag{24}$$

$$n\mathbf{v} = \sum_{i=1}^{I} f_i\mathbf{e}_i + \frac{1}{2}\mathbf{F} \tag{25}$$

Equations (19)–(25) together with the new nonlocal pressure equation (11) complete the definition of the mean-field free energy LBM for liquid-vapor systems.

Numerical Implementation

To implement the modified LBM numerically, a representation to the local free-energy density $\psi(n)$ is needed. Van Kamper [15] obtained the local free-energy density as

$$\psi(n) = nk_bT\ln\frac{n}{1-bn} - an^2 - nk_bT \tag{26}$$

where a is a measure of the interparticle attractive potential, b is the hard sphere volume of one particle, k_b is the Boltzmann constant, and T is the temperature. Substitution of Eq. (26) into Eq. (4) results in the van der Waals' equation of state; that is,

$$p_0 = n\psi' - \psi = \frac{nk_bT}{1-bn} - an^2 \tag{27}$$

The representation of free-energy density in Eq. (26) is used in our current numerical implementation. In the framework of the LBM, for the validation of the current theoretical development, we specify $a=9/49$ and $b=2/21$. K_bT is specified according to the temperatures studied in different cases.

To maintain the symmetry of the interparticle attraction potential $-w(\mathbf{r},\mathbf{r}')$, the computational domain is discretized into a D2Q7 lattice configuration, such that $D=2$, $I=6$, $c=1$, and

$$\mathbf{e}_0 = [0,0] \tag{28}$$

$$\mathbf{e}_i = \left[\frac{\cos\pi(i-1)}{3}, \frac{\sin\pi(i-1)}{3}\right], \quad i = 1,2,\ldots,6 \tag{29}$$

The interparticle attraction potential $-w(\mathbf{r},\mathbf{r}')$ can be approximated by a form similar to the attraction term in Eq. (13). In all cases, the potential decays rapidly with distance. For example, based on the -6 power law, the magnitude of the attraction potential reduces by a factor of 64 across the first and second nearest lattices. Considering that in a practical LBM simulation, each lat-

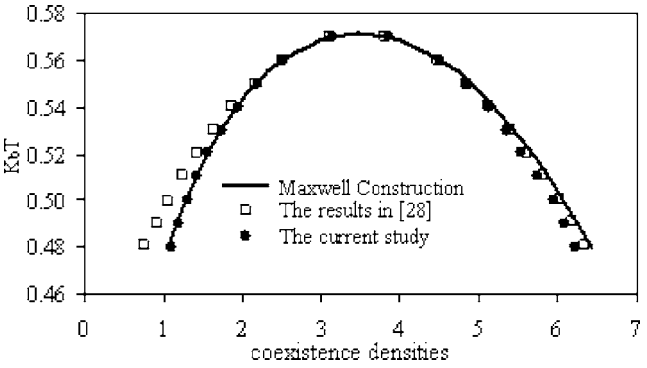

Fig. 1 Comparison between LBM simulations and analytical Maxwell constructions of liquid-vapor coexistence densities

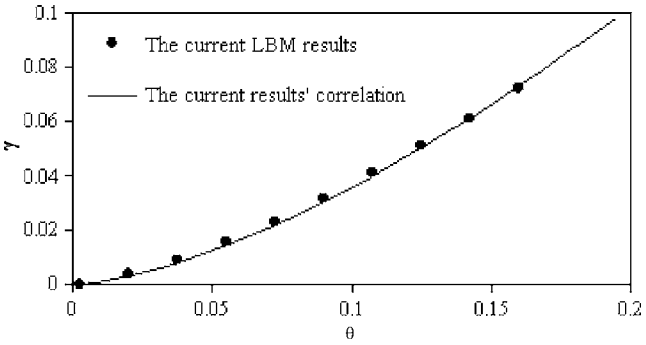

Fig. 2 Planar interface surface tension versus normalized temperature

tice site represents a large number of molecules and that the physical length scale between lattices is orders of magnitude larger than the atomic scale, the nearest lattice can be assumed to be the effective relevant range of the interparticle attraction potential. Thus, the attraction potential $-w(\mathbf{r},\mathbf{r}')$ is approximated as

$$-w(\mathbf{r},\mathbf{r}') = \begin{cases} -K, & |\mathbf{x}'-\mathbf{x}| = c \\ 0, & |\mathbf{x}'-\mathbf{x}| \neq c \end{cases} \tag{30}$$

where $-K$ is a constant representing the effective interparticle attraction potential when the attractive range is approximated to one lattice length $|\mathbf{x}'-\mathbf{x}|=c$. $K=0.01$ is used for all the calculations in this paper.

Equation (30), together with Eq. (11), is implemented in the LBM through Eq. (22) to represent the pressure in inhomogeneous systems.

Numerical Results

In this section, the LBM is validated against theoretical solutions, which include comparisons of liquid-vapor coexistence densities from Maxwell constructions, the variation of surface tension with temperature near the critical point, density profiles across the liquid-vapor interface, the dispersion relationship of capillary wave dynamics, and oscillating droplets in vapor. Finally, the application of the LBM to droplet coalescence is also illustrated.

Maxwell Constructions, Surface Tensions, and Interface Profiles of Equilibrium Planar Interfaces. The simulations are conducted on a periodic lattice of size $128\times 64\sqrt{3}$ for temperatures $K_bT=0.48$–0.55 with a relaxation time $\tau=1/0.90$ and the constant $d_0=0.25$. The initial velocity is set to zero with an initial density distribution specified such that half of the domain is set to a high density and the other half to a lower density.[1] Under these conditions, the liquid-vapor system attains its equilibrium state after ~6000 time steps of iterations, where the density profile across the interface changes little. The following planar interface properties are all displayed at the same time step of 10,000, where the maximum residual velocity is of order of 10^{-5} and the averaged residual velocity reaches an order of 10^{-6}.

Figure 1 shows a comparison of liquid-vapor coexistence densities between the results from Maxwell constructions [36] (solid line), those simulated with the current LBM (solid circles), and also those calculated by [28] (hollow squares). It is shown that the equilibrium fluid densities of the current LBM agree very well with the Maxwell constructions, in general. When temperature is close to the critical point, the agreement between the current LBM and the Maxwell constructions is much better. As the state of the system moves further away below the critical point, the difference in the results between the LBM and the Maxwell constructions tends to become larger. However, even at $K_bT=0.48$, the lowest temperature presented in Fig. 1, the maximum error of the current LBM is just 3.29%. In contrast, the LBM simulations of [28] show larger discrepancies as the state of the system deviates from the critical point, leading to errors as high as 28% in the prediction of the vapor density.

The surface tension at the liquid-vapor interface can be computed by integrating the excess free energy across the interface region [17]. Figure 2 shows the surface tension γ of the planar interface versus the normalized temperature, $\theta=(T_c-T)/T_c$, where T_c represents the critical temperature. The solid circles in Fig. 2 are the numerical results, whereas the line represents the best fit to the results. Surface tension increases exponentially as the temperature deviates from the critical point and the variation is given by the relationship $\gamma=\text{const}\cdot\theta^{\beta}$ [37]. Analytical mean-field theory gives $\beta=3/2$, while both molecular dynamics and experimental measurements result in $\beta=1.49\pm0.01$ [37]. The current LBM gives $\beta=1.5$ which agrees accurately with the analytical solution. In contrast, the LBM results from [28] give an exponent of 1.68, which is 12% in error.

Figure 3 shows the comparison of three density profiles of the planar interfaces between analytical results and the current LBM. The three lines are obtained analytically by minimizing Eq. (1) at three different temperatures $K_b=0.54$, 0.55, 0.56, and the symbols are the current LBM simulation for the same three temperatures. It is shown again that good agreement is obtained between the analytical solution and the current LBM simulations.

Liquid Droplets in Vapor at Equilibrium. The new nonlocal pressure equation is next tested for droplets in vapor at equilibrium and agreement with the Laplace's law of capillarity is evaluated. For the initial conditions, a rectangular block of static liquid is located in the middle of the domain surrounded by a low-

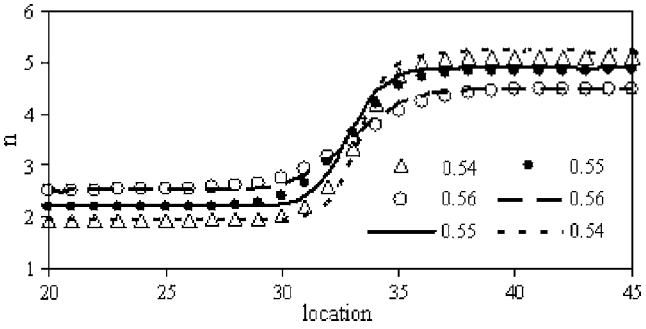

Fig. 3 Comparison of analytical solution and the current LBM simulation for the density profiles of the planar interfaces at $K_bT=0.54$, 0.55, 0.56; lines: the analytical solutions, symbols: the current LBM

[1]It was established that the initial distribution had no effect on the final solution, only on how quickly the solution equilibrated.

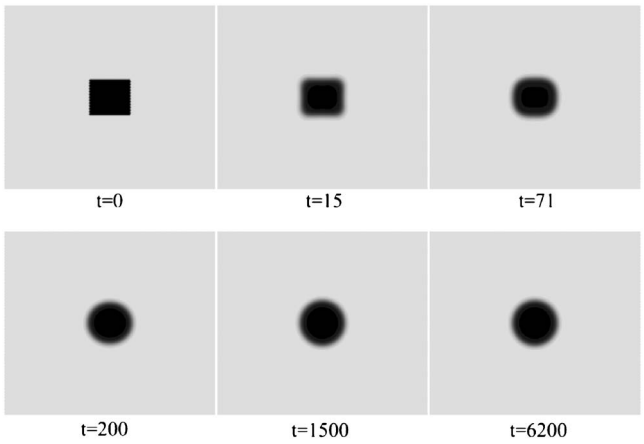

Fig. 4 Snapshots of the droplet iteration process

density static vapor distributed everywhere else. The periodic condition is applied around the four sides of the domain. In the simulations, we choose the lattice size $128\times64\sqrt{3}$, relaxation time $\tau=1$, and $d_0=0.40$. Figure 4 displays several snapshots of the droplet at different time steps. It is seen that the droplet evolves from the initial square shape to a circular shape by 1500 iterations, beyond which the shape changes little. The spurious residual velocity at the time step 10,000 is of order 10^{-6} over the whole simulation domain.

Figure 5 shows the fluid density profiles of six droplets of different radii at $K_bT=0.55$ and time step of 10,000. For each of the six droplets, the density profiles are plotted from the droplet center along the four directions: the north, west, south, and east. It is shown that each droplet displays good symmetry and the density profiles of every droplet in all four directions fall on top of each other.

Laplace's law of capillarity relates pressure inside and outside a droplet with surface tension and radius of curvature of the droplet

$$p_{\text{in}}-p_{\text{out}}=\frac{\gamma}{R} \tag{31}$$

Figure 6 represents the pressure difference inside and outside of a droplet for different sizes, where the solid circles and triangles are the simulation results with the current LBM for $K_bT=0.52$ and $K_bT=0.55$, respectively. The solid lines are the linear correlations of the respective LBM results. For both cases, it is shown that the droplet pressure difference increases linearly with a decrease of the droplet radius, as depicted by the Laplace equation.

According to the Laplace's law of capillarity, the slope of the correlation line gives the surface tension, which is obtained from the data in Fig. 6 to be $\gamma=0.00764$ for $K_bT=0.55$ and $\gamma=0.0310$ for $K_bT=0.52$. Based on the equation $\gamma=\text{const}\cdot\theta^{1.5}$ obtained from Fig. 2 and theory, the predicted surface tension is 0.00824 for $K_bT=0.55$, and 0.0307 for $K_bT=0.52$, which agree to within 7% and 1%, respectively, with the predicted surface tensions from Eq. (31). This establishes the consistency of the current theoretical model in computing the surface tension between the mechanical method through Eq. (31) and the thermodynamic approach through the integration of the excess free-energy approach.

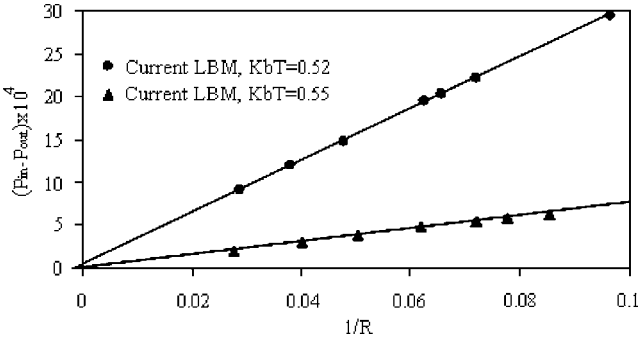

Fig. 6 Pressure difference between inside and outside for different droplet sizes: Solid lines are the linear correlations of the LBM data, which give the surface tension 0.00764 for $K_bT=0.55$ and 0.0310 for $K_bT=0.52$

To verify numerically that the current LBM is Galilean invariant, we examine droplet shape response to an initial horizontal flow speed U_0. The shape distortion is measured by the ratio of the droplet radius in the horizontal direction r_h over the radius in the vertical direction r_v. Figure 7 displays the ratio of the two radii of a droplet versus initial velocity. It is shown that the droplet distortion is quite small in the presence of the imposed velocity field and that the modified LBM is Galilean invariant according to Kalarakis et al. [38].

Capillary Waves. Capillary waves or ripples are used to validate the model in simulating dynamic characteristics of liquid-vapor interfaces. The exact solution of capillary waves gives the dispersion relation of capillary waves, which is the relation between wave frequency ω and wave number k as follows [39,40]:

$$\omega^2\sim k^3 \tag{32}$$

In this simulation, periodic boundary conditions are applied for the left and right sides of the domain. Both top and bottom sides are treated as nonslip, solid boundaries. Nine different domains are chosen as those shown in Table 1 such that: (a) The domain height $\hbar$ is much bigger than the wave length ℓ such that the "shallow water" effect is negligible; (b) the wave length is much bigger than the wave amplitude, such that it is consistent with the assumption of a small amplitude wave; and (c) the wave amplitude is much bigger than the interface thickness, such that the

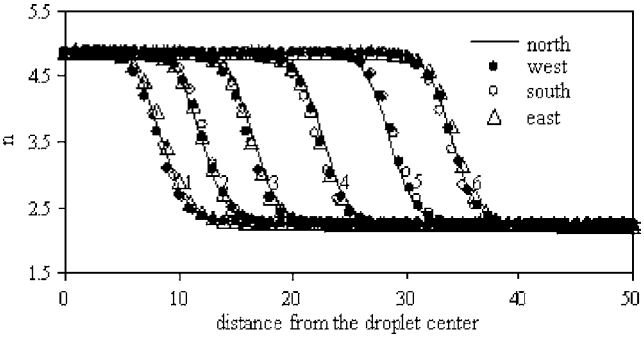

Fig. 5 Density profiles of six droplets in different directions: the north, west, south, and east, $K_bt=0.55$, time step=10,000

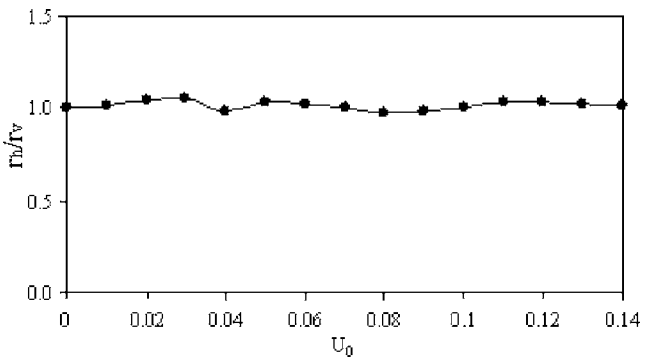

Fig. 7 Droplet shape (r_h/r_v) response to initial speed U_0

Table 1 Current LBM simulation, domain height $\hbar$, width ℓ, wave number k, and wave frequency ω

Case	ℓ	$2\hbar/\sqrt{3}$	k	ω
1	135	623	0.046542	0.002094
2	107	501	0.058721	0.003256
3	81	375	0.077570	0.004924
4	65	299	0.096664	0.006920
5	53	245	0.118551	0.009578
6	45	207	0.139626	0.011855
7	39	181	0.161107	0.015177
8	33	153	0.190400	0.020010
9	29	133	0.216662	0.025133

change of wave amplitude is clearly distinguishable. During the simulations of the capillary waves, we choose kinetic viscosity $\nu=(\tau-0.5)/4=0.01786$, the constant $d_0=0.40$, and temperature $K_bT=0.52$. Initial conditions consist of zero velocity with liquid and vapor densities specified in the bottom and top half of the computational domain, respectively. The iterations are continued until an equilibrium planar interface is formed and the density profile across the interface shows little change. At this time, a single-period sine wave is imposed along the planar interface and the evolution of the interface location is then recorded.

Figure 8 displays the snapshots of capillary waves at several time steps of a complete wave period for case 4 listed in Table 1, where the domain width is $\ell=65$ and domain height is $\hbar=299\sqrt{3}/2$. The relative time step Δt, shown in Fig. 8, is counted from the time step when the sine wave is just imposed, as shown in Fig. 8(*a*), where $\Delta t=0$. Figures 8(*c*) ($\Delta t=454$) and 8(*f*) ($\Delta t=908$) are the snapshots at the middle and at the end of the wave period, respectively, which give the wave frequency of 0.00692, as shown in Table 1. The rest of the snapshots are the intermediate wave profiles. Table 1 summarizes the wave numbers and frequencies for all cases studied. Figure 9 displays the current LBM results shown in Table 1. The solid line in Fig. 9 is the best linear fit to the nine LBM points, which yields the slope of the straight line as 1.551. The exact solution of the slope, as shown in Eq. (32), is 1.50 and the error between the two is 3.4%.

Oscillation of Droplets in Vapor. A pulsating droplet is another case used to test the model in simulating the dynamic characteristics of liquid-vapor interfaces. The exact solution of an oscillating droplet gives the relation between droplet oscillating frequency ω and droplet radius R as follows [39,40]:

$$\omega \sim R^{-3/2} \tag{33}$$

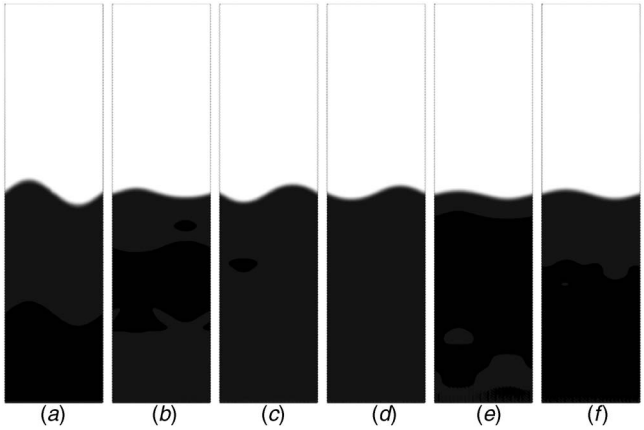

Fig. 8 Snapshots of capillary waves at different time steps, $K_bT=0.52$, case 4, $\ell=65$, $\hbar=299\sqrt{3}/2$: (*a*) $\Delta t=0$, (*b*) $\Delta t=180$, (*c*) $\Delta t=454$, (*d*) $\Delta t=580$, (*e*) $\Delta t=850$, and (*f*) $\Delta t=908$

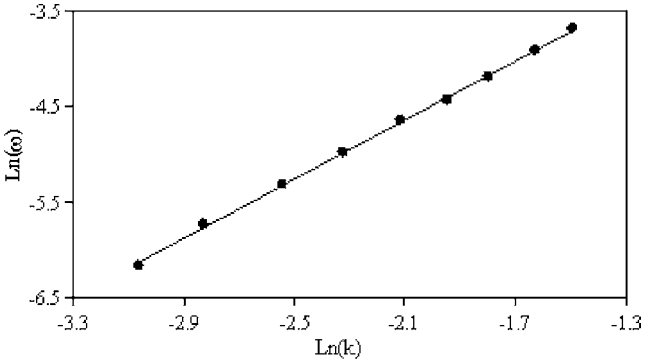

Fig. 9 Dispersion relation of capillary waves, $K_bT=0.52$; solid circle: the current LBM, solid line: correlation for the LBM, which gives the line slope of 1.551; exact solution gives the slope of 1.50

In simulating oscillating droplets, periodic boundary conditions are applied for the four sides and the lattice dimensions are $256\times128\sqrt{3}$. We choose kinetic viscosity $\nu=(\tau-0.5)/4=0.01389$, constant $d_0=0.40$, and temperature $K_bT=0.50$. Initially, a static droplet in vapor is simulated until the droplet attains an equilibrium state. Then the equilibrium circular droplet is transformed to an elliptic droplet in vapor with specified large and small radii, R_L and R_S, respectively. Six different elliptic droplets are simulated with the dimensions of $R_L\times R_S$: 25×18, 30×22, 40×29, 60×43, 70×50, and 80×58, and the droplet shape is recorded.

Figure 10 displays the snapshots of a complete oscillating period of the droplet $R_L\times R_S=25\times18$, which shows the viscous decay of the oscillating amplitude of the droplets. Figure 11 plots the oscillating frequency versus the final equilibrium droplet radius, where the solid circles are the current LBM simulation results and the line is the best linear fit of the results. The linear fit gives the slope of the line as −1.458, while the exact solution, as shown in Eq. (33), has a slope of −1.5. The difference between the two is 2.8%.

Binary Droplet Coalescence. Droplet coalescence has a number of applications in DNA analysis, protein crystallization, and cell encapsulation, to name a few. However, complex interface dynamics and the related capillary interactions of droplet coalescence make the numerical simulations quite challenging with discontinuous interface techniques. In this section, the potential of the current LBM is shown by simulating binary droplet

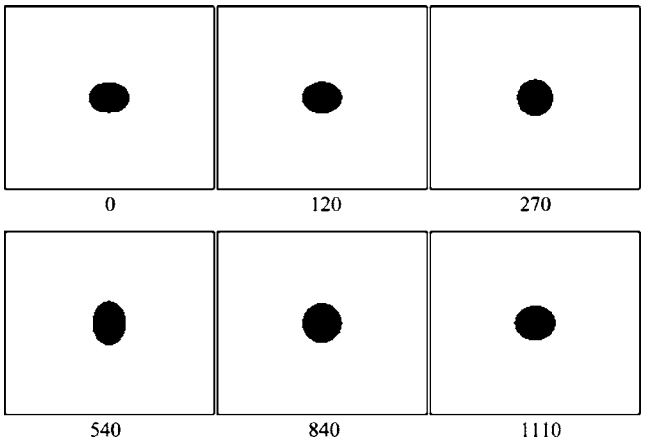

Fig. 10 Snapshot of an oscillating droplet with the initial dimension of $R_L\times R_S=25\times18$, $K_bT=0.50$

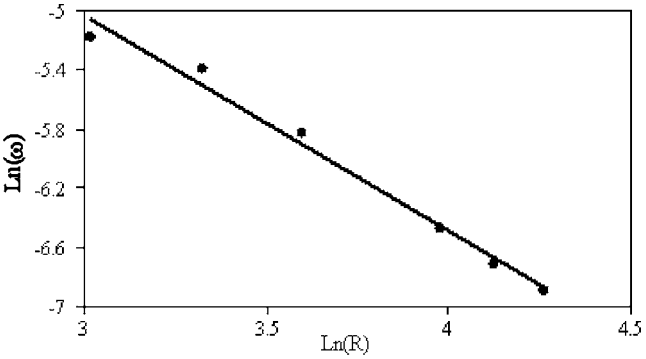

Fig. 11 Oscillating frequency versus droplet radius, $K_bT=0.50$; solid circles: the current LBM results; line: the linear correlation of the LBM results, giving the slope of the line −1.458; the analytical solution gives the slope of −1.50

coalescence.

Initially, two precomputed liquid droplets at $K_bT=0.55$ are embedded into the domain filled with a uniformly distributed vapor and zero initial velocity is imposed over the whole domain. The two droplets are of the same size (diameter of 12.7 lattice units) and density distribution, and at the beginning of the simulation they are separated by ten lattice units from the droplet boundaries, which are defined as the location having the averaged density of the bulk liquid and vapor. Figure 12 displays the simulated results of a binary droplet coalescence process. It is shown in Fig. 12 that the two droplets are attracted to each other and start to touch at the time step 480, where the complex topological transition occurs. After that, the two droplets merge quickly. After the two droplets combine with each other to form a rounded rectangular droplet, the shape evolves to first an oval and then a circle. After 8000 time steps, the droplet becomes very steady in shape and density distribution and the final droplet mass is the sum of the masses of the initial two droplets. This simulated coalescence is the well-known Ostwald ripening phenomenon [41]. Within the framework of the diffuse interface model, no special numerical treatment is required to simulate the merging of the two interfaces.

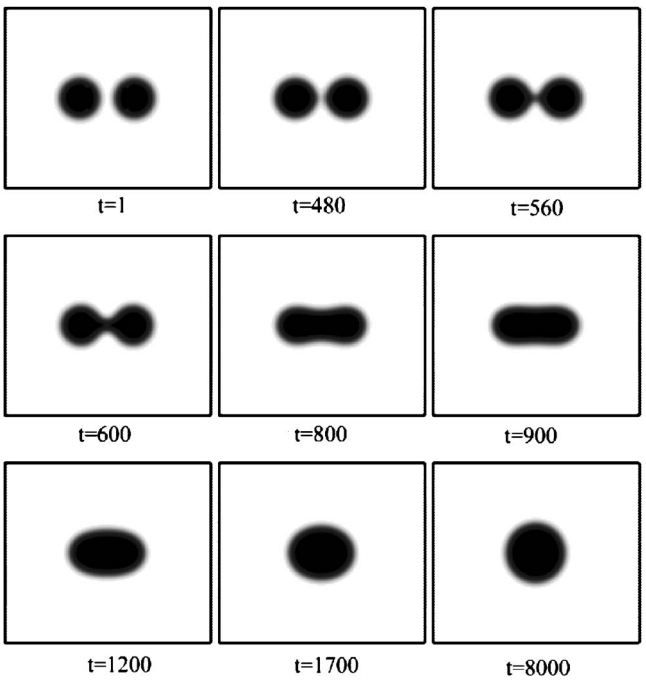

Fig. 12 Simulation of droplet coalescence process, $K_bT=0.55$

Summary and Conclusions

A nonlocal pressure equation is proposed for simulating liquid-vapor interfaces using the mean-field free energy diffuse interface theory. It is shown analytically that the nonlocal pressure equation is a general form of the van der Waals' density square-gradient theory. The new nonlocal pressure is implemented in the LBM for simulating liquid-vapor interfaces. The method is numerically validated with a number of theoretical results. It is shown that the LBM results agree to within 3.4% with Maxwell construction of liquid-vapor densities down to the scaled temperature $K_bT=0.48$. Variation of surface tension with temperature obtained by integrating the excess free energy across the liquid-vapor interface is identical to analytical results and agrees to within 7% with surface tension calculated by applying Laplace's law to equilibrium droplets. Dynamic tests conducted on capillary waves and oscillating droplets show excellent agreement with theory.

Acknowledgment

This work was performed under a grant from the National Science Foundation, No. CCR-0121616. The support is gratefully acknowledged. The authors would also like to thank Dr. Daniel Y. Kwok of University of Alberta for his advice in clarifying some questions pertaining to the implementation of the LBM [28].

Nomenclature

a = measure of the interparticle attractive potential or the van der Waals constant
b = hard sphere volume of a particle or the van der Waals constant
c = lattice particle speed
d_0 = fraction of rest particles at equilibrium
D = spatial dimensionality
$\boldsymbol{e}_i$ = lattice link vector in ith direction
f_i = particle distribution function in ith lattice direction
f_i^{eq} = equilibrium particle distribution function in ith lattice direction
$\mathbf{F}$ = force term representing nonlocal pressure
$\hbar$ = domain height
H = total Helmholtz free energy of liquid-vapor system in a domain
I = lattice link number
k = wave number of capillary waves
k_b = Boltzmann constant
K = effective interparticle attraction potential
ℓ = domain width
LMB = lattice Boltzmann method(s)
m = fluid mass within volume Λ
n = fluid density
p = fluid pressure
p_{in} = fluid pressure inside a droplet
p_o = fluid pressure of a bulk phase
p_{out} = fluid pressure outside a droplet
$\mathbf{r}$ = spatial location vector
$\mathbf{r}'$ = spatial location vector
r_h = skewed droplet radius in the horizontal direction
r_v = skewed droplet radius in the vertical direction
R = droplet radius
R_L = long axis length of an elliptic droplet
R_S = short axis length of an elliptic droplet
t = LBM time step
T = fluid temperature
T_c = critical temperature of a liquid-vapor system

$\mathbf{u}$ = equilibrium fluid velocity
U_0 = initial flow speed in simulating a droplet in vapor flow
$\mathbf{v}$ = fluid velocity
V = total volume of a domain
w = interparticle pairwise attraction potential
$w_{\text{L-J}}$ = Lennard-Jones potential
$\mathbf{x}$ = location vector of LBM lattice site

Greek Letters

β = exponent for the relation between surface tension and temperature
ε = constant of Lennard-Jones potential
γ = liquid-vapor interface surface tension
κ = constant representing the strength of interparticle attraction potential
Λ = fluid volume of a very small domain
ν = kinetic viscosity of fluid
θ = dimensionless temperature, $\theta=(T_c-T)/T_c$
σ = constant of Lennard-Jones potential
τ = collision relaxation time
ω = wave frequency
ψ = free-energy density of a bulk phase
Ψ = free-energy density of nonhomogeneous fluid

References

[1] Hirt, C. W., and Nichols, B. D., 1981, "Volume of Fluid (VOF) Methods for the Dynamics of Free Boundaries," J. Comput. Phys., **39**(1), pp. 201–225.
[2] Johnson, A. A., and Tezduyar, T. E., 1997, "3D Simulation of Fluid-Particle Interactions With the Number of Particles Reaching 100," Comput. Methods Appl. Mech. Eng., **145**(3-4), pp. 301–321.
[3] Hu, H. H., Patankar, N. A., and Zhu, M. Y., 2001, "Direct Numerical Simulations of Fluid-Solid Systems Using Arbitrary-Lagrangian-Eularian Techniques," J. Comput. Phys., **169**(2), pp. 427–462.
[4] Brackbill, J. U., Kothe, D. B., and Zemach, C., 1992, "A Continuum Method for Modeling Surface Tension," J. Comput. Phys., **100**(2), pp. 335–354.
[5] Unverdi, S. O., and Tryggvason, T., 1992, "Computations of Multi-Fluid Flows," Physica D, **60**(1-4), pp. 70–83.
[6] Unverdi, S. O., and Tryggvason, T., 1992, "A Front-Tracking Method for Viscous, Incompressible, Multi-Fluid Flows," J. Comput. Phys., **100**(1), pp. 25–37.
[7] Osher, S., and Sethian, J. A., 1988, "Fronts Propagating With Curvature-Dependent Speed: Algorithms Based on Hamilton-Jacobi Formulations," J. Comput. Phys., **79**(1), pp. 12–49.
[8] Sethian, J. A., 1996, *Level Set Methods*, Cambridge University Press, Cambridge, England.
[9] Antanovskii, A., 1995, "A Phase Field Model of Capillarity," Phys. Fluids, **7**(4), pp. 747–753.
[10] Jasnow, D., and Vinals, J., 1996, "Coarse-Grained Description of Thermo-Capillary Flow," Phys. Fluids, **8**(3), pp. 660–669.
[11] Anderson, D. M., McFadden, G. B., and Wheeler, A. A., 1998, "Diffuse-Interface Methods in Fluid Mechanics," Annu. Rev. Fluid Mech., **30**, pp. 139–165.
[12] Jacqmin, D., 1999, "Calculation of Two-Phase Navier-Stokes Flows Using Phase-Field Modeling," J. Comput. Phys., **155**(1), pp. 96–127.
[13] Jacqmin, D., 2000, "Contact Line Dynamics of a Diffuse Fluid Interface," J. Fluid Mech., **402**, pp. 57–88.
[14] Jamet, D., Lebaigue, O., Coutris, N., and Delhaye, J. M., 2001, "The Second Gradient Method for the Direct Numerical Simulation of Liquid-Vapor Flows with Phase Change," J. Comput. Phys., **169**(2), pp. 624–651.
[15] Van Kampen, N. G., 1964, "Condensation of a Classical Gas With Long-Range Attraction," Phys. Rev., **135**(2A), pp. A362–A369.
[16] Sullivan, D. E., 1981, "Surface Tension and Contact Angle of a Liquid-Solid Interface," J. Chem. Phys., **74**(4), pp. 2604–2615.
[17] Rowlinson, J. S., and Widow, B., 1982, "*Molecular Theory of Capillarity*," Clarendon Press, Oxford.
[18] Rowlinson, J. S., 1979, "Translation of J. D. van der Waals' 'The Thermodynamic Theory of Capillarity Under the Hypothesis of a Continuous Variation of Density," J. Stat. Phys., **20**(2), pp. 197–244.
[19] Cahn, J. W., and Hilliard, J. E., 1958, "Free Energy of a Nonuniform System. I. Interfacial Free Energy," J. Chem. Phys., **28**(2), pp. 258–267.
[20] Swift, M. R., Osborn, W. R., and Yeomans, J. M., 1995, "Lattice Boltzmann Simulation of Nonideal Fluids," Phys. Rev. Lett., **75**(5), pp. 830–833.
[21] He, X., and Doolen, G. D., 2002, "Thermodynamic Foundations of Kinetic Theory and Lattice Boltzmann Models for Multiphase Flows," J. Stat. Phys., **107**(1-2), pp. 309–328.
[22] Gunstensen, A. K., Rothman, D. H., and Zaleski, S., 1991, "Lattice Boltzmann Model of Immiscible Fluids," Phys. Rev. A, **43**(8), pp. 4320–4327.
[23] Shan, X., and Chen, H., 1993, "Lattice Boltzmann Model for Simulating Flows With Multiple Phases and Components," Phys. Rev. E, **47**(3), pp. 1815–1819.
[24] Shan, X., and Chen, H., 1994, "Simulation of Nonideal Gases and Liquid-Gas Phase Transitions by the Lattice Boltzmann Equation," Phys. Rev. E, **49**(4), pp. 2941–2948.
[25] Swift, M. R., Orlandini, E., Osborn, W. R., and Yeomans, J. M., 1996, "Lattice Boltzmann Simulations of Liquid-Gas and Binary-Fluid Systems," Phys. Rev. E, **54**(5), pp. 5041–5052.
[26] He, X., Shan, X., and Doolen, G. D., 1998, "Discrete Boltzmann Equation Model for Nonideal Gases," Phys. Rev. E, **57**(1), pp. R13–R16.
[27] Luo, L., 1998, "Unified Theory of Lattice Boltzmann Models for Nonideal Gases," Phys. Rev. Lett. **81**(8), pp. 1618–1621.
[28] Zhang, J., Li, B., and Kwok, D. Y., 2004, "Mean-Field Free-Energy Approach to the Lattice Boltzmann Method for Liquid-Vapor and Solid-Fluid Interfaces," Phys. Rev. E, **69**(3), 032602.
[29] Van Giessen, A. E., Bukman, D. J., and Widom, B., 1997, "Contact Angles of Liquid Drops on Low-Energy Solid Surfaces," J. Colloid Interface Sci., **192**(1), pp. 257–265.
[30] Briant, A. J., Papatzacos, P., and Yeomans, J. M., 2002, "Lattice Boltzmann Simulations of Contact Line Motion in a Liquid-Gas System," Philos. Trans. R. Soc. London, Ser. A, **360**(1792), pp. 485–495.
[31] Briant, A. J., Wagner, A. J., and Yeomans, J. M., 2004, "Lattice Boltzmann Simulations of Contact Line Motion. I. Liquid-Gas Systems," Phys. Rev. E, **69**(3), 031602.
[32] Li, S.-M., and Tafti, D. K., 2006, "Contact Line Dynamics in Liquid-Vapor Flows Using Lattice Boltzmann Method," *Proc. of FEDSM2006, 2006 ASME Joint U.S.–European Fluids Engineering Summer Meeting*, July 17–20, Miami, ASME, New York, ASME Paper No. FEDSM2006-98022.
[33] Chen, S., Chen, H. D., Martinez, D., and Mathhaeus, W. H., 1991, "Lattice Boltzmann Model for Simulation of Magnetohydrodynamics," Phys. Rev. Lett., **67**(27), pp. 3776–3779.
[34] Qian, Y. H., D'Humieres, D., and Lallemand, P., 1992, "Lattice BGK Models for Navier-Stokes Equation," Europhys. Lett., **17**(6), pp. 479–484.
[35] Chen, H., Chen, S., and Mathhaeus, W. H., 1992, "Recovery of the Navier-Stokes Equations Using a Lattice-Gas Boltzmann Method," Phys. Rev. A, **45**(8), pp. R5339–R5342.
[36] Stanley, H. E., 1971, *Introduction to Phase Transitions and Critical Phenomena*, Oxford University Press, London, Chap. 5.
[37] Van Giessen, A. E., Blokhuis, E. M., and Bukman, D. J., 1998, "Mean Field Curvature Correlation to the Surface Tension," J. Chem. Phys., **108**(3), pp. 1148–1156.
[38] Kalarakis, A. N., Burganos, V. N., and Payatakes, A. C., 2002, "Galilean Invariant Lattice-Boltzmann Simulation of Liquid-Vapor Interface Dynamics," Phys. Rev. E, **65**(5), 056702.
[39] Lamb, H., 1945, *Hydrodynamics*, 6th ed., Dover, New York, Chap. 9.
[40] Landau, L. D., and Lifshitz, E. M., 1987, *Fluid Mechanics*, Pergamon Press, New York, 2nd ed., Chap. 7.
[41] Voorhees, P. W., 1985, "The Theory of Ostwald Ripening," J. Stat. Phys., **38**(1-2), pp. 231–252.
[42] Bhatnagar, P. L., Gross, E. P., and Krook, M., 1954, "A Model for Collision Processes in Gases. I. Small Amplitude Processes in Charged and Neutral One-Component System," Phys. Rev. A, **94**, pp. 511–525.

Theoretical Parameter Study of Aerodynamic Vectoring Particle Sorting

Dane N. Jackson

Barton L. Smith

Mechanical and Aerospace Engineering,
Utah State University,
Logan, UT 84322

A new particle sorting technique called aerodynamic vectoring particle sorting (AVPS) has recently been shown to be effective at sorting particles without particles contacting surfaces. The technique relies on turning a free jet sharply without extended control surfaces. The flow turning results in a balance of particle inertia and several forces (pressure, drag, added mass, and body forces) that depend on particle size and density. The present paper describes a theoretical study of particle sorting in a turning flow. The purpose of this study is to extend AVPS to parameter spaces other than those that are currently under investigation. Spherical particles are introduced into a turning flow in which the velocity magnitude increases like r. The trajectory of each particle is calculated using the particle equation of motion with drag laws that are appropriate for various Knudsen number regimes. Large data sets can be collected rapidly for various particle sizes, densities, turning radii, flow speeds, and fluid properties. Ranges of particle sizes that can be sorted are determined by finding an upper bound (where particles move in a straight line) and a lower bound (where particles follow flow streamlines). It is found that the size range of particles that can be sorted is larger for smaller turning radii, and that the range moves toward smaller particles as the flow speed and the particle-to-fluid density ratio are increased. Since this flow is laminar and 2-D, and particle loading effects are ignored, the results represent a "best case" scenario.
[DOI: 10.1115/1.2742732]

1 Introduction

Particle manufacturing processes are often incapable of making uniform-sized particles. If a uniform size is necessary, sorting of the particles is required. In addition, sorting is often used as a diagnostic tool to determine the number of particles of a given size in a sample. When detection of particles such as pathogens is required, it is beneficial to concentrate a sample, which can be achieved using a sorting apparatus.

While methods for particle sorting may differ greatly from one application to another, the principles involved are often similar. For over a century, particle sorting has been accomplished through use of plate, and more recently, virtual impactors [1]. In either case, the main flow is subject to an angular acceleration, which serves as the primary means for separating particles. The plate impactor accelerates the particle laden flow through a nozzle onto an impinging surface where the main flow turns parallel to the plate. Larger particles impact an adhesive surface while smaller particles remain in the flow. Torczynski and Rader [2] described some problems stemming from these methods. Placing a plate in the flow path can cause contamination of physical or chemical properties. In addition, impaction of particles on a surface may lead to fragmentation or agglomeration, or particles may be re-entrained into the main flow. Furthermore, pressure drops can be large for impact-based approaches, which can limit transport rates and increase device size and pumping energy requirements.

Virtual impactors (VIs) operate with the main flow exiting through side openings due to low pressure regions while only a minor flow continues in a straight path. Sorting with VIs depends on a cutoff point; particles are separated into large and small bins [3]. Further sorting requires multiple VIs, which leads to large pressure drops.

Utah State University's Experimental Fluid Dynamics Laboratory is currently developing a sorting technique based on free vectoring of a jet. Prediction of the size and densities of particles that can be sorted with free vectoring for ideal conditions is the motivation for the work presented in this paper. The sorting device is illustrated in Fig. 1. The proper application of secondary flows near the exit plane of a jet can result in the flow turning upstream of the exit. It was shown by Bettridge et al. [4] that vectoring of a laminar or turbulent jet can be achieved by applying steady blowing and suction flows on the order of 10% of the primary jet flow through two slots near the jet exit, as shown in Fig. 1(*a*). More recently, it has been discovered that larger vector angles can be achieved with less fluctuation by imposing pure suction at higher flow rates (e.g., 30% of the primary jet flow rate [5]), as shown in Fig. 1(*b*). The low pressure region generated by the suction flow results in the jet turning toward the low pressure region.

Computational fluid dynamics (CFD) can predict particle motion. However, CFD is expensive if one desires to examine a wide range of parameters. An analytical model of the forces on the particle has been developed to examine the effects of several parameters on the path of a particle. This model will provide an evaluation of particle sorting characteristics in a timely manner without new test facilities or numerical models.

2 AVPS Model

Predicting a particle's trajectory and sorting a particle by size are made possible by a calculation of the particle forces found in the governing equations of particle motion. Models of the forces on a particle in motion date back a century. Millikan [6–8] performed a famous oil drop experiment in the early twentieth century to provide empirical data that was used to modify the Stokes [9] drag force equation:

Contributed by the Fluids Engineering Division of ASME for publication in the JOURNAL OF FLUIDS ENGINEERING. Manuscript received July 21, 2006; final manuscript received January 10, 2007. Assoc. Editor Theodore Heindel. Paper presented at the 2006 ASME Fluids Engineering Division Summer Meeting and Exhibition (FEDSM2006), Miami, FL, July 17–20, 2006.

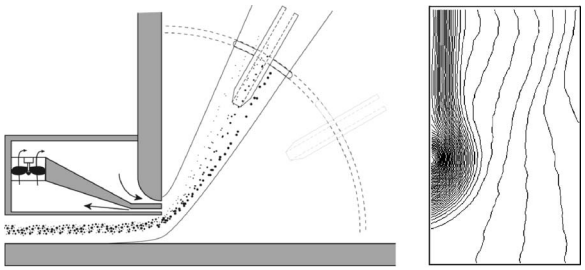

(*a*) (*b*)

Fig. 1 (*a*) AVPS particle sorter designed to select a variable band of particle sizes from a sample. Vectoring occurs due to the combined effect of the blowing and suction slots near the jet exit. (*b*) Contours of the stream function of the velocity field of a vectoring result from [5] showing the circular 90 deg vectoring possible with pure suction. The lower left edge of the domain is the jet exit.

$$\text{Drag} = -6\pi\mu a\{V_i(t) - u_i[\mathbf{Y}(\mathbf{t}),\mathbf{t}]\} \tag{1}$$

where a is the particle diameter, u_i is the fluid velocity at the particle location $\mathbf{Y}(\mathbf{t})$, V_i is the particle velocity, and μ is the dynamic viscosity.

The particle size relative to the mean free path of the fluid is accounted for in the more sophisticated model [10]

$$\text{Drag} = \frac{-6\pi\mu a\{V_i(t) - u_i[\mathbf{Y}(\mathbf{t}),\mathbf{t}]\}}{\left[1 + \text{Kn}(A + Qe^{\frac{-B}{\text{Kn}}})\right]} \tag{2}$$

where A, B, and Q are Cunningham slip coefficients, and Kn is the Knudsen number. $\text{Kn} = 2\lambda/a$, where λ is the mean free path. The equation is valid for Knudsen numbers ranging from 0.01 to 100. Knudsen numbers greater than 100 are described as "large" while values less than 0.01 are described as "small." Other improvements came from Basset [11] for Knudsen numbers much less than unity and by Epstein [12] in 1924 for Knudsen numbers much greater than unity.

For the present study, depending on particle size, one of three analytical models is used to calculate the particle drag term in the particle equation of motion. Particles of Knudsen numbers smaller than 0.01 have a drag calculated by the following equation derived by Basset [11]:

$$D = \frac{-3\pi\mu a\{V_i(t) - u_i[\mathbf{Y}(\mathbf{t}),\mathbf{t}]\}}{m_p + \frac{m_f}{2}}\left[1 - \frac{\text{Kn}}{\sigma}(2 - \sigma)\right] \tag{3}$$

where σ is the accommodation coefficient. Equation (3) is used to calculate acceleration due to drag by dividing the force by the particle mass and half the displaced fluid mass. Particles of Knudsen numbers between 0.01 and 100 have a drag calculated by

$$D = \frac{-3\pi\mu a\{V_i(t) - u_i[\mathbf{Y}(\mathbf{t}),\mathbf{t}]\}}{\left[1 + \text{Kn}\left(\alpha + Qe^{\frac{-\beta}{\text{Kn}}}\right)\right]}\frac{1}{m_p + \frac{m_f}{2}} \tag{4}$$

where the constants α, Q, and β are the Cunningham slip coefficients [6–8] for water particles in air.

The drag of particles of Knudsen numbers greater than 100 is calculated by

$$D = \frac{-3\pi\mu a[V_i(t) - u_i\{\mathbf{Y}(\mathbf{t}),\mathbf{t}\}](\mathbf{8} + \pi\sigma)}{18\text{Kn}}\frac{1}{m_p + \frac{m_f}{2}} \tag{5}$$

derived from Epstein's [12] theoretical solution.

In 1956, Corrsin and Lumley [13] provided a more concise set of equations of motion that included other forces such as pressure effects (the force on a sphere due to the pressure field of the undisturbed flow) and added mass. In the present paper, the forces acting on a particle under acceleration will be calculated using the particle equation of motion developed by Maxey and Riley [14]:

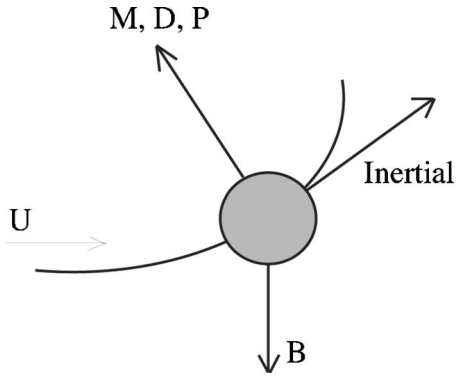

Fig. 2 Forces acting on a spherical particle to balance inertia

$$m_p\frac{dV_i}{dt} = P + M + D + B \tag{6}$$

$$P = m_f\left(\frac{Du_i}{Dt} - \nu\nabla^2 u_i\right)_{Y(t)} \tag{7}$$

$$M = -\frac{m_f}{2}\frac{d}{dt}\{V_i(t) - u_i[\mathbf{Y}(\mathbf{t}),\mathbf{t}]\} \tag{8}$$

$$B = (m_p - m_f)g_i \tag{9}$$

These forces are referred to as the pressure (Eq. (7)), added mass (Eq. (8)), drag (Eqs. (3)–(5)), and body forces (Eq. (9)). The pressure term represents the force exerted by the pressure gradient at the location of the particle if the particle had no influence on the flow. The added mass term represents the force required to accelerate a mass of fluid from the ambient at the particle location. Drag is the force due to differences in particle and fluid velocities. The body force is the force due to gravity. These forces are illustrated in Fig. 2. The particle equation of motion is solved using a fourth-order Runge-Kutta method. The horizonal and vertical velocities of the particle are compared to the velocity of the flow for each point to calculate the forces.

Our flow model is a two-dimensional solid body rotation meant to simulate the turning region found by Bettridge et al. [4], and, more directly, the recent result of Humes et al. [5] shown in Fig. 1(*b*). We wish to learn the effects of many fluid, geometric, and particle parameters. Thousands of test cases are required to examine the effects of each parameter on the others. A simplified flow field allows for the study of a large number of cases in a timely manner.

The magnitude of the velocity increases like r. As each streamline maintains a constant angular velocity independent of turning radius, shear effects are not present. Particles are introduced at the start of the turning and initially have the same velocity as the fluid.

In order to determine the particle size and density limits for AVPS, rejected particle path cases are categorized as follows: "Streamline" cases are those in which, either due to its small diameter or small density, a particle's deviation from a fluid streamline is less than a specified amount. An example of a streamline case is the innermost path shown in Fig. 3. "Straight line" cases are those in which a particle's inertia carries it through the domain with little or no deviation from its initial path. A straight line example is the straightest path seen in Fig. 3. Both streamline and straight line cases represent particles that cannot be collected into sorted groups, and will therefore constitute the sorting limits.

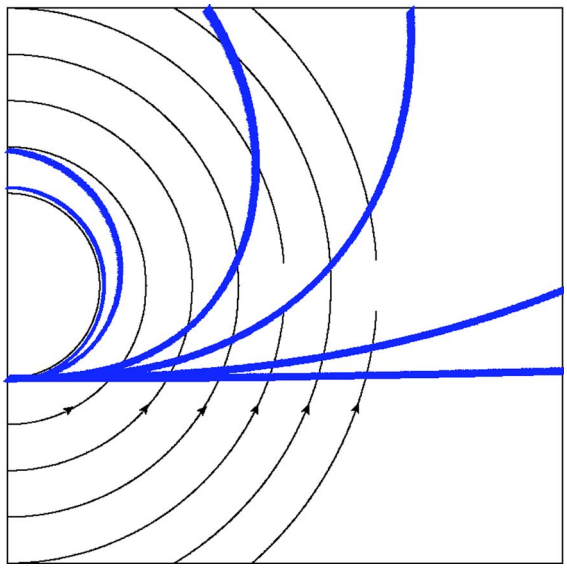

Fig. 3 Acceptable data between particles following streamlines and particles with little or no change in their trajectory. Particle paths are shown with thick lines. The thin lines represent flow streamlines. Four paths of acceptable data between two paths of unacceptable data are shown.

3 Results

Six cases of particles in air were modeled to find the range of sortable particles for particle-to-fluid density ratios of 100:1, 500:1, 1000:1, 2500:1, 5000:1, and 10,000:1. Each case included several subcases that tracked a single particle through the flow. The inlet velocity and the inlet distance from the flow center, or turning radius r, were varied. The inlet velocities for each case were $U=1$, 5, and 10 through 100 m/s in increments of 10 m/s. The distances to the flow center were 2 mm to 9 mm in increments of 1 mm.

The paths of acceptable particle diameters are shown in Fig. 4 for particle sizes from three different cases. The x-axis is the horizontal distance and the y-axis is the vertical. The particle enters the flow in the lower-left portion of the field. It can be seen that the particle's deviation from the streamlines increases with particle diameter.

The effect of inlet velocity is shown in Fig. 5. The paths of particles with the same diameter, density ratio, and turning radius are shown for various inlet velocities. Particles deviate more from the streamlines with increasing inlet velocity for a given turning radius.

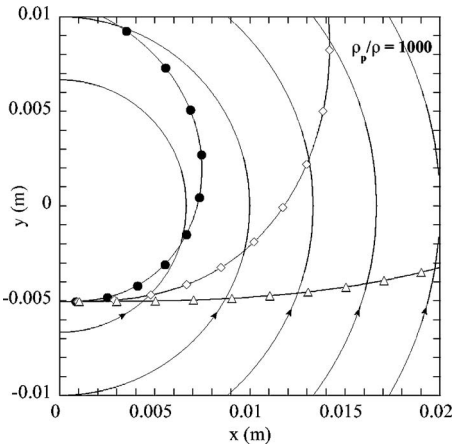

Fig. 4 Various particle diameters in the flow field. Particle diameter is (●) 2 μm, (◇) 5 μm, (△) 20 μm. The other curves are flow streamlines. Inlet velocity is 30 m/s.

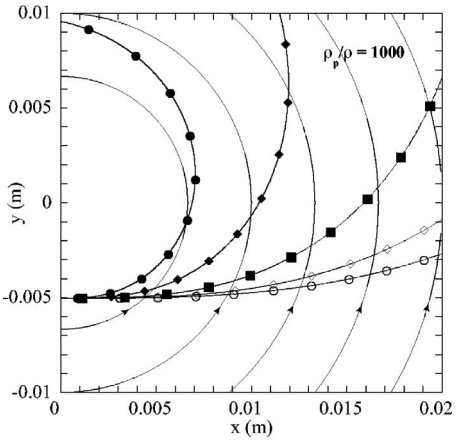

Fig. 5 Particles of varying inlet velocity in the flow field. Particle inlet velocity of (●) 1 m/s, (♦) 5 m/s, (■) 20 m/s, (◇) 50 m/s, (○) 90 m/s. The other curves are flow streamlines. Particle diameter is 10 μm.

The effect of particle-to-fluid density ratio is shown in Fig. 6. Paths for particles of the same diameter, inlet velocity, and turning radius are shown for various particle-to-fluid density ratios. Particles deviate more from the streamlines with increasing density ratio for a given turning radius. This is expected since particles of higher particle-to-fluid density ratios will have relatively more inertia.

The sorting limits for the cases of particle-to-density ratios of 100:1 and 10,000:1 are shown in Figs. 7 and 8, respectively. The lines plotted with solid symbols represent the upper (straight line) limits and open symbols for the lower (streamline) limits for various inlet speeds. Figures 7 and 8 each demonstrate that with increasing turning radius, the streamline limit increases while the straight line limit decreases. A wider range of particles can be sorted as turning radius is decreased. This is because the sharper turn generates larger accelerations that are able to accelerate larger particles more while requiring less inertia for smaller particles to remain entrained. The cases not shown follow the same trends.

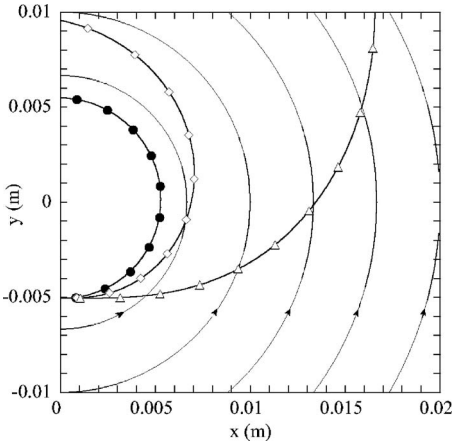

Fig. 6 Particle paths of various particle-to-fluid density ratios and an inlet velocity of 50 m/s. Particle-to-fluid density ratio: (●) ρ_p/ρ=100, (◇) ρ_p/ρ=1000, (△) ρ_p/ρ=10,000. All other lines are flow streamlines. The particle diameter is 10 μm and inlet velocity is 1 m/s.

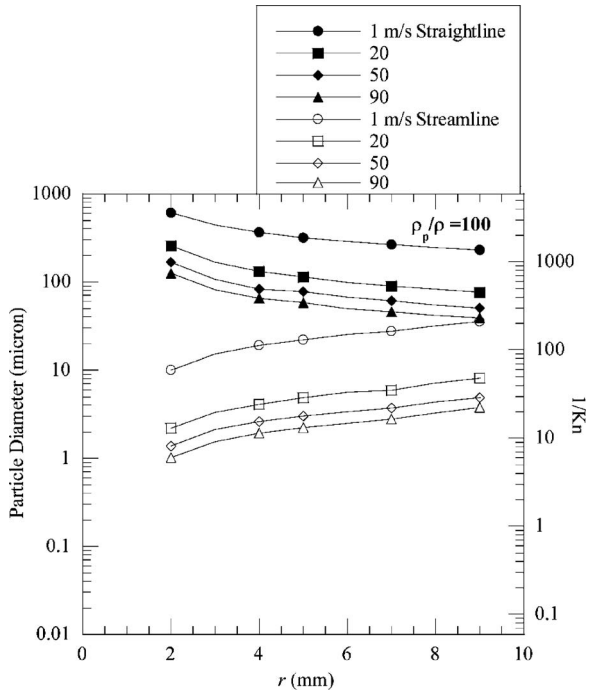

Fig. 7 Streamline and straight line limits for a particle-to-fluid density ratio of 100

It can also be seen that the streamline and straight line limits decrease together as inlet velocity is increased. Figure 9 illustrates the streamline and straight line limits of different particle-to-fluid density ratios for inlet velocities of 50 m/s. Generally, the range of sizes that can be sorted remains constant (between one and two orders of magnitude depending on the turning radius). Larger density ratios shift both the lower and upper limits downward.

It should be noted that the results presented in this paper apply only to an ideal case where the flow is laminar and 2-D, the particles are spherical, and particle loading is small. Departure from any of these conditions will likely result in similar mean results, but may cause large standard deviations in the particle size at any location.

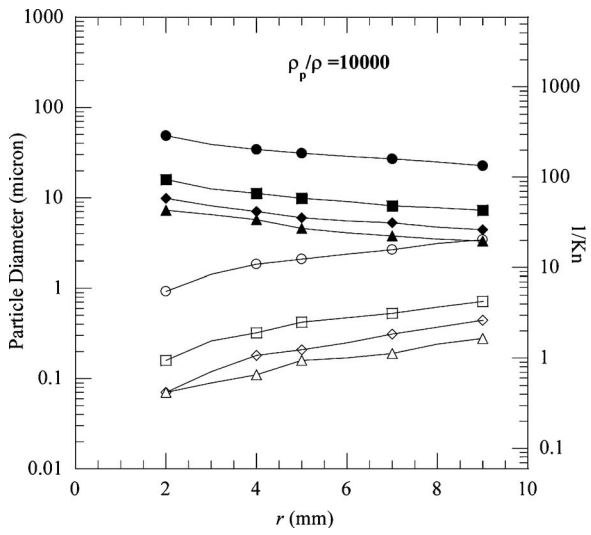

Fig. 8 Streamline and straight line limits for a particle-to-fluid density ratio of 10,000. Symbols are the same as Fig. 7.

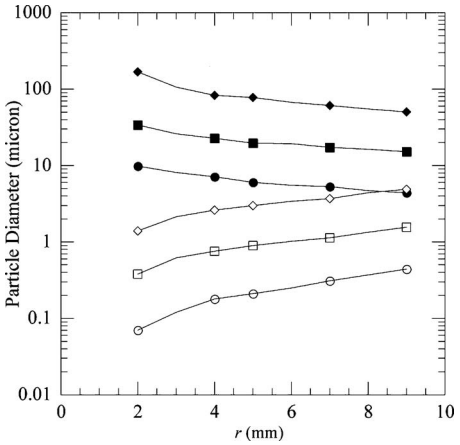

Fig. 9 Streamline and straight line limits for various particle-to-fluid density ratios. For straight line limits, (♦) ρ_p/ρ=100, (■) ρ_p/ρ=1000, (●) ρ_p/ρ=10,000. Streamline limits are indicated with open symbols.

The upper and lower limits of particle sorting have been found to be a function of the turning radius, the particle density, and the inlet velocity. Based on dimensional analysis and the data from this study, the two limits of the sorting range are cast dimensionlessly. Specifically, the upper (streamline) limit relative to the turning radius is found to be

$$\left(\frac{a}{r}\right)_{\text{streamline}} = \left(\frac{1.38}{\text{Re}}\frac{\rho}{\rho_p}\right)^{0.5} \tag{10}$$

where $\text{Re}=Ur/\nu$, U is the inlet velocity, ν is the fluid kinematic viscosity, r is the initial distance to the flow center, and ρ_p/ρ is the particle-to-fluid density ratio. The fit of the data from the present study to Eq. (10) is shown in Fig. 10. The equation adequately represents all of the data.

The straight line limit diameter is normalized by the mean free path and is a function of the same parameters (see Fig. 11)

$$\text{Kn} = \left[\gamma\frac{\rho_p}{\rho}\frac{\text{Re}_\lambda^{1.8}}{\text{Re}^{0.8}}\left(\frac{r}{\lambda}\right)^{1.3}\right]^{0.5} \tag{11}$$

where $\text{Re}_\lambda=U\lambda/\nu$, $\gamma=3.3\times10^{-10}$, and λ is the mean free path of air.

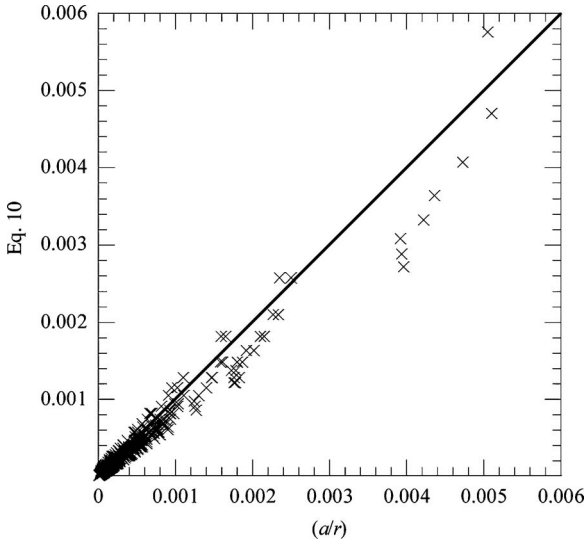

Fig. 10 Comparison of the data to Eq. (10) for the streamline (lower) limit

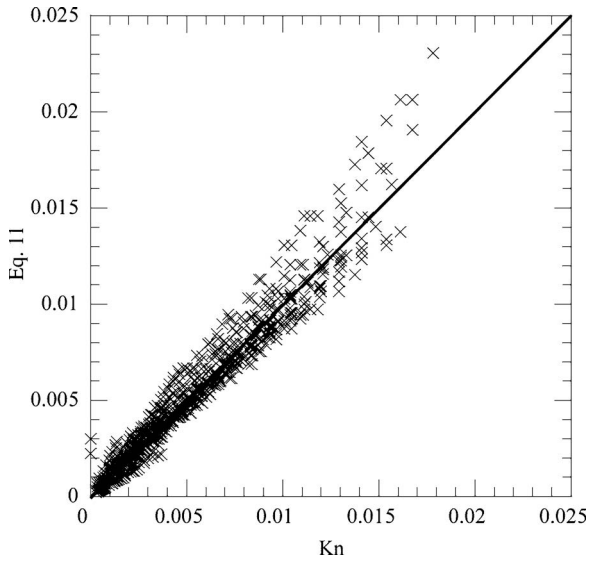

Fig. 11 Comparison to model results for Knudsen number (Eq. (11))

4 Validation

Earlier work [5,15] described experiments performed on an AVPS apparatus. Since the experimental flow is not infinite in extent (the jet has a finite width, after which particles move into a largely stagnant region) and does not turn exactly on a circular path, the best comparison of the experimental result with the present theoretical result is to examine the particle trajectory angle as a function of the particle size at one downstream location very near the jet exit. The theoretical speed is matched to the experiment (16.8 m/s), as is the density of the particles ($\rho_p/\rho=600$). At this location, the particles in both the experiment and the theoretical study have been under the influence of the aerodynamic forces for a short time, and therefore the trajectory angle of each particle has been altered according to size. Since the experiment acquired data over a small but finite region (about 2×3 mm square), at any one location, a small band of trajectory angles will be present for each particle size. For comparison, the theoretical "data" are also collected in the same-sized region. The gray band in Fig. 12 represents all possible trajectory angles that the particles of various sizes could have inside the window. The symbols represent the measured particles in the same window. Although the theoretical result seems to indicate a smaller degree of sorting, the range of particle sizes at each angle in the window is similar for the experimental and the theoretical result. The trends of both cases are similar, and indicate that the model is a good representation of the effects of a turning flow on particle paths.

Furthermore, in our recent unpublished experimental study, particles with a density 2.5 times that of water in the range 5 to 45 μm were sorted. Equations (10) and (11) would predict a range of 3.5 μm to 50 μm.

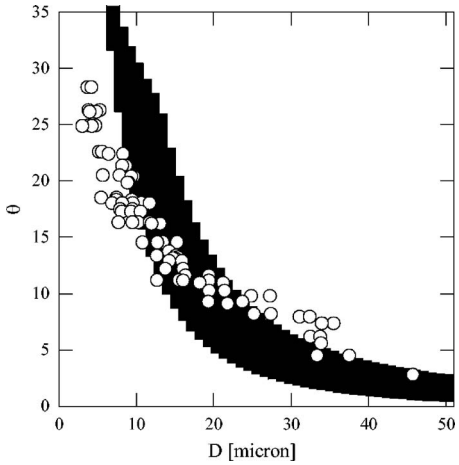

Fig. 12 Experimentally measured particle trajectory angles (○) (glass spheres, $\rho_p/\rho=600$) compared to the present results indicated by the shaded regions

5 Conclusions

A theoretical model has been constructed to determine the limits of particle sorting by rapidly turning a free jet. The theoretical model is verified by comparing the trajectory of a wide range of particle sizes to experimental results. It has been demonstrated that sorting particles over a wide range of diameters is possible using the AVPS arrangement. Particles that are too large to be sorted move in a straight line in a turning flow. Particles that are too small follow flow streamlines. The streamline and straight line limits decrease as the inlet velocity is increased. The streamline and straight line limits decrease as the particle-to-fluid density ratio is increased. A wider range of particles can be sorted as the turning radius is decreased. This effect is especially important for small turning radii.

These trends are quantified in a pair of equations fit to the theoretical results—one for the lower limit (Eq. (10)), and a second for the upper limit (Eq. (11)). These equations are useful for scaling a sorting apparatus. For instance, if one wishes to sort particles five times the density of water down to 0.5 μm, a flow speed of 30 m/s and a turning radius of 2 mm would suffice. A jet with an exit velocity of 30 m/s would need to be no larger than 2.5 mm in order to remain laminar. On the other hand, if it were desired to sort to 0.1 μm of the same material, a flow speed of 100 m/s would require a turning radius of 0.2 mm and a jet less than 0.75 mm wide. Clearly, the practicality of this method decreases rapidly with particle size in the neighborhood of 1 μm.

It should be noted that the results presented in this paper apply only to an ideal case where the flow is laminar and 2-D, the particles are spherical, and particle loading is small. Departure from any of these conditions will likely result in similar mean results, but may cause large standard deviations in the particle size at any location.

References

[1] Marple, V. A., 2004, "History of Impactors—The First 110 Years," Aerosol Sci. Technol., **38**, pp. 247–292.
[2] Torczynski, J. R., and Rader, D. J., 1997, "The Virtual Cyclone: A Device For Nonimpact Particle Separation," Aerosol Sci. Technol., **26**, pp. 560–573.
[3] Gotoh, K., and Masuda, H., 2000, "Improvement of the Classification Performance of a Rectangular Jet Virtual Impactor," Aerosol Sci. Technol., **32**, pp. 221–232.
[4] Bettridge, M. W., Spall, R. E., and Smith, B. L., 2006, "Aerodynamic Jet Steering Using Steady Blowing and Suction," Exp. Fluids, **40**(5), pp. 776–785.
[5] Humes, Z., Smith, B. L., and Minichiello, A., 2006, "Particle Sorting by Aerodynamic Vectoring," Bull. Am. Phys. Soc., p. 39.
[6] Millikan, R. A., 1911, "The Isolation of an Ion, a Precision Measurement of its Charge, and the Correction of Stokes's Law," Phys. Rev., **32**, pp. 349–397.
[7] Millikan, R. A., 1923, "Coefficients of Slip in Gases and the Law of Reflection of Molecules From the Surfaces of Solids and Liquids," Phys. Rev., **21**, pp. 217–238.
[8] Millikan, R. A., 1923, "The General Law of Fall of a Small Spherical Body Through a Gas, and Its Bearing Upon the Nature of Molecular Reflection From Surfaces," Phys. Rev., **22**, pp. 1–23.
[9] Stokes, G. G., 1851, Trans. Cambridge Philos. Soc., 9(8).

[10] Slowik, J., Stainken, K., Davidovits, P., Williams, L., Jayne, J., Kolb, C., Worsnop, D., Rudich, Y., DeCarlo, P., and Jimenez, J., 2004, "Particle Morphology and Density Characterization by Combined Mobility and Aerodynamic Diameter Measurements. Part 2: Application to Combustion-Generated Soot Aerosols as a Function of Fuel Equivalence Ratio," Aerosol Sci. Technol., **38**, pp. 1206–1222.
[11] Basset, A. B., 1961, *Hydrodynamics*, Dover, New York, Vol. II.
[12] Epstein, P. S., 1924, "On the Resistance Experienced by Spheres in Their Motion Through Gases," Phys. Rev., **23**, pp. 710–733.
[13] Corrsin, S., and Lumley, J., 1956, "On the Equation of Motion for a Particle in a Turbulent Fluid," Appl. Sci. Res., Sect. A, **6**, pp. 114–116.
[14] Maxey, M. R., and Riley, J. J., 1983, "Equations of Motion for a Small Rigid Sphere in a Nonuniform Flow," Phys. Fluids, **26**, pp. 883–889.
[15] Smith, B. L., Humes, Z., and Minichiello, A., 2006, "Aerodynamic Vectoring Particle Sorting," *Proceedings of FEDSM2006, ASME Fluids Engineering Summer Conference*, July 2006, Paper No. 2006-98266.

Acceleration Methods for Coarse-Grained Numerical Solution of the Boltzmann Equation

Husain A. Al-Mohssen

Nicolas G. Hadjiconstantinou

Mechanical Engineering Department,
Massachusetts Institute of Technology,
Cambridge, MA 02139

Ioannis G. Kevrekidis

Department of Chemical Engineering and PACM,
Princeton University,
Princeton, NJ 08540

We present a coarse-grained steady-state solution framework for the Boltzmann kinetic equation based on a Newton-Broyden iteration. This approach is an extension of the equation-free framework proposed by Kevrekidis and coworkers, whose objective is the use of fine-scale simulation tools to directly extract coarse-grained, macroscopic information. Our current objective is the development of efficient simulation tools for modeling complex micro- and nanoscale flows. The iterative method proposed and used here consists of a short Boltzmann transient evolution step and a Newton-Broyden contraction mapping step based on the Boltzmann solution; the latter step only solves for the macroscopic field of interest (e.g., flow velocity). The predicted macroscopic field is then used as an initial condition for the Boltzmann solver for the next iteration. We have validated this approach for isothermal, one-dimensional flows in the low Knudsen number regime. We find that the Newton-Broyden iteration converges in $O(10)$ iterations, starting from arbitrary guess solutions and a Navier-Stokes based initial Jacobian. This results in computational savings compared to time-explicit integration to steady states when the time to steady state is longer than $O(40)$ mean collision times.
[DOI: 10.1115/1.2742725]

Introduction

The objective of the work presented here is the development of efficient simulation tools for modeling flows in micro/nanoscale devices. In this paper we will focus on dilute gas flows. The development of accurate engineering models of such flows is important for the fundamental understanding, but also in the design [1,2], and even fabrication of such devices [3,4].

It is well known [5,6] that when the mean free path becomes comparable to the flow characteristic length scale, the flow deviates from the Navier-Stokes (NS) description. This deviation is typically quantified by the Knudsen number $\mathrm{Kn}=\lambda/L$, where λ is the molecular mean free path and L is the characteristic flow lengthscale. When the Knudsen number exceeds ~ 0.1, kinetic effects become important in appreciable parts of the flow, whereas for $\mathrm{Kn} \gtrsim 0.5$ the Navier-Stokes description cannot be used [21], and one typically turns to a kinetic description, such as the Boltzmann equation (BE), given below in nondimensional form for a hard-sphere gas [7]

$$\frac{\partial f}{\partial t} + \vec{c} \cdot \frac{\partial f}{\partial \vec{x}} + \vec{a} \cdot \frac{\partial f}{\partial \vec{c}} = I(\vec{x},\vec{c},t)$$

$$I(\vec{x},\vec{c},t) = \frac{1}{\mathrm{Kn}} \int \int (f' f_1' - f f_1) V \sigma d\Omega d\vec{c}_1 \qquad (1)$$

Here, $f=f(\vec{x},\vec{c},t)$ is the single-particle probability distribution function, $\vec{x}=(x,y,z)$ is the position vector, $\vec{c}=(c_x,c_y,c_z)$ is the molecular velocity vector, $f_1=f(\vec{x},\vec{c}_1,t)$, $f_1'=f(\vec{x},\vec{c}_1',t)$, $f'=f(\vec{x},\vec{c}',t)$, and $\vec{a}$ is the acceleration due to an applied external field; the above quantities are nondimensionalized by the gas reference number density n_o, the most probable molecular speed $c_m=\sqrt{2kT/m}$, and the characteristic flow length scale L, where k is Boltzmann's constant, T is the gas temperature, and m is the molecular mass. V, Ω, and σ are the relative velocity, scattering angle, and collision cross section of colliding particles, respectively. The collision cross section is nondimensionalized by d, the hard sphere gas diameter; finally, time is nondimensionalized by the molecular collision time given by $\tau=\sqrt{\pi}\lambda/(2c_m)$, where $\lambda = 1/(\sqrt{2}\pi n_o d^2)$ is the molecular mean free path.

One of the most widely used methods for solving the Boltzmann equation is the direct simulation Monte Carlo (DSMC), a stochastic particle-based *simulation* method. The major drawback of this method is the rapid increase in the number of samples required to resolve the flow as the flow speed (Mach number Ma) becomes small (in fact, the cost that scales like $1/\mathrm{Ma}^2$). Recently, Baker and Hadjiconstantinou [8] proposed a method of solving the Boltzmann equation that is particularly suited to low-speed applications: by considering only the deviation from equilibrium, they derive a new Monte Carlo procedure for calculating the collision integral, which exhibits significantly reduced relative statistical uncertainty (and, hence, computational cost) that is also independent of the Mach number, implying that simulation of arbitrarily low flow speeds is possible [8,9] in sharp contrast to DSMC.

In the present paper, we are interested in accelerating the solution of steady-state problems. These become expensive to resolve by explicit integration methods as L grows when one uses a time step appropriate to a kinetic description ($\Delta t \ll \tau$). Although as L grows such that $\mathrm{Kn} \leq 0.1$ a Navier-Stokes description may be used, in this paper, we are targeting a particular class of *multidimensional* problems with large aspect ratios that exhibit both long global evolution (steady-state) timescales but also NS failure.[1]

Contributed by the Fluids Engineering Division of ASME for publication in the JOURNAL OF FLUIDS ENGINEERING. Manuscript received June 1, 2006; final manuscript received December 4, 2006. Assoc. Editor: Subrata Roy. Paper presented at the 4th International Conference on Nanochannels, Microchannels and Minichannels (ICNMM2006), June 19–21, 2006, Limerick, Ireland.

[1] Although implicit solution methods based on a finite difference discretization of the Boltzmann equation have also been developed, these have been found to converge slowly or not at all for lower values of Kn [15].

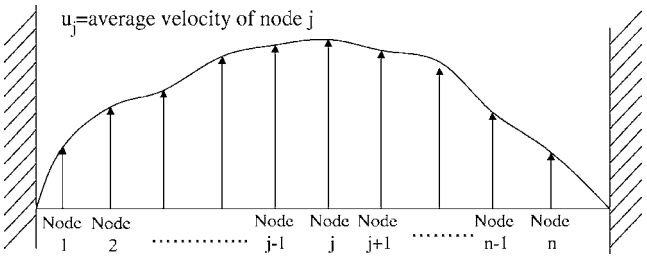

Fig. 1 Sketch of 1D computational domain

The major ingredients of our work are the low-noise solution method of Baker and Hadjiconstantinou [8] and ideas from the "equation-free" simulation framework of Kevrekidis et al. [10–14]. It is important to note that the "microscopic" solver here is a Monte Carlo method for solving the Boltzmann equation; consequently, steady-state solutions are to be understood as *stationary* solutions for the particle distribution moment fields, and—here, in particular—of a coarse-grained velocity field; while the particles continue their motion, their coarse-grained description approaches a steady state. Finally, we would like to emphasize that the variance reduction achieved by the method of [8] is essential in making the method described below successful for practical problems.

Problem Description and Proposed Approach

Figure 1 shows the basic setup of the one-dimensional (1D) model problem studied in this paper, where the macroscopic flow velocity $\vec{u}(\vec{x},t)=\int_{-\infty}^{\infty}\vec{c}f(\vec{x},\vec{c},t)d\vec{c}$ is nonzero only in the x direction and varies only in the y direction, i.e., $\vec{u}(\vec{x},t)=(u(y,t),0,0)$, $f=f(y,\vec{c},t)$. Now, let $\{u_j(t)\}=[u_1(t),u_2(t),\ldots,u_j(t),\ldots,u_n(t)]^T$ be the spatially discrete form of the flow velocity field, such that $u_j(t)$ is the flow velocity at physical-space node j, i.e., $u_j(t)=u(y_j,t)$.

To proceed, we define $F(\{u_j\})=\partial\{u_j(t)\}/\partial t$, which represents the rate of the change of the (discrete in space) macroscopic velocity field. Finding the steady-state solution $\{u_j\}_{SS}$ can then be posed as the problem of finding the flow field $\{u_j\}_{SS}$, which solves the (in general) nonlinear set of equations $F(\{u_j\}_{SS})=\{0\}$.

Our approach here is to solve the above system of equations using a variant of Newton's method. For many degrees of freedom, each iteration (i) of Newton's method [16] updates the guess solution for $\{u_j\}_{SS}^{(i+1)}$ using the value of the function $F^{(i)}(\{u_j\})$ (obtained by fitting the slope of $\{u_j(t)\}^{(i)}$ versus time from solution of the BE) and the Jacobian matrix of derivatives $[J]^{(i)}$. As the Jacobian matrix is not analytically available, it would be very expensive to directly estimate $[J]$ through finite differences, particularly for a fine discretization (large number of nodes) in the presence of fluctuations. To circumvent this limitation, we use a Broyden update formula to successively update the Jacobian at every step, using the most recent evaluation of the function and the previously available Jacobian (in other words, $[J]^{(i)}$ is updated using $[J]^{(i-1)}$, $\{u_j(t)\}^{(i)}-\{u_j(t)\}^{(i-1)}$, and $F^{(i)}-F^{(i-1)}$) [16,17].

Calculation of the Collision Integral Using Variance Reduction. In this section, we give a brief description of the variance-reduction method used to evaluate the collision integral $I(\vec{x},\vec{c},t)$. More details can be found in [8].

The method is based on the "weak" form of the collision integral [6,8]

$$I(\vec{x},\vec{c},t)=\frac{1}{2\mathrm{Kn}}\int\int\int(\delta_1'+\delta_2'-\delta_1-\delta_2)f_1f_2V\sigma\,d\Omega\,d\vec{c}_1d\vec{c}_2 \tag{2}$$

where $\delta_1=\delta^3(\vec{c}_1-\vec{c})$, $\delta_2=\delta^3(\vec{c}_2-\vec{c})$, $\delta_1'=\delta^3(\vec{c}_1'-\vec{c})$, $\delta_2'=\delta^3(\vec{c}_2'-\vec{c})$, and $f_2=f(\vec{x},\vec{c}_2,t)$. By expanding the nonequilibrium distribution function about an arbitrary Maxwell-Boltzmann distribution and using the fact that the contribution of the equilibrium Maxwell-Boltzmann (MB) distribution to the collision integral is zero, we obtain [8] the following form:

$$I(\vec{x},\vec{c},t)=\frac{1}{2\mathrm{Kn}}\int\int\int(\delta_1'+\delta_2'-\delta_1-\delta_2)\times(2f_1^{\mathrm{MB}}+f_1^d)f_2^dV\sigma d\Omega\,d\vec{c}_1d\vec{c}_2 \tag{3}$$

where $f^d\equiv f-f^{\mathrm{MB}}$ is the deviation from the equilibrium distribution f^{MB}.

As suggested by the above form, in the numerical implementation, the collision integral is evaluated by summing the contributions of a large number ($\mathcal{M}$) of simulated collisions (between a particle of velocity $\vec{c}_1$ and one of velocity $\vec{c}_2$)

$$I(\vec{x},\vec{c},t)\approx\frac{2\pi}{\mathrm{Kn}\mathcal{M}}\hat{\mathcal{N}}\sum_{i=1}^{\mathcal{M}}(\delta_{1,i}'+\delta_{2,i}'-\delta_{1,i}-\delta_{2,i})\times\mathrm{sgn}(2f_{1,i}^{\mathrm{MB}}+f_{1,i}^d)\,\mathrm{sgn}(f_{2,i}^d)V_i\sigma_i \tag{4}$$

where, according to (3), the particle of velocity $\vec{c}_1$ is chosen with probability

$$\frac{|2f^{\mathrm{MB}}(\vec{c}_1)+f^d(\vec{c}_1)|}{\int|2f^{\mathrm{MB}}(\vec{c})+f^d(\vec{c})|d\vec{c}}$$

and the particle with velocity $\vec{c}_2$ is chosen with probability

$$\frac{|f^d(\vec{c}_2)|}{\int|f^d(\vec{c})|d\vec{c}}$$

Here,

$$\hat{\mathcal{N}}\equiv\int|2f^{\mathrm{MB}}(\vec{c})+f^d(\vec{c})|d\vec{c}\times\int|f^d(\vec{c})|d\vec{c}$$

and $\mathrm{sgn}(x)=\pm1$ for $x\gtrless0$. The number of simulated collisions is a parameter that affects the statistical uncertainty associated with the evaluation of (4). For convenience, the precollision velocities $\vec{c}_1$ and $\vec{c}_2$ are chosen to lie on nodes of the computational grid, while the contributions of post-collision velocities are assigned to the nearest node. This was shown in [8] to provide excellent accuracy provided a sufficiently fine discretization is used.

Implementation Challenges. To successfully implement the above general approach, a number of issues have to be tackled. These are described in the following sections.

Initializing the Jacobian. Although the Broyden update formula for the Jacobian is robust, the algorithm requires an initial Jacobian. Directly estimating this Jacobian using forward differences would require $n+1$ BE solutions and could be prohibitively expensive, particularly when a fine spatial grid is used. The alternative strategy used here is to use an analytic Jacobian based on the best available closure (the Navier-Stokes description of the flow) as a starting point. We have found this strategy to work very well even when we start from a Jacobian that is quite distant from the correct one,[2] provided we use an L-1 norm in the line search of Newton's method [17].

[2]E.g., when the initial Jacobian corresponds to a different flow profile.

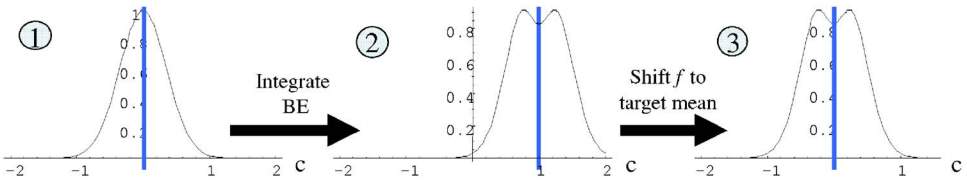

Fig. 2 Sketch of different steps of the maturing procedure

Initializing the Distribution Function. Solution methods which in some way couple macroscopic and microscopic degrees of freedom are usually faced with the problem of "reconstructing" physically consistent (correct) microscopic states from macroscopic data. This is a problem of general interest in molecular simulation, also encountered when developing hybrid atomistic-continuum methods [18]. In the equation-free framework of Theodoropoulos et al. [10], this is called the *lifting* step.

This challenge presents itself here as the need to specify an initial condition for the BE solver in the form of a distribution function, $f^*(\{y_j\},\vec{c})$, after the Newton-Broyden procedure provides the next guess for the steady-state solution $\{u_j\}_{SS}^{(i+1)}$(which in the interest of simplicity we will denote as $\{u_j\}$ from now on). The challenge lies in the fact that the flow velocity $\{u_j\}$ corresponds to the first moment of the distribution function and thus does not uniquely determine the distribution function. In other words, out of a large number of possible distributions with a first moment equal to $\{u_j\}$ only the correct distribution function $f^*(\{y_j\},\vec{c})$ is the one that has a first moment equal to $\{u_j\}$ but also exhibits the correct rate of change $F(\{u_j\})$ when integrated by the BE solver. One may assume that the desired $f^*(\{y_j\},\vec{c})$ is the distribution that would naturally arise had it been previously "matured" through direct integration from an *appropriate* set of initial conditions. Instead of searching for these appropriate initial conditions, the approach taken in this paper (and described in the next paragraph) is to iteratively relax the distribution function while constraining the first moment to remain at the desired value. Once the procedure is converged, $F(\{u_j\})$ is sampled for the next Newton-Broyden iteration. Obtaining the correct "matured" $f^*(\{y_j\},\vec{c})$ is critical in ensuring the accuracy of $F(\{u_j\})$ and, consequently, the correct steady-state solution $\{u_j\}_{SS}$.

The approach used here for maturing distributions is an adaptation of the procedure proposed by Kevrekidis and coworkers [14,19,20]; it appears to give a robust estimate of $f^*(\{y_j\},\vec{c})$ and can be summarized as follows: (1) we start with a Maxwell-Boltzmann distribution that has the correct macroscopic moments (in this case $\{u_j\}$); (2) we integrate the Boltzmann equation for a short period of time which allows $f(\{y_j\},\vec{c})$ to relax toward a microscopically consistent distribution; in general, the macroscopic velocities u_j will drift due to the integration; (3) we compensate for the drift by shifting $f(\{y_j\},\vec{c})$ to ensure that its first moment is equal to $\{u_j\}$; and (4) finally, we repeat steps 2 and 3 until convergence. This process, in effect, relaxes the distribution function constrained on $\{u_j\}$ without explicitly including a Lagrange multiplier to enforce the constraint. In our implementation, convergence (of the maturing part) means $F(\{u_j\})$ does not change if steps 2 and 3 are repeated. Figure 2 provides a schematic of the maturing procedure steps which in our experience has a computational cost comparable to that of directly integrating the system for a time of about $1-4\tau$ at low Ma numbers.

The computational cost of the maturing process can be reduced by starting this process with the mature distribution function from the previous Broyden step (with a mean shifted to equal $\{u_j\}$) rather than a Maxwell-Boltzmann distribution. This approach takes advantage of the fact that, close to convergence, guess solutions do not change significantly; preliminary results indicate that this approach reduces the computational cost of the maturing process by a factor of 2 or more.

A schematic diagram of the algorithm for finding the steady-state solution of the Boltzmann equation can be seen in Fig. 3.

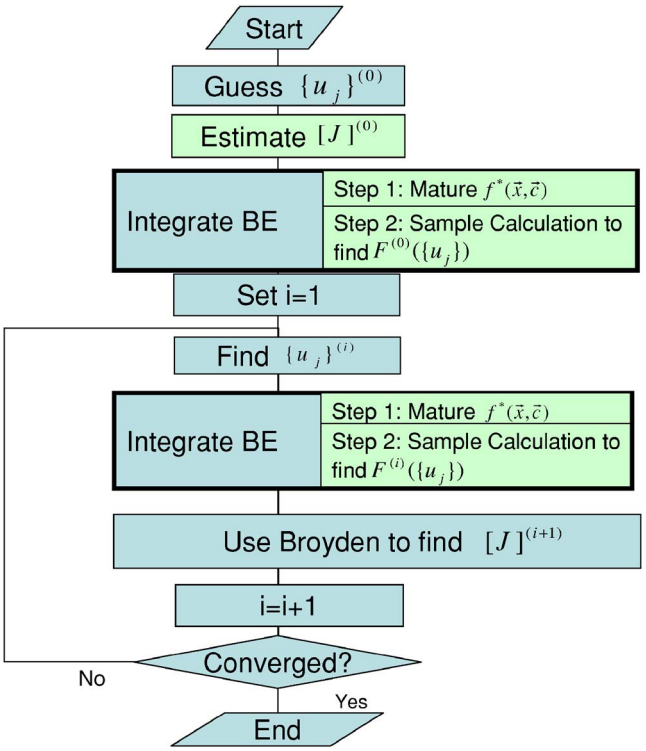

Fig. 3 Flowchart of the solution algorithm as explained in the text

Verification Examples

Below we present results for a 1D Couette flow with a normalized wall velocity of ±0.05; these results are representative of other flow configurations that we explored (e.g., Poiseuille). Also note that while the Couette flow problem has a trivial solution within the NS description, the presence of a kinetic boundary layer at the wall, known as the Knudsen layer [6,21], makes this problem nontrivial.

Figure 4 shows a comparison between the Knudsen layers[3] of a Kn=0.1 flow obtained using our proposed approach and the "exact" solution obtained via explicit time integration. As we can see, the agreement between the two layers is quite good; the relative error is ~0.2%. Figure 5 shows a convergence history plot for a Couette flow problem; it also shows that the error decays fast, and then saturates to a value determined by the sampling uncertainty in $F(\{u_j\})$ (recall that our Boltzmann equation solution method

[3]The Knudsen layer is "extracted" by subtracting the straight-line (slip-flow) Navier-Stokes result [21].

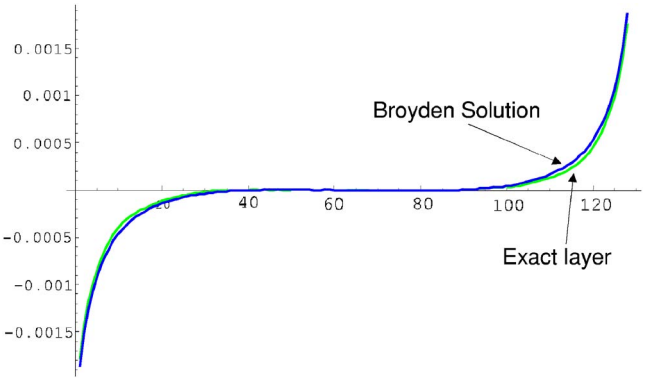

Fig. 4 Exact and Broyden Knudsen layer

still has relatively small but finite statistical uncertainty). This plot is representative of our results in the sense that convergence is typically achieved within <10 iterations *regardless of the number of discretization nodes in physical space*. Using a Navier-Stokes-based initial Jacobian was instrumental in keeping the total number of BE solution calls low and independent of the number of discretization nodes.

Computational Performance and Limitations

The method proposed here has an approximately constant computational cost that is independent of the characteristic time scale (time to steady state) of the system being considered. The most expensive part of this procedure is the maturing step that has to be repeated at every iteration. Clearly, the proposed method will be more efficient than straightforward time integration if the total time integrated using this method—approximately given by $O(10*Iterations)*[Maturing\ time+Sampling\ time]$—is shorter than the time to steady state. In the particular problem studied here, the total time integrated is $\approx 40\tau$, making the present method more efficient for flows characterized by $\mathrm{Kn} \lesssim 0.2$.

Of course, the break-even point will, in general, be implementation dependent and will depend on the target error; the latter is important because it affects the number of iterations required for convergence, but also because of the statistical uncertainty associated with the Boltzmann solution method and the associated sampling time. Fortunately, the drastically reduced statistical uncertainty associated with the present collision integral calculation method means that unless extremely small error tolerances are required, the effect of statistical error on the computational cost is small. The interaction of linear algebra techniques with random noise is a subject which is starting to gain momentum in the numerical analysis literature [22–24]—insights from these theoretical developments will be useful in understanding the limitations of approaches like the ones described here.

Finally, the proposed method becomes significantly more efficient as characteristic length scales increases (Kn decreases) since (for $\mathrm{Kn} \lesssim 1$) the time to steady-state scales as $1/\mathrm{Kn}^2$. We thus expect this method to be very efficient for *multidimensional* problems which can exhibit both long evolution time scales and Navier-Stokes breakdown.

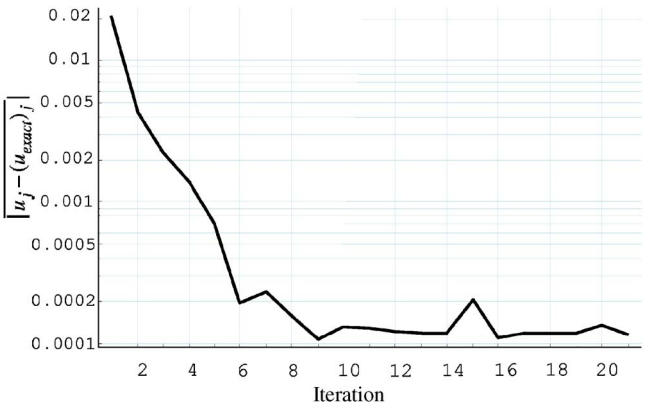

Fig. 5 Convergence history for a Kn=0.1 problem. The error is averaged over all spatial nodes (512 Total) and an L-1 Norm is used for the error.

Discussion and Future Work

In this paper, we described a Newton-Broyden approach for solving the kinetic Boltzmann equation. Our method is intended for problems that have larger characteristic time scales and are consequently hard to solve by explicit time integration. In one-dimensional low-Knudsen-number problems, our approach converges in $O(10)$ iterations from an arbitrary guess solution and a Navier-Stokes derived initial Jacobian; moreover, the number of iterations is independent of the number of nodes in physical space.

The excellent agreement between the "exact" and the Broyden solutions for low Knudsen number flows for *kinetic* features of the flow, such as the Knudsen layer and slip at the wall, demonstrates that the maturing procedure is reliable in the presence of kinetic effects. In other words, this is evidence that an accurate macroscopic equation can close in terms of only the flow velocity, even though we cannot write this equation explicitly. This can be taken to imply that higher-order moments become functionals of the velocity field over simulation times of the order of the maturing time. This is consistent with the kinetic theory description of the Knudsen layer [25]: in the latter, the underlying distribution function, despite being far from the equilibrium and Chapman-Enskog distributions (the latter corresponding to the Navier-Stokes description [5]), is still similar to the Chapman-Enskog in the sense that it is parametrized by the local Navier-Stokes solution. Because in one-dimensional transition-regime problems ($0.1 \lesssim \mathrm{Kn} \lesssim 10$) the time to steady state is of the order of the maturing time, it is unclear whether a macroscopic description comprising of only the flow velocity will be sufficient to describe general transition-regime flows. Recall, however, that, if required, this framework can be readily extended to include any number of higher moments of the distribution function (e.g., stress) as independent macroscopic variables [10]. We expect to address this issue when we apply our methodology to two- and three-dimensional problems with long evolution time scales. It is also worth noting that the same type of approach allows for a quantitative stability analysis of the computed steady states through matrix-free iterative eigencomputations.

Acknowledgment

The authors would like to thank L. L. Baker for help with computations and A. T. Patera for useful comments and suggestions. This work was suppported, in part, by DOE through the Center for Multiscale Plasma Dynamics, and, in part, by Sandia National Laboratory.

References

[1] Aoki, K., Sone, Y., Takata, S., Takahashi, K., and Bird, G. A., 2001, "One-way Flow of a Rarefied Gas Induced in a Circular Pipe With Periodic Temperature Distribution," *Rarefied Gas Dynamics 23rd International Symposium*, T. J. Bartel and M. A. Gallis, eds., AIP, Melville, NY, pp. 940–947.

[2] Ho, C. M., and Tai, Y. C., 2001, "Micro-Electro-Mechanical Systems (MEMS) and Fluid Flows," Annu. Rev. Fluid Mech., **30**, pp. 579–612.

[3] Gallis, M. A., Torczynski, J. R., and Rader, D. J., 2006, "An Approach for Simulating the Transport of Spherical Particles in a Rarefied Gas Flow Via the Direct Simulation Monte Carlo," Phys. Fluids, **13**, pp. 3482–3492.

[4] Al-Mohssen, H. A., and Hadjiconstantinou, N. G., 2004, "Arbitrary-Pressure Chemical Vapor Deposition Modeling Using Direct Simulation Monte Carlo With Nonlinear Surface Chemistry," J. Comput. Phys., **198**, pp. 617–627.

[5] Vincenti, W. G., and Kruger, C. H., 1965, *Introduction to Physical Gas Dynamics*, Krieger, Melbourne, FL.

[6] Cercignani, C., 1988, *The Boltzmann Equation and its Applications*, Springer-Verlag, Berlin.
[7] Bird, G. A., 1994, *Molecular Gas Dynamics and the Direct Simulation of Gas Flows*, Clarendon Press, Oxford.
[8] Baker, L. L., and Hadjiconstantinou, N. G., 2005, "Variance Reduction for Monte Carlo Solutions of the Boltzmann Equation," Phys. Fluids, **17**, p. 051703.
[9] Hadjiconstantinou, N. G., Garcia, A. L., Bazant, M. Z., and He, G., 2003, "Statistical Error in Particle Simulations of Hydrodynamic Phenomena," J. Comput. Phys., **187**, pp. 274–297.
[10] Theodoropoulos, K., Qian, Y. H., and Kevrekidis, I. G., 2000, "'Coarse' Stability and Bifurcation Analysis Using Timesteppers: A Reaction Diffusion Example," Proc. Natl. Acad. Sci. U.S.A., **97**(18), pp. 9840–9843.
[11] Gear, C. W., Kevrekidis, I. G., and Theodoropoulos, C., 2002, "'Coarse' Integration/Bifurcation Analysis Via Microscopic Simulators: Micro-Galerkin Methods," Comput. Chem. Eng., **26**, pp. 941–963.
[12] Kevrekidis, I. G., Gear, C. W., Hyman, J. M., Kevrekidis, P. G., Runborg, O., and Theodoropoulos, K., 2003, "Equation-Free Coarse-Grained Multiscale Computation: Enabling Macroscopic Simulators to Perform System-Level Tasks," Commun. Math. Sci., **1**, pp. 715–762; original version can be obtained as physics/0209043 at arXiv.org.
[13] Kevrekidis, I. G., Gear, C. W., and Hummer, G., 2004, "Equation-Free: The Computer Assisted Analysis of Complex, Multiscale Systems," AIChE J., **50**, pp. 1346–1355.
[14] Gear, C. W., Kaper, T. J., Kevrekidis, I. G., and Zagaris, A., 2005, "Projecting on a Slow Manifold: Singularly Perturbed Systems and Legacy Codes," SIAM J. Appl. Dyn. Syst., **4**(3), pp. 711–732.
[15] Aristov, V. V., 2001, *Direct Methods for Solving the Boltzmann Equation and Study of Nonequilibrium Flows*, Kluwer, Dordrecht.
[16] Press, W. H., Teukolsky, S. A., Vetterling, W. T., and Flannery, B. P., 1992, *Numerical Recipes in C*, 2nd ed., Cambridge University Press, Cambridge, England.
[17] Kelley, C. T., 2003, *Solving Nonlinear Equations With Newton's Method*, SIAM, Philadelphia.
[18] Wijesinghe, H. S., and Hadjiconstantinou, N. G., 2004, "Discussion of Hybrid Atomistic-Continuum Methods for Multiscale Hydrodynamics," Int. J. Multiscale Comp. Eng., **2**, pp. 189–202.
[19] Gear, C. W., and Kevrekidis, I. G., 2005, "Constraint-Defined Manifolds: A Legacy-Code Approach to Low-Dimensional Computations," J. Sci. Comput., **25**(1), pp. 17–28.
[20] Erban, R., Kevrekidis, I. G., and Othmer, H. G., 2006, "An Equation-Free Computational Approach for Extracting Population-Level Behavior From Individual-Based Models of Biological Dispersal," Physica D, **215**, pp. 1–24.
[21] Hadjiconstantinou, N. G., 2005, "Validation of Second-Order Slip Model for Dilute Gas Flows," Microscale Thermophys. Eng., **9**, pp. 137–153.
[22] Simoncini, V., and Szyld, D. B., 2003, "Theory of Inexact Krylov Subspace Methods and Applications to Scientific Computing," SIAM J. Sci. Comput. (USA), **25**, pp. 454–477.
[23] van den Eshof, J., and Sleijpen, G. L. G., 2004, "Inexact Krylov Subspace Methods for Linear Systems," SIAM J. Matrix Anal. Appl., **26**, pp. 125–153.
[24] Bouras, A., and Fraysse, V., 2005, "Inexact Matrix-Vector Products in Krylov Methods for Solving Linear Systems: A Relaxation Strategy," SIAM J. Matrix Anal. Appl., **26**, pp. 660–678.
[25] Sone, Y., 2002, *Kinetic Theory and Fluid Dynamics*, Birkhauser, Boston.

F. Rousset[1]
e-mail: francois.rousset@univ-lyon1.fr

S. Millet

V. Botton

H. Ben Hadid

Université de Lyon,
Université Lyon 1, INSA de Lyon,
Ecole Centrale de Lyon,
Laboratoire de Mécanique des Fluides et d'Acoustique,
UMR CNRS 5509,
Villeurbanne, 69622, France

Temporal Stability of Carreau Fluid Flow Down an Incline

This paper deals with the temporal stability of a Carreau fluid flow down an inclined plane. As a first step, a weakly non-Newtonian behavior is considered in the limit of very long waves. It is found that the critical Reynolds number is lower for shear-thinning fluids than for Newtonian fluids, while the celerity is larger. In a second step, the general case is studied numerically. Particular attention is paid to small angles of inclination for which either surface or shear modes can arise. It is shown that shear dependency can change the nature of instability. [DOI: 10.1115/1.2742737]

1 Introduction

The hydrodynamics of a fluid under gravity is not only of practical interest in many engineering applications, such as coating processes, but also in many geophysical phenomena (e.g., glaciers, mud, and lava flows). Among the various aspects of falling films that have been explored over the years, particular attention was devoted to the investigation of the stability of Newtonian flow down an inclined plane for single-layer systems. This problem was first theoretically discussed by Benjamin [1] and Yih [2]. These authors obtained critical conditions for the onset of instability via linear stability analysis for long surface waves. Smith [3] proposed a physical mechanism for the long-wave instability. He described how a disturbance to the interface produces a motion in the layer and how this motion can amplify the disturbance by studying energy transfer from the basic state to the disturbance. Many authors have made numerical contributions to this topic, especially in the case of small angles of inclination. De Bruin [4] found that shear modes have lower critical Reynolds number than do surface modes when the angle of inclination is very small. This work was extended by Floryan et al. [5] who took into account surface tension at the interface between the liquid and the passive gas that bounds it. The authors found that growth rates of surface waves are reduced by an increase of surface tension or by a decrease of the angle of inclination. In contrast, the critical Reynolds number for shear modes exhibits a nonmonotonic relation with the surface tension. The authors thus showed that particular attention has to be paid to this parameter.

All the above studies are based on the Newtonian fluid model. However, the rheological behavior of many fluids cannot be properly described by the Newtonian model. For example, mudflows are pseudoplastic, saccharified honey is known to be a shear-thickening fluid, whereas polymers exhibit generally a large elastic component. Some authors focused on non-Newtonian film flows down an inclined plane, such as Yih [6] for a triply nonlinear constitutive equation, Gupta [7] for a second-order fluid, Liu and Mei [8] for a Bingham fluid, Lai [9] and Shaqfeh et al. [10] for an Oldroyd-B fluid, Hwang et al. [11] for a power-law liquid, Andersson and Dahl [12] for a Walters' liquid B″, and Chen [13] for an upper convected Maxwell model. The instability mechanism of viscoelastic fluids has been described by Huang and Khomami [14].

Among the studies on the stability of non-Newtonian film flows, little attention was paid to the four-parameter Carreau inelastic model proposed by Carreau et al. [15] although it is frequently used in chemical engineering. For instance, it fits reasonably well with polymer solutions' behavior in many flow situations. This model describes the behavior of a purely viscous fluid whose viscosity changes with increasing rate of deformation. It predicts, in particular, a region in which a linear relation between viscosity and shear rate is observed (on the usual log-log coordinates). The Carreau law thus predicts a so-called power-law region. However, unlike the power-law or Ostwald-De Waele model, it predicts a viscosity that remains finite as the shear rate approaches zero. For that reason, the Carreau constitutive equation suits well for free surface flows. Weinstein [16] studied numerically the influence of shear-thinning rheology on spatial stability of a film flow down an inclined plane. In order to assess the effect of shear-thinning behavior on a single-layer system, the author compared his results to the two limiting Newtonian cases constructed with the minimum and maximum viscosities attained in the shear-thinning layer. He observed that the shear-thinning results lie between these two Newtonian cases except at very low frequencies. The author finally proposed a mechanism that models the different cases based on energy considerations.

In the present work, we have studied the influence of shear-dependant rheology on the temporal stability of a liquid flow down an inclined plane. This case has not been treated before. Following the approach developed by Benjamin [1] and Yih [2], we have examined, analytically, the flow stability for long-wave perturbations in the limit of small non-Newtonian behavior. For doing so, we carried out a stability analysis based on analytical expressions for velocity field and film thickness proposed by Weinstein [16]. We have also investigated the flow stability numerically. Special attention has been paid to small angles of inclination. Our approach thus extends the results obtained by De Bruin [4] and Floryan et al. [5] to shear-thinning fluids.

2 Formulation

2.1 Basic Flow. We study an incompressible fluid flow driven by gravity down a plate inclined to the horizontal at angle β as shown in Fig. 1. We make use of a Cartesian coordinate system aligned with the plane in which the x-axis points down the slope and the y-axis is taken normal to the plane and oriented toward it. The origin is taken at the unperturbed free surface. Let $y=\zeta(x,t)$ be the equation of the free surface at time t.

The governing equations are

[1]Corresponding author.

Contributed by the Fluids Engineering Division of ASME for publication in the JOURNAL OF FLUIDS ENGINEERING. Manuscript received September 7, 2006; final manuscript received January 16, 2007. Assoc. Editor: Dennis Siginer. Paper presented at the EFMC6 (2006).

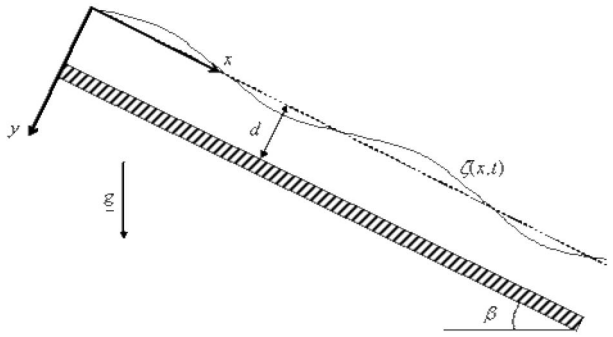

Fig. 1 Definition sketch

$$\frac{\partial u}{\partial x} + \frac{\partial v}{\partial y} = 0 \tag{1}$$

$$\rho\left(\frac{\partial u}{\partial t} + u\frac{\partial u}{\partial x} + v\frac{\partial u}{\partial y}\right) = -\frac{\partial p}{\partial x} + \left(\frac{\partial \sigma_{xx}}{\partial x} + \frac{\partial \sigma_{xy}}{\partial y}\right) + \rho g \sin\beta \tag{2}$$

$$\rho\left(\frac{\partial v}{\partial t} + u\frac{\partial v}{\partial x} + v\frac{\partial v}{\partial y}\right) = -\frac{\partial p}{\partial y} + \left(\frac{\partial \sigma_{xy}}{\partial x} + \frac{\partial \sigma_{yy}}{\partial y}\right) + \rho g \cos\beta \tag{3}$$

where u and v are respectively the x and y velocity components, ρ is the density, p is the pressure, g is the gravitational acceleration, and σ_{ij} are the deviatoric stress tensor components. The fluid is supposed to be purely viscous; that is, its viscosity depends only on the shear rate. Its constitutive equation is a generalization of Newton's law and has the following form:

$$\sigma_{ij} = 2\eta(|\dot{\gamma}|)D_{ij} \tag{4}$$

where D_{ij} are the strain rate tensor components. The non-Newtonian viscosity η is a function of the second invariant of the strain rate tensor defined by

$$|\dot{\gamma}| = (2D_{ij}D_{ij})^{1/2} \tag{5}$$

The viscosity is assumed to fit with the four parameters Carreau model [15]

$$\frac{\eta - \eta_\infty}{\eta_0 - \eta_\infty} = [1 + (\delta|\dot{\gamma}|)^2]^{(n-1)/2} \tag{6}$$

where η_0 and η_∞ are the viscosity at low and high shear rate, respectively, δ is a characteristic time, and n is a dimensionless parameter. The fluid exhibits nearly Newtonian behavior both at low and high shear rate, whereas in-between the behavior is nearly that of a power-law fluid. Note that this model is suitable for free surface flows because the viscosity remains finite at zero shear rate, contrary to what is predicted by the power-law model. The fluid is Newtonian if $n=1$, shear thinning (or pseudoplastic) if $0<n<1$ and $\eta_\infty < \eta_0$. A Newtonian behavior can also be obtained by setting δ equal to zero, whatever the value of n. Note that a shear-thickening or so-called dilatant behavior can also be obtained through this model but is out of the scope of the present paper.

The primary flow is assumed to be parallel and steady. The velocity U varies only with y, and the pressure gradient in the x direction is zero. As a consequence, Eq. (1) is identically satisfied. For a given flow rate per unit width Q, the film thickness cannot be explicitly calculated; therefore, it cannot be taken as a length scale. Weinstein [16] proposed a length scale denoted by d_s and defined by

$$d_s = \left(\frac{\eta_0 Q}{\rho g \sin\beta}\right)^{1/3} \tag{7}$$

Dimensionless quantities, denoted by an overbar, are introduced as follows:

$$(\bar{x},\bar{y}) = (x/d_s, y/d_s) \quad (\bar{u},\bar{v}) = \left(\frac{ud_s}{Q}, \frac{vd_s}{Q}\right) \quad \bar{p} = \frac{pd_s^2}{\rho Q^2} \quad \bar{t} = \frac{tQ}{d_s^2} \tag{8}$$

Denoting the dimensionless velocity of the basic flow as $\bar{U} = Ud_s/Q$, the only non-zero dimensionless component of the stress tensor is supposed to have the following form:

$$\bar{\sigma}_{xy} = \bar{\eta}\frac{d\bar{U}}{d\bar{y}} \tag{9}$$

where

$$\bar{\eta} = I + (1-I)\left[1 + \left(L\frac{d\bar{U}}{d\bar{y}}\right)^2\right]^{(n-1)/2} \tag{10}$$

with $I = \eta_\infty/\eta_0$ and $L = \delta Q/d_s^2$.

Equations (2) and (3) become

$$\frac{d\bar{\sigma}_{xy}}{d\bar{y}} = -1 \tag{11}$$

$$\frac{d\bar{P}}{d\bar{y}} = \frac{\cot\beta}{\mathrm{Re}} \tag{12}$$

where $\bar{P}$ is the dimensionless basic hydrostatic pressure and the Reynolds number (Re) is defined by $\mathrm{Re} = \rho Q/\eta_0$. The no-slip condition at the solid boundary and the zero shear condition at the free surface are respectively given by

$$\bar{U}(\bar{d}) = 0 \tag{13}$$

$$\bar{\sigma}_{xy}(0) = 0 \tag{14}$$

where $\bar{d} = d/d_s$ is the dimensionless thickness. The governing equations integrate to

$$\bar{\sigma}_{xy} = -\bar{y} \tag{15}$$

$$\bar{P} = \frac{\bar{y}\cot\beta}{\mathrm{Re}} \tag{16}$$

Equations (9), (10), and (15) yield the following differential equation:

$$\left\{I + (1-I)\left[1 + \left(L\frac{d\bar{U}}{d\bar{y}}\right)^2\right]^{(n-1)/2}\right\}\frac{d\bar{U}}{d\bar{y}} = -\bar{y} \tag{17}$$

Equation (17) has to be solved for $\bar{y} \in [0,\bar{d}]$ with the boundary condition (13). A further relation is given by the fact that the dimensionless flow rate is equal to unity; that is,

$$\int_0^{\bar{d}} \bar{U}d\bar{y} = 1 \tag{18}$$

Equations (13), (17), and (18) constitute a nonlinear problem to determine the velocity field and the film thickness. It cannot be solved analytically in the general case. Weinstein [16] proposed an asymptotic solution when L approaches zero that is in the limit of a small non-Newtonian behavior. He obtained expansions in series of L for the velocity field and film thickness as

$$\bar{U} = \tfrac{1}{2}(3^{2/3} - \bar{y}^2) + \tfrac{1}{40}(I-1)(n-1)(3^{4/3} - 5\bar{y}^4)L^2 + O(L^4) \tag{19}$$

$$\bar{d} = 3^{1/3} - \tfrac{3}{10}(1-I)(n-1)L^2 + O(L^4) \tag{20}$$

We use the previous expressions for velocity and thickness in the asymptotic approach of the flow stability. To investigate the general case, the system has to be solved numerically. We use a

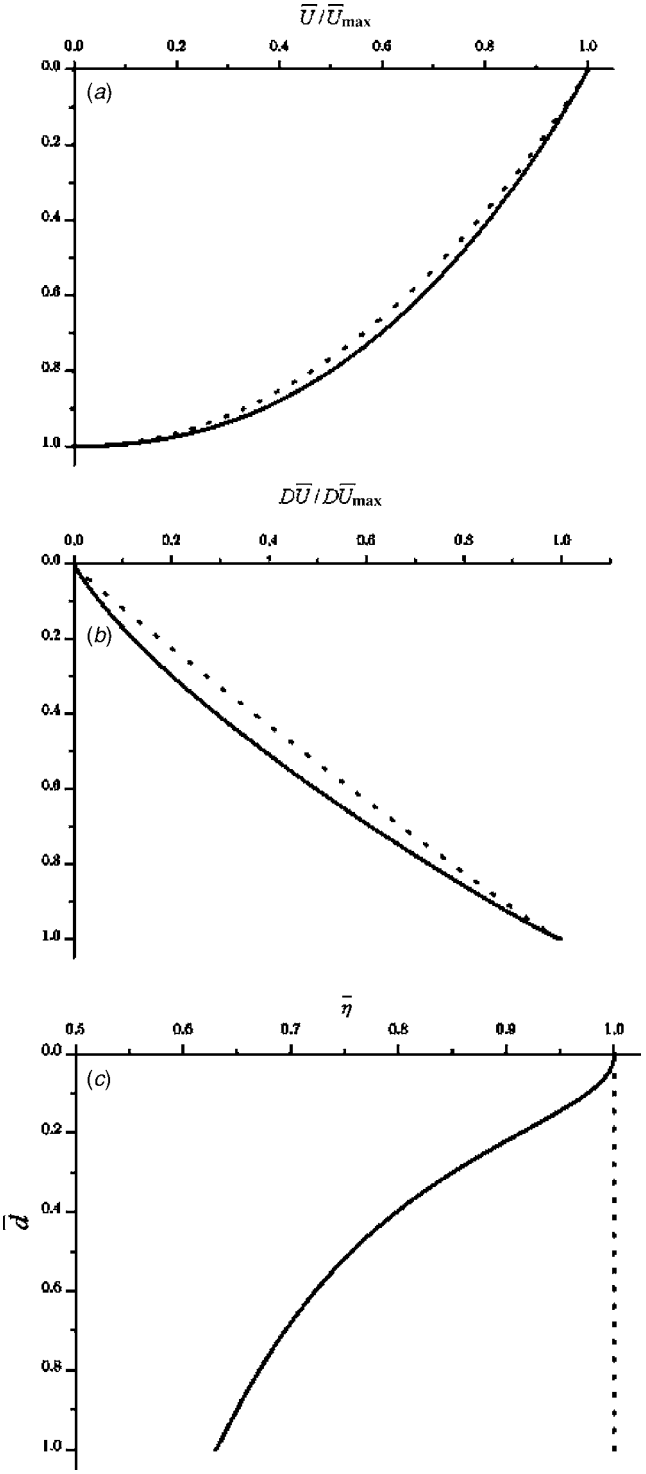

Fig. 2 Effect of shear-thinning behavior. Solid lines stand for the shear-thinning fluid (I=0, L=5, and n=0.8) and dotted lines for the Newtonian fluid. Comparison is made at equal angle β and at equal Reynolds number: (*a*) Velocity profiles, (*b*) rates of strain profiles, and (*c*) viscosity profiles.

finite difference scheme to convert the system of differential equations into a set of algebraic equations. The numerical solutions of the problem are used in the numerical approach of the stability analysis.

Some characteristics of the flow are illustrated through an example on Fig. 2. We compare the flows of a Newtonian fluid and of a shear-thinning fluid down an inclined plane at angle β. The comparison is made at equal flow per unit width Q, density ρ, and zero shear rate viscosity η_0 that is at equal Reynolds number. As a consequence, the length scale defined by Eq. (7) is the same for both fluids. Moreover, we set for the shear-thinning fluid I=0, L=5, and n=0.8. It is found that the film thickness is smaller in the shear-thinning case than for the Newtonian fluid. Indeed, we found $\bar{d}=1.2629$ for the shear-thinning fluid and $\bar{d}=3^{1/3}\approx 1.4422$ in the Newtonian case. In the following, the ordinates axis is normalized so that the film thickness is equal to unity in both cases. The maximum velocity denoted by U_{max} is reached at the free surface. It is greater for the shear-thinning fluid (U_{max} =1.1333) than for the Newtonian one (U_{max}=1.0289). Figure 2(*a*) displays the normalized velocity profiles U/U_{max} for both cases. In the shear-thinning case, we note a positive deviation compared to the classical parabolic velocity profile. The maximum strain rate, denoted by DU_{max} and reached at the solid boundary, is greater for the shear-thinning fluid for which DU_{max}=2.0020 than for the Newtonian one for which DU_{max}=1.4331. Figure 2(*b*) gives the normalized rates of strain profiles DU/DU_{max}, where DU denotes the rate of strain, whereas Fig. 2(*c*) shows the variation of viscosity $\bar{\eta}$. As one might expect, the viscosity is smaller than the zero shear rate viscosity everywhere except at the free surface. As a result, the normalized strain rate is found to be smaller than the one associated with the Newtonian fluid.

2.2 Stability Analysis. The stability problem is formulated following the small perturbation technique. Pressure and velocity components of the perturbed flow can be written as

$$\bar{u} = \bar{U}(\bar{y}) + \bar{u}'(\bar{x},\bar{y},\bar{t}) \tag{21}$$

$$\bar{v} = \bar{v}'(\bar{x},\bar{y},\bar{t}) \tag{22}$$

$$\bar{p} = \bar{P}(\bar{y}) + \bar{p}'(\bar{x},\bar{y},\bar{t}) \tag{23}$$

where a prime is used to denote the small perturbations. The fluctuation of the interface takes the following form:

$$\bar{\zeta} = \bar{\zeta}'(\bar{x},\bar{t}) \tag{24}$$

where $\bar{\zeta}=\zeta/d_s$.

In the following, we shall omit the overbars over dimensionless variables. We neglect the second-order terms in the primed quantities and make use of the fact that U and P satisfy the basic flow equations, so that the linearized governing equations for the disturbance become

$$\frac{\partial u'}{\partial x} + \frac{\partial v'}{\partial y} = 0 \tag{25}$$

$$\mathrm{Re}\left(\frac{\partial u'}{\partial t} + U\frac{\partial u'}{\partial x} + v'\frac{\partial u'}{\partial y}\right) = -\mathrm{Re}\frac{\partial p'}{\partial x} + \frac{\partial \sigma'_{xx}}{\partial x} + \frac{\partial \sigma'_{xy}}{\partial y} \tag{26}$$

$$\mathrm{Re}\left(\frac{\partial v'}{\partial t} + U\frac{\partial v'}{\partial x}\right) = -\mathrm{Re}\frac{\partial p'}{\partial y} + \frac{\partial \sigma'_{xy}}{\partial x} + \frac{\partial \sigma'_{yy}}{\partial y} \tag{27}$$

where

$$\sigma'_{xx} = 2\bar{\eta}\frac{\partial u'}{\partial x} \quad \sigma'_{yy} = 2\bar{\eta}\frac{\partial v'}{\partial y} \quad \sigma'_{xy} = \bar{\theta}\left(\frac{\partial u'}{\partial y} + \frac{\partial v'}{\partial x}\right)$$

and

$$\bar{\theta} = I + (1-I)\left[1 + n\left(L\frac{dU}{dy}\right)^2\right]\left[1 + \left(L\frac{dU}{dy}\right)^2\right]^{(n-3)/2} \tag{28}$$

At the solid boundary, the no-slip condition yields

$$\begin{cases} u' = 0 \\ v' = 0 \end{cases} \quad \text{at} \quad y = d \tag{29}$$

The kinematic condition at the free surface gives

$$v' = \frac{\partial \zeta}{\partial t} + U\frac{\partial \zeta}{\partial x} \quad \text{at} \quad y = 0 \tag{30}$$

At the free surface, the shear stress must vanish and the normal stress has to balance the normal stress induced by surface tension. These two conditions are given, respectively, by

$$\sigma'_{xy} - \zeta' = 0 \quad \text{at} \quad y = 0 \tag{31}$$

$$p'\mathrm{Re} + \zeta' \cot\beta - 2\bar{\eta}\frac{\partial v'}{\partial y} - \frac{1}{Ca}\frac{\partial^2 \zeta'}{\partial x^2} = 0 \quad \text{at} \quad y = 0 \tag{32}$$

where $Ca = \eta_0 Q/(Td_s)$, T being the surface tension. We now assume that there are two-dimensional normal mode solutions of the following form:

$$f' = \hat{f}(y)e^{i\alpha(x-ct)}$$

where variable f stands for u, v, p, and ζ, and the longitudinal wave number α is real and c is the complex velocity of the disturbance. The real part of c, denoted by c_R, is the phase speed and αc_I is the temporal growth rate, where c_I is the imaginary part of c. The flow is respectively stable, unstable, or neutrally stable according to whether c_I is negative, positive, or zero. Substituting these expressions into Eqs. (25)–(27) and the corresponding boundary conditions (29)–(32), and then eliminating p' and u', one obtains the linear stability equation for the flow. It is a generalized Orr-Sommerfeld equation for a purely viscous fluid as stated, for example, by Olsson and Henningson [17] but with additional terms introduced by the Carreau model

$$(D^2 + \alpha^2)[D^2\bar{\theta} + 2D\bar{\theta}D + \bar{\theta}(D^2 + \alpha^2)]\hat{v} - 4\alpha^2 D(\bar{\eta}D\hat{v}) = i\alpha\mathrm{Re}[(U - c)(D^2 - \alpha^2) - D^2 U]\hat{v} \tag{33}$$

where D denotes derivative with respect to y. The no-slip condition (29) becomes

$$\begin{cases} D\hat{v} = 0 \\ \hat{v} = 0 \end{cases} \quad \text{at} \quad y = d \tag{34}$$

and the kinematic condition (30) takes the form

$$[1 + (U - c)(D^2 + \alpha^2)]\hat{v} = 0 \quad \text{at} \quad y = 0 \tag{35}$$

The normal component of the dynamic boundary condition (32) becomes

$$i\alpha\mathrm{Re}[(c - U)D + DU]\hat{v} - 4\alpha^2\bar{\eta}D\hat{v} + (D^2 + \alpha^2)\left[\bar{\theta}D + D\bar{\theta} + i\alpha\bar{\theta}\left(\cot\beta + \frac{i\alpha^2}{Ca}\right)\right]\hat{v} = 0 \quad \text{at} \quad y = 0 \tag{36}$$

Equations (33)–(36) makeup a generalized eigenvalue problem, which enables one to determine the complex velocity c as a function of the wave number α.

3 Results

3.1 Asymptotic Approach. We study here, analytically, the stability of the flow with respect to long waves compared to the length scale d_s, i.e., for α in the vicinity of zero. For this purpose, we expanded $\hat{v}$ and c as regular perturbation series of α as follows:

$$\hat{v} = \hat{v}_0 + \alpha\hat{v}_1 + O(\alpha^2)$$

$$c = c_0 + \alpha c_1 + O(\alpha^2)$$

In addition, we suppose that the fluid is weakly non-Newtonian (i.e., for L tending toward zero) so that we can use Eqs. (19) and (20) as analytical expressions for film thickness and velocity field. Let us first examine the zero-order solution. Collecting the zero-order terms in Eq. (33) yields

$$\bar{\theta}D^4\hat{v}_0 + 2D\bar{\theta}D^3\hat{v}_0 + D^2\bar{\theta}D^2\hat{v}_0 = 0 \tag{37}$$

The no-slip condition takes the form

$$\begin{cases} D\hat{v}_0 = 0 \\ \hat{v}_0 = 0 \end{cases} \quad \text{at} \quad y = d \tag{38}$$

The normal component of the dynamic boundary condition becomes

$$D^3\hat{v}_0 = 0 \quad \text{at} \quad y = 0 \tag{39}$$

Moreover, a normalization condition is arbitrarily added, so that $\hat{v} = 1$ at $y = 0$. It means that at the free surface $\hat{v}_0 = 1$ and $\hat{v}_i = 0$, with $i \geq 1$. The zero-order solution is

$$\hat{v}_0 = \left(1 - \frac{2}{3^{1/3}}y + \frac{1}{3^{2/3}}y^2\right) + \left\{\frac{3^{2/3}}{60}(I - 1)(n - 1)y[-33y + 3^{1/3}(18 + 5y^3)]\right\}L^2 + O(L^4) \tag{40}$$

The kinematic condition (35) yields

$$\hat{v}_0 + (U - c_0)D^2\hat{v}_0 = 0 \quad \text{at} \quad y = 0 \tag{41}$$

The eigenvalue c_0 is determined as

$$c_0 = 3^{2/3} + \tfrac{9}{10}3^{1/3}(I - 1)(n - 1)L^2 + O(L^4) \tag{42}$$

An equation for the first-order approximation is obtained by collecting terms in order α^1 in Eq. (33)

$$\bar{\theta}D^4\hat{v}_1 + 2D\bar{\theta}D^3\hat{v}_1 + D^2\bar{\theta}D^2\hat{v}_1 = i\mathrm{Re}[(U - c_0)D^2\hat{v}_0 - \hat{v}_0 D^2 U] \tag{43}$$

The boundary conditions are

$$\begin{cases} D\hat{v}_1 = 0 \\ \hat{v}_1 = 0 \end{cases} \quad \text{at} \quad y = d \tag{44}$$

$$D^3\hat{v}_1 + i\{\mathrm{Re}[(c_0 - U)D\hat{v}_0 + \hat{v}_0 DU] + \cot\beta D^2\hat{v}_0\} = 0 \quad \text{at} \quad y = 0 \tag{45}$$

$$\hat{v}_1 = 0 \quad \text{at} \quad y = 0 \tag{46}$$

The first-order eigenvector is thus

$$\hat{v}_1 = \left(\frac{-iy}{180}\right)[\mathrm{Re}(-63 + 48 \times 3^{2/3}y - 30 \times 3^{1/3}y^2 + 3^{2/3}y^4) + 20\cot\beta(3 - 2 \times 3^{2/3}y + 3^{1/3}y^2)] + \left(\frac{-iy}{25200}\right)(I - 1)(n - 1) \times [\mathrm{Re}(-5679 \times 3^{2/3} + 10368 \times 3^{1/3}y - 5040y^2 + 1680 \times 3^{2/3}y^3 - 1953 \times 3^{1/3}y^4 + 130 \times 3^{2/3}y^6) - 140\cot\beta(24 \times 3^{2/3} - 60 \times 3^{1/3}y + 33y^2 + 10 \times 3^{2/3}y^3 - 9 \times 3^{1/3}y^4)]L^2 + O(L^4) \tag{47}$$

The kinematic condition (35) becomes

$$\hat{v}_1 + (U - c_0)D^2\hat{v}_1 - c_1 D^2\hat{v}_0 = 0 \quad \text{at} \quad y = 0 \tag{48}$$

Finally, we obtain the expression of the first-order eigenvalue

$$c_1 = \frac{i}{5}(6\mathrm{Re} - 5\cot\beta) + \frac{3^{5/3}}{175}i(I - 1)(n - 1)(-35\cot\beta + 113\mathrm{Re})L^2 + O(L^4) \tag{49}$$

Setting $c_I = \alpha c_1$ equal to zero yields then the critical Reynolds number

Table 1 Critical Reynolds number versus N for $\beta=1'$, $I=0.1$, $n=0.5$, and $\delta=0.05$

Number of modes N	90	120	150	180
Critical Reynolds number	3206	3197	3196	3196

$$\mathrm{Re}_{cr} = \frac{5}{6}\cot\beta - \frac{71}{28\times 3^{1/3}}(I-1)(n-1)\cot\beta L^2 + O(L^4) \tag{50}$$

In the case of Newtonian fluids, i.e. $L=0$ and/or $n=1$, the celerity and the critical Reynolds number given by Eqs. (42) and (50), respectively, are in agreement with those given by Benjamin [1] and Yih [2].

Equation (50) leads to the conclusion that for the shear-thinning case ($I<1$ and $n<1$), the critical Reynolds number is less than that for the Newtonian case although it remains proportional to $\cot\beta$. Moreover, the phase speed c_R is found larger than that corresponding to the Newtonian fluid. The increase of the celerity c_0 with L is steeper than that of the free surface velocity $\bar{U}(0)$. Benjamin [1] and Yih [2] showed that the celerity is twice the free surface velocity for a Newtonian fluid. This ratio is all the more important as the fluid is shear thinning and could have a non-negligible role in the stability characteristics of the layer.

The destabilizing effect of the perturbation flow convection by the base flow underscored by Smith [3] is indeed proportional to $U(0)-c_0$; as this term is increased, it becomes more and more important in comparison to the stabilizing pressure gradient.

3.2 Numerical Approach

3.2.1 Numerical Procedure. The numerical part of this work consists of solving the Orr-Sommerfeld generalized eigenvalue problem (33)–(36). A spectral collocation method based on Chebyshev polynomials is chosen for the discretization. This method is extensively described by Olsson and Henningson [17]. The eigenfunctions are expanded in Chebyshev series

$$\hat{v}(y) = \sum_{n=0}^{N} v_n T_n(y)$$

with N the number of modes. The kth derivative is obtained by

$$D^{(k)}\hat{v}(y) = \sum_{n=0}^{N} v_n T_n^{(k)}(y)$$

The system (33)–(36) has to be solved at the Gauss-Lobatto collocation points $y_j=\cos(j\pi/N)$. It has to be set in the following form:

$$[A]\hat{v} = c[B]\hat{v} \tag{51}$$

with $\hat{v}$ the vector containing the algebraic values of the disturbance velocity at each collocation point. The dimension of the square matrices $[A]$ and $[B]$ is determined by the number of modes N. Equation (51) is a generalized eigenvalue problem whose eigenvalues are the complex velocities c. For each eigenvalue, we define the associated growth rate as $\omega_I=\alpha c_I$. The linear stability is determined by the sign of the maximum growth rate. We then identify the most unstable mode and determine if the flow is stable ($\omega_I\leq 0$) or unstable ($\omega_I>0$).

The border between stable and unstable regions is said neutral curve.

The number of modes N is set to 150 to provide sufficient accuracy. The case of small angles of inclination ($\beta<0.5$ deg) has been chosen to check computations accuracy. Indeed, as shown by Floryan [5], the critical Reynolds number for the onset of instabilities varies very fast with β. Table 1 shows the calculated critical Reynolds number versus N through an example. For N over 120, numerical results do not vary significantly.

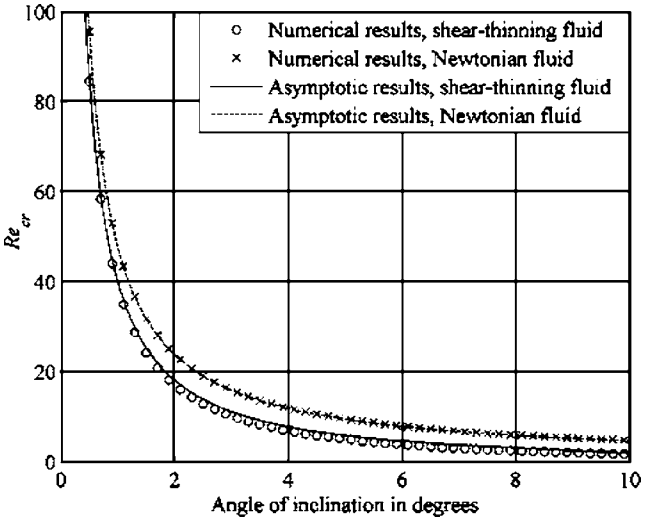

Fig. 3 Critical Reynolds number R_c versus β with $I=5\times10^{-5}$ and $n=0.5$. Parameter δ is set to 0 in the Newtonian case and to 0.1 in the shear-thinning case.

We look for the flow stability for various values of the governing parameters L, n, and β. The systematic study of the influence of I have not been carried out. Indeed, parameter I represents the relative positions of Newtonian viscosities η_0 and η_∞. In all our computations, shear rates remain moderate and I is taken small. Consequently, this parameter does not directly influence the shear-thinning behavior of the fluid. Note that each comparison is made at equal value of viscosity ratio I.

Two kinds of instabilities may arise: surface and shear instabilities. A way to identify which one occurs is to compare the phase speed c_R to the free surface velocity $\bar{U}(0)$. An instability is known as a surface mode when $c_R>\bar{U}(0)$ and as a shear mode in the opposite case. Note that the instability type can also be determined according to the range of the disturbance wavelength. Indeed, surface tension tends to stabilize small wavelength instabilities so that only long wavelength surface instabilities can grow up.

3.2.2 Comparison Between Newtonian and Shear-Thinning Cases. The Newtonian case is a particular shear-thinning case and can be obtained by setting $\delta=0$ or $n=1$ in Eq. (6). The Newtonian case is first considered in order to check the agreement of both the asymptotic and the numerical approaches with previous results from Yih [2] and Floryan et al. [5]. The study is then extended to the shear-thinning case, over a wider range of parameter values than those used in the asymptotic approach and only valid in the nearly Newtonian region.

The curves displayed in Fig. 3 give the evolution of the critical Reynolds number versus the angle of inclination. The lines correspond to the asymptotic approach based on the long-wave approximation: the dashed line gives the results for a Newtonian fluid and the full line for a shear-thinning fluid. The crosses and dots represent the numerical results in the shear-thinning and Newtonian cases, respectively. From Fig. 3, it is clear that the asymptotic approach gives results that are quantitatively in good agreement with those of the numerical approach. This validates the long-wave asymptotic approach for the investigated set of parameters. It is important to note that for angles of inclination larger than $\beta>0.5'$, the instabilities observed for large wavelengths are surface instabilities. This result is in agreement with those of the literature from Floryan et al. [5].

3.2.3 Effect of Shear-Thinning Properties. The effects of the

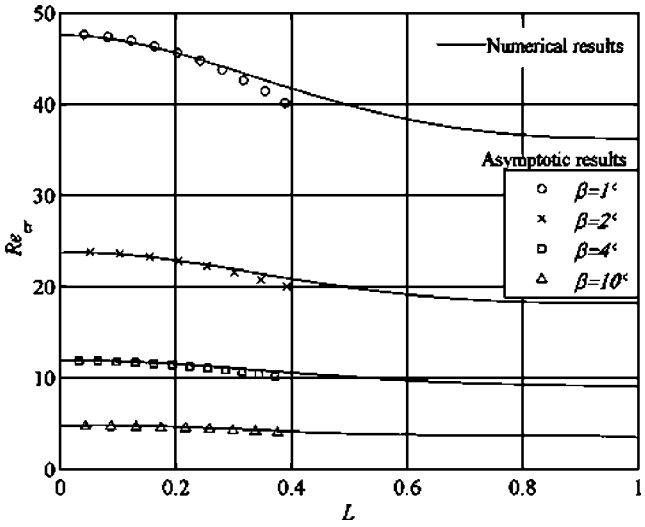

Fig. 4 Critical Reynolds number versus L for different angles of inclination with $I=5.10^{-5}$ and $n=0.5$

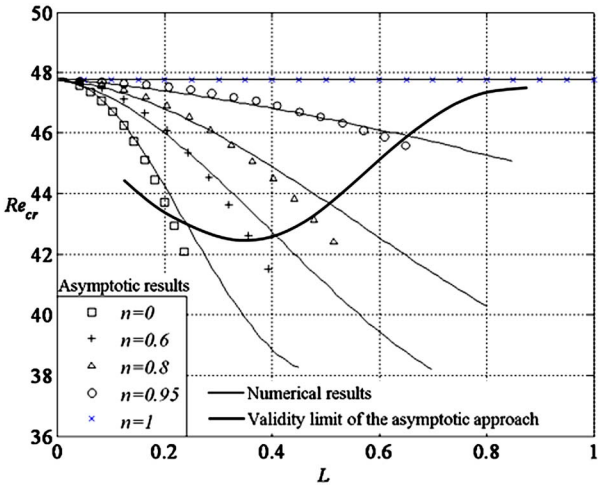

Fig. 6 Critical Reynolds number versus L for different values of n with $I=5\times10^{-5}$ and $\beta=1°$

shear-thinning property on the stability of a film flowing down an inclined plane are examined by considering the influence of two particular parameters L and n, which appear in the dimensionless Carreau model given by Eq. (10). Figure 4 gives the evolution of the critical Reynolds number versus parameter L for different angles of inclination. The lines are obtained through the asymptotic approach and the points through the numerical one. Note that increasing L means an increase in the nonlinearity of the tangential stress with respect to velocity gradients. Both methods lead to the conclusion that increasing L will make the flow more unstable. Moreover, we show in Fig. 4 that this tendency is enhanced as β decreases. In the case of a small non-Newtonian behavior ($L\ll1$), it can be expected from Eq. (50) that the critical Reynolds number is proportional to $(5/6)\cot\beta$. It has been verified in Fig. 5 that normalizing the ordinate axis of Fig. 4 by the maximum value of the critical Reynolds number $\mathrm{Re_{cr}}\max=(5/6)\cot\beta$, which corresponds to the critical Reynolds number for the Newtonian case ($L=0$), results in a collapse of the curves, so that the plot is independent of β. Thus, the angle of inclination is found to be a proportionality factor for the critical Reynolds number whatever the value of L. The obtained single curve reveals three behaviors: for $L<0.2$, it is found to fit with asymptotic results given by Eq. (50), for $0.2<L<0.6$, a linear evolution is observed, and for much larger values of L, the curve seems to tend asymptotically toward 0.75.

In Fig. 6 several curves are sketched representing the stability limit for a shear-thinning fluid versus parameter L for different values of n ranging from 0 to 1. We note that the film becomes more unstable as n decreases because it corresponds to a decrease in the mean viscosity. This fact has been pointed by Hwang et al. [11] for power-law fluids. Let us compare asymptotic and numerical results. In the particular case of the Newtonian fluid ($n=1$ whatever the value of L, or $L=0$ whatever the value of n), numerical and asymptotic results are in good agreement. It remains valid for small values of L and when n is in the vicinity of 1. The agreement progressively decreases as L and n are moved away from these conditions. In the asymptotic approach the shear-thinning fluid case is considered with its linearized form for the viscosity based on the assumption that $L^2DU_{\max}^2\ll1$. Thus, it is desirable to have an idea concerning the effect of this linearization on the stability results. We then derived parameter ε, which measures the relative difference between the linearized part of the viscosity expression, and its corresponding nonlinearized form used respectively in the asymptotic and numerical approaches as

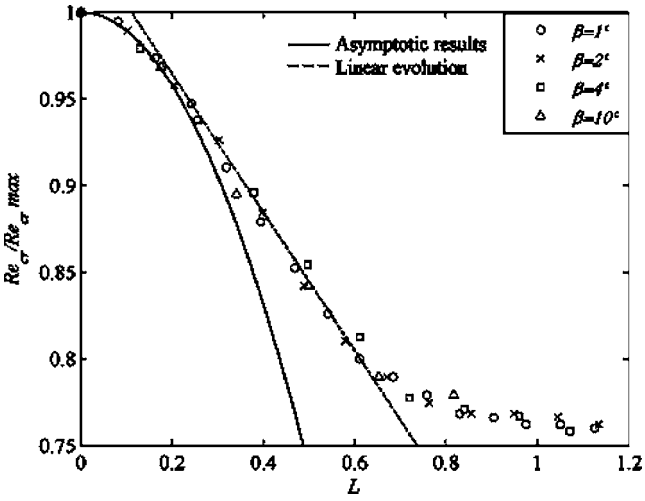

Fig. 5 Normalized critical Reynolds number versus L for different angles of inclination with $I=5\times10^{-5}$ and $n=0.5$

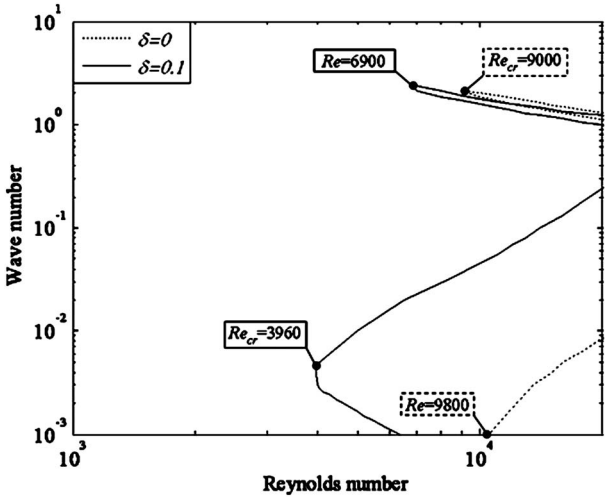

Fig. 7 Neutral curves for $\beta=0.3'$, $I=0.1$, and $n=0.5$

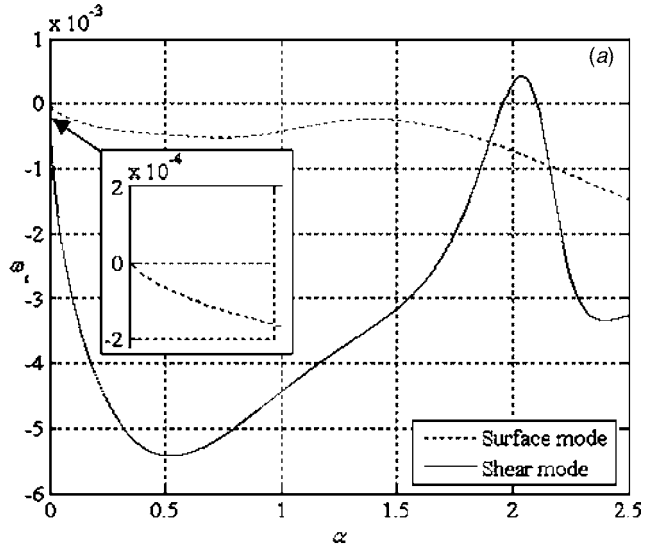

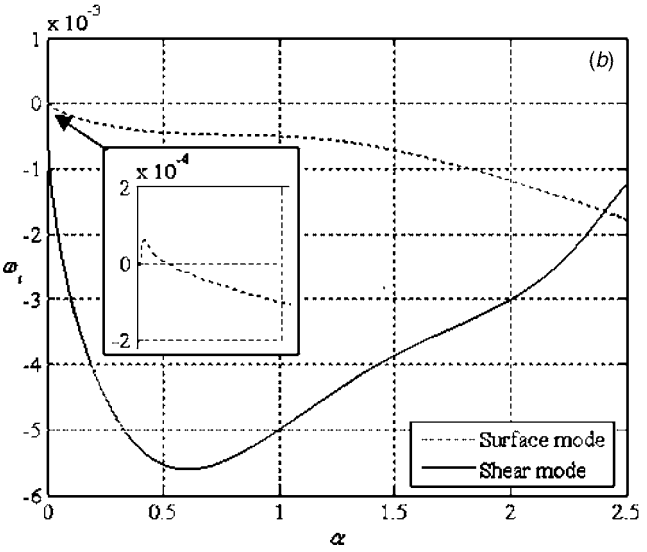

Fig. 8 Growth rate ω_I versus wave number α for $\beta=0.3'$, $I=0.1$, and $n=0.5$: (*a*) $\delta=0$ and Re=9500, (*b*) $\delta=0.1$ and Re =6000

$$\varepsilon = \left| \frac{(1+L^2 D U_{\max}^2)^{(n-1)/2} - \left(1 + L^2 \frac{n-1}{2} D U_{\max}^2\right)}{(1+L^2 D U_{\max}^2)^{(n-1)/2}} \right| \quad (52)$$

It is possible to determine the domain of validity of the asymptotic approach by giving a maximum admissible value for ε. We set arbitrarily $\varepsilon=10^{-3}$ as a limit above which the two methods diverge significantly. This limit is shown in Fig. 6 by a thick line. It tends asymptotically towards the line $n=1$ as $\varepsilon=0$ for a Newtonian fluid.

The results concerning a small inclination angle $\beta=0.3'$ are shown in Fig. 7. In this figure, the two neutral curves correspond to a Newtonian ($\delta=0$) and a shear-thinning ($n=0.5$, $\delta=0.1$, and $I=0.1$) fluid, respectively. They both exhibit two relative minima in terms of Reynolds number; the values of these minima are specified in Fig. 7. For Newtonian fluids, Benjamin [1] identified the instability that can occur as a surface mode in the long-wave approximation. Floryan et al. [5] identified, for small inclination angles $\beta<0.5'$, a second kind of unstable mode, which is the shear mode characterized by a wavelength on the order of the layer thickness and a wave speed c_R smaller than the undisturbed surface velocity.

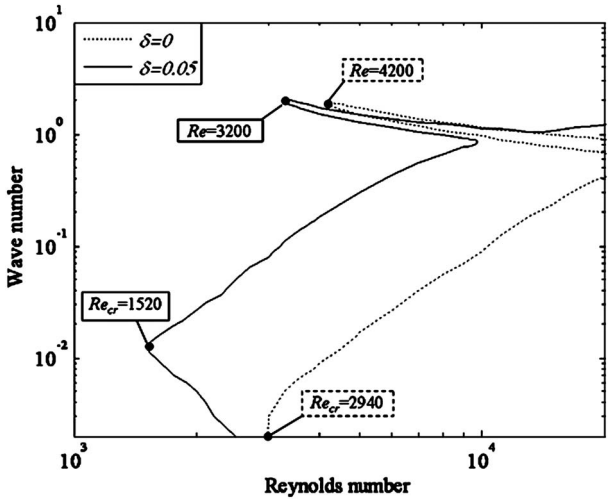

Fig. 9 Neutral curves for $\beta=1'$, $I=0.1$, and $n=0.5$

The results presented in Fig. 8 clearly show that in the Newtonian fluid case the most unstable mode is a surface mode, whereas for a shear-thinning fluid, the most unstable mode is the shear mode. To illustrate this clearly, we displayed the evolution of the growth rate $\omega_i=\alpha c_i$ with the wave number α, in Fig. 8(*a*) for a Newtonian fluid ($\delta=0$) and in Fig. 8(*b*) for a shear-thinning fluid ($\delta=0.1$). The values of Reynolds numbers have to be correctly chosen in order to point out only one of the two kinds of instabilities. From Fig. 8(*a*), the only positive growth rate giving rise to instabilities is located at a wave number α close to 2. One can check that this is indeed a shear mode because the celerity of this mode is lower than the base surface velocity as shown in Table 2. On the contrary, in Fig. 8(*b*), the other mode arises. It is a surface mode for a wave number α close to 0.

As we can note from Fig. 9, which shows the results for $\beta=1'$, in the Newtonian fluid case ($\delta=0$) as well as in the shear-thinning fluid ($n=0.5$ and $\delta=0.05$), the shear mode is now always preceded by the surface mode whatever the value of δ. The only instability that can grow up is thus a surface instability as shown in Table 3.

The previous results bring us to the conclusion that the stability of the layer can be deeply influenced by the viscosity distribution so that it can change the nature of the instability. However, this property to change the nature of the instability disappears when the inclination angle becomes larger than $0.5'$.

Table 2 Instability type for $\beta=0.3'$, $I=0.1$, and $n=0.5$ related to Fig. 7

δ	α	Re	$U(y=0)$	c_R	Instability type
0	2.05	9500	0.440	0.173	Shear mode
0.1	0.00255	6000	0.246	2.406	Surface mode

Table 3 Instability type for $\beta=1'$, $I=0.1$, and $n=0.5$ related to Fig. 9

δ	α	Re	$U(y=0)$	c_R	Instability type
0	0.01	2000	0.232	2.311	Surface mode
0.05	0.001	4000	0.283	2.027	Surface mode

4 Conclusions

Linear stability analysis has been carried out to investigate the stability characteristics of a shear-thinning fluid (Carreau fluid) flowing down an inclined plane. Two approaches have been used: a long-wave asymptotic approach applied to quasi-Newtonian fluids and a numerical approach based on the solution of a generalized eigenvalue problem, obtained from the discretization of the Orr-Sommerfeld equation. It has been shown that at the layer surface the waves travel faster for a shear-thinning fluid than for a Newtonian fluid. The critical Reynolds number for the onset of the instabilities is found proportional to cot β because as it is the case for Newtonian fluids. However, the proportionality factor decreases when the shear-thinning behavior becomes stronger. The threshold is thus always lower than that in the Newtonian case. In some range of the governing parameters ($L \to 0$ and $n \to 1$), the long wave asymptotic approach gives results in good agreement with those of the numerical approach. Depending on the angle of inclination, the stability of a shear-thinning fluid can be somewhat influenced by the viscosity distribution. The nature of the instability changes from shear instability to surface instability for an angle of inclination slightly lower than that given in the literature for Newtonian fluids.

Acknowledgment

We would like to thank T. Akbar for fruitful discussions. We also thank the referees for the care they brought to the reading of this paper.

References

[1] Benjamin, T. B., 1957, "Wave Formation in Laminar Flow Down an Inclined Plane," J. Fluid Mech., **2**, pp. 554–573.

[2] Yih, C., 1963, "Stability of Liquid Flow Down an Inclined Plane," Phys. Fluids, **6**(3), pp. 321–334.

[3] Smith, M. K., 1976, "The Mechanism for the Long-Wave Instability in Thin Liquid Film," J. Fluid Mech., **217**, pp. 469–485.

[4] De Bruin, J. G., 1974, "Stability of a Layer of Liquid Flowing Down an Inclined Plane," J. Eng. Math., **8**, pp. 259–270.

[5] Floryan, J. M., Davis, S. H., and Kelly, R. E., 1987, "Instability of a Liquid Film Flowing Down a Slightly Inclined Plane," Phys. Fluids, **30**, pp. 983–989.

[6] Yih, C., 1965, "Stability of a Non-Newtonian Liquid Film Flowing Down an Inclined Plane," Phys. Fluids, **8**(7), pp. 1257–1262.

[7] Gupta, A. S., 1957, "Stability of a Visco-Elastic Liquid Film Flowing Down an Inclined Plane," J. Fluid Mech., **28**, pp. 17–28.

[8] Liu, K. F., and Mei, C. C., 1989, "Slow Spreading of a Sheet of Bingham Fluid on an Inclined Plane," J. Fluid Mech., **207**, pp. 505–529.

[9] Lai, W., 1967, "Stability of an Elastico-Viscous Liquid Film Flowing Down an Inclined Plane," Phys. Fluids, **10**, pp. 844–847.

[10] Shaqfeh, E. S. G., Larson, R. G., and Fredrickson, G. H., 1989, "The Stability of Gravity Driven Viscoelastic Film-Flow at Low to Moderate Reynolds Number," J. Non-Newtonian Fluid Mech., **31**, pp. 87–113.

[11] Hwang, C. C., Chen, J. L., Wang, J. S., and Lin, J. S., 1994, "Linear Stability of Power Law Liquid Film Flows Down an Inclined Plane," J. Phys. D, **27**, pp. 2297–2301.

[12] Andersson, H. I., and Dahl, E. N., 1999, "Gravity-Driven Flow of a Viscoelastic Liquid Film Along a Vertical Wall," J. Phys. D, **32**, pp. 1557–1562.

[13] Chen, K. P., 1992, "The Onset of Elastically Driven Wavy Motion in the Flow of Two Viscoelastic Liquid Films Down an Inclined Plane," J. Non-Newtonian Fluid Mech., **45**, pp. 21–45.

[14] Huang, C. T., and Khomami, B., 2001, "The Instability Mechanism of Single and Multilayer Newtonian and Viscoelastic Flows Down an Inclined Plane," Rheol. Acta, **40**, pp. 467–484.

[15] Carreau, P. J., De Kee, D., and Daroux, M., 1979, "An Analysis of the Viscous Behavior of Polymeric Solutions," Can. J. Chem. Eng., **57**, pp. 135–141.

[16] Weinstein, S. J., 1990, "Wave Propagation in the Flow of Shear-Thinning Fluids Down an Incline," AIChE J., **36**(12), pp. 1873–1889.

[17] Olsson, P. J., and Henningson, D. S., 1995, "Optimal Disturbance Growth in Watertable Flow," Stud. Appl. Math., **94**, pp. 183–210.

Assessment and Modification of One-Equation Models of Turbulence for Wall-Bounded Flows

M. Elkhoury
Assistant Professor
Department of Mechanical Engineering,
Lebanese American University,
P. O. Box 36,
Byblos, Lebanon
e-mail: mkhoury@lau.edu.lb

This work assesses the performance of two single-equation eddy viscosity transport models that are based on Menter's transformation of the k-ε and the k-ω closures. The coefficients of both models are set exactly the same and follow directly from the constants of the standard k-ε closure. This in turn allows a cross-comparison of the effect of two different destruction terms on the performance of single-equation closures. Furthermore, some wall-free modifications to production and destruction terms are proposed and applied to both models. An assessment of the baseline models with and without the proposed modifications against experiments, and the Spalart-Allmaras turbulence model is provided via several boundary-layer computations. Better performance is indicated with the proposed modifications in wall-bounded nonequilibrium flows.
[DOI: 10.1115/1.2743666]

Introduction

Since the advent of the computational resources, turbulence modeling has become an increasingly useful tool in the aerodynamics design of aerospace vehicles. Before the evolution of single-equation models, algebraic models such as Cebeci Smith [1] and Baldwin Lomax [2] were used to determine the eddy viscosity based on an algebraic length scale, which becomes harder to determine in complex nonequilibrium flows. Two-equation closures such as the k-ε and the k-ω models were also used for aerodynamic flows where the eddy viscosity is calculated from the two dependent variables k and ε (or ω). These models perform very well in simple separated flows. However, they fail in many nonequilibrium turbulent flows [3]. As a result, several modifications have been proposed that improve the predictive capabilities of the two-equation models. Speziale [4] and Rubinstein and Barton [5] proposed two-equation models that are nonlinear in the mean strain rate. An explicit algebraic stress equation was also proposed by Gatski and Speziale [6] and successfully applied to nonequilibrium turbulent flows by Abid et. al [3].

Single-equation models solve directly for the eddy viscosity without computing the full range of turbulent time and length scales. This form of transport equation has recently been an interest to many researchers [7–10] due to its accuracy, simplicity of implementation, and less demanding computational requirements. The Baldwin Barth (BB) model [11] was among the first single-equation models to be self-consistent by avoiding the use of algebraic length scales and the first that was derived using the k-ε closure. During the transformation, however, some other major assumptions were made that broke the link with its parent k-ε model. As a result, the BB model performs totally different from its underlying k-ε model, even in simple equilibrium flows [9].

To a large extent, the failure of the BB turbulence model lies in the destruction term. Besides being sensitive to the free-stream value of the turbulent Reynolds number, the BB model tends to respond strongly to an adverse pressure gradient, in the sense that it always predicts a large decrease in skin friction relative to the measured values [12–14]. It also yields unexpected results, such as prediction of separation in attached flows with mild to strong adverse pressure gradients. In addition, the diffusive term that was not directly connected to the k-ε model renders the equation ill conditioned in the shear layer regions. However, the BB model has good near-wall benign properties such as the linear behavior of its transport property, which in turn does not require a finer grid than an algebraic model would. Spalart and Allmaras (SA) [15] derived their model using empirical criteria and arguments from dimensional analysis. Their model is not linked to the k-ε equations. The motivation for this approach is that the BB model is constrained by assumptions inherited from the k-ε model. The model was calibrated for a certain class of flows that includes airfoils and wings, and has a provision for transition onset built in to trip the boundary layer.

Menter [9], in his transformation from the k-ε closure to the single-equation model, has shown a closer bond than the BB model in his use of Bradshaw's assumption (i.e., the shear stress in the boundary layer is proportional to the turbulent kinetic energy). Menter also indicated that using Bradshaw's assumption seems to be more effective in nonequilibrium flows. However, transforming the k-ε closure may carry many of its deficiencies, such as the bad performance in wall-bounded flows in the presence of mild adverse pressure gradients. It should be noted that Menter aimed to establish a firm connection between the one- and two-equation models rather than endorsing a new model.

In this work, two one-equation models that differ only in the form of the destruction term are assessed against each other. These models follow from the transformation of the k-ε and k-ω closures. Because of the transformation complexity, the wall-limiting behavior is extremely hard to derive from the low-Reynolds-number (LRN) terms of the k-ε model, and thus Menter's near-wall damping functions are used for all models. Although the author believes that a specific form of damping functions has little to no effect on the results of high-Reynolds-number (HRN) flows, using Menter's damping functions eliminates the criticism of having different LRN formulations and their effect on the predictive capabilities of the considered models. Furthermore, both models are assigned the same constants that are based on the transformation of the k-ε closure. Therefore, the impact of different destruction terms on the predictive capabilities is studied via several boundary-layer computations.

With this baseline, further modifications are proposed to both

Contributed by the Fluids Engineering Division of ASME for publication in the JOURNAL OF FLUIDS ENGINEERING. Manuscript received September 19, 2006; final manuscript received January 25, 2007. Assoc. Editor: Ugo Piomelli.

models and assessed against experiments and the SA model. The proposed modifications have no effect for zero pressure gradient flows. However, they improve the predictive capabilities of the models in wall-bounded nonequilibrium flows and retain their wall-distance-free feature. The latter renders these models more flexible to utilize in highly complex flows compared to the SA model.

Menter Turbulence Model and Proposed Modifications

Menter Eddy Viscosity Transport Model. The HRN form of the two-equation k-ε model is written in boundary-layer coordinates as follows:

$$\frac{Dk}{Dt} = \tilde{\nu}_T\left(\frac{\partial u}{\partial y}\right)^2 + \frac{\partial}{\partial y}\left(\frac{\tilde{\nu}_T}{\sigma_k}\frac{\partial k}{\partial y}\right) - \varepsilon$$

$$\frac{D\varepsilon}{Dt} = c_{\varepsilon 1}\frac{\varepsilon}{k}\tilde{\nu}_T\left(\frac{\partial u}{\partial y}\right)^2 + \frac{\partial}{\partial y}\left(\frac{\tilde{\nu}_T}{\sigma_\varepsilon}\frac{\partial \varepsilon}{\partial y}\right) - c_{\varepsilon 2}\frac{\varepsilon^2}{k} \tag{1}$$

where $D(\,)/Dt$ stands for the substantial derivative. The eddy viscosity is defined as

$$\tilde{\nu}_T = C_\mu \frac{k^2}{\varepsilon} \tag{2}$$

Following Baldwin and Barth, a transport equation for the eddy viscosity can be defined (by taking the substantial derivative of Eq. (2)) as follows:

$$\frac{D\tilde{\nu}_T}{Dt} = 2\frac{\tilde{\nu}_T}{k}\frac{Dk}{Dt} - \frac{\tilde{\nu}_T}{\varepsilon}\frac{D\varepsilon}{Dt} \tag{3}$$

The substantial derivatives for k and ε in Eq. (3) are replaced by substituting the right-hand side of Eq. (1). The transport equation for the eddy viscosity is obtained as

$$\frac{D\tilde{\nu}_T}{Dt} = F(\tilde{\nu}_T, k, \varepsilon) \tag{4}$$

Equation (4) depends on k, ε, and the eddy viscosity. The turbulence energy dissipation (ε) can be eliminated by using Eq. (2), which leaves the eddy transport equation a function of the turbulent kinetic energy and the eddy viscosity. The Bradshaw relation or the turbulent structure parameter is used to eliminate k:

$$|-\overline{uv}| = \sqrt{C_\mu}k = \tilde{\nu}_T\left|\frac{\partial u}{\partial y}\right| \tag{5}$$

The main assumption in the derivation of the one-equation model is that the turbulent shear stress is proportional to the turbulent kinetic energy, which is equivalent to the assumption of $\text{Production}_k = \text{Dissipation}_k$ in standard two-equation models. The second assumption that is used in deriving the transport equation is $\sigma = \sigma_\varepsilon \equiv \sigma_k$. A more detailed derivation can be found in Ref. [9] and is not repeated here. The resulting HRN transport equation for the eddy viscosity follows as

$$\frac{D\tilde{\nu}_T}{Dt} = c_1\tilde{\nu}_T\left|\frac{\partial u}{\partial y}\right| + \frac{\partial}{\partial y}\left(\frac{\tilde{\nu}_T}{\sigma}\frac{\partial \tilde{\nu}_T}{\partial y}\right) - c_2\frac{\tilde{\nu}_T^2}{L_{\text{VK}}^2} \tag{6}$$

This is the Menter model (with no damping function). L_{VK} is the von Karman mixing length scale defined as

$$\frac{1}{L_{\text{VK}}} = \frac{\dfrac{\partial}{\partial y}\left|\dfrac{\partial u}{\partial y}\right|}{\left|\dfrac{\partial u}{\partial y}\right|} \tag{7}$$

The model's coefficients c_1 and c_2 are related to the k-ε constants by

$$c_1 = (c_{\varepsilon 2} - c_{\varepsilon 1})\sqrt{C_\mu} \tag{8}$$

and

$$c_2 = \frac{(c_{\varepsilon 2} - c_{\varepsilon 1})\sqrt{C_\mu}}{\kappa^2} + \frac{1}{\sigma} \tag{9}$$

where $\kappa = 0.41$ is the Karman constant. Note that σ was chosen equal to σ_k and not equal to σ_ε. With the latter choice, the transformation leads to $c_2 = 2/\sigma_\varepsilon$. Furthermore, the production term in Eq. (6) results from the imbalance of the production and destruction processes in the ε equation. A similar procedure is followed to transform the k-ω model into the following one-equation model:

$$\frac{D\tilde{\nu}_T}{Dt} = c_1\tilde{\nu}_T\left|\frac{\partial u}{\partial y}\right| + \frac{\partial}{\partial y}\left(\frac{\tilde{\nu}_T}{\sigma}\frac{\partial \tilde{\nu}_T}{\partial y}\right) - c_2\frac{\tilde{\nu}_T}{L_{\text{VK}}}\left|\frac{\partial \tilde{\nu}_T}{\partial y}\right| \tag{10}$$

This is the one-equation k-ω based model (from now on referred to as $(k\text{-}\omega)_{1\text{E}}$ based model) with no damping functions. The constants c_2 and c_1 corresponding to Eqs. (8) and (9), respectively, are calculated based on the values of the standard k-ε closure ($c_{\varepsilon 1} = 1.44$ and $c_{\varepsilon 2} = 1.92$), and the diffusion coefficient was taken as $\sigma = 1.0$. All occurrences of the strain rates are replaced by the absolute value of the vorticity S:

$$\left|\frac{\partial u}{\partial y}\right| \rightarrow S \tag{11}$$

Alternative formulations like the strain rate $\sqrt{U_{ij}U_{ij}}$ are also possible, with little difference in thin shear flows [9]. The inverse of the von Karman mixing length scale follows as

$$\frac{1}{L_{\text{VK}}^2} \rightarrow \frac{\dfrac{\partial S}{\partial x_j}\dfrac{\partial S}{\partial x_j}}{S^2} \tag{12}$$

Two damping functions that were introduced by Menter [9] are used in all models. The final forms of the original one-equation models with the limiters [9] to prevent singularity in the destruction term if $L_{\text{VK}} \rightarrow 0$ are

$$\frac{D\tilde{\nu}_T}{Dt} = D_1 c_1 \tilde{\nu}_T S + \frac{\partial}{\partial x_j}\left(\frac{\tilde{\nu}_T}{\sigma}\frac{\partial \tilde{\nu}_T}{\partial x_j}\right) - c_2 c_3 \min\left(\frac{\tilde{\nu}_T^2}{c_3 L_{\text{VK}}^2}, \frac{\tilde{\nu}_T^2 S\sqrt{\tilde{\nu}_T/\nu}}{\nu}\right) \tag{13}$$

$$\frac{D\tilde{\nu}_T}{Dt} = D_1 c_1 \tilde{\nu}_T S + \frac{\partial}{\partial x_j}\left(\frac{\tilde{\nu}_T}{\sigma}\frac{\partial \tilde{\nu}_T}{\partial x_j}\right) - c_2 c_3 \min\left(\frac{\tilde{\nu}_T}{c_3 L_{\text{VK}}}\left|\frac{\partial \tilde{\nu}_T}{\partial x_j}\right|, \frac{\tilde{\nu}_T^2 S\sqrt{\tilde{\nu}_T/\nu}}{\nu}\right) \tag{14}$$

with the damping function in front of the production term given as

$$D_1 = \frac{\nu_T + \nu}{\tilde{\nu}_T + \nu} \tag{15}$$

Equations (13) and (14) are the Menter model and the $(k\text{-}\omega)_{1\text{E}}$ based model with (k-ε) constants, as implemented by the author for all results that will be presented later. The constant c_3 is set to 7.0 [9]. In most flows $\tilde{\nu}_T^2/c_3 L_{\text{VK}}^2 \ll (\tilde{\nu}_T^2 S\sqrt{\tilde{\nu}_T/\nu})/\nu$ and the original formulations are recovered. Furthermore, the numerical results are not sensitive to the value of c_3 as referred to by Menter [9] as well as tested and verified by the author in the present formulations. The eddy viscosity and the damping function D_2 are computed using

$$\nu_T = \tilde{\nu}_T D_2 \quad \text{with} \quad D_2 = 1 - e^{-(\tilde{\nu}_T/A^+\kappa\nu)^2} \tag{16}$$

The coefficient A^+ is set equal to 13.0 when the damping functions D_1 and D_2 are used with Eq. (13) and to 17.0 when used with Eq. (14). Note that the only difference between Eqs. (13) and (14) is

the destruction term. Thus, comparing results using the Menter model and the $(k\text{-}\omega)_{1E}$ based model with $(k\text{-}\varepsilon)$ constants will directly show the effects of the different forms of the destruction term.

Proposed Modifications. Various damping functions of the $k\text{-}\varepsilon$ model have been tested before [16,17] for different flow types. The results showed little to no dependency on the specified damping function. Hence, the author believes that different damping functions have very little effect on the predicted velocity and skin friction profiles. Damping functions are only used to reduce the eddy viscosity in the sublayer while ensuring numerical stability without excessive grid resolution near the wall. Moreover, varying a model's constants may improve the results of a specific type of flow but may lead to deterioration in the results of another. Therefore, the author believes that effective modifications should be made to the HRN form of the model.

Late separation in adverse pressure gradient test cases was observed by Menter [9]. This in turn suggests that the transformation of the $k\text{-}\varepsilon$ closure carried this deficiency to the Menter model. Since the $k\text{-}\omega$ model has better predictive capabilities than the $k\text{-}\varepsilon$ model in wall-bounded adverse pressure gradient flows [17], it is expected that this behavior will carry through its transformation to the present one-equation model. The destruction term that results from the transformation of $k\text{-}\omega$ model, i.e., $(\tilde{\nu}_T/L_{VK})(\partial\tilde{\nu}_T/\partial y)$, is a mix of both Menter and BB models and includes a term from each of them. Due to this similarity with the BB's destruction term, i.e., $(\partial\tilde{\nu}_T/\partial y)(\partial\tilde{\nu}_T/\partial y)$, a concern arises as to whether this term is sensitive to the free-stream value of the turbulence viscosity. Indeed, the first tests reported by Menter [9] using the coefficients that follow directly from the $k\text{-}\omega$ closure indicated some dependency on the free-stream values of the turbulent viscosity. At first, the author used the following multiplier on the destruction term to preclude this dependency:

$$f_d = \begin{cases} 1 & \text{if } \phi > 0 \\ 0 & \text{otherwise} \end{cases}$$
$$\phi = \frac{\partial V_{\text{Total}}}{\partial x_j}\frac{\partial(\tilde{\upsilon}_T)}{\partial x_j} \tag{17}$$

$$V_{\text{Total}} = [(U-U_0)^2 + (V-V_0)^2 + (W-W_0)^2]^{\frac{1}{2}} \tag{18}$$

However, after extensive testing with high values of free-stream turbulence viscosity, the $(k\text{-}\omega)_{1E}$ based model with $(k\text{-}\varepsilon)$ constants showed no sensitivity to the free-stream value of turbulence viscosity. Here, $[U_0, V_0, W_0]$ is the velocity vector of the reference frame in Cartesian coordinates. Furthermore, after numerical testing, the condition seemed to improve the predictive capabilities of the models and was hence adopted and applied on the destruction term of both modified models. It is worth noting that in open flows, this multiplier is usually effective near shear-layer edges, where the gradient of $\tilde{\upsilon}_T$ is negative. For the $(k\text{-}\omega)_{1E}$ based model with $(k\text{-}\varepsilon)$ constants, the destruction term vanishes naturally at the location of maximum $\tilde{\upsilon}_T$. The above multiplier retains f_d=0 from that point to the boundary-layer edge. In closed flow problems, f_d=0 when either gradient of the velocity or turbulent viscosity is negative. The impact of the f_d function on the solution is presented in the results later.

The main modification is of an empirical nature and performed on the production term. The turbulent shear stress and the turbulent kinetic energy that results from standard two-equation models can be written as

$$|-\overline{uv}| = a_1\left(\frac{\text{production}_k}{\text{dissipation}_k}\right)^{1/2} k \tag{19}$$

In nonequilibrium adverse pressure gradient flows, the ratio of production/dissipation can become significantly larger than one in the outer region of the boundary layer and the two-equation models over-predict the shear stress. Using Bradshaw's relation, i.e., $|-\overline{uv}| = a_1 k$, in the transformation of the two-equation models improved the prediction of the single-equation models [9]. However, the shear stress predicted by one-equation models that are transformed from two-equation closures, i.e., $|-\overline{uv}| = \tilde{\nu}_T|\partial u/\partial y|$, does not exactly follow Bradshow's relation. To further improve their prediction and better satisfy this relation, the shear stress or the production term in the present work is multiplied by a term $\propto$ (dissipation/production)^n of the corresponding one-equation model and not that of the k-equation. Here n is different than 1/2 and has to be found by numerical optimization over several nonequilibrium flow test cases.

The limiter f_p introduced in front of the production term of Menter's model is found to be

$$f_p = \min[1.0, \max(r^{0.1}, e^{-\frac{\tilde{\upsilon}_T}{400\upsilon}}, 0.7)] \tag{20}$$

with the dissipation to production ratio of Eq. (13) expressed as

$$r \equiv \frac{\tilde{\nu}_T}{S\kappa^2 L_{VK}^2} \tag{21}$$

For the $(k\text{-}\omega)_{1E}$ based model with $(k\text{-}\varepsilon)$ constants model, the f_p limiter is

$$f_p = \min[1.0, \max(r, e^{-\frac{\tilde{\upsilon}_T}{400\upsilon}}, 0.7)] \tag{22}$$

Similarly, the dissipation to production ratio of Eq. (14) gives

$$r \equiv \frac{\left|\frac{\partial\tilde{\nu}_T}{\partial x_j}\right|}{S\kappa^2 L_{VK}} \tag{23}$$

The value of r is less than unity in the outer part of the boundary layer in nonequilibrium flows and is unity in the logarithmic layer for zero pressure gradient flows. The 0.7 value is put as a lower bound, whereas the exponent $e^{-\tilde{\upsilon}_T/400\upsilon}$ is an active limiter in near-wall regions, where $\tilde{\nu}_T \leq \nu$.

The final forms of the modified models are

$$\frac{D\tilde{\nu}_T}{Dt} = f_p D_1 c_1 \tilde{\nu}_T S + \frac{\partial}{\partial x_j}\left(\frac{\tilde{\nu}_T}{\sigma}\frac{\partial\tilde{\nu}_T}{\partial x_j}\right) - f_d c_2 c_3 \min\left(\frac{\tilde{\nu}_T^2}{c_3 L_{VK}^2}, \frac{\tilde{\nu}_T^2 S\sqrt{\tilde{\nu}_T/\nu}}{\nu}\right) \tag{24}$$

and

$$\frac{D\tilde{\nu}_T}{Dt} = f_p D_1 c_1 \tilde{\nu}_T S + \frac{\partial}{\partial x_j}\left(\frac{\tilde{\nu}_T}{\sigma}\frac{\partial\tilde{\nu}_T}{\partial x_j}\right) - f_d c_2 c_3 \min\left(\frac{\tilde{\nu}_T}{c_3 L_{VK}}\left|\frac{\partial\tilde{\nu}_T}{\partial x_j}\right|, \frac{\tilde{\nu}_T^2 S\sqrt{\tilde{\nu}_T/\nu}}{\nu}\right) \tag{25}$$

Equations (24) and (25) are the modified Menter model and the modified $(k\text{-}\omega)_{1E}$ based model with $(k\text{-}\varepsilon)$ constants, respectively. The boundary conditions used are $\tilde{\nu}_T$=0 at the wall and $\tilde{\nu}_T \leq \nu_\infty$ as initial condition and free-stream inflow, respectively.

Numerical Method

An implicit, thin-layer, time dependent, compressible or incompressible Navier-Stokes solver was employed. The governing equations in a curvilinear coordinate system (ξ, ζ) are given as follows:

$$\partial_t\hat{\mathbf{Q}} + \partial_\xi\hat{\mathbf{F}} + \partial_\zeta\hat{\mathbf{G}} = \mathbf{Re}^{-1}\,\partial_\zeta\hat{\mathbf{S}} \tag{26}$$

where $\hat{\mathbf{Q}}$ is the vector of conserved variables, $1/J(\rho, \rho u, \rho w, e)$, $\hat{\mathbf{F}}$ and $\hat{\mathbf{G}}$ are the convection flux vectors, and $\hat{\mathbf{S}}$ is the thin layer approximation of the viscous fluxes in the ζ direction normal to a solid boundary. The convective fluxes are evaluated using a third-order-accurate Osher's upwind biased flux difference splitting

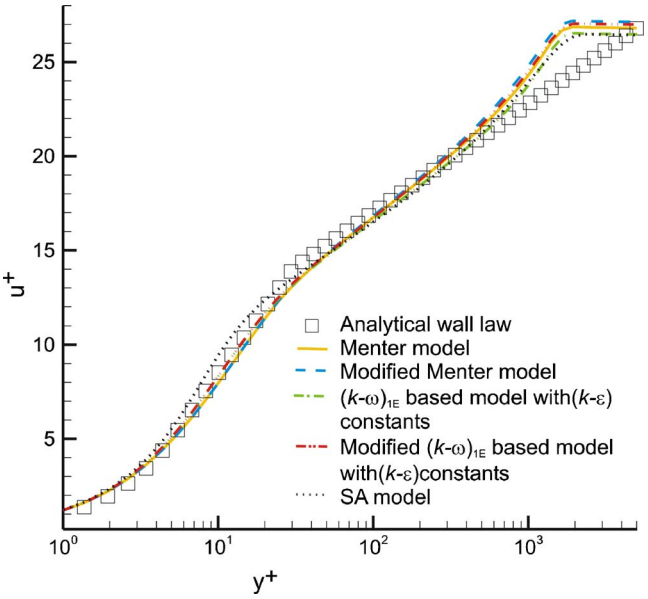

Fig. 1 Analytical law-of-the-wall profile for the flat plate case

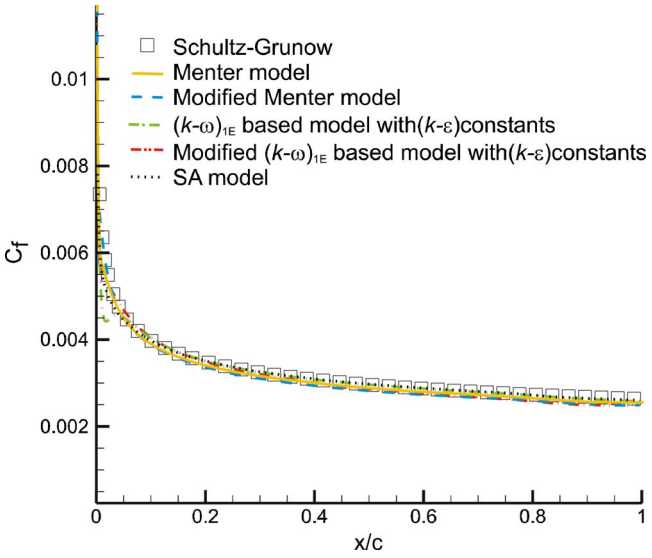

Fig. 2 Skin friction profile for the flat plate case

scheme. The viscous fluxes are computed with second-order-accurate central differences. The discretized Navier-Stokes equations and all models are solved and decoupled using an implicit approximate factorization method. Further details regarding the numerical implementation are available in Refs. [18,19].

Results and Discussion

The two modified models (Eqs. (24) and (25)) and the $(k\text{-}\omega)_{1E}$ based model with $(k\text{-}\varepsilon)$ constants (Eq. (14)) are evaluated and compared to the SA model, and the original Menter turbulence model (Eq. (13)) as well as to theoretical and experimental data for six different test cases. The first test case is flow over a flat plate with zero pressure gradient. The second test case is of a NACA 4412 at large angle of attack. The third test case deals with the flow over the Aerospacial A-Airfoil, whereas two other cases involve transonic flows over two different airfoils: RAE 2282 and NACA 0012. The last test case is a low speed flow in a channel with a slanted backstep. A C-type grid was used for all airfoil test cases. A grid study was conducted for all test cases with considerable care taken to ensure grid independence. The free-stream turbulent eddy viscosity is set to one-tenth of the laminar eddy viscosity. The f_p function was mainly determined using an adverse pressure gradient flow test case, and a shock-boundary-layer interaction test case, namely, the NACA 4412 and the RAE 2282 test cases.

Flow Over a Flat Plate at Zero Pressure Gradient. This case was one of the building blocks for testing all modifications in an equilibrium flow test case. The free-stream Mach number was set to 0.3 and the Reynolds number was taken as 6.0×10^6. The flow was computed on an 81×81 grid with the first point off the wall yielding a y^+ value around 0.5. As expected, the present modifications show no effect in equilibrium flow cases and hence, all turbulence models yield good predictions for the flat plate turbulent boundary layer. Comparisons of all model results with analytical wall-law profile are given in Fig. 1. The computational profile was taken at 60% of the plate. The analytical wall-law profile was plotted according to $u^+=y^+$ in the viscous sublayer, $u^+=5.0\ln(y^+)-3.05$ in the buffer layer, and $u^+=2.5\ln(y^+)+5.5$ in the logarithmic layer. The results of all models collapse very closely on the analytical solution. The skin friction is plotted along the flat plate in Fig. 2. All models are compared to the empirical correlation by Schultz-Grunow: [20] $C_f/2=0.185/(\log_{10}\mathrm{Re}_x)^{2.584}$. The skin friction profile is very well predicted by all models.

Flow Over NACA 4412 Airfoil. This validation case focuses on reproducing exact velocity profiles and predicting separation location. The flow over this airfoil was computed at a 13.87 deg angle of attack with a Reynolds number of 1.52×10^6. A 257×91 grid was used with 191 nodes lying on the airfoil surface with a minimum wall-distance of $y^+\approx1$ and an outer boundary extent of approximately 22 chords. A 307×135 grid was also used to ascertain grid independence of the reported mesh results. Computed results were compared with the experimental data by Coles and Wadcock [21]. Trip-strips were employed in the experiment and artificially modeled in the present computation on the suction and pressure sides at $x/c=0.025$ and 0.103, respectively. Figure 3 compares the computed mean velocity profiles of the SA, Menter, modified Menter, $(k\text{-}\omega)_{1E}$ based model with $(k\text{-}\varepsilon)$ constants, and the modified $(k-\omega)_{1E}$ based model with $(k\text{-}\varepsilon)$ constants turbulence models at different stations on the upper surface of the airfoil with the experimental measurements. The solution obtained by both modified models gives satisfactory results by accounting for the significant nonequilibrium effect through correct prediction of the separation bubble height. The $(k\text{-}\omega)_{1E}$ based model with $(k-\varepsilon)$ constants, SA, and Menter models generally over-predict the mean velocity profiles for the stations exhibiting separation. Both modified models, in comparison with the other models, consistently give results that are in better agreement with the experimental data. All models predict velocities that are more consistent with the experimental data closer to the leading edge, but the discrepancies of the SA, Menter, and $(k\text{-}\omega)_{1E}$ based model with $(k\text{-}\varepsilon)$ constants magnify further downstream.

The skin friction data are not available. Furthermore, the separation predicted by modified $(k\text{-}\omega)_{1E}$ based model with $(k\text{-}\varepsilon)$ constants, modified Menter, and the SA models fall well within the experimental range of $x/c=0.75-0.8$, reported by Coles and Wadcock [21]. The Menter model and the $(k\text{-}\omega)_{1E}$ based model with $(k\text{-}\varepsilon)$ constants predict a mild and delayed separation taking place at $x/c=0.94$ and 0.86, respectively. This in turn suggests that the destruction term resulting from the transformation of the $k\text{-}\omega$ closure brought about a slight improvement as compared to that of the $k\text{-}\varepsilon$ model.

Flow Over NACA 0012 Airfoil. This case is one of the most challenging cases for turbulence models in terms of shock loca-

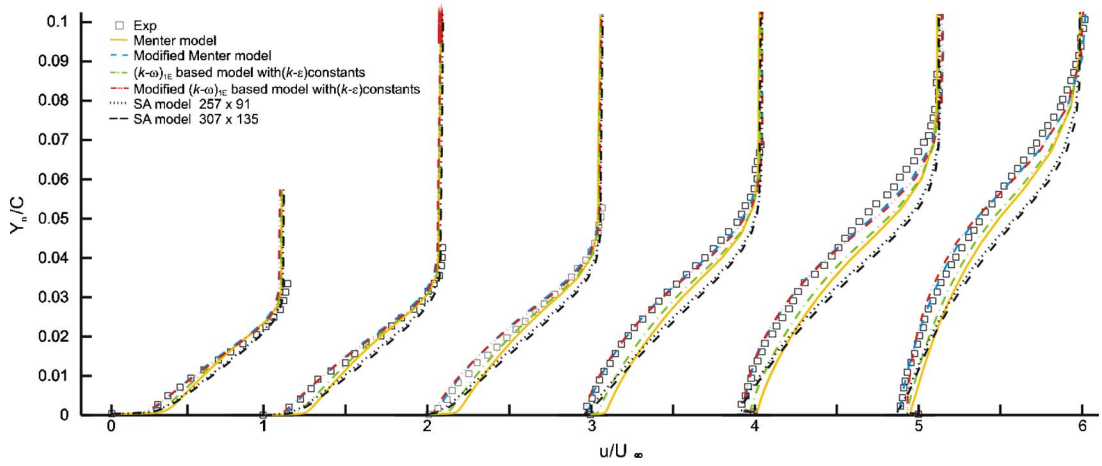

Fig. 3 Mean velocity profiles for NACA 4412 airfoil at $x/c=0.675$, 0.731, 0.786, 0.842, 0.897, and 0.953 on the suction surface of airfoil

tion and prediction of the aft-shock variation. The airfoil's angle of attack was set at 2.26 deg and the Reynolds number, based on the chord and the free-stream velocity, was 9.0×10^6 with a Mach number of 0.799. The computation was performed on a 257×69 grid with 223 points lying on the airfoil surface. The far field was located approximately 23 chords from the airfoil surface. The first grid point in the off-body mesh was located at an average of $y^+\approx1$. Furthermore, the sensitivity of the turbulence models is expected to be considerably more pronounced in such flow cases due to shock-induced separation. Figure 4 shows the variation of the surface pressure coefficient in comparison to the pressure measurement given by Harris [22]. Encouragingly, both modified turbulence models and the SA model return a marked improvement in terms of the shock location relative to Menter and the $(k\text{-}\omega)_{1E}$ based model with $(k\text{-}\varepsilon)$ constants that indicate shock location too far downstream. The modified Menter model seems to be relatively closer to experimental data in the aft-shock location than the modified $(k\text{-}\omega)_{1E}$ based model with $(k\text{-}\varepsilon)$ constants. Unlike the known behavior of the $k\text{-}\varepsilon$ and $k\text{-}\omega$ two-equation models in shock-boundary interaction flows, the Menter model is more precise in predicting the shock location than the $(k\text{-}\omega)_{1E}$ based model with $(k\text{-}\varepsilon)$ constants.

Flow Over RAE 2822 Airfoil

The flow over the RAE 2822 Case 10 transonic airfoil provides a stringent test for the present model due to the shock-induced flow separation and therefore, the sensitivity of the models is expected to be considerably pronounced. The computation was carried out using a 249×69 grid with 223 points lying on the airfoil surface with the first y^+ in the off-body mesh being at an average location of 1. The far field was located approximately 22 chords from the airfoil surface. Computed results were compared with the experimental data given by Cook et al. [23]. The flow over this airfoil was computed with a Reynolds number of 6.2×10^6, a Mach number of 0.75, and a corrected angle of attack of 2.81 deg. The computed surface pressure coefficient is given in Fig. 5. The location of the shock wave found in simulations is consistently aft of that found experimentally, with the present modified models best predicting the shock location. This can be ascribed to the correct eddy viscosity predicted in that region. Again, the Menter model seems to predict the shock location slightly better than the $(k\text{-}\omega)_{1E}$ based model with $(k\text{-}\varepsilon)$ constants.

The skin friction coefficient is compared with experimental data in Fig. 6. All models satisfactorily predict the skin friction coefficient distribution upstream of the shock wave. In the post-shock

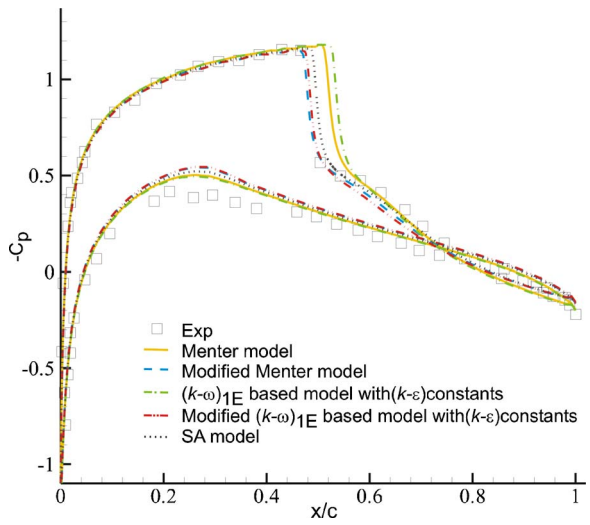

Fig. 4 Surface pressure distribution over the NACA 0012 airfoil

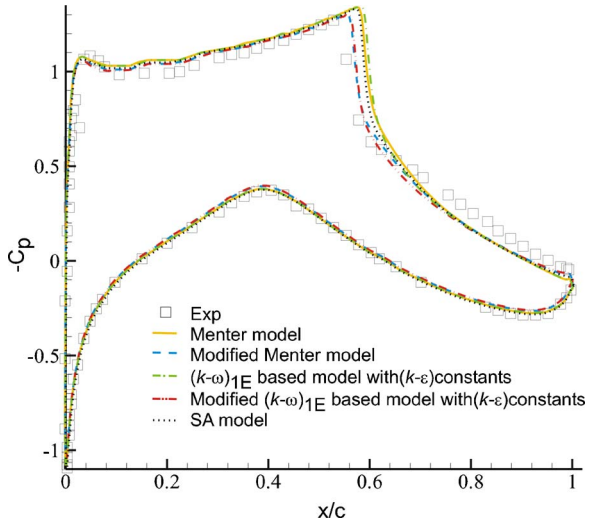

Fig. 5 Surface pressure distribution over the RAE 2822 Case 10 airfoil

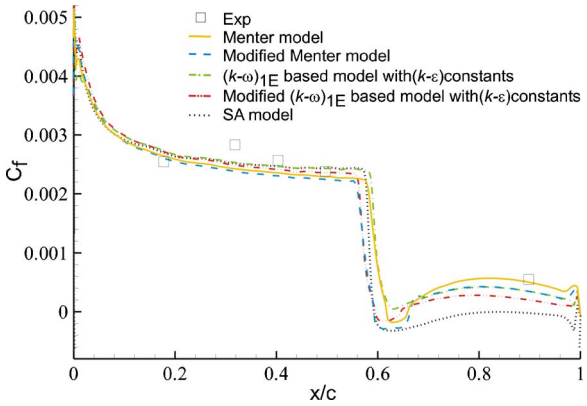

Fig. 6 Surface skin friction distribution over the upper surface of the RAE 2822 Case 10 airfoil

region the Menter model follows exactly several two-equation models reported by Kral [12] for the same test case predicting a mild separation. Interestingly enough, the $(k\text{-}\omega)_{1E}$ based model with $(k\text{-}\varepsilon)$ constants predicts no separation and a sluggish post-reattachment boundary layer recovery, which is due solely to a different destruction term. It must be said, however, that the behavior of the two-equation $k\text{-}\omega$ closure is superior to that of the $k\text{-}\varepsilon$ model in wall bounded adverse-pressure gradient flows [14,17]. The modified $(k\text{-}\omega)_{1E}$ based model with $(k\text{-}\varepsilon)$ constants indicates a mild separation but with a slower post-reattachment boundary layer recovery compared to the $(k\text{-}\omega)_{1E}$ based model with $(k\text{-}\varepsilon)$ constants. The deepest separation is predicted by both the modified Menter and the SA model where they overlap downstream of the shock and predict a larger separation bubble compared to the Menter model. The SA model fails to recover, whereas the modified Menter model with the deepest separation bubble recovers the most.

Flow Over Aerospatiale-A Airfoil. The Aerospatiale-A airfoil test case was performed using a grid size of 341×61, with the node closest to the wall located at about $y^+ \approx 0.2$ In addition, the airfoil's angle of attack was set at 13.3 deg and the Reynolds number, based on the chord and the free-stream velocity, was 2.0×10^6. Predictions of the flow were obtained by artificially tripping the boundary layer at 12% and 30% of the chord on the respective upper and lower surfaces of the airfoil. This was achieved by setting the value of the eddy viscosity to zero upstream of the aforementioned locations.

The skin friction coefficient on both sides of the airfoil is given in Fig. 7. All model predictions are relatively close to the experimental measurements with the Menter model over-predicting the skin friction coefficient distribution the most. A mild laminar separation bubble is detected on the suction surface near $x/C = 0.1$. The development of this bubble is consistent with the experimental measurements [24].

The mean streamwise components of the velocity profiles are given in Fig. 8 for the streamwise locations of $x/C = 0.3, 0.7, 0.87, 0.96$, and 0.99. Both of the modified models return better prediction relative to other models. However, neither of the models could accurately reproduce the experimental profiles. The modified Menter model shows a sluggish recovery towards the boundary-layer edge relative to the modified $(k\text{-}\omega)_{1E}$ based model with $(k\text{-}\varepsilon)$ constants. It must be stated, however, that the results of the shear stress transport (SST) model reported by Kotapati-Apparao et al. [25] did not produce qualitatively better results than the presently modified models. Furthermore, the author is unaware of any eddy-viscosity model that is able to reproduce the measured experimental profiles for the same transition test case.

Low Speed Flow in a Channel With 45 deg Slated Backstep.

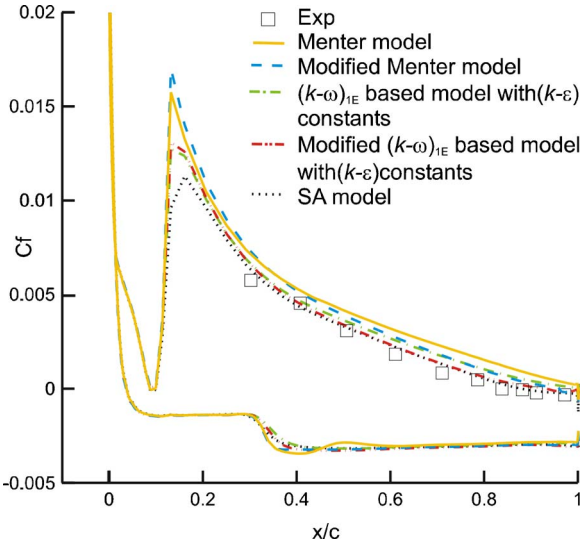

Fig. 7 Surface skin friction coefficient distribution for the Aerospatiale-A airfoil

This test case is one of the well examined experiments of Ruck and Makiola [26] with a 45 deg step angle. The inflow Mach number was set to 0.1 and the Reynolds number based on the channel height upstream of the step, was 64,000 with an expansion ratio of 2. Neumann boundary conditions were applied at the outlet, located at $x/H = 50$. A no-slip boundary condition was imposed on all solid surfaces. The calculated data of a fully developed channel flow are used at the inlet. A 181×101 grid was employed with the first point off solid surface located at $y^+ < 1.0$. The computed results of the mean velocity profiles at $x/H = 1$, $x/H = 2$, $x/H = 8$, and $x/H = 15$ are shown in Figs. 9 and 10, respectively. The velocity profiles, shown in Fig. 9, confirm that at $x/H = 1$, all models are in good agreement for $y/H > 1$ and only the modified Menter model and the $(k\text{-}\omega)_{1E}$ based model with $(k\text{-}\varepsilon)$ constants follow the experimental data down to $y/H = 0.5$. The SA model and the modified $(k\text{-}\omega)_{1E}$ based model with $(k\text{-}\varepsilon)$ constants almost reproduce the same profile down to the wall, whereas the Menter model predicts a reattachment. This is clearly noticed at $x/H = 2$, where it predicts an incipiently attached flow. On the contrary, the SA model predicts a deeper reverse flow. Furthermore, the $(k\text{-}\omega)_{1E}$ based model with $(k\text{-}\varepsilon)$ constants is generally in better agreement with the experimental data compared to the Menter model, which is solely due to the difference in the destruction term. Both the modified models along with the $(k\text{-}\omega)_{1E}$ based model with $(k\text{-}\varepsilon)$ constants predict correct near-wall behavior of the mean velocity profile.

In Fig. 10, the SA, Menter, and $(k\text{-}\omega)_{1E}$ based model with $(k\text{-}\varepsilon)$ constants under-predict the extent of the separation bubble at $x/H = 8$ with the latter being a little closer than Menter model to the experimental values. Furthermore, the modified Menter model and $(k\text{-}\omega)_{1E}$ based model with $(k\text{-}\varepsilon)$ constants are in good agreement and capture the location of the reattachment point acceptably. The improvement of the modified models is slightly detected at $x/H = 15$, where all models fail to reproduce the velocity profile correctly.

The computed results of the modified Menter model with $f_d = 1.0$ are also shown in Figs. 9 and 10. The improved prediction of the mean velocity profile at $x/H = 1$ does not carry over throughout the channel. Indeed, at $x/H = 2$, the predicted velocity profile is close to the original Menter model while it considerably deviates from the experimental results and all predicted profiles by other models at $x/H = 8$ and 15. This in turn shows the effect of the f_d multiplier on the predictive capability of the model. The

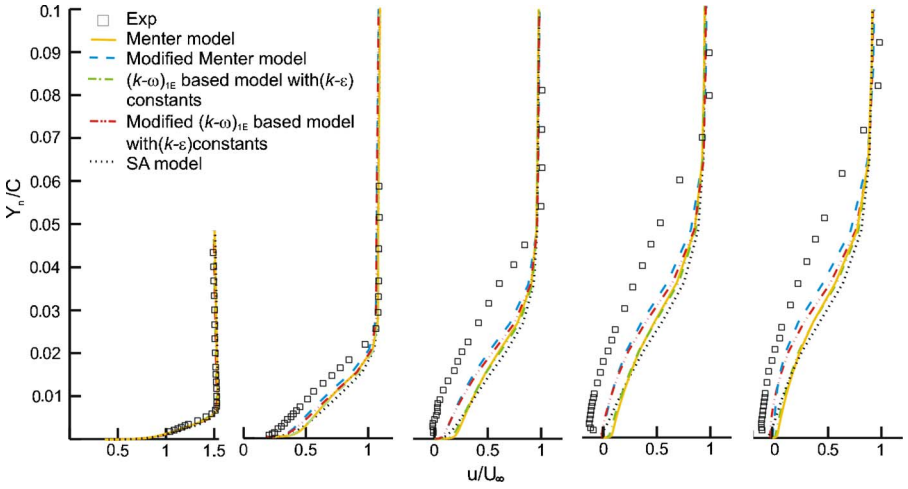

Fig. 8 Mean streamwise velocity profiles for the Aerospatiale-A airfoil at $x/c=0.3$, 0.7, 0.87, 0.96, and 0.99 on the suction side of the airfoil

presence of the f_p alone does not seem to improve the model's prediction, which is due mainly to the f_p calibration in the presence of the f_d multiplier.

Conclusion

The present study pursued two main objectives. The first was to examine the difference between two different one-equation model forms: one derived from the k-ε equations while the other was derived from the k-ω equations. The only difference between the one-equation forms is in their destruction terms. The second objective was to assess the ability of two one-equation turbulence models with the proposed modifications to better account for nonequilibrium effects in comparison to their baseline models.

The major conclusions emerging from the study may be summarized as follows:

- It may be claimed that the modified models consistently predict a higher level of accuracy, leading to an improved agreement with experimental data in most of the flow cases considered in this study.
- The modified models return superior predictions relative to the original models and the SA model in all test cases examined herein. Furthermore, these modified models retain the wall-distance-free feature, which in turn renders them advantageous to the SA model.
- The Menter model returns a marked improvement in shock-boundary layer interacting flows (in terms of the shock location and post-reattachment recovery) relative to the $(k$-$\omega)_{1E}$ based model with $(k$-$\varepsilon)$ constants model, which is attributed to the difference in the destruction term.
- The general prediction of the modified $(k$-$\omega)_{1E}$ based model with $(k$-$\varepsilon)$ constants model is somehow inferior to that of the modified Menter model in all considered test cases. Therefore, the latter is recommended for engineering applications.

It is important to validate the models that incorporate the von Karman length scale further in future work to determine whether this length scale is sufficient for describing more complex three-dimensional flow fields.

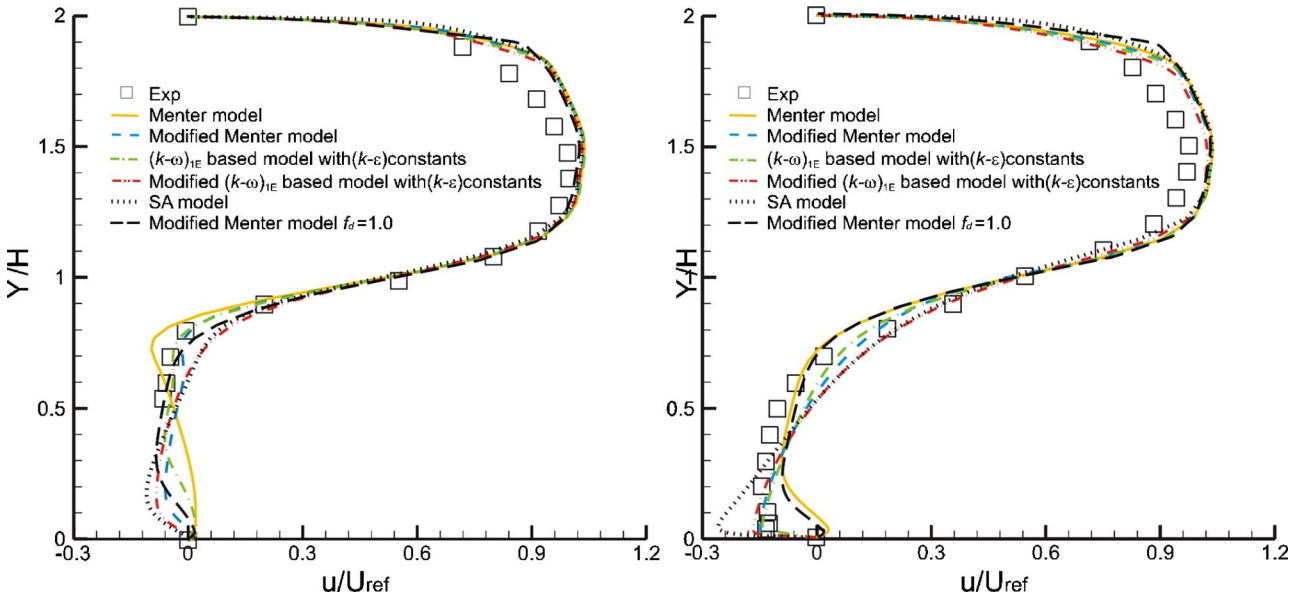

Fig. 9 Mean velocity profiles for a 45 deg slanted backstep at $x/H=1$, and 2

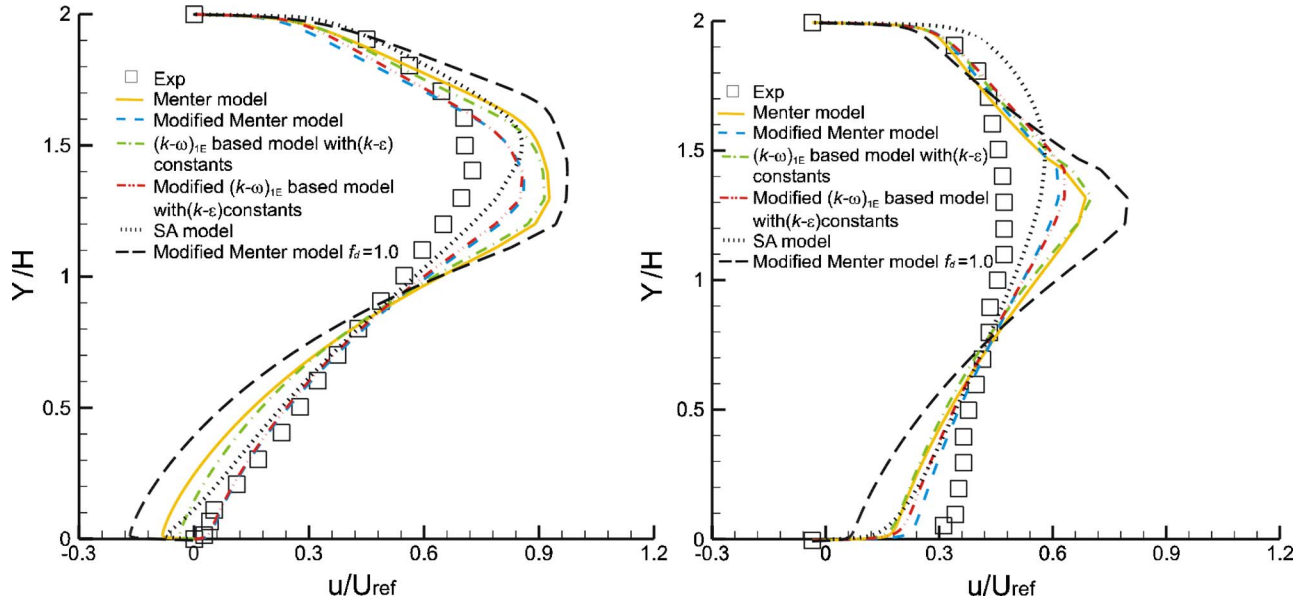

Fig. 10 Mean velocity profiles for a 45 deg slanted backstep at $x/H=8$, and 15

References

[1] Cebeci, T., and Smith, A. M. O., 1974, *Analysis of Turbulent Boundary Layers*, Academic Press, New York, pp. 215–217.

[2] Baldwin, B. S., and Lomax, H., 1978, "Thin-Layer Approximation and Algebraic Model for Separated Turbulent Flows," AIAA Paper No. 78-257.

[3] Abid, R., Rumsey, C., and Gatski, T. B., 1995, "Prediction of Nonequilibrium Turbulent Flows With Explicit Algebraic Stress Models," AIAA J., **33**, pp. 2026–2031.

[4] Speziale, C. G., 1987, "On Nonlinear *k-l* and *k-ε* Models of Turbulence," J. Fluid Mech., **178**, p. 459.

[5] Rubinstein, R., and Barton, J. M., 1990, "Nonlinear Reynolds Stress Models and the Normalization Group," Phys. Fluids A, **2**, p. 1472.

[6] Gatski, T. B., and Speziale, C. G., 1993, "On Explicit Algebraic Stress Models for Complex Turbulent Flows," J. Fluids Eng., **254**, pp. 59–78.

[7] Goldberg, U., 2000, "Hypersonic Flow Heat Transfer Prediction Using Single Equation Turbulence Models," ASME J. Heat Transfer, **123**, pp. 65–69.

[8] Goldberg, U., 2003, "Turbulence Closure With a Topography-Parameter-Free Single Equation Model," Int. J. Comput. Fluid Dyn., **17**, pp. 27–38.

[9] Menter, F. R., 1997, "Eddy Viscosity Transport Equations and Their Relation to the $k-\varepsilon$ Model," ASME J. Fluids Eng., **119**, pp. 876–884.

[10] Nagano, C., Pei, C., and Hattori, H., 2000, "A New Low-Reynolds-Number One-Equation Model of Turbulence," Flow, Turbul. Combust., **63**, pp. 135–151.

[11] Baldwin, B., and Barth, T., 1990, "A One-Equation Turbulent Transport Model for High Reynolds Number Wall-Bounded Flows," NASA TM-102847.

[12] Kral, L. D., 1998, "Recent Experience With Different Turbulence Models Applied to the Calculation of Flow Over Aircraft Components," Prog. Aerosp. Sci., **34**, pp. 481–541.

[13] Sai, V. A., and Lutfy, F. M., 1995, "Analysis of the Baldwin-Barth and Spalart-Allmaras One-Equation Turbulence Models," AIAA J., **33**, pp. 1971–1974.

[14] Wilcox, D. C., 2000, *Turbulence Modeling for CFD*, Second ed., DCW Industries Inc., La Cacada, CA.

[15] Spalart, P., and Allmaras, S., 1992, "A One-Equation Turbulence Model for Aerodynamic Flows," AIAA Paper No. 92-0439.

[16] Michelassi, V., and Shihi, T.-H., 1991, "Elliptic Flow Computation by Low Reynolds Number Two-Equation Turbulence Models," NASA TM-105376, CMOTT-91-11.

[17] Wilcox, D. C., 1993, "Comparison of Two-Equation Turbulence Models for Boundary Layers With Pressure Gradient," AIAA J., **31**(8), pp. 1414–1421.

[18] Ekaterinaris, J. A., Cricelli, A., and Platzer, M. F., 1994, "A Zonal Method for Unsteady Viscous, Compressible Airfoil Flows," J. Fluids Struct., **8**, pp. 107–123.

[19] Rai, M. M., and Chakravarthy, S. R., 1986, "An Implicit Form of the Osher Upwind Scheme," AIAA J., **24**, pp. 735–743.

[20] Schlichting, H., 1979, *Boundary Layer Theory*, McGraw-Hill, New York.

[21] Coles, D., and Wadcock, A. J., 1979, "Flying Hot Wire Study of Flow Past an NACA 4412 Airfoil at Maximum Lift," AIAA J., **17**, pp. 321–328.

[22] Harris, C., 1981, "Two-Dimensional Aerodynamic Characteristics of the NASA 0012 Airfoil in the Langley 8-Foot Transonic Pressure Tunnel," NASA TM-81927.

[23] Cook, P. H., McDonald, M. A., and Firmin, M. C. P., 1979, "AIRFOIL RAE 2822 Pressure Distributions, Boundary Layer and Wake Measurements," AGARD Advisory Report No. 138.

[24] Mellen, C. P., Froölich, J., and Rodi, W., 2002, "Lessons From the European LESFOIL Project on LES of Flow Around an Airfoil", AIAA Paper No. 2002-0111.

[25] Kotapati-Apparao, R., Squires, K. D., and Forsythe, J. R., 2004, "Prediction of the Flow Over an Airfoil at Maximum Lift," AIAA Paper No. 2004-0259.

[26] Ruck, B., and Makiola, B., 1993, "Flow Separation Over the Step With Inclined Walls," *Near-Wall Turbulent Flows, Proceedings of the International Conference*, R. M. C. So, C. G. Speziale, and B. E. Launder, eds., Tempe, AZ, March 15–17, 1993, Elsevier, Amsterdam, p. 999.

The Asymmetry of the Large-Scale Structures in Turbulent Three-Dimensional Wall Jets Exiting Long Rectangular Channels

J. W. Hall[1]
e-mail: jwhall@unb.ca

D. Ewing[2]
e-mail: ewingd@me.queensu.ca

Department of Mechanical Engineering,
McMaster University,
Hamilton, Ontario, L8S 4L7,
Canada

The development of the large-scale structures in three-dimensional wall jets formed using long rectangular channels with aspect ratios of 1 and 4 was investigated using measurements of the fluctuating wall pressure and point measurements of the turbulent velocity throughout the near and intermediate field. The instantaneous pressure fluctuations in both jets were laterally asymmetric causing the fluctuating wall pressure to be poorly correlated across the jet centerline. A frequency-dependent proper orthogonal decomposition (POD) of the fluctuating pressure measurements indicated that the first two mode shapes were opposite and each mode made similar contributions to the mean square fluctuations at all frequencies in order to capture the instantaneous asymmetry of the pressure field. The mode shapes in the intermediate field of both jets were strongly frequency dependent, and a subsequent wavelet analysis indicated that there are both large-scale horseshoe structures that span one-half of the jet and separate, smaller, near-wall structures located near the jet centerline. The initial development of the large-scale structures in the two jets differed, with the most energetic fluctuations being more antisymmetric in the square jet. [DOI: 10.1115/1.2742721]

Introduction

Wall jets are formed when a jet of fluid is directed at or along a wall. Wall jets occur frequently in engineering practice, particularly in heating and cooling applications. One of the most remarkable features of the turbulent three-dimensional wall jet (Fig. 1) is that the far-field lateral growth of the jet parallel to the wall is typically five times larger than the vertical growth normal to the wall [1–4]. Launder and Rodi [3] proposed that this behavior was caused by two pairs of counterrotating mean streamwise vorticity on either side of the jet centerline that were oriented to drive the flow down toward the wall and laterally outward. Later, Iida and Matsuda [5] measured the mean streamwise vorticity in the near field of the wall jet and found evidence of two regions of counterrotating mean streamwise vorticity located near the wall and on either side of the jet centerline. The two regions of concentrated streamwise vorticity were initially beside each other, but the outer region lifted from the wall and became more diffuse as the wall jet developed downstream. Sun and Ewing [6] later reported measurements of a single component of the mean streamwise vorticity, $\partial W/\partial y$, and showed that the outer regions continued to reorient themselves throughout the intermediate field until they were roughly aligned on top of each other similar to the model proposed by Launder and Rodi [3].

Matsuda et al. [7] recognized that these regions of vorticity were related to the passage of quasi-periodic vortical structures and used conditionally averaged velocity measurements to examine these structures in the near field of the wall jet. Their results suggested that the outer regions of vorticity were caused by the passage of large-scale horseshoe vortices formed when the ring structures generated at the jet outlet interacted with the wall. Ewing and Pollard [8] and Ewing et al. [9] later examined the large-scale structures in the three-dimensional wall jet closer to the wall in the near and intermediate field. They argued that the inner regions of streamwise vorticity were generated by the passage of smaller horseshoe structures. These smaller structures were thought to be connected to the larger structures proposed by Matsuda et al., as shown in Fig. 2. Ewing and Pollard [8] and Ewing et al. [9] suggested that the reorientation of the outer region of mean streamwise vorticity was caused by the outer leg of the vortical structures becoming more angled to the centerline as the structures evolved downstream. Sun [6] extended these measurements to the far field and found that the fluctuating velocities measured on opposite sides of the jet centerline were not well correlated with each other. He suggested that this behavior was due to lateral meandering of the structures in across the wall jet, although no instantaneous measurements were performed to verify this.

The objective of this investigation was to examine the *instantaneous development* of the large-scale structures in the three-dimensional wall jet with particular attention given to the lateral symmetry of the structures in the flow. This was done using simultaneous multipoint measurements of the fluctuating wall pressure across a wall jet exiting a long rectangular channel with aspect ratio of 4. Time-resolved pressure measurements were used to investigate the dynamics of the structures in the flow since they are much easier to obtain than temporally and spatially resolved

[1]Present address: Department of Mechanical Engineering, University of New Brunswick, 15 Dineen Drive, Fredericton, NB, E3B 5A3.

[2]Present address: Department of Mechanical and Materials Engineering, Queens University, Kingston, ON, K7L 3N6 Canada.

Contributed by the Fluids Engineering Division of ASME for publication in the JOURNAL OF FLUIDS ENGINEERING. Manuscript received November 16, 2005; final manuscript received January 15, 2007. Review conducted by Ugo Piomelli. Paper presented at the 2005 ASME Fluids Engineering Division Summer Meeting and Exhibition (FEDSM2005), June 19–23, 2005, Houston, TX.

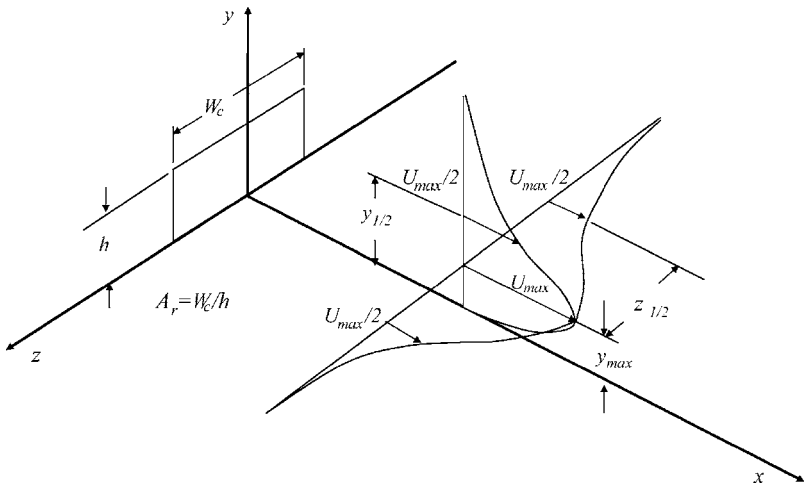

Fig. 1 Schematic of a three-dimensional wall jet exiting a rectangular nozzle

velocity measurements. Similar measurements were performed in a wall jet exiting a square channel to examine how the outlet aspect ratio affected the development of the coherent structures in the two jets. Hall and Ewing [10] showed that the length scales in the two jets collapsed when the streamwise coordinate was scaled using the square root of the nozzle cross-sectional area [11]. This scaling is used to compare the development of the two wall jets examined here.

Experimental Setup

The facility used in this investigation, shown in Fig. 3, is the same as used previously by Hall and Ewing [10]. The three-dimensional wall jets exit a long channel with variable width W_c. The airflow to the channel was conditioned in a settling chamber equipped with three air filters, a flow straightener, and a wire mesh. The flow entered the channel through an adjustable bell-mouth that could be varied along with the width of the channel. The height of the channel h was fixed at 2.54 cm, and the width could be set from 0 to 25 cm so the aspect ratio of the channel could be continually varied from 0 to 10. Measurements are reported here with the channel set to $A_r=1$ and 4. The length of the channel was 2.5 m and the velocity profiles measured at the channel exit for aspect ratios of 1–8 were in good agreement with fully developed profiles [12].

On exiting the channel, the jet evolved over a horizontal plate with a width of 2.4 m and a length of 1.8 m. The base of the channel was mounted flush with the wall so that the jet interacts with the wall immediately after exiting the channel. A 1.2 m high wall with a width of 2.4 m was mounted flush with the channel exit to block entrainment of air from behind the exit. In all cases, the centerline velocity of the jet at the channel exit was 55.0 m/s corresponding to a Reynolds number based on the channel height and the centerline velocity of $\mathrm{Re}_h=89{,}600$.

The development of the large-scale structures in the three-dimensional wall jets was characterized by measuring the distribution of the fluctuating wall pressure across the jet using a specially made 16 channel, Panasonic WM-61B electret microphone system. The response of the microphones was flat for frequencies between 20 Hz and 5000 Hz. The microphones were mounted directly in the wall for increased frequency response and sensitivity to the flow. The microphones sensed the flow via a 0.8 mm hole drilled through the wall. At each downstream location considered here, one hole was drilled on the jet centerline and seven additional holes were equally spaced on either side of the centerline for a total of 15 pressure measurements.

The velocity field in the wall jet was measured using an Auspex $u-w$ boundary layer cross-wire probe connected to an eight-channel anemometry system designed and manufactured at McMaster University [6]. The hot-wire probe was traversed to 21 different heights above each microphone using an automated traverse so that correlations of the fluctuating wall pressure and the streamwise and lateral velocity could be obtained. The ambi-

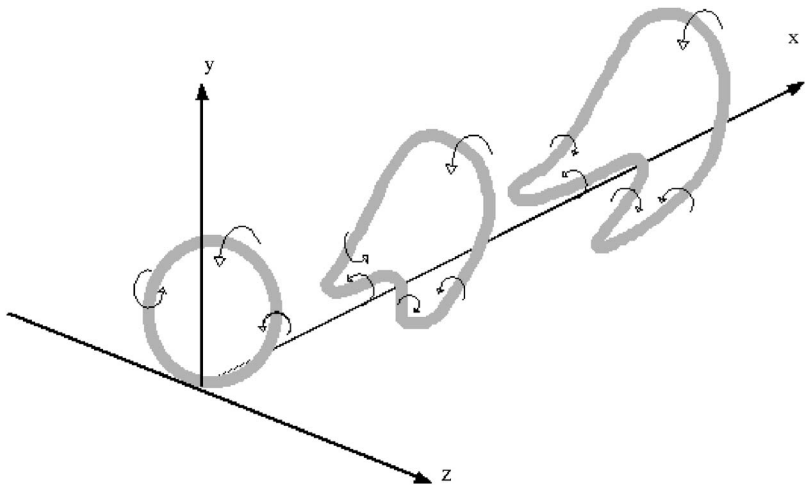

Fig. 2 Proposed development of the vortex structure in a three-dimensional wall jet formed using a round nozzle [8]

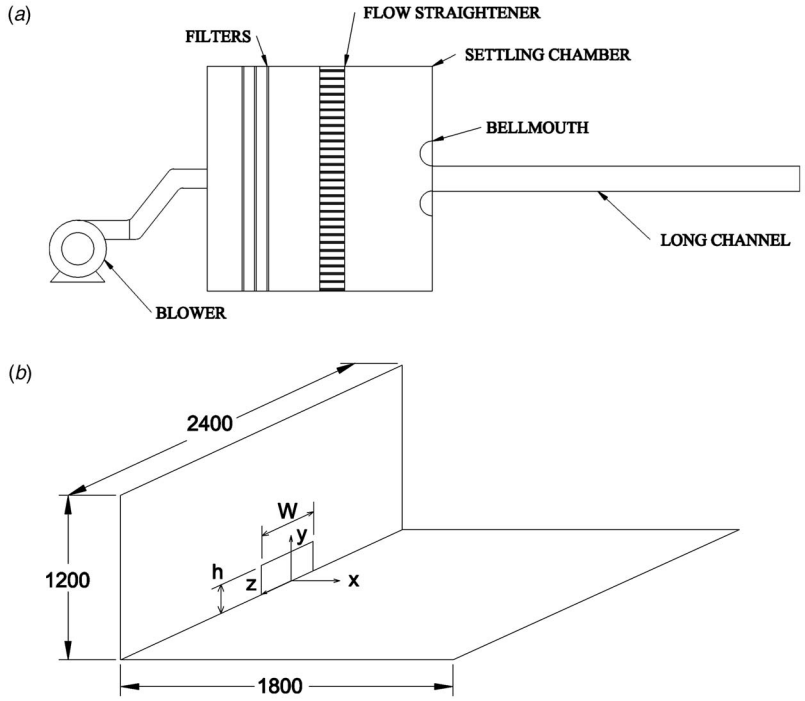

Fig. 3 Schematic of: (*a*) The channel and flow conditioning for the variable aspect-ratio channel and (*b*) the wall-jet facility. All dimensions are in millimeters.

ent room temperature was monitored with a thermistor, and the hot-wire probe response was corrected for changes in the room temperature using the scheme suggested by Beuther [13]. The voltage signals from the hot wires, the microphones, and the thermistor were simultaneously sampled at 10,000 Hz using a 14 bit Microstar 5600a A/D board. At each measurement location, 100 independent blocks of 0.25 s duration were recorded for each channel, yielding in excess of 30,000 independent blocks of pressure data. The uncertainty in the lateral velocity measurements due to the finite sampling time at the 95% confidence interval was $<5\%$ within the region $0 \leq y \leq y_{1/2}$ and $-z_{1/2} \leq z \leq z_{1/2}$. Further details of the uncertainty in these measurements can be found in Hall [12].

The present analysis focused primarily on measurements of the fluctuating wall pressure in the two wall jets. The mean from each full pressure record was subtracted from the combined blocks of data because there was a small DC offset on some of the microphones. The fluctuating pressure records were then Fourier transformed in time and used to compute the cross-spectra of the fluctuating pressure. The spectra were computed from over 15,000 blocks of data the uncertainty in the estimate of the spectra and cross-spectra so the 95% confidence interval was $<2\%$ [14]. The spectra and cross-spectra were then symmetrized at each frequency across the centerline of the jet so that the proper orthogonal decomposition (POD) technique could be applied to these spectra and cross-spectra to decompose the flow in the lateral direction. In all cases, the pressure measurements were symmetrical on either side of the centerline to within ±15%. The instantaneous contributions of the POD modes were then examined by projecting the instantaneous pressure onto the POD modes as discussed below.

Experimental Results

The link between the fluctuating pressure field and the velocity field was first examined by comparing the standard deviation of the fluctuating wall pressure, p_{rms}, with one component of the mean streamwise vorticity, $\partial W/\partial y$. The results in the $A_r=4$ jet at $x/h=6$, 20, and 40 (or $x/\sqrt{A}=3$, 10, and 20) are shown in Fig. 4. On either side of the jet centerline there are two peaks in the fluctuating pressure that correspond to the regions of oppositely signed $\partial W/\partial y$. This close correspondence suggests that the pressure fluctuations are related to the mean streamwise vorticity and are thus likely caused by the coherent vortical motions in the wall jet. Initially, oppositely signed regions of large $\partial W/\partial y$ are concentrated on either side of the lateral edges of the jet causing large, narrow peaks in the pressure fluctuations. As the flow evolves downstream, the outer regions of $\partial W/\partial y$ become more diffuse and lift slightly from the wall, consistent with previous investigations in wall jets formed using round openings [5–9]. This reorientation of vorticity causes the pressure fluctuations to decrease in magnitude and become broader. The largest pressure fluctuations, however, do remain approximately beneath the inner regions of strong $\partial W/\partial y$.

The relationship between the fluctuating wall pressure and the turbulent velocity field was examined using the two-point, two-time correlations given by

$$\rho_{pu}(y=0,y',z,z',\tau)=\frac{\overline{p(y=0,z,t)u(y',z',t+\tau)}}{p_{\mathrm{rms}}(y=0,z)u_{\mathrm{rms}}(y',z')} \tag{1}$$

The results on the $y-z$ plane for different time delays at $x/h=6$ and 20 are shown in Figs. 5 and 6, respectively. In each case, the turbulent velocity has been correlated with the fluctuating pressure at $z_{\max}$, the location where the standard deviation of the pressure fluctuations was a maximum. The time delay in these correlations τ has been normalized using the maximum streamwise velocity $U_{\max}$ and the vertical half-widths of the jet $y_{1/2}$. This scaling was shown by Hall [12] to reasonably collapse the time scale for the passage of the structures at different downstream locations in these jets. At both downstream locations, the fluctuating velocity is well correlated with the fluctuating wall pressure on the same side of the jet as the reference pressure, even well away from the wall. This behavior indicates that the passage of the structures that cause the fluctuating wall pressure are not, on average, symmetric

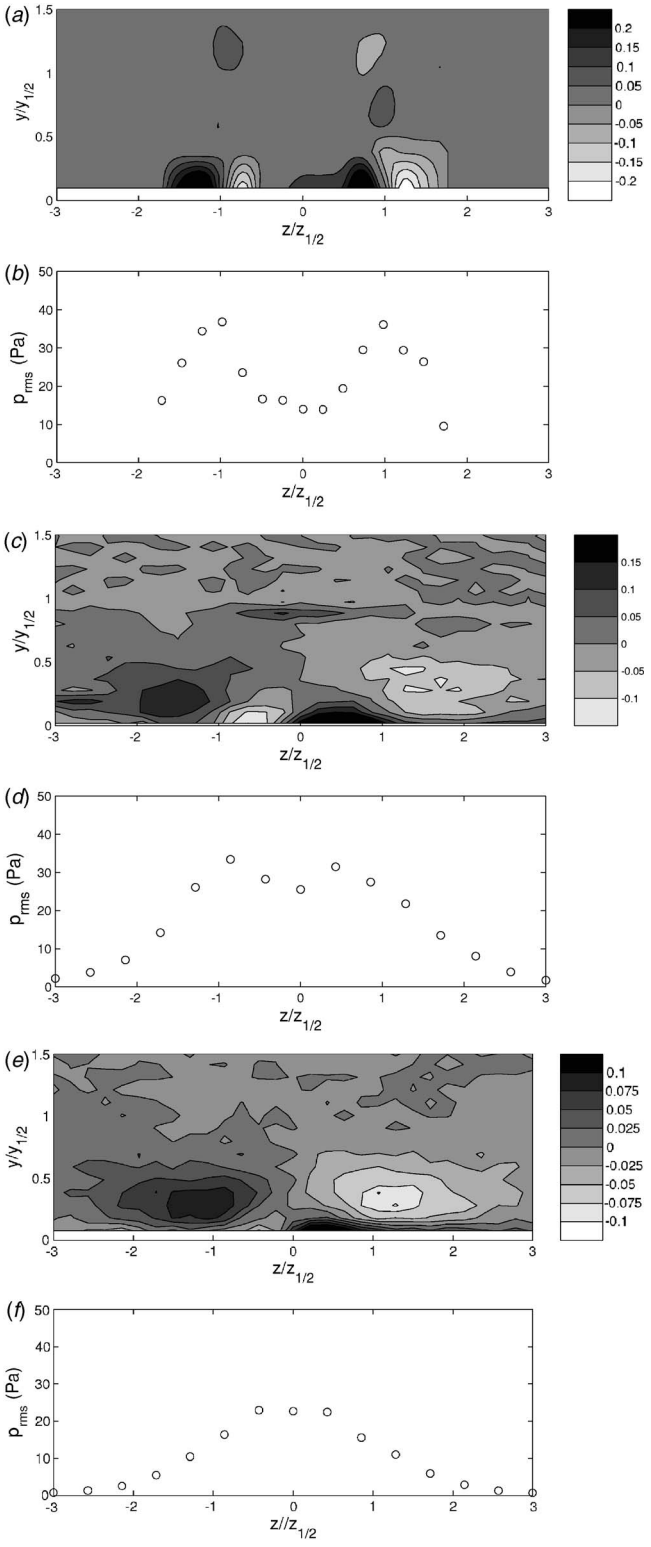

Fig. 4 Comparison of $(\partial W/\partial y)(h/U_{max})$ and p_{rms} at (*a*) and (*b*) $x/h=6$, (*c*) and (*d*) $x/h=20$, and (*e*) and (*f*) $x/h=40$ for the wall jet formed using the $A_r=4$ channel

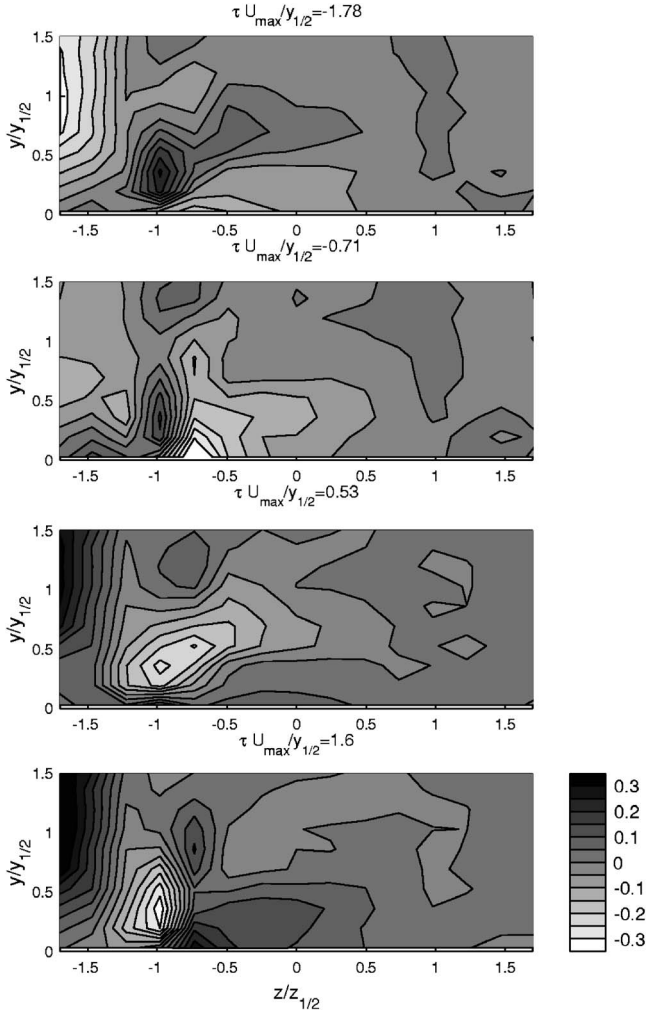

Fig. 5 Sequence of correlations of the fluctuating pressure at $z/z_{1/2}=-1$ with the streamwise fluctuating velocity measured at $x/h=6$

across the jet centerline. These results are consistent with those of Sun [6], who found that the turbulent velocity fluctuations were not well correlated across the jet centerline. These correlations also suggest that the topology of the structure changes significantly from $x/h=6$ to $x/h=20$. For example, at $x/h=6$, there appear to be two oppositely signed regions near the wall at $\tau U_{max}/y_{1/2}=-0.71$ and 1.6. These regions closely correspond to the mean vorticity shown in Fig. 4. Further downstream at $x/h=20$, the correlations appear more indicative of cane or horseshoe vortex structures, which apart from the lack of symmetry across the jet, are consistent with the previously proposed vortex models in the three-dimensional wall jet.

The asymmetry of the organized motions in the flow was also evident in the normalized two-point, two-time correlations of the fluctuating pressure given by

$$\rho_{pp}(z,z',\tau)=\frac{\overline{p(z,t)p(z',t+\tau)}}{p_{\rm rms}(z)p_{\rm rms}(z')} \tag{2}$$

The correlations at $x/h=6$, 20, and 40 are shown in Fig. 7. At each downstream position, the fluctuating pressures at z_{max} are well correlated with the fluctuating pressure on the same side of the jet but poorly correlated with the pressure on the opposite side of the jet centerline. There was a significant time delay across the jet at $x/h=20$ and 40, as marked by the bold line connecting the correlation maxima, that was not evident at $x/h=6$. This suggests that the structures are becoming angled to the jet centerline as they evolve downstream, particularly near the outer edges of the jet. This behavior is consistent with the reorientation of the outer leg of the vortical structures proposed by Ewing and Pollard [8].

The asymmetry of the organized flow structures was further analyzed by applying the POD to the fluctuating wall pressure

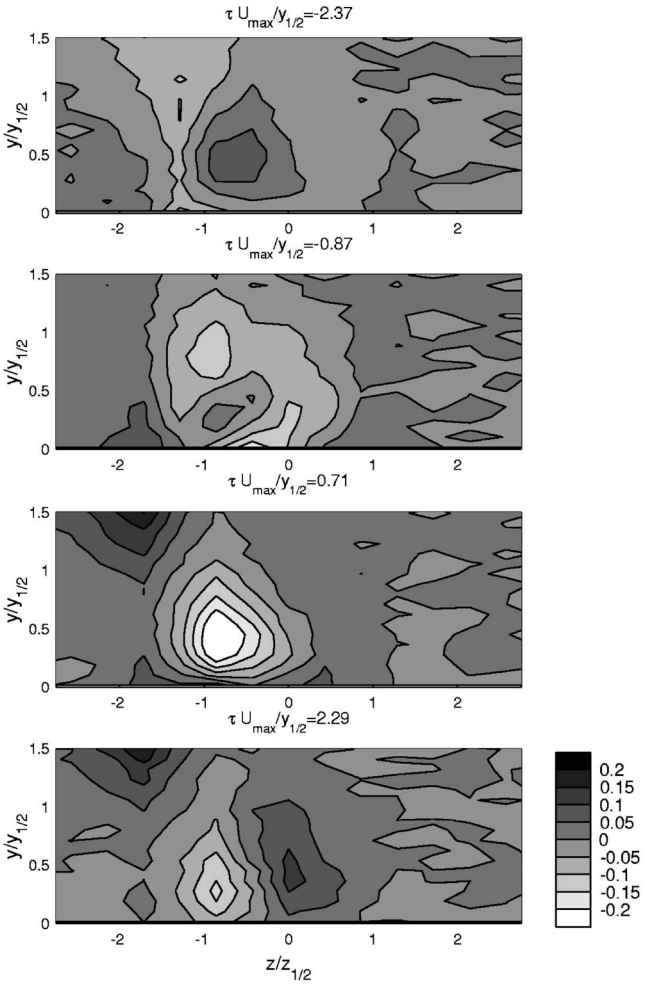

Fig. 6 Sequence of correlations of the fluctuating pressure at $z/z_{1/2}=-0.86$ with the streamwise fluctuating velocity at $x/h=20$

Table 1 Relative contribution of the first three POD modes to the mean square pressure for the jet formed using the $A_r=4$ channel

x/h	$n=1$	$n=2$	$n=3$	$n=1,2,3$
		(%)		
6	49.0	38	7	94
20	37.0	27.7	10.6	75.3
40	36.3	26.2	14.9	77.4

measured across the jet. The fluctuating pressure signals were Fourier transformed in time before the POD was applied. The resulting POD basis functions are solutions to the frequency dependent integral eigenvalue problem given by [15–17]

$$\int_{-\infty}^{\infty} \phi_{pp}(z,z',f)\psi^{(n)}(z',f)dz' = \lambda^{(n)}(f)\psi^{(n)}(z,f) \tag{3}$$

where $\psi^{(n)}(z,f)$ is the eigenvectors, $\lambda^{(n)}(f)$ is the eigenspectrum for the nth modes, and ϕ_{pp} is the cross-spectral tensor given by

$$\overline{\hat{p}(z,f)\hat{p}^*(z',f')} = \phi_{pp}(z,z',f')\delta(f-f') \tag{4}$$

The integral eigenvalue problem was discretized using a trapezoidal weighting scheme and solved at each frequency using the method outlined by Glauser et al. [18].

The contribution from the first three POD modes over all frequencies to the variance of the fluctuating pressure

$$\xi_R^{(n)} = \frac{\int_f \lambda^{(n)}(f)df}{\sum_{i=1}^{m}\int_f \lambda^{(m)}(f)df} = \frac{\int_f \lambda^{(n)}(f)df}{p_{\text{rms}}^2} \tag{5}$$

is shown in Table 1. The first three POD modes capture 94% of p_{rms}^2 at $x/h=6$, and whereas 87% of p_{rms}^2 is contained in the first two POD modes indicating that there are organized pressure fluc-

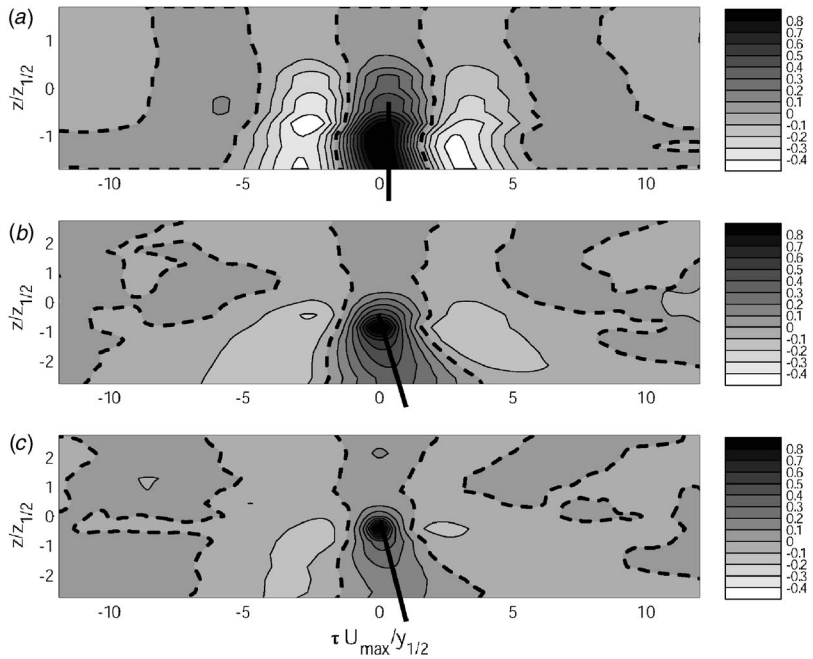

Fig. 7 Normalized two-point two-time correlation of the fluctuating wall pressure, $\rho_{pp}(z/z_{1/2}=z_{\max}/z_{1/2},z',\tau y_{1/2}/U_{\max})$, at (*a*) $x/h=6$, (*b*) $x/h=20$, and (*c*) $x/h=40$ in the jet exiting the $A_r=4$ channel. The contours of zero correlation are marked by the dashed lines.

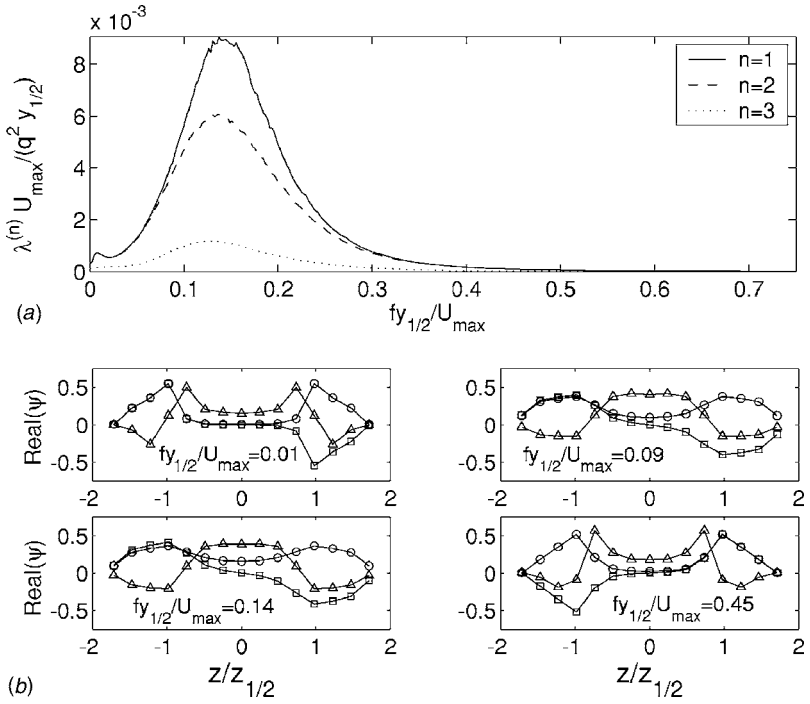

Fig. 8 Comparison of (*a*) the eigenspectra and (*b*) the mode shapes of the first 3 POD modes at $x/h=6$ in the jet formed using the $A_r=4$ channel: ○ $n=1$, □ $n=2$, and △ $n=3$

tuations in the near field of the wall jet. The first three modes contribute less to the pressure fluctuations at $x/h=20$ and $x/h=40$, indicating that the flow is becoming less organized as it evolves downstream. However, the first three POD modes still do contribute to at least 75% of the mean square pressure fluctuations (and the first two modes together contribute more than 60%), so indicating there are still prominent organized motions in the flow at these downstream locations.

The eigenspectra of the first three POD modes and typical mode shapes for various frequencies at $x/h=6$, 20, and 40 are shown in Figs. 8–10. The eigenspectra of the first two POD modes at all downstream positions have single peaks at $fy_{1/2}/U_{\max}$

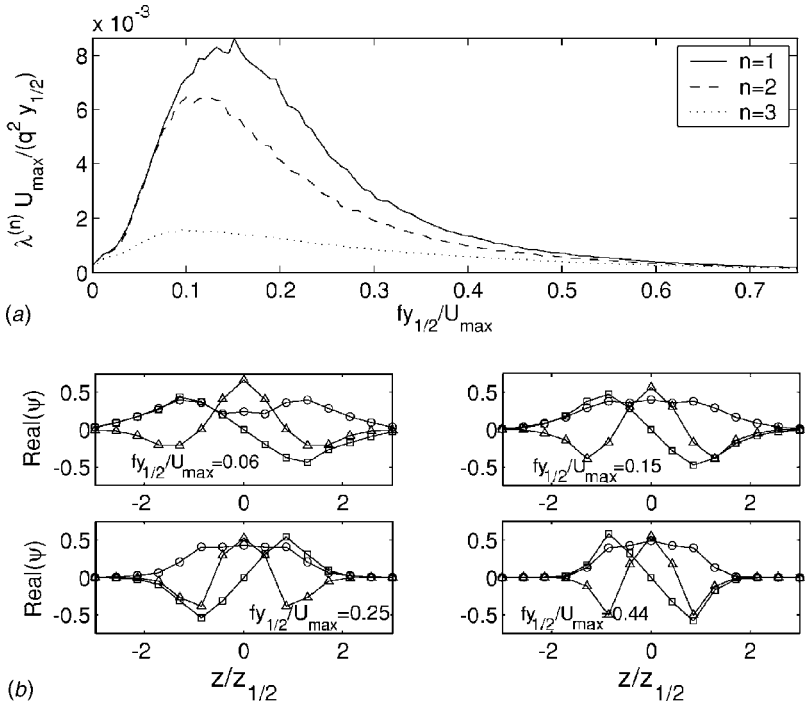

Fig. 9 Comparison of (a) the eigenspectra and (b) the mode shapes of the first 3 POD modes at $x/h=20$ in the jet formed using the $A_r=4$ channel: ○ $n=1$, □ $n=2$, and △ $n=3$

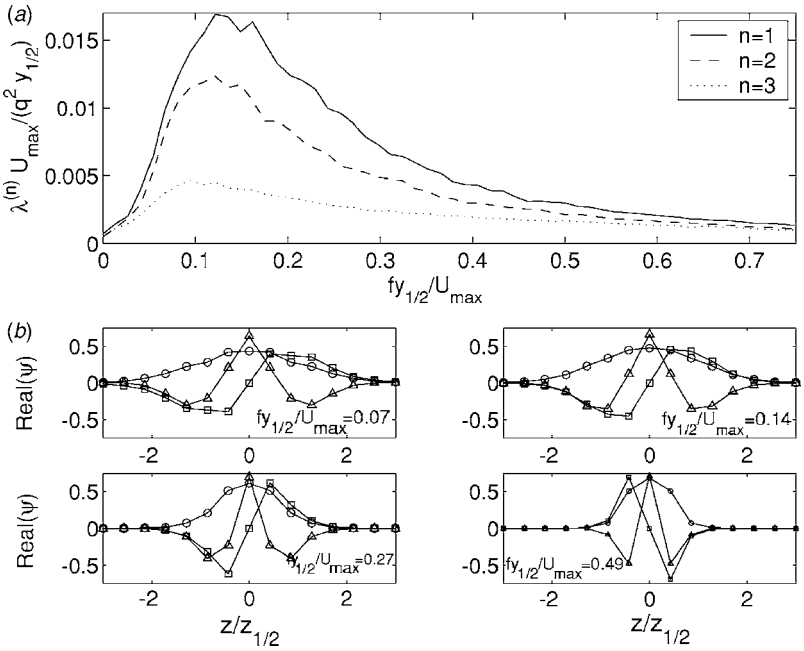

Fig. 10 Comparison of (*a*) the eigenspectra and (*b*) the mode shapes of the first 3 POD modes at $x/h=40$in the jet formed using the $A_r=4$ channel: ○ $n=1$, □ $n=2$, and △ $n=3$

$\approx 0.12-0.14$, again demonstrating that the time scale $y_{1/2}/U_{\max}$ aptly captures the change in the characteristic frequency of the structures. The mode shapes for the first POD mode at all downstream locations are symmetric about the jet centerline with peaks near the jet half width, while the mode shapes for the second mode are antisymmetric with peaks at similar locations. The shapes of the first two POD modes are relatively independent of frequency at $x/h=6$, particularly for the most energetic frequencies. At $x/h=20$ and 40, however, the mode shapes for the first two POD modes are significantly wider at the lower frequencies than those at the higher frequencies. Such frequency-dependent mode shapes have not been observed in previous POD investigations and may be caused by the passage of different width structures in the flow wall jet.

The instantaneous contribution from the first three POD modes was examined by temporally Fourier transforming the simultaneous measurements of the time-resolved fluctuating pressure across the jet and projecting them onto the POD basis functions, i.e.:

$$a_n(f) = \int \hat{p}(z,f)\psi^{(n)*}(z,f)dz \tag{6}$$

The instantaneous contribution of the POD modes in frequency space was computed using

$$\hat{p}^{\text{rec}}(z,f) = \sum_{m=1}^{N} a_m(f)\psi^{(m)}(z,f) \tag{7}$$

and then inverse Fourier transformed back into time to yield a low-order reconstruction of the instantaneous pressure field. A comparison of the transients of the fluctuating pressure field at $x/h=6$ to the contribution to the fluctuating pressure from each of the first three individual modes, the first and second modes, and the first three modes is shown in Fig. 11. The reconstructed pressure field for the first POD mode is symmetric about the jet centerline and appears periodic with peaks at the location of the lateral shear layers, i.e., $\pm z/z_{1/2}=1$. The second mode is antisymmetric with peaks located at roughly the same lateral position as for the first mode. This mode is more intermittent than the first mode but appears to reinforce the contribution from mode 1 on one side of the jet and to negate the contribution from mode 1 on the other side of the jet, such as from $tU_{\max}/y_{1/2}=45-55$. The combination of these modes is asymmetric similar to the full fluctuating pressure field. The opposite nature of the first two POD mode shapes and the relatively even distribution of energy between the first two POD modes allows these modes to combine to capture the instantaneously lateral asymmetry in the fluctuating pressure field. The pressure fluctuations associated with the third mode are smaller in magnitude and very intermittent, and appear to link the pressure fluctuations across the jet. The overall features of the fluctuating pressure field are reasonably recovered using the contribution from both the first two POD modes, while the first three POD modes do capture most of the features of the fluctuating pressure field. For the rest of this investigation, the first three POD modes will be used to produce an accurate, instantaneous, low-order description of the fluctuating wall pressure.

The three-mode reconstruction spatially filters the fluctuations with smaller lateral length scales. To be consistent, the contribution of the high-frequency motions (primarily associated with the smaller-scale structures in the streamwise direction) should be removed by low-pass filtering the eigenspectra. This was performed at a normalized cutoff frequency of $f_c y_{1/2}/U_{\max}=0.4$. The contribution of the POD modes to the mean square pressure fluctuations after this filtering process is shown in Table 2. The filtering reduces the contribution from the first three modes particularly at $x/h=40$, where the peak in the spectra is broader, but in all cases the reduction is modest. Transients of the resulting reconstructed pressure fields across the jet at $x/h=6$, 20, and 40 are shown in Fig. 12. At $x/h=6$, the pressure fluctuations are rarely symmetric and often accompanied by negative pressure fluctuations on the other side of the jet. Downstream at $x/h=20$, the pressure fluctuations are more irregular, though large pressure fluctuations occasionally appear linked to large, liked-sign fluctuations on the other side of the jet at later times ($tU_{\max}/y_{1/2}=20-35$). The asymmetry in the pressure fluctuations is still somewhat apparent at $x/h=40$ even though the pressure fluctuations are much more irregular. In all cases, there is no evidence of lateral meandering in the recon-

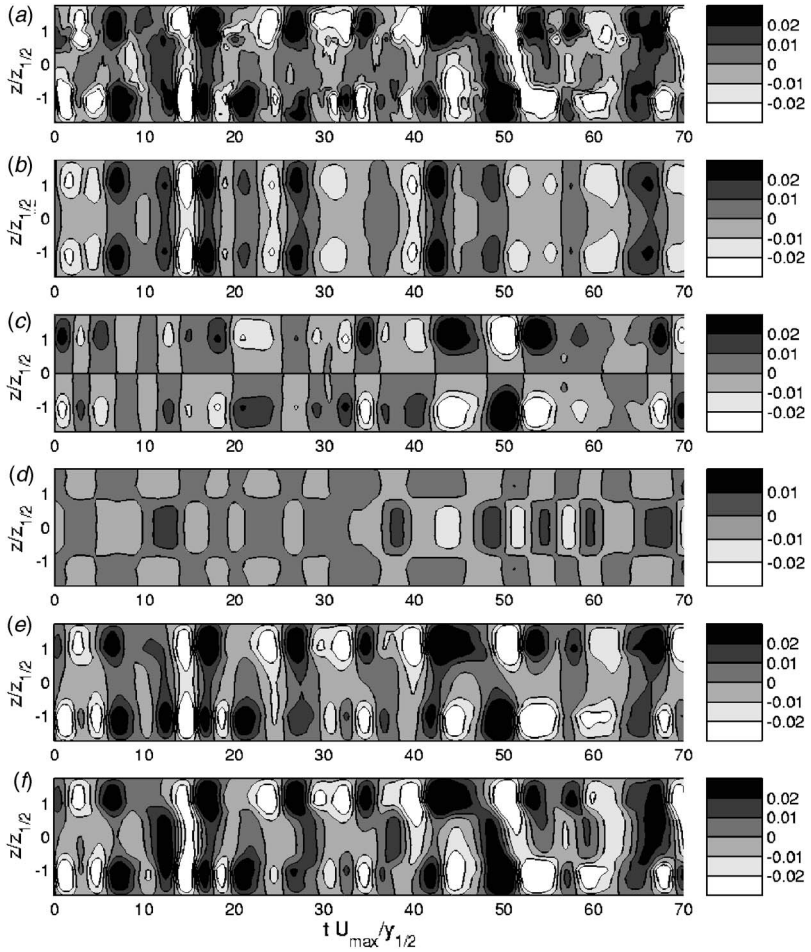

Fig. 11 Transient fluctuating pressure field across the jet normalized by the local dynamic head of jet at $x/h=6$: (*a*) original field, (*b*) reconstructed using only the first POD mode, (*c*) using only the second POD mode, (*d*) using only the third POD mode, (*e*) using the first and second POD modes, and (*f*) using the first three POD modes

structed pressure fields, indicating that the poor correlation of the pressure fluctuations across the jet is a feature of the structures themselves.

The varying lateral extent of the different frequencies noted in the POD mode shapes was examined by applying a continuous wavelet transform to the reconstructed pressure field

$$P(a,\tau)=\frac{1}{\sqrt{a}}\int_{-\infty}^{\infty}p^{\mathrm{rec}}(t)\Psi^{*}\left(\frac{(t-\tau)}{a}\right)dt \tag{8}$$

where a is the scale of the wavelet and τ is the temporal translation parameter. The decomposition was performed using the Morlet wavelet

Table 2 The contribution of the first three POD modes at $0<fy_{1/2}/U_{\max}\leq 0.4$ to the mean square pressure in the jet formed using the $A_r=4$ channel

A_r	x/h	$f_c y_{1/2}/U_{\max}$	$n=1$	$n=2$	$n=3$ (%)	$n=1,2,3$
4	20	≤ 0.40	34.4	25.5	8.8	68.7
4	40	≤ 0.41	25.6	18.3	8.1	52.3

$$\Psi(t)=\frac{1}{\sqrt{2\pi}}e^{\omega_{\Psi}it}e^{-t^2/2} \tag{9}$$

where ω_{Ψ} was set to 5 to force admissibility as discussed by Farge [19]. The modulus and real portion of the wavelet coefficients determined using a three POD mode reconstruction of the fluctuating pressure are shown in Fig. 13 at two different lateral locations. Plotting the modulus of the wavelet coefficients allows the oscillating nature of the mother wavelet to be negated, whereas examination of the real portion of the coefficients yields instantaneous information about the both the magnitude and phase between the two lateral locations. The contributions from the first three POD modes near the center of the jet, such as at $z/z_{1/2}=-0.43$, are rich in frequency content. The largest pressure fluctuations occur primarily at frequencies from $fy_{1/2}/U_{\max}=0.1-0.2$, similar to the peak in the eigenspectra for these POD modes. There are also more intermittent higher-frequency pressure fluctuations at $fy_{1/2}/U_{\max}=0.25-0.50$. The pressure fluctuations near the outer edge of the jet, such as $z/z_{1/2}=-1.71$, however, occur primarily in a narrow frequency band centered at $fy_{1/2}/U_{\max}=0.1$ coincident with the pressure fluctuations at these frequencies near the centerline of the jet. Thus, the low-frequency fluctuations that persist across the jet are consistent with the passage of vortex structures that affect the flow over at least half of the lateral span of the jet. The higher-frequency fluctuations are more localized to

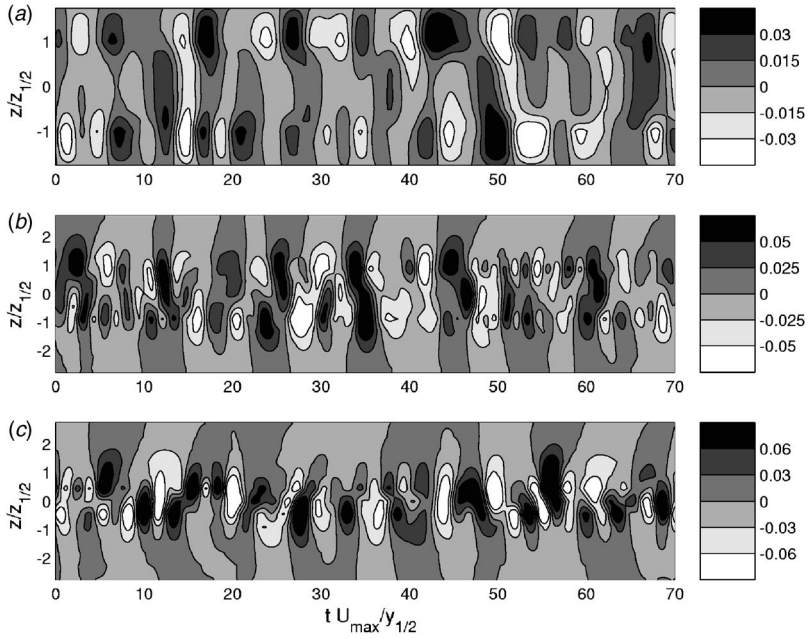

Fig. 12 Transient fluctuating pressure field across the jet normalized by the local dynamic head of jet, $0.5\rho_o U_{max}^2$, reconstructed using the first three POD modes with frequencies $0 < fU_{max}/y_{1/2} \leq 0.4$ at (*a*) $x/h=6$, (*b*) $x/h=20$, and (*c*) $x/h=40$

the centerline of the jet and could be associated with the passage of a second shorter structure like those proposed by Ewing and Pollard [8]. The higher-frequency fluctuations do not appear to be related to the low-frequency events, suggesting that the two structures are not directly linked.

Similar measurements were performed in a three-dimensional wall jet formed with the channel set to $A_r=1$. These measurements are compared to the results for the $A_r=4$ jet by normalizing the streamwise coordinate by the square root of the channel area, $\sqrt{A}$. Contours of $\partial W/\partial y$ and profiles of p_{rms} at $x/h=10$ and 20 in the $A_r=1$ wall jet are compared in Fig. 14. The cross-wire measurements could not be performed in this jet at $x/h=3$ to compare to the measurements at $x/h=6$ in the $A_r=4$ jet. Again, the maxima in the standard deviation of the fluctuating pressure are located beneath the inner regions of large $\partial W/\partial y$. The outer regions of

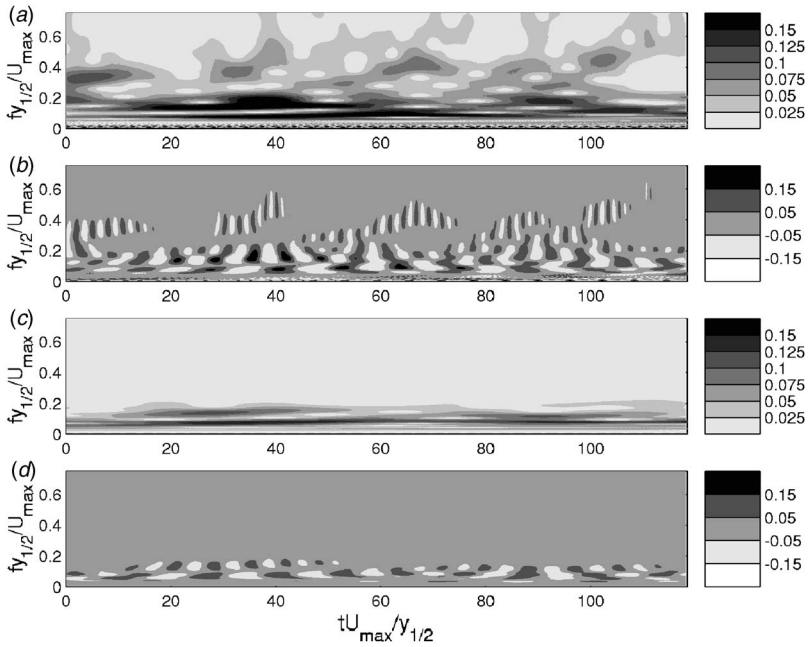

Fig. 13 Comparison of (*a*) and (*c*) the modulus of the wavelet coefficients and (*b*) and (*d*) the real part of the wavelet coefficients for the contribution of the first three POD modes at (*a*) and (*b*) $z/z_{1/2}=-0.43$, and (*c*) and (*d*) $z/z_{1/2}=-1.71$

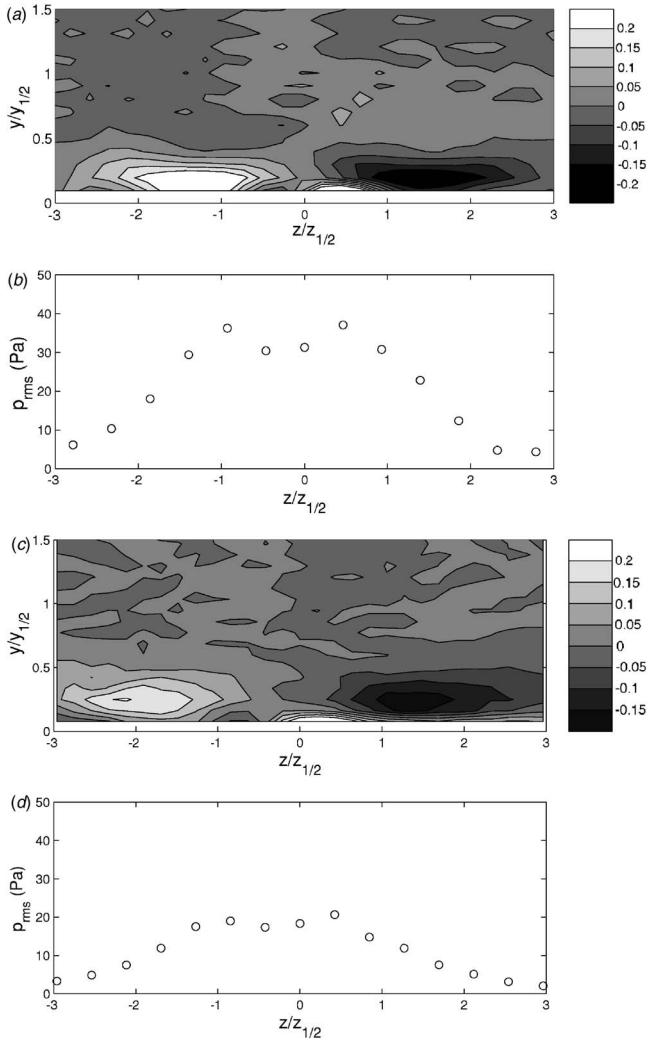

Fig. 14 Comparison of $(\partial W/\partial y)(h/U_{max})$, and p_{rms} at (*a*) and (*b*) $x/h=10$ and (*c*) and (*d*) $x/h=20$ for the jet formed using the $A_r=1$ channel

$\partial W/\partial y$ are located closer to the wall and are more concentrated, thereby causing larger pressure fluctuations in this flow than in the $A_r=4$ jet.

The eigenspectra and mode shapes determined in this jet at $x/h=10$ and 20 are shown in Figs. 15 and 16. The eigenspectra of the first two POD modes at $x/h=10$ have peaks at $fy_{1/2}/U_{max}=0.18-0.19$, higher than the normalized peak frequency in the eigenspectra for the $A_r=4$ wall jet. The first POD mode shapes are antisymmetric about the jet centerline for frequencies corresponding to the peak in the eigenspectra ($0.1<fy_{1/2}/U_{max}<0.35$) and symmetric for all other frequencies. The second POD mode shapes behave in the opposite manner, being symmetric near the peak frequencies and antisymmetric at the other frequencies. Integrating the portions of the eigenspectra associated with the symmetric and antisymmetric mode shapes separately revealed that the antisymmetric mode is more prominent. Downstream, at $x/h=20$, the first POD mode is symmetric and the second mode is antisymmetric similar to the jet exiting the larger aspect-ratio channel. In both cases, the width of the mode shapes decreases with frequency, again suggesting that there are multiple width structures in this flow. The frequency of the peak in the eigenspectra for the second POD mode decreases more significantly than for the first mode from $x/h=10-20$. A similar but less prominent decrease occurred in the jet exiting the larger channel between $x/h=20-40$.

Transients of the fluctuating pressure reconstructed from the first three POD modes in the two jets at $x\sqrt{A}=10$ and 20 are shown in Fig. 17. The reconstructed fields have been low-pass filtered at $f_c y_{1/2}/U_{max}=0.5$ in the $A_r=1$ jet, slightly higher because of the higher characteristic frequencies here than in the $A_r=4$ jet. Again, the filter did not have a significant effect on the contribution from the first three POD modes as summarized in Table 3. As suggested by the eigenspectra, there are differences in the normalized time scale of the motions between the jets indicating $U_{max}/y_{1/2}$ does not collapse the differences in the time scales between the two jets. The reconstructed pressure fluctuations at $x/\sqrt{A}=10$ in the square jet are more regular than in all other cases and often clearly antisymmetric ($tU_{max}/y_{1/2}\approx 7$, 22, or 41). The prevalence of the antisymmetric mode here suggests that the antisymmetry of the structures may develop in the near field of the $A_r=1$ jet. The pressure fluctuations at $x/\sqrt{A}=20$ in the square jet are simply asymmetric, consistent with the results for the larger aspect-ratio jet. The overall differences in the results for the two jets are more significant than could be attributed to improperly scaling the streamwise coordinate, suggesting that there are fundamental differences in the development of the structures in these two flows.

Concluding Remarks

The development of the large-scale structures in three-dimensional wall jets formed using long channels with aspect ratios of 1 and 4 was investigated using simultaneous measurements of the fluctuating pressure and velocity across the jet. In both jets, the fluctuating wall pressure was not well correlated with either the fluctuating velocity or the fluctuating pressure across the jet centerline. Instantaneous measurements revealed that this was not due to lateral meandering of the structures as previously thought, but was because the structures themselves are asymmetric. This feature of the large-scale structures has not been incorporated in previous coherent structures models for three-dimensional wall jets and may suggest that the development of the jet could be modified by promoting or reducing the instantaneous lateral symmetry of the flow. Since previous measurements in a wall jet exiting a round opening have also shown poor correlation across the jet centerline [6], it is likely that the lack of lateral symmetry in the structures is not particular to the jet outlets investigated here.

The POD was performed on the fluctuating pressure measurements to characterize the lateral extent of the motions in the jet. The first two POD mode shapes were symmetric and antisymmetric, respectively, and made similar and prominent contributions to the mean square pressure fluctuations at all downstream locations. The interplay between these modes recovered the asymmetry observed in the instantaneous pressure fluctuations. A wavelet analysis of the spatially filtered fluctuating wall pressure indicated that there were at least two different type structures in the wall jet. Specifically, low-frequency fluctuations coincident across one side of the jet are likely related to the angled outer leg of the vortex structures proposed by Matsuda et al. [7], whereas higher-frequency events at the center of the jet could be related to the passage of shorter inner structures like those proposed by Ewing and Pollard [8]. Here though, it appears that these are two independent structures in the flow. The present results indicate that the contribution of the two structures may be effectively isolated by combining temporal bandpass filtering with lateral POD filtering. The full relationship between the pressure-velocity correlations and the vortex structures is currently under investigation.

A comparison of the fluctuating wall pressure measured in the three-dimensional wall jet exiting the square channel with the measurements in the $A_r=4$ channel indicated that there were differences in the development of the large-scale structures in the

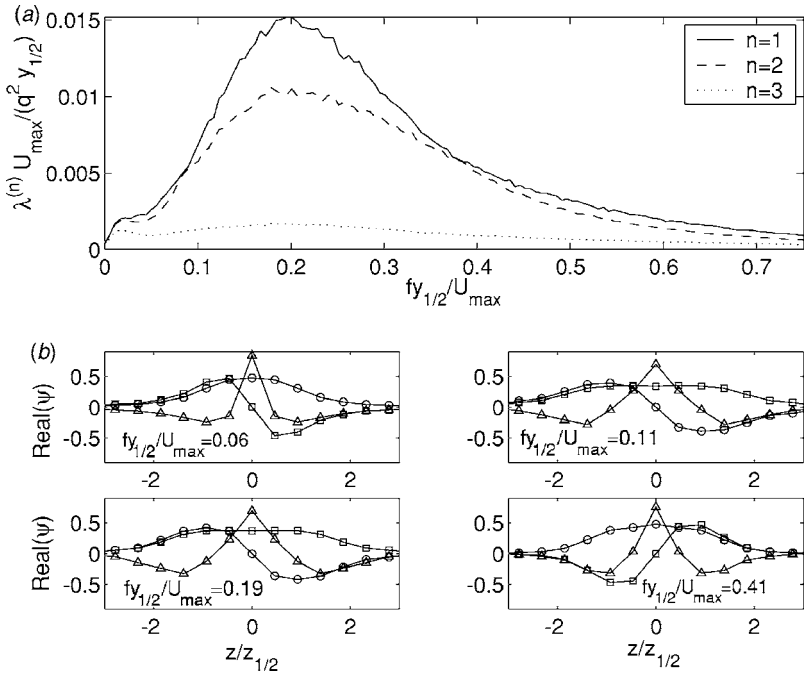

Fig. 15 Comparison of (*a*) the eigenspectra and (*b*) the mode shapes of the first three POD modes at $x/h=10$ in the jet formed using the $A_r=1$, channel: ○ $n=1$, □ $n=2$, and △ $n=3$

two flows. The results in the jet exiting the square nozzle at $x/h=10$ were more antisymmetric than those in the larger aspect-ratio wall jet, the outer structures were closer to the wall in the $A_r=1$ jet, and the characteristic frequency of the motions normalized by the local maximum velocity and jet half width differed by ~30% in the intermediate field. Overall, the differences in the development of the structures seemed larger than could be explained by improperly scaling the streamwise development of the jet. Thus, the structures do appear to depend on the initial conditions of the jet, at least in the region examined here.

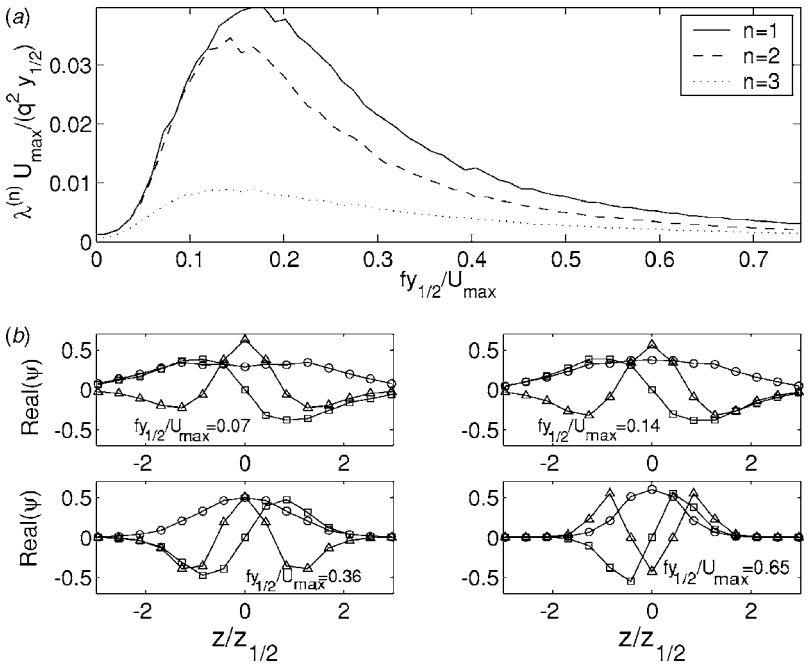

Fig. 16 Comparison of (*a*) the eigenspectra and (*b*) the mode shapes of the first three POD modes at $x/h=20$ in the jet formed using the $A_r=1$ channel: ○ $n=1$, □ $n=2$, and △ $n=3$

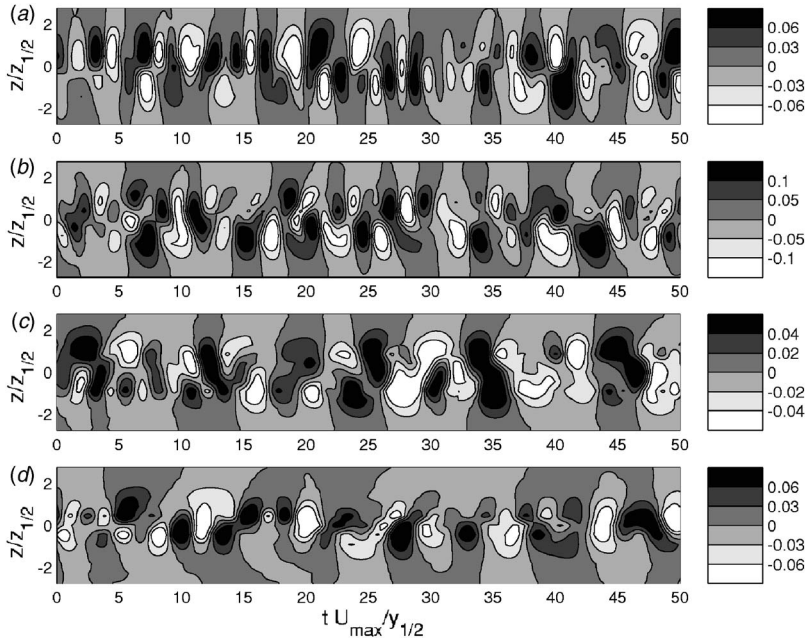

Fig. 17 Transient pressure field normalized by the local dynamic head of the jet, $0.5\rho_o U_{max}^2$, reconstructed using the first three POD modes for frequencies $0 < fU_{max}/y_{1/2} \leq 0.5$ at (*a*) $x/\sqrt{A}=10$, (*b*) $x/\sqrt{A}=20$ in jet formed using $A_r=1$ channel and for frequencies $0 < fU_{max}/y_{1/2} \leq 0.5$ at (*c*) $x/\sqrt{A}=10$, and (*d*) $x/\sqrt{A}=20$ in jet formed using $A_r=4$ channel

Table 3 The contribution to the mean square pressure fluctuations of the first three POD modes integrated over all frequencies and for $0 < fy_{1/2}/U_{max} \leq 0.5$ in the wall jet formed using the $A_r=1$ channel

A_r	x/h	$f_c y_{1/2}/U_{max}$	$n=1$	$n=2$	$n=3$ (%)	$n=1,2,3$
1	10	unfiltered	45.6	35.6	7.9	89.2
1	10	0.50	41.4	32.7	6.4	80.1
1	20	unfiltered	36.7	27.9	11.3	75.9
1	20	0.51	29.9	23.1	7.9	60.9

Acknowledgment

The authors are grateful for the financial support of the Natural Sciences and Engineering Research Council of Canada and the Ontario Graduate Scholarship Program.

Nomenclature

a = wavelet scale
A = channel cross-sectional area
A_r = channel aspect ratio, $A_r=W_c/h$
f = frequency, Hz
h = height of channel, m
j = $j=\sqrt{-1}$
t = time, s
T = block length, s
N = number of blocks
P = wavelet coefficients, Pa
p = fluctuating wall pressure, Pa
p_{rms} = standard deviation of fluctuating pressure, Pa
p_{max} = maximum standard deviation of fluctuating pressure, Pa
$\overline{p^2}$ = variance of fluctuating pressure, Pa^2
R_{pp} = pressure correlation function, Pa^2
U_{exit} = exit streamwise flow velocity, m/s
U_{max} = maximum streamwise flow velocity, m/s
W = mean lateral flow velocity, m/s
W_c = width of channel, m,
x = streamwise coordinate, m
y = vertical coordinate, m
$y_{1/2}$ = vertical jet half width, m
z = lateral coordinate, m
z_{max} = location of maximum variance of fluctuating wall pressure, m
$z_{1/2}$ = lateral jet half width, m
$\lambda^{(n)}$ = energy in nth POD mode, Pa^2
ν = kinematic velocity, m^2/s
$\xi^{(n)}$ = energy recovered using n POD modes relative to $\overline{p^2}$, %
ρ_o = ambient fluid density, kg/m^3
ρ_{pp} = normalized correlation of fluctuating wall pressure
τ = time lag, s
ϕ_{pp} = cross-spectra of fluctuating wall pressure, Pa^2/Hz
Ψ = mother wavelet
ψ = POD mode shape
Ω_x = streamwise component of mean vorticity

References

[1] Davis, M. R., and Winarto, H., 1980, "Jet Diffusion From a Circular Nozzle Above a Solid Plane," J. Fluid Mech., **101**, pp. 193–218.
[2] Launder, B. E., and Rodi, W., 1981, "The Turbulent Wall Jet," Prog. Aerosp. Sci., **19**, pp. 81–128.
[3] Launder, B. E., and Rodi, W., 1983, "The Turbulent Wall Jet-Measurements and Modelling," Annu. Rev. Fluid Mech., **15**, pp. 429–459.
[4] Abrahamsson, H., Johansson, B., and Lofdahl, L., 1997, "The Turbulence Field of a Fully Developed Three-Dimensional Wall Jet," Tech. Report No. 91-1, Chalmers University of Technology, Sweden.
[5] Iida, S., and Matsuda, H., 1988, "An Experimental Study of Circular Turbulent Wall Jet Along a Convex Wall," Trans. Jpn. Soc. Mech. Eng., Ser. B, **54**, pp. 354–360.
[6] Sun, H., 2002, "The Effect of Initial Conditions on the Development of the

Three-Dimensional Wall Jet," Ph.D. thesis, McMaster University, Hamilton, Ontario, Canada.
[7] Matsuda, H., Iida, S., and Hayakawa, M., 1990, "Coherent Structures in Three-Dimensional Wall Jet," ASME J. Fluids Eng., **112**, pp. 462–467.
[8] Ewing, D., and Pollard, A., 1997, "Evolution of the Large-Scale Motions in a Three-Dimensional Wall Jet," 28th AIAA Fluid Dynamics Conference/4th AIAA Shear Flow Control Conference, AIAA Paper No. 97-1964.
[9] Ewing, D., Benaissa, A., Pollard, A., Citriniti, J., Abrahamsson, H., and Lofdahl, L., 1997, "Contribution of Large Structures to the Anisotropic Spread Rate in a Wall Jet Issuing From a Round Nozzle," 10th International Symposium on Transport Phenomena in Thermal Science and Process Engineering, Kyoto, Japan.
[10] Hall, J. W., and Ewing, D., 2007, "Three-Dimensional Turbulent Wall Jets Issuing from Moderate-Aspect-Ratio Rectangular Channels," AIAA J., **45**(6), pp. 1177–1186.
[11] Rajaratnam, N., and Pani, B. S., 1974, "Three-Dimensional Turbulent Wall Jets," J. Hydr. Div., **HV1**, pp. 69–83.
[12] Hall, J. W., 2005, "The Role of The Large-Scale Structures in the Development of Turbulent Wall Jets," Ph.D. thesis, McMaster University, Hamilton, Ontario, Canada.
[13] Beuther, P. D., 1980, "Experimental Investigation of the Axisymmetric Turbulent Bouyant Plume," Ph.D. thesis, SUNY, Buffalo.
[14] Bendat, J. S., and Piersol, A. G., 1993, *Engineering Applications of Correlation and Spectral Analysis*, Wiley, New York.
[15] Lumley, J. L., 1967, "The Structure of Inhomogeneous Turbulence," *Atmospheric Turbulence and Wave Propagation*, A. M. Yaglom and V. I. Tatarski, eds., Nauka, Moscow, pp. 166–178.
[16] Glauser, M. N., 1987, "Coherent Structures in the Axisymmetric Turbulent Jet Mixing Layer," Ph.D. thesis, State University of New York at Buffalo.
[17] Holmes, P., Lumley, J. L., and Berkooz, G., 1996, *Turbulence, Coherent Structures, Dynamical Systems and Symmetry*, Cambridge University Press, Cambridge, England.
[18] Glauser, M. N., Leib, S. J., and George, W. K., 1987, "Coherent Structures in the Axisymmetric Mixing Layer," *Turbulent Shear Flows 5*, F. Durst, ed., Springer-Verlag, Berlin, pp. 4.21–4.26.
[19] Farge, M., 1992, "Wavelet Transforms and Their Applications to Turbulence," Annu. Rev. Fluid Mech., **24**, pp. 395–457.

Experimental and Numerical Investigation of a Swirl Stabilized Premixed Combustor Under Cold-Flow Conditions

P. A. Strakey
e-mail: peter.strakey@netl.doe.gov

M. J. Yip

National Energy Technology Laboratory,
3610 Collins Ferry Road,
P.O. Box 880,
Morgantown, WV 26507

Planar velocity measurements under cold-flow conditions in a swirl-stabilized dump combustor typical of land-based gas turbine combustors were carried out using two-dimensional particle image velocimetry (PIV). Axial, radial, and tangential velocity components were measured sequentially using two experimental configurations. Mean and root-mean-squared velocity components are presented along with instantaneous realizations of the flowfield. A numerical study of the flowfield using large-eddy simulation (LES) and Reynolds-averaged Navier-Stokes (RANS) techniques was conducted in an effort to help understand the complex hydrodynamics observed in the experiments. The agreement between the experimental data and LES simulation was good with both showing evidence of a precessing vortex core. The results of the RANS simulation were not as encouraging. The results provide a fundamental understanding of the complex flowfield associated with the relatively simple geometry and also serve as a baseline validation dataset for further numerical simulations of the current geometry. Validation of LES models in a highly swirled, nonreacting flowfield such as the work presented here is an essential step towards more accurate prediction in a reacting environment. [DOI: 10.1115/1.2743665]

1 Introduction

Lean premixed combustion has become the favored approach to land based gas turbine power generation using natural gas due mainly to the inherently low emissions of NO_x and CO with this approach. Some of the problems associated with lean premixed combustion include combustion dynamics and a sensitivity to operating conditions and fuel type. There is a growing interest within the Department of Energy in fueling gas turbine combustors with syngas or other hydrogen-rich fuels derived from the gasification of coal. There is, however, very little experimental data and general understanding of the effects of fuel variability on combustor performance and pollutant emissions.

Increasing the fuel hydrogen content will greatly accelerate the chemical kinetics of the combustion process and the flame speed, which can improve stability at lean conditions and extend operation to leaner conditions and lower NO_x emissions [1]. Hydrogen has been studied as an additive to natural gas in gas turbine applications for NO_x reduction [1], and is of special interest due to the growing popularity of integrated gasification combined cycle (IGCC) power generation systems. In IGCC syngas based fuels, the hydrogen content of the fuel can vary widely. For example, syngas can be derived from various sources, with fuel hydrogen contents varying from 9% to 62% by fuel volume [2]. There has also been a growing interest in carbon sequestration in the U.S. in the past few years, which provides an even greater driver for developing gas turbines that can run on high hydrogen content fuels. This wide fuel composition variation alone is likely to complicate the development process for future gas turbine combustors, and will add significant complexity, time, and cost to the combustor and turbine development process.

Even for gas turbine systems utilizing solely natural gas, the cost of developing new low-emission turbine combustors is high. A typical development program can last for several years and requires repeated hardware testing and redesign to resolve unexpected problems with combustion stability, hardware life, and emissions performance. Adapting a low-emission combustor to a fuel with a different composition may require a similar investment, and the high development cost is one factor that prevents routine engine deployment where low emissions are sought on "opportunity" fuels such as biogas, or hydrogen-rich syngas. While the use of different opportunity fuels would be beneficial for energy production, the cost of developing fuel-specific combustors or redeveloping existing combustors is often too great to justify development for a specific fuel application.

A reliable, low-cost method to evaluate combustor performance during operation with various fuels could greatly reduce the time and cost required to develop these new turbine combustors. Progress in computational fluid dynamics (CFD) modeling of combustion systems has advanced to the point where basic design features are now routinely assessed on the computer. In many instances, these simulations have produced useful qualitative information about the effects of proposed design changes. However, a quantitatively accurate prediction of combustion dynamics, pollutant emissions, and the effects of specific fuel chemistry are beyond the capability of current computational models. Technical progress in this area could provide a low-cost method to evaluate the behavior of new fuels in proposed combustor designs.

The advancement of computational modeling tools is limited by the availability of experimental data for model development and validation. Central problems in model development include: providing an accurate, computationally tractable representation of key processes in the flame such as turbulence-chemistry interaction, sub-grid mixing, and accurately representing the acoustic, flow, and thermal boundary conditions. In simple laboratory flames, considerable progress has been made on sub-model development using experimental data from well-characterized diffusion flames [3]. However, similar data are less available for the type of premixed flames that are used in low-emission gas turbine combustors.

Contributed by the Fluids Engineering Division of ASME for publication in the JOURNAL OF FLUIDS ENGINEERING. Manuscript received April 3, 2006; final manuscript received January 18, 2007. Review conducted by Joseph Katz.

The majority of studies conducted on lean premixed combustors has focused on measuring global phenomena such as pollutant emissions and stability. There have been a limited number of studies in which detailed flowfield measurements have been made. Wicksall et al. [4] used PIV to study the effects of hydrogen addition on a methane based lean premixed flame in a swirl stabilized combustor operating at atmospheric pressure. They showed the significant effects of hydrogen on the flame structure as well as the ability of PIV to provide detailed experimental data over a large portion of the flowfield.

Griebel et al. [5] presented detailed PIV and hydroxyl radical (OH) planar laser-induced fluorescence data for premixed methane air flames at elevated pressures (up to 10 bar). This work was conducted in a generic combustor using grid generated turbulence without the use of swirl to stabilize the flame. Measurements included mean and rms values of axial and radial velocities as well as integral length scale and flame-front location. This is one of the very few studies conducted at elevated pressure.

Cabot et al. [6] made a variety of measurements in a scaled down model of an industrial gas turbine combustor under unstable operation at atmospheric pressure. Measurements included dynamic pressure, CH chemiluminescence, and CO and NO_x emissions. This study was focused on the effects of combustion dynamics and primary dilution air on flame structure and pollutant emissions.

The need to develop and validate computational tools for designing and understanding the complex physical and chemical processes occurring in gas turbine combustors is universal. This is especially true in the evolution of fuel flexible combustors capable of burning hydrogen or syngas type fuels. The purpose of this study is to provide much needed datasets for validating and developing computational tools under conditions representative of industrial gas turbine combustors. This paper presents the first such dataset, which is comprised of two-dimensional PIV measurements within a combustor operating at atmospheric pressure cold-flow conditions. While these conditions of course do not simulate the combustion environment, they do lay the groundwork for more complex experiments that are aimed at making detailed flowfield measurements under high-pressure combustion conditions. In addition, these data present an opportunity to validate LES codes in a highly swirling flowfield in the absence of combustion, which can often obscure problems associated with LES sub-models and numerical approaches.

Experimental

The combustor used in the investigation here, referred to as SimVal, is shown schematically in Fig. 1. It consists of a slot swirler, a nozzle section, and a combustor section that is encased by a 180 mm diam quartz tube followed by an exhaust section. Further details of the combustor along with pollutant measurements can be found elsewhere [7]. For the cold-flow measurements made here, both the inlet and exhaust choke were removed and the combustor was operated at ambient temperature and pressure. Air flowrate through the combustor was regulated upstream of the combustor with a control valve and flowmeter, which was accurate to ±1%. For the data presented here, the maximum air flowrate was 0.137 kg/s and there was no fuel flow. The combustor was mounted on a hydraulic jackstand that allowed the combustor to be raised or lowered with respect to the laser sheet and camera. In this fashion, the combustor was moved while the optics remained fixed.

Since the planar PIV technique used here was only capable of measuring two velocity components, two basic experimental configurations were used to sequentially measure the axial and tangential velocity components. This was accomplished by passing the laser sheet through the combustor in either a "horizontal" configuration (as shown in Fig. 2), which yields tangential and radial

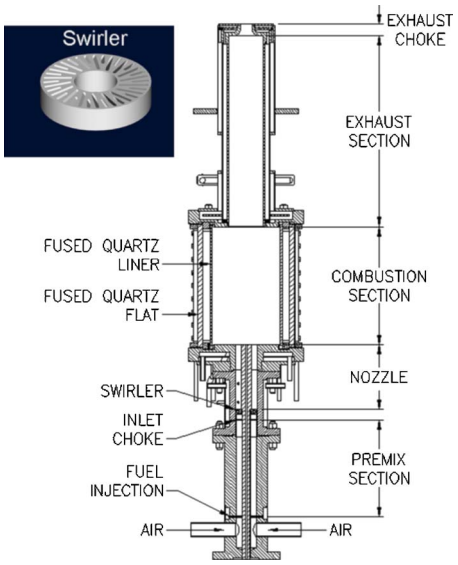

Fig. 1 Schematic of the SimVal combustor with inset showing swirl plate

velocity components, or in a "vertical" configuration in which the sheet is perpendicular to the combustor exit plane and passed through the centerline of the combustor. For the horizontal configuration shown in Fig. 2, the camera was configured to view the light sheet through the exhaust section of the combustor using a mirror located just above the combustor exit. For the vertical configuration, the CCD camera was oriented normal to the laser sheet and was viewing through the wall of the quartz liner without the use of a mirror. This configuration yielded the axial and radial velocity components over one-half of the annulus as the field of view was not large enough to capture the entire flowfield.

The airflow was seeded with aluminum oxide powder of 1 μm nominal diameter. Seeding was accomplished by passing approximately 1% of the total airflow through a membrane dryer followed by a cyclone seeder designed specifically for the high flowrates studied here. The seeder consisted of a 15 cm diam cylinder approximately 25 cm high. Air was introduced to the seeder by a pair of tangentially oriented inlet tubes near the bottom of the chamber. The seeder was filled with approximately 5 cm of aluminum oxide powder and a four-blade paddle located at the bottom of the seeder continuously stirred the powder to prevent caking and maintain a steady flow of seed. A 38 mm diam cyclone separator was located inside the seeder at the exit to remove any large agglomerates that may be entrained in the flow.

The PIV system was a commercial two-dimensional system manufactured by TSI Inc. It consisted of a two-head YaG laser (Gemini model 15 Hz, New Wave Research Inc.) with approximately 100 mJ of output at 532 nm per head. The sheet forming optics consisted of a 2 m spherical lens located 1.8 m from the center of the combustor followed by a −25 mm cylindrical lens. The spherical lens was intentionally located away from the focal point of the lens (~1.8 m) in order to increase the thickness of the laser sheet in the combustor section, which was measured to be 1.2 mm at the $1/e^2$ beam waist. The relatively thick laser sheet was necessary in order to minimize the loss of particle image pairs in the strongly swirling flowfield.

The PIV camera was a TSI Powerview frame-straddling model 630149 camera with 2048×2048 resolution. A 200 mm f4.0 micro-Nikkor lens with a 12 mm spacer ring was used to collect the scattered light. The lens was always operated at f5.6 and was located at 1.3 m from the laser sheet yielding a field of view of 91×91 mm and a resolution of 44 μm per pixel. The long focal length lens was necessary to reduce error in the velocity measure-

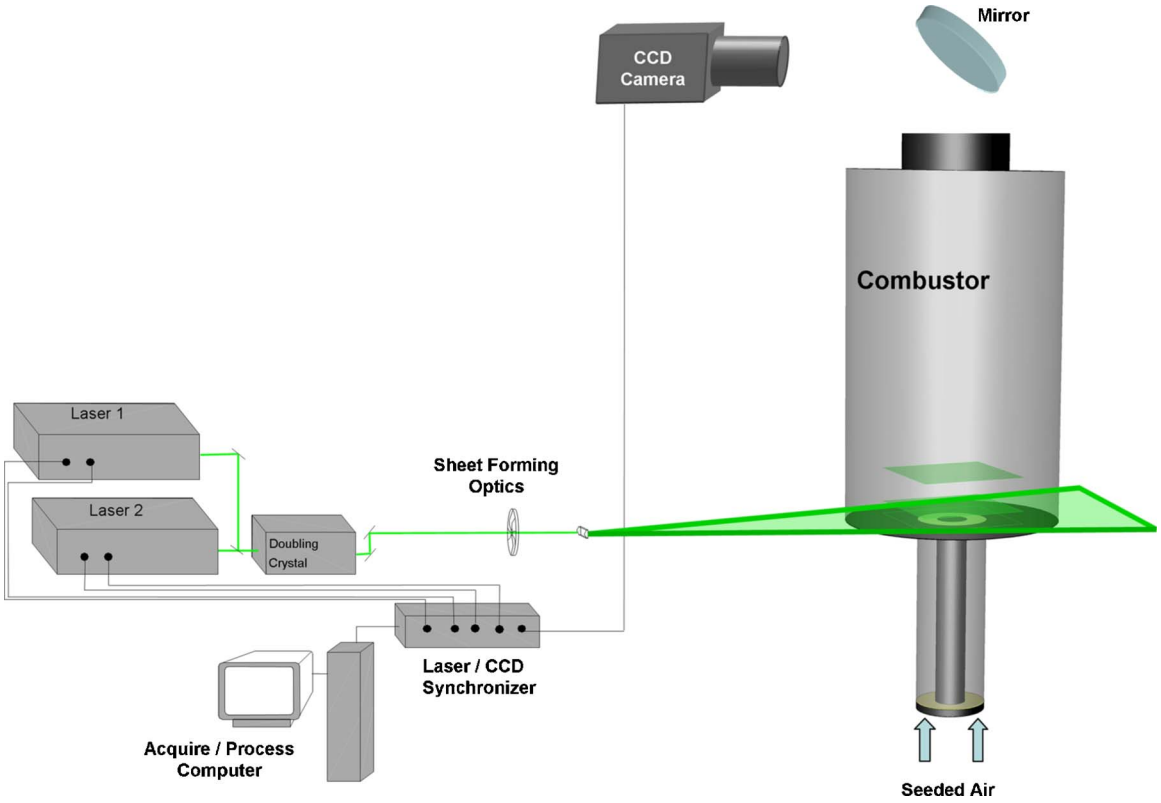

Fig. 2 Layout of the two-dimensional PIV system in the "horizontal" light-sheet configuration

ment due to perspective error. Perspective error is caused by the out-of-plane motion of the particles combined with the finite collection angle of the lens. As the particles move either toward or away from the camera, there is an apparent motion in either the vertical or horizontal direction due to the fact that the camera is viewing the particles at an angle. Since the viewing angle increases toward the edges of the image, this is where the largest errors occur. Although this error cannot be eliminated in a 2D PIV system, it can be minimized by reducing the viewing angle as defined by the focal length of the lens and the field of view. With the current optical configuration, the maximum viewing angle at the edge of the image is 2.0 deg.

In order to estimate the magnitude of this source of error, it is necessary to know the magnitude of the swirling velocity component as well as the axial and radial components. Since all three velocity components were measured at several overlapping regions, it was possible to estimate the error on the mean velocity as ±2% in the axial component and as much as ±20% in the radial component. The larger percentage error in the radial component is due to the fact that the radial velocities are small compared to the axial and tangential velocity components.

The software used to process the image pairs was TSI Insight version 3.5. The software uses a Gaussian peak searching algorithm to locate the theoretical particle image center at a sub-pixel accuracy. This algorithm has been estimated to yield accuracies as high as ±0.1 pixel for an idealized particle image, although it is difficult to estimate the realistic accuracy for nonspherical particle images [8]. A two-frame, fast Fourier transform based cross-correlation algorithm is used to determine the average particle displacement within each interrogation region. For all of the data presented here, a 32×32 pixel interrogation region was used with 50% overlap in both the vertical and horizontal directions. This yielded a final system resolution of 1.4 mm $\times$ 1.4 mm with a depth of field of 1.2 mm as determined by the laser sheet thickness.

After processing, the vector field was validated using a 3-standard deviation criterion to remove spurious vectors. Further validation was ensured using a "mean" filter of 50% of the bulk flow velocity in the nozzle over a 3×3 neighborhood. Typical validation rates were in the range of 90–95% with most of the rejections occurring in regions where reflections from the combustor face were significant. A typical run included the capture of 100 images at a rate of about 1 image per second. The number of images in each dataset was limited by computer memory and by the deposition of the alumina seed particles on the quartz liner, which increased the stray scattered light reaching the camera and decreased the signal-to-noise ratio of the data. Statistical significance was checked by capturing several sequences of 100 images at the same location and flowrate and by examining the variation in mean velocity between the different sets of data. The maximum variation in mean velocity between data sets was roughly 12% and occurred in the regions of highest velocity gradient. Within the regions of high velocity, the typical variation in mean velocity between datasets was about 5%.

Most of the data collected were at a flowrate of 0.137 kg/s, which corresponds to a bulk flow velocity in the nozzle section of 54 m/s. For this flowrate, a laser pulse separation time of 2 μs was found to yield the maximum vector validation rate. The optimization of the PIV system at this relatively short pulse separation time is due to the out-of-plane motion, which results in significant numbers of particles passing out of the laser sheet between pulses for longer pulse separation times. For the nominal velocity of 54 m/s, this results in a particle displacement of 108 μm or 2.4 pixels within the laser sheet. With an estimated sub-pixel interpolation accuracy of 0.1 pixel, this results in a velocity uncertainty of ±2.3 m/s.

Data was also collected at one-tenth the nominal flowrate (0.0137 kg/s) for purposes of comparison. For these runs, the pulse separation time was increased by a factor of 10 (20 μs) and

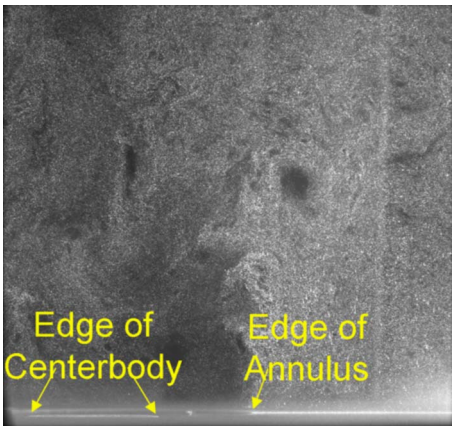

Fig. 3 Raw scattered light image for flowrate of 0.137 kg/s

particle displacement is similar to the higher flowrate case. The uncertainty due to sub-pixel accuracy for this case is ±0.23 m/s.

Results

A single-shot image of the raw scattered light from the vertical configuration is shown in Fig. 3 for the air flowrate of 0.137 kg/s. The flow is emerging from the bottom of the image in the space between the edges of the centerbody and the annulus. Note that only one-half of the annular flow is imaged with the annulus exit placed roughly in the center of the image. The laser sheet is approaching from the right. Some haziness in the image can be seen near the dump plane of the combustor (bottom of image). This is due to a diffuse reflection from the combustor dump plane as well as some fouling of the quartz liner that the camera is viewing through. The fouling of the quartz liner was greatest near the bottom of the combustor where a corner recirculation zone was created by the expanding, swirling flow. This flow pattern is typical of swirl stabilized dump combustors. Some nonuniformity in the seeding density can be observed in Fig. 3, particularly in the high velocity region at the exit of the annulus in which the seed density appeared to be somewhat lower than in the corner recirculation zone (lower right-hand corner of image). This was typical for the high flowrate case and is attributed to the accumulation of a small fraction of large agglomerated particles that become trapped in the recirculation zone. For the lower flowrate case, this was not observed as the flowfield appeared to be uniformly seeded.

A contour plot of the mean axial velocity field is shown in Fig. 4(*a*) for the high flowrate case of 0.137 kg/s.[1] Velocity vectors are superimposed on the contour plot. Only every fourth vector is shown for purposes of clarity. The data in Fig. 4(*a*) are for the vertical light-sheet arrangement and correspond to the average of 200 raw scattered light images shown in Fig. 3. The bottom of the contour plot is approximately 2 mm from the dump plane of the combustor ($Z=0$ mm) and the centerline of the combustor is defined as a radial location of $X=Y=0$ mm. The location of the centerbody and annulus are illustrated on the bottom of the figure. The velocity field shown in Fig. 4(*a*) is typical of swirl-stabilized lean premixed combustors and shows the swirling annular jet expanding in the combustor section in the form of a reverse cone at an angle of roughly 16 deg with respect to the centerline. The expansion of the jet and the ensuing breakdown of the vortex results in a central recirculation zone being formed, characterized by negative axial velocity (dark blue region) as well as a corner recirculation zone. This recirculation provides the flame anchoring in a swirl-stabilized combustor operating under combusting conditions.

Near the centerbody, the mean axial velocity was nearly zero, although the instantaneous axial velocity was fluctuating tremendously with both large positive and negative (reversed flow) values. This can be seen in Fig. 4(*b*), which is a contour plot of the rms fluctuating axial velocity component with mean velocity streamlines overlaid. It is clear that the region near the tip of the

[1]Full datasets can be obtained by contacting the author (peter.strakey@netl.doe.gov).

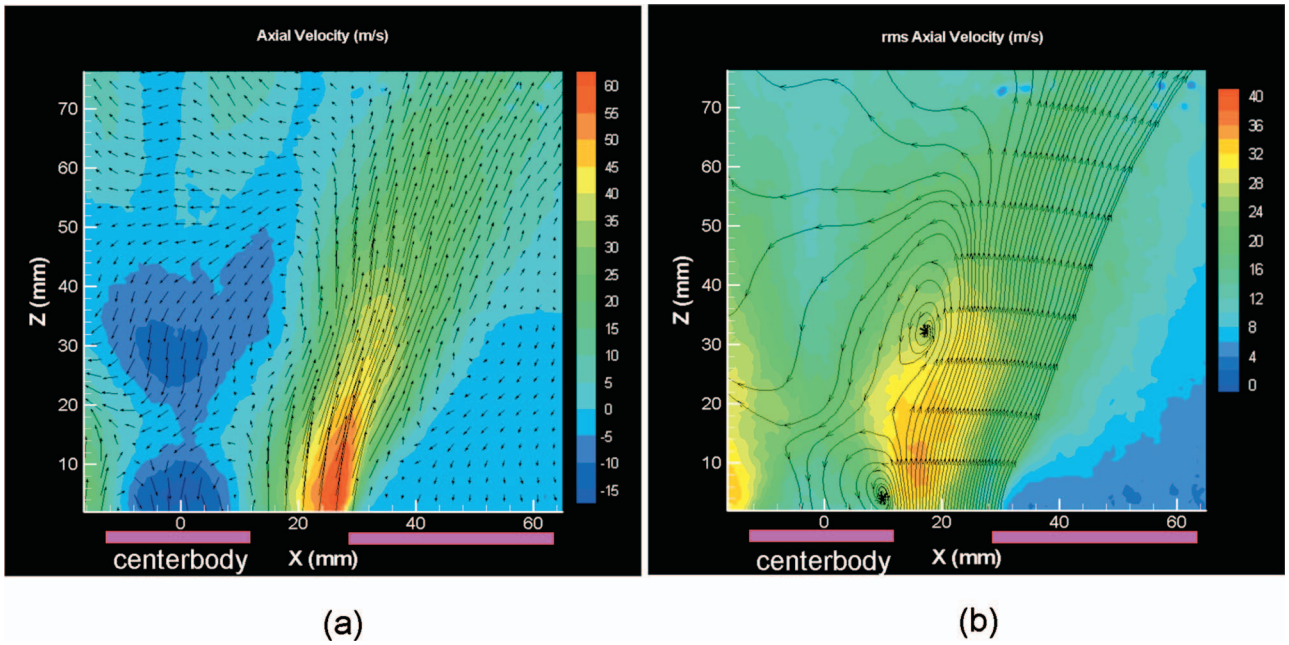

Fig. 4 (*a*) Contour plot of mean axial velocity with vectors overlaid and (*b*) contour plot of rms fluctuating velocity with streamlines overlaid. PIV data at 0.137 kg/s flowrate. Centerbody and annulus are annotated on the bottom of the figure. *Z*=axial location from dump plane, *X*=radial distance from center.

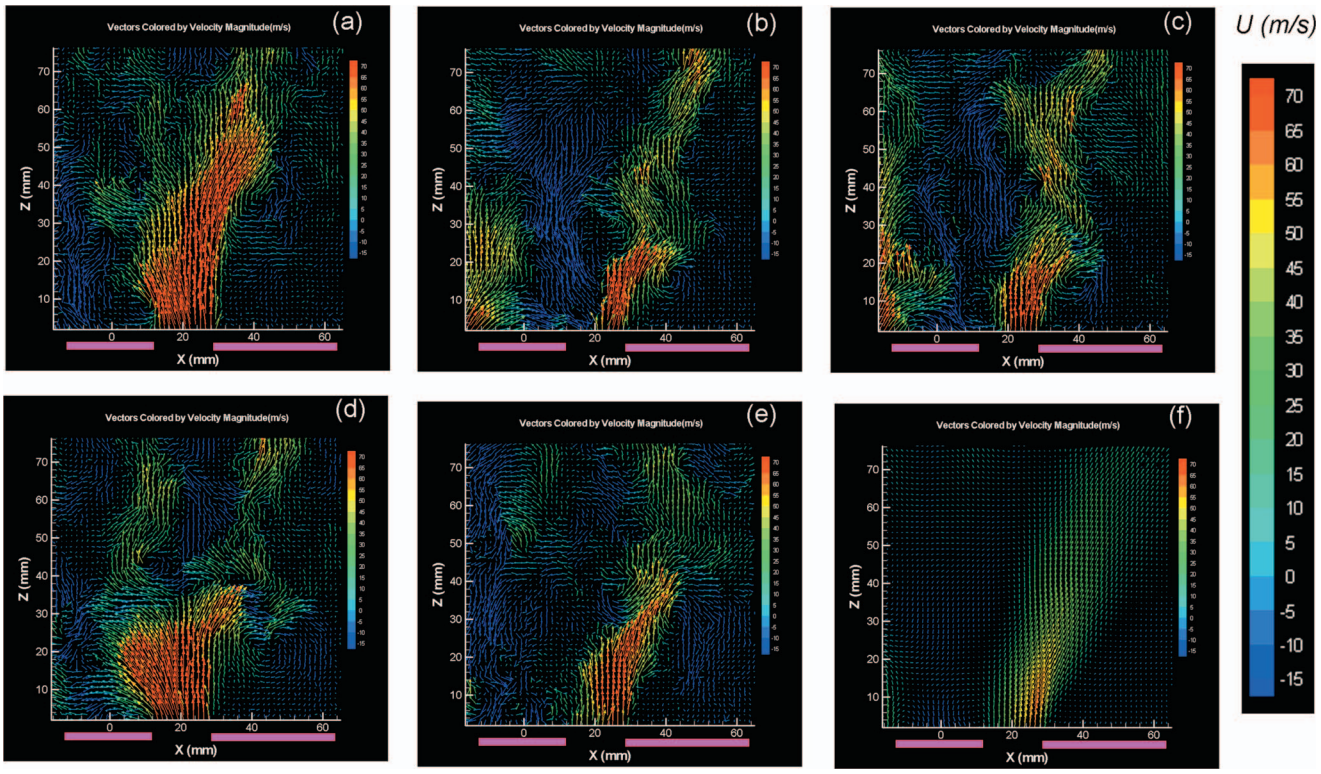

Fig. 5 Instantaneous vector fields from five realizations (*a*)–(*e*), along with mean vector field averaged over 200 realizations (*f*). PIV data at 0.137 kg/s flowrate. Vectors colored by velocity magnitude. Centerbody and annulus are annotated on the bottom of the figure.

centerbody is an area of high turbulence intensity and flow recirculation. In this region, the turbulence intensity, characterized by $U_{\text{rms}}/U_{\text{mean}}$ reaches values well over 100%. Earlier observations of this combustor under lean-premixed hot-fire conditions indicate that the flame is aerodynamically anchored in this region.

The highly dynamic nature of the flowfield is evident in the series of vector plots shown in Fig. 5. Figures 5(*a*)–5(*e*) are five instantaneous realizations of the flowfield, each one obtained approximately 1 s apart in time. Figure 5(*f*) shows the 200 shot average vector field. In all of the vector plots, the vectors are colored by velocity magnitude and only every other vector is shown to aid in clarity. The individual snapshots reveal that the jet issuing from the annulus never resembles the average velocity field shown in Fig. 5(*f*). The experimental repeatability of the average field in Fig. 5(*f*) is, however, very good.

Contour plots of the mean tangential velocity component with every fourth velocity vector superimposed are provided in Fig. 6 for the horizontal light-sheet configuration at axial locations of 3, 13, and 43 mm from the dump plane. Each plot represents the average of 100 instantaneous velocity images. Except for the centerline of the combustor where the tangential velocity is truly zero, the regions of zero tangential velocity in the plots are really due to areas of low data validation as a result of reflections off of the dump plane of the combustor. The circles annotated in Fig.

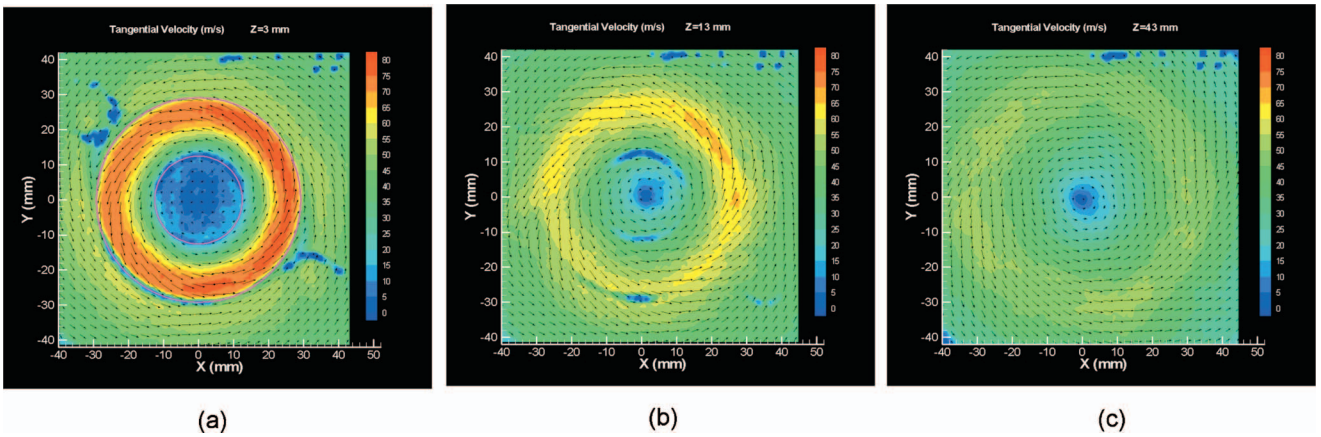

Fig. 6 Contour plots of mean tangential velocity at: 3 mm (*a*), 13 mm (*b*), and 43 mm (*c*) axial locations with vectors overlaid. PIV data at 0.137 kg/s flowrate. Centerbody and annulus are annotated by the concentric circles in (*a*).

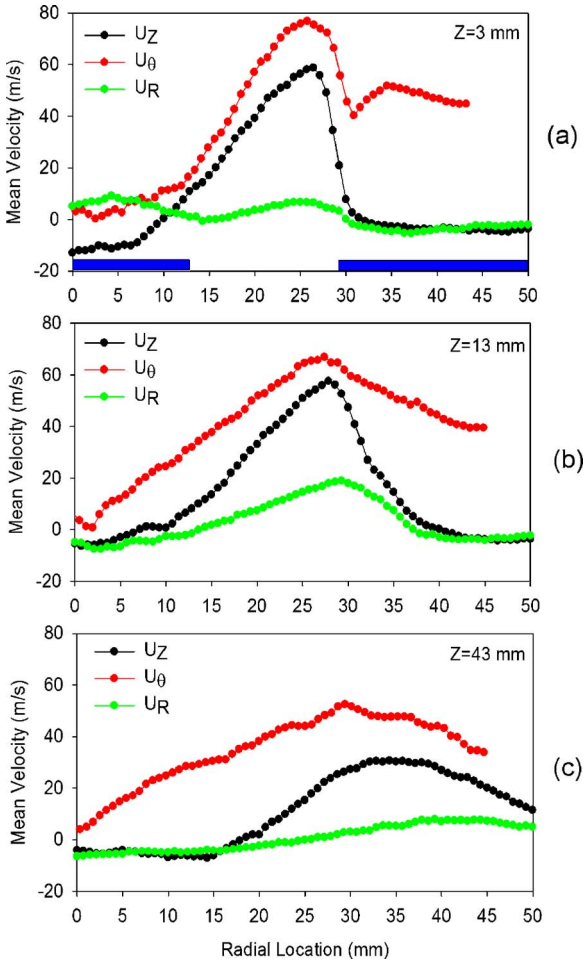

Fig. 7 Mean velocity components at: 3 mm, (*a*), 13 mm (*b*), and 43 mm (*c*) axial locations. PIV data at 0.137 kg/s. Centerbody and annulus are annotated in (*a*).

6(*a*) represent the edges of the centerbody and annulus. It is interesting to note in Fig. 6(*a*), that even at 3 mm from the dump plane, there is a significant tangential velocity component throughout the interrogation region (~40 m/s), indicating that the entire combustor flowfield is swirling. At the axial location of 43 mm, the tangential velocity profile is more uniform and is indicative of "solid body" rotation.

Profiles of mean axial, radial, and tangential velocities at the axial locations of 3, 13, and 43 mm, respectively, are provided in Fig. 7. The profiles were extracted from the planar data at the locations where the vertical and horizontal planar slices intersected to provide common locations where all three velocity components are obtained. Axial and radial velocity components were taken from the vertical slices, while the tangential component was obtained with the horizontal slices. At the exit of the annulus ($Z=3$ mm), the radial velocity component is low and the flow is mostly axial and tangential with the maximum velocity occurring near the outer wall of the annulus.

It is also interesting that the peak tangential velocity is around 75 m/s, which is larger than the peak axial velocity of 60 m/s, which corresponds to a swirl angle ($\tan^{-1}(U_\theta/U_z)$) of 51 deg. Integration of the tangential and axial velocity profiles across the exit of the annulus yields a mass-weighted average swirl angle of 56 deg. The swirl angle of the slot swirler used here is 30 deg, but due to the blockage of the swirler, there is a downstream deceleration of axial velocity within the nozzle section. The blockage ratio of the swirler as defined by the ratio of area in the annulus to the total open area of slots is 3.0. After exiting the slots, the axial velocity decreases by a factor of 3.0 and conservation of angular momentum therefore dictates an increase in swirl angle to a theoretical value of 60 deg which is reasonably close to the measured average value of 56 deg. The difference is likely due to some degree of viscous dissipation of tangential momentum. Following the classic definition of swirl number, S is defined as the ratio of axial flux of tangential momentum to axial momentum flux:

$$S = \frac{\int_{R_i}^{R_o} U_Z U_\theta r^2 dr}{R_o \int_{R_i}^{R_o} U_Z^2 r dr} \tag{1}$$

where R_i and R_o are the inner and outer radii of the annulus, respectively. The swirl number calculated using the measured profiles of axial and tangential velocity just downstream of the dump plane (Fig. 7(*a*)) correspond to $S=1.17$, indicating that this geometry produces a relatively strongly swirling flow.

Examination of the instantaneous velocity realizations at the dump plane of the combustor using the horizontal light-sheet configuration reveals an interesting feature. Figure 8 shows six sequential tangential velocity snapshots, each one obtained about 1 s apart. The flow is rotating counterclockwise, as viewed in the images. The sequence shows a region of high tangential velocity that varies in location with time. Since the PIV system is not capable of resolving temporal features of the flowfield, a series of experiments was conducted using a hot-wire probe to measure the velocity in the annulus at the dump plane of the combustor.

The hot wire, which was actually a one-dimensional cylindrical hot-film sensor approximately 3 mm long and 150 μm in diameter, was oriented in the flowfield at an angle to capture both axial and tangential velocity components. The signal from the hot-wire was analyzed with a TSI model IFA-100 analyzer and a digital spectrum analyzer and simultaneously recorder on a digital tape recorder. A sample of the power spectrum from the spectrum analyzer for the flowrate of 0.0137 kg/s is provided in Fig. 9 and shows that a periodic velocity component was present in the flow. A second harmonic was also observed and is shown in Fig. 9. To ensure that the periodic signal was not an artifact of electronic noise, the flowrate through the combustor was varied from the low flowrate case of 0.0137 kg/s up to the maximum flow of 0.137 kg/s. The two peak frequencies, as measured on the spectrum analyzer, are plotted in Fig. 10 as a function of flowrate. It is clear that the periodic motion behaves linearly with flowrate.

As a secondary verification of the periodic nature of the flow, a microphone was used to capture the audible noise generated by the combustor without the quartz containment section in place. The signal from the microphone was fed to a digital spectrum analyzer and a clear frequency was observed at each flowrate and corresponded to the dominant mode measured with the hot-wire anemometer.

A simple analysis shows that the frequency measured with the hot wire is very close to the rotational frequency of the flow ($\omega = U_\theta/\pi D$) where U_θ and D are the maximum tangential velocity and location within the annulus, respectively. This corresponds to a Strouhal number ($\mathrm{St}=\omega\pi D/U_\theta$) of 1. This implies that the low-pressure vortex core formed in the combustor section is not instantaneously symmetric about the axis, but rather follows an eccentric pattern around the annulus, which in turn drives the flow in the annulus through pressure-velocity coupling.

A review of the literature reveals that periodic behavior in swirling flows is commonly observed and is often referred to as a precessing vortex core (PVC) [9,10]. The PVC has been identified as a naturally occurring hydrodynamic instability. This phenomenon has been observed in swirling flows both with and without a

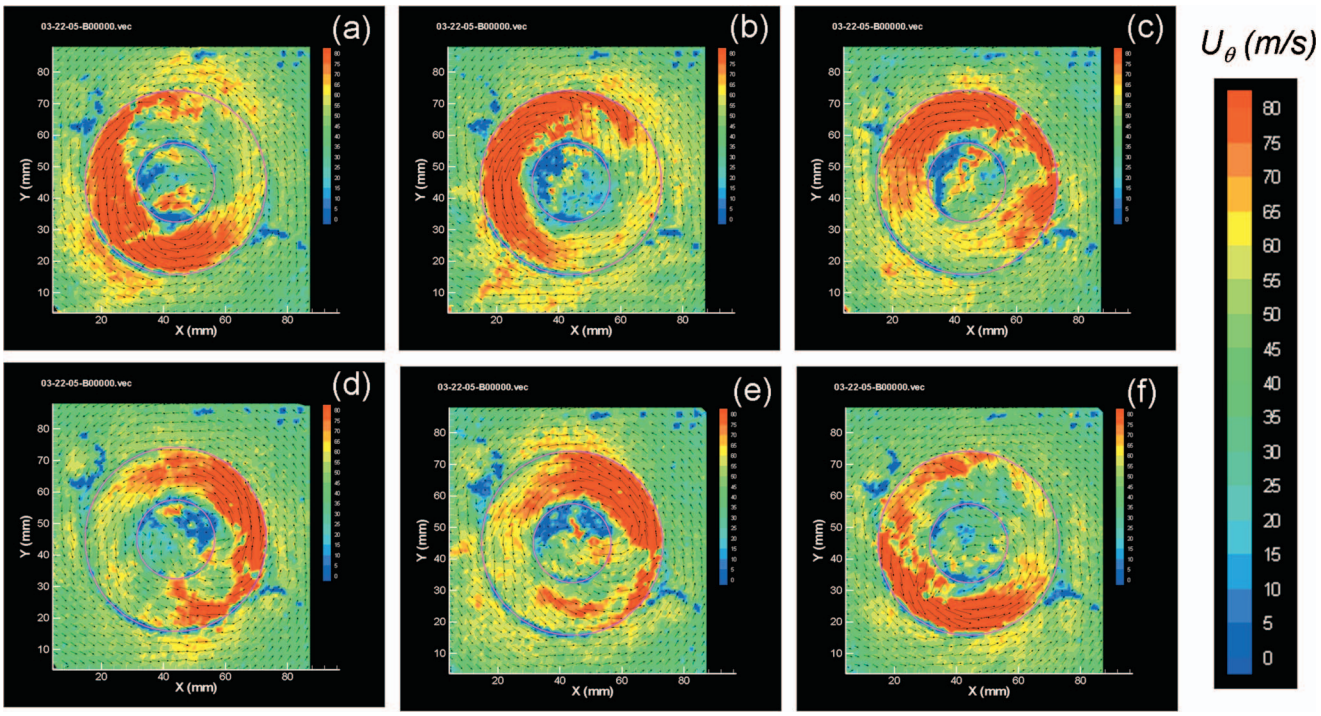

Fig. 8 (*a*)–(*f*) Instantaneous contour plots of tangential velocity with vectors overlaid from six realizations at an axial location of 3 mm. PIV data at 0.137 kg/s flowrate. Centerbody and annulus are annotated by the concentric circles in the figures. Flow is counterclockwise.

centerbody and is even suspected of being a possible trigger for combustion instabilities [11]. While the details of PVCs are not well understood, it is clear that this is a phenomenon associated with a swirling flow followed by a sudden expansion and has been observed both in reacting and nonreacting flows.

The linear scaling of the precession frequency with flowrate implies a self-similarity in the flowfield. To verify this, PIV data collected at the highest and lowest flowrate (0.137 and 0.0137 kg/s), respectively, are compared in Fig. 11. In the figure, mean axial and tangential velocity components at $Z=3$ mm are normalized by the bulk flow velocity for each flowrate. The bulk flow velocities were 55 m/s and 5.5 m/s for the high and low flowrate cases, respectively. The similarity in both axial and tangential velocity fields for the two cases implies a self-similarity in the flowfield. This would be expected even in the absence of a PVC, since the Reynolds number based on the annular gap size (Re=5700) indicates fully turbulent flow even at the lowest flowrate.

LES Modeling

In an effort to aid in understanding the unique features of the flowfield studied here, as well as to assess the current capabilities of CFD codes, a series of simulations was performed on the current geometry for conditions equivalent to those studied experimentally. The simulations were performed in parallel to the experimental effort and were in fact used to guide the experiments.

The code used here is FLUENT 6.2, which is a commercial finite-volume based CFD code with a broad range of modeling capabilities. A Reynolds-averaged Navier-Stokes (RANS) type of turbulence modeling approach and an LES approach were used to

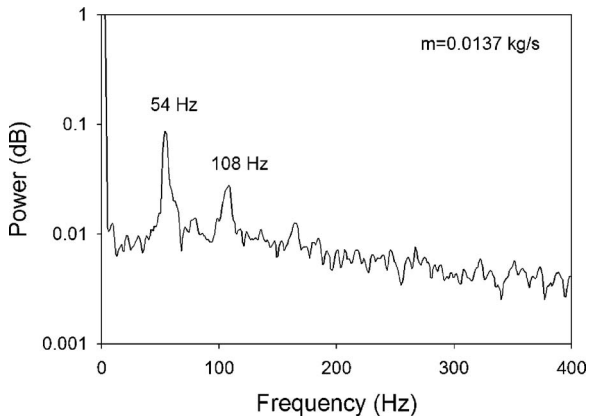

Fig. 9 Power spectrum from hot-wire measurement at dump plane. Flowrate of 0.0137 kg/s.

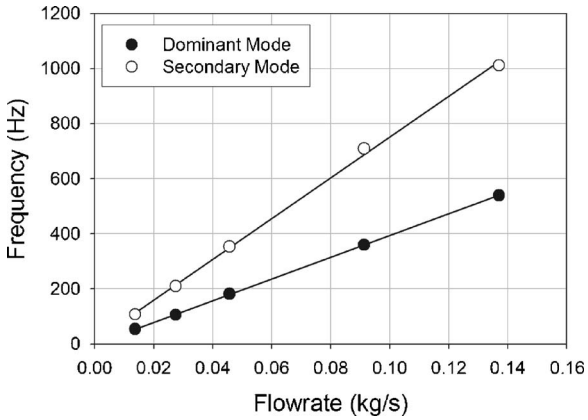

Fig. 10 Dominant and secondary frequencies measured with the hot wire at the dump plane as a function of flowrate

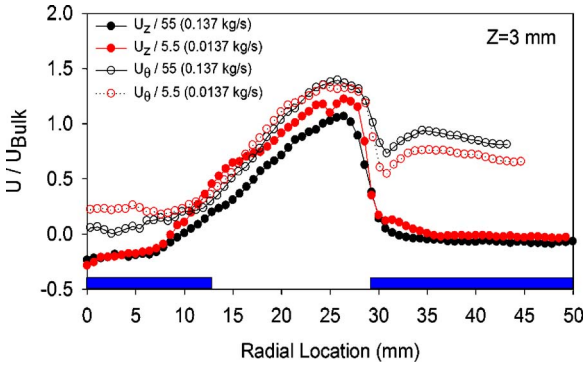

Fig. 11 Mean axial and tangential velocity normalized by bulk-flow velocity versus radial location at axial location of 3 mm for flowrates of 0.0137 kg/s and 0.137 kg/s from PIV measurements

simulate the flowfield, but it was obvious from the experiments that only an unsteady method such as LES would be able to capture the periodic motion of the PVC. The three-dimensional computational domain encompassed the region from the exit of the swirl plate to 9 cm into the exhaust section and was comprised of approximately 2.2×10^6 hexahedral cells in a multiblock structured grid. The grid was partitioned into 32 blocks and calculations were performed on a Linux PC cluster using 3.0 GHz Intel® Zeon® processors. Each simulation required approximately 2 weeks to run for 30,000 time steps.

The individual slots at the entrance to the domain were modeled as velocity inlets with specified axial and tangential velocity components of 133 m/s and 77 m/s, respectively, which is equal to a 30 deg flow angle and corresponds to the 0.137 kg/s flowrate case. The vortex method was used to synthesize the turbulence present in the inlet stream with a turbulent kinetic energy of 300 m^2/s^2 and a dissipation rate of 2×10^6 m^2/s^3. The inlet turbulence quantities were determined by separately modeling one of the inlet slots using a RANS approach to estimate the turbulence at the exit of the slot. A simulation performed later using a laminar inlet condition for the LES boundary showed that the turbulence in the inlet stream has very little effect on the flow in the combustor due to the very large levels of turbulence generated in the wake of the swirl plate. The exit in the exhaust section was modeled as a pressure outlet and the fluid used was air at constant density and viscosity, thus, the simulations were incompressible.

The sub-grid viscosity model used here was the dynamic Smagorinski model and the discretization scheme used was a second-order accurate bounded central differencing scheme in space and a second-order backward differencing scheme for the temporal discretization. The bounded central differencing scheme uses pure central differencing by default, but reverts to a blend of central differencing and upwinding schemes when the convection boundedness criteria is violated. The time step used was 2 μs, which corresponded to a maximum Courant-Friedrich-Levy number of 1 near the inlet and about 0.25 in the nozzle section. The simulation was run for about 60 msec, which corresponded to about 25 flow-through times of the nozzle section. This was found to be more than adequate to obtain good statistical quantities.

Figure 12 shows cross-sectional slices of instantaneous and mean axial velocity through the center of the combustor from the LES simulation. The contour lines on the mean axial velocity plot denote the location of zero axial velocity to show the location of the recirculation zones. The snapshot in Fig. 12(*a*) provides another illustration of the unsteadiness of this particular flowfield.

The PIV data generated here are well suited for direct comparison with LES simulation. Both experiment and computation produce a temporally resolved and spatially filtered velocity field with a similar (~1 mm) spatial filter size. Time averaging of the PIV and LES velocity fields provides directly comparable velocity statistics.

Figure 13 contains simulation results of mean and rms fluctuating axial velocity near the dump plane with a field of view equal to that of the PIV experiments. The mean and rms fluctuating axial velocity component plotted in Fig. 13 can be compared to the PIV data presented in Fig. 4. The LES simulation agrees reasonably well with the PIV data for both mean and fluctuating values. It should be pointed out that the rms velocities in both the experimental data and simulations are the result of both turbulent fluctuations as well as the periodic motion in the mean flow due to the precessing vortex. Since the PIV data was not phase locked to the motion of the PVC, it was impossible to separate out this effect on the fluctuating velocity component.

A more quantitative comparison between the PIV data and LES simulations is presented in Fig. 14 for the three axial locations of 3, 13, and 43 mm. In each plot, all three mean velocity components are shown. In general, the simulations agree very well with the experimental data although the simulations tended to over-

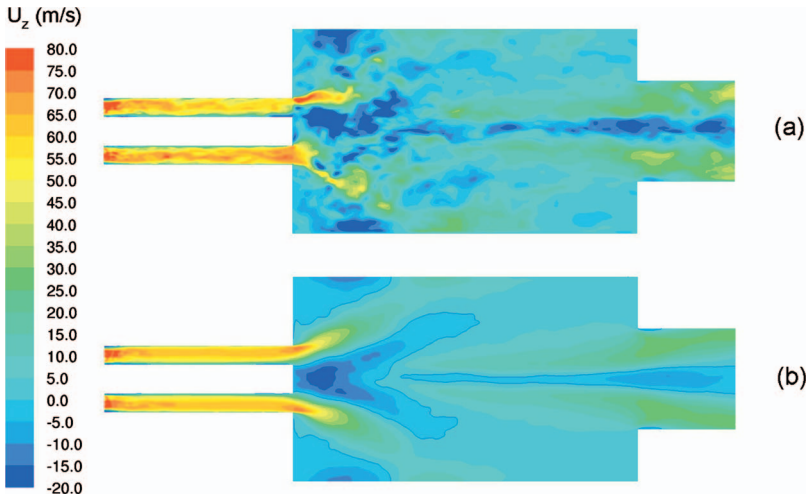

Fig. 12 Instantaneous snapshot of axial velocity field (*a*), and mean axial velocity field (*b*) with contour lines of zero axial velocity along cutting plane through center of combustor. LES simulation at 0.137 kg/s flowrate.

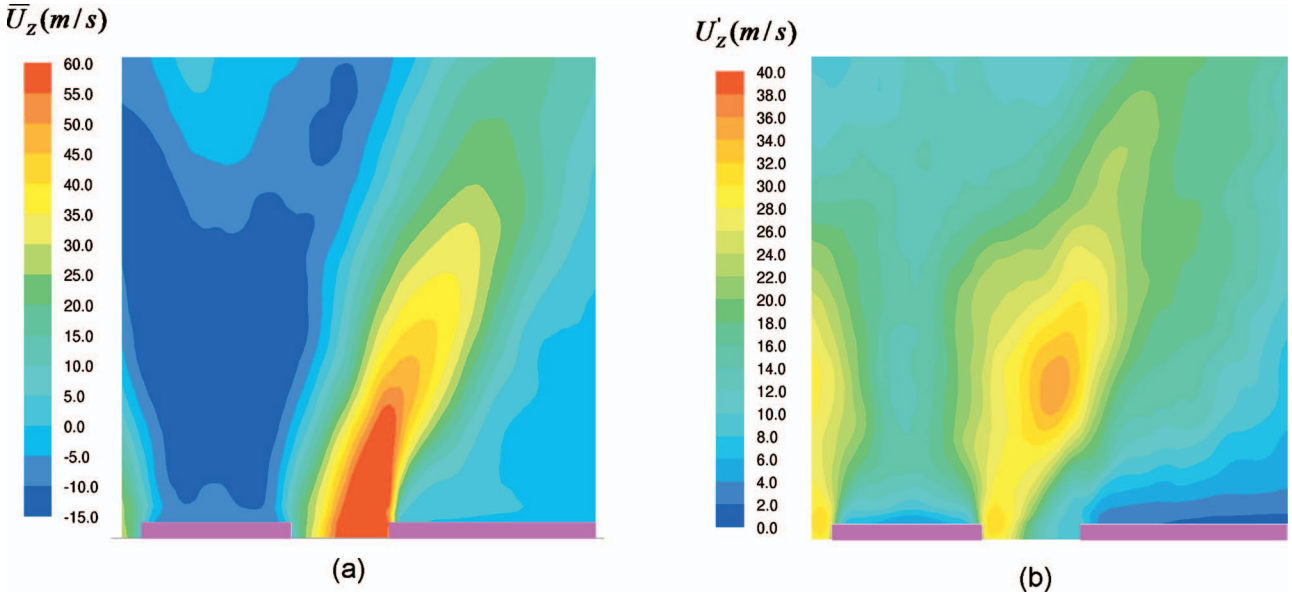

Fig. 13 Contour plots of mean axial velocity (*a*), and rms fluctuating axial velocity (*b*) along cutting plane through center of combustor. LES simulation at 0.137 kg/s flowrate with field of view equal to Fig. 4. Centerbody and annulus annotated on bottom of figures.

predict the axial velocity while under-predicting the tangential velocity. The disparity between the experimental data and simulations for the axial location of 3 mm and radial locations greater than 30 mm is believed to be due to the proximity of this location to the dump plane of the combustor and the boundary layer formed there. The simulations indicate a marked sensitivity to an axial location this close to the wall, and the accuracy in positioning the laser sheet in the PIV experiments is estimated to be about ±0.5 mm.

The LES simulation was found to do an excellent job of capturing the PVC that was identified in the experimental effort. In fact, it was the simulation results that identified the existence of the PVC in the experiments and led to additional experimental efforts, including the hot-wire studies to confirm the results. Spectral analysis of the tangential velocity at the dump-plane showed the precessing motion to be occurring at about 550 Hz, which was close to the frequency of 540 Hz measured with the hot-wire probe. Figure 15 shows a sequence of contour plots of instantaneous tangential velocity at the dump plane from the LES simulation. The plots were extracted at 300 μs intervals, so that the sequence of six plots represents approximately one revolution of the PVC that was rotating counterclockwise in the figure. Although the PIV data presented in Fig. 8 do not resolve the temporal evolution of the precessing motion as the LES simulation presented in Fig. 15, the results are strikingly similar.

The behavior of the PVC is similar to that described in a review paper on vortex breakdown by Lucca-Negro and O'Doherty [12] in which the core of the vortex lies on the boundary of the recirculation zone, which in turn is very near the centerbody. Examination of the axial and tangential velocity and pressure at a single point located at the dump plane midway between the centerbody and outer annulus in Fig. 16 shows that the axial and tangential velocity components are about 60 deg out of phase, while the axial velocity and pressure are exactly 180 deg out of phase with one another. This behavior is classic PVC behavior and is caused by the coupling between the pressure and velocity field in that the low-pressure zone at the core of the vortex drives the high axial velocity. The "noise" that is superimposed on the periodic signals in Fig. 16 is the turbulence resolved by the LES approach.

The agreement between the LES simulation and the PIV data was somewhat surprising since the computational grid, even with

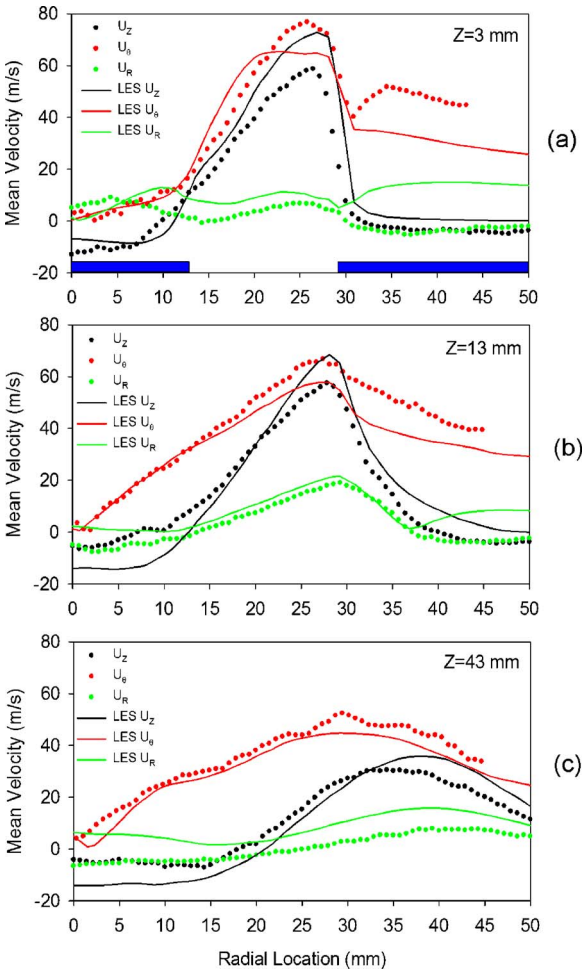

Fig. 14 Mean velocity components at: 3 mm (*a*); 13 mm (*b*); and 43 mm (*c*) axial locations. PIV data (symbols) and LES simulation (lines) at 0.137 kg/s. Centerbody and annulus are annotated in (*a*).

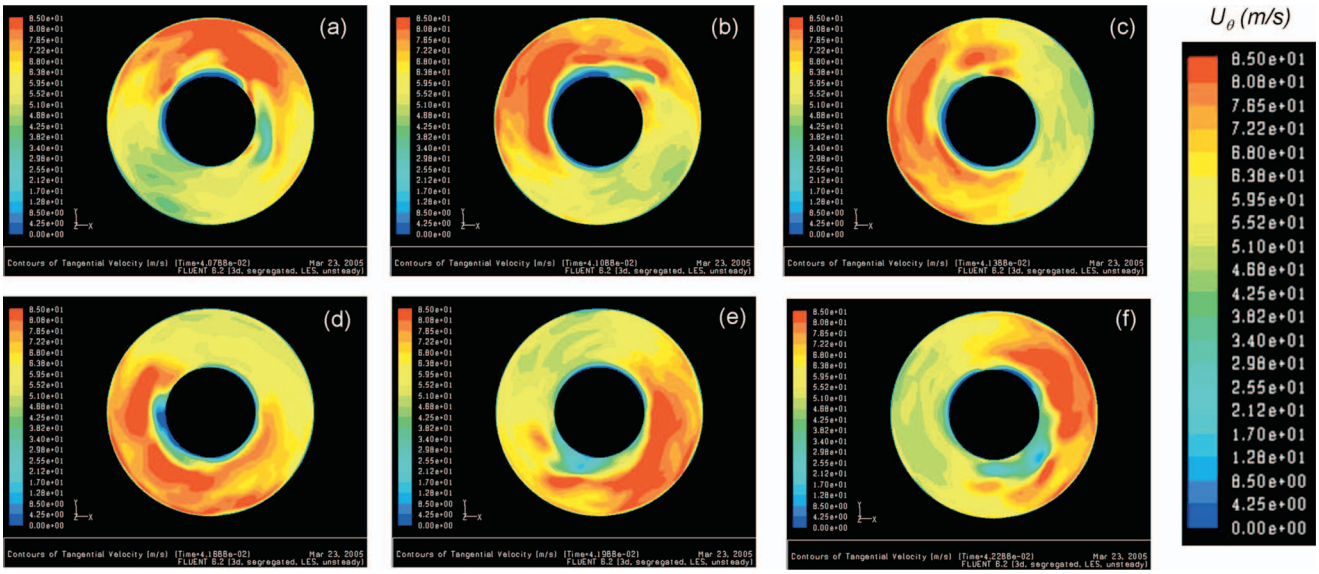

Fig. 15 Sequence of instantaneous contour plots of tangential velocity at the dump plane showing one full revolution of the PVC. Plots (*a*)–(*f*) are at 300 μs intervals. LES simulation at 0.137 kg/s flowrate. Flow is counterclockwise.

2.2×10^6 cells, was relatively coarse. The characteristic cell length in the combustor section just downstream of the dump plane was about 1.2 mm, which is about a factor of 2 larger than the Taylor micro-scale, which was estimated to be around 0.5 mm in this region, based on a RANS simulation of the flowfield. The Taylor micro-scale is usually a good estimate of the necessary grid resolution for a LES simulation. Even so, the ability of LES to provide quantitative predictions of the unsteady, nonreacting flowfield studied here was encouraging. It is also noteworthy that this agreement was accomplished without tuning any turbulence model constants that is typically done in RANS calculations.

For purposes of comparison, an unsteady RANS simulation was performed on the same grid used in the LES study. A standard k-ε turbulence model was used and second-order upwinding was used for all variables. The time step was kept the same as the LES simulations at 2 μs. Although the RANS approach usually warrants a larger time step and coarser grid than LES, it was decided to keep these the same so that a direct comparison could be made between the two approaches. A comparison between the PIV data, LES simulation, and unsteady RANS simulation at the dump plane is provided in Fig. 17. Although the LES approach was more accurate, the RANS simulation did provide reasonably good predictions of mean axial and tangential velocity at the dump plane. The rms turbulent fluctuating velocity was, however, severely under-predicted by the RANS model. For both the LES and RANS model, the rms fluctuating velocity was taken to be the sum of the resolved fluctuating velocity and the modeled turbulent velocity:

$$u' = u'_{\text{resolved}} + \left(\frac{2k}{3}\right)^{\frac{1}{2}}$$

The disparity between the simulations and the data for radial locations greater than 35 mm is believed to be due to the strong sensitivity to axial location in this region, as pointed out in the discussion of Fig. 14.

The RANS simulation showed no evidence of a PVC, and in fact, most of the large-scale turbulent motions were damped out by the model. The lack of the PVC in the RANS simulation is largely responsible for the under-prediction of the turbulent fluctuating velocity. These results provide strong evidence that RANS models are not capable of accurately representing the flowfield in a highly swirled combustor such as that studied here.

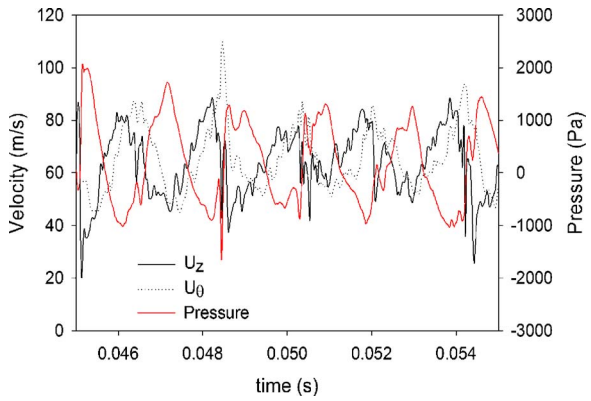

Fig. 16 Time trace of axial and tangential velocity and pressure at a single point located midway in the annulus at the dump plane. LES simulation at 0.137 kg/s flowrate.

Conclusions

The velocity field in a swirl-stabilized combustor was experimentally characterized under atmospheric pressure cold-flow conditions using PIV. Numerical simulations were also performed using the LES and RANS turbulence modeling techniques. A number of conclusions can be drawn from the results presented here.

Both the PIV measurements and LES simulations showed the flowfield to be highly unsteady with very high levels of turbulence. The unsteadiness was in part due to the presence of a precessing vortex core, which was found to have a precession frequency that was a linear function of flowrate. The presence of the PVC was confirmed experimentally with hot-wire measurements and was also observed in the LES simulations. The frequency of the PVC was found to be equal to the ratio of the mean tangential velocity to the annular circumference, corresponding to a Strouhal number of 1.

The LES model was found to perform relatively well in predicting mean and rms velocities in the combustor in comparison to the PIV measurements. The LES model was also able to capture the precession frequency and behavior of the vortex core. The identification and understanding of the hydrodynamics associated

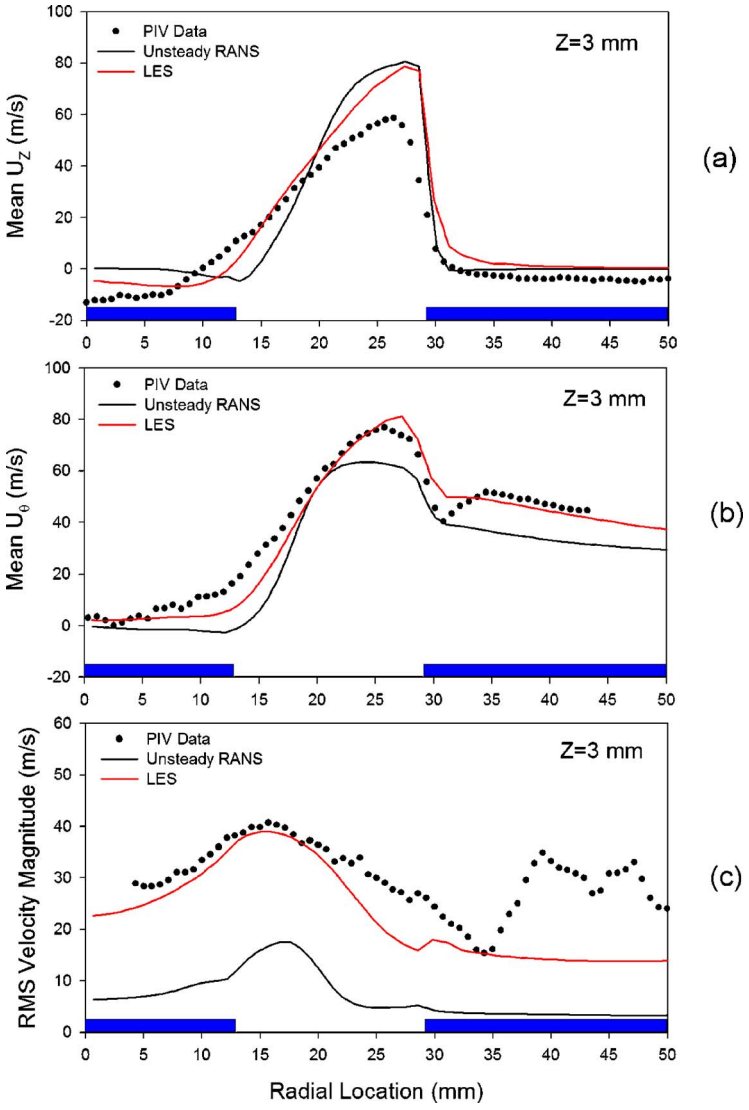

Fig. 17 Mean axial velocity component (*a*), mean tangential velocity (*b*), and rms fluctuating velocity (*c*) at an axial location of 3 mm from the PIV data (symbols), LES simulation, and an unsteady RANS simulation. Centerbody and annulus are annotated on the bottom of the figures.

with a PVC may play a role in understanding a possible cause of combustion instabilities. In addition, the inherent unsteadiness observed in this type of flowfield provides a compelling argument for using more computationally expensive time accurate modeling approaches such as LES over more traditional RANS techniques.

The PIV technique provides data that are directly comparable to LES simulations. This is achieved through similar spatial filtering of both the PIV data and LES simulation. Statistical quantities such as mean and rms fluctuating velocities are obtained in a similar fashion in both experiment and simulation.

These data provide an excellent opportunity to validate any computational tool aimed at prediction of highly swirling flowfields. The absence of combustion allows for validation of turbulence modeling and numerical approaches without the complicating effects of turbulence chemistry interaction. Validation under the conditions presented here is a key step towards the development of accurate computational tools for gas turbine applications.

Current efforts are now focused on obtaining velocity field measurements in the combustor during high-pressure combusting conditions. In addition, further analysis of the current data is expected to produce other useful scalar quantities such as integral length scale and dissipation rate that can be used to further validate and improve modeling tools.

References

[1] Phillips, J. N., and Roby, R. J., 1999, "Enhanced Gas Turbine Combustor Performance Using H2-Enriched Natural Gas," *Proceedings of the ASME Turbo Expo 1999: Power for Land, Sea and Air*, ASME, New York, Paper No. 99-GT-115.

[2] Todd, D. M., 2000, "Gas Turbine Improvements Enhance IGCC Viability," Gasification Technologies Conference 2000, Gasification Technologies Council, Arlington, VA.

[3] *The 5th International Workshop on Measurements and Computation of Turbulent Nonpremixed Flames*, 2000, A. Mbiock, R. Barlow, and D. Roekaerts, eds., Delft, The Netherlands.

[4] Wicksall, D. M., Agrawal, A. K., Schefer, R. W., and Keller, J. O., 2005, "Influence of Hydrogen Addition on Flow Structure in Confined Methane Flame," J. Propul. Power, **21**(1), pp. 16–24.

[5] Griebel, P., Scharen, R., Siewert, P., Bombach, R., Inauen, A., and Kreutner, W., 2003, "Flow Field and Structure of Turbulent High-Pressure Premixed Methane/Air Flames," *Proceedings of ASME Turbo Expo 2003*, Atlanta, GA, June 16–19, 2003, ASME, New York.

[6] Cabot, G., Vauchelles, D., Taupin, B., and Boukhalfa, A., 2004, "Experimental

Study of Lean Premixed Turbulent Combustion in a Scale Gas Turbine Chamber," Exp. Therm. Fluid Sci., **28**, pp. 683–690.
[7] Sidwell, T., Richards, G., Casleton, K., Straub, D., Maloney, D., Strakey, P., Ferguson, D., Beer, S., and Woodruff, S., 2006, "Optically-Accessible Pressurized Research Combustor for Computational Fluid Dynamics Model Validation," AIAA J., **44**(3), pp. 434–443.
[8] Raffel, M., Willert, C., and Kompenhans, J., 1998, *Particle Image Velocimetry: A Practical Guide (Experimental Fluid Mechanics)*," Springer-Verlag, Germany, pp. 129–133.
[9] Singh, K. K., Mongeau, L., Frankel, S. H., and Gore, J. P., 2005, "Acoustic Detection of Anomalies in Swirling Flows and Flames," *Proceedings of the 2005 Joint Meeting of the U.S. Sections of the Combustion Institute*, Drexel University, Philadelphia, PA, March 20–23.
[10] Reddy, A. P., Sujith, R. I., and Chakravarthy, S. R., 2005, "Swirler Flow Field Characteristics in a Sudden Expansion Combustor Geometry Using PIV," *43rd AIAA Aerospace Sciences Meeting and Exhibit*, Reno, NV, January 10–13 2005, Paper No. AIAA 2005-217.
[11] Huang, Y., Sung, H., Hsieh, S., and Yang, V., 2003, "Large-Eddy Simulation of Combustion Dynamics of Lean-Premixed Swirl-Stabilized Combustor," J. Propul. Power, **19**(5), pp. 782–794.
[12] Lucca-Negro, O., and O'Doherty, T., 2007 "Vortex Breakdown: A Review," Prog. Energy Combust. Sci., **27**, pp. 431–481.